Evaluation des performances de l'analyse statistique et physique d'images hyperspectrales de Mars. Application au capteur multi-angulaire CRISM

Xavier Ceamanos Garcia Ceamanos Garcia

UNIVERSITÉ DE GRENOBLE

THÈSE

Pour obtenir le grade de

DOCTEUR DE L'UNIVERSITÉ DE GRENOBLE

Spécialité : **Sciences de la terre, de l'univers, et de l'environnement**

Arrêté ministériel : 7 août 2006

Présentée par

Francisco Javier CEAMANOS GARCÍA

Thèse dirigée par **M. Sylvain DOUTÉ**

préparée au sein de l'**Institut de Planétologie et d'Astrophysique de Grenoble**
dans **l'École Doctorale Terre-Univers-Environnement**

Évaluation des performances de l'analyse statistique et physique d'images hyperspectrales de Mars
Application au capteur multi-angulaire CRISM

Thèse soutenue publiquement le **25 octobre 2011**
devant le jury composé de :

M. Jérôme MARS
Professeur, Gipsa-lab, Président du jury
M. Stéphane ÉRARD
Astronome, Laboratoire d'Études Spatiales et d'Instrumentation en Astrophysique - Observatoire de Paris, Rapporteur
M. Antonio PLAZA
Associate professor, Escuela Politécnica de Cáceres - University of Extremadura, Rapporteur
M. Patrick PINET
Directeur de recherche, Institut de Recherche en Astrophysique et Planétologie - Université de Toulouse, Examinateur
M. Stéphane LE MOUÉLIC
Ingénieur de recherche, Laboratoire de Planétologie et Géodynamique - Université de Nantes, Examinateur

"The most incomprehensible thing about the universe is that it is comprehensible." - Albert Einstein

Pel meu avi. Per ser sovint el meu mirall.

Per la Sílvia i la meva família. Per tot el que m'heu ensenyat.

This work has been done within the framework of the Vahiné project funded by the “Centre National d’Études Spatiales” (CNES) and the “Agence Nationale de la Recherche” (ANR) under the reference ANR-07-MDCO-013.

Acknowledgments

Tout d'abord je voulais remercier les membres de mon jury de thèse pour avoir accepté ce rôle. Merci à mes deux rapporteurs, Stéphane Érard et Antonio Plaza, pour leurs commentaires pertinents qui ont amélioré substantiellement ce manuscrit de thèse. Je remercie aussi mes examinateurs, Patrick Pinet et Stéphane Le Mouélic, qui m'ont fait me poser des questions sur ma thèse auxquelles je n'avais jamais pensé auparavant, le jour même de ma soutenance ! Finalement, un grand merci aussi à Jérôme Mars qui a été un excellent président du jury, mais aussi mon professeur de télédétection pendant mon master de recherche.

Le plus grand merci est pour mon directeur de thèse, Sylvain Douté. Merci Sylvain pour ces trois ans pendant lesquels j'ai beaucoup appris à ton côté, non seulement sur la planète Mars mais aussi sur les petits plaisirs de la vie et sur ce qu'est la recherche juste et rigoureuse. Si je parle de Sylvain, je parle aussi du projet Vahiné auquel j'ai participé ces trois ans. J'en profite donc pour remercier mes collaborateurs au GIPSA-Lab, Bin Luo et Jocelyn Channussot. Merci aussi Jocelyn pour avoir été mon initiateur dans le monde de la télédétection (et pour m'avoir fait découvrir un pays aussi beau que l'Islande !). Aussi dans le projet Vahiné, je tiens à remercier Mathieu Fauvel et les gens de l'équipe Mistis à l'INRIA.

Je voudrais remercier spécialement à mes collaborateurs "photométriques" Jennifer Fernando, Patrick Pinet et Frédéric Schmidt pour leur travail fantastique qui a permis que ce manuscrit soit plus abouti. Merci aussi à l'équipe transversal Mars de l'IPAG pour vos questions toujours pertinentes pendant mes séminaires et présentations, merci donc à Bernard Schmitt, Pierre Beck et Wlodek Kofman, parmi d'autres. Also, I would like to write some words to sincerely thank Alexei Lyapustin who hosted me during a week in his office at the Goddard Space Flight Center. Thank so much Alexei for your warm welcome and for the excellent coffee we had together several times! Honestly, I enjoyed a lot our discussions on atmospheric correction and your excellent algorithm маяк. I hope that what I learnt from you those days is visible in this dissertation. Speaking of Greenbelt, Maryland, I will never forget the great help of Yuliya Tarabalka that made this research visit possible.

Since I already switched to English, I would like to thank the members of the CRISM team: Mike Wolff, for sharing his knowledge on martian aerosols, Mike Smith, for our interesting discussion in Goddard, and Frank Morgan, for helping me out with the CAT and the WC CDR. Also, I specially thank Mario Parente for our discussions on spectral unmixing, spectral smile, and others, but especially for being an electrical engineer in the planetology community. I know what it feels like, Mario. Eventually, I would like to extend my sincere gratitude to Dave Humm. Thank you Dave for helping me since the beginning, for your extensive and comprehensive explanations on the beautiful instrument that CRISM is, and for introducing me to the team. You all made an outstanding instrument and I have no doubt that excellent findings on Mars are about to come thanks to it!

I would not like to forget the special role that the community of Earth observation has had in this work. My sincere gratitude to the team leaded by Jón Atli Benediktsson, Jocelyn Chanussot, and Antonio Plaza, who have been my mentors in remote sensing. Unas palabras especiales para Antonio que, a parte de un examinador severo pero justo, ha sido un amigo durante estos tres años. Espero que el destino nos vuelva a cruzar pronto, como ya lo ha hecho varias veces en el Cairo, Hawai'i, Vancouver y otros lugares.

Je continue en français en remerciant Jean-Yves Bonnet pour trois ans de co-bureautage géniaux pendants lesquels nous avons partagé nos goûts musicaux, nos projets professionnels et personnels (il faut que tu attaque ta luge ou tu vas quitter l'IPAG avant...), mais surtout des caramels au beurre salé ! Je suis content qu'on ait pu visiter Nantes ensemble. Maintenant c'est moi qui t'attends à Barcelone. Je continue avec Thomas Appéré qui a été sans doute mon collègue le plus martien. Merci Thomas pour être toujours prêt à passer dans mon bureau pour me poser des questions sur CRISM (en même temps que tu embêtais Jean-Yves, bien évidemment !). Honnêtement, je te remercie pour partager ta passion aussi inspiratrice sur Mars et sur tout ce que tu fais. J'espère que tu la garderas toujours avec toi. Je tiens à remercier à Alexandre Ratajczak pour son esprit toujours positif, pour ses blagues parfois un peu incompréhensibles, pour m'avoir appris ce qu'est "une fouine", et pour les moments passés autour d'un barbecue. Un grand merci aussi à Gaël Cessateur, pour m'avoir pas laissé tout seul faire les courses pour le barbecue, à Cyril Grima, pour m'apprendre à jouer avec des xenomorphes, à Zuriñe Yoldi Martínez de Mandojana et à Alix Guillot, pour être les filles les plus sympas du laboratoire (en même temps il y a pas beaucoup de filles... je plaisante !), et à Hélène Ménager pour être ma collègue anti-JdD. Un merci spéciale pour Stéphane Dichiaro (je sais que Messi te fait rêver...) et Alberto Villa, même si tu étais au GIPSA-lab, tu as été un de mes meilleurs collègues de travail.

À l'IPAG je tiens à remercier aussi à Ulysse Marboeuf, Nicolas Blind, Ludovic Léau-Mercier, Yann Berquin, Florence Grisolle, Antoine Pommerol, Adrien Tavernier, Roland Thissen, Olivier Brissaud, Beatrice Pibaret, Akila Mokhtari, Mathieu Barthelemy, et encore Odile Dutuit.

Vull agrair també a la meva família per la seva confiança en mi i per haver-me motivat sempre a continuar el meu recorregut científic que ja dura uns quants anys. Espero algun dia poder-vos tornar d'alguna manera tot aquest temps que he passat lluny de casa. Un enorme gracias para Silvia sin la que todo esto no sería posible: no sería doctor, la teledetección no me apasionaría, y no habría sido tan feliz tanto tiempo en el extranjero. Siempre has sido mi luz en este camino.

Je finis en remerciant tout le monde rencontré à Grenoble et en France, tous ceux qui m'ont accueilli très chaleureusement dans ce que je considère maintenant ma deuxième maison. Merci beaucoup.

Abstract

A new generation of imaging spectrometers is emerging in the field of planetary remote sensing by adding an additional view of measurement, the angular dimension. Multi-angle imaging spectroscopy is conceived to provide a more accurate characterization of planetary materials and a higher success in separating the signals coming from the atmosphere and the surface. The Compact Reconnaissance Imaging Spectrometer for Mars (CRISM) aboard the Mars Reconnaissance Orbiter is a hyperspectral camera that operates systematically in multi-angle mode from space. Multi-angle hyperspectral images are nonetheless related to problems of manipulation, visualization and analysis because of their size and complexity. In this framework this thesis proposes robust statistical and physical algorithms to analyze images acquired by the CRISM instrument in an efficient manner. First, I propose a tailor-made data pipeline aimed at improving the radiometric quality of CRISM data and generating advanced products, the latter data being devised to perform fine analysis of the planet Mars. Second, I address the atmospheric correction of CRISM imagery by exploiting the multi-angle capabilities of this instrument. An innovative physically-based algorithm that compensates for atmospheric effects is put forward in order to retrieve the reflectance of the surface of Mars. In this thesis this approach is used to infer the photometric properties of the materials coexisting in a specific site of Mars, the Gusev crater. Third, I perform an intercomparison of a selection of state-of-the-art techniques aimed at performing spectral unmixing of hyperspectral data acquired by the CRISM instrument. This family of techniques is proved to be useful to analyze hyperspectral images in an unsupervised manner, that is, without any a priori on the scene. An original strategy is proposed to discriminate the most suitable techniques for the exploration of Mars based on ground truth data built from independent high resolution imagery.

Contents

Introduction

Space exploration began when our ancestors started gazing upon the sky. These first astronomers called the bright objects moving among the stars "planets", or the wanderers. They were named after Roman deities and since then have driven the curiosity of the human race. Among all planets **Mars** has given rise to many questions such as whether life exists, or ever existed, in outer space. This inquisitiveness still persists nowadays largely because of the findings provided by the set of techniques named "remote sensing". **Remote sensing** allows the exploration of planetary objects through spacecrafts from orbit and has been used by more than fifty years now, from the pioneering Sputnik 1 satellite, launched in 1957, to the modern Mars Reconnaissance Orbiter (MRO), launched in 2006. Technological improvements have made possible the development of increasingly sophisticated instruments to arm spacecrafts. Nowadays different types of instruments provide unique data on topics such as the formation, the geology and the atmospheric conditions of planetary objects. The planet Mars has especially benefited from remote sensing techniques with a few tens of unmanned missions that have provided an unprecedented view on the Red Planet, improving our understanding of the mysteries that Mars hosts.

Remote sensing is commonly divided into passive and active techniques. While the instruments based on the latter technique emit a signal that is subsequently sensed after reflecting on a planet, **passive remote sensing** is based on the illumination of planetary objects by the Sun. Solar photons go through planetary atmospheres, reflect on the surface and reach the sensors after a second path through the atmosphere. The physical interactions happening along this path modulate the signal sensed by passive scanners providing clues on the composition of materials at the surface and atmospheric components. A few tens of years ago technological improvements in the field of spectroscopy and traditional imaging gave rise to **hyperspectral imaging**. This passive technique couples spectroscopy and imaging to determine the spatial distribution of the materials at the surface and of their physical properties. Hyperspectral imaging expands traditional imagery to the range of the electromagnetic spectrum that is invisible to the human eye. In this way hyperspectral sensors have the capability of discriminating between different materials that look similar in the visible range. In front of this potential planetary spacecrafts have been equipped with hyperspectral imagers since the late 1980s. Nowadays two hyperspectral instruments orbit the planet Mars, the Observatoire pour la Minéralogie, l'Eau, les Glaces, et l'Activité (OMEGA) aboard the Mars Express orbiter, launched in 2003, and the **Compact Reconnaissance Imaging Spectrometer for Mars** aboard MRO.

The OMEGA and the CRISM instruments provide unprecedented data on Mars. However, the voluminousness and the complexity of hyperspectral images entail challenges regarding the visualization, manipulation and exploitation of these data. This is particularly the case of the CRISM sensor whose major technical improvements with respect to OMEGA are its higher spatial resolution and the fact

that CRISM is the first hyperspectral imager to operate systematically in **multi-angle mode** from space. The first attribute allows CRISM to provide a finer spatial outlook on the surface of Mars while maintaing the spectral resolution of OMEGA. Second, the mechanical configuration of CRISM allows it to spectrally explore a given martian scene at different observation geometries. This exclusive novelty of CRISM is originally intended to improve the characterization of the atmosphere of Mars. As a result of these two technical capabilities the images released from the CRISM instrument are not only related to a unique information but also to an unprecedented complexity and size.

In this framework this thesis proposes a series of **statistical and physical algorithms** to process and analyze CRISM hyperspectral images. These tools are conceived to help planetary scientists to address fine analysis of the planet Mars using data acquired by CRISM. This thesis looks into the fields of planetary sciences and Earth observation to develop state-of-the-art tools to process CRISM data. The major goals are to develop unsupervised techniques to perform automatic processing of CRISM images for the retrieval of meaningful planetary features and to propose physically-based approaches to carry out fine analysis of the physical and chemical properties of materials at the surface of Mars. These two objectives are addressed taking into consideration the multi-angle capabilities of the CRISM instrument, not only for a better characterization of the atmosphere but also in the seek of photometric properties of the surface according to observation geometry. The latter data shall indeed give significant hints about the physical state of surface materials, which are nowadays largely unknown. Additionally, this dissertation investigates the sensitivity of the CRISM instrument to instrumental artifacts coming from its demanding technological requirements. In this matter, the improvement of the radiometric accuracy of the CRISM data is also explored. Although the proposed algorithms in this thesis are recurrently tested and validated on selected CRISM images they are reusable in other contexts and are not limited to a particular case.

This Ph.D. dissertation is divided into four major parts:

- In the **first part** I introduce the **context of the present thesis**. The first chapter starts with a summary of the exploration of Mars and the use of hyperspectral imagers, in particular. Afterward, I detail the instruments and products related to the hyperspectral imaging of planetary objects followed by the description of the CRISM instrument. In the second chapter I provide an overview on the physics related to passive remote sensing, that is, the radiative transfer between solar photons, the atmosphere, and the surface. This chapter sets the background for the third part of this document. The first part of the dissertation concludes by detailing the **objectives of this thesis**, that is, the solutions that I propose to overcome the challenges associated to the remote sensing of Mars using the CRISM instrument.
- In the **second part** I investigate the automatic processing of CRISM multi-angle data by introducing a tailor-made **data pipeline**. First, this set of routines aims at improving the radiometric quality of CRISM data by addressing the correction of several instrumental artifacts. These technical limitations compromise the analysis of CRISM data by the algorithms that shall be proposed in this thesis. Second, the data pipeline is devised to produce advanced CRISM products taking into consideration the geometric, atmospheric, and instrumental conditions under which CRISM images are acquired. In this way I shall explore the compensation for heterogeneous illumination conditions and atmospheric effects that may disguise the features related to the surface. Likewise, the proposed data pipeline produces multi-angle products encompassing the full angular

information made available by CRISM from a single martian site.

- In the **third part** I explore further the **atmospheric correction** of CRISM data by proposing an original approach that exploits the multi-angle capabilities of the CRISM instrument for the sake of an accurate compensation of atmospheric effects. This technique is devised to retrieve the information related to the surface from at-sensor data with a higher fidelity than when using traditional atmospheric correction methods. In this part of the thesis I shall go further by investigating the photometric properties according to the geometry of acquisition of the materials of a given site of Mars. This photometric study is made possible thanks to the proposed atmospheric correction algorithm and supposes a pioneering investigation of this type using orbital imagery.
- In the **fourth part** I investigate the use of statistic techniques to extract physically meaningful features from CRISM imagery in an unsupervised manner. In particular I propose the use of **spectral unmixing** techniques that are able to transform a voluminous hyperspectral image into a set of a few feature images, some of them related to the existent materials at the surface. These techniques represent a remarkable tool to process hyperspectral data in an automatic and significant manner. In addition the unmixing concept makes possible a compact visualization of hyperspectral images due to the mentioned dimensionality reduction. In this part of the dissertation I perform a comparison between some state-of-the-art techniques typically used for analyzing terrestrial hyperspectral images. The most appropriate techniques for the remote sensing of Mars are identified by a validation strategy based on original ground truth data built from independent high resolution imagery.

Each of the aforementioned parts begins with a short introduction to the problems to be addressed and concludes with the related conclusions and outlook. A chapter summarizing the main points discussed along the thesis and highlighting the major conclusions and future prospects is included at the end of this dissertation. This thesis is concluded by a series of appendices describing different aspects related to the topics discussed along this work.

Part I.

Background

Introduction

Since the very first close-up of the Red Planet taken in the 1960s spacecraft missions to Mars have revealed a world somewhat familiar yet different enough to trigger our curiosity. Every time we feel close to understanding Mars, new discoveries make us review existing theories. Like Earth, Mars has polar ice caps, seasonal weather patterns, clouds in its atmosphere, volcanoes, canyons and other recognizable features. However, conditions on Mars greatly vary from those on Earth. Over the past five decades space exploration programs have led the discover that Mars is cold and rocky beneath its reddish hazy sky. The first part of this Ph.D. thesis starts with an introduction on the planet Mars and its most relevant geological features in section 1.1.

Space exploration is mainly accomplished by remote sensing techniques. The term "remote sensing" is commonly used to describe the science of identifying, observing, and measuring an object without coming into direct contact with it. The technology of modern remote sensing began with the invention of the camera, more than 150 years ago. However, the idea of looking down at the Earth's surface emerged in the 1840s when pictures were taken from cameras secured to balloons for mapping purposes. This was the precedent of the current observation and exploration satellites performing remote sensing of planetary objects using several types of sensors. In this thesis I focus on passive remote sensing which uses the radiation of the Sun as source of illumination. In the following section 1.2 I provide a brief review on the space exploration of the planet Mars by means of remote sensing orbiters and rovers on the surface. The latter crafts will indeed help us to complement and validate the results obtained from space.

Recent advances in remote sensing have led the way for the development of hyperspectral sensors. Hyperspectral remote sensing, also known as imaging spectroscopy, is a relatively new technology that is currently being investigated by researchers and scientists with regard to the detection, identification, and characterization of minerals, ices, and other materials at the surface. These techniques have been incorporated to space missions since the late 1980s and have provided unprecedented data on the surface and atmosphere of the Red Planet. In section 1.3 I give a review on the principles of imaging spectroscopy and the related instruments, products and analysis techniques. The chapter is concluded in section 1.4 by introducing the Compact Reconnaissance Imaging Spectrometer for Mars, which represents the main instrument of study of this thesis.

Because satellites measure radiation, the interpretation of their data requires the study of radiative transfer in the atmosphere and through the upper few millimeters to centimeters of the surface. Radiative transfer is the physical phenomenon of energy transfer in the form of electromagnetic radiation and is crucial to understand the at-sensor signal that eventually forms hyperspectral images. In chapter 2 I explain the radiative phenomena happening in the remote sensing of planetary surfaces. The main elements such as the atmospheric gases, the aerosols, and the surface itself are described by their scat-

tering and absorption properties that condition the travel of light from the Sun to the spacecraft. This radiative interaction characterizes the spectral signatures that will be sensed by imaging spectrometers and that will be key in the exploitation of hyperspectral images that will be accomplished in this dissertation. As a matter of fact, chapter 2 establishes the basis of some of the physically-based methods that shall be presented in this thesis to process and analyze multi-angle hyperspectral images of Mars.

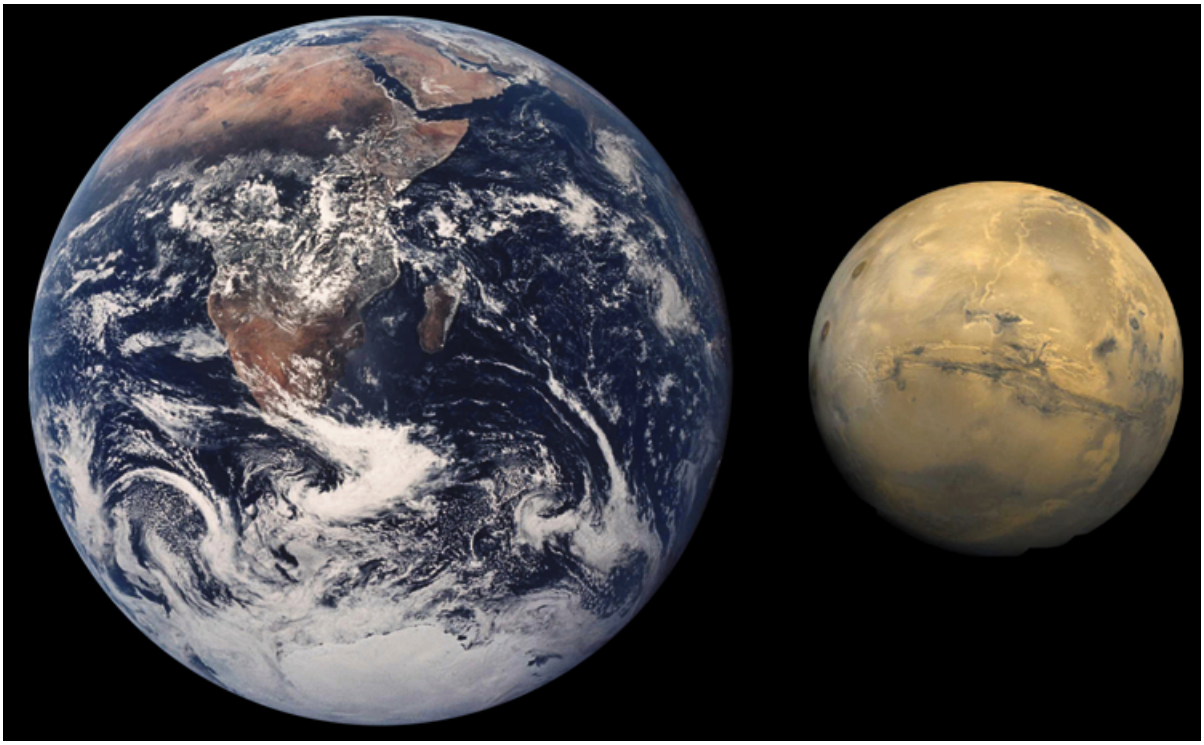

Size comparison of Earth and Mars.

Contents

1

Remote sensing of Mars

The first chapter of this thesis is divided into four sections. First, I give a description of the planet Mars and the geological and atmospheric features that have been discovered by remote sensing from space. The second section is devoted to the exploration of Mars by the combination of orbiters, landers and rovers. In this way I detail the successful (and fruitless) unmanned missions that have been carried out to the date, introducing the main on board instruments that shall be considered in this dissertation. Third, I describe a specific imaging technique to explore planetary surfaces, imaging spectroscopy. Imaging spectrometers, or hyperspectral imagers, provide a unique insight into the chemical composition and physical state of materials at the surface and particles in the atmosphere. This technique represents the principal remote sensing tool that will be used in this thesis. Eventually, the hyperspectral imager named Compact Reconnaissance Imaging Spectrometer for Mars (CRISM) aboard the Mars Reconnaissance Orbiter is introduced in the fourth section by detailing its technical attributes and the resulting image products.

1.1. The planet Mars

Our curiosity for Mars goes back in time to the ancient eras. A legacy of it is our use of the name Mars, which comes from the ancient Roman God of war. Nonetheless, other ancient civilizations already named the planet after warrior gods due to its reddish-orange color. Absolute fascination, however, began in the late 19th century when several astronomers theorized on the presence of liquid water on the surface of Mars based on telescopic observations. This speculation was founded on an observed network of dark straight lines in the equatorial regions of Mars that were interpreted to be irrigation channels. These "canals" were first observed by the Italian astronomer Giovanni Schiaparelli in 1877 (see Figure 1.1) and confirmed by later observers. Some people went further with their speculations and even proposed these patterns to be irrigation canals built by a intelligent civilization on Mars!

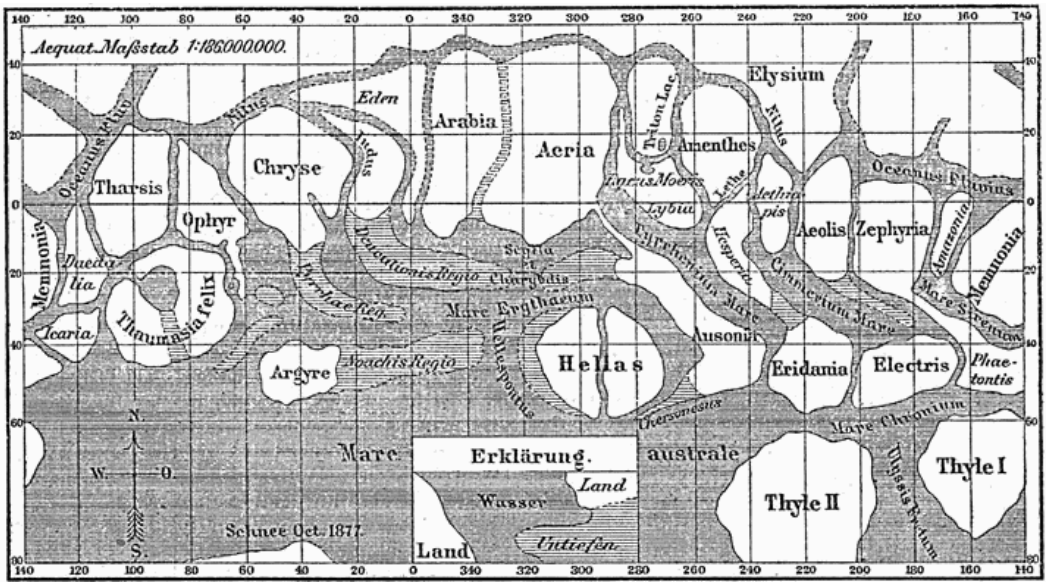

Figure 1.1.: Historical map of planet Mars from Giovanni Schiaparelli.

This enigma, among other mysteries of the universe, has made the human race to spare no effort in exploring space in order to learn about the planetary objects of the Solar system. Sadly for believers, advanced astronomical observations revealed in the early 20th century that the aforementioned "canals" were an optical illusion. Today, high resolution mapping of the Martian surface aboard spacecrafts shows no such features. Although this might be considered to be disappointing, unmanned missions have gathered information on other enigmas. In the recent times, for example, spacecrafts on orbit and rovers on the surface have collected geological evidence suggesting that Mars once had water coverage at large scale on its surface. The human race hence keeps wondering.

The planet Mars is half the size of the Earth and represents the fourth planet closest to the Sun at a distance of more than 230 millions of kilometers. The British astronomer William Herschel determined in the 19th century its rotational period to be 24 hours 37 minutes, only 41 minutes longer than a day on Earth. Mars is related to other Earth-like characteristics such as its seasonal cycles that result from a similar obliquity of its rotational axe than Earth's. During a journey around the Sun of a little more than two Earth years, Mars goes through the first day of spring in the northern hemisphere at $L_S = 0°$[1], the northern summer solstice at $L_S = 90°$, the northern autumnal equinox at $L_S = 180°$ and the northern winter solstice at $L_S = 270°$. In this voyage Mars is accompanied by its two moons, Deimos (panic) and Phobos (fear) named after the horses that pulled the chariot of the Greek war god Ares and discovered in 1877 by the American astronomer Asaph Hall. Table 1.1 summarizes some of the mentioned characteristics of Mars among other physical attributes.

Regarding its geology, the surface of Mars is mainly composed of basalt often mantled by a layer of finely grained iron oxide dust. Also, latest discoveries have revealed the presence of hydrated sulphates and phyllosilicates at the surface. Mars has many features similar to the valleys, polar caps, deserts, and volcanoes of Earth as well as the impact craters of the Moon. Mars is the site of Valles Marineris, the largest known canyon in the Solar System, and Olympus Mons, the highest known mountain with more than 21 km from the base to the summit. The lowest point is situated in the Hellas impact

[1] L_S is the **longitude of the Sun** and is widely referred to determine the position of Mars in relation to the Sun

Attribute	Mars	Earth
Mass	6.42×10^{23} kg	58.35×10^{23} kg
Equatorial radius	3396 km	6378 km
Solar day	24h 37m	23h 56m
Surface gravity	3.71 ms^{-2}	9.78 ms^{-2}
Bond albedo	0.250	0.306
Orbital period	779.94 days	365.25 days
Obliquity	25.19°	23.44°
Distance to Sun	2.3×10^{8}km	1.5×10^{8}km

Table 1.1.: Orbital, rotational and physical characteristics of Mars.

basin at less than -8 km. This huge difference in elevation is evidenced in Figure 1.2, displaying the hemispheric dichotomy between the elevated southern highlands and the lower northern plains.

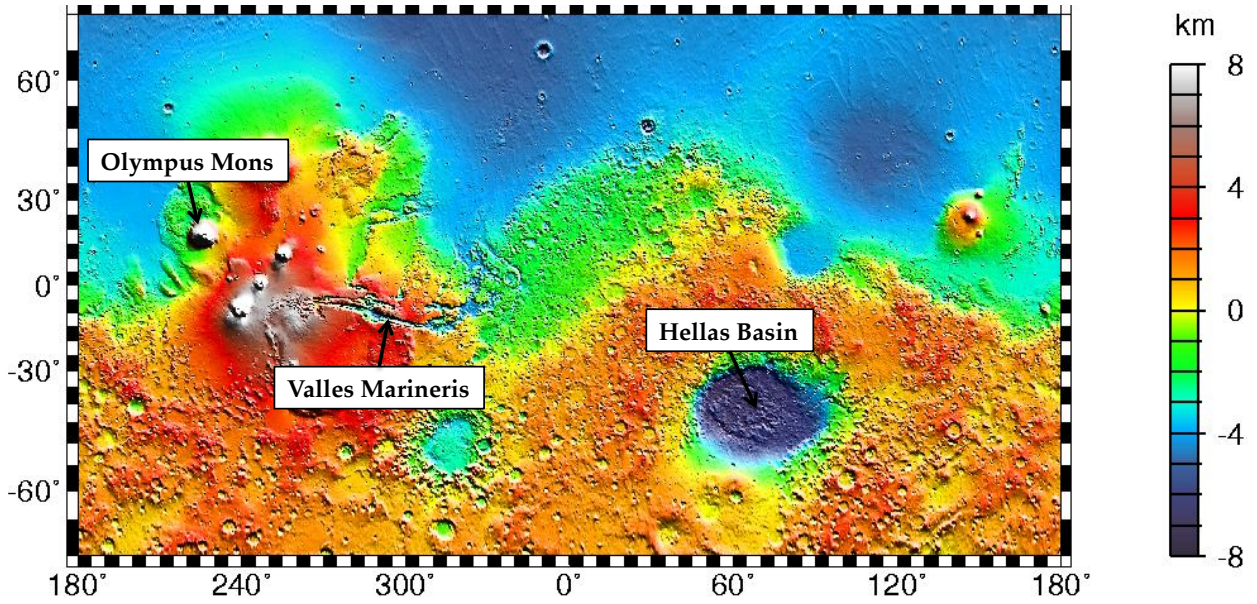

Figure 1.2.: Global topography of Mars from the Mars Global Surveyor Mars Orbiter Laser Altimeter experiment. The geological features named in the text are highlighted. Credit: National Aeronautics and Space Administration.

Although Mars lost its magnetosphere a few billion years ago, a thin atmosphere remains. The atmosphere of Mars is composed of 95% carbon dioxide (CO_2) and contains suspended dust and water ice particles called aerosols. These particles can be highly mobilized during the storms that happen on Mars, ranging from local storms to huge global storms that can cover the entire planet.

As for the existence of water on Mars, the Mars Pathfinder rover measured a pressure on the surface too low to host liquid water (i.e. a few millibars). Nevertheless, large quantities of water ice are known to be stocked in the poles of Mars. The polar caps at both poles consist primarily of water ice covered by a thin layer of frozen carbon dioxide about one meter thick on the northern cap in winter only and by a permanent eight-meter thick layer made of the same component on its southern twin cap. Water ice is indeed predominant in both poles as the northern permanent polar cap has an average thickness of 2 km and a diameter of roughly 1000 km (see Figure 1.3) while the southern permanent polar cap

has a thickness of 3 km and a diameter of 350 km. Only the volume of water stored in the southern ice cap would be sufficient to cover the entire planet with a resulting depth of 11 meters.

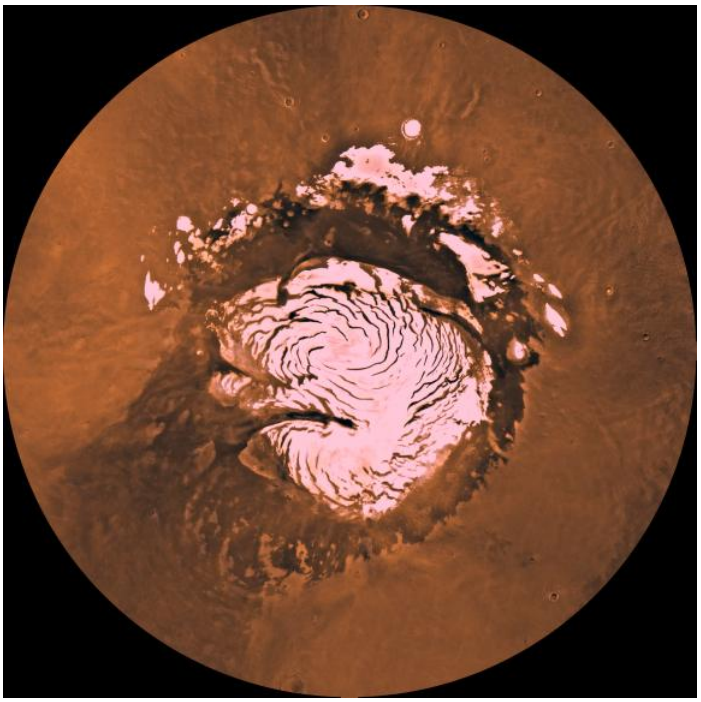

Figure 1.3.: Viking Orbiter's view of the northern ice cap of Mars.

Apart from being huge reservoirs of water ice, the poles of Mars drive the massive CO_2 cycle that happens on the Red Planet. During winter, the poles lie in complete darkness, cooling off the surface and causing that up to 30% of the atmosphere condenses generating deposits of seasonal CO_2 ice sometimes in the form of thick slabs. When the spring comes, the frozen CO_2 on the poles sublimes due to exposition to sunlight, creating winds. These seasonal effects transport large amounts of dust and water vapor, giving rise to cirrus clouds and Earth-like frost. As the regions permanently covered by frost warm with the arrival of spring, pressure from subliming CO_2 increases under the seasonal slabs, elevating and ultimately rupturing it. This leads to geyser-like eruptions of CO_2 gas mixed with dust.

These processes, among many others, represent the type of targets aimed by remote sensing exploration. As a matter of fact, the instruments mounted on spacecrafts orbiting around Mars have been decisive to detect, monitor and quantify the aforementioned attributes and processes of Mars. In the following section, I detail in brief the 50 years of exploration of Mars principally accomplished by remote sensing techniques.

1.2. Space exploration

Mars has been the focus of intense scientific study throughout history. Even before the invention of the telescope by Galileo in 1609, the Polish astronomer Nicolas Copernicus already performed observations of the Red Planet with the naked eye. Later on, telescopic observations expanded our knowledge by revealing, for example, the presence of polar caps and atmosphere on Mars. However,

their compositions remained unknown. Progress on the size and the types of telescopes have greatly increased the quality and kinds of martian observations in recent years.

Most of the contemporary understanding on Mars has been acquired thanks to unmanned space missions composed by orbiters, landers and rovers. Mars has been indeed a popular destination of spacecrafts since the early days of space exploration. This is explained not only by its proximity to Earth but also because of the question of whether life could ever have existed on the Red Planet. In the present section of the thesis, I briefly summarize the exploration of Mars since the first mission. I recommend, however, the excellent works of Barlow and Bell that provide a much more detailed story on this subject [8, 11].

Albeit the considerable interest in Mars, the Red Planet has not been the easiest place to explore. Indeed, up to this day, about two-thirds of all space missions directed to the Red Planet have been partially or completely failed. The Soviets were the first to send a spacecraft to Mars with the Mars 1 mission, launched on 1 November 1962. This spacecraft was designed to photograph the planet and determine if Mars had a magnetic field. Unfortunately, after some critical failures, data were never returned. The United States took over from the Soviets and launched the Mariner 3 and 4 spacecrafts in Mars 1964. Although both missions were launched successfully, the solar panels powering Mariner 3 did not deploy properly and that mission ended up in solar orbit. Mariner 4, however, returned the first ever close-up photos of Mars, revealing a heavily cratered surface (see Figure 1.4). Additionally, Mariner 4 confirmed the existence of an atmosphere primarily composed of carbon dioxide and a faint magnetic field.

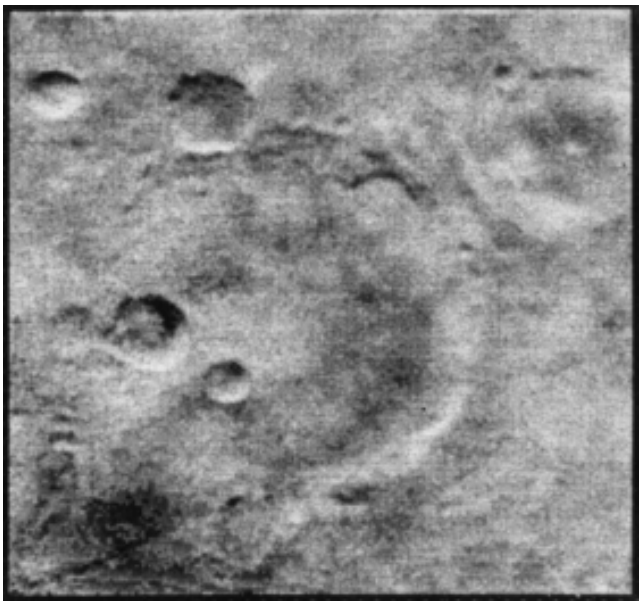

Figure 1.4.: View of the martian surface taken by the Mariner 4 spacecraft. Craters can be seen, but little else is discernible in this image. Credit: National Aeronautics and Space Administration/Jet Propulsion Laboratory.

Also in the mid-sixties the Soviets sent a couple of spacecrafts, Zond 2 and Zond 3, which failed because of different technical reasons. A few years later, Mariners 6 and 7 expanded on the discoveries made by Mariner 4 by reaching Mars in mid-1969. Instruments on these two spacecrafts revealed a heavily cratered, geologically dead world that sadden the planetary community, eager of finding life

on Mars. However, the question of life on Mars arose again right after Mariner 9 entered orbit on November 1971. Among the several findings made during this mission, Mariner 9 observed channels on the surface that were though to be formed by a flowing liquid. These geological features seemed to indicate that conditions could have changed through martian history.

A few weeks after Mariner 9 arrived at Mars, the Soviet Mars 2 and 3 orbiters achieved orbit (see Figure 1.5). Their temperature observations of the north polar cap were close to the condensation temperature of carbon dioxide, indicating that CO_2 is a major component of the ice caps. Both Mars 2 and 3 also carried landers which were meant to be the first human artifacts to explore in-situ the surface of Mars. Unfortunately, both of them crashed onto the surface and contact was lost. Although the same happened with Mars 6 and 7 landers in mid-1973, the Soviets got more lucky with Mars 4 and 5 orbiters that acquired substantial data from the surface and the atmosphere of the planet.

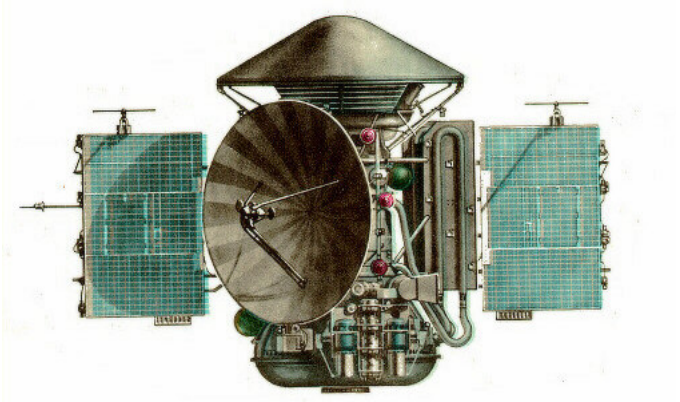

Figure 1.5.: Artist's conception of the Soviet Mars 2 spacecraft. The Mars 2 and Mars 3 missions consisted of identical spacecrafts, each with an orbiter and an attached lander. The latter were the first human artifacts to impact the surface of Mars.

At the end of the space race between the Soviet Union and the United States, the next two missions of the National Aeronautics and Space Administration (NASA), Vikings 1 and 2, were launched on August and September 1975, respectively. These two missions included landers which successfully landed and explored the soil for evidence of microorganisms. Both returned the first color views of the surface of Mars, revealing a rocky and dusty surface. Viking 2 provided one of the first proofs that water might exist on the surface by observations of water frost (see Figure 1.6). In addition to the landers, each mission also consisted of an orbiter to provide detailed views of the entire planet. The Viking orbiters mapped the entire surface of Mars and acquired more than 50000 images, becoming one of the most successful first missions in the space exploration of Mars.

The Soviets were definitely out of luck as both the Phobos 1 and 2 spacecrafts, launched on July 1988, suffered from critical failures. As the spacecraft names suggest, the main target was Mars' largest moon, Phobos. Phobos 2 managed, however, to made a limited number of observations of Mars, including the first near-infrared (NIR) spectra acquired by the infrared spectrometer (ISM), the ancestor of imaging spectrometers such as the CRISM instrument. The United States had not better luck than the Soviets as the communications with the ambitious Mars Observer mission, launched on September 1992, were lost while the spacecraft was entering Mars orbit.

The first mission to recover some of the initial investigations of Mars Observer was Mars Global Surveyor (MGS) which was launched on November 1996 and operated during ten years. The data acquired

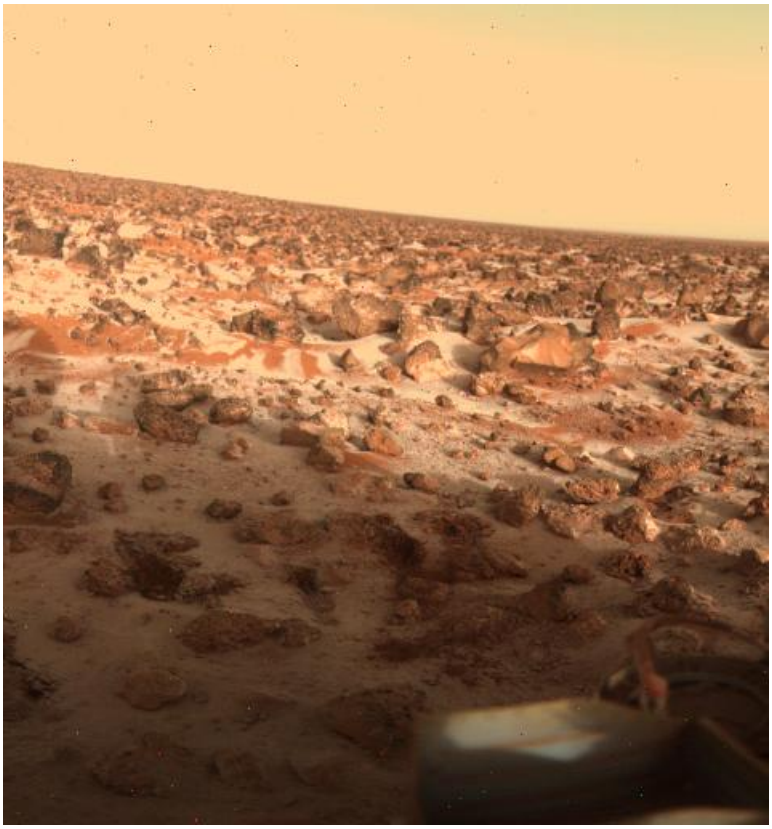

Figure 1.6.: Pictured acquired by the Viking Lander 2 showing an unusual image of the martian surface in 1979 sporting a thin layer of seasonal water ice in the form of frost.

by MGS have proved to be of an excellent quality and are still used in current studies. MGS was equipped with severals instruments out of which I highlight the Mars Orbiter Camera that provided unprecedented high-resolution imagery (1.5 to 12 m/pixel resolution) and the Mars Orbiter Laser Altimeter (MOLA) that used laser pulses to determine the topography of the surface. Russia tried to compete with MGS with the ambitious Mars 96 mission containing an orbiter, two surface landers, and two penetrators. Mars 96 was launched in November 1996 but a failure affecting the rockets caused the mission to crash into the ocean. One month later, the American Mars Pathfinder lander was launched to become the first mission to carry a robotic rover. The lander safely landed on Mars and the rover traveled a distance of a hundred meters during which it characterized the composition of some soils and rocks.

The end of the 90s was disastrous for Mars exploration. First, Japan attempted to join the international exploration of Mars in July 1998 with the Nozomi mission. However a malfunctioning valve caused the spacecraft to lose some fuel that eventually led to the abandon of the mission. Second, the American Mars Climate Orbiter and Mars Polar Lander missions failed due to different technical reasons in 1998 and 1999, respectively.

The success came back with Mars Odyssey orbiter, launched on April 2001. In this orbiter, I highlight the Thermal Emission Imaging System (THEMIS) instrument which still observes the planet in both visible (18 m/pixel resolution) and infrared (100 m/pixel resolution) wavelengths. Two years later, the two Mars Exploration Rovers (MER) Spirit and Opportunity were sent to Mars to investigate sites which were thought to contain evidence of ancient water. Each rover carries a Panoramic Camera (Pan-

cam) to survey the surrounding areas among other instruments. In this thesis, data coming the Pancam instrument of Spirit is used in Part III. While Spirit got definitely stuck in May 2009, Opportunity keeps exploring the surface of Mars at the present time.

The European Space Agency (ESA) joined the exploration of Mars in June 2003 with the launch of Mars Express (MEX). MEX consisted of an orbiter and the Beagle 2 surface lander, although unfortunately no signal was detected from Beagle 2 after its landing. The MEX orbiter, however, has been very successful as all of its instruments are returning precious data nowadays. Instruments include several that were lost on the Mars 96 mission, including the Observatoire pour la Minéralogie, l'Eau, les Glaces, et l'Activité (OMEGA). OMEGA is an imaging spectrometer with co-aligned channels working in the visible and near-infrared (VNIR) range and the short wavelength infrared (SWIR) range. OMEGA has provided evidence of water ice in the martian polar caps and mineralogical variations across the surface. I specially call attention to this instrument as it represents the predecessor of CRISM, the main instrument that shall be studied in this thesis. Likewise, recurrent references will be made to OMEGA and even some particular experiments are conducted based on its characteristics (e.g. see chapter 11). I recommend the Ph.D. dissertation of Schmidt for a detailed outlook on the OMEGA instrument and the science that it makes possible [157]. Aboard MEX, I also highlight the High Resolution Stereo Camera (HRSC), which has produced impressive three-dimensional images of the martian surface as the one shown in Figure 1.7.

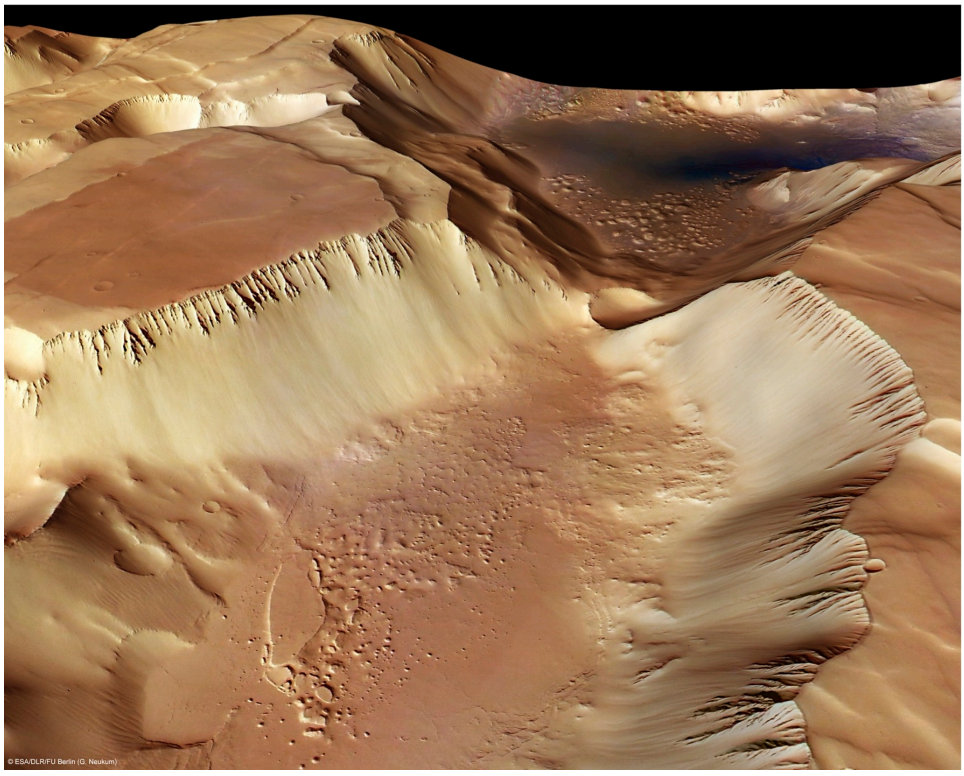

Figure 1.7.: This image of the Noctis Labyrinthus region on Mars was taken by the HRSC onboard MEX. The HRSC took these pictures with a ground resolution of approximately 16 m/pixel. This future prospect view has been calculated from the digital terrain model derived from the stereo channels. Credit: ESA / German Aerospace Center / Freie Universität Berlin

The last orbiter to be launched has been the Mars Reconnaissance Orbiter (MRO). MRO is a NASA multipurpose spacecraft which entered Mars orbit on March 2006. As MRO reached Mars it joined

four other active missions, namely MGS, MEX, Mars Odyssey and MER, a then record. MRO contains a host of scientific instruments such as the High Resolution Imaging Science Experiment (HiRISE) (25 cm/pixel) and the imaging spectrometer CRISM, which is aimed at analyzing the surface and atmosphere of Mars. In November 2008, MRO completed its primary science phase which started in November 2006. The MRO spacecraft operates in a sun-synchronous, near-circular (255×320 km altitude) and near-polar orbit and it is expected to transfer more data to Earth than all previous planetary missions combined.

Eventually, the Phoenix lander descended on Mars on May 25, 2008. Phoenix was NASA's sixth successful landing out of seven attempts and is the most recent spacecraft to land successfully on Mars as well as the first successful landing in a martian polar region. Indeed, Phoenix discovered the presence of shallow subsurface water ice. The mission was declared concluded on late 2008, after engineers were unable to re-contact the craft.

The Phoenix lander concludes the race for martian exploration for now. More advanced instruments will follow the steps started by the Soviet Mars 1 mission such as the upcoming Mars Science Laboratory carrying the rover Curiosity that is scheduled to launch in late 2011. The Curiosity rover will help assess whether Mars is or ever was an environment able to support microbial life. The show has just begun.

1.3. On the use of imaging spectroscopy

For more than a decade visible and infrared imaging spectroscopy, or hyperspectral imaging, has been an active area of research and development. With the recent imaging spectrometers, or hyperspectral imagers, devised for space exploration and Earth observation, hyperspectral imaging constitutes a key remote sensing technique to study planetary objects. The advantage of spectral imaging, as opposed to single-field-of-view spectrometers and traditional imaging systems, is its ability to simultaneously detect, identify, and map compositional units on planetary surfaces. As solar light is transmitted, reflected and diffused by interaction with the atmosphere and the surface, the analysis of reflectance spectra allows the identification, characterization and quantification of chemical species. As a matter of fact, chemical components have characteristic spectral features in the VNIR and SWIR observed by imaging spectrometers that allow the investigation of the geochemical evolution of surfaces as well as the compositional properties of atmospheres.

In planetary sciences the first imaging spectrometer was the ISM aboard the Phobos 2 mission. Before contact was definitely lost with this spacecraft, ISM obtained a few thousand spectra in the NIR and SWIR (from 0.75 to 3.2 μm) in the equatorial areas of Mars, with a spatial resolution ranging from 7 to 25 km/pixel, and a few hundred spectra of Phobos at 700 m/pixel resolution. These observations made possible the first mineralogical maps of the planet and its satellite. The ISM instrument was followed by the Near Infrared Mapping Spectrometer (NIMS) experiment on the Galileo spacecraft. The Galileo mission was launched in October 1989 and was aimed at the exploration of Jupiter and its moons, the Galilean satellites (see Figure 1.8 for a picture of the moon named Europa acquired during the Galileo mission). After six years traveling through space, Galileo arrived at Jupiter. On the travel to the red giant, the NIMS camera, along other instruments aboard Galileo, explored the planet Venus, the Earth/Moon system and a couple of asteroids. NIMS provided unprecedented information to the

scientific community on the composition of each of these planetary objects.

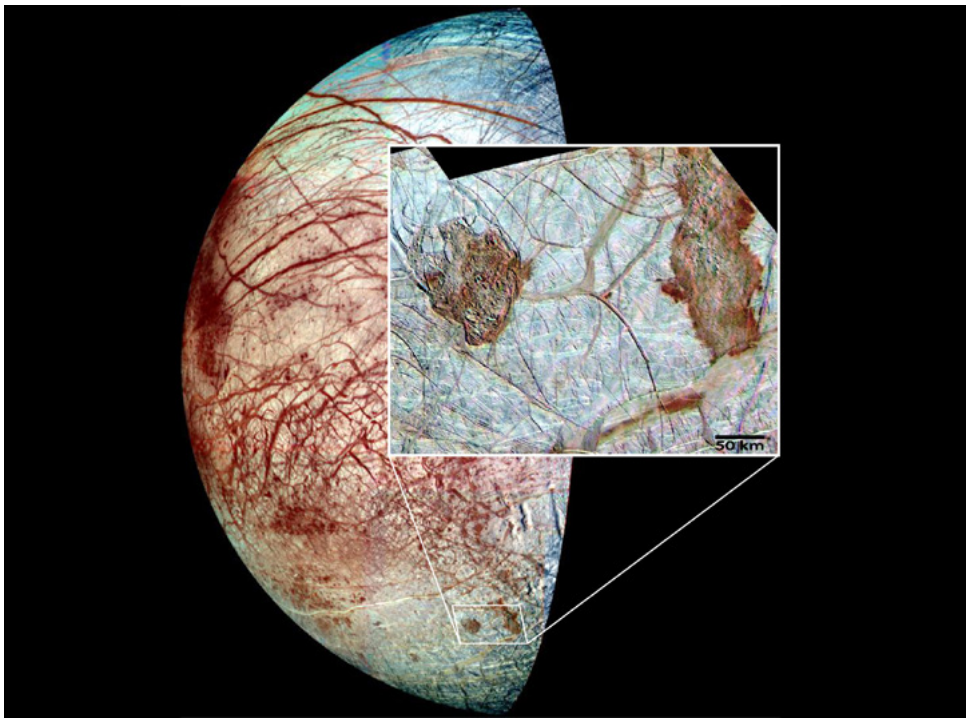

Figure 1.8.: This image of Europa and an enlargement of the Thrace region gives visual evidence of the dramatic advance in our knowledge of Jupiter's second Galilean satellite due to the Galileo mission. Credit: Arizona State University.

The Phobos 2 and Galileo missions were pioneers in using imaging spectroscopy for the study of planetary objects. Later on the ISM and NIMS instruments were followed by other hyperspectral imagers such as the Visual and Infrared Mapping Spectrometer sensor on the Cassini spacecraft, the OMEGA instrument aboard MEX, the CRISM sensor aboard MRO and the Visible and Infrared Thermal Imaging Spectrometer (VIRTIS) experiment on the Venus Express mission. This series of increasingly powerful sensors has been decisive in addressing issues related to the surface and the atmosphere of Saturn, its moons, Mars and Venus. Furthermore, imaging spectroscopy represents a key remote sensing technique to study not only the planets of the Solar system but the Earth itself. I recommend the reading of the Ph.D. dissertation of Guanter in which a comprehensive review of the imaging spectrometers used in Earth observation is given [68].

Nowadays, we find two imaging spectrometers orbiting around Mars, the OMEGA and the CRISM instruments. Similarly to other hyperspectral imagers, both instruments have provided substantial clues on environmental conditions and present and past activity. For example, ESA announced in 2004 the discovery of water ice in the south polar ice cap, using data taken with the OMEGA instrument. In particular, the orbiter detected a polar ice cap whose bulk composition is dominated by water ice with various amounts of dust overlaid by a veneer of carbon dioxide ice 10-15 meters thick over a fraction of its surface [3]. In 2005, Poulet et al. reported on the presence of hydrated sulphates, silicates and various rock-forming minerals using OMEGA data [144]. Alternatively, in the primary science phase of CRISM, international researchers performed a comprehensive investigation of past aqueous environments, structure of the planet's crust, past climate and current meteorology [128]. The main technological difference between CRISM and OMEGA is that the former instrument is the first

hyperspectral imager to operate systematically in multi-angle mode at high spatial resolution from orbit. As it shall be seen in this thesis, this attribute represents a state-of-the-art advance toward a more complete understanding of the Red Planet.

In the following I detail the advantage of using imaging spectroscopy complementarily to classical techniques. The data products generated by these instruments, the different systems of acquisition as well as the major analysis trends are detailed afterward.

1.3.1. Exploring the surface

Imaging spectroscopy begins with sunlight reflected off a delimited area of a planet. Hyperspectral imagers have the ability of decomposing this light into a few hundreds of wavelengths forming the measured spectra. The use of a broad spectral range provides hyperspectral imagers with the ability of determining the composition of the observed area. The science of using reflected radiation leaving materials at a set of wavelengths to measure composition is called **reflectance spectroscopy**. In the same way that someone with a little familiarity with rocks can recognize a piece of basalt (black, hardened volcanic lava) or limestone (whiter, sedimentary rock) by their color and texture, spectroscopy extends mineral and rock discrimination based on wavelength (or color in the case of the "rock expert") to spectral ranges that are not visible to the eye (e.g. the infrared).

The concept of spectroscopy is based on the fact that each chemical component is more likely to absorb solar radiation at certain wavelengths, defining intrinsic spectral signatures. Low signals in a reflectance spectrum occur at wavelengths where the observed material absorbs light, the so-called **absorption bands**. The portion of the electromagnetic spectrum that is not absorbed is named **spectrum continuum**. These two fingerprints characterize each type of material as well as its physical state. Figure 1.9 highlights these spectral features for a spectrum of olivine, an igneous mineral common on Mars. The dotted line depicts the spectrum continuum while arrows point to absorption bands. As it can be seen, the fingerprints of olivine are different than the other two kinds of pyroxenes, becoming distinctive features of the former material. Other typical martian materials such as water ice or frozen CO_2 have likewise distinctive fingerprints which are sensed by spectrometers working in the visible and infrared ranges. Data acquired by this type of instruments are hence unique to detect and characterize the materials coexisting in planetary surfaces.

The advantage of imaging spectrometers in front of single-shot spectrometers, that is, acquiring a single spectrum, is that the mentioned discrimination between materials can be extended to a whole spatial scene. Imaging spectrometers produce hyperspectral images in which each pixel is related to a spectrum, allowing a compositional mapping over the full extent of the image.

1.3.2. Hyperspectral images

A hyperspectral image is a compilation of typically a few hundred spectral images, each one expressing the sensed radiance coming from a given scene at a given wavelength. The stacking of spectral images produces hyperspectral images, or data cubes, in which two axis correspond to the two spatial dimensions and the third one to the spectral dimension according to wavelength. Generally, hyperspectral images cover the visible ($400 < \lambda < 700$ nm), the near-infrared range ($0.7 < \lambda < 3.5$ μm) and the shorter wavelengths of the thermal infrared ($3.5 < \lambda <\sim 5$ μm). Figure 1.10 depicts the three

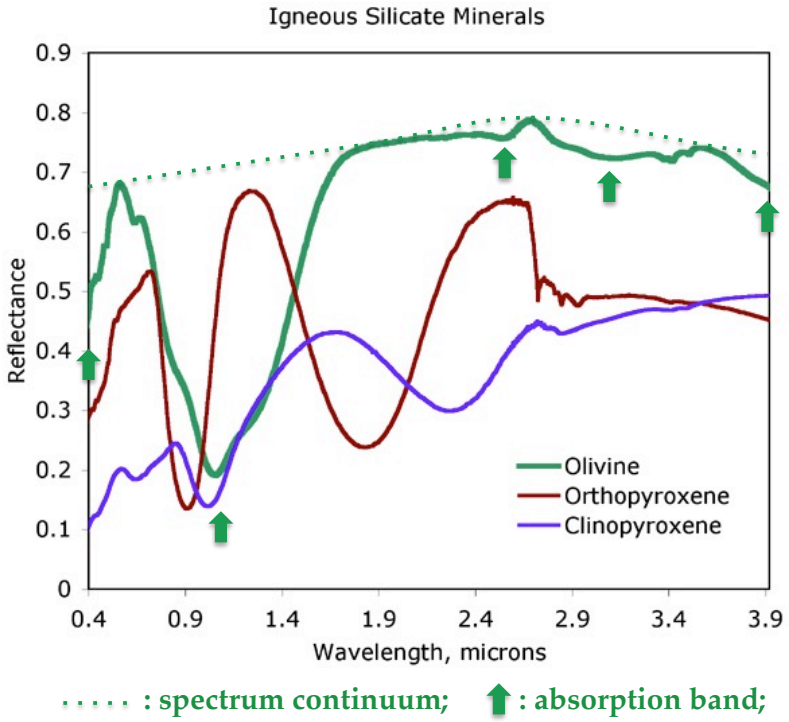

Figure 1.9.: Spectra of typical minerals at the martian surface. The dotted line and the arrows point to the spectrum continuum and the absorption bands of the olivine spectrum. Credit: http://crism.jhuapl.edu.

mentioned dimensions as well as the major elements in a hyperspectral image. Each stacked image composed by a set of pixels corresponding to a given wavelength is called a **spectral band**. However, if we refer to the spectral data contained within a given spatial position, we use the term **spectrum**. A spectrum expresses the variance according to wavelength of the measured radiance. Figure 1.9 shows the spectra corresponding to three different materials. I note, however, that a spectrum may not correspond to a single material at the surface but a mixture of a few components due to an insufficient spatial resolution, for instance. The issue of mixed spectra constitutes a major issue in hyperspectral imagery and shall be addressed in Part IV. From a spectral point of view, a hyperspectral image can be considered as an ensemble of spectra arranged according to their original position at ground. In this case each element composing a spectrum is no longer named a pixel but a **spectel**.

1.3.2.1. Geometry of acquisition

Passive remote sensing of planetary surfaces is sensitive to the position of the spacecraft with respect to the scene of study and with respect to the Sun. This sensitivity comes from the scattering properties of the surface and the variation of the amount of energy falling on the surface depending on the Sun elevation (more details on these processes are given in chapter 2). For this reason hyperspectral images are typically released along with ancillary data that describe the acquisition conditions under which each single spectrum was acquired.

I define the **acquisition geometry** related to a remote sensing problem as the following triplet of angles (see Figure 1.11 for complementary details):

- The angle of incidence of the Sun, or **Sun zenith angle** (SZA), determines the illumination, or

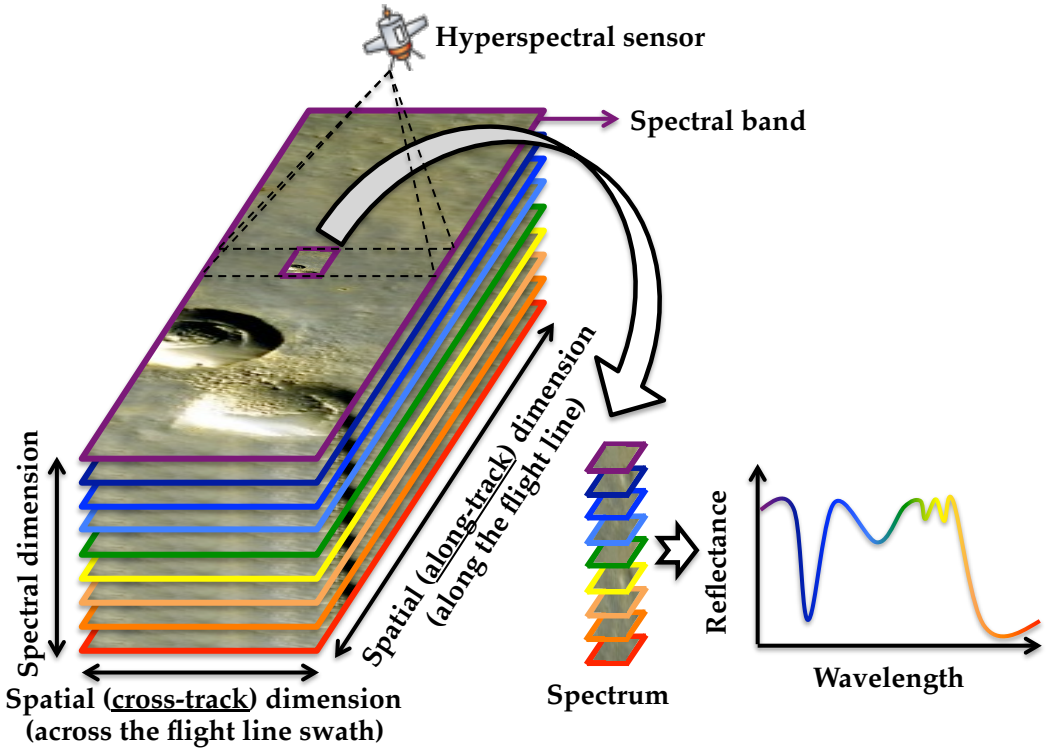

Figure 1.10.: Scheme of a hyperspectral image. Note that the image is composed by a set of pixels, each one assigned to a spectrum like the one in the example. In hyperspectral images acquired by spaceborne or airborne instruments, the two spatial axis are called **along-track dimension** and **cross-track dimension**. These two notions are further described in subsection 1.3.3.

incidence, direction in the scene of study. It is defined as the angle between the direction of the Sun as regards the target and the zenith and is usually mentioned by symbol θ_0. The SZA is crucial to determine the solar energy per unit of surface as higher values of θ_0 result in lower radiation over an elementary terrain unit. This fact is taken into account in the study of surface photometry (see subsection 4.2.3). The SZA can also be expressed in its cosine form $\mu_0 = \cos\theta_0$.

- The angle of emergence, or **view zenith angle** (VZA), determines the elevation of the spacecraft in relation to the ground. The VZA is defined as the angle between the zenith and the viewing (or emergence) direction, namely the line that goes from the target to the craft. VZA is usually expressed by the symbol θ. The angle of emergence is important when dealing with surfaces whose appearance changes according to the viewing direction such as ices and some minerals. Spacecrafts working at **nadir** correspond to $\theta \approx 0^o$. The VZA can also be expressed in its cosine form $\mu = \cos\theta$.
- The relative azimuth, or simply **azimuthal angle**, indicates the relative position of the Sun and the spacecraft projected on ground. The relative azimuth is defined as the angle between the projections of the Sun and spacecraft positions on ground and is referred to as φ. There is one case in which this angle relating the source and the craft becomes useless, namely the presence of materials at the surface with privileged scattering directions. In this case, a reference point is necessary to define the absolute azimuth of the Sun φ_0 and that of the spacecraft φ (e.g. these two angles are usually given with the north as reference). In this thesis, I will use the symbol φ as the relative azimuth $\varphi_0 - \varphi$, unless mentioned in the text otherwise, as most martian materials

do not have privileged scattering directions.

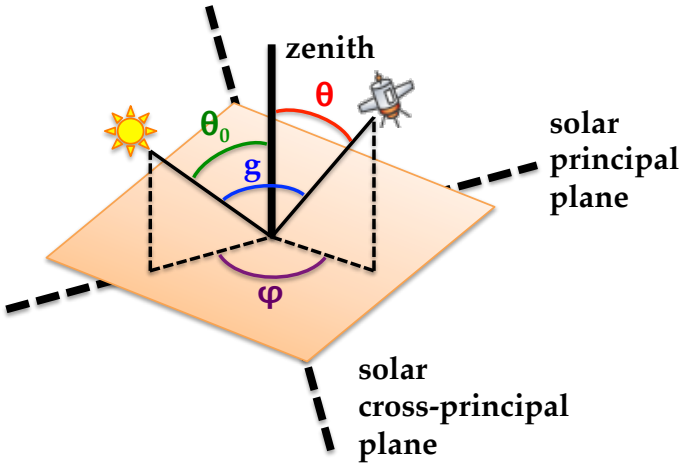

Figure 1.11.: Scheme of the acquisition geometry in remote sensing of planetary surfaces.

These three angles fully determine the geometry of acquisition in a passive remote sensing problem. Alternatively, this acquisition triplet can be expressed by replacing the relative azimuth by the phase angle. The **phase angle** g is defined as the angle between the illumination and the viewing directions and can be calculated such that $\cos g = \cos\theta_0 \cos\theta + \sin\theta_0 \sin\theta \cos\varphi$. The phase angle is useful when analyzing scattering processes by atmospheric particles or by the surface.

Figure 1.11 also details two other concepts related to the geometry of acquisition, the **solar principal plane** and the **solar cross-principal plane**. The former direction is defined by the infinite imaginary line determined by $\varphi = 0^o$ and $\varphi = 180^o$. Contrarily, the cross-principal plane is defined as being orthogonal to the principal plane.

Eventually, we define the **airmass**, or ν, that is the geometrical path length along the incidence and emergence directions through a planet's atmosphere such that:

$$\nu = \frac{1}{\cos(\theta_0)} + \frac{1}{\cos(\theta)}. \tag{1.1}$$

Following this expression, the airmass cannot be lower than 2. This extreme value corresponds to the case in which the sensor operates at nadir $\theta = 0^o$ and the Sun is at zenith $\theta_0 = 0^o$. Airmass increases as the angle between the source and the zenith, or the spacecraft and the zenith, increases too. In this thesis, the parameters g and ν will allow us to reduce the acquisition geometry triplet to two parameters or even a single one. This is useful in those cases in which three angles result too confusing or lower computational times become necessary. However, I stress that multiple combinations of Sun and view zenith angles may produce the same airmass, for example.

1.3.2.2. Units of hyperspectral images

To conclude with this section I define some of the units typically used for hyperspectral images. A more detailed look on the following physical concepts will be given in chapter 2. For a comprehensive reading on this subject I recommend the seminal work of Nicodemus in [133] or the most recent work

of Schaepman-Strub et al. in [154].

A hyperspectral imager senses the amount of reflected light that it receives from a planet in each wavelength band. In addition to surface reflectance, which exclusively depends on the surface properties and what we actually aim at retrieving, the spectral radiance measured by an orbital sensor depends on several aspects of the remote sensing chain, namely:

1. The spectrum of the input solar energy.
2. The geometry of illumination.
3. The interactions of this energy during its downward and upward passages through the atmosphere.
4. The characteristics of the sensor system.

The last aspect intervenes on board when the intensity of sensed radiation is transformed into digital number (DN) units. DNs are related to the intrinsic sensitivity of the instrument. Data preprocessing before the release of the data (see Part II) transforms DN units into radiance units. **Radiance** is a radiometric measure, noted L, that describes the amount of light that passes through or is emitted from a particular area and falls within a given solid angle in a specified direction. The units of radiance is watts per steradian per square meter $[Wsr^{-1}m^{-2}]$.

The first aspect of the list above is also typically considered in preprocessing steps by transforming radiances into I/F units. **I/F** units make data independent on the spectral properties of the light source, the Sun in the case of passive remote sensing (see Figure 1.12). In particular, I/F stands for the ratio of measured intensity to solar flux, where the **intensity** I $[Wsr^{-1}]$ is the measure of the energy flux $[W]$ per unit of solid angle $[sr]$ and the **solar flux** F $[W]$ is the rate of transfer of energy through a surface adjusted for the squared distance between the observed surface and the Sun. I/F units are $[sr^{-1}]$ and are used by several imaging spectrometers such as the CRISM instrument.

In order to take into account the decrease of energy as function of θ_0 (second aspect of the list above), **spectral reflectance** $r(\lambda)$ is defined as the fraction of incident radiation reflected by a surface to the incident irradiance (i.e. flux per squared meter) from a collimated source[2] as a function of wavelength λ. In order to transform I/F data into reflectance units, illumination conditions are typically taken into account making

$$r \approx q_L = \frac{I/F}{\cos\theta_0} = \frac{I/F}{\mu_0} \tag{1.2}$$

This expression weights the I/F data by the amount of received energy (e.g. the fainter light at high SZA is compensated by higher $1/\cos\theta_0$ values). If we assume equal scattering in all directions (i.e. **isotropic scattering**), a property only accomplished by the so-called **Lambertian surfaces**, the latter can be characterized by a reflectance value not depending on illumination direction called **Lambert albedo** or q_L [94]. In this thesis, we shall also use the term **apparent reflectance**, or R, to refer to Lambert albedos in order to emphasize that atmospheric effects have not yet been accounted for. Indeed, aspect number 3 of the list above shall be considered when performing atmospheric correction (see subsection 4.2.2 and Part III).

[2] **Collimated light** is radiation whose rays are nearly parallel defining a single illumination direction.

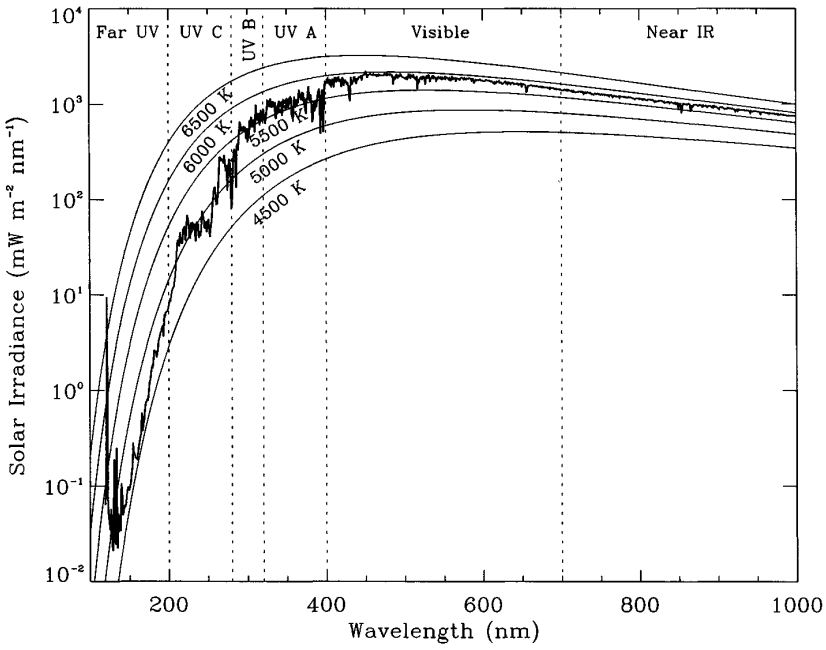

Figure 1.12.: Extraterrestrial solar irradiance E $[Wm^{-2}]$ measured by a spectrometer on board an Earth-orbiting satellite. The vertical lines divide the various spectral subranges that are typically defined in the literature. The smooth curves are calculated blackbody spectra for a number of emission temperatures. Credit: [170].

Nevertheless, most materials are, however, non-Lambertian and therefore their reflectance must be expressed depending on the directional distribution of incoming radiation and the viewing direction. This is done by defining the **bidirectional reflectance distribution function** (BRDF) that characterizes the scattering properties of a surface accurately. The BRDF is defined as the ratio of the reflected radiance $L(\theta_0, \theta, \varphi, \lambda)$ $[Wsr^{-1}m^{-2}]$, in an infinitesimal solid angle in the direction (θ_0, θ) to the incident irradiance at ground, $E(\theta_0, \lambda)$ $[Wm^{-2}]$ such that

$$f(\theta_0, \theta, \varphi, \lambda) = \frac{L(\theta_0, \theta, \varphi, \lambda)}{E(\theta_0, \lambda)} \left[sr^{-1}\right], \tag{1.3}$$

Unfortunately, BRDF values are not accessible directly by measurement in most field studies since natural light is not collimated but includes both direct solar and diffuse radiations [154]. In other words, in remote sensing problem we can only deal with the term $L(\theta, \varphi, \lambda)$ instead of $L(\theta_0, \theta, \varphi, \lambda)$. In this case, the unitless **hemispherical directional reflectance function** (HDRF) represents the accessible parameter, which means that the incident beam is integrated over the whole incident hemisphere Ω_+ such that

$$h(\theta, \varphi, \lambda) = \frac{L(\theta, \varphi, \lambda)}{\int_{2\pi} E(\theta_0, \lambda) \cos\theta_0 d\Omega_+}, \tag{1.4}$$

To conclude, I define a last parameter, namely the **spectral spherical albedo**. The also called bi-hemispherical reflectance is the ratio of reflected radiation to the incident irradiance at a given wavelength after integration in the upper incidence and emergence hemispheres. This measure is also called

Bond albedo and is measured on a scale from zero, for no reflecting power of a perfectly black surface, to unity, for perfect reflection of a white surface. The Bond albedo depends on the frequency of the radiation and is crucial to determine the energetic balance of an objet[3].

$$q(\lambda) = \frac{1}{\pi} \int_{2\pi} \int_{2\pi} f(\theta_0, \theta, \varphi, \lambda) \cos\theta_0 \cos\theta d\Omega_+ d\Omega_-. \tag{1.5}$$

1.3.2.3. Processing hyperspectral data

Hyperspectral imaging is used in a wide array of applications ranging from remote sensing of planetary surfaces to surveillance purposes on Earth. However, this type of images present some challenges for the analyst. While providing the fine spectral resolution needed to characterize the spectral properties of surface materials, the volume of data in a single scene may be overwhelming. Additionally, the difference in spectral information between two adjacent spectral bands may be apparently rather small. Nonetheless, embedded in these data there is critical information that can be used to identify the ground surface materials. Finding appropriate tools and approaches for visualizing and analyzing the essential information in a hyperspectral scene is an area of active research. Most approaches to analyze hyperspectral images concentrate on the spectral information in individual pixels, although spatial variations start being considered as well, creating advanced analysis algorithms. Here I briefly detail some of the principal families of analysis methods in hyperspectral imaging.

1. **Spectral classification** consists in the assignment of each spectrum in the image into classes such that spectra in the same class are similar in some sense. The use of conventional analysis methods is, however, not adequate for classifying high-dimensional data due to the so-called curse of dimensionality, referring to the fact that the classification problem becomes intractable as the number of spectral bands increases. Therefore, more sophisticated classifiers are considered such as those based on machine learning principles. Support Vector Machines (SVM) are the state of the art in this analysis field [23, 28]. Advanced classification methods are, however, often supervised, thus requiring ground truth to train the classifier. This represents a major drawback in planetary remote sensing as ground truth data are very scarce.
2. **Dimensionality reduction** algorithms aim at overcoming the curse of dimensionality by reducing the number of features (i.e. the spectral bands in the case of hyperspectral images) under consideration. This family of methods are divided into feature selection and feature extraction. The latter techniques have the capability to transform the data into a feature space in which resulting features may be more significant than those in the original spectral space. Dimensionality reduction techniques are useful in planetary sciences and shall be used in this thesis. A pair of examples are the classical Principal Component Analysis (PCA) and the Maximum Noise Fraction (MNF), the latter producing new features ordered according to signal-to-noise ratio (SNR) after two cascaded PCA transformations and a noise whitening step [67] (see section 14.1 for a detailed explanation of the MNF). In planetary sciences the PCA has been widely used to detect and map materials at the surface as it is done in [33, 141].

[3] Adapted from [133, 154].

3. **Spectral unmixing** is based on the premise that a scene is composed by a certain number of materials, or endmembers, with distinct spectral properties. When the spatial resolution is moderate, it is likely that more than one material contributes to an individual spectrum measured by the sensor. The result is a composite or mixed spectrum composed by a combination of the endmember spectra. Spectral unmixing aims firstly at identifying the endmember spectra, and secondly at unmixing each pixel spectrum to identify the relative abundances to each endmember material. Assuming a linear mixture model, each spectrum can be modeled as the sum of the fractional abundances multiplied by the corresponding endmember spectra. Spectral unmixing techniques based on the linear assumption are potentially interesting tools in planetary exploration as they are totally unsupervised and provide satisfactory results [143]. In addition, spectral unmixing techniques perform dimensionality reduction of hyperspectral images as they transform them into a few abundance images. The use of these techniques on planetary hyperspectral data shall be investigated in Part IV.
4. **Segmentation** aims at partitioning an image into multiple regions encompassing similar pixels. These techniques differ from classification approaches in the fact that they generally take into account the spatial information while the latter approaches are devised in a pixel-wise fashion. In addition, pixels classified as a same class do not necessarily have to form an ensemble of contiguous pixels while segmented regions are usually defined as spatially continuous segments. In hyperspectral imagery, classical segmentation techniques are improved by incorporating the spectral dimension [176]. Nonetheless, these techniques still are in an early stage of development and thus will not be considered in this dissertation.
5. **Anomaly detection** aims at detecting and identifying spatially resolved or unresolved objects on the basis of spectral signatures. If each material had a unique spectrum, the solution of detection and identification problems would be straightforward. Unfortunately, variabilities in material composition and atmospheric propagation, in addition to sensor noise, introduce random spectral variations. Also, for pixels containing unresolved objects, the measured spectrum includes a mixture of object and background contributions. Thus, every detection algorithm has to overcome two major obstacles, namely spectral variability and background interference [112]. The study of these techniques is not addressed in this thesis as they are more oriented toward Earth observation issues.

1.3.3. Imaging spectrometers

Hyperspectral images are produced by instruments called imaging spectrometers. The development of these complex sensors has involved the convergence of two related but distinct technologies: spectroscopy and imaging.

A **spectrometer** is an instrument used to measure the properties of light over a specific range of the electromagnetic spectrum. Spectrometers are typically used in spectroscopic analysis to identify different types of materials by their spectral properties. A single-shot spectrometer generates a spectrum according to wavelength, or wavenumber, after the incident light from the target goes through a slit, is scattered according to wavelength using a diffraction grating and is eventually projected onto a line of photodetectors, each one receiving a given wavelength (see Figure 1.13).

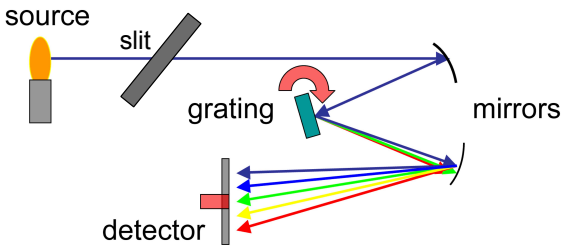

Figure 1.13.: Scheme of a spectrometer.

An **imaging spectrometer** is an instrument used in hyperspectral imaging to acquire a spectrally resolved image of the observed scene. The operating principle is the same than that of single-shot spectrometers with the expansion of the acquisition to two spatial dimensions thanks to a mechanical system and/or the use of a two dimensional matrix of detectors. Due to this technological improvement, imaging spectrometers offer advanced spatial performances whereas accurate calibration to avoid optical aberrations becomes sometimes challenging. Examples of the most common types of imaging spectrometers used in planetary sciences and Earth observation include the whiskbroom scanner and the pushbroom scanner. Since this thesis exclusively focuses on imaging spectrometers, I therefore may often use the term spectrometer instead of imaging spectrometer for brevity.

- **Whiskbroom sensors**, also known as cross-track scanners, acquire a series of lines (i.e. an image) in the direction perpendicular to the satellite orbital motion based on a single-shot spectrometer and a mechanical system. First, a limited set of detectors, sensitive to a specific wavelength range, captures the radiation reflected by the planet at one edge of the swath. The remaining points of the swath are then sensed thanks to a continuously rotating mirror (see Figure 1.14). The motion of the spacecraft allows the scanning of the next line at ground. As Figure 1.14 illustrates, the **field of view** (FOV) of the scanner is set by the length of the sweep. Since each scan line at the ground consists of multiple ground cells to be sensed, the resulting dwell time for each ground cell, characterized by its **instantaneous FOV** (IFOV), is very short, compromising the related SNR of the resulting hyperspectral image.

  Under this design, whiskbroom sensors achieve high spectral and spatial uniformity if long integration times are available. Therefore, these scanners are more appropriate for airborne rather than orbiting platforms, as the limited integration time of the latter spacecrafts due to the higher speed on ground may result in inadequate SNR performance. However, a whiskbroom scanner owns a single linear photodetector array and thus careful calibration of the response of each detector element suffices to eliminate most artifacts. The whiskbroom approach is implemented on the terrestrial Airborne Visible Infrared Imaging Spectrometer (AVIRIS) sensor, which is a standard of high-accuracy hyperspectral imager. In planetary exploration, the SWIR channel (0.93-5.1 μm) of the OMEGA instrument operates in the whiskbroom mode. In this case, a scanning mirror in front of the telescope provides cross-track swaths 16-128 pixels wide corresponding to a maximum FOV of 8.8°.

- **Pushbroom sensors**, or along-track scanners, differ from the whiskbroom design in the replacement of the rotating mirror by an array of detectors that capture simultaneously a single scan line at ground. Each row of the two-dimensional detector array used in pushbroom scanners is indeed an independent spectrometer. The detector array is typically a charged-coupled device

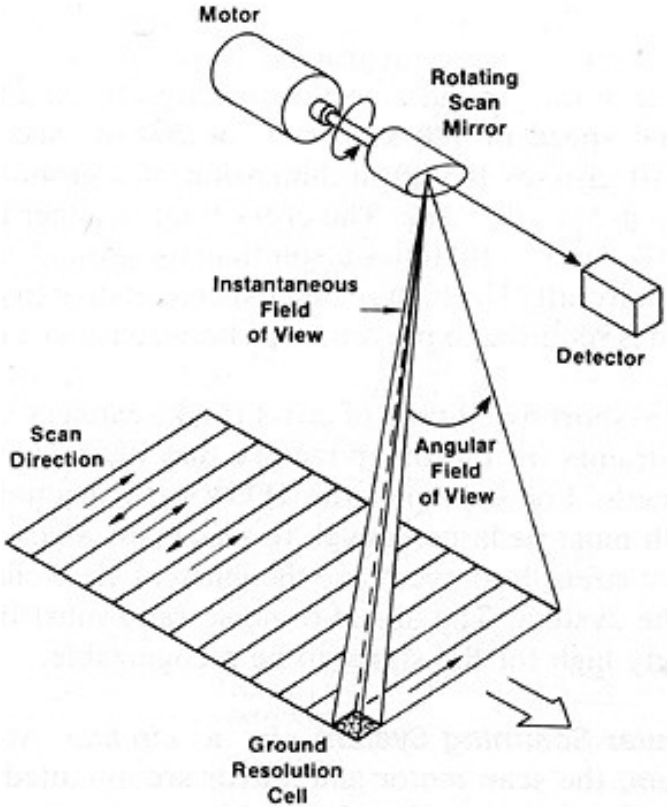

Figure 1.14.: Scheme of a whiskbroom scanner.

in which one axis corresponds to the cross-track dimension and the second to wavelength (see Figure 1.15 for a scheme). The number of cross-track pixels is equal to the number of ground cells for a given swath, and thus defines the FOV of the sensor. Similarly to whiskbroom scanners, the motion of the spacecraft provides the along-track dimension of hyperspectral images. Pushbroom scanners are the standard for orbital imaging spectrometers as integration times are longer than in the whiskbroom concept, and thus the SNR performances. Examples of pushbroom scanners in planetary sciences are the VNIR channel (0.38-1.05 μm) of the OMEGA instrument and the CRISM imaging spectrometer.

While pushbroom spectrometers offer excellent performances regarding SNR, spatial alignment and spatial resolution, I highlight other intrinsic problems. In particular, these scanners are affected by non-uniformities of their spatial-spectral detector matrix. For example, it would be desirable to have the same point spread function (PSF), or spectral response, for all detectors in a given row of the array, that is to say, the detectors belonging to the same wavelength. That of course is not straightforward as it multiplies the already demanding whiskbroom calibration procedure by the number of spatial pixels, typically several hundreds. In this thesis I shall address the compensation of a typical artifact of pushbroom sensors in subsubsection 4.1.2.1. To conclude I recommend the reader the seminal work of Mouroulis et al. for an in-depth outlook on pushbroom-type imaging spectrometers [123].

In the following section I describe the CRISM imaging spectrometer that constitutes the main instrument of study in this thesis.

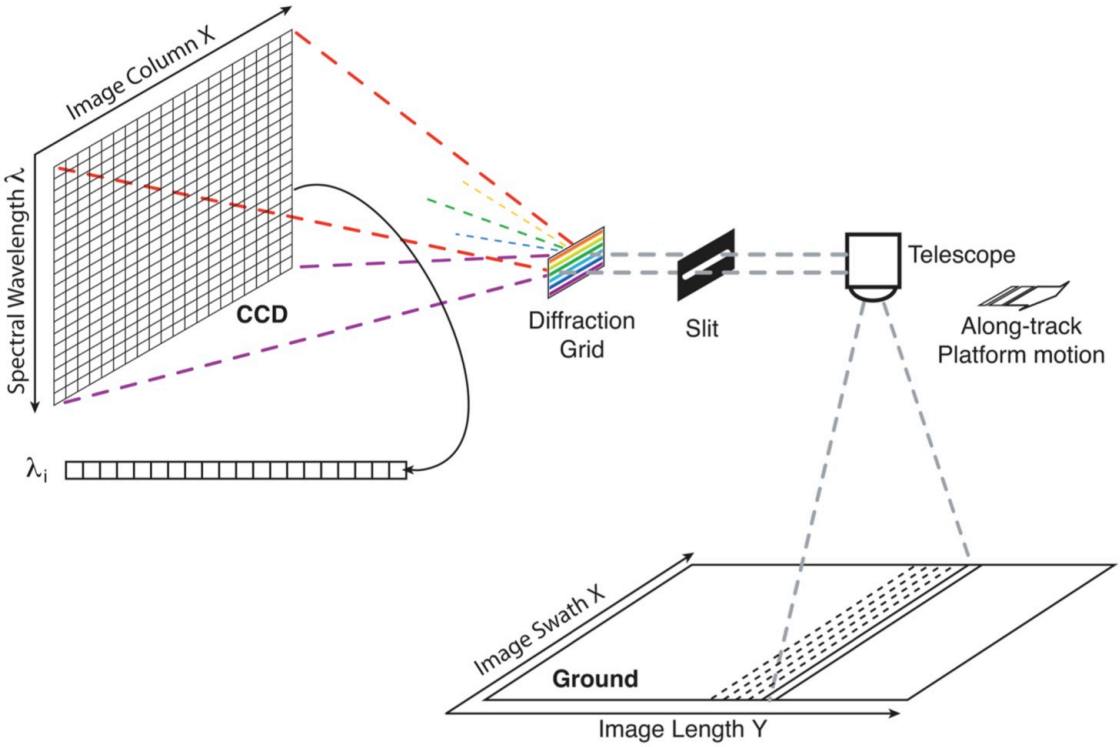

Figure 1.15.: Scheme of a pushbroom scanner. Credit: [7].

1.4. Description of the CRISM instrument

The Compact Reconnaissance Imaging Spectrometer for Mars is a visible and infrared imaging spectrometer operating around Mars aboard MRO since November 2006. CRISM was designed, built, and tested by the Johns Hopkins University Applied Physics Laboratory under the supervision of principal investigator Scott Murchie. The present Ph.D. dissertation is focused on the remote sensing of Mars made possible through CRISM and therefore this instrument constitutes a keystone of it. In the following, I provide a summary of the design, attributes and functioning of the CRISM instrument. For further reading on this sensor, I recommend the main article on CRISM of Murchie et al. [126].

The scientific objectives of the CRISM instrument are summarized as follow:

1. To map the entire surface using a subset of bands to characterize crustal mineralogy.
2. To map the mineralogy of key areas at high spectral and spatial resolution.
3. To measure spatial and seasonal variations in the atmosphere.

In addition, CRISM is being used to identify locations on Mars that may have hosted water. In fact, the seek for evidence of aqueous or hydrothermal activity is one of the major goals of the MRO mission [192]. CRISM addresses this problem by mapping the presence of minerals and chemicals that may indicate past interaction with water such as iron and oxides, which can be chemically altered by water, and phyllosilicates and carbonates, which form in the presence of water. All these materials have characteristic fingerprints in their visible and infrared spectra that are readily seen by CRISM. In addition, CRISM monitors CO_2 and H_2O seasonal deposits at the surface and dust and water ice particles in the martian atmosphere to study the martian seasons and climate.

In order to achieve the mentioned objectives, the CRISM imaging spectrometer senses the electro-

magnetic spectrum from 362 to 3920 nm in more than 500 spectral bands. CRISM is designed as a combination of three assemblies. The largest, the Optical Sensor Unit (OSU), contains optics, detectors, radiators, and a cryogenic system, all of which can be gimbaled, or pivoted, to track the martian surface. A Data Processing Unit (DPU) provides power, command and control, and data editing and compression, and the Gimbal Motor Electronics (GME) runs the gimbal. A close-up of the three assemblies is given in Figure 1.16.

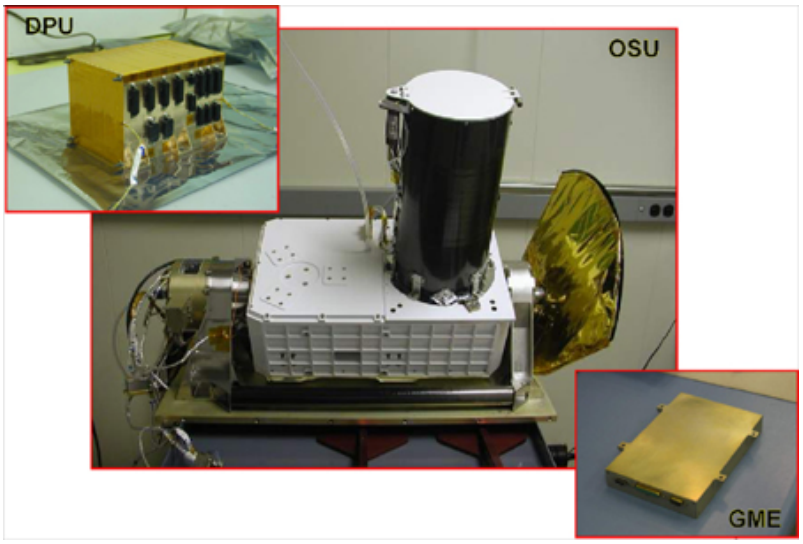

Figure 1.16.: Picture of the three main assemblies of CRISM, namely OSU, DPU and GME. Credit: http://crism.jhuapl.edu/instrument/innoDesign.php.

Being this thesis on remote sensing, I focus on the OSU, containing two pushbroom imaging spectrometers. After the light passes through a common telescope and slit, a beam splitter directs it to two independent diffraction gratings with separate detectors. In each spectrometer, a scan line of the planet is dispersed into its component wavelengths that are projected onto different rows of that spectrometer's 2D detector. One spectrometer uses an array of silicon photodiodes to capture hyperspectral images covering the wavelengths 362-1053 nm. In this thesis, I shall denote this spectrometer as **VNIR channel**. The other spectrometer uses an array of HgCdTe diodes to take hyperspectral images at 1002–3920 nm. I will denote this spectrometer as **IR channel**. Both VNIR and IR channels sample the electromagnetic spectrum at an average step of 6.55 nm per detector row, that is to say, two contiguous spectral bands are separated by only $\Delta\lambda = 6.55$ nm, $\Delta\lambda$ constituting the **spectral sampling** of CRISM. Both detectors have a 640×480 (spatial×spectral) format, giving acquisition scan lines one-pixel high and 640-column wide. Each element of this line contains a data spectrum. Similar to other pushbroom scanners, CRISM constructs a hyperspectral image by stacking multiple scan lines as MRO flies over the surface. When the MRO spacecraft is at an altitude of 300 km, each CRISM line scan on the Martian surface is about 18 meters long (the maximum **spatial resolution** of CRISM) and ~11 km across. The latter figure results in a FOV of 2.1°. This and other technical attributes of the CRISM instrument are summarized in Table 1.2 along with a comparison with those of its ancestor, the imaging spectrometer OMEGA.

As support to following sections, I briefly detail the spectral attributes of CRISM. In order to distinguish spectrally similar materials at the surface, adequate spectral resolution is necessary. This requires not only a high spectral sampling but a sufficiently high spectral resolution. **Spectral resolution** is set

Attribute	CRISM	OMEGA
Spectral range	0.36-3.92 μm	0.38-5.10 μm
Spectral sampling	6.5 nm (544 bands)	13.4 nm (352 bands)
Spectral resolution	FWHM = 8-15 nm	FWHM = 7-20 nm
Spatial resolution	> 18 m/pixel	> 350 m/pixel
Signal-to-noise ratio	> 100 dB	> 100 dB
Field of view	2.1°	8.8°

Table 1.2.: Technical attributes of the imaging spectrometers CRISM and OMEGA.

by the full-width at half maximum (FWHM) of the instrument spectral response, or PSF. CRISM was designed such that FWHM is 8±2 nm and 10-15±2 nm across the FOV in the VNIR channel and the IR channel, respectively. The broader spectral responses correspond to the off-axis detectors. The point spread function $PSF(\lambda)$ of the elements of the detector array were determined by pre-launch calibration and modeled by a 3-Gaussian function such that

$$PSF(\lambda) = \sum_{i=1}^{3} \alpha_i e^{-\gamma_i(\lambda-\Lambda_i)^2} \tag{1.6}$$

where the three values of terms α_i, γ_i and Λ_i are unique to each position of the detector matrix and are stored in calibration data records as it will be further detailed in Part II.

The CRISM instrument has two modes of functioning:

- In the multispectral **untargeted mode**, CRISM senses the martian surface using fixed pointing (i.e. the gimbal is disabled) and 72 of its 544 spectral bands at a resolution of 200 m/pixel. This spatial degradation is performed by an internal ×10 spatial pixel binning. CRISM mapped half of the planet Mars in this mode within the period from June to September 2007 (see Figure 1.17) [128]. The untargeted mode is meant to identify new scientifically interesting locations to be further investigated by the targeted mode. The untargeted multispectral mode is, however, not considered in this thesis.
- In the hyperspectral **targeted mode**, the CRISM spectrometer measures energy covering 0.36-3.92 microns using all 544 spectral bands. In targeted observations the gimbal is used to track a point on the surface and prevent smear from motion of the spacecraft. If the surface is scanned at the full spatial resolution of 18 m/pixel, the product is called "**full-resolution targeted**" (FRT). Alternatively, spatial resolution can also be set to 36 m/pixel using a 2× binning, producing products named "half-resolution short" (HRS) or "half-resolution long" (HRL). Ten additional abbreviated, 10× spatially binned images are taken before and after the main image, or **central scan**, providing measurements of the same scene with different path lengths through the atmosphere. This sequence of multiple measurements at different geometries is called an **emission phase function** (EPF). As I show in Part III, when analyzed using a radiative transfer model that incorporates a model of surface scattering and wavelength-dependent attenuation by atmospheric gases and aerosols, the combination of the main image and the EPF allows separation of atmospheric and surface contributions. As mentioned before, the multi-angle properties of the CRISM instrument represent its main innovative attribute along with its high spatial resolution.

Figure 1.17.: Coverage by multispectral survey data acquired during the primary science phase. Credit: [128]

Targeted observations are aimed to specific martian sites whose scientific interest requires a more in-depth investigation than that made possible by untargeted observations. Figure 1.18 details the coverage of this type of products during the primary science phase.

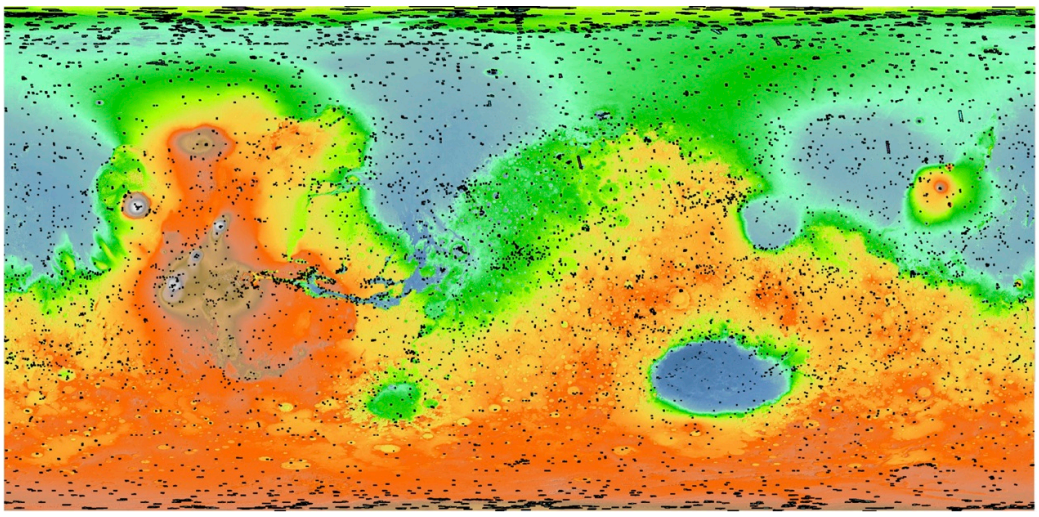

Figure 1.18.: Coverage of Mars by CRISM targeted observations taken during the primary science phase, indicated by black symbols overlain on a color-coded MOLA elevation map in which redder colors indicate higher elevations. Credit: [128]

In this dissertation, I define the set of eleven hyperspectral images taken during the gimbal's tracking of a target as a **CRISM multi-angle observation**, or simply CRISM observation. Each one of the eleven hyperspectral images are referred to as **CRISM scans**, or simply CRISM images.

In Figure 1.19, I detail the acquisition geometry of a targeted observation. The eleven scans forming the observation are numbered in hexadecimal notation, that is, '01', '02', '03', '04', '05', '07', '09', '0A', '0B', '0C', and '0D'. The central scan '07' corresponds to the main image at full spatial resolution while the rest form the bracketing EPF. Scans with labels '06' and '08' are not data images as they correspond to shutter close measurements that are used to calibrate in-flight internal noise (see Part II). According

to the motion of MRO, EPF scans from '01' to '05' correspond to the **inbound direction** while those ranging from '09' to '0D' are related to the **outbound direction**. Typically, the relative azimuth φ in a CRISM observation presents two main values, or modes, one for the inbound direction $\varphi_{inbound}$ and another for the outbound direction $\varphi_{outbound}$. The central scan '07' is divided by the two **azimuthal modes** as the border between them happens for the central scan lines acquired at nadir, $\theta \approx 0^{o}$. Regarding the VZA, targeted images present variations by more than 70^{o} between the most extreme scans, '01' and '0D', and the central scan '07'. Regarding the main image '07', variations of 30^{o} in VZA are expected. This attribute of CRISM is driven by the combination of the gimbal and the motion of MRO (see Figure 1.19) and represents an unprecedented opportunity to study Mars from a multi-angular point of view.

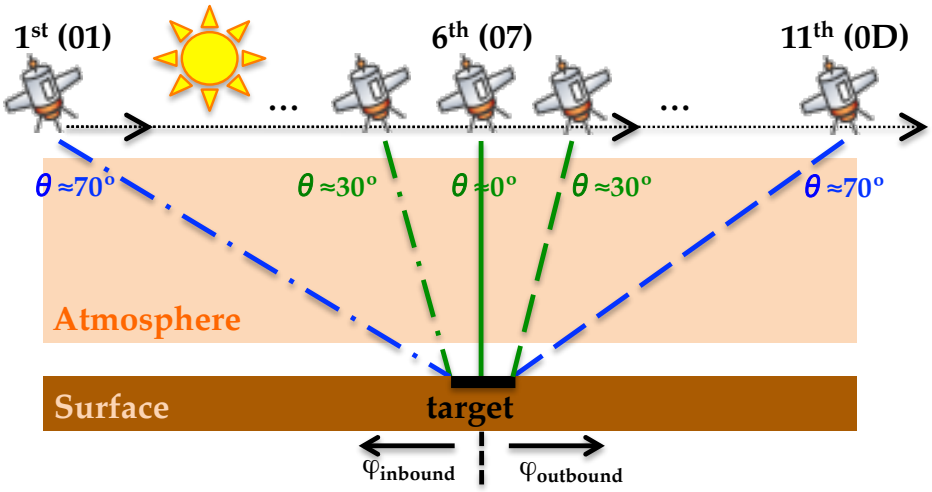

Figure 1.19.: Scheme of a targeted observation acquired by the CRISM sensor. Only three scans out of the total eleven are shown in this figure. Green color corresponds to the central scan at high resolution '07' while the presented EPF scans, '01' and '0D', are detailed in blue. Dash-dotted lines correspond to the first scanned line of a CRISM image. Conversely, dashed lines indicate the last line that is sensed. All scans are acquired as a combination of the gimbal and the MRO motion. In the quasi-nadir central scan, viewing angles can range from 0^{o} to 30^{o}.

Figure 1.20 shows the difference in spatial resolution between the central scan and the accompanying EPF. The bracketing images are indeed degraded aboard MRO by a binning factor of 10 in order to reduce the size of the images before sending them to Earth. Indeed, the EPF was originally intended exclusively for atmospheric studies and thus the higher heterogeneity of the surface was not meant to be preserved [126]. This attribute will represent a limitation when exploiting CRISM multi-angle observation for studying the surface in Part III. As it can be seen in Figure 1.20, all eleven scans are projected onto a map space. Originally, each CRISM scan is, however, released in the **image space**, which is defined by the width of the detector matrix and the scanning time of a CRISM image both divided by the binning factor (i.e. typically 640×420 pixels for a FRT central scan and 15×60 pixels for the EPF individual images). Each CRISM image comes with an ancillary data set containing the acquisition and geographic attributes of each pixel, among other information. In particular, each pixel is characterized by its latitude, longitude and acquisition angular triplet (θ_0, θ, φ) by the information enclosed in the corresponding **Derived Data Record** (DDR) that accompanies each CRISM image. In this way, the data in the image space can be projected onto a **map space** (i.e. the one defined by

the latitude and longitude dimensions and by a given projection system) by placing each pixel in its geographic coordinates.

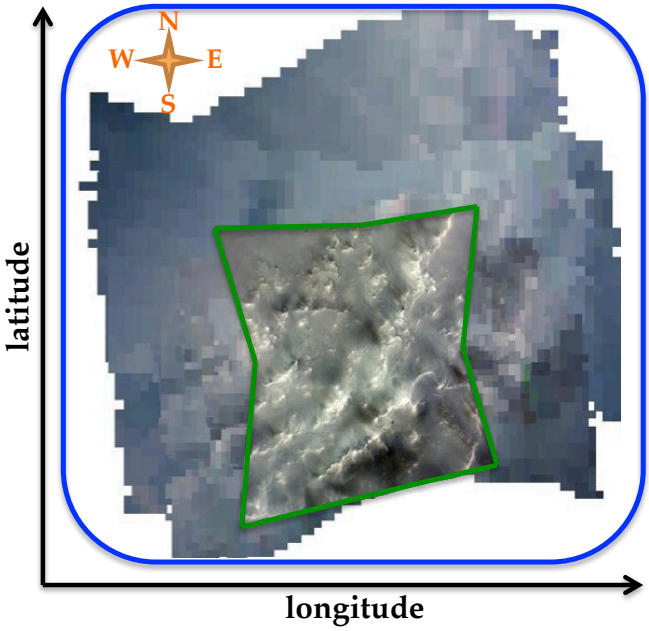

Figure 1.20.: Projection onto the map space of the eleven scans of a CRISM observation. Note the different coverage and footprint of the different eleven hyperspectral images. Also, remark the higher spatial resolution of the central scan (encompassed by a green line) in front of the accompanying EPF (embraced by a blue box).

In conclusion the CRISM instrument represents an unprecedented tool to study the planet Mars, especially because of its unprecedented multi-angle capabilities. Extraction of mineralogically useful spectral data at high spatial and spectral resolution requires high SNR, which is met by CRISM thanks to its pushbroom concept. In general most requirements that were set up by the CRISM team are satisfied. However, Murchie et al. argue that there are some cases in which small deviation in actual performance are expected [126]. These limitations are greatly overcome by the data pipeline undergone by CRISM data before being released to the scientific community. After this data pipeline, targeted observations are called Targeted Reduced Data Records (TRDR), namely radiometrically calibrated CRISM spectra. For the majority of the length of this Ph.D., the version of the data pipeline has been TRDR version 2 (**TRDR2** for brevity) while some products with the improved TRDR version 3 (**TRDR3** for brevity) started to be released in the previous months of the writing of this dissertation. Unfortunately, some residual anomalies coming from intrinsic limitations of CRISM are not fully resolved in the TRDR products and thus may compromise the radiometric quality of the data. These issues shall be addressed in Part II.

2

Radiative transfer

In the present chapter I provide an introduction to the interaction between surface, atmosphere and radiation. The following notions represent the basis of the atmospheric correction of remote sensing data that will be addressed in Part III. For this purpose I describe the absorption and scattering processes affecting the solar electromagnetic radiation in its path across the atmosphere toward the sensor. A brief description of atmospheric components, namely gases and aerosols, is given as well as their influence on radiation. The mathematical formulation of the macroscopic radiative transfer (RT) is then detailed. Eventually, I discuss on different models of the surface bidirectional reflectance. For a more complete outlook on RT in planetary atmospheres I recommend to the reader the seminal and comprehensive book of Thomas and Stamnes [170].

2.1. Extinction in the atmosphere

The atmosphere of Mars can be considered as a series of parallel atmospheric layers, each layer containing a mixture of gas and aerosols that define the optical thickness of the layer. The **optical thickness**, or depth, or opacity, is a measure of transparency of a medium related to the fraction of radiation that goes directly through the atmosphere without finding any obstacle. The other fraction of radiation is said to be extinct, or attenuated. **Extinction** is the result of two different phenomena, absorption and scattering. In this thesis we consider that there is no emission by particles. All these concepts are defined below. The optical depth therefore expresses the quantity of light removed from a beam by scattering or absorption during its path through a medium as Figure 2.1 illustrates.

If $E_0(\lambda)$ is the irradiance of radiation at wavelength λ at the top of the atmosphere (TOA), and $E_d(\lambda)$ is the direct irradiance at the surface after a given atmospheric path (see Figure 2.1), the intrinsic optical

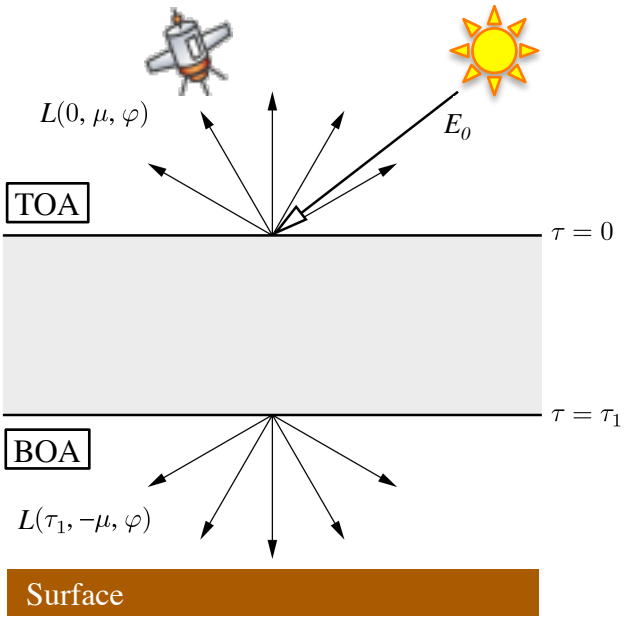

Figure 2.1.: Scheme of a single-layer atmosphere characterized by its intrinsic optical thickness τ_1. E_0 is the incident irradiance on the layer that is partially transmitted downward after going through extinction. $L(\tau_1, -\mu, \varphi)$ is the radiance incident on the surface. The upward radiance $L(0, \mu, \varphi)$ results from the transmitted radiation that has been previously reflected on the surface and from the solar irradiance reflected by the atmosphere alone. The two vertical positions TOA (**top-of-atmosphere**) and BOA (**bottom-of-atmosphere**) are depicted.

depth $\tau(\lambda)$ of the medium is defined as

$$E_d(\lambda) / E_0(\lambda) = e^{-\tau(\lambda)}. \tag{2.1}$$

In this way $\tau(\lambda) \ll 1$ when the atmosphere is transparent and $\tau(\lambda) \gg 1$ when it is opaque. I stress that the previous expression is only true for the coherent direct fraction of the irradiance along the incident direction and not for the incoherent part resulting from the multi-scattering of the former.

2.1.1. Atmospheric absorption

Absorption is the process by which incident radiant energy is retained by the atmosphere. When the atmosphere absorbs energy, the result is an irreversible transformation of radiation into another form of energy, typically heat. This energy is transformed according to the nature of the absorbent medium.

A large fraction of the absorbed light in the atmosphere is due to atmospheric gases since aerosols are related to a **single scattering albedo** close to unity in the SWIR (our preferred spectral range in this thesis)[1]. The atmosphere of Mars consists of 95% carbon dioxide, 3% nitrogen, 1.6% argon and contains traces of oxygen and water. Out of the optically active molecules, CO_2 is the most influencing component due to its predominance in the atmosphere and its numerous absorption bands in the

[1]Single scattering albedo is the ratio of scattering efficiency to total extinction efficiency. A single scattering albedo close to unity implies that almost all particle extinction is due to scattering. Conversely, a single scattering albedo of zero implies that all extinction is due to absorption.

visible, NIR and SWIR spectrum. A typical **transmittance** (i.e. the fraction of incident light that passes through a medium) spectrum of gaseous carbon dioxide is plotted in Figure 2.2 in the SWIR region covered by the IR channel of CRISM. The main absorption bands due to carbon dioxide are pointed out. These often strong absorption features modulate the radiation leaving the surface that is eventually sensed at the TOA by imaging spectrometers.

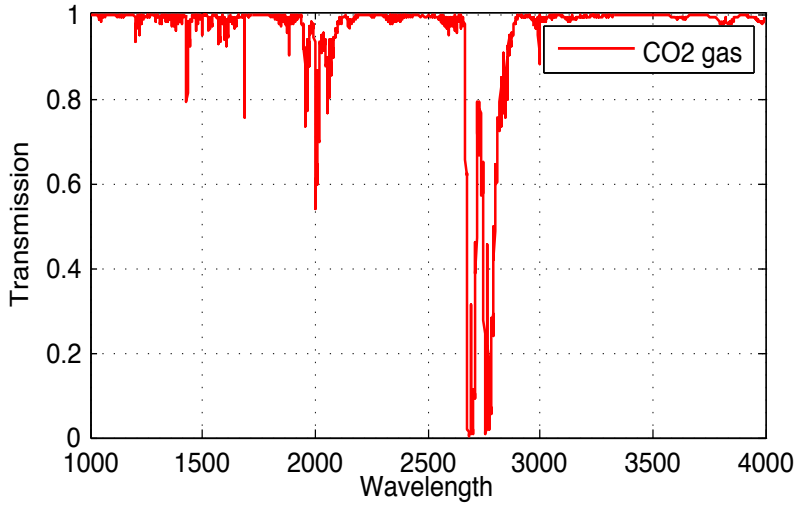

Figure 2.2.: Typical one way transmission spectrum through the CO_2 dominated martian atmosphere in the near-infrared range.

In this context the absorption of gases is typically expressed by the **transmission function of the atmosphere** $T_{gaz}(\lambda)$ along a single vertical path depending on wavelength. On Mars this term can be approximated by the transmission of the gaseous CO_2 after accounting for the elevation of the target (i.e. the lower the elevation, the thicker the atmosphere). Atmospheric transmission functions are used in the literature to take into account the impact of gases on TOA radiance and therefore shall be considered in the atmospheric correction algorithms proposed in subsection 4.2.2 and Part III.

2.1.2. Atmospheric scattering

Scattering is the process by which small particles suspended in a medium of a different **refractive index**[2] diffuse a portion of the incident radiation in other directions. Contrarily to absorption, scattering does not involve an energy transformation but a change in the directional distribution of it. In the atmosphere of Mars light is mainly scattered by **aerosols**, suspended particulates about 1.5 μm in diameter which give the Martian sky an orange-brown color when seen from the surface (see Figure 2.3).

Scattered, or diffuse, radiation results from collisions of photons with atmospheric particles. Assuming that the shape of these particles is spherical and much smaller than the radiation wavelength, this extinction phenomenon can be evaluated using the Maxwell equations. John William Strutt, most known as Lord Rayleigh, proposed in 1871 a solution based on this hypothesis [147]. This solution explains the blue color of the sky on Earth, for instance.

[2]The refractive index of a substance is expressed as a ratio of the speed of light in vacuum relative to that in the considered medium.

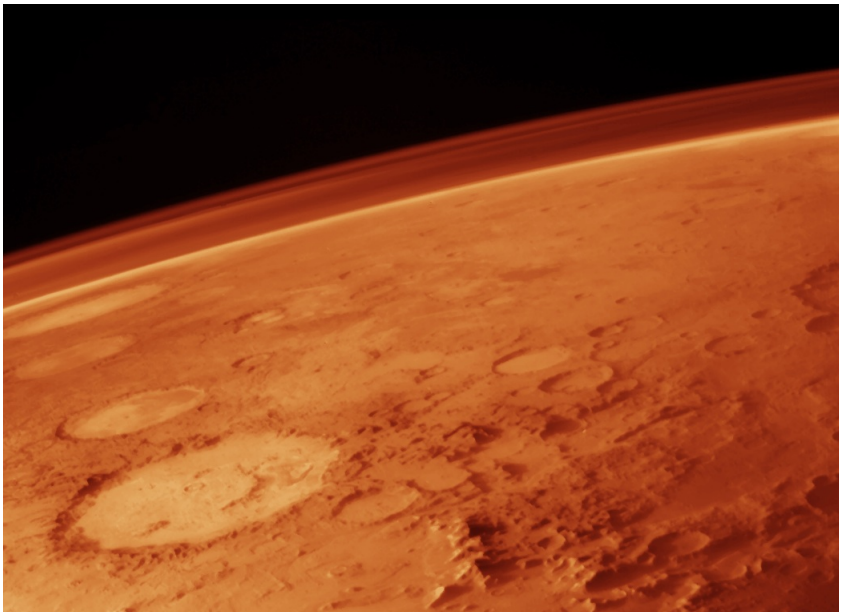

Figure 2.3.: The tenuous atmosphere of Mars, visible on the horizon in this low-orbit photo taken by the Viking Orbiter.

The Rayleigh theory is, however, not valid when the particle size is similar to the incident radiation wavelength. Lorenz and Mie independently developed a similar and more general theory in 1890 and 1908, respectively, relying on classical electromagnetic equations with continuity conditions at the boundary between the particle and its surroundings. The Lorenz-Mie, or simply Mie, scattering theory derives a solution for the interaction of a plane wave with an isotropic homogeneous sphere, although the theory can be extended to any size and some shapes of regular geometry[120].

The effect of particle size on scattering is inferred by a physical term called **size parameter** x. In the case of a spherical particle it is defined as the ratio of the particle circumference to the incident wavelength λ such that $x = 2\pi r/\lambda$, where r is the particle radius. If we define λ in meters, three cases are defined such that (i) when $x \ll 1$, scattering is well explained by the **Rayleigh theory**, (ii) when $x \gg 1$, scattering is analyzed by means of classical **geometric optics**, and (iii) in the intermediate case, scattering is interpreted by the **Mie theory**. Figure 2.4 details the shape of scattering in each case. Even though the nature and the shape of the atmospheric aerosols is highly variable, the Mie theory is usually employed for the study of their radiative properties.

In those media with a high concentration of scatterers the photons scattered by a particle are likely to collide with other ones, a process called multiple scattering. **Multiple scattering** happens when radiation is scattered more than once, making that some of the incident light that has been first scattered away from a single direction may reappear in this direction. Multiple scattering is the source of **diffuse radiation**. This is an important process for the transfer of radiant energy in the martian atmosphere, especially when aerosols are involved.

Two parameters must be introduced to quantify the scattered light, the phase function $P(g)$, and the scattering cross section σ_s. The **phase function** describes the spatial distribution of the scattered

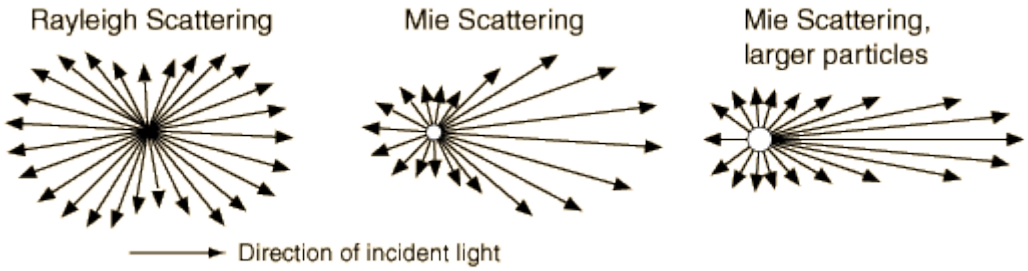

Figure 2.4.: The scattering from molecules and very tiny particles is predominantly Rayleigh scattering. For particle sizes larger than a wavelength, Mie scattering predominates. This scattering produces a pattern like an antenna lobe, with a sharper and more intense forward lobe for larger particles. Note that the scattering in larger particles tend to a simple reflection and refraction of light explained by geometric optics.

radiation. It is normalized in the way

$$\int_{4\pi} P(g)\, dg = 4\pi, \tag{2.2}$$

where g is the phase angle defined in subsection 1.3.2. Phase functions can also be defined depending on the **scattering angle** Θ, which is simply equal to $\pi - g$.

A widely used phase function is the so-called **Henyey-Greenstein function** [74]. This expression was originally devised to mimic the angular dependence of light scattering by small particles of interstellar dust clouds. The Henyey-Greenstein scattering function is determined by the anisotropy factor ξ and has proved to be useful in approximating the angular scattering dependence of single scattering events in many fields (see Figure 2.6 for a couple of phase function examples). The Henyey-Greenstein function is expressed as

$$P_{HG1}(g) = \frac{1-\xi^2}{[1+2\xi\cos g+\xi^2]^{3/2}}, \tag{2.3}$$

However, the previous function only allows a single scattering lobe. In order to consider phase functions with two scattering lobes, Henyey and Greenstein proposed the 2-lobe phase function such that

$$P_{HG2}(g) = c\frac{1-b^2}{[1-2b\cos g+b^2]^{3/2}} + (1-c)\frac{1-b^2}{[1+2b\cos g+b^2]^{3/2}}, \tag{2.4}$$

In this case b is the asymmetry parameter describing the width of both lobes. This term ranges in $0 < b < 1$, larger b values corresponding to narrower and greater lobes. The backward scattering fraction c is also comprised in the interval $0 < c < 1$. If $c > 0.5$ the particle is predominantly backscattering, whereas $c < 0.5$ implies predominant forward scattering. There exist several conventions respecting the b and c parameters. In this thesis I use the convention used by many authors such as Cord et al. in [40].

The **scattering cross section** represents the amount of incident energy that is removed from the original direction because of a single scattering event such that the energy is redistributed on the area of a sphere whose center is the scatterer and whose radius is r. The scattered intensity is proportional to those variables, and can be expressed, for molecules and aerosols, by

$$I(\Theta, \lambda) = I_0 \frac{\sigma_s}{4\pi r^2 \lambda^4} P(\Theta). \tag{2.5}$$

where I_0 is the intensity of the incident radiation.

As I mentioned before martian aerosols are the principal scattering elements in the atmosphere of Mars. This is especially true in the NIR and SWIR range where Rayleigh scattering coming from martian gases is negligible because of a faint atmosphere (~6 mbar of pressure on average at the martian surface) and because the fact that scattering cross section falls off as λ^4. In this thesis we therefore define the **aerosol optical thickness** (AOT) as the value resulting from integrating the optical thickness exclusively due to aerosols along the vertical of the atmosphere. This parameter, namely $\tau_{aer}(\lambda)$, is usually calculated at reference wavelength 1 μm in which the transmission of martian gases is roughly 1. This integration along the vertical is adequate because the atmosphere is usually well mixed. In this way $\tau_{aer}(\lambda)$ characterizes the degree of transparency of the whole atmosphere outside the absorption bands of the gases.

2.1.3. Martian aerosols

The influence of the atmosphere on radiation leaving the surface demands an adequate characterization of atmospheric aerosols. In this way the corresponding attenuation and scattering contribution to the measured TOA radiances can be compensated by atmospheric correction algorithms. Figure 2.5 gives an example on the effect of martian mineral aerosols on a typical H_2O ice spectrum in the SWIR.

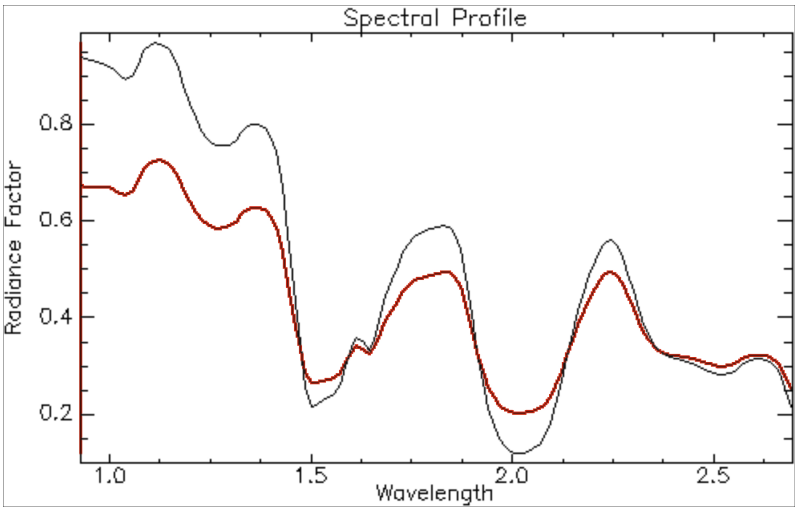

Figure 2.5.: Effect of heavy aerosol content on a NIR spectrum of water ice. The black line corresponds to an opacity $\tau_{aer} = 0.1$ while red line is associated to a thicker atmosphere $\tau_{aer} = 2$. Note the decrease in spectral contrast affecting the ice spectrum. As a matter of fact, aerosols make bright surfaces to look darker and dark surfaces to look brighter.

The atmospheric dust drifting over Mars is a key radiative factor in the heating of the atmosphere and plays an important role in radiative and dynamical models of the martian atmosphere [134]. These suspended particles are related to different sizes, origins and optical properties, as well as to strong spatial and temporal variability. While martian gases are well-known, scattering by martian aerosols is still largely unknown. Indeed, optical properties of martian aerosols such as the scattering phase function are still somewhat imprecise. Furthermore, the typically strong forward component of aerosol scattering makes RT modeling difficult. A correct parametrization of aerosols is crucial for atmospheric modeling and, thus atmospheric correction[3].

Recent studies have improved our understanding on the optical properties of Martian mineral aerosols [93]. In some cases composition, shape, size distribution, and phase function are evaluated in the visible and infrared using multi-instrumental observations at nadir or limb (i.e. $\theta \approx 90^{o}$). This is achieved by considering the particles to be homogeneous and using models of regular geometries such as spheres or cylinders. Orbital observations are then inverted based on these models using numerical algorithms founded on the Mie theory or the T-Matrix method, the latter approach being used for light scattering by non-spherical particles.

Clancy and Lee characterized the radiative properties of martian aerosols using EPF data from the Infrared Thermal Mapper and the Thermal Emission Spectrometer of the Viking orbiters [34]. Contrarily, a complete scattering model for the martian aerosols is developed by Drossart et al. using quasi-nadir ISM/Phobos-2 observations [56]. This model was corroborated later on by the independent study of Erard et al. using multi-angle ISM data [59]. Another approach consists in constructing a synthetic model of the aerosol optical properties based on experimental data. In this matter Ockert-Bell et al. addressed the characterization of absorption and scattering properties (e.g. single scattering albedo and phase function, among other parameters) of martian suspended dust using Viking lander images and a 1-lobe Henyey-Greenstein phase function with $\xi = 0.63$ [134]. Similarly, Tomasko et al. exploit the upward-viewing geometry of the Imager for Mars aboard the rover Pathfinder to estimate the aerosol properties minimizing the impact of the surface [173]. Almost ten years later, Vincendon et al. use the same scattering model than Ockert-Bell's based on orbital OMEGA observations [180, 181]. This phase function is, however, valid only for the phase angle range spanned by OMEGA nadir observations as the Henyey-Greenstein function proves to be somewhat inaccurate for the broader CRISM angular operating range. In this thesis I favor the optical properties retrieved in the CRISM spectral range by Wolff et al. in [187] using CRISM multi-angular observations. In this case a non-parametric phase function based on cylindrical particles is considered (see Figure 2.6). Nonetheless, Wolff et al. stress that such radiative properties may be specific to the very dusty observations that were used for their inversion and therefore may be somewhat incorrect under other atmospheric conditions.

This section is concluded by defining the **adjacency effect** that will be mentioned in **Part IV**. Aerosol scattering implies that the signal received by a satellite is a combination of the radiance leaving the target pixel and radiance from surrounding pixels. Because the apparent signal at the TOA of a pixel comes also from adjacent pixels, this effect is called adjacency effect [178].

[3] Although water ice crystals may also be frequently present drifting over Mars, they are not considered in this thesis for simplicity and because this is out of the scope of my work.

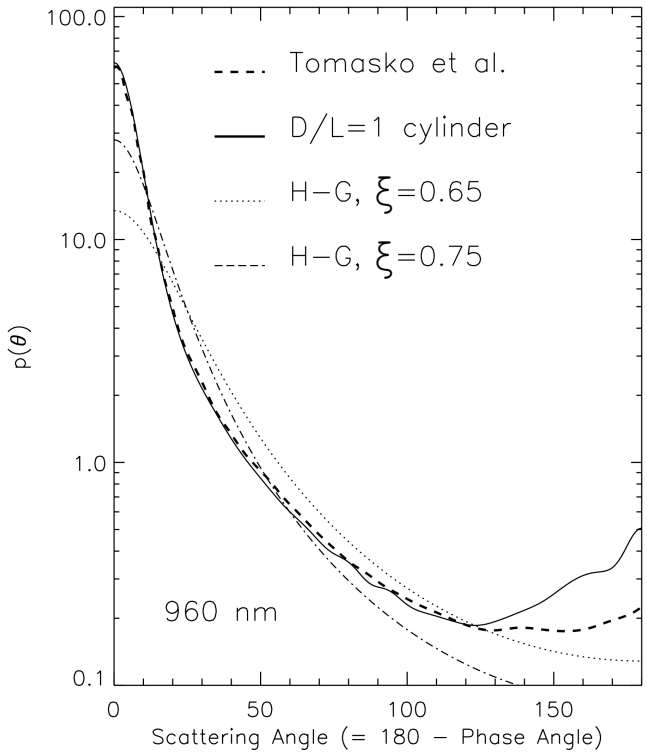

Figure 2.6.: Different phase functions of martian aerosols calculated based on orbital observations. Plain line corresponds to the phase function retrieved by Wolff et al. from CRISM observations used in this thesis. We also show two Henyey-Greenstein phase functions using asymmetry parameter ξ=0.65 and ξ=0.75. Credit: [187]

2.2. Atmosphere/surface radiative transfer

The theory of radiative transfer originated in astrophysics with the work of Chandrasekhar for stellar atmospheres [30]. As we have seen, the propagation of radiation through a medium is affected by emission, absorption and scattering processes. The **radiative transfer equation** (RTE) describes mathematically at each point of the medium the balance between the gains and the losses affecting the multidirectional fluxes of radiant energy. RTEs have application in remote sensing as they allow simulating the multiple diffuse reflections occurring between the surface and the atmosphere in terms of radiation, helping in the study of atmospheric effects affecting at-sensor signal. In this way **forward simulation** of RT models enhances our understanding on the sensitivity of measured radiance to external parameters such as atmospheric or acquisition conditions. Contrarily, **inverse simulations** are necessary to compensate TOA radiances for these external effects in the retrieval of surface properties. The availability of a solid mathematical base to formulate the RT problem is crucial to implement the RT codes that will carry out these simulations.

There exist many algorithms for atmospheric RT. Analytic solutions to the RTE exist for simple cases but advanced numerical methods are required for media with more realistic multiple scattering effects. In this thesis I use the Discrete Ordinates Radiative Transfer Program for a Multi-Layered Plane-Parallel Medium (DISORT) which is a general and versatile RT code applicable to problems within a broad range of the electromagnetic spectrum. DISORT solves the RTE by means of a proper implementation of the so-called discrete ordinate method developed by Chandrasekhar in the 1950s [168]. The physical

processes included in DISORT and of interest in this thesis are scattering, absorption and bidirectional reflection at the lower boundary, the surface. However, the use of DISORT, as well as other similar RT codes, is related to high computational times, and I will thus limit its use to some specific computations in which high accuracy is required. The main factor for such a computational burden is that the boundary condition at the bottom of the atmosphere, the surface BRDF, is considered in the RT problem. As a consequence, each time DISORT simulates a radiance value at any point of the atmosphere it considers each combination of physical parameters of the surface (see section 2.3 for some examples on parametrized surface reflectance models) as well as those related to the atmosphere (e.g. τ_{aer}). Numerical methods such as discrete ordinates are therefore traditionally used for the problem with a Lambertian surface (i.e. $f(\theta_0, \theta, \varphi, \lambda) \approx q_L(\lambda)$), which reduces significantly the computational burden. Anisotropic reflectance, if considered, is usually treated by means of numerical integration [92].

In this thesis I propose to adopt an alternative, robust, and fast resolution of the RTE problem based on the Green's function formulation[4] allowing a partial decoupling of RT between the surface and the atmosphere. This formulation will be the basis of the algorithm for atmospheric correction of CRISM multi-angle observations introduced in Part III.

2.2.1. Expression of the top-of-atmosphere radiance

Throughout this thesis I make a few suppositions regarding the RT in the atmosphere and surface of Mars. The former medium is considered to be vertically stratified with respect to solar radiation according to a plane-parallel geometry. Likewise, the surface is supposed to be flat. Under these circumstances I am considering a one-dimensional RT problem in which potential interactions between different facets of the surface are not considered. Three different types of illumination on the surface are distinguished as (i) **direct illumination** coming directly from the Sun, (ii) **diffuse illumination** coming from photons scattered once or many times by aerosols, and (iii) illumination resulting from **round trips** (multiple diffuse reflection) undergone by photons between the surface and the aerosols. The mentioned assumptions and concepts form the basis of the surface/atmosphere RT formulation that I shall consider for the atmospheric correction for CRISM data. For an operational version of the correction as described in subsection 4.2.2, we will additionally consider the surface to be Lambertian in terms of reflection. Contrarily, in Part III I propose an advanced atmospheric correction approach that considers an anisotropic surface. In this case, however, the atmosphere is described by a single layer characterized by a sole optical thickness, as the example illustrated in Figure 2.1.

The concept of the Green's formulation has been used in many works on RT recently [22, 145]. I retain the seminal work of Lyapustin and Knyazikhin in which an application of the Green's function formulation to the one-dimensional RT problem with a non-Lambertian surface is described [107]. This work is carried out under similar conditions regarding the atmosphere and the surface as mentioned above. Lyapustin and Knyazikhin propose a robust expression for the **spectral radiance at the top of the atmosphere** $L_{TOA}(\lambda)$ accounting for the interactions of radiation with the atmosphere and the surface detailed in previous sections. In the present chapter I give a brief introduction to the basis of this RT formulation. Some necessary terms are introduced as follow:

[4] The use of the Green's function method in remote sensing is detailed in subsection 5.3.1.

- s_0, s: incidence and emergence directions defined by pairs of zenith and azimuthal angles (θ_0, φ_0) and (θ, φ), respectively.
- μ_0, μ: cosines of SZA and VZA; the z axis is pointed downward, so $\mu_0 > 0$ for the solar beam and $\mu < 0$ for the reflected beam.
- Ω_+, Ω_-: incidence (or downward) and emergence (or upward) upper hemisphere, respectively.
- πS: extraterrestrial solar spectral irradiance as detailed in Figure 1.12.
- ρ: surface **bidirectional reflectance factor** (BRF). ρ is given by the ratio of the reflected radiant flux from the surface to the reflected radiant flux from an ideal Lambertian surface under identical view geometry and illumination direction. BRF is unitless as it is proportional to the BRDF $[sr^{-1}]$ of the surface by a factor π $[sr]$ such that $\rho(\theta_0, \theta, \varphi, \lambda) = \pi f(\theta_0, \theta, \varphi, \lambda)$.
- ρ_1 and ρ_2 are different moments of the BRF and will be detailed in section 5.3.
- c_0, q: spherical albedo of the atmosphere and the surface, respectively (review Equation 1.5).
- D: **atmospheric path radiance** made by the photons that reach the sensor without interacting with the surface.
- G^d: the Green's function of the diffuse component of the atmosphere, or bi-directional upward diffuse transmittance divided by π. The **diffuse Green's function** stands for the response of the atmosphere illuminated from below with an elementary and collimated beam of light. The calculation of this term can be achieved with classical RT codes such as DISORT as I shall explain in section 5.4.

The method in [107] is based on three main ideas regarding the parametrization of the RT in the atmosphere as follow:

1. The total upward radiance L_l at level of the atmosphere l, with optical thickness τ_l and with direction of propagation s is decomposed into a term embracing the radiance of those photons that did not interact with the surface D_l, and the radiance coming from the rest J_l.
2. If we apply any kind of upward radiance L at the bottom of the atmosphere, the response of the atmosphere in terms of radiation can be calculated with G^d as a weighted sum of elementary contributions.
3. Radiance resulting from the interaction with the surface J is considered as a convergent series of terms $\sum_{i=0}^{\infty} J_i$ that quantifies the energy of group of photons having undergone a given number of round trips i in the system atmosphere-surface.

The formal expression of the upward radiation at any point of the atmosphere resulting from these ideas cannot be used in practice due to its complexity. A couple of assumptions are hence made to simplify the expression.

1. After a sufficiently large number of round trips in the atmosphere/surface system, two successive terms in the series of terms of J become proportional. Under this assumption, a maximum-eigenvalue method allows faster calculation of the series only requiring the first three orders of the surface-reflected radiance.
2. The multiple reflections in the surface-atmosphere system can be approximated as a Lambertian contribution.

These two suppositions result in a simplified expression of the upward radiance at the bottom of the atmosphere as the sum of intelligible contributions. The last step is the transfer by direct and diffuse

transmission of this radiance into the TOA radiance (i.e. the one sensed by a sensor in orbit) thanks to the Green's function. After all radiance at the sensor level L_{TOA} is expressed as the sum of the following terms:

- The atmospheric path radiance:

  $$L_{TOA}(s_0, s) = D(s_0, s) \tag{2.6}$$

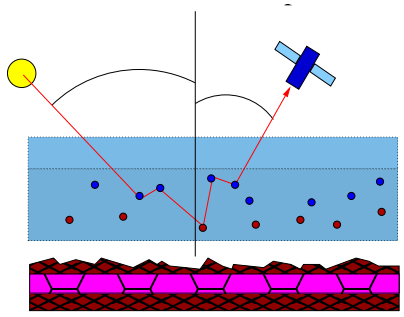

- The direct collimated flux reflected by the surface and directly transmitted to the sensor:

  $$+S\mu \exp(-\tau/\mu_0) \exp(-\tau/\mu) \rho(s_0, s)$$

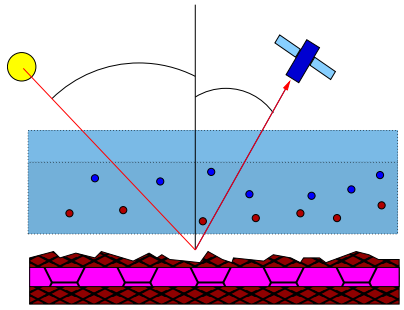

- The direct collimated flux reflected multiple times by the system surface/atmosphere and directly transmitted to the sensor:

  $$+S\mu \exp(-\tau/\mu_0) \exp(-\tau/\mu) \rho(s_0, s) \frac{c_0 \rho_1(s) \rho_2(s_0)}{1 - q c_0}$$

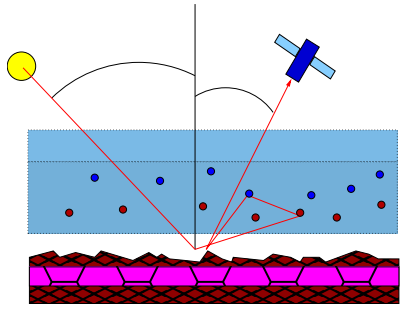

- The diffuse flux reflected multiple times by the system surface/atmosphere and directly transmitted to the sensor:

  $$+\frac{1}{\pi(1 - q c_0)} \exp(-\tau/\mu) \int_{\Omega_0} D(\tau, s, s') \rho(s', s) \mu' ds'$$

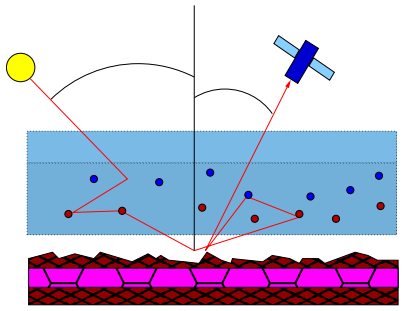

- The direct collimated flux reflected by the surface and transmitted by multiple scattering to the sensor:

$$+\int_{\Omega} S\mu_0 \exp\left(-\tau/\mu_0\right) \rho\left(s,s'\right) G^d\left(s',s\right) ds'$$

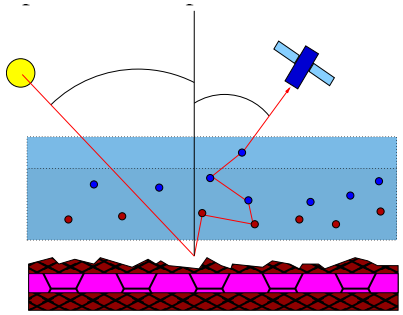

- The direct collimated flux reflected multiple times by the system surface/atmosphere and transmitted by multiple scattering to the sensor:

$$+\int_{\Omega} S\mu_0 \exp\left(-\tau/\mu_0\right) \frac{c_0\rho_1\left(s'\right)\rho_2\left(s\right)}{1-qc_0} G^d\left(s',s\right) ds'$$

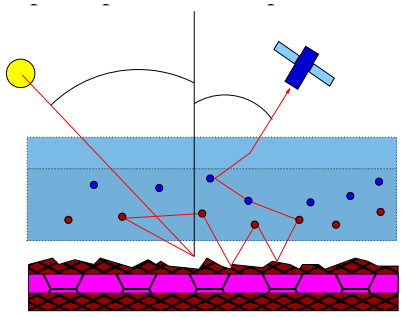

- The diffuse flux reflected multiple times by the system surface/atmosphere and transmitted by multiple scattering to the sensor:

$$+\int_{\Omega} G^d\left(s_1,s\right) \frac{1}{\pi\left(1-qc_0\right)} ds_1 \int_{\Omega_0} D\left(\tau,s,s'\right) \rho\left(s',s_1\right) \mu' ds'.$$

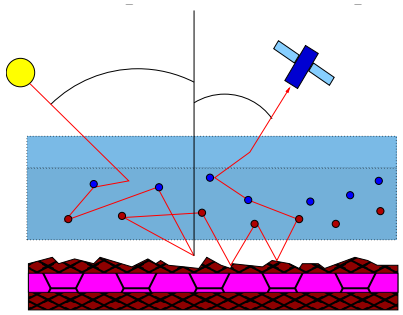

This expression of the radiance at the top of the atmosphere provides the means for robust forward and inverse simulations of the remote sensing RT problem. This will be further discussed in Part III.

2.3. Modeling the surface reflectance

As introduced in the previous section, formulation of the RT happening in planetary atmospheres considers a lower boundary determined by the surface medium. Materials at the surface are characterized by their reflectance properties, which are described by the BRDF. This distribution function provides the reflectance of the surface as a function of illumination and viewing geometries and has been already briefly introduced in Equation 1.3.

In other words, the BRDF simply expresses the fact that objects look differently when viewed from different angles, and when illuminated from different directions. Figure 2.7 provides an example of the anisotropic BRDF of a soil surface in terms of phase angle g. The observed soil looks featureless for small phase angles while details increase for higher phase angles (i.e. with the Sun in front of the observer). At this point, I note that in the case of a Lambertian, or isotropic, surface both images would look similar. The anisotropy expressed by the BRDF depends on wavelength (although definitions in this section will not express this dependence for brevity) and is determined by the optical and structural properties of the materials at the surface through multiple scattering, absorption, shadow-casting, and facet orientation distribution, among others phenomena. The BRDF is crucial in remote sensing applications such as correction of view and illumination angle effects or atmospheric correction as it represents the lower boundary condition of the RTE.

One of the major challenges in RT is the use of parametric yet realistic BRDF models that represent accurately the different materials at the surface. In the following, I provide a brief review on BRDF models, including those that shall be used in this dissertation. For a more extensive review on BRDF models I strongly recommend the study of Jupp in [86].

2.3.1. BRDF models

If the scattering surface is sufficiently smooth, it will behave like a mirror, resulting in **specular scattering** or specular reflection. In this limiting case of surface scattering, radiation incident from direction (θ_0, φ_0) is scattered only into the direction $(\theta = \theta_0, \varphi = \varphi_0 - \pi)$. The opposite limiting case in terms of scattering is that of an ideally rough surface, resulting in **Lambertian scattering**. Lambertian surfaces have the property that, for any illumination that is uniform across the surface, the scattered radiation is distributed isotropically. Therefore, the BRDF has a constant value $f_L(\theta_0, \theta, \varphi) = q_L/\pi$, or BRF

Figure 2.7.: A soil field with rough surface. (left) backscattering direction, Sun behind observer. Note at the bottom of the picture the bright region (hotspot) where all shadows are hidden. (right) forward scattering direction, Sun opposite to the observer. Note the specular, or mirror-like, reflection. Soils with similar scattering properties are common on Mars. Credit: http://www-modis.bu.edu/brdf/.

$\rho_L(\theta_0, \theta, \varphi) = q_L$, where q_L is the Lambertian albedo. Both limiting cases of scattering are illustrated in Figure 2.8 (a) and (c).

In the recent times, researchers have proposed many BRDF models that consider the physics behind the scattering of light by surfaces and that are useful to be included in the RTE.

2.3.1.1. Minnaert's model

A simple modification of the Lambertian scattering is the Minnaert's analytical model. This empirical model originated in the study of the photometric properties of the Moon by Minnaert in the 40s [121]. The Minnaert's scattering model depends on a constant k, commonly called Minnaert's constant or index of limb darkening effect. This model is associated with the limb region because the roughness plays an important role in the photometry of airless bodies observed obliquely. The model is written as follows:

$$\rho_{Minnaert}(\mu_0, \mu, g) = q_{Minnaert}\mu_0^k \mu^{k-1}, \tag{2.7}$$

where $q_{Minnaert}$ is the Minnaert's albedo and parameter k has the effect of increasing or decreasing the radiance scattered in the direction of the surface normal. An example with $k = 2$ is given in Figure 2.8 (d). Lambertian scattering is the special case of the Minnaert's model when $k = 1$.

However, the Minnaert's model does not account for the fact that real surfaces may also show additional backscattering or specular scattering. These attributes can be incorporated by devising an empirical model combining a Lambertian or Minnaert's components with, for example, a quasi-specular

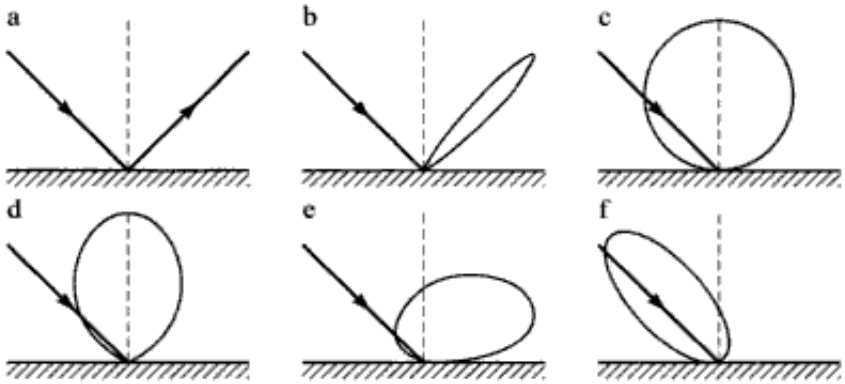

Figure 2.8.: Schematic illustration of different types of surface scattering. The lobes describe the strength of radiation and how diffuse it is. (a) Specular reflection. (b) quasi-specular scattering. (c) Lambertian scattering. (d) Minnaert's model with $k = 2$. (e) 1-lobe Henyey-Greenstein model of forward scatter ($\xi = 0.7$). (f) 1-lobe Henyey-Greenstein model of backscatter ($\xi = -0.5$). Credit: [148].

term [see Figure 2.8 (d)]. One common modification is to multiply the Lambert or Minnaert's BRDF by a Henyey-Greenstein term (see Equation 2.3) as it is done in Figure 2.8 (e) and (f) [148].

2.3.1.2. Hapke's model

Although being a satisfactory first approximation, analytical models such as Minnaert's are empirical (i.e. founded on observations) and often fail to reproduce accurately the different scattering processes. Contrarily, theoretical analytical BRDF models are based on RTEs and hence provide more realistic expressions for the surface bidirectional reflectance. In this matter a widely used model for studying the scattering properties of surfaces is the scattering model of Hapke [71]. This model is based on the equations of RT taking into account several phenomena at the cost of additional parameters. The Hapke's model was originally developed for the study of granular surfaces, and has been applied satisfactorily to different types of soils in the Solar system [84, 85, 44]. Being ω the single scattering albedo of a volume element and $P(g)$ its phase function, the BRF of an arbitrary surface can be expressed as

$$\rho_{Hapke}(\mu_0, \mu, g) = \frac{\omega}{4} \frac{1}{\mu_0 + \mu} \left\{ [1 + B(g)] P(g) + H(\mu_0) H(\mu) - 1 \right\}, \tag{2.8}$$

where

$$B(g) = \frac{B_0}{1 + (1/h) \tan(g/2)}, \tag{2.9}$$

$$H(x) \simeq \frac{1 + 2x}{1 + 2x\sqrt{1 - \omega}}. \tag{2.10}$$

where B_0 and h are the strength and the angular width of the **opposition effect**, respectively. Both B_0 and h characterize the non-linear increase in brightness with decreasing phase angle shown in

Figure 2.9. As for the phase function $P(g)$ the Henyey-Greenstein function defined in Equation 2.3 or Equation 2.4 is commonly adopted for the Hapke's model [84, 44, 80, 188].

Figure 2.9.: Apollo 11 photo taken by Neil Armstrong of the terrain in front of the lunar module. Note how the opposition effect brightness the area around Armstrongs's shadow due to the backscattering properties of lunar regoliths. Credit: NASA, Neil Armstrong.

In addition to the opposition effect the Hapke's model accounts for other physical processes such as multiple scattering and anisotropy of surfaces. An improved version of this BRDF model also includes the surface macroscopic roughness. **Surface roughness** is a measure of the complex geometry of the interface between the surface materials and the atmosphere quantified for example by the vertical deviations of a real surface from its ideal form (see Figure 2.10). If these deviations are large, the surface is rough while if they are small, the surface is smooth. Roughness plays an important role in determining how light interacts with its environment and its consideration results in more realistic scattering models.

There are three important effects of macroscopic roughness that may modify the reflectance (i) scattering of light from one facet to another may increase the reflectance, (ii) unresolved shadows cast on one part of the surface by another may decrease the reflectance, and (iii) as the surface is viewed and illuminated at increasing zenith angles, the facets that are tilted away from the observer or source may tend to be hidden or in shadow. In order to account for the latter two effects Hapke writes the rough-surface bidirectional reflectance factor $\rho_{Rough-Hapke}(\mu_0, \mu, g)$ as the product of a shadowing function $S(\mu_0, \mu, g)$ and the original Hapke's BRF $\rho_{Hapke}(\mu_0, \mu, g)$ of a smooth surface of effective area A_e tilted so as to have effective angle of incidence θ_{0e}, effective angle of emergence θ_e, with the same phase angle g such that

$$\rho_{Rough-Hapke}(\mu_0, \mu, g) = \frac{\omega}{4} \frac{1}{\mu_{0e} + \mu_e} \{[1 + B(g)] p(g) + H(\mu_{0e}) H(\mu_e) - 1\} S(\mu_0, \mu, g), \tag{2.11}$$

Hapke defines $\bar{\theta}$ as the mean roughness slope angle or, in other words, the averaged mean slope angle

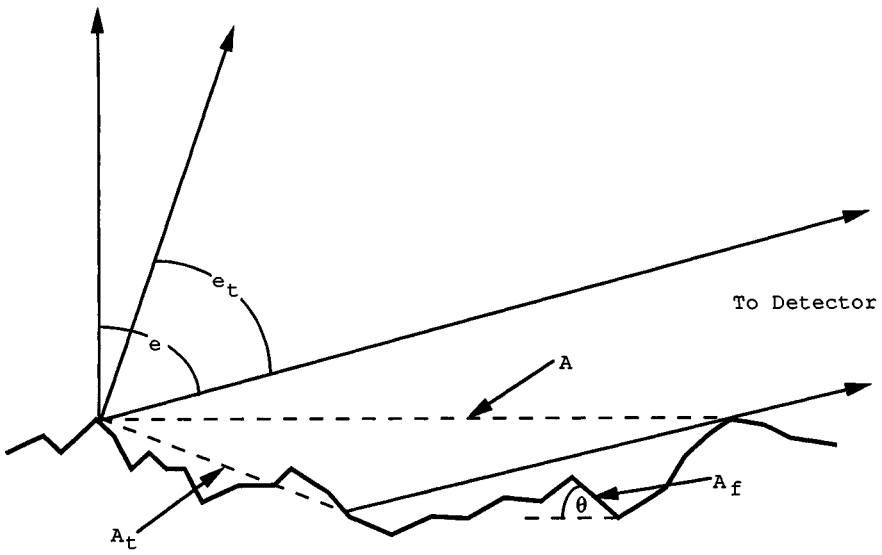

Figure 2.10.: Schematic diagram of the intersection of the surface and a vertical plane containing the detector. Shown are the actual surface, consisting of a multitude of unresolved facets A_f, the nominal surface A, and the effective tilted surface A_t. Credit: [71].

over all spatial scales on the surface between some upper and lower limits that are determined by the angular resolution of the detector and the physics of the RTE. The upper limit is the footprint of the detector on the surface of the planet, which in planetary remote sensing is typically tens of centimeters to kilometers. Being μ_e and μ_{0e} the modified angle cosines, two cases are defined such that:

- if $\theta_0 < \theta$,

$$S(\mu_0, \mu, g) \simeq \frac{\mu_e}{\mu_e(0)} \frac{\mu_0}{\mu_{0e}(0)} \frac{\chi(\bar{\theta})}{1 - t(\varphi) + t(\varphi)\chi(\bar{\theta})[\mu_0/\mu_{0e}(0)]}, \tag{2.12}$$

$$\mu_{0e} \simeq \chi(\bar{\theta}) \left[\cos\theta_0 + \sin\theta_0 \tan\bar{\theta} \frac{\cos\varphi E_2(\theta) + \sin^2(\varphi/2) E_2(\theta_0)}{2 - E_1(\theta) - (\varphi/\pi) E_1(\theta_0)}\right], \tag{2.13}$$

$$\mu_e \simeq \chi(\bar{\theta}) \left[\cos\theta + \sin\theta \tan\bar{\theta} \frac{E_2(\theta) - \sin^2(\varphi/2) E_2(\theta_0)}{2 - E_1(\theta) - (\varphi/\pi) E_1(\theta_0)}\right], \tag{2.14}$$

- if $\theta_0 \geq \theta$,

$$S(\mu_0, \mu, g) \simeq \frac{\mu_e}{\mu_e(0)} \frac{\mu_0}{\mu_{0e}(0)} \frac{\chi(\bar{\theta})}{1 - t(\varphi) + t(\varphi)\chi(\bar{\theta})[\mu/\mu_e(0)]}, \tag{2.15}$$

$$\mu_{0e} \simeq \chi(\bar{\theta}) \left[\cos\theta_0 + \sin\theta_0 \tan\bar{\theta} \frac{E_2(\theta_0) - \sin^2(\varphi/2) E_2(\theta)}{2 - E_1(\theta_0) - (\varphi/\pi) E_1(\theta)}\right], \tag{2.16}$$

$$\mu_e \simeq \chi(\bar{\theta}) \left[\cos\theta + \sin\theta \tan\bar{\theta} \frac{\cos\varphi E_2(\theta_0) + \sin^2(\varphi/2) E_2(\theta)}{2 - E_1(\theta_0) - (\varphi/\pi) E_1(\theta)}\right], \tag{2.17}$$

where $t(\varphi)$ is the fraction of the visibility shadow hidden in the illumination shadow,

$$t(\varphi) = \exp\left(-2\tan\frac{\psi}{2}\right), \tag{2.18}$$

$\mu_{0e}(0)$ and $\mu_e(0)$ are the effective cosines at o°,

$$\mu_e(0) \simeq \chi(\bar{\theta}) \left[\cos\theta + \sin\theta \tan\bar{\theta} \frac{E_2(\theta)}{2 - E_1(\theta)}\right], \tag{2.19}$$

$$\mu_{0e}(0) \simeq \chi(\bar{\theta}) \left[\cos\theta_0 + \sin\theta_0 \tan\bar{\theta} \frac{E_2(\theta_0)}{2 - E_1(\theta_0)}\right], \tag{2.20}$$

and

$$E_1(x) = \exp\left(-\frac{2}{\pi}\cot\bar{\theta}\cot x\right), \tag{2.21}$$

$$E_2(x) = \exp\left(-\frac{1}{\pi}\cot^2\bar{\theta}\cot^2 x\right), \tag{2.22}$$

$$\chi(\bar{\theta}) = 1/(1 + \pi\tan^2\bar{\theta})^{1/2}. \tag{2.23}$$

These equations can be used to calculate the effects of macroscopic roughness on light scattered by a surface having an arbitrary diffuse-reflectance function. This improved Hapke's model is often used in the literature and shall be also used in this thesis. The main deficiency of this model is its neglect of inter-facet multiple scattering. This will be negligible if the reflectances of the facets are low, but it can be important if the surface is bright, especially at high phase angles where many shadows are visible but are partially diffusely illuminated.

2.3.1.3. Rahman-Pinty-Verstraete model

The main drawback of the Hapke's model is related to its complexity due to its numerous physical parameters (up to six if we consider a 2-lobe Henyey-Greenstein phase function). The Hapke's model is hence not practical in inverse surface-atmosphere simulations of the RT because of the high computational cost of retrieving all parameters and its non-linearity. In this thesis, I shall use the Hapke's model to fit atmospherically corrected TOA radiances by other inverse methods. Even in this case, however, some parameters may remain unconstrained if enough measurements are not available [84].

In an effort to develop simpler parametric models, Rahman et al. propose the Rahman-Pinty-Verstraete (RPV) model [146]. This fully parametric model expresses bidirectional reflectance of the surface as dependent on the Minnaert's parameter k, the spherical albedo of the surface q, and parameter ξ such that

$$\begin{aligned} \rho_{RPV}(\mu_0, \mu, \varphi) &= qM(k) P_{HG1}(g, \xi) H(q) \\ M(k) &= [\mu\mu_0(\mu + \mu_0)]^{k-1} \\ H(\rho_0) &= \left\{1 + \tfrac{1-q}{1+G}\right\} \end{aligned} \tag{2.24}$$

where $G = \sqrt{\tan^2\theta_0 + \tan^2\theta + 2\tan\theta_0\tan\theta\cos(\varphi)}$ and $P_{HG1}(g, \xi)$ is simply the 1-lobe Henyey-Greenstein phase function.

A modified version of the RPV model (MRPV) is used in the atmospheric correction algorithm for the Multi-angle Imaging SpectroRadiometer (MISR) aboard the NASA Terra spacecraft by simply replacing $P_{HG1}(g, \xi)$ for $\exp\alpha\cos\xi$, yielding a quasi-linear expression for the model parameters after logarithmic

transformation [113]. The MRPV has proved to be adequate to represent very anisotropic surfaces such as snow in [106].

2.3.1.4. Ross-Thick Li-Sparse model

Recently, a few RT algorithms adopt the kernel-based semi-empirical Ross-Thick Li-Sparse (RTLS) model. In [151] Roujean et al. develop a parametric scattering model for the correction of surface bidirectional effects in time series of satellite observations, where both Sun and viewing angles are varying. The RTLS model defined in [102] inherits the basis of Roujean's model to describe the surface by only three adjustable parameters, k_L, k_G and k_V. This model considers that the observed surface bidirectional reflectance is the sum of three terms operating at a local scale: (i) an isotropic contribution, (ii) a diffuse reflection component taking into account the geometrical structure of opaque reflectors on the surface, and shadowing effects, and (iii) a volume scattering contribution by a collection of dispersed facets which simulates the volume scattering properties of canopies and bare soils. The RTLS model decomposes the BRF as follows:

$$\rho_{RTLS}\left(\mu_0,\mu,\varphi\right) = k^L + k^G f_G\left(\mu_0,\mu,\varphi\right) + k^V f_V\left(\mu_0,\mu,\varphi\right). \tag{2.25}$$

where subscripts refer to isotropic (L), volumetric (V) and geometric (G) components. The RTLS model uses predefined geometric functions (kernels) f_G, f_V to describe different angular shapes which are independent on land conditions. Since the BRF of a pixel is characterized by a linear combination of three kernel weights $\vec{K} = \{k_L, k_G, k_V\}$, this model is very advantageous to be included in RT algorithms to process remote sensing data in an efficient and rapid manner. The RTLS model is used in operational atmospheric correction algorithms for the Moderate Resolution Imaging Spectroradiometer (MODIS) aboard the Terra and Aqua spacecrafts [153, 108]. In this thesis I shall use the RTLS in the atmospheric correction of CRISM multi-angle observations presented in Part III.

Regarding the predefined kernel functions, a suitable expression for f_V was derived by Roujean et al. [151]. It is called the Ross-Thick kernel and was developed for a dense leaf canopy. This kernel is a single-scattering approximation of RT theory consisting of a layer of small scatterers with uniform leaf angle distribution, a Lambertian background, and equal leaf transmittance and reflectance. Figure 2.11 (left) shows some curves of f_V according to VZA and SZA. As I will prove in Part III the fact that the Ross-Thick kernel was defined based on vegetation does not affect its suitability to recreate martian surfaces. The form of this kernel, normalized to zero for $\theta_0 = 0$, $\theta = 0$, is

$$f_V\left(\mu_0,\mu,\varphi\right) = \frac{\left(\pi/2 - g\right)\cos g + \sin g}{cos\theta_0 + cos\theta} - \frac{\pi}{4} \tag{2.26}$$

A suitable expression for f_G that works well with observed data was derived by Wanner et al. [184]. It is called the Li-Sparse kernel for its assumption of a sparse ensemble of surface objects casting shadows on the background, which is assumed Lambertian. This geometric term is given by the proportions of sunlit and shaded scene components in a scene consisting of randomly located spheroids of height-to-center-of-crown and crown h vertical-to-horizontal radius ratio b/r. Figure 2.11 (right) shows some

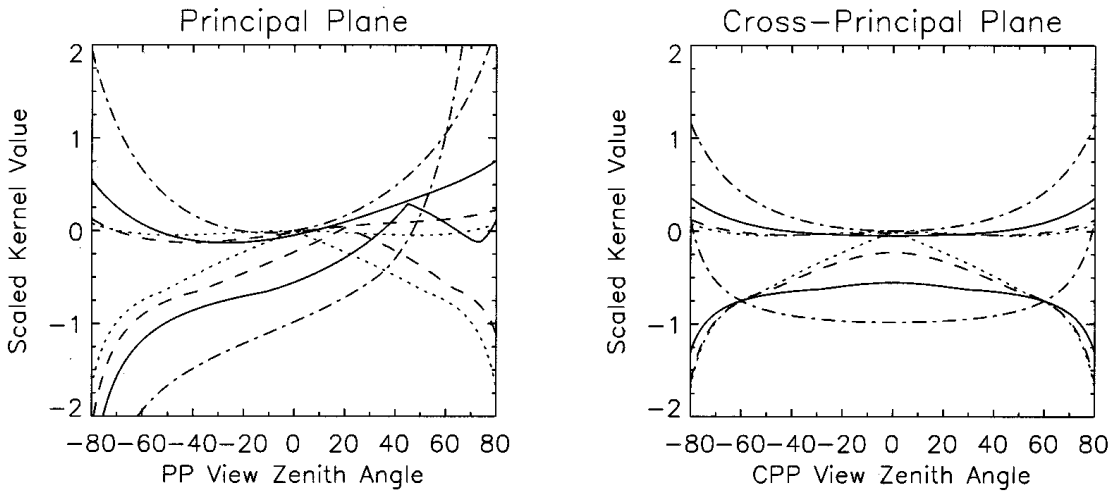

Figure 2.11.: Principal plane and cross-principal solar plane plots of the Ross-Thick (upper curves) and Li-Sparse (lower curves) BRDF model kernel values (arbitrary units; the Li-Sparse kernel values were divided by 2 for better plotting). The Sun is located at positive zenith angles of 0° (dotted lines), 20° (dashed lines), 45° (solid lines), and 70° (dashed-dotted line) solar zenith angle. The parameter h/b of the Li-Sparse kernel was set to 2 and the parameter b/r to 1. Credit: [102].

curves of f_G according to VZA and SZA. The original form of this kernel is not reciprocal in θ_0 and θ, a property that is approximately expected from homogeneous natural surfaces viewed at coarse spatial scale. The main reason for this non-reciprocity is that the scene component reflectances are assumed to be constants independent of solar zenith angle. If the sunlit component is simply assumed to vary as $1/\cos\theta_0$, the kernel takes on the reciprocal form given here

$$f_G(\mu_0, \mu, \varphi) = O(\mu_0, \mu, \varphi) - \sec\theta_0' - \sec\theta' + \frac{1}{2}(1 + \cos g')\sec\theta_0' \sec\theta' \tag{2.27}$$

where

$$O = \frac{1}{\pi}(t - \sin t \cos t)\left(\sec\theta_0' + \sec\theta'\right) \tag{2.28}$$

$$\cos t = \frac{h}{b}\frac{\sqrt{D^2 + (\tan\theta_0' \tan\theta' \sin\varphi)^2}}{\sec\theta_0' + \sec\theta'} \tag{2.29}$$

$$D = \sqrt{\tan^2\theta_0' + \tan^2\theta' - 2\tan\theta_0' \tan\theta' \cos\varphi} \tag{2.30}$$

$$\cos g' = \cos\theta_0' \cos\theta' + \sin\theta_0' \sin\theta' \cos\varphi \tag{2.31}$$

$$\theta_0' = \tan^{-1}\left(\frac{b}{r}\tan\theta_0\right), \theta' = \tan^{-1}\left(\frac{b}{r}\tan\theta\right) \tag{2.32}$$

Similar to the MPRV scattering model, the fully parametric RTLS model has proved to be useful to recreate BRF of very anisotropic surfaces such as snow-covered regions [106]. However, in this thesis this model is preferred to the RPV model as its linear expression has very convenient mathematical properties that allow the linearization of the RTE. As for the drawbacks, the RTLS model becomes less accurate for large zenith angles due to the increasing values of the kernels at extreme angles

(see Figure 2.11). Likewise, the RTLS kernels are not orthogonal, not positive-only functions, and the geometric-optical function f_G is normalized with a rather arbitrary convention that is not related to RT theory [102]. Eventually, the RTLS model does not have a kernel to model the opposition effect. The advantage and drawbacks of the RTLS model shall be made clear in Part III.

Summary and objectives of the thesis

In the first part of the dissertation I have provided the basis of the hyperspectral remote sensing of Mars. First, I have described the major attributes of the Red Planet and the geological and atmospheric features that shall be of interest in this thesis. Afterward, the technique named as imaging spectroscopy has been introduced as it represents the remote sensing tool for which I shall propose analysis algorithms. I remind the reader that the major advantage of imaging spectrometers with respect to other imaging systems is their ability to decompose a given scene of study into the spectral dimension, thus providing unique information in the spectral range which is invisible to the human eye. In this matter I have introduced the main concepts of hyperspectral imagery, the associated products, and the main instrument whose data I shall exploit in the following chapters, the Compact Reconnaissance Imaging Spectrometer for Mars instrument. In the second chapter I have introduced some principles of the radiative transfer in the atmosphere of Mars in interaction with the materials at the surface. The main physical phenomena controlling the signal received by an orbital sensor have been introduced as well as the elements originating such effects (e.g. the martian aerosols). I have likewise proposed a robust parametrization of the RT by adopting a smart expression of the at-sensor signal that decomposes the several contributions of the radiance at the top of the atmosphere. Eventually, a review on the models that are devised to recreate the scattering properties of different types of surfaces has been made.

Mars is an appropriate scenario for the use of imaging spectroscopy. Quite different materials coexist in the surface of the Red Planet ranging from dark soils to bright ices, each one related to specific fingerprints. These spectral features have been the key to some of the discoveries of Mars in which imaging spectrometers have played an important role. Technological improvements such as the multi-angle capabilities of the CRISM instrument are devised to further improve our understanding of the planet Mars. Nonetheless, I focus attention on some remaining hurdles toward the exploitation of the full potential of this pioneering instrument:

1. Advanced imaging spectrometers such as CRISM are related to increasingly demanding technological performances that augment their sensitivity to potential instrumental artifacts. Unfortunately, these limitations are only partially overcome by pre-launch calibration and preprocessing before the release of the data. Further processing is therefore required to overcome to the potentially limited radiometric quality of the data.
2. Data acquired by the CRISM instrument are released without fully exploiting the mentioned multi-angle characteristics of this instrument. As a matter of fact, each hyperspectral image forming a single CRISM observation is released separately. The consideration of this multi-angle data sets as a sole product is crucial to perform advanced studies of the photometric properties of the atmosphere and the surface of Mars according to incidence angle.
3. Remote sensing of surfaces is typically disturbed by the presence of an overlaying atmosphere.

On Mars, the predominant mineral aerosols significantly alter the radiance incident on spacecrafts, thus masking the features of interest at the surface. Advanced techniques are therefore required to perform accurate atmospheric correction. In this matter RTEs are useful as they allow the modeling of the energy transfer of photons through the atmosphere/surface system to the sensor. However, RT formulations may be very complex and at-sensor signal may become intractable when exploited by RT-based inversion methods.

4. Insufficient spatial resolution or intimate microscopic mixtures of several components, among other causes, result in the sensing of mixed spectra. In the first situation each individual spectrum may be linearly decomposed into several spectral signatures that are differently weighted according to its predominance in the area delimited by the corresponding pixel at ground. Mixed spectra are very common in planetary remote sensing as materials at the surface are commonly mixed, each type of mixture forming spatially well defined terrain units.
5. Imaging spectrometers are related to a high technical complexity and voluminous data sets. These two facts results in more challenging, manually-unfeasible data analysis and processing than for traditional imaging. Moreover, the increased complexity of CRISM data due to the multi-angle dimension make traditional analysis methods such as PCA not enough powerful. Advanced and unsupervised algorithms are therefore required for the automatic analysis of hyperspectral data in order to extract the most significant data features.
6. Eventually, one of the major hurdles in planetary remote sensing is the scarcity of ground truth data to validate the scientific results provided by the mentioned methods applied on in-orbit data. Ground truth data on Mars are available only for a few specific places and dates, being too scarce to perform operational validation of algorithms that are meant to work on any site of Mars.

In this dissertation I suggest to address the previous issues as follow:

- In Part II I propose to overcome obstacle number 1 by putting forward a data pipeline that improves the radiometric quality of the data acquired by the CRISM instrument. The proposed pipeline is composed by original tailor-made algorithms that aim at correcting those instrumental artifacts that compromise the data accuracy. In this part of the dissertation I also address hurdle number 2 by devising a data pipeline module that generates advanced products embodying the eleven hyperspectral images that form a single CRISM multi-angle observation. Point number 3 is also considered as I adopt existing atmospheric correction techniques into the proposed data pipeline. Eventually, point number 5 is partially addressed as the present data pipeline is fully automated, performing the improvement and processing of CRISM observations in a totally unsupervised manner.
- In Part III I propose to simultaneously address both drawbacks 2 and 3 by proposing an original atmospheric correction approach for CRISM multi-angle observations. In this part of the thesis I suggest to exploit the multi-angle capabilities of the CRISM instrument to devise an advanced approach that compensates aerosol scattering effects taking into account the anisotropic reflectance of the surface. The proposed algorithm compensates for atmospheric effects based on the robust radiative transfer formulation that has been presented above. I further address point number 2 by retrieving unprecedented and meaningful multi-angle products of the surface, namely photometric curves in units of bidirectional reflectance. This is achieved after applying the proposed

atmospheric correction approach onto a specific area of Mars, the Gusev crater. The study of the photometry of this location gives meaningful hints about the physical state of the materials at the surface.

- In Part IV I propose to address hurdles number 4, 5 and 6 by investigating on the use of spectral unmixing techniques for analyzing hyperspectral data of Mars. I overcome point number 4 by distinguishing the most relevant unmixing techniques in the martian case thanks to an intercomparison between a selection of state-of-the-art techniques. The selected techniques represent a reliable tool in the unsupervised processing of large collections of hyperspectral images because of its speed and the fact that they are not based on any a priori on the scene. These two properties, as well as the intrinsic dimensionality reduction performed by spectral unmixing strategies, overcome obstacle number 5. In the last part of the dissertation, I also investigate the capabilities of the mentioned reduction of dimensionality as a tool to provide physically meaningful quick look products for planetary scientists in the form of abundance maps. Eventually, I propose to overcome point number 6 for a specific region of Mars by setting up an original strategy that builds ground truth data from independent high resolution imagery. This ground truth data, not available otherwise, are actually used as a reference in the aforementioned intercomparison between spectral unmixing techniques.

Part II.

Data pipeline for postprocessing CRISM observations

Introduction

The first part of the dissertation has been committed to the introduction of the main concepts that shall be used throughout this thesis. For instance, the imaging spectrometers that are currently exploring the planet Mars have been presented along with their main instrumental characteristics. This is the case of the CRISM camera aboard the MRO spacecraft that represents a unique tool in the exploration of the Red Planet. Imaging spectrometers such as CRISM are complex sensors as they are related to demanding instrumental requirements. One of the most challenging attributes is the combination of high spectral and spatial capabilities. In general remote sensing instruments emphasize one of the two requirements by providing either high spatial resolution in the case of panchromatic cameras (down to tens of centimeters per pixel at a single spectral band) or high spectral resolution in the case of traditional spectrometers (a single acquired spectrum at a few hundreds of spectral bands). In addition to dealing with both requirements, imaging spectrometers must confront other instrumental exigencies such as satisfactory spatial coverages at ground (resulting in quite large detector matrices), precise pre-launch detector alignment (to exactly determine the wavelength corresponding to each spectral band) and satisfactory SNR levels [123].

As it has been described in subsection 1.3.3 push-broom imaging spectrometers such as CRISM particularly satisfy the required SNR performances because of the 2-D detector matrix. Nonetheless, push-broom imaging spectrometers do not easily yield high-quality spectroscopic data caused by non-uniformities affecting the multiple elements of the detection matrix. Recovered spectra of planetary features may hence contain significant artifacts that compromise the identification of the features of interest. Instrumental artifacts may indeed cause image processing algorithms to fail, producing unsatisfactory results.

In this context accurate calibration of data acquired by push-broom imaging spectrometers becomes necessary before their release to the scientific community. The CRISM team established a data pipeline to process orbital observations for improvement of the radiometric calibration and for cleaning of instrumental artifacts. Nonetheless, processing hyperspectral data is generally delicate since faulty correction for artifacts may result in disturbances making the original data unrecoverable. Therefore, the data pipeline that CRISM data undergo before being released was devised to correct only the major artifacts corrupting the data. In this way the resulting radiometric accuracy is acceptable for many scientific studies tolerating some inaccuracies in the data (e.g. a classification method based on a band ratio thresholding does not require the same level of radiometric accuracy than a RT-based atmospheric correction approach).

Further processing of CRISM observations is, however, required to achieve the objectives of this thesis defined in the conclusions of Part I. Optical artifacts such as the so-called spectral smile effect detailed in subsubsection 4.1.2.1 are not overcome by the original data pipeline while they prove to be critical

for fine data processing such as atmospheric correction and investigations related to icy surfaces. In this part of the thesis I put forward an original postprocessing pipeline for fine calibration of CRISM observations. The proposed pipeline also addresses the transformation of CRISM observations into advanced products that take into account the multi-angle capabilities of CRISM, for example. The exploitation of the multi-angular capabilities of CRISM is indeed not addressed in the original data pipeline. This part of the thesis is twofold. First, I briefly summarize the data pipeline undergone by CRISM data before being released in chapter 3. Second, I describe the proposed postprocessing data pipeline that is adapted to the scientific interests of this thesis.

The Compact Reconnaissance Imaging Spectrometer for Mars aboard the Mars Reconnaissance Orbiter is devised to study water occurring as polar ice, as clouds and vapor in the atmosphere, locked in minerals, and as ice or groundwater below the surface. Credit: NASA/JPL-Caltech.

Contents

3

Preprocessing CRISM data

In this chapter I briefly detail the processing that data acquired by the CRISM instrument undergo before the release via the Planetary Data System (PDS). This information is crucial to understand the postprocessing pipeline that has been developed in this thesis.

The attributes of the CRISM instrument were characterized by calibration and testing strategies before and after integration onto the MRO spacecraft [126]. Two types of calibration are defined:

- **Ground calibration**. Before launching MRO, the CRISM team calibrated the attributes of the instrument that are difficult to measure in-flight and are detector-specific. For example, the spectral response function of the elements of the detector matrix were calibrated using a laboratory monochromator and collimator. Likewise, the VNIR and IR detectors were aligned in the optical assembly for best focus and to minimize optical distortions.
- **In-flight calibration**. Some attributes of the instrument are highly time-variable and thus must be calibrated in-flight. For example, the bias and the thermal background (i.e. different types of thermal noise) in the infrared spectral range depend on the temperature of the detector and the spectrometer housing, and therefore are measured periodically throughout the MRO mission.

Data resulting from the ground and in-flight calibrations are stored in the so-called **CRISM calibration data records** (CDR). These data are crucial for processing CRISM hyperspectral images accounting for the technical attributes of this imaging spectrometer. Table 3.1 summarizes the CDR that shall be used in this thesis for the improvement of the radiometric quality of released CRISM data.

Like any spacecraft instrument the CRISM imaging spectrometer requires corrections beyond the basic calibration due to instrument artifacts. I distinguish three types of effects that cause these artifacts:

- **Electronic effects** that come from electrical disturbances affecting the electronics in the instrument. For example, I highlight the so-called spikes that denote pixel-dependent non-linearities resulting in anomalous, or "bad", pixels, or the so-called stripes that originate in the non-uniformities of electronic attributes of the detector elements (see subsection 4.1.1 for details).

Product	Acronym
Bias file: time-tagged, fitted VNIR and IR images	BI
Bad pixel mask: time-tagged map of bad pixels	BP
Non-uniformity file: time-tagged flat-field correction	NU
Full width half maximum determined on ground for each pixel	SB
Time-tagged uncertainties in short-exposure images for each pixel to calculate bias	UB
Wavelength determined on ground for each pixel	WA
CRISM temperature dependent wavelength shift coefficient table	WC

Table 3.1.: Description of CRISM Calibration Data Records used in this thesis.

Electronic artifacts corrupt the data by creating false radiance values that may mask physical features. In this matter in-flight calibration generates periodically the BP CDR storing a "bad" pixel mask, for example.

- **Thermal effects** are originated in the noise produced by the intrinsic temperature of the spectrometer components. The impact of thermal artifacts is similar to electronic effects as they may result in "bad" pixels, or spikes, and random bias levels affecting the columns in the data, or stripes. As for the calibration of thermal effects, the evolution of the detector thermal bias measured in-flight is stored in the BI CDR based on shutter-closed measurements, for example. In addition to random noise, thermal effects have an impact on the optics of CRISM as it is explained in subsection 4.1.1.
- **Optical effects** coming from limitations of the optics of the CRISM instrument such as the fold mirrors, the diffraction grating or the telescope (see subsection 1.3.3). Artifacts related to optical inaccuracies include the second order leakage, which corrupts the IR channel, and the so-called spectral smile effect, which makes the CRISM spectral response dependent on the column position in the image space (see subsection 4.1.2 for details). The latter artifact is common to push-broom sensors and impacts CRISM data in particular. Due to the presence of the spectral smile the CRISM team defined the so-called **sweet spot** that encompasses the central spatial elements of the VNIR and IR detectors in which optical distortions are minimal. Without further calibration of the data, it is recommended to work in this restricted area to avoid unsatisfactory results. As for the optical ground calibration of CRISM, the measured wavelengths of the detector matrix are stored in the WA CDR while the shape of the individual spectral responses are stored in the SB CDR, for example.

In order to overcome these artifacts data are processed before the data release by the CRISM data pipeline (hereafter referred to as **CRISM-DP**). I recommend the article of Murchie et al. for precise details on this preprocessing stage [126]. The main calibration process is briefly summarized as follows:

1. After uncompressing the data and dividing them by exposure time, thermal and electronic artifacts are corrected in a first approximation. For example, thermal bias is subtracted from the raw data using the corresponding BI CDR. Similarly, electronic artifacts such as spikes are corrected using a function that considers the BP CDR.
2. Optical effects coming from the second order leakage affecting the IR channel are partially overcome by the CRISM-DP. However, the correction for other optical artifacts such as the spectral smile effect is not addressed.

3. The CRISM-DP eventually converts the original DN units, to physical units of at-sensor spectral radiance L $[Wsr^{-1}m^{-2}]$. In a second step, radiance units are converted to apparent I/F $[sr^{-1}]$ (see subsubsection 1.3.2.2).

The resulting data are released via the PDS at http://pds.nasa.gov/ in radiance and I/F units.

Even though the most significant artifacts were found early enough during calibration either to be corrected or to be characterized sufficiently to be removed during postprocessing, residues remain after the CRISM-DP. There is therefore a real need for postprocessing CRISM observations. The major issues are:

1. Residual thermal and electronic effects such as spurious striping and spiking effects.
2. Optical problems affecting the spectral accuracy of CRISM such as the spectral smile which is not addressed by the CRISM-DP.
3. The independent functioning of the the VNIR and IR channels. The CRISM-DP treats each channel independently and thus fully consistent spectra (from 0.4 μm to 4.0 μm) are not available for the scientific community.
4. Photometric effects in the images due to a heterogeneous acquisition geometry are not considered.
5. There is lack of multi-angle products that combine the eleven hyperspectral images composing a single CRISM multi-angle observation.

In this matter the **CRISM Analysis Toolkit** (CAT) was developed by the CRISM science team. The CAT is a collection of ENVI[1] and IDL[2] routines for reading, displaying, and analyzing CRISM data released through the PDS[3]. However, the CAT addresses only the first point of the list above, namely the correction of residual thermal and electronic noise. Issues 2-5 therefore remain unsolved nowadays, thus not allowing fine processing of CRISM data required to carry out some of the objectives of this thesis.

In this context one of the first tasks of this thesis has been to devise a postprocessing data pipeline (hereafter referred to as **IPAG-DP**) to complement the original CRISM-DP and to replace the CAT. Figure 3.1 shows the scheme of the processing of CRISM data since their acquisition to their processing by the IPAG-DP. As it shall be presented in chapter 4, the IPAG-DP is designed as a combination of tailor-made algorithms and existing routines from the CAT. The IPAG-DP has been crucial for automating the process of CRISM hyperspectral observations in this thesis.

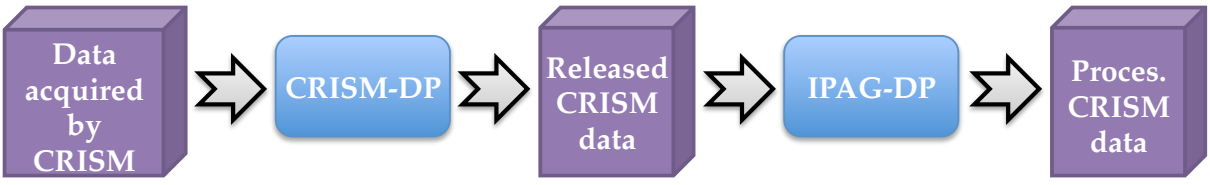

Figure 3.1.: Block diagram illustrating the processing of CRISM data from their acquisition to their improvement by the proposed data pipeline after the release via the PDS. The position of the two data pipelines, CRISM-DP and IPAG-DP, is highlighted.

[1] http://www.ittvis.com/language/en-US/ProductsServices/ENVI.aspx
[2] http://www.ittvis.com/language/en-US/ProductsServices/IDL.aspx
[3] The CAT software is available for downloading at http://pds-geosciences.wustl.edu/missions/mro/crism.htm.

Before detailing the different blocks of the IPAG-DP I remark that the presented CRISM-DP processes data corresponding to the TRDR2 version (see section 1.4). Since mid-2011 CRISM products are being released with the TRDR3 version, including improved calibration procedures [160, 159]. Compared to TRDR2, TRDR3 products present a lesser presence of instrumental artifacts and noise. The IPAG-DP that I present in this thesis was developed at the beginning of this Ph.D. (i.e. early 2009) and therefore is originally adapted to TRDR2 data. Nonetheless, most of the procedures are valuable for TRDR3 data and therefore the IPAG-DP is still used at the present time.

4

Postprocessing CRISM data

The proposed IPAG-DP is summarized in Figure 4.1 by detailing its two main parts, the first step related to the improvement of the radiometric accuracy of the data, and the second step involving the generation of advanced products. In section 4.1 I first propose to enhance the radiometric quality of the PDS-released data in both the spatial and the spectral domains. In particular the IPAG-DP is devised to address substantial correction for (i) instrumental artifacts that are not considered in the CRISM-DP and (ii) residues of those anomalies that have been partially addressed. As a second step I propose in section 4.2 to further process CRISM hyperspectral products toward the generation of advanced outcomes. These products shall be crucial to perform fine analysis of the planet Mars. In this second block of the IPAG-DP the data corresponding to the two CRISM spectral channels VNIR and IR are first combined to produce hyperspectral images in the full spectral range (i.e. 0.4-4.0 μm). CRISM data are then corrected for atmospheric effects to generate products revealing the features specifically linked to the surface. Additionally, I propose to investigate the normalization of the heterogeneous illumination conditions of CRISM targeted observations by traditional and advanced strategies. Eventually, the proposed IPAG-DP is designed to generate multi-angle products that combine the high resolution central scan and the EPF of a single CRISM observation. I note that the proposed IPAG-DP is conceived to process any type of hyperspectral observation produced by the CRISM instrument, namely FRT, HRL, and HRS products.

The present chapter describes the several blocks that form the IPAG-DP. Two different types are distinguished. On the one hand, I underline those blocks that have been adopted from existing procedures in the CAT (e.g. subsubsection 4.1.1.1), that have not been completely devised in the framework of this thesis (e.g. subsection 4.2.2), or that had been already developed before this Ph.D. (e.g. subsection 4.2.4). These blocks are only briefly introduced in this thesis while they are further detailed in the appendix chapter 14. On the other hand, I highlight those blocks that have been specifically conceived for this thesis in order to overcome those hurdles that remained unsolved. In this matter I detail each one of the developed strategies as they represent a main contribution of this thesis. First, I

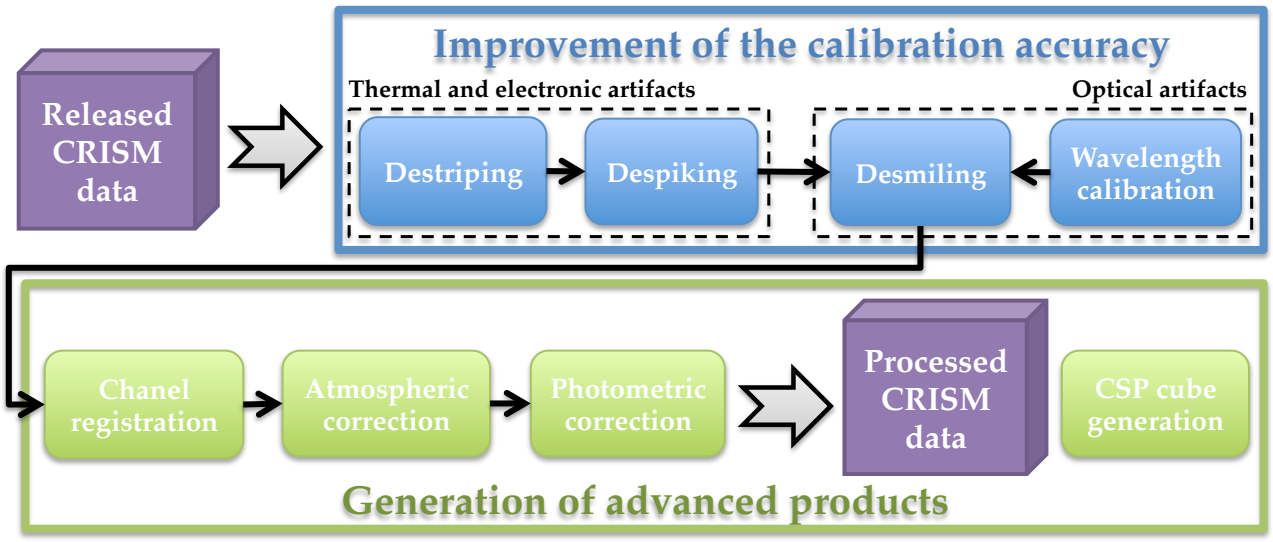

Figure 4.1.: Block diagram illustrating the IPAG-DP proposed in this thesis. The calibration accuracy of the PDS-released CRISM data is first improved while the second part of the IPAG-DP is aimed at generating advanced data products. The position of the IPAG-DP in the processing of CRISM data is illustrated in Figure 3.1.

introduce each processing step by detailing the instrumental artifact to be corrected or the undesired effects to be compensated. I follow with the summary of the state of the art on the subject. The strategy that is adopted for each block of the IPAG-DP is eventually introduced by describing the related technical procedure and the testing that has been performed for its validation.

4.1. Improvement of the radiometric accuracy

The first stage of the IPAG-DP is the refinement of the radiometric accuracy of the CRISM hyperspectral products released via the PDS. With this aim I propose to address the correction of the previously identified instrumental artifacts (i.e. thermal, electronic and optical residues) by a combination of tailor-made approaches and routines of the CAT. The different blocks of the first part of the IPAG-DP are presented in their actual order of execution by detailing the attributes of the artifacts and the adopted correction algorithms. The sole exception is the wavelength calibration step that, although it is executed before the spectral smile correction, is detailed afterwards for the sake of clarity. In this way an arbitrary CRISM hyperspectral image is first corrected for thermal and electronic artifacts as explained in subsection 4.1.1. Optical artifacts such as the spectral smile effect are then minimized in subsection 4.1.2. Previous to the correction of this particular optical artifact, the set of wavelengths of the CRISM instrument are calibrated from in-flight data in subsection 4.1.3. The order of execution shall be justified in the following sections.

4.1.1. Electronic and thermal artifacts

Hyperspectral remote sensing images are generally affected by different types of thermal and electronic noise. According to our experience with CRISM data I distinguish three major artifacts affecting the PDS-released products:

- **Thermal spectral shift**: CRISM suffers from an additive shift to the nominal wavelengths that were estimated on ground for all spectral bands. Smith et al. found that the wavelength for a given CRISM band varies by as much as 1.5 nm caused by the instrument temperature [165]. This thermal effect was also observed by McGuire et al. when performing atmospheric correction [117]. In this way warmer (colder) temperatures lead to a slight shift toward higher (lower) wavelengths affecting all CRISM spectral bands. Although this amount of shift is not important for many applications (the shift is much lower than the CRISM spectral sampling), some applications need its consideration in the original set of wavelengths to perform accurate processing. For example, Smith et al. state that the wavelengths shift makes difficult to retrieve the weak and narrow absorption bands corresponding to carbon monoxide. In our case a wrong calibration of the instrument may impact fine atmospheric correction (see section 14.2).
- **Stripes**: The so-called striping effect results in complex disturbance patterns that arise in a large number of push-broom imaging instruments. These spatial anomalies are characterized by a vertical (or horizontal) pattern caused by the random variation of the intensity of a homogeneous imaged area according to column (or line). Stripes are intrinsic to the image formation process and affect the radiometric quality of cross-track sensors such as CRISM but also the Compact High Resolution Imaging Spectrometer (CHRIS) aboard the PRoject for On–Board Autonomy (PROBA) spacecraft or the MODIS instrument [65, 16, 175]. In the case of CRISM this anomaly is manifested by a columnar pattern in the image space, the dimension corresponding to the along-track dimension (see subsection 1.3.3). Figure 4.2 illustrates the typical striping effect affecting the CRISM sensor by showing a spectral band of the central scan FRT64D9. As it can be seen, each data column is affected by a different bias value that can be negative (darker stripes) or positive (brighter stripes).

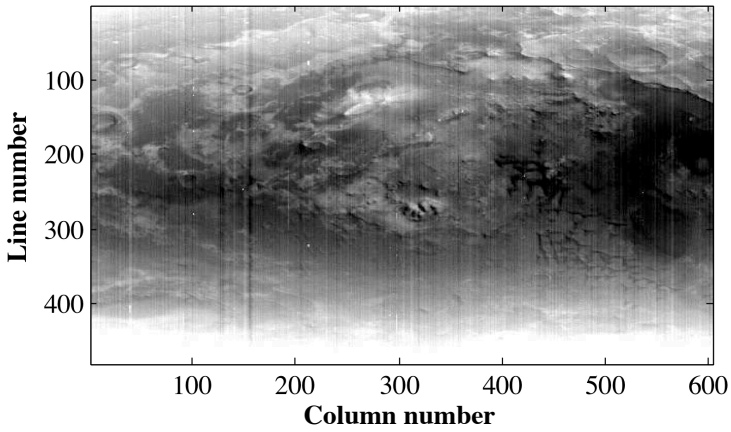

Figure 4.2.: FRT64D9 IR band 10. Note the strong striping effect arranged in a columnar organization.

Regarding the causes of the striping effect I recommend the Ph.D. dissertation of Bouali on destriping of MODIS data [15]. Bouali describes two main types of stripes:

  - **Periodic stripes** caused by a poor radiometric calibration of the relative gain and offset of the individuals detectors of the acquisition system. These slight deviations between the input/output transfer function of neighboring elements of the detector matrix remain constant with time. Periodic stripes are also originated in variations in the width of the slit along its length. The bias induced by these stripes can be straightforwardly characterized to set up

a correction algorithm such as the common flat fielding, already included in the CRISM-DP (see subsubsection 4.1.3.1).

- **Random stripes** caused by thermal noise or random fluctuations in the sensor response. This type of disturbance results in bright and dark stripes with random length within the along-track dimension. The complexity of this instrumental artifact lies in the impossibility of characterizing permanently the resulting spurious bias caused by its random variation with the spectral dimension of the CRISM detector matrix and time.

The main effects of the residual stripes affecting CRISM is the reduction of the quality and interpretability of the associated hyperspectral images. Stripes may introduce strong biases in the outcomes of posterior processing aimed at extracting qualitative and quantitative parameters. For example, the southern seasonal cap of Mars is scrutinized in the work of Langevin et al. for the detection of water ice using an approach based on a ratio of three spectral bands of the OMEGA instrument [95]. These spectral ratios aim at detecting the materials that coexist at the surface level by removing the principal atmospheric features, for example. In this way subtle contributions in the image are revealed. The quality of such a method may be severely impacted due to the randomness of random stripes.

In this matter the CRISM-DP addresses the correction of this artifact by deriving the quasi-instantaneous detector bias from flight measurements with the shutter closed (CRISM scans '06' and '08', see section 1.4), stored as the BI CDR (see Table 3.1), and subtracted in the radiometric calibration. Figure 4.3 illustrates the detector bias captured within a CRISM dark frame with the shutter closed that varies with detector temperature [126]. The high variability of random stripes may result in persistent residual stripes after the mentioned correction, however.

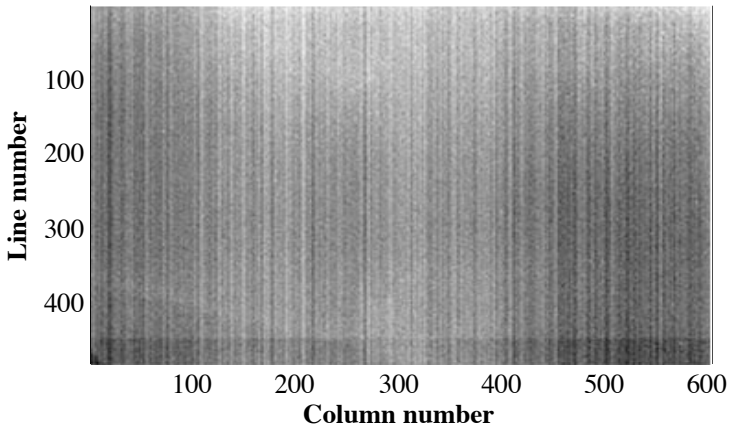

Figure 4.3.: Frame acquired by CRISM with shutter close showing column-arranged bias. Although this noise is partially corrected by the CRISM-DP, residual random stripes may remain in the PDS-released data.

- **Spikes**: Dropouts, or spikes, are those pixels whose effective SNR or available dynamic range are adversely impacted, thus resulting in anomalous high radiance values [65]. According to our experience the location and value of these erroneous pixels is fully random and they often form small clusters of spikes that are visible in the spectral bands of CRISM observations (see Figure 4.4). The CRISM team attributes these dropouts to pixel-dependent non-linearities and partially correct them in the CRISM-DP based on the BP CDR [126].

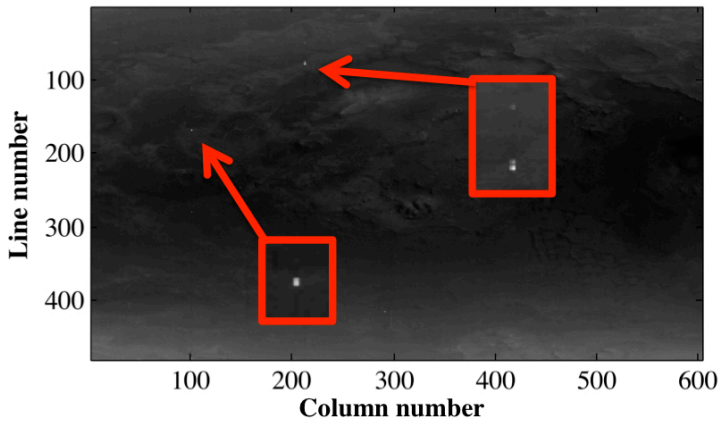

Figure 4.4.: FRT64D9 IR band 10. This figure is the same than Figure 4.2 using a gray stretch whose upper value is set to the value of the spurious spikes. Red boxes frame two spikes formed by a few pixels.

Regarding the correction of the aforementioned artifacts I adopt several strategies to be integrated in the IPAG-DP. First, the CRISM team shared with us the WC CDR (see Table 3.1) that tabulate the spurious spectral shift according to the temperature of CRISM. The thermal shift is then overcome by the IPAG-DP by simply updating the pre-launch wavelengths stored in WA CDR by the shift value that corresponds to the temperature of the image to be processed. This is done by adding (subtracting) the corresponding positive (negative) spectral shift. Second, after some investigations that shall be detailed below I decide to overcome the striping effect by integrating the proposed methodology in the CAT to the IPAG-DP. This selection is justified based on a comparison of the CAT method against the state of the art in destriping methods (see subsubsection 4.1.1.1). As said before, only a brief description on the adopted destriping method is given while further details can be found in the appendix section 14.1. Third, I investigate the spiking artifact by examining the state-of-the-art algorithms for their correction in subsubsection 4.1.1.2. Similarly to the striping effect, I evaluate the strategy adopted by the CAT to overcome this artifact against the methods proposed in the literature. By contrast, this time I suggest an alternative tailor-made despiking algorithm that suits better the purposes of this thesis.

4.1.1.1. Destriping CRISM data

Investigation of several CRISM images proves that albeit periodic stripes seem to be overcome by the CRISM-DP random stripes strongly persist. In this matter the CRISM science team argues that, in operational situations, postprocessing approaches are preferable to a full pre-launch characterization of the whole system producing gain correction factors and allowing an improved calibration [126]. The reason is that the latter solution is not practical due to random stripes. In addition, Murchie et al. argue that the system may be affected due to the rocket launch in such a way that the characterization would never completely remove the noise. Under these circumstances I decide to incorporate a destriping algorithm into the IPAG-DP. As a first step toward this objective I investigate the state of the art concerning this instrumental artifact.

The correction of hyperspectral images for spurious stripes has been widely addressed by the remote sensing community. I distinguish two main families of destriping algorithms as follow:

1. **Filtering approaches** are based on the application of a filter to the data to normalize the sensor

response. In other words, the filtering process aims at eliminating the spurious contributions introduced by the instrument in order to produce a constant output for a bland input. In the literature Gomez-Chova et al apply a low-pass filter to the perturbed data using a cut off frequency that is independently estimated for each image [65]. In this way the contribution of the spatial high frequencies of the surface is excluded from the stripes removal based on the information contained in the spectral domain. Similarly to [65], Tsai and Chen propose the destriping of remotely sensed image by edge-detection and line-tracing algorithms in [175]. The stripes are first flagged by treating gray values of each line or column as a piecewise spline curve. After identifying the positions of the stripes, noise-free pixels of each line or column are collected and used as control points to construct a cubic spline of reference. This destriping system is restricted by limiting the maximum stripe thickness to five pixels because of an unreliable spline interpolation in this case. Contrarily to [65] and [175], Liu and Morgan propose a destriping algorithm based on a frequency-domain filtering via the Fast Fourier Transform (FFT) [101]. In the spectral domain the stripes are easily recognized by frequency spots due to the periodic pattern of the striping noise. The main idea of [101] is to mask the spurious spots off before performing the inverse FFT back to the original space.

On the one hand, filtering techniques produce visual improvement by reducing the periodic and random stripes. In addition, they are sensor-independent, straightforward to implement and applicable to small images. On the other hand, the main disadvantage of these techniques is related to the risk of filtering out spatial components that are not due to the striping effect but to real features of the observed area. This issue may result in a lost of information, or blurring, in methods similar to [65], and ringing phenomena, or the so-called Gibbs phenomenon, in the case of the FFT-based destriping strategy in [101]. In addition, the method proposed by Liu and Morgan in [101] requires information on the spatial frequency content to define the optimal frequency filter. Regarding the destriping method proposed by Tsai and Chen in [175], investigation of CRISM images reveals multiple stripes that are thicker than five pixels. In conclusion this family of methods present a good trade-off between efficiency and simplicity but may compromise the radiometric accuracy of the data.

2. **Statistical methods** represent an alternative to remove artifact stripes from hyperspectral images by statistical modeling. This is the case of the destriping algorithm developed by Carfantan et al. in which a statistical unsupervised method is proposed to perform linear response correction based on a Markov random field (MRF) model [24]. The main disadvantage of this method lies in the assumption of a linear response of the detectors. In addition, the efficiency of the destriping process depends on the validity of the MRF model. Alternatively, Bouali and Ladjal propose a variational approach for the destriping of orbital MODIS images [16]. In functional analysis the calculus of variations is a set of methods for determining the critical points or extremal functionals using the Euler-Lagrange equation. Variational principles, which are statistical or physical principles expressed in a variational form, are used in the field of computer vision to develop general methods for finding functions which minimize, or maximize, the value of quantities that depends upon those functions. The geometric shape of the unidirectional variations of stripes is considered as statistical principle by Bouali and Ladjal in their work. These authors then define an iterative method based on the minimization of distortion indicators leading to the estimation of the optimal correction factor. In particular the correct definition of this factor is the main

hurdle of this algorithm as there exists a trade-off between the full removal of the stripes and the distortion minimization. Likewise, testing on CRISM data proved that this iterative process results in high computational times.

The main advantage of this family of destriping methods are the low interference with the radiometric accuracy of the data. Furthermore, statistical methods have the ability (though not always exploited) of dealing with non-linear detector responses. On the other hand, statistical destriping methods are usually developed for a specific sensor while filtering approaches can be used for data acquired by different imaging spectrometers. Statistical assumptions also represent a major drawback as the input of all elements of the detector matrix are assumed to have similar statistical characteristics in order to correct response functions of the detectors. Eventually, statistical methods are proved to be ineffective on small-size images, in particular when the image contains along track-oriented structures that are not related to stripes. Unfortunately, I consider this disadvantage to be critical for the correction of hyperspectral images forming the EPF, which are only 15×60 pixels.

In front of the striping effects the CRISM team put forward a destriping technique in the flavor of the work of Gomez-Chova et al. in [65] that is available via the CAT. This filtering method was proposed by Parente in [136] and is detailed in section 14.1. As it is demonstrated by the experiments detailed in the appendix, the CAT destriping method is found to be appropriate for the correction of CRISM hyperspectral images. The satisfactory results obtained after applying this method to several CRISM images justify the integration of the CAT destriping algorithm into the IPAG-DP. The adopted destriping method is fast and tunable in order to embrace different striping magnitudes. In the current implementation of the IPAG-DP I adapt the CAT destriping algorithm by defining a '**cleaning flag**' that allows three degrees of destriping, namely 'LOW', 'MODERATE' and 'HIGH', the second being the option by default. In this way, if a given CRISM presents atypically low or high striping effects, this intrinsic flag of the IPAG-DP can be modified accordingly by the user. This flag shall also be used in the despiking process presented in the following section[1].

4.1.1.2. Despiking CRISM data

Extensive exploration of several CRISM images led to the discover that residual, rather strong spikes remain after the CRISM-DP. Although seeming a cosmetic correction spikes compromise the reliability of some processing steps (e.g. the smile correction in subsubsection 4.1.2.1) and therefore correction methods become necessary. Under these circumstances I propose to include a despiking method into the IPAG-DP. Contrarily to the destriping algorithm included in the CAT, the despiking approach is not appropriate in our case as it is demonstrated below. I therefore propose an alternative tailor-made algorithm to overcome residual spikes. Again, I first summarize the state of the art in correction of dropout pixels.

In the literature spikes are typically corrected using a twofold strategy. The first step consists in detecting the pixels owning an anomalous radiance value compared to its neighbors. The flagged pixels are corrected in a second step by a restoration strategy that typically consists in assigning the

[1] The new calibration TRDR3 is related to an improved radiometric accuracy thanks to the consideration of a statistical model of the noise in the CRISM-DP. The new calibration version therefore enhances the quality of the images in terms of striping noise, making the destriping algorithm less crucial.

average radiance value of the surrounding spectral/spatial neighbors. This is the case of the work of Gomez-Chova et al. aiming at the cleaning of CHRIS hyperspectral images [65]. First, dropouts are selected as those pixels whose difference with contiguous pixels is larger than the difference with the pixels two columns away. The detected dropout errors are then corrected based on both spatial and spectral context of the anomalous pixel. In particular each invalid pixel value is replaced by a weighted average of the values of the spatial neighboring pixels, the weights being computed by a similarity test. Similarly, Davies et al. correct CHRIS data for dropout pixels by subtracting a smoothed version of each spectral image to the original spectral band [46]. The smoothing is done by taking the logarithm to base 10 of the column averages and convolving a smoothing kernel with the logarithm of the column average values. The differences between the smoothed and non-smoothed data are considered as dropout pixels.

Alternatively, the proposed method in the CAT is based on the work of Parente [136]. The work of Parente differs from other methods in the fact that a dropout pixel is defined as a disturbance in the spectral dimension affecting the radiance value of a given spectel. This disturbance must satisfy two conditions:

1. The value of the spectel needs to vary from its spectral neighbors, at one spectral band of distance, by more than a user-defined threshold.
2. The given pixels is declared as a spike only if the adjacent pixels are both higher, or both lower, than the current pixel. A different sign is considered as a steep slope, otherwise.

After the spikes are flagged following the previous conditions, the spectra are corrected by classical interpolation. In order to avoid the artificial smoothing of regions of high spectral frequency Parente adds a preprocessing filter to remove high frequency signals. By dividing all spectra by the average spectrum of the image, all of the features which are consistent over the spatial domain, are minimized. In this way the dominant, high frequency atmospheric variations are isolated and removed. In addition, each spectral band is similarly divided by the average band of the entire image cube. By the application of these two filters, Parente considers all that is left as noise and variation due to change in composition, easing the retrieving of the spikes. At the end, the spectral and spatial information is reincorporated by multiplying by the filters.

Similarly to the striping effect, I first considered the integration of the despiking method proposed by CAT into the IPAG-DP. Unfortunately, exhaustive testing of this algorithm on several CRISM images resulted in unsatisfactory results. I conclude that the filtering by the average spectrum and the average spectral band does not consider cross-track variations due to the spectral smile effect [see Figure 4.7 (left)], which severely modulate the radiance value of pixels at the edges of some spectral images (this shall be explained in detail in subsubsection 4.1.2.1). Therefore, these anomalous pixels due to the smile effect are mistakenly considered as dropout pixels by the CAT strategy. In addition, I consider that the second condition that defines a spike in the CAT (see item 2) is not always satisfied as spikes can be found in very steep portions of spectra. In this case the values of the neighboring spectels may be associated to a higher or lower radiance value than the spike.

As a result of these unsatisfactory results I put forward an alternative despiking strategy for the IPAG-DP. This innovative algorithm is in the flavor of the method proposed in [65] and has been specially adapted to the nature of the CRISM spikes. The proposed technique is twofold:

1. **Detection**: The distance of every pixel $x_{l,c}$ to its $n \times n$ neighbors $\mathbf{X}_{l,c} = \{x_{l-\Delta,c-\Delta}, \ldots, x_{l+\Delta,c+\Delta}\}$,

where $\Delta = \frac{n-1}{2}$, is computed for every spectral band by a $n \times n$ filtering mask $\mathbf{M}$ illustrated in Table 4.1. This mask is devised to be robust against clusters of spikes in the form of rather small squared (3×3 inner kernel set to zero) and vertical (central column set to zero) structures that can impact the detection of spikes otherwise (see an example of spike cluster in Figure 4.4). The parameter n is typically set to 11 as this value provides a good trade-off between a successful detection of all types of spikes and a satisfactory degree of correction. A distance image $\mathbf{D} = \{d_{1,1}, \ldots, d_{n,n}\}$ is then generated by the following expression:

$$d_{l,c} = \frac{x_{l,c}}{\sum \mathbf{X}_{l,c} \cdot \mathbf{M}}. \tag{4.1}$$

Equation 4.1 assigns dropout pixels to large $d_{l,c}$ values. In this way two different populations are usually distinguished when inspecting the histogram of the matrix distance $\mathbf{D}$, (i) a Gaussian-shaped population centered at unity belonging to the majority of the pixels and (ii) some outliers with distances $d_{l,c}$ which are significantly higher than unity. The pixels belonging to the latter population are considered to be spikes. Dropout pixels are flagged by thresholding the histogram by a predefined cutoff value. This parameter has three possible values that are predefined according to three typical magnitudes of the spiking effect and that is chosen by the user through the 'cleaning flag' also used in the destriping method (see subsubsection 4.1.1.1).

$$\mathbf{M} = \frac{1}{104} \begin{vmatrix} 1 & 1 & 1 & 1 & 1 & 0 & 1 & 1 & 1 & 1 & 1 \\ 1 & 1 & 1 & 1 & 1 & 0 & 1 & 1 & 1 & 1 & 1 \\ 1 & 1 & 1 & 1 & 1 & 0 & 1 & 1 & 1 & 1 & 1 \\ 1 & 1 & 1 & 1 & 1 & 0 & 1 & 1 & 1 & 1 & 1 \\ 1 & 1 & 1 & 1 & 0 & 0 & 0 & 1 & 1 & 1 & 1 \\ 1 & 1 & 1 & 1 & 0 & 0 & 0 & 1 & 1 & 1 & 1 \\ 1 & 1 & 1 & 1 & 0 & 0 & 0 & 1 & 1 & 1 & 1 \\ 1 & 1 & 1 & 1 & 1 & 0 & 1 & 1 & 1 & 1 & 1 \\ 1 & 1 & 1 & 1 & 1 & 0 & 1 & 1 & 1 & 1 & 1 \\ 1 & 1 & 1 & 1 & 1 & 0 & 1 & 1 & 1 & 1 & 1 \\ 1 & 1 & 1 & 1 & 1 & 0 & 1 & 1 & 1 & 1 & 1 \end{vmatrix}$$

Table 4.1.: Filtering mask used in the despiking of CRISM spectral bands when $n = 11$. See text for details.

2. **Restoration**: Flagged pixels are corrected by a simple spatial interpolation. I assign each selected pixel to the average of the 3×3 adjacent neighbors in the same spectral band. If one of the adjacent neighbors is also detected as a spike, its value is not considered in the interpolation. In the infrequent case of small clusters of spikes I suggest to use a larger neighboring window (e.g. 5×5) to obtain a realistic output radiance value. Contrarily to the study of Gomez-Chova in [65], I do not consider spectral interpolation in the despiking method adopted by the IPAG-DP as this might bias the corrected I/F value for spectral bands within steep portions of spectra.

As for the experiments, Figure 4.5 shows the IR band 10 of central scan FRT64D9 after applying the proposed despiking procedure (see Figure 4.4 for comparison). As it can be seen, the spikes that were initially highlighted by the red boxes have completely disappeared. According to the similar results

obtained on many spectral bands of different CRISM images, the proposed despiking technique is incorporated to the IPAG-DP.[2].

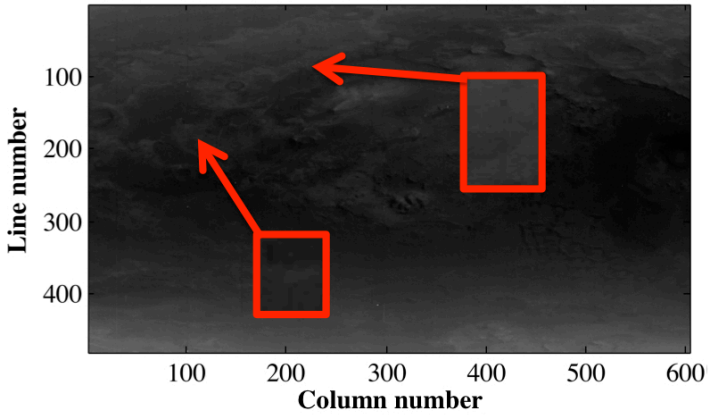

Figure 4.5.: Same figure as Figure 4.4 but after applying the despiking correction proposed in this thesis and adopted by the IPAG-DP. Red boxes frame two previous spikes formed by a few pixels that have been satisfactorily corrected.

Eventually, I investigate the order of execution of the destriping and despiking algorithms by considering several issues. On the one hand, striping disturbances are found to affect the new pixel value produced by the despiking algorithm if the local average is performed by using contiguous columns due to the different multiplicative factors of each image column. On the other hand, dropout pixels can alter the estimation of the detection matrix in the destriping algorithm due to the high spurious radiance values. Based on the latter reason Gomez-Chova et al. apply the despiking technique before the correction for stripes by considering only the values of the vertical neighbors for the despiking interpolation [65]. In our case I decide contrarily to apply the destriping technique in the first place because of (i) the presence of vertical spikes that make impossible an interpolation restricted to only the vertical dimension, and (ii) the use of a trimmed average in the destriping step for the estimation of the detector image (see section 14.1). Due to the latter strategy the presence of spikes have a null impact on the destriping algorithm and the despiking algorithm can deal with destriped data.

4.1.2. Optical artifacts

As it is introduced in chapter 3 two main optical effects are identified to affect CRISM observations. On the one hand, the spectral bands at >2600 nm are corrupted by residual light coming from lower wavelengths. On the other hand, the spectral bands embracing strong absorption features coming from the atmosphere or the surface are altered by the so-called spectral smile effect. The two artifacts are detailed as follow.

- **Second order leakage**: One of the side effects of imaging spectrometers based on diffraction gratings such as CRISM is the existence of multiple orders. Multiple orders make that a percentage of the light corresponding to the spectral band at 1000 nm (first order) is refracted on those bands at 2000 nm (second order), a smaller percentage is refracted at 3000 nm (third order) and so forth [99]. In the design of the CRISM instrument higher orders were prevented from

[2]While the recently released TRDR3 data present a slightly reduced number of dropout pixels, the despiking method is still used in the IPAG-DP due to the presence residual spikes and its low computational time.

contaminating first-order light by using blocking filters [126]. In particular the installed filters admit up to 3% of the second order light from the grating at wavelengths 1400-1950 nm that falls at spectral bands whose nominal wavelengths are 2800-3900 nm. Band leakage is found in this spectral range with a peak at a nominal wavelength of 3400 nm [see Figure 4.6 (left)]. In addition, the relative magnitude of the leakage is enhanced up to tens of percent of the total signal caused by the falloff of both the solar spectrum and the martian reflectance spectrum and the increase of the thermal noise at this wavelength range. Figure Figure 4.6 (right) shows the SNR expected for a full resolution targeted observation and the corresponding falloff at wavelengths >2600 nm. Murchie et al. state that while pre-launch optical testing provided sufficient data for an empirical correction for this effect, the correction was not included in the TRDR2 calibration [126]. As a consequence, the accuracy of the IR detector at >2600 nm and the magnitude of the expected residues are unknown.

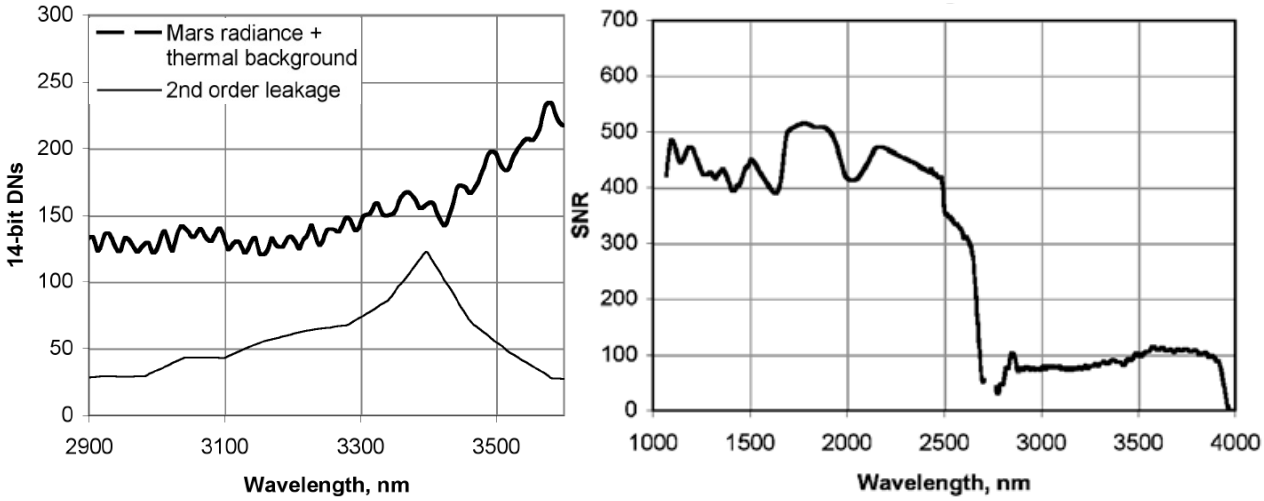

Figure 4.6.: (left) Estimated magnitude of the leakage relative to nominal signal, including effects of the solar spectrum and martian reflectance spectrum. (right) Expected SNR for the CRISM IR detector for a reference surface material expected during targeted observations without spatial binning. Credit: [126].

- **Spectral smile effect**: The CRISM instrument is affected by a common artifact to push-broom-type sensors, the so-called spectral smile effect. The smile effect is generally described as low-frequency artifacts affecting some spectral bands in hyperspectral images as that shown in Figure 4.7 (left). These spurious effects were discovered at the very beginning of this Ph.D. with the visualization of the first CRISM images. The origin of this instrumental artifact comes from limitations of the intrinsic functioning of push-broom spectrometers. Optical aberrations degrade the quality of the scattered light projection depicted in Figure 1.15, thus creating spectral artifacts in the generated hyperspectral images [123]. The impact of the optical aberrations onto the sensor spectral response is summarized by two major effects:

  1. The distorted shape of the light projection makes that the photons corresponding to a given wavelength are sensed by detector elements that are assigned to a different spectral range. Figure 4.8 illustrates this spectral anomaly by plotting the projection of the decomposed light in the absence and in the presence of the optical aberrations. As a consequence of this distortion, the central wavelengths of the PSFs of the CRISM instrument vary according to

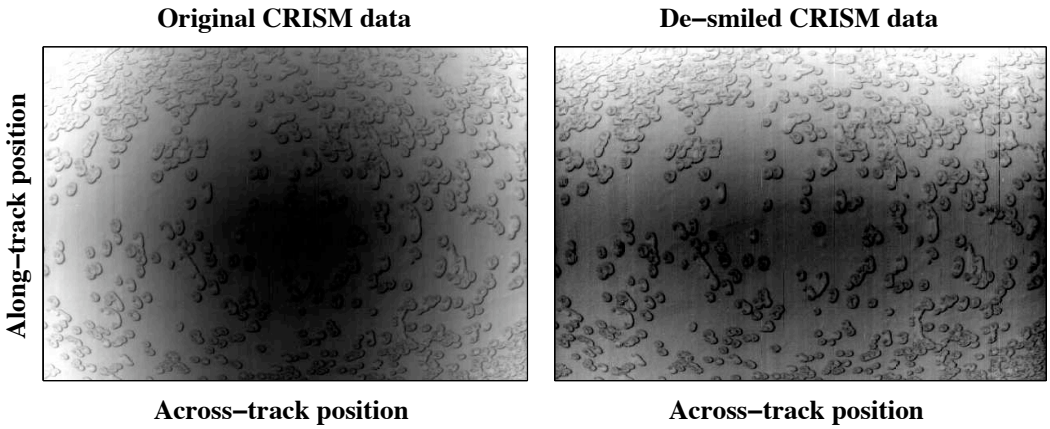

Figure 4.7.: Spectral band at 2013 nm of the CRISM central scan FRT5AE3 (left) before and (right) after correction for the smile effect. In the first image, note the typical cross-track brightness gradient caused by this spectral artifact.

the spatial dimension of the detector matrix (the columns in the image space).

2. The spectral resolution of the CRISM instrument becomes poorer progressing toward the off-axis detectors elements because of a degraded sharpness of the projection. Hence, the width of the CRISM PSFs is also dependent on the spatial dimension of the detector matrix. While this consequence of the optical aberrations is traditionally ignored in the literature, it proves to be as critical as the wavelength shift (see subsubsection 4.1.2.1).

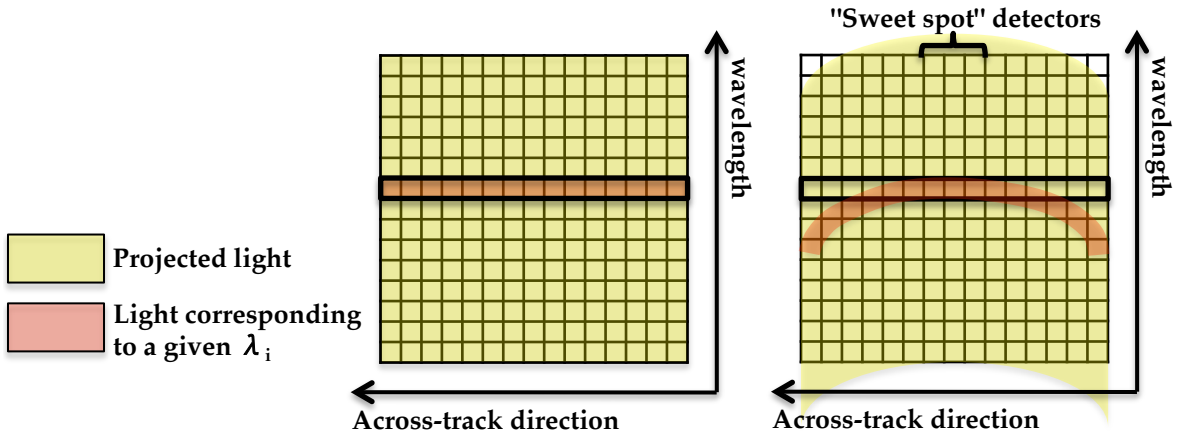

Figure 4.8.: Projection of the light scattered by the grating of a push-broom spectrometer onto the detector matrix in the (left) absence and (right) presence of optical aberrations leading to the so-called spectral smile effect.

These two anomalies are illustrated in Figure 4.9 in which I explore the pre-launch calibration measurements that are stored in WA CDR and SB CDR (see Table 3.1). On the left hand side, the PSF corresponding to three different spatial positions of the CRISM spectral band centered at 2013 nm are plotted. The dashed line corresponds to the average PSF of the CRISM sweet spot where the distortions are minimal [126]. The plain lines illustrate the alteration of the PSF central wavelength and width for the most off-axis detectors. Figure 4.14 (right) further explores the variation of these two parameters along the whole cross-track dimension. Considering the sweet spot as the detectors owning the best performances, CRISM shows increasing optical aberrations

as the off-axis detector elements are inspected.

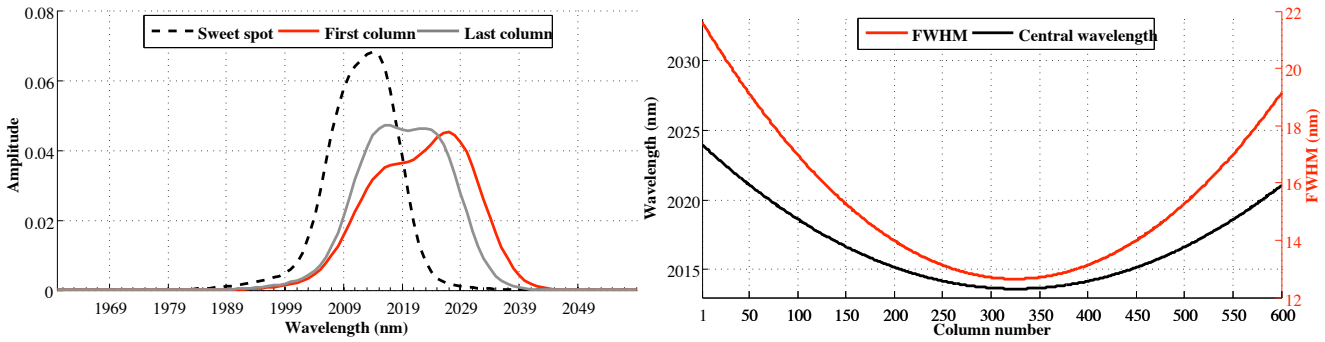

Figure 4.9.: (left) PSF belonging to three cross-track positions of CRISM channel at 2013 nm. Dashed line corresponds to the average PSF of the CRISM sweet spot. (right) Central wavelength and FWHM according to column position of CRISM at 2013 nm.

The aforementioned optical aberrations result in the generation of hyperspectral images whose spectra are collected using different spectral responses. Spectral analysis becomes very challenging under these circumstances as the majority of techniques developed for analyzing hyperspectral images are based on the assumption that data within a given spectral band are acquired under the same spectral conditions. The distortions in the shape and the spectral position of the CRISM PSFs particularly affect the acquisition of off-axis spectra, which suffer from strong spectral shifting and amplitude smoothing. These two effects are shown in Figure 4.12 (top) and are especially aggravated for spectra having strong and thin absorption bands (e.g. solid or gaseous CO_2). In this case, the slightest inaccuracy in the acquisition results in a significant error bias. Contrarily, slowly varying spectra such as most of martian minerals are less affected by the smile effects.

Unfortunately, the planet Mars is a challenging scenario in terms of smile correction due to the predominance of atmospheric CO_2. Indeed, the related strong absorption bands in the near-infrared (see Figure 2.2) produce smile effects in the data, thus affecting all orbital CRISM images. Except in atmospheric studies, CRISM data can be corrected for smile effects by performing an accurate atmospheric correction considering the real set of PSFs for each column. However, CO_2 is also found on the surface of Mars in the form of frozen carbon dioxide in the high latitudes. Since CO_2 ice also shows strong absorption features that result in notable smile effects, an accurate atmospheric correction alone is insufficient to desmile the images of these regions of Mars.

Based on the previous description of the smile effect, the cross-track artifact illustrated in Figure 4.7 (left) can be now explained. This spectral band corresponds to a narrow spectral range centered at 2013 nm of the CRISM central scan FRT5AE3. This particular spectral range encompasses a strong absorption feature of the predominant gaseous and solid CO_2 in the atmosphere and the surface, respectively. The conjugation of the strong variation of the radiance level in this spectral range and the mentioned optical aberrations of CRISM result in the observed cross-track brightness gradient, which is typically called the smile effect. This instrumental artifact introduces non-linearities in the hyperspectral data that may impact following data processing.

As regards the correction of the aforementioned optical artifacts, I decide to adopt several strategies to be included in the IPAG-DP. First, I propose to overcome the second order leakage by working only with the spectral range lower than 2600 nm of the IR channel (spectral bands IR 1-250). This wavelength range has proved to be sufficient enough for a first analysis of the planet Mars as it hosts many spectral features of the atmosphere and the surface[3]. Second, I propose the development of an original algorithm that compensates substantially for the smile effects. This correction approach represents one of the main contributions of this thesis due to the complexity of the artifact and the importance of its correction for upcoming analysis of CRISM data. The description of the desmiling method as well as its application to real CRISM data is presented in the following section.

4.1.2.1. Correction for the spectral smile effect

The correction for the smile effects has been addressed by many authors since the appearance of push-broom-type imaging spectrometers. This has been the case of the Hyperion sensor aboard the Earth Observing-1 satellite. According to the literature I distinguish two main families of desmiling methods:

1. First, we find those techniques that are driven by the artifacts observed in the data. In particular I highlight the work of Dadon et al. who propose the combination of derivative calculations issued from atmospheric absorption features and the MNF transformation (see section 14.1 for a description of this technique) for detecting and correcting the smile effects in Hyperion images [45]. In that study the spectral smile is overcome by adapting the MNF component that embodies the cross-track brightness gradient before rotating the data set back to the radiance space. The desmiling of Hyperion images is also addressed by Goodenough et al. in [66]. The problem is first tackled by a method that uniforms the average value of all columns to the average of the corresponding spectral band. Goodenough et al. state, however, that this technique proves to be inadequate when performed on either the radiance or the MNF space due to the apparition of false spectra caused by the assumption of the image cross-track uniformity. Similarly, Jupp et al. investigate the desmiling of Hyperion images in [87]. First, the MNF component that encompasses the smile effects is de-trended by a polynomial fit before rotating the data back to the radiance space. Another strategy is based on the cross-track illumination correction in the ENVI software. In this method, each value is corrected by subtracting the difference regarding a polynomial that is fitting the averaged line of the corresponding spectral band. These two techniques also fail to provide satisfactory results because of the apparition of false spectra. The main drawback of these methods is their lack of instrumental basis.
2. Second, the second family embraces those techniques that are based on the knowledge of the instrument characteristics. For instance, the works of Goodenough et al. and Jupp et al. address similar desmiling techniques that aim at resampling all spectra to a set of reference wavelengths resulting from the Hyperion pre-launch calibration [66, 87]. The accuracy of this kind of approach is increased by linearly interpolating the data before the resampling. Albeit some smile residues are still detected in the mentioned works, this approach is considered to provide reasonable results. Contrarily, Schläpfer et al. underline the need to correct not only the bias induced by the varying central wavelength of the PSFs but also the non-uniformities coming from the inconstant

[3]The second-order IR leakage is partially solved in the TRDR3 calibration. Therefore, full analysis of the IR channel can be considered now.

spectral width [156]. In this matter Schläpfer et al. suggest a degradation of the imagery to obtain a uniform spectral response on the basis of the broadest occurring PSF. Nevertheless, this strategy is not tested on real data.

The spectral smile effect is a recurrent problem for planetary scientists working with CRISM data. In this matter McGuire and the CRISM team overcome the varying spectral response by modifying their albedo retrieval method in [118]. In particular CRISM spectra are corrected for atmospheric absorption effects in the major CO_2 gas bands by using an approach that is applied separately for the sweet spot and the off-axis columns. Alternatively, Smith et al. overcome the smile effects by performing their atmospheric study only on the sweet-spot columns, thus minimizing the optical distortions in the data [165]. Similarly, Massé et al. limit their study on the detection of gypsum in the north polar cap of Mars to the center of the image [114]. Sadly, this method ignores more than 80% of the data in a CRISM observation. Recently, Seelos and the CRISM team proposed a empirical smile correction that is applied to some specific products belonging to the TRDR3 version [159]. The proposed method is based on the resampling of the data to a set of reference wavelengths in the flavor of the aforementioned techniques developed for the Hyperion instrument. Unfortunately, to our knowledge there is no study addressing the correction of the bias induced by the non-uniformities of the PSF width.

In front of the absence of a standard method to perform a full correction of the smile effects I propose to tackle the desmiling of CRISM data by defining an innovative and robust method. The desmiling approach is based on the combination of a traditional resampling technique and the correction for the non-uniform PSF width, as suggested by Schläpfer [156] but maintaining the spectral resolution at the level of the sweet spot for the whole image. The main goal is to minimize the smile effects while preserving the quality of the information coming from Mars. This original method belongs to the second family of mentioned desmiling techniques as the consideration of the instrumental characteristics is crucial for the sake of an accurate smile correction. With that aim a detailed investigation of the CRISM CDR that could be useful to the desmiling algorithm was carried out[4].

The desmiling method is threefold and is defined as follows:

1. **Smile indicator**. First, I propose a measure of the extent of the smile effects in a CRISM image based on the transformation of the hyperspectral data onto the MNF space. This measure is also adopted by other authors [66, 87, 45]. In the MNF space CRISM images typically show an eigenimage corresponding to a high eigenvalue (i.e. the smile effects are generally related to a high SNR) that encompasses the repetitive brightness gradient that affect some spectral bands [see Figure 4.7 (left)]. Figure 4.10 (right) shows the MNF eigenimage (hereafter referred to as **MNF-smile**) related to the central scan of the CRISM observation FRT64D9 embracing the typical cross-track artifact. I therefore propose the eigenvalue of the MNF-smile eigenimage as an estimation of the significance, or energy, of the smile effect. Other transformations such as PCA or the Independent Component Analysis (ICA) were investigated in this thesis but discarded right after as they perform worse than the MNF when retrieving a component related to the smile (see chapter 15 for more details).
2. **Spectral resampling**. The second step of the proposed desmiling method aims at overcoming the non-uniform central wavelength by resampling all spectra to the sweet-spot parameters. With

[4]In this dissertation I briefly detail the proposed desmiling algorithm. Further details can be found in [26] that is attached to this dissertation in chapter 15.

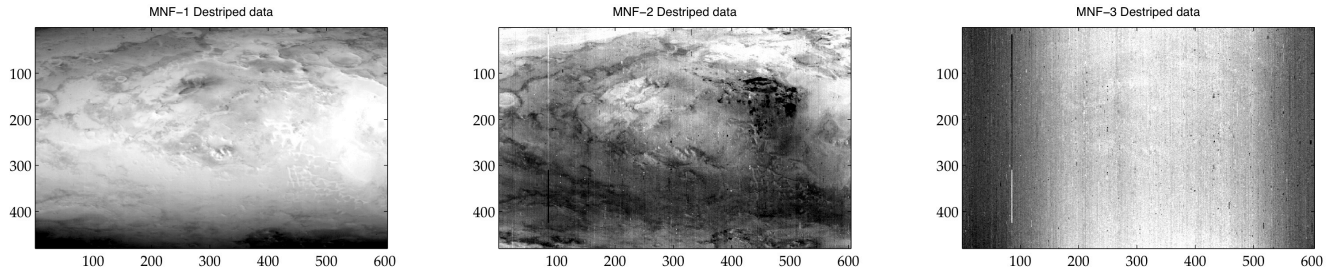

Figure 4.10.: MNF eigenimages of the central scan of observation FRT64D9 corresponding to the three highest eigenvalues. Note the cross-track brightness pattern introduced by the spectral smile in the third eigenimage.

this aim, the central wavelength of each element in the detector matrix is retrieved from the WA CDR. Each reflectance value is then recomputed at the corresponding sweet-spot wavelength after locally interpolating the spectrum by a cubic spline. I consider this interpolation as being meaningful because wavelength shifts caused by the smile are hardly ever a whole number of the spectral sampling $\Delta\lambda$. The use of cubic splines to interpolate is preferred as they reproduce the fidelity of steep absorption features contrarily to linear interpolation methods as it is done in [66]. In this way the proposed approach assumes that the missing data between two consecutive spectels correspond to the points resulting from the interpolation. This hypothesis is reasonable since CRISM is close in meeting the Nyquist sampling theorem for the off-axis detectors (in particular, FWHM$\gtrsim 2\Delta\lambda$, see section 1.4), which undergo a stronger smile correction [126]. The interpolation step underlines the relevance of the despiking algorithm presented in subsubsection 4.1.1.2 as the interpolation of dropout pixels would propagate the error toward the bracketing spectral bands. A weakness of the resampling of CRISM data is the strong sensitivity to potential inaccuracies in the WA CDR. For example, the IPAG-DP is conceived to modify the WA CDR for each CRISM image by adding the corresponding wavelength shift caused by the thermal effects (review subsection 4.1.1). In subsubsection 4.1.3.2 I detail another wavelength anomaly that is taken into account by the IPAG-DP to perform a more accurate resampling of the data.

3. **Spectral sharpening**. In the third step of the desmiling approach I propose to overcome the non-uniform spectral resolution within a given spectral band. The last stage of the desmiling approach is rather innovative as it represents the first attempt in the literature toward the improvement of the non-uniform spectral resolution in push-broom spectrometers. This heterogeneity causes sharp absorption features to be convolved by increasingly wider PSFs as we depart from the sweet-spot columns. As a consequence, spectra become over-smoothed progressively (i.e. the absorption feature becomes shallower), thus contributing to the cross-track brightness gradient. Instead of a global degradation of the spectral resolution as it is suggested in [156], I propose to implement an original sharpening approach inspired by image processing techniques in order to mimic a global increase of the spectral resolution up to the one of the sweet spot. In this way, the spectral contrast of the data is normalized for all the image columns while preserving all the physically meaningful information. In this processing step, the PSF of each detector element (review section 1.4) is assumed to be represented by a single equivalent Gaussian function for

simplicity such that:

$$PSF^{c,b}(\lambda) = \sum_{i=1}^{3} \alpha_i^{c,b} e^{-\gamma_i^{c,b}\left(\lambda-\Lambda_i^{c,b}\right)^2} \approx \alpha_E^{c,b} e^{-\gamma_E^{c,b}\left(\lambda-\Lambda_E^{c,b}\right)^2} \tag{4.2}$$

where $\gamma_E^{c,b}$ stands for the width of the equivalent spectral response for column c and spectral band b. The proposed sharpening algorithm aims at making this term constant regardless of column such that $\gamma_E^{c,b} \approx \gamma_E^b$, $\forall c$. This objective is achieved in a few sub-steps as follow:

- **Estimation of the spectral smile energy**: The energy E^S of the smile effects affecting a hyperspectral CRISM image is estimated as the eigenvalue of the MNF-smile component.
- **Selection of the smile-affected spectral bands**: I propose to perform spectral sharpening only on those spectral bands that are significantly affected by the smile effect. In this way, the inherent risk of sharpening techniques to increase the noise in the data is limited. In this band selection, I include those spectral bands that are affected by the cross-track brightness gradient. This selection is automatically done by exploring the eigenvector related to the MNF-smile component and choosing those spectral bands whose corresponding value is higher than a given threshold. In addition, the spectral bands that are systematically critical in the martian scenario are included, that is, those encompassing the CO_2 gas absorption features (see Figure 2.2).
- **Sharpening**: Every previously selected spectral band is sharpened in order to increase the local spectral resolution. For this processing step, I consider sharpening techniques that are classically applied in image processing for contrast enhancing [155]. Spectral sharpening is individually adapted to each spectral band by taking into account the local shape of the spectra and the instrument spectral response by the following expression

$$r_\lambda^{sh}(c) = \frac{r_\lambda(c) - \omega_\lambda(c)\left(r_{\lambda-1}(c) + r_{\lambda+1}(c)\right)/2}{1-\omega_\lambda(c)} \tag{4.3}$$

  where $r_\lambda(c)$ is the reflectance of spectral band λ for column c and any line position and $\omega_\lambda(c)$ is the sharpening degree within $[0 \ldots 1)$ such that

$$\omega_\lambda(c) = \rho_\lambda \kappa_\lambda(c) = \rho_\lambda \frac{fwhm_\lambda(c) - \min(fwhm_\lambda)}{\max(fwhm_\lambda) - \min(fwhm_\lambda)} \tag{4.4}$$

  where $fwhm_\lambda$ is the FWHM of all detector elements (retrieved from the SB CDR) and ρ_λ is the largest sharpening degree for the spectral band λ. Using the FWHM of the CRISM detector elements, I impose the degree of the desmiling correction to be dependent on the degradation in spectral resolution. Equation 4.4 is defined such that the parameter $\omega_\lambda(c)$ is zero for the sweet-spot spectra (i.e. corresponding to a null sharpening) and maximum for the off-axis data (the most affected by the smile effect). In addition, the sharpening approach is defined to become negligible when flat spectra are processed since $r_\lambda^{sh} \approx r_\lambda$ if $r_{\lambda-1} \approx r_\lambda \approx r_{\lambda+1}$.
- **Sharpening degree determination**: The optimal sharpening degree strongly depends on the shape of the observed spectra. I therefore propose an iterative strategy that determines the

set of optimal ρ_λ factors based on the minimization of the smile energy E^S. For every selected spectral channel, the sharpening degree ρ_λ is set as the value which makes E^S minimal without degrading the quality of the image. More details on this iterative procedure can be found in chapter 15.

- **Desmiling of CRISM observations**: After desmiling the central scan of a CRISM observation, each bracketing image forming the EPF is corrected similarly by undergoing a sharpening strategy applied to the same spectral bands and using the same set of ρ_λ values that those determined for the central scan in the first place. Nevertheless, the set of FWHM functions is of course specific to the EPF as this parameter is intrinsic to the instrument and not to the desmiling approach. This choice is made to perform a spectrally uniform sharpening on the eleven hyperspectral images forming a single CRISM observation. In addition, the individual desmiling of the EPF is almost unfeasible as the 15×60-pixel images are too small to define the MNF-smile component. Indeed, the smile indicator is based according to the typical cross-track pattern induced by the smile, which is not always distinguishable in such small images.

4.1.2.1.1. Application to CRISM data The proposed desmiling technique is applied to the central scan of the CRISM observation FRT5AE3. This observation was acquired over the so-called "Swiss cheese" terrains in the southern latitudes of Mars (see Figure 4.11). According to recent studies this area of Mars is very rich in CO_2 ice [21]. For this reason, the observation FRT5AE3 is singularly challenging in terms of desmiling due to the presence of frozen carbon dioxide in the surface in addition to the atmospheric CO_2 over it.

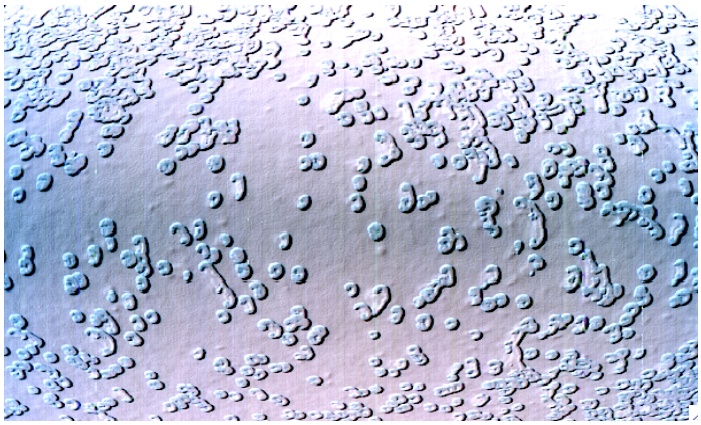

Figure 4.11.: Central scan of the CRISM FRT5AE3 observation acquired over the southern residual cap at 86° S, 6° W. This image is the original image space and in approximative real color. The so-called "Swiss cheese" features can be observed. Credit: CRISM team.

In this experiment I only consider spectral bands from number 138 to 168 of the IR channel for the evaluation of the smile correction method. Indeed, the corresponding spectral range is particularly demanding as it embraces the strong 2-μm absorption feature due to CO_2. This feature is of great interest in (i) many scientific atmospheric studies for the determination of the surface pressure [167] or the retrieval of the AOT (see section 14.2), (ii) processing by spectral unmixing techniques as it is explained in Part IV, or (iii) physical characterization of the remotely sensed signal by modeling as in

Part III. In order to monitor the correctness of the results the spectra forming the FRT5AE3 central scan are carefully inspected at the mentioned spectral range. In Figure 4.12 I explore the evolution of the spectra throughout the desmiling process depending on the number of column. Albeit this image is quite homogeneous I decide to average the central 100 lines of the central scan to minimize the remaining heterogeneity of the surface. These data are explored at each step of the desmiling process as follow:

1. Figure 4.12 (top) illustrates the spectral shift and the degradation in spectral resolution as the off-axis positions of the PDS-released data are explored. The red spectrum, which corresponds to the average of the first column in the left hand side of the detector matrix, is shifted close to two spectral bands (~10 nm) toward lower wavelengths. Furthermore, we note that the lower contrast of this spectrum is close to eliminate the weak absorption features at the spectral bands IR 158-162. The eigenvalue corresponding to the MNF-smile component E^S is detected to be equal to 100.1.
2. After the resampling step Figure 4.12 (center) underlines the removal of the spectral shift. At this point the CO_2 ice absorption features of the four averaged spectra share the same spectral position. Nonetheless, spectra close to the edges of the detector matrix are still too smooth in comparison with the spectrum corresponding to the sweet spot. In this figure the impact of the non-uniform spectral resolution on the spectra is highlighted in comparison to Figure 4.12 (top). After the resampling step, the smile energy E^S undergoes a decrease of ~90% down to a value of 7.6.
3. As for the last step of the desmiling technique, Figure 4.12 (bottom) illustrates the increase of the local spectral contrast of the CO_2 absorption features. Indeed, the proposed sharpening technique enhances the spectra by focusing particularly on the spectra belonging to the off-axis columns. By contrast, the sweet-spot spectrum remains untouched. We note that the fidelity of the spectra is preserved and there are no spikes caused by overcorrection. However, special attention must be paid to the features around the spectral band IR 162. Unfortunately, the strong, original degradation caused by the poor spectral response of the off-axis detectors makes impossible to enhance the spectra in this case. Eventually, the inspection of the smile energy E^S shows a second decrease of ~70% down to a value of 2.1, which is close to the noise threshold in a MNF transformation, usually set to unity [67].

In addition to the previous investigation the benefits of the desmiling approach are also evident in the spatial dimension of CRISM data, the spectral bands, as Figure 4.7 (right) illustrates. The spurious cross-track brightness gradient is greatly corrected revealing a secondary along-track gradient coming from the anisotropic photometry of the planet Mars, mostly due to atmospheric aerosols. The residual cross-track trend in the form of a darker pattern in the center of the image may come from the limitations of the desmiling method or, again, the anisotropic photometry of the planet Mars. As a matter of fact the highest cross-track variation in VZA in central scans (~5°) happens for the central lines and therefore highly anisotropic scenes, such as the one presented by the FRT5AE3 due to the presence of ice and aerosols, are suitable to present a cross-track component coming that is not spurious.

In conclusion a special effort is dedicated to the correction of the smile effects in CRISM observations. This artifact corrupts the data in a very particular manner that puts in danger some of the primary objectives that are defined in this thesis. First, smile effects impact severely the absorption features

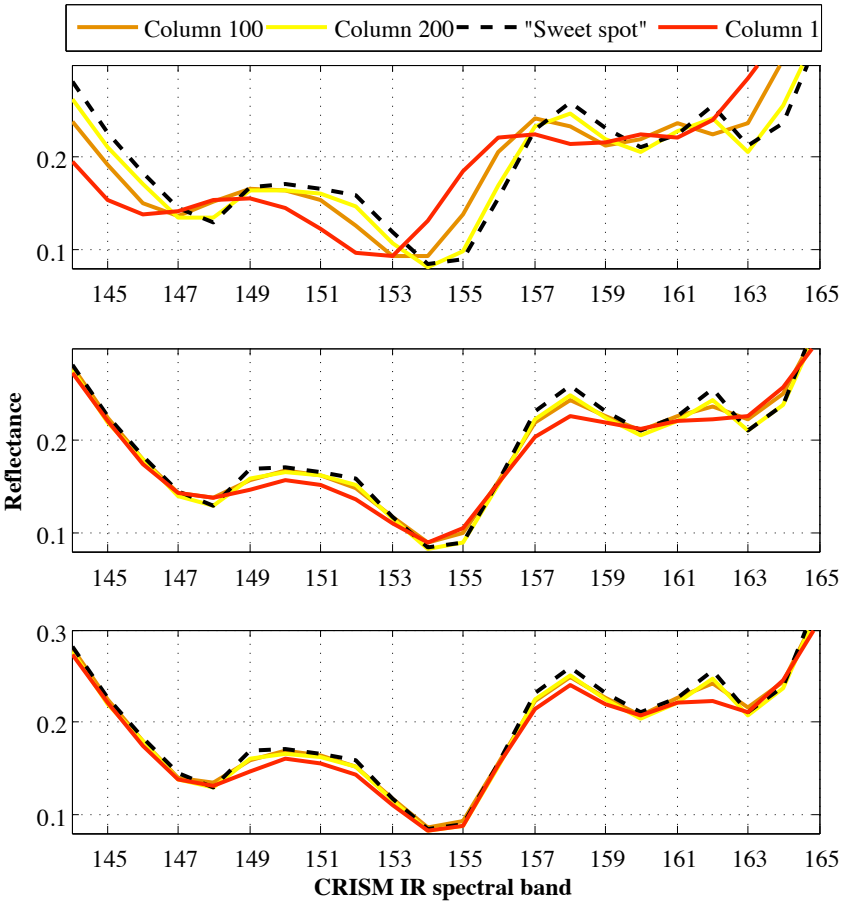

Figure 4.12.: Spectra belonging to four different column positions throughout the desmiling process (top to bottom). All spectra are the result of averaging the 100 central lines of the FRT5AE3 central scan.

related to the atmospheric CO_2. As it is explained in section 14.2, the accuracy of the adopted atmospheric correction strategy for CRISM data depends on the knowledge of the exact wavelengths of the CRISM detectors and on the fidelity of the shape of the 2-μm absorption features.

An example on the benefits of the proposed desmiling method for this thesis is summarized in Figure 4.13. In this figure I investigate a set of photometric curves retrieved from a CRISM multi-angle observation (see subsection 4.2.4 for a definition of photometric curve). Figure 4.13 plots as black crosses the whole ensemble of at-sensor apparent reflectance values of the CRISM observation FRT5AE3 (i.e. the central scan and the EPF) at 2013 nm. Data are plotted according to phase angle, which is a key descriptor of the acquisition geometry. As it can be seen, the data clusters (corresponding to each of the eleven scans) show a recurrent curved pattern caused by the simultaneous variation according to column of the brightness intensity due to the smile effect and the phase angle. Furthermore, this artifact is annoying in the fact that a given terrain unit sensed by the eleven scans within a CRISM observation is typically observed by detector elements belonging to different column positions, and thus to different spectral responses. The smile effect may thus corrupt the processing of these angular signatures in the retrieval of the surface BRDF as it is done in Part III. The gray crosses in Figure 4.13 represent the apparent reflectance data after undergoing the proposed desmiling method. According to the presented results, data are strongly compensated for the smile bias while

the apparent reflectance preserves the main dependence on the phase angle.

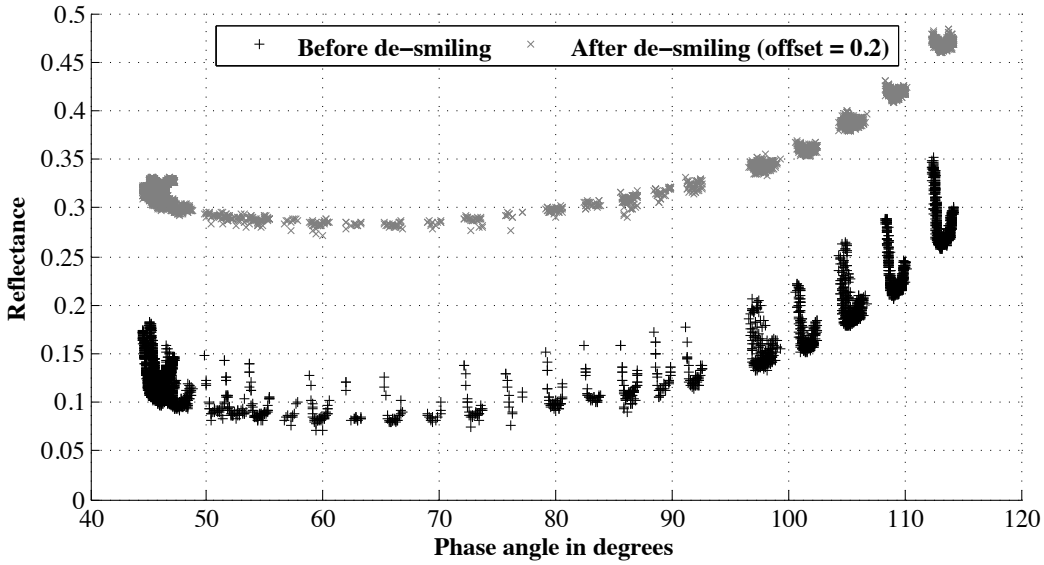

Figure 4.13.: Apparent reflectance values of spectral band IR 155, observation FRT5AE3. The data of the 11 scans are plotted before and after desmiling (offset for clarity).

4.1.2.1.2. Discussion and future prospects As one of the initial objectives of this thesis I have proposed an original technique for the correction of the so-called spectral smile effect. The desmiling algorithm aims at normalizing the non-homogeneous spectral response of CRISM along the cross-track dimension of the matrix detector. According to the presented experiments, among others performed during this thesis, the proposed method is robust even for challenging CRISM observations. Furthermore, the proposed algorithm is suitable to correct for smile effects affecting other push-broom sensors as long as accurate pre-launch calibration records are available.

Regarding the limitations of this original method I highlight the sensitivity of the resampling method to existent inaccuracies in the pre-launch measurements. Indeed, some disagreements were found between the pre-launch WA CDR and the operative wavelengths as it shall be explained in subsection 4.1.3. These discrepancies may result in a deficient resampling of the spectral data. Furthermore, the sharpening procedure may be unsatisfactory when enhancing absorption features that have nearly disappeared in the off-axis columns due to a very degraded spectral resolution. Unfortunately, the deconvolution of the signal performed by the sharpening process is no longer possible under these circumstances. In this case I remark that a spectral degradation of the image as it is proposed in [156] may be more appropriate than the current spectral improvement. It is important to bear in mind that sharpening techniques are intrinsically related to noise increase. Albeit the amount of sharpening is carefully set to cause the minimum noise increase the method is not optimized for considering all the variability embraced by CRISM observations. In order to constrain the optimal set of correction factors ρ_λ I propose as a future future prospect the use of quantitative indexes that evaluate the impact of the spectral sharpening on the corrected spectral bands. Some possible distortion indicators are summarized in the Ph.D. dissertation of Bouali in which these tools are used to measure the image degradation introduced by destriping algorithms [15]. Eventually, I point out that the rather high computational time of the desmiling algorithm may trouble the processing of large collections of CRISM images. Indeed, the

iterative process to determine the set of optimal sharpening factors ρ_λ is based on the monitoring of a MNF transformation. In this context the large size of CRISM observations (~100e6 pixels) results in executions times around a few hours in a regular computer. Alternative and less computing demanding definitions of the smile energy E^S may be considered to lighten the computational burden such as the correlation coefficient between the MNF-smile eigenimage and each of the CRISM spectral bands.

4.1.3. Calibration of in-flight wavelengths

Another spectral anomaly was discovered while testing the presented desmiling correction. Accurate investigation of CRISM spectra after the resampling step of the desmiling algorithm (see item 2) revealed a persistent column-dependent spectral shift affecting the position of some absorption features. In Figure 4.14 I illustrate this anomaly for the central scan of observation FRT5089 acquired over icy terrains of Mars. In this figure only the spectral range embracing the strong 1.43-μm absorption band related to CO_2 ice is considered. Each curve is the result of averaging all spectra belonging to columns 1, 50, 100 or those forming the sweet spot. This averaging is appropriate while analyzing the image FRT5089 as it embraces a very homogeneous area of the CO_2-ice dominated southern polar cap of Mars. On the left hand side of Figure 4.14, a typical negative spectral shift due to the smile effect can be observed as we depart from the sweet spot. Given that the ice is homogeneously present all over the image, the depicted absorption maximum should be situated at the same wavelength regardless of the number of column. In Figure 4.14 (right) I show the same spectral range after resampling the FRT5089 central scan to the sweet spot wavelengths, that is, after undergoing the first step of the proposed desmiling method in subsubsection 4.1.2.1. As it can be seen, the spectral shift not only persists but its sign is inverted. In this case the resampling overcorrects the spectra by introducing a positive shift that still corrupts the radiometric accuracy of the data. This anomaly is observed with different intensities for several absorption features. In this context I proposed to investigate the causes of this anomaly as this irregularity does not allow to carry out fine spectral analysis of CRISM data (e.g. atmospheric correction).

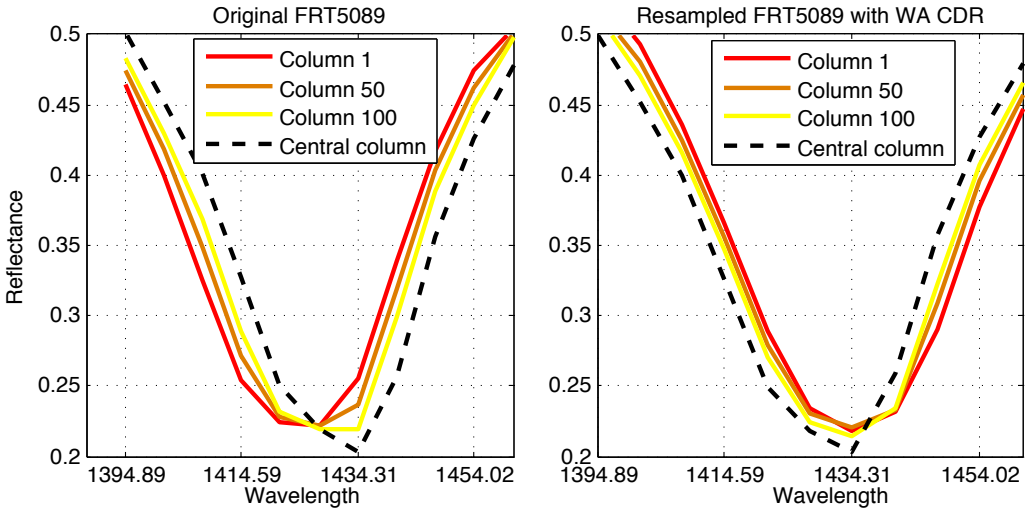

Figure 4.14.: Line-averaged spectra according to different column positions of the central scan of the CRISM FRT5089 before and after spectral resampling using the WA CDR.

This anomaly was first mistakenly thought to belong to a disagreement between the pre-launch cali-

brated wavelengths and the in-flight ones. I came to this preliminary conclusion since it agreed with the typical mismatch described in the literature affecting other imaging spectrometers such as the Hyperion sensor caused by vibrations during the spacecraft launch. Figure 4.15 illustrates this anomaly in Hyperion data in the study of Neville et al. in [132]. As it can be seen, the curves of the in-flight wavelengths retrieved for different Hyperion images do not agree with the pre-launch calibration measurements. In this matter Murchie et al. detail that, although vibration testing for CRISM exceeded expected launch vibrations by 50%, spectral shifting during launch can not be ruled out [126]. I therefore was ready to address the characterization of the on-orbit radiometric performance of CRISM to compare it against the performance established during pre-flight acceptance tests. This type of study has been done in the past by many authors such as in [9, 62, 70].

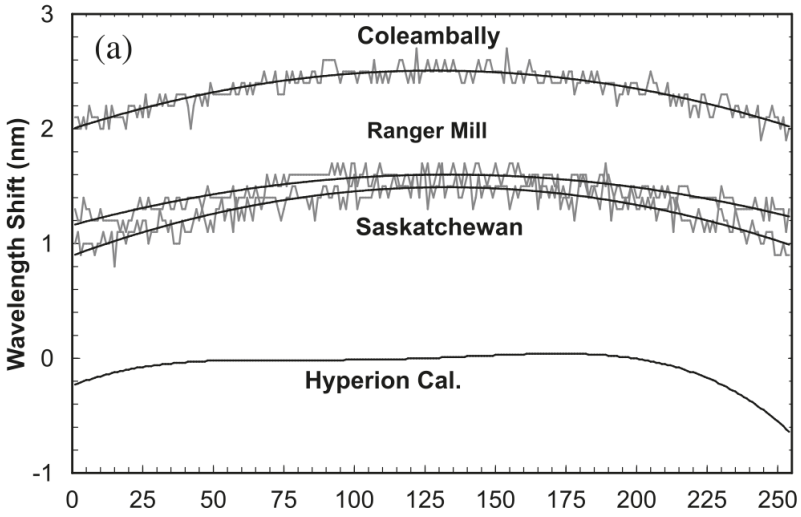

Figure 4.15.: In-flight wavelengths calculated at the 1136 nm water vapor band, with their polynomial fits, for three Hyperion data sets: Coleambally, Ranger Mill and Saskatchewan. The laboratory calibration for the Hyperion 1134 nm band is included. The disagreement in shape between both can be observed. Credit: [132]

Unexpectedly, further investigation proved that the strength of this anomaly varies for different CRISM images acquired within a short interval of time. Albeit some modifications of the capabilities of CRISM are expected due to temperature variations, the intensity of the observed fluctuations made us look at other instrumental reasons. After discussion with some engineers of the CRISM team we found out that this spectral anomaly comes from a faulty processing step of the CRISM-DP, the so-called flat field correction[5].

In this thesis I suggest to incorporate to the IPAG-DP an original algorithm to compensate for the effects of the presented anomaly. In subsubsection 4.1.3.1 I briefly detail the anomaly caused by the flat fielding on the CRISM spectral bands encompassing strong absorption features. I then introduce the innovative method that estimates the operative in-flight wavelengths based on synthetic reference data in subsubsection 4.1.3.2. This set of retrieved wavelengths may be used for performing a refined correction for the smile effects as in subsubsection 4.1.2.1. I conclude this section by testing the calibration method on the central scan of the CRISM observation FRT5089.

[5]The origin of the spectral anomaly was indeed discovered (partially based on our observations) by David Humm from the John's Hopkins University Applied Physics Laboratory. David Humm is part of the CRISM team and has collaborated with us during this Ph.D.

4.1.3.1. Flat fielding anomaly

As it has been shown in previous sections, push-broom imaging spectrometers suffer from several non-uniformities. In particular the elements of the detector matrix are not homogeneous in responsivity (i.e. the input-output gain of a detector system), which, furthermore, varies during flight due to thermal shifts (see chapter 3). This varying heterogeneity of the sensor results in artifacts affecting the data. **Flat fielding** techniques are a standard calibration procedure used to correct this effect from conventional digital cameras to high precision optical telescopes. Particularly, flat field correction aims at uniforming the responsivity of each spectral band at all spatial positions. After a detector matrix is appropriately flat-fielded, a uniform signal as input creates a uniform output, that is to say, free of systematic errors. The so-called flat-field refers to the set of weights by which the input data must be rationed to be flat fielded [135].

In order to overcome these non-uniformities, a classical flat field correction is integrated by the CRISM team into the CRISM-DP [126]. Flat fields are generated periodically using flight data by taking an average of many lines of several CRISM images of bland scenes of Mars. The resulting spatial-spectral array is considered as an estimate of the detector matrix responsivity at that time and is stored in a NU CDR (see Table 3.1). Each CRISM image is divided by the closest NU CDR in time as part of the CRISM-DP. Figure 4.16 shows the flat field stored in the NU CDR which corresponds to the CRISM image FRT5089. The construction of flat fields based on pre-launch calibration data is not considered by the CRISM team due to launch shifts, thermal shifts, and other factors.

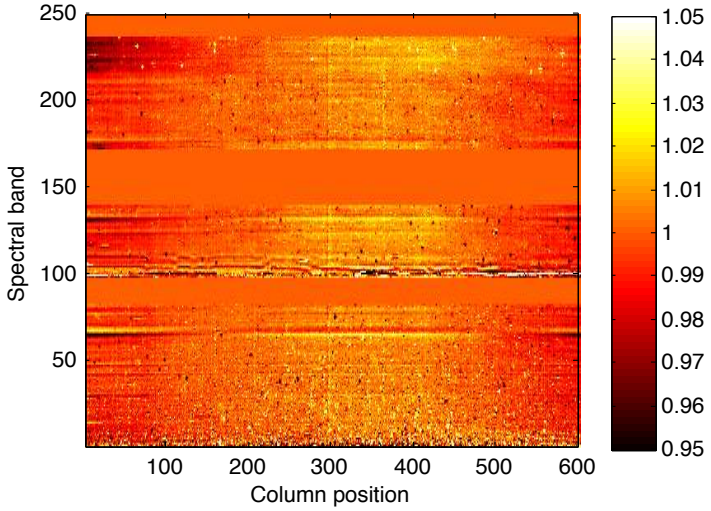

Figure 4.16.: Flat field used for the spectral range from 1 μm to 2.6 μm of the CRISM image FRT5089. Note the spectral ranges for which the flat field is disabled (put to unity) and the ones affected by the spectral smile artifact (e.g. spectral band IR 67).

A side effect of this preprocessing step is the interaction of the smile effects with the flat field correction. In the NIR spectrum, fairly sharp spectral features (i.e. mainly absorption maxima of atmospheric gases) affect the bland scenes that are used to generate the flat fields. In the presence of spectral smile, the flat field used for correcting a given spectral band is not acquired at the same wavelength, and therefore the typical smile brightness gradient is considered as being part of the non-uniformitites that must be flat fielded. In other words, the flat field is formed by the non-uniform responsivity of the detectors plus the smile effects, the latter being often stronger than the former. The objectives of the flat

field correction do not include the correction of the smile effects (in fact, a simple rationing with the NU CDR cannot accurately desmile the data), and therefore the flat fielding is disabled in the CRISM-DP for those spectral bands embracing strong CO_2 gas absorption features (i.e. 1546-1638 nm, 1921-2126 nm and 2563-2933 nm. See red strips in Figure 4.17 and the result in NU CDRs in Figure 4.17) [126]. In these precise spectral bands, the uniformity in responsivity is not assured but stronger artifacts coming from the smile effect are prevented.

This conservative flat fielding is appropriate for most CRISM images in which the absorption maxima due to the CO_2 gas are the unique source of the smile. However, the high latitudes of Mars encompass another hazard in terms of smile effects, namely the terrains covered by CO_2 ice. In particular the CRISM spectral bands encompassing the strong absorption features of this type of ice (e.g. at 1.43 μm) are outside the spectral range in which the flat fielding is disabled. The smile effects at these wavelengths may be therefore mistaken for the instrument responsivity (note the higher variations of the flat field for spectral band number 67, corresponding to 1.43 μm, in Figure 4.16). As a consequence, the flat fielding mistakenly removes the brightness gradient due to the smile that is found in the bland scenes. This miscorrection of the smile effects is not adequate as the strength of the smile artifact is generally different from image to image (and thus is not the same for the bland scenes and the flat fielded image) due to different chemical composition. In other words, a faulty flat fielding may imitate a desmiling correction if both strengths are equal while the spurious spectral shift will be overcorrected or under-corrected otherwise (as it happens for FRT5089 in Figure 4.14). This anomaly results in a spectral shifting of the affected absorption bands, making "apparent" in-flight wavelengths no longer correspond to pre-launch measurements.

The present faulty flat fielding may severely impact the analysis of CRISM data from the high latitudes of Mars at the wavelengths that correspond to the ice absorption features, for example. I highlight the work of Appéré et al. who monitor the CO_2 deposits of the northern terrains of Mars observed by the OMEGA instrument using a method based on the CO_2 feature at 1.43 μm [4]. A similar study cannot be done using PDS-released CRISM data even with an accurate desmiling of the data. As a matter of fact, fine data processing such as spectral smile or atmospheric correction are based on the exact knowledge of the position of the operating wavelengths (which are typically retrieved from the WA CDR) and therefore inaccuracies caused by the faulty flat fielding may remarkably impact the results.

4.1.3.2. Methods

After the faulty flat fielding has been identified, I propose a novel method to overcome the resulting anomalies in the data. This calibration improvement is included in the IPAG-DP and can be applied to those images which especially suffer from this artifact, typically those containing CO_2 ice such as the central scan FRT5089.

I address the faulty flat fielding by considering that it produces a typical wavelength miscalibration. In other words, I consider that the stored WA CDR do not correspond to the operating wavelengths (hereafter refereed to as apparent wavelengths) within the affected spectral ranges as it is shown in Figure 4.14. This assumption is verified by the observation of Figure 4.14. In this context, I propose a method for estimating the in-flight apparent wavelengths inspired by those studies that address the on-board calibration of the Hyperion spectrometer such as the works of Neville et al. [132] and Barry et al. [9]. In the former study, the central wavelength and the width of the Hyperion PSFs are estimated by

iterative atmospheric corrections considering different spectral responses. The optimal PSF parameters are the ones that yield to the smoothest surface spectra after atmospheric correction. Contrarily, the work of Barry et al. retrieves the in-flight wavelengths based on a reference atmospheric spectrum at the sensor spectral resolution. These synthetic data are used to estimate the apparent wavelengths of a given spectral band of the affected image by comparison with the closest absorption feature in the reference spectrum. In this thesis I propose to implement a wavelength calibration method in the flavor of [9] but adapting it to consider a reference solid CO_2 spectrum. The proposed method is fast, simple and accurate enough to determine the apparent CRISM wavelengths of those spectral bands corresponding to the critical absorption features. The wavelength calibration is performed for each absorption feature that is depicted by an arrow in Figure 4.17 and not falling within the red strips as follows:

1. A synthetic CO_2 ice spectrum is generated at very high spectral resolution by the RT model in [54] using optical properties of ice measured in the laboratory by [158]. The physical properties of the ice are chosen to be representative of the polar terrains of Mars. Likewise, a typical transmission spectrum of the gases in the high latitudes of Mars is simulated to be multiplied by the ice spectrum. In this way, the realism of the resulting reference spectrum is improved.
2. The reference spectrum is convolved by the CRISM spectral response retrieved from the ancillary data SB CDR. I do this for every spatial position of the detector matrix, thus generating a reference spectrum for each of the 600 columns of CRISM. Figure 4.17 shows, at the CRISM spectral resolution, the CO_2 ice spectrum, the vertical transmission of the gases and the resulting spectrum after multiplication of an arbitrary column in green, red and blue, respectively. Likewise, the corresponding average spectrum of the image FRT5089 is plotted in gray to underline the realism of the reference spectrum.

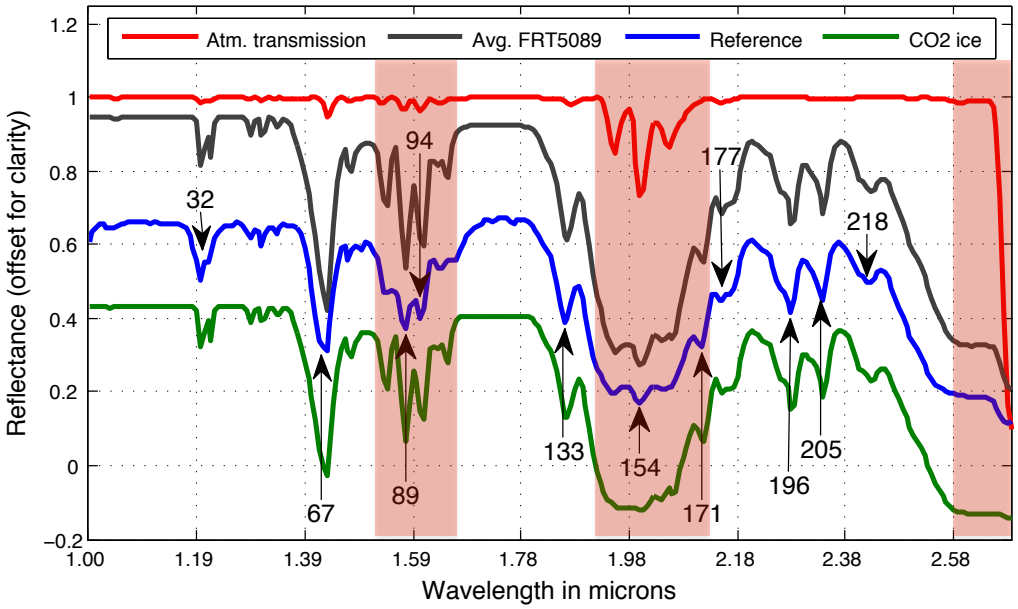

Figure 4.17.: Reference and real spectra summarizing the wavelength calibration strategy. All spectra except for the atmospheric transmission spectrum in red are modified by an offset for clarity. Arrows point to the potentially-affected ice absorption features and identify the number of the corresponding CRISM spectral bands. Red strips highlight those spectral ranges in which the flat fielding has been disabled. See text for details.

3. In the processing of a given CRISM image, the apparent wavelength of each ice absorption feature is determined, for each column, for both the reference and the in-flight spectra based on a minima search strategy. If the CRISM image is homogeneous enough, spectra can be averaged along the line dimension to increase the SNR in the minima search.
4. The apparent wavelengths of the spectral bands close to the absorption feature are obtained by extrapolation (taking $\Delta\lambda$=6.55 nm [126]). Reference and in-flight data are interpolated with cubic splines for retrieving accurate in-flight wavelengths. I prefer cubic splines rather than other interpolation methods according to the satisfactory results provided for the desmiling approach. Figure 4.18 details an example in which the reference and real spectra corresponding to a given column are fitted by cubic splines before determining the absorption maxima around 1.43 μm (green and orange dashed lines, respectively). The wavelength axis corresponds to the reference spectrum while the horizontal axis of the real spectrum is considered unknown due to the faulty flat fielding. By assuming that the separation between spectral bands is 6.55 nm, the difference between the real minimum and the reference minimum can be straightforwardly determined (i.e. 1.5 nm in the example). This calculation is repeated for each column position in order to plot the curve that determines the wavelength distance for the closest spectral band, namely the IR band 67 in the example in Figure 4.18.

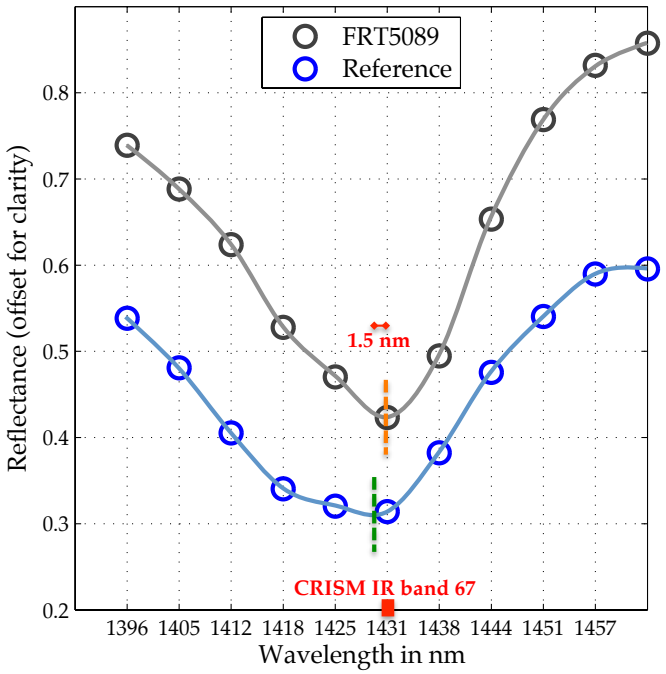

Figure 4.18.: Example on the determination of the wavelength distance between real and reference spectra. See text for details.

The accuracy of the proposed method is tested empirically by calibrating the CRISM-like reference data set, whose wavelengths are known. Comparison of the estimated wavelengths with the WA CDR curves, which are used to generated the reference data set, gives a maximum error of $\pm$0.01 nm.

The calibration method is included in the IPAG-DP to estimate the in-flight wavelengths for a given CRISM image, at every column, for each absorption feature that is affected by the faulty flat fielding. I

remark that in the absence of spatially extended CO_2 ice, the presented wavelength calibration could be done if a synthetic spectrum of the material having the strongest absorption features is made available. For example, the faulty calibration in spectral bands corresponding to atmospheric absorption features could be overcome by considering a synthetic atmospheric spectrum as it is done in [9]. As for mineral materials, they do not generally present strong absorption features, and thus the faulty flat fielding does not have a remarkable impact.

4.1.3.3. Experiments and discussion

Before including this processing step in the IPAG-DP, several experiments were carried out on different CRISM images. In this thesis, I detail the calibration of the central scan of the CRISM observation FRT5089 from 1.0 to 2.6 μm. This image is indeed very challenging as there are many strong absorption bands due to the presence of CO_2 ice.

Table 4.2 details the compatibility of the estimated in-flight wavelengths with the WA CDR for each ice absorption feature detailed by an arrow in Figure 4.17. In this experiment, spectral bands that are already well calibrated due to a disabled flat fielding are also processed for comparison with the affected ones. The fourth column of Table 4.2 details the average of the set of spectral shifts obtained as in Figure 4.18. As it can be seen, spectral bands for which the flat fielding is disabled present lower spectral shifts while absorption features outside the red strips in Figure 4.17, and thus affected by the faulty flat fielding, present average shifts up to 1.1 nm. The average value of the former group (i.e. ~0.34 nm) is acceptably low and may be explained by inaccuracies in the thermal shift (as it is explained in subsubsection 4.1.2.1). By contrast, the latter group of absorption features, which show significant spectral shifts, correspond to strong absorption features that are affected by the faulty flat fielding (e.g., IR bands 32, 67 and 133). The reason why features corresponding to greater wavelengths (> 2.15 μm) are less impacted may be a weaker strength of the absorption feature.

Wavelength	Spectral band	Flat fielding	Average spectral shift
1.20 μm	32	Enabled	1.13 nm
1.43 μm	67	Enabled	0.87 nm
1.58 μm	89	Disabled	0.25 nm
1.61 μm	94	Disabled	0.44 nm
1.87 μm	133	Enabled	1.10 nm
2.00 μm	154	Disabled	0.26 nm
2.11 μm	171	Disabled	0.43 nm
2.16 μm	177	Enabled	0.71 nm
2.28 μm	196	Enabled	0.64 nm
2.34 μm	205	Enabled	0.70 nm
2.43 μm	218	Enabled	0.40 nm

Table 4.2.: List of absorption features of the CO_2 ice encompassed by the CRISM spectral range considered in this study. The average spectral shift between the apparent and the WA CDR wavelengths is detailed according to the use or not of the flat field correction.

Further testing is performed by exploring a couple of representative absorption features. In particular Figure 4.19 details the wavelength calibration in a similar way to Figure 4.15. The red lines correspond to the estimated apparent wavelengths while the pre-launched measurements WA CDR are shown

by the black dashed lines. As it can be seen, both curves match satisfactorily for the feature at 2 μm due to the lack of flat field correction [see Figure 4.19 (left)]. Small differences are explained by the quadratic approximation that was used to fit pre-launch measurements [126]. Contrarily, the absorption feature at 1.43 μm suffers from the faulty flat fielding according to the distorted red line shown in Figure 4.19(right). This behavior is observed for other problematic bands. As it can be seen, there exists a correlation between the sign of the wavelength shift regarding the WA CDR and the flat field value. A flat field value greater than unity (e.g. central columns) induces a spectral shift toward greater wavelengths while spectra are shifted in opposite for a flat field value lower than unity (note the offset applied to the flat field curve in Figure 4.19).

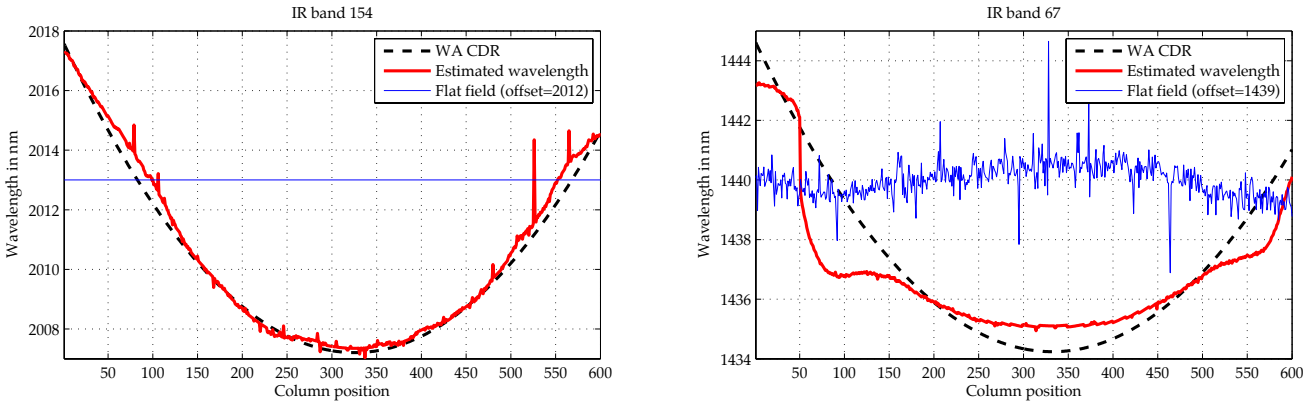

Figure 4.19.: Calibration results corresponding to (left) the spectral band IR 154 at 2 μm and (right) the spectral band IR 67 at 1.43 μm are plotted in red. The dashed black line corresponds to the WA CDR and the flat field (extracted from the corresponding NU CDR) is shown in blue with an offset for clarity.

The use of the WA CDR curve instead of the distorted red one in the desmiling resampling results in the deficient results shown in Figure 4.14. In this context, I propose the use of calibrated apparent wavelengths for data processing that needs an accurate knowledge of the CRISM spectral response (e.g. correction for smile effects and atmospheric correction). This calibration must be performed independently for each CRISM observation because of the dependence of the anomaly magnitude on the physical properties of the flat fielded image and the bland scenes that are used for generating the flat field.

In this matter, I perform a last experiment to underline the substantially better performances that are obtained based on the estimated in-flight wavelengths when correcting for the smile effects among other processing. The original spectra of the central scan FRT5089 are resampled to the sweet spot wavelengths as detailed in subsubsection 4.1.2.1 using, on the one hand, the typical WA CDR, and, on the other hand, the estimated wavelengths by the proposed original method. A third experiment is performed by processing the TRDR3 version of the image FRT5089. As a matter of fact, this new calibration disables the flat field correction in the spectral ranges corresponding to the CO_2 ice absorption features among other improvements[6]. Table 4.3 shows the energy associated to the smile artifacts by means of the MNF transformation (see subsubsection 4.1.2.1) before and after resampling. As it can be seen, the eigenvalue related to the MNF component embracing the smile effects is very similar

[6]The release of the TRDR3 data started in mid-2011. The proposed method was developed in early 2010 as an alternative solution to the faulty flat fielding. This work was used among other studies by the CRISM team to define the spectral ranges for which the flat fielding should be disabled [159].

when using the in-flight wavelengths for the processing of the TRDR2 image and the WA CDR for the improved TRDR3 image. It is important to remark that the MNF-smile eigenvalue pertains to all wavelengths affected by the smile and not only to those suffering from a faulty flat-fielding. That is the reason why the MNF-smile eigenvalue also decreases significantly (although to a lesser extend than otherwise) after resampling when the TRDR2 + WA CDR is considered.

FRT5089	TRDR2+WA CDR	TRDR2+in-flight wave.	TRDR3+WA CDR
Original MNF eigenv.	743	743	754
Resampled MNF eigenv.	139	113	112

Table 4.3.: Eigenvalue of the MNF component corresponding to the spectral smile effects for three different cases. See text for details.

According to the presented results, the in-flight wavelengths retrieved by the proposed calibration method may compensate the distortion produced by the faulty flat fielding in spectral bands encompassing a strong absorption feature. I therefore consider this innovative method to be appropriate to be integrated in the IPAG-DP for processing those CRISM images which require fine processing.

4.2. Generation of advanced products

After the refinement of the radiometric accuracy of CRISM hyperspectral products, the second part of the IPAG-DP is devoted to the generation of advanced data products. Remotely sensed images are intended to be used in many types of scientific applications such as the analysis of planetary atmospheres or surfaces. Each scientific study is thus performed at specific spectral ranges, determined spatial locations and for relevant physical units (e.g. TOA radiance, surface reflectance, etc.). In our case I devise the IPAG-DP to carry out fine analysis of the surface of Mars at the whole spectral range of CRISM. In this way I first put forward a fusion algorithm in subsection 4.2.1 that combines the channels VNIR and IR into a single hyperspectral image ranging from the visible to the mid-wavelength infrared wavelengths. Likewise, an atmospheric correction step is included in the IPAG-DP to correct hyperspectral CRISM data for atmospheric effects that coexist with, and thus pollute, the signal coming from the materials at the surface (see subsection 4.2.2). In subsection 4.2.3 I propose the transformation of I/F data into reflectance units by considering the heterogeneous conditions in illumination that happen within a single CRISM observation. The IPAG-DP is designed to conclude by generating a new data product that incorporates the eleven hyperspectral images forming each CRISM multi-angle observation. The resulting multi-angle data product is crucial for the fine analysis that is carried out in Part III, for example.

4.2.1. Fusion of VNIR and IR channels

As explained in section 1.4 the CRISM instrument is composed by two different spectral channels VNIR and IR that share some optical elements such as the telescope and the shutter. The side effects of this division are exposed in scientific studies that are based on the exact wavelength range that separates both channels (i.e. ~1 μm) or full spectra coming simultaneously from both channels. In particular I highlight the work of Clénet et al. who address the detection and characterization of mafic minerals on

Mars [37]. Different types of these chemical components (e.g. olivine and pyroxenes) are discriminated by specific spectral features around 1 μm. Clénet et al. utilize a method that models a given spectrum by a sum of Gaussian functions and a polynomial for the spectral continuum. However, the absorption band at 1 μm cannot be reproduced with the PDS-released CRISM data. In front of this limitation I propose a method that addresses the combination of the VNIR and IR hyperspectral images of a same CRISM observation. In this way full spectra from 0.4 to 4.0 μm are made available for the surface of Mars.

Unfortunately, a simple stacking of the spectral bands is not appropriate for the fusion of the VNIR and IR channels. As a matter of fact, the area at the surface imaged by the VNIR detector matrix is slightly larger that the one of the IR channel. In addition, a higher number of detector columns are operational in the latter detector matrix (an arbitrary martian scene is sensed by columns 25-625 of the VNIR detector and 29-632 of the IR detector). These two effects results in a lower spatial resolution for the VNIR channel. In this context, a simple stacking of the VNIR and IR data cubes into a single product would make correspond the VNIR and IR spectral ranges of an arbitrary spectrum to two different points at the surface. This effect is illustrated in Figure 4.20 in which a full spectrum (in red) is plotted after the simple stacking of the VNIR and IR channels of the CRISM central scan FRT6415. This CRISM observation acquired over the Alga crater of Mars is particularly significant as it is used to detect mafic rocks in the study of Clénet et al. [37]. As it can be seen, the red spectrum is affected by a notable falloff at 1 μm. Although some radiometric inaccuracies are expected for the extreme bands of both detectors (corresponding to the largest wavelengths of the VNIR channel and the lowest wavelengths of the IR channel) due to higher noise, the observed discontinuity is anomalous. Such fall-off is explained by the fact that each spectral range (0.4 to 1.0 μm for the VNIR, and 1.0 to 4.0 μm for the IR) corresponds to a different point at the surface.

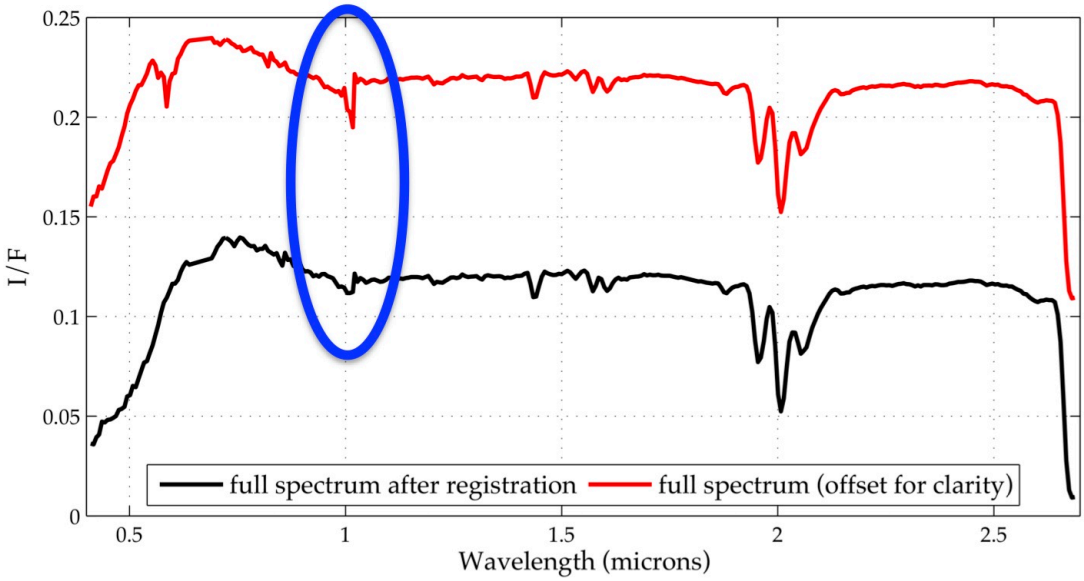

Figure 4.20.: Full spectrum extracted from the CRISM observation FRT6415 after combining the VNIR and the IR channels based on a simple band stacking in red, and the proposed fusion strategy in black. Note the blue ellipse pointing at the spectral falloff at 1 μm for the red spectrum caused by the different instrumental characteristics of the CRISM instrument in the VNIR and IR channels.

The spectral anomaly shown in Figure 4.20 is repeated for all the area covered by a CRISM observation.

I thus decide to consider these disturbances as a faulty registration of both images. To illustrate this Figure 4.21 (centre) shows the ratio between two spectral bands of the central scan FRT6415, namely the VNIR spectral band corresponding to 0.95 μm and IR spectral band at 1.05 μm. I note that the direct comparison of the same wavelength is not possible because the spectral bands within the common spectral interval between the two channels (~1 μm) are quite noisy as they are situated in the extrema of the detector matrices. For this reason I decide to compare two spectral bands that are separated by 0.1 μm. This spectral gap is expected to introduce a negligible bias because this spectral range corresponds to a continuum in the spectra for the majority of the image. In this way Figure 4.21 (centre) is a useful indicator to assess the presented spectral drop-off by assigning a value different to unity to those areas in the image that are most affected by the faulty registration of the CRISM channels. Likewise, these inaccuracies may be combined with the spectral variations around 1 μm produced by the presence of different types of mafic minerals. Both contributions can be distinguished in some cases such as the craters situated in the south of the displayed area. As it can be seen the misregistration between the two channels results in the occurrence of low ratio values in the shadows casted by the contour of the craters. Such discontinuous patterns come from the instrumental limitations and not from the variability of the surface. In order to overcome the spurious patterns in Figure 4.21 (centre) I incorporate in the IPAG-DP an original and accurate fusion strategy for the VNIR and IR channels.

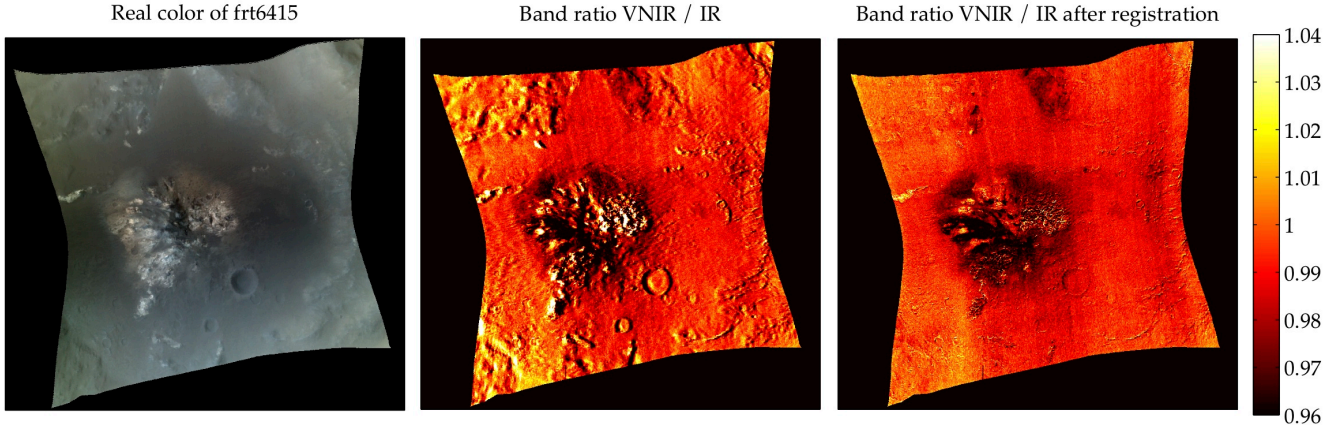

Figure 4.21.: Channel registration. (left) Real color CRISM image FRT6415. (center) Band ratio between VNIR band at 0.95 microns and IR band at 1.05 microns. (right) Previous band ratio after channel registration.

In the IPAG-DP I consider the fusion of the VNIR and IR channels as a traditional image registration problem. **Image registration** is the process of transforming different sets of data into one common coordinate system in order to be able to compare or integrate the data obtained from these different measurements. A comprehensive review of the state of the art in this subject is found in the seminal work of Zitová and Flusser [190]. In planetary sciences a similar problem to the one introduced in this section for CRISM is found for the OMEGA sensor. As a matter of fact the OMEGA channels VNIR and SWIR cannot be directly combined as the latter sensor owns an improved spatial resolution. In the Ph.D. thesis of Clénet the registration of both OMEGA channels is addressed based on a set of control points and a warping of the VNIR image to match the characteristic of the SWIR channel [36]. Contrarily, I decide to implement an innovative method that performs accurate registration between the CRISM VNIR and IR channels based on the ancillary DDR data set that is provided along with

each CRISM observation. In this way misregistration inaccuracies resulting from the definition of the control points and the warping process are avoided. DDR data contain the geographic position of each pixel in latitude and longitude. The accuracy of these geographic data is generally very high and some potential inaccuracies can be ignored as the generation process of these auxiliary data relies on the same spacecraft orbit/altitude models and data for both CRISM channels [126].

The scheme in Figure 4.22 describes the original channel fusion strategy that I propose to integrate in the IPAG-DP. This method is based on the projection of the VNIR data set $\mathbf{X}^{VNIR} = \left\{\mathbf{x}_{1,1}^{VNIR}, \ldots, \mathbf{x}_{Nl,Nc}^{VNIR}\right\}$, where $\mathbf{x}_{l,c}^{VNIR}$ is the spectrum that corresponds to the l^{th} line and c^{th} column, onto the IR image space. The $Nl \times Nc$ image space is geographically characterized by the set of latitude coordinates $\mathbf{lat}^{IR} = \left\{lat_{1,1}^{IR}, \ldots, lat_{Nl,Nc}^{IR}\right\}$ and the set of longitude coordinates $\mathbf{lon}^{IR} = \left\{lon_{1,1}^{IR}, \ldots, lon_{Nl,Nc}^{IR}\right\}$, which are retrieved from the ancillary DDR data corresponding to the IR image. The transformation of $\mathbf{X}^{VNIR}$ into an improved registered product $\mathbf{Y}^{VNIR} = \left\{\mathbf{y}_{1,1}^{VNIR}, \ldots, \mathbf{y}_{Nl,Nc}^{VNIR}\right\}$ is preferred to the processing of $\mathbf{X}^{IR}$ because of the lower number of spectral bands of the former data set (i.e. 107 against 437) and the resulting lower computational time. Note that $\mathbf{Y}^{VNIR}$ is associated to the geographical coordinates $\mathbf{lat}^{IR}$ and $\mathbf{lon}^{IR}$. For a given spatial position of $\mathbf{Y}^{VNIR}$ defined by l^{th} line and the c^{th} column and related to the latitude $lat_{c,l}^{IR}$ and longitude $lon_{c,l}^{IR}$, we fulfill the position $\mathbf{y}_{l,c}^{VNIR}$ by the "closest" spectrum $\mathbf{x}_{c',l'}^{VNIR}$ in the original VNIR data set $\mathbf{X}^{VNIR}$ in which the duplet (c', l') is generally not equal to (c, l) because of the aforementioned differences between the VNIR and the IR spectrometers and because of a resampling that we apply to the VNIR channel. The channel fusion strategy is described as follows:

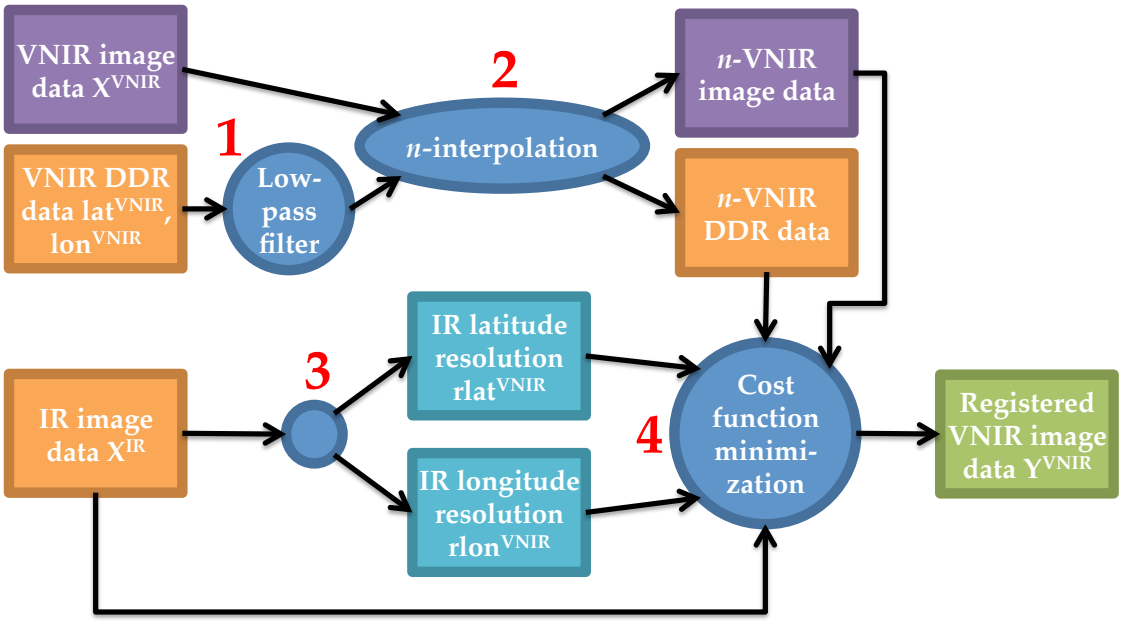

Figure 4.22.: Scheme of the fusion strategy for combining the VNIR and IR CRISM channels.

1. First, the VNIR ancillary DRR data $\mathbf{lat}^{VNIR}$ and longitude $\mathbf{lon}^{VNIR}$ are processed by a classical low-pass filter. In this way I correct for disturbances that are originated in thermal and electronic noise affecting the georeferencing system of the MRO spacecraft. Spurious high-frequency features affecting the smooth variations in latitude and longitude are filtered out by a classical mean filter. Testing on several CRISM images proved that a mean filter based on a 17×17 kernel is satisfactory when dealing with FRT central scans.

2. In order to build the output image $\mathbf{Y}^{VNIR}$ with the closest spectra to the corresponding set of $\mathbf{lat}^{IR}$ and $\mathbf{lon}^{IR}$ coordinates I increase the spatial density of points of $\mathbf{X}^{VNIR}$ by a factor n based on a linear interpolation. This processing step is found to be judicious in the common case in which the position (c,l) corresponding to $\left(lat^{IR}_{l,c}, lon^{IR}_{l,c}\right)$ is in the middle way between two pixels of the VNIR image space. The increase of the density of points provides an estimate of the spectrum corresponding the originally missing position $\left(lat^{IR}_{l,c}, lon^{IR}_{l,c}\right)$ by assuming a certain spatial homogeneity in the image. The factor n is generally set to 4 as it offers a good trade-off between accuracy in retrieving the closest spectrum and acceptable computational time. This data extrapolation is performed to obtain the VNIR image $\mathbf{Y}^{VNIR}$ and the ancillary data $\mathbf{lat}^{VNIR}$ and $\mathbf{lon}^{VNIR}$.
3. The spatial resolution of a CRISM image is not uniform due to variations in the altitude of MRO and the VZA angle. I decide to overcome this heterogeneity by computing the spatial resolution of $\mathbf{X}^{IR}$ in units of latitude and longitude. In this way the search for the "closest" spectra is performed on a normalized image space in which the distance between two pixels is homogenous over the whole image space. The spatial resolution in latitude $\mathbf{rlat}^{IR} = \left\{rlat^{IR}_{1,1}, \ldots, rlat^{IR}_{Nl,Nc}\right\}$ (longitude $\mathbf{rlon}^{IR} = \left\{rlon^{IR}_{1,1}, \ldots, rlon^{IR}_{Nl,Nc}\right\}$) is calculated based on the average difference between the latitude $lat^{IR}_{l,c}$ (longitude $lon^{IR}_{l,c}$) of an arbitrary pixel and that of its adjacent neighbors at a one-pixel distance.
4. The improved spectrum $\mathbf{y}^{VNIR}_{l,c}$ is filled by the spectrum in the interpolated version of $\mathbf{X}^{VNIR}$ that minimizes the following cost function

$$d = \sqrt{\left(\frac{\mathbf{lon}^{VNIR} - lon^{IR}_{l,c}}{\mathbf{rlon}^{IR}}\right)^2 + \left(\frac{\mathbf{lat}^{VNIR} - lat^{IR}_{l,c}}{\mathbf{rlat}^{IR}}\right)^2} \tag{4.5}$$

The evaluation of the presented algorithm for combining the VNIR and IR channels has been tested on several CRISM images. In this dissertation I summarize the results obtained on the central scan FRT6415 in Figure 4.20, Figure 4.21 and Figure 4.23. First, the black line in Figure 4.20 represents the full spectrum from 0.4 to 2.6 μm that is obtained after the fusion of the two channels. I note that the data in the VNIR spectral range is not the same contrarily to the IR spectrum. According to this figure the absorption band at 1 μm has been satisfactorily recreated by the fusion approach except for a small dropout in the first spectral band of the IR channel due to noise. Likewise, Figure 4.21 (right) corroborates the correctness of the proposed approach by showing the same spectral band ratio as the one displayed in Figure 4.21 (center) but after the registration of the VNIR image. As it can be seen, most of the spurious features have been substantially removed making the band ratio much smoother. Thanks to this processing step, the absorption band at 1 μm can be satisfactorily modeled by the approach of Clénet et al. in [37]. From that work I highlight Figure 4.23 in which an image product mapping the chemical properties of pyroxenes is shown over the area covered by the CRISM image FRT6415 in the vicinity of Valles Marineris. These results come from the analysis of the 1-μm feature and are obtained using the full spectra obtained after combining the VNIR and IR channels by the proposed methodology. As it can be seen, the pixels in Figure 4.21 (right) that do not correspond to unity reveal a different composition of the surface expressed by Figure 4.23.

The previous study among others would be unfeasible without the proposed fusion of the VNIR and IR channels. Hence, I include this fusion strategy in the IPAG-DP to systematically process each CRISM

observation.

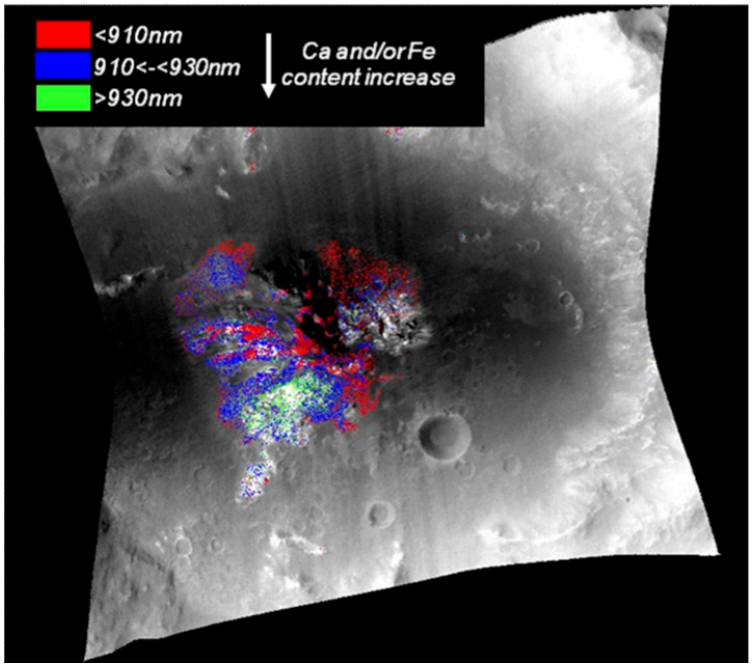

Figure 4.23.: Absorption centers around 1 μm as an indicator of pyroxene chemical composition. The position of the absorption center is directly related to the content in calcium and iron. This image product has been generated based on full spectra data of the CRISM central scan FRT6415 resulting from the channel fusion approach. Credit: [37].

4.2.2. Atmospheric correction

Although the atmosphere of Mars is fainter than Earth's, its composition dominated by CO_2 gas results in many strong absorption bands that often overlap with surface features such as the CO_2 ice. In addition to atmospheric gases, suspended mineral and water ice particles generally drift over the martian surface. These aerosols have a strong influence on the observed spectra of the surface that varies with time and location. In this thesis I envisage accurate analysis of the materials at the surface and therefore I require a previous modeling and correction for the atmospheric effects.

Atmospheric correction, or compensation (as we rarely know what we have to correct for exactly), is not straightforward and often unconstrained. In that matter many algorithms for atmospheric correction have been proposed in the literature. These algorithms often result from a combination of the consideration of the real physics behind the remote sensing problem and acceptable assumptions that ease the retrieval of the surface properties. In subsection 5.1.2 I provide a detailed state of the art on the algorithms that have been developed in planetary sciences and Earth observation.

The IPAG-DP integrates an original method that corrects CRISM observations in TOA radiance units for the effects of atmospheric gases and aerosols. This method was developed by Douté during the time of this Ph.D. and is detailed in section 14.2. The adopted method takes into account the multi-angle capabilities of the CRISM spectrometer in order to refine the accuracy of the atmospheric compensation in front of that performed for single-shot spectrometers. The IPAG-DP first retrieves the integrated optical thickness due to aerosols (i.e. the AOT) at the reference wavelength of one micron by the

so-called β-method using at once the central scan and the EPF of a same CRISM observation. The Lambertian albedo of the surface q_L (see subsubsection 1.3.2.2) is then inferred based on the AOT estimate. As a matter of fact, one of the main drawbacks of the adopted algorithm is the assumption that the surface behaves as a Lambertian reflector or, in other words, that the quantity of scattered light is the same regardless of the viewing direction. This limitation is overcome by the advanced atmospheric correction method that is presented in Part III. This improved technique retrieves the surface BRF $\rho\left(\theta_0, \theta, \varphi, \lambda\right)$ that depends on illumination and viewing directions.

I conclude this section by remarking the importance of an accurate radiometric accuracy of the CRISM data. According to our experience, bias in the TOA radiances may result in faulty atmospheric correction by the adopted method. This issue underlines the importance of previous corrections for instrumental artifacts such as the non-uniformity of the detector response, the smile effect, and the calibration of in-flight wavelengths. In particular the last spectral anomalies in the data can result in residual distortions in the spectral bands encompassing the strongest atmospheric absorption features as it is detailed in section 14.2.

4.2.3. Photometric normalization

The local illumination angle, or SZA, is typically heterogeneous in an arbitrary CRISM image due to the sometimes rugged topography of Mars. The emergence angle varies for the same reason but also owing to the motion due to the gimbaled OSU of CRISM (see section 1.4). These variations cause significant alterations in the solar reflected radiance acquired from orbit [174]. In this context photometric models of the surface are usually used in accurate analysis by transforming radiance data into reflectance units that limit the effects of the varying illumination and viewing conditions. In this section I investigate the techniques that allow this objective.

Photometry is the study and the measurement of electromagnetic radiation depending on the incidence and emergence directions. In the exploration of planetary surfaces the photometry is applied to the study of the interaction between the solar radiation and the studied area at the surface. Indeed, solar photons reaching the surface are partly absorbed, transmitted, diffused and reflected according to the physical state and chemical properties of the terrain of study. Properties of the surface can be therefore retrieved based on a photometric model and the study of the reflected radiation sensed by a spacecraft at varying acquisition geometries. The main difficulty of these photometric models is to understand what is the relationship and the meaning between parameters and physical characteristics of the observed surface. I recommend the Ph.D. dissertation of Jehl for a comprehensive lecture on the photometry of planetary surfaces [79].

CRISM data are released via the PDS in radiance or I/F units which are dependent on surface photometric effects. The widely adopted photometric normalization in the literature is based on the classical Lambert's cosine law defined in Equation 1.2. This simple photometric model divides I/F data by the cosine of the Sun incidence angle θ_0 and is valid in the often restrictive case in which the surface is isotropic, or Lambertian (review subsubsection 1.3.2.2). Despite the obvious limitations of this photometric model, the Lambertian assumption is widely adopted for processing CRISM data due to its simplicity and its correctness at first order [129, 118, 20]. The resulting Lambertian albedo q_L is typically considered as the real reflectance for following processing. The Lambert's model may be replaced by more realistic and complex models such as the Hapke's model described in subsubsection 2.3.1.2.

However, a priori knowledge on the scattering properties of the surface is required in that case, which is rarely the case (see [44] for an example). I therefore propose to adopt the classical photometric normalization for the IPAG-DP in order to treat systematically all CRISM observations due to its simplicity and correctness at first order.

The aforementioned practice to overcome the heterogeneous illumination conditions is based on the corresponding ancillary DDR data. In particular these auxiliary data provide the solar incidence angle that is computed in-flight for each pixel. Unfortunately, the routines used for the CRISM team consider the incidence angle that is relative to the martian geoid[7] θ_0' and not the angle relative to the surface normal θ_0. Consequently, the topography of the image is not considered in the photometric normalization of CRISM data and thus the Lambert's method results in false reflectance values in most of the cases (see Figure 4.24). The resulting error is specially severe for images acquired over rugged surfaces for which θ_0' is far from being close to θ_0. This particularity of the classical normalization adds another limitation that combines with the likely error coming from the Lambertian assumption. In this thesis I investigate the improvement of this procedure by considering the topography of the surface in the photometric normalization of some particular CRISM observations.

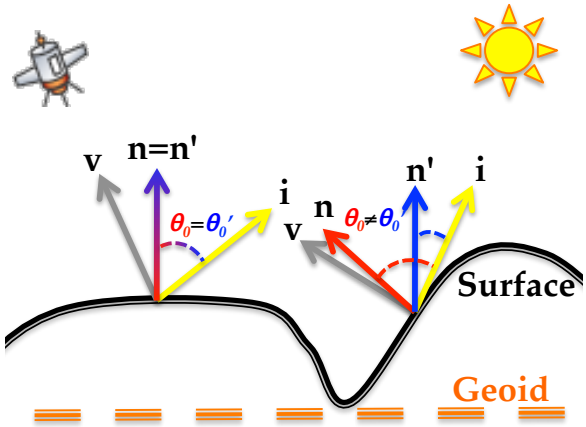

Figure 4.24.: Scheme illustrating the error introduced by adopting the incidence angle with respect to the martian geoid. In the presence of a perfectly flat surface (example on the left), the normal vector to the surface **n** is identical to the normal vector to the geoid **n**′, and so the two SZAs. Nonetheless, this equality becomes false in the presence of rugged terrains (example on the right).

4.2.3.1. On the use of Digital Terrain Models

In order to improve the accuracy of the aforementioned classical photometric normalization, I explore the use of digital terrain models (DTM) to compute the Sun incidence angle that is relative to the surface normal θ_0. A DTM is a digital representation of the ground surface topography that expresses the elevation of a given spatial point. The normal vector to the surface can be straightforwardly obtained using a DTM by calculating the inclination of the slope and its azimuth from north. The local SZA is then determined knowing the Sun elevation above the geoid, which is simply the complementary angle of θ_0'. More details on this strategy can be found in the work of Shibata et al. [162]. This strategy has been adopted by many authors such as Jehl et al. or Walter et al. when processing HRSC/MEX

[7]The **martian geoid** is the hypothetical shape of the Red Planet defined by a reference ellipsoid based on a model gravity.

data in [80] and [182], respectively, and has been validated based on terrestrial ground experiments in [174].

As for the availability of DTMs on the surface of Mars, we find those generated by the MOLA altimeter or the HRSC multi-angle sensor (see section 1.2). Nonetheless, both instruments provide DTMs that own an insufficient spatial resolution for processing ~18-m/pixel CRISM images (i.e. ~400 m/pixel for MOLA [164] and down to ~200 m/pixel for HRSC [80]). Such difference in spatial resolution makes impossible a photometric normalization based on these DTMs without degrading the CRISM spatial resolution. Contrarily, DTMs are generated at 1 m/pixel for a few specific areas of Mars by stereoscopic acquisitions acquired by the HiRISE camera [115]. In addition to a sufficiently high spatial resolution, HiRISE DTMs are acquired over areas of Mars that are also sensed by CRISM since both instruments are often coordinated. For example, Figure 4.25 shows the HiRISE DTM that is generated for the Russell dune in the south of Mars and that shall be used in subsection 10.1.1.

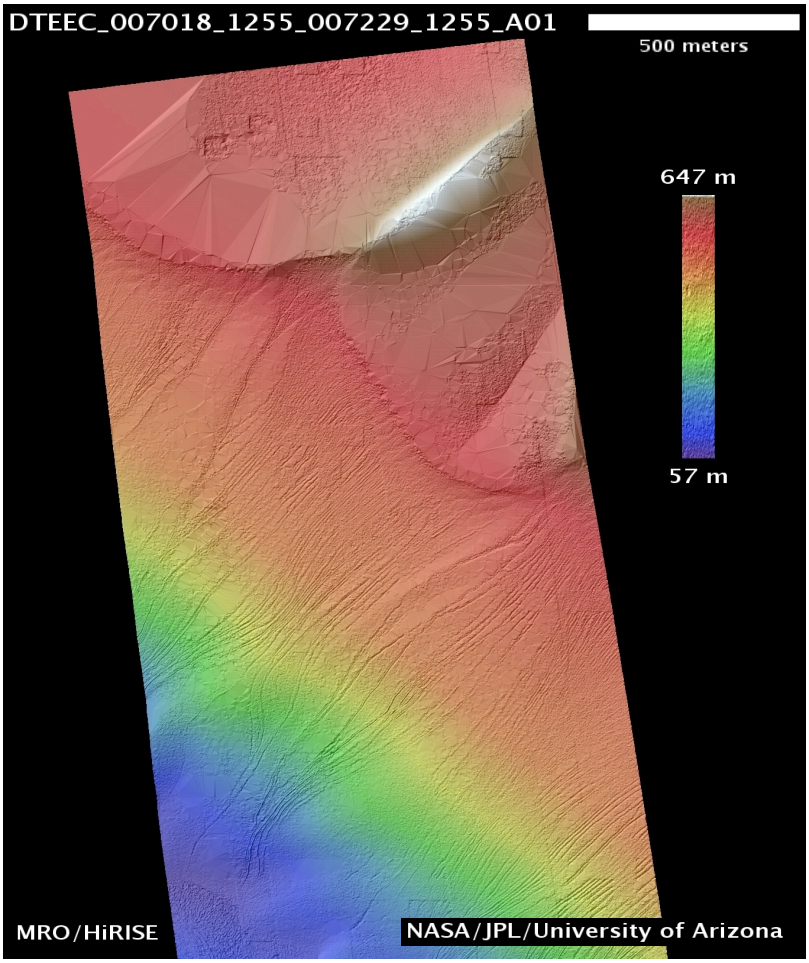

Figure 4.25.: Detail on the DTM of the Russell crater dune of Mars generated by the HiRISE instrument. Credit: http://hirise.lpl.arizona.edu/dtm/dtm.php?ID=PSP_007018_1255.

In this thesis I investigated the exploitation of high resolution HiRISE DTMs for fine photometric normalization of those CRISM images for which a DTM is available. According to the conducted experiments, albeit the spatial resolution of the HiRISE DTMs is large enough for calculating the real incidence angle for each CRISM pixel, photometric normalization based on these products is not straightforward due to intrinsic problems that are especially critical for areas with accentuated relief.

A pixel-wise photometric normalization requires indeed an optimal registration between the DTM and the CRISM image, which are acquired by two different instruments. This issue becomes very challenging due to the high spatial resolution and the large size of the data sets. Comprehensive testing revealed that expectable inaccuracies coming from a non-optimal registration are combined with intrinsic noise of the DTM that remains even after downsampling it to a lower resolution. The mentioned inaccuracies result in notable bias affecting the photometric normalization since variations of the illumination angle at the pixel scale magnify the smallest inaccuracy of the DTM or the registration process [80]. As a matter of fact, a slightly faulty value of θ_0 in Equation 1.2 may produce considerable bias in the calculation of the corresponding Lambertian albedo. Also in this thesis, a procedure based on clustering the image according to θ_0 was investigated to minimize the aforementioned issues. However, this strategy was found to be unsatisfactory as the surface features are critically corrupted after correcting for the average photometry of each area homogeneous in θ_0.

I conclude this investigation by stating that the normalization for photometric effects based on DTMs requires high quality DTMs optimally registered with the image data, which is not the case in reality. As stated above, the classical procedure assuming a Lambertian surface is therefore used in this thesis by the IPAG-DP. Although the Lambert's normalization can be considered as accurate at first order, we must keep in mind the potential limitations of this postprocessing. In some specific cases DTMs have been used to perform a homogeneous photometric normalization using the average θ_0 of the region of interest instead of θ'_0. In this way more realistic levels of reflectance are obtained for very rugged areas that are far from being flat as assumed by the martian geoid. This particular procedure is considered in Part IV, subsection 10.1.1.

4.2.4. Generation of an integrated multi-angle product

One of the main objectives of this thesis is the exploitation of the multi-angle capabilities of the CRISM instrument. Albeit CRISM represents a unique opportunity to scan the surface of Mars with up to eleven hyperspectral images at different emergence angles, the CRISM-DP releases separately these scans via the PDS. In this thesis the multi-angle sampling of CRISM shall be further exploited in Part III for the exploration of the surface and the atmosphere of Mars in the angular dimension, combined with the classical spatial and spectral dimensions. The spatial exploration of surfaces at several emergence angles is performed on Earth observation using multi-angle data coming from the imaging spectrometers CHRIS in [57] and MISR in [188]. Multi-angle imaging spectrometers are unprecedented tools to retrieve spectro-photometric signatures of materials at the surface depending on the observation geometry (see Figure 4.13). A **spectro-photometric curve** is defined as the ensemble of spectra corresponding to the same terrain unit under different observation conditions. In the same way a **photometric curve** is defined as a spectral sample of spectro-photometric curves, or in other words, the radiation observed from a given area at different geometries at a single wavelength. This two types of products are of great interest to delineate and characterize planetary terrain units by image processing and modeling, respectively.

The IPAG-DP concludes by spatially rearranging the spectra corresponding to the set of eleven hyperspectral images into an original data set, namely the CSP cube ("courbe spectro-phométrique", spectro-photometric curve in French). The generation of a CSP cube from a given CRISM multi-angle observation is integrated into the IPAG-DP from existing codes that had been developed in our lab-

oratory before this Ph.D.. The CSP cube represents an innovative and efficient way to retrieve the spectro-photometric curve, or one of the photometric curves, corresponding to a given point at the surface. Details on the generation of the CSP cube are given in the appendix section 14.3.

Summary and future prospects

In the present part of this thesis I have proposed a robust and original data pipeline for postprocessing hyperspectral CRISM images. After carefully investigating the processing that CRISM data undergo before being released through the PDS I have put forward a series of routines that transform PDS-released CRISM images into advanced data products owing an improved radiometric accuracy. This decision is justified by three main reasons. First, the automatic processing of PDS-released data into advanced products represents a crucial objective of this thesis. Second, although the radiometric accuracy of the PDS-released data is reliable, it is somewhat insufficient for fine processing. Third, this Ph.D. started during the preliminary science phase of the CRISM instrument in which some improvements still had to be done. Many improvements and routines aimed at enhancing the quality of CRISM products have been released during the time of this thesis (and still do!). Nonetheless, a IPAG-DP has been necessary to overcome the existing limitations meanwhile.

I hence put forward a postprocessing data pipeline based on two primary objectives. First, the IPAG-DP takes into consideration the substantial improvement of the radiometric accuracy of the CRISM hyperspectral products due to residual artifacts coming from thermal, electronic and optical limitations. Second, the PDS-released CRISM images are further processed to generate advanced products fully exploiting the capabilities of the CRISM instrument. In this matter the proposed IPAG-DP has been designed to produce original outcomes that make use of the full spectral resolution, the multi-angle information encompassed by CRISM observations and the information coming from the materials at the surface. As shown in the present part of the thesis, both objectives are satisfactorily achieved by the IPAG-DP. Consequently, the current postprocessing pipeline has become a very demanded tool not only in the IPAG but also in the planetary science community. I highlight, for example, the work of Clénet et al. in which advanced products generated by the IPAG-DP are used to perform studies on the surface of Mars [37]. Furthermore, several blocks of the proposed data pipeline may be used for other instruments. For example, I cite the Moon Mineralogy Mapper aboard the Chandrayaan-1 spacecraft which produces hyperspectral images affected by stripes due to its push broom design [139]. These data may benefit from the destriping method in the IPAG-DP.

Regarding the hurdles that were initially defined to be overcome by the IPAG-DP, I specially highlight those artifacts that affect the spectral properties of the CRISM instrument. In this family of anomalies we find the spectral smile effect that results in complex spurious effects on the data produced by the CRISM instrument. The desmiling algorithm that I have developed and integrated into the IPAG-DP reflects the efforts that have been required for the sake of its compensation. In my opinion the principal reason for such an issue is the conjugation of the intrinsic optical limitations of CRISM and the abundance of CO_2 on Mars. As we have seen, the conjugation of the smile and the very sharp spectra related to this chemical component in its gaseous or solid form deteriorates the spectral capabilities

of CRISM making some spectral bands unprofitable without further processing. Carbon dioxide is indeed involved in the most challenging issues regarding the processing of CRISM data. For example, images acquired over the high latitudes of Mars are usually rich in CO_2 ice and therefore result in higher spectral smile effects, worse spectral calibration due to the faulty flat fielding, the failure of the despiking method proposed in the CAT, as well as a more complex atmospheric correction due to the superposition of the solid and the gaseous carbon dioxide. Being interested in these particular areas of the Red Planet, the IPAG-DP is developed to address all the aforementioned challenges while remaining operational for the rest of CRISM observations.

I believe that this part of the dissertation represents a brief but substantial review of the limitations that commonly affect push-broom imaging spectrometers, their impact on the produced data, and the state-of-the-art methods to overcome them. As a matter of fact the development of the IPAG-DP in the beginning of this Ph.D. resulted in a deep and complete comprehension of the functioning of the CRISM instrument that has been crucial in accomplishing the other objectives of this thesis.

Some indications have already been given regarding the future prospects to carry out for each block of the IPAG-DP. For instance, a detailed outlook on the improvement of the desmiling algorithm has been given in paragraph 4.1.2.1.2. In my opinion future prospects must be also led toward the consideration of the surface topography in the postprocessing of CRISM data. According to subsection 4.2.3 the non-consideration of the real terrain unavoidably forces us to adopt the Lambertian surface assumption and the martian geoid to compute the solar incidence angle over a scene. This simplistic, yet rarely avoidable, hypothesis represent a crucial hurdle toward the obtention of accurate properties of the surface. A clue toward that direction is based on the use of improved registration algorithms that may allow the satisfactory superposition of an arbitrary hyperspectral image with its accompanying DTM. Another future prospect would be the improvement of the flat fielding of a given CRISM observation using the proposed desmiling technique. As a consequence of the faulty flat fielding, spectral bands encompassing some specific absorption features are not corrected for non-uniformities affecting the sensor's detector matrix in the CRISM-DP. This conservative strategy was adopted by the CRISM team to avoid greater bias coming from the combination of the flat fielding and the smile effect. I therefore propose to correct the bland scenes that are used to generate the flat field for smile effects. In this way the corresponding CRISM observation may be flat fielded without having to exclude any spectral band. To conclude I highlight a limitation of the proposed post-DC, the supposition by the adopted atmospheric correction algorithm that the surface is isotropic. This restrictive assumption shall be overcome in an original way in the following Part III.

Part III.

Atmospheric correction of CRISM observations and surface retrieval

Introduction

Part II of this dissertation has been devoted to the introduction of a data pipeline to improve the radiometric quality of released CRISM data and to produce advanced products to carry out specific planetary studies. As stated in Part I, one of the major objectives of this thesis is the exploitation of the multi-angle capabilities of the CRISM instrument for the fine analysis of the planet Mars. Until now the algorithm adopted by the IPAG-DP to evaluate the AOT (see section 14.2) represents the sole example in this matter. In the present part of the thesis I introduce an approach that uses the full angular coverage that is made available by CRISM in order to retrieve unprecedented photometric information on the surface of Mars from space.

Although other instruments aboard MRO such as the Mars Color Imager and the Mars Climate Sounder sensors are exclusively designed for atmospheric studies, the multi-angle capabilities of CRISM may greatly enhance the characterization of the atmosphere in the spectral range in which CRISM works [192]. As a matter of fact the EPF in CRISM observations is originally intended to allow atmospheric studies such as the observation of water vapor, carbon monoxide and dust aerosols as it is done in [165, 187]. These investigations benefit substantially from multi-angle measurements providing information corresponding to several atmospheric path lengths at different azimuthal configurations. These data allow an in-depth characterization of the atmosphere of Mars that is not possible with traditional single-shot imaging spectrometers. In this thesis I propose to investigate the potential of the angular coverage of CRISM to compensate targeted observations for atmospheric effects. Atmospheric correction represents the first step toward the retrieval of the reflectance of the materials at the surface.

As it has been explained in Part I atmospheric aerosols and materials at the surface are related to anisotropic scattering properties that depend on illumination and viewing directions. Currently adopted methods for atmospheric correction of data acquired by single-shot spectrometers cannot deal properly with the atmosphere/surface RT problem due to the lack of multiple measurements of the same target. In this context the supposition that solid surfaces behave as a Lambertian scatterer (see subsubsection 1.3.2.2) is generally adopted to constraint the inverse problem of retrieving surface reflectance from orbital data. This is the case, for example, of the atmospheric correction technique integrated into the IPAG-DP. The Lambertian hypothesis is, however, not realistic since most types of surfaces are anisotropic in terms of scattering. The common strategy to solve correctly the atmosphere/surface RT problem entails the consideration of the unknown surface BRDF. In practice this procedure makes the atmospheric correction problem unconstrained when a sole measurement is available. Multi-angle imaging spectroscopy may, however, constrain this problem.

The community of Earth observation has recently led some efforts toward the use of multi-angle measurements for improved atmospheric corrections. In this thesis I investigate the development of an innovative strategy in this direction to be applied to CRISM targeted observations. In this part of

the dissertation I eventually come up with an original method that inherits the work done in Earth observation, namely the Multi-angle Approach for Retrieval of Surface Reflectance for CRISM Observations (MARS-ReCO). MARS-ReCO is an original atmospheric correction algorithm for the retrieval of surface reflectance. This approach represents an improvement regarding other atmospheric correction techniques as it considers a non-Lambertian surface. The algorithm MARS-ReCO achieves the extraction of accurate photometric signatures of surface materials depending on acquisition geometry and wavelength from CRISM targeted observations. These signatures of the surface shall be of great interest to delineate and characterize martian terrain units by image processing and modeling.

This part of the thesis is threefold. First, I describe the proposed approach MARS-ReCO in chapter 5 by detailing the RT formulation and the atmospheric correction strategy on which it is based. Afterward a sensitivity study is carried out in chapter 6 to validate the proposed algorithm using simulated data. In this way I identify the most problematic atmospheric and acquisition configurations to perform accurate surface retrievals. In chapter 7 MARS-ReCO is applied to a set of CRISM observations to retrieve photometric signatures of mineral surfaces which shall be validated with data from independent studies. This part is concluded eventually by evaluating the benefits of adopting a non-Lambertian surface in the atmospheric correction of CRISM data.

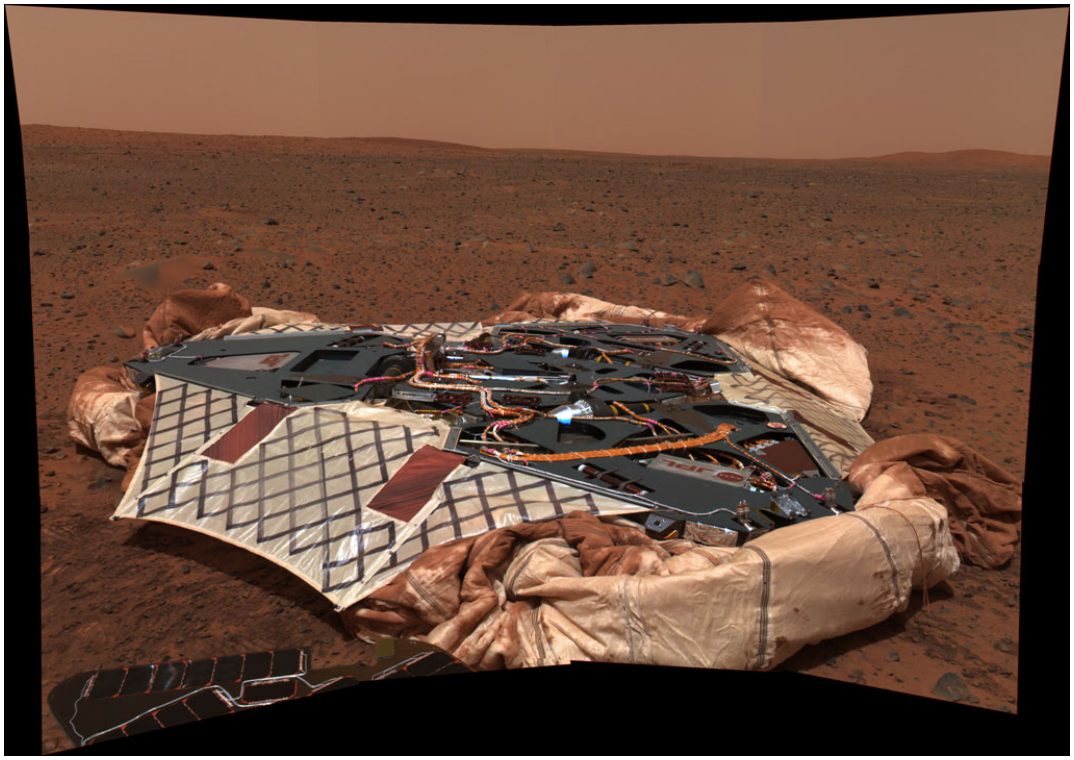

This image mosaic taken by the panoramic camera Pancam onboard the MEX rover Spirit shows the rover's landing site, the Columbia Memorial Station, at Gusev Crater, Mars. A portion of Spirit's solar panels appear in the foreground. Credit: NASA.

Contents

5

Multi-angle Approach for Retrieval of Surface Reflectance for CRISM Observations

In the following chapter I introduce the algorithm referred to as Multi-angle Approach for Retrieval of Surface Reflectance for CRISM Observations (MARS-ReCO) by giving some notions on inverse problems, by reviewing the state of the art in atmospheric correction of orbital data, and by detailing the technical aspects of this novel algorithm.

5.1. Atmospheric correction, surface retrieval and radiative transfer

5.1.1. Inverse problems

Retrieving surface parameters from remotely sensed images is a classic inverse problem. To predict the result of a measurement $\mathbf{y} = (y_1, ..., y_m)$ we require a model of the system under investigation and a relationship $F(\cdot)$ linking the parameters of the model to the measurements. Given the values of the parameters $\mathbf{x} = (x_1, ..., x_n)$ that define the model, the prediction of observations constitutes the so-called forward problem $\mathbf{y} = F(\mathbf{x})$. Figure 5.1 illustrates the forward and inverse problem. The **inverse problem**, which is expressed as $\mathbf{x} = F^{-1}(\mathbf{y})$, consists in using the measurement to infer the values of the parameters characterizing the system under investigation. In the case of inversion of remote sensing data $\mathbf{y}$ correspond to the set of TOA radiances sensed by the camera, and $\mathbf{x}$ are the physical parameters that define the model such as the BRDF of the surface, the atmospheric AOT or the acquisition geometry expressed by the angular triplet θ_0, θ and φ. The physical theory $F(\cdot)$ to pass from a set of parameters to another resides with the RT model of the atmosphere, the surface being the lower boundary condition. Inverse problems may be difficult to solve for, at least, two different reasons, (i) the problem may be unconstrained and different values of $\mathbf{x}$ may be consistent with the measurement $\mathbf{y}$ (knowing the weight of an elephant is not sufficient for calculating its age), and (ii)

discovering the values of the model parameters may require the exploration of a enormous parameter space (finding a bottle with a message in the ocean is complicated).

In this thesis I deal with the inverse problem that is defined as the retrieval of surface properties, $\mathbf{x}$ (e.g. by means of the BRDF), from TOA measurements, $\mathbf{y}$. This problem is typically solved by performing atmospheric correction, that is, the inverse method.

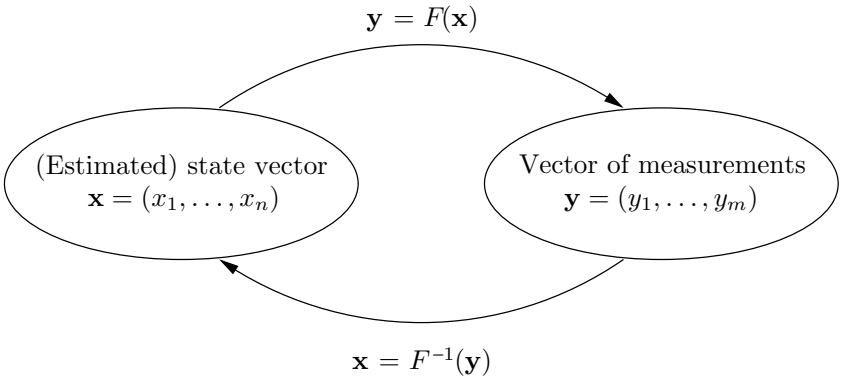

Figure 5.1.: Scheme of forward and inverse problems. In remote sensing applications, $\mathbf{y} = (y_1, ..., y_m)$ stands for the remotely sensed data and $\mathbf{x} = (x_1, ..., x_n)$ encompasses the physical parameters that correspond to the measurements.

One of the hurdles toward an accurate inversion of TOA radiances is to provide a realistic model $F(\cdot)$, that is, a robust expression for TOA radiance. In subsection 2.2.1 I detail an expression that is not only robust but analytically invertible as it shall be shown. Another difficulty is related to the accuracy of the measurements $\mathbf{y}$. In this matter it is important to work with the most accurate measured radiance values and therefore the IPAG-DP introduced in Part II becomes crucial for the sake of a satisfactory atmospheric correction. I note that in the case of the inversion of TOA radiances for retrieval of surface reflectance $\mathbf{y}$ may be complemented by some other input parameters. For example, the triplet of acquisition angles are available for all CRISM images thanks to the corresponding ancillary data DDR [127]. Likewise, the atmosphere can be modeled using the radiative properties of gases and aerosols that have been estimated in previous works [180, 187, 52]. Side effects coming from intrinsic limitations of TOA measurements can also be minimized by considering other a priori information such as experimental BRDF measurements that help constraining the inverse problem. Last but not least, the major obstacle for a robust retrieval of surface properties is the scarcity of measurements at different acquisition angles. Aerosols in the atmosphere and materials at the surface scatter light depending on illumination and viewing directions and therefore the success in retrieving accurate estimates of surface parameters drastically depends on the number and the distribution of the available angular measurements.

5.1.2. State of the art and motivation

After presenting the atmospheric correction problem I investigate the efforts that have been done in this direction in the literature. In the past years imaging spectrometers around Mars have been traditionally corrected by the so-called volcano-scan technique [96]. In this method, used by the OMEGA and CRISM science teams, a reference transmission spectrum of the atmosphere is built by ratioing two spectra acquired nearly simultaneously, one over the summit of the volcano Olympus Mons and one

from the base of it. Both spectra are acquired over areas with minimal amounts of aerosols to minimize their effects on the reference spectrum. This ratio gives the transmission through the atmospheric column between the summit and the base of Olympus Mons. The reference spectrum is then scaled to a spectrum of interest such that, after division by the scaled reference, the Lambertian albedo of the surface is forced to be the same at a wavelength outside the atmospheric CO_2 absorption bands (typically 1.89 μm) and another wavelength inside a CO_2 absorption feature (typically 2.01 μm). In this way the volcano-scan method can remove the gas absorption bands of any spectrum. McGuire et al. adapted and improved this atmospheric correction technique for CRISM in [117]. Unfortunately, this technique does not correct for aerosol effects and cannot operate for surfaces made of CO_2 ice.

In the literature we find advanced methods that address the correction of aerosols drifting over the surface. In this matter Vincendon et al. [180] quantify the contribution of mineral aerosols in the SWIR based on multi-temporal nadir OMEGA observations corresponding to significantly different SZA. In this way the AOT is inferred and the aerosol-free surface reflectance is retrieved. Nonetheless, this method relies on the restrictive assumption that the AOT remains constant during the time spanned by the employed acquisitions. Furthermore the authors of [180] select a Lambertian hypothesis for the surface considering that the signal variations at the TOA with the illumination and phase angles are exclusively related to the contribution of aerosols. In this case the surface is characterized by a wavelength-dependent single value of albedo. In [181] the same authors monitor the AOT above the south polar cap of Mars based on the assumption that the reflectance in the 2.64-μm saturated absorption band of the CO_2 ice at the surface is due only to the light scattered by aerosols. Although a single observation is sufficient in this case and the Lambertian hypothesis has no influence on the retrieved AOT (as the surface is assumed to be totally absorbing at 2.64 μm), the AOT retrieval is restricted to the areas of Mars covered by pure CO_2 ice. Alternatively, Douté proposes efficient RT-based algorithms and tailor-made methods for operational retrieval of surface reflectance using single-shot and multi-temporal OMEGA images [52]. Similarly to [180], Douté considers the surface as isotropic. In the literature the Lambertian assumption becomes unavoidable when processing single-view sensors such as OMEGA for atmospheric correction [52]. This limitation can be eased if series of multi-temporal images are considered to build a single multi-angular data set [180]. In this case other hurdles arise as we must suppose that the surface did not change in the time spanned by the images, and the atmospheric conditions must be treated independently since each image corresponds to a different AOT.

The Lambertian assumption is generally adopted, even when multi-angle data are available (e.g. [180]), as it largely simplifies the RT model, reduces the size of the look-up tables (LUTs) used in the inversion, and creates faster algorithms. All these factors are crucial in operational processing [177]. Although the Lambertian surface assumption may work in some limited cases (e.g. very turbid atmospheres), it has been proved that anisotropic scattering properties play a significant role for most minerals [163, 84, 166] (see Figure 5.2 for an example on Mars) and ices [106]. The fact that the martian surface is not Lambertian has also been proved using Earth-based observations of the Red Planet [47]. In this context the Lambertian hypothesis creates systematic angle-dependent biases in derived surface reflectance, thus reducing the anisotropy of final reflectance [111]. I shall further discuss this point in section 7.4.

As for the atmospheric correction of CRISM data, McGuire and the CRISM science team define a DISORT-based model to retrieve the AOT caused by dust and water ice particles using the measured

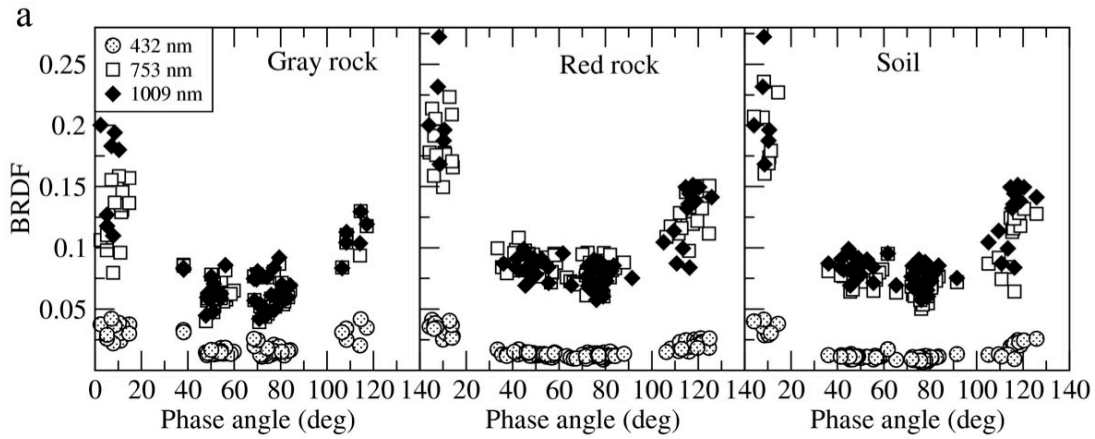

Figure 5.2.: Phase curves of BRDF corrected for diffuse skylight extracted from a Pancam image aboard the MER Spirit. These curves correspond to the mineral units (Gray rocks, Red rocks, and Soils) found in the east and west from the Cahokia region at West Spur on Mars. The different symbols stand for three wavelengths for each unit of interest. The anisotropy of the three surface units according to phase angle can be observed. Credit: [84]

I/F spectrum by CRISM and independent data records [118]. In that study the surface spectrum is computed in Lambertian albedo units after correction of the gaseous and aerosol contributions. This algorithm does not, however, retrieve the AOT from the images nor takes advantage of the multi-angle capabilities of the CRISM instrument. Alternatively, Brown et al. propose a first attempt in this direction by proposing a DISORT-based algorithm to model the remotely sensed signal at a single wavelength [19]. In that study three parameters (i.e. surface albedo, dust opacity and water ice opacity) are iteratively adjusted in order to fit a set of TOA radiances from the same terrain unit that have been observed with different emergence angles. Nevertheless, this method is very time consuming and the surface is assumed to reflect light isotropically, that is, under a Lambertian hypothesis. In all the mentioned studies as well as the method adopted by the IPAG-DP (see [53]) the Lambertian albedo of the surface ρ_L is inferred after retrieving the AOT based on the assumption of an isotropic surface.

In Earth observation we find identical problems regarding the atmospherical correction of remote sensing data. In this twin field of study most inversion algorithms for retrieval of surface reflectance from multi-angle data also make assumptions regarding the scattering properties of the surface. In particular the Lambertian assumption is commonly adopted such as in the work of Guanter et al. in which multi-angle hyperspectral observations acquired by the CHRIS instrument are corrected for atmospheric effects under this assumption [69]. Alternatively, some works propose an effort towards the relaxation of the Lambertian assumption by adopting a surface retrieval strategy based on a converging iteration loop [76, 178]. In the first iteration the BRF of the surface is retrieved adopting the Lambertian assumption. The inferred model of the surface is then injected into the iterative process as an input parameter. This process is repeated until convergence is reached, thus improving the quality of the final BRF estimate. Nonetheless, this method is not plausible for highly anisotropic surfaces such as snow or ice since the error in the first iteration greatly impacts the succeeding retrievals.

Alternative assumptions are made on the angular shape of the surface BRDF. For example, the MODIS BRDF/Albedo algorithm utilizes a priori knowledge on the likely anisotropy of the surface reflectance that is characterized by the semi-empirical RTLS model (see subsubsection 2.3.1.4) [153]. In particular

archetypal BRDF shapes coming from either well-sampled field data or previous retrievals by MODIS are assumed for those pixels with insufficient or poor angular sampling. Alternatively, the currently adopted algorithm for the multi-angle MISR instrument assumes that the implied angular shape of the surface BRDF is similar among the five MISR wavelengths (i.e. 446, 558, 672, and 866 nm) [50]. Although the angular reflectance shapes may be somewhat similar, the authors of [50] affirm that they are not necessarily identical, especially in such a large spectral range.

Further investigation on the impact of the commonly adopted assumptions regarding the scattering properties of the surface leads us to devise an atmospheric correction method based on as little assumption as possible. In the following I describe the two major motivations that justify such decision.

1. It has been proved that the Lambertian supposition induces a substantial error, even for low anisotropic surfaces [111]. In that study Lyapustin proves that the error in terms of BRF caused by the Lambertian approximation is as high as 10-15% for moderate view angles at $\tau = 0.5$ and up to 30% in the principal plane (see Figure 5.3 for details). Furthermore, this assumption creates flatter BRF patterns, the true BRF being more anisotropic. This consequence may impact processing of CRISM observations acquired over the high latitudes of Mars mostly composed of ice and snow, which are highly anisotropic, or even over equatorial areas where surface materials may also be anisotropic (e.g. see Figure 5.2). In a complementary study Hu et al. study the interrelationship between surface BRF retrieval and atmospheric correction [76]. The results of this work corroborates that the assumption of a Lambertian surface causes relative errors in the retrieved surface reflectances up to about 15% under turbid atmospheric conditions.

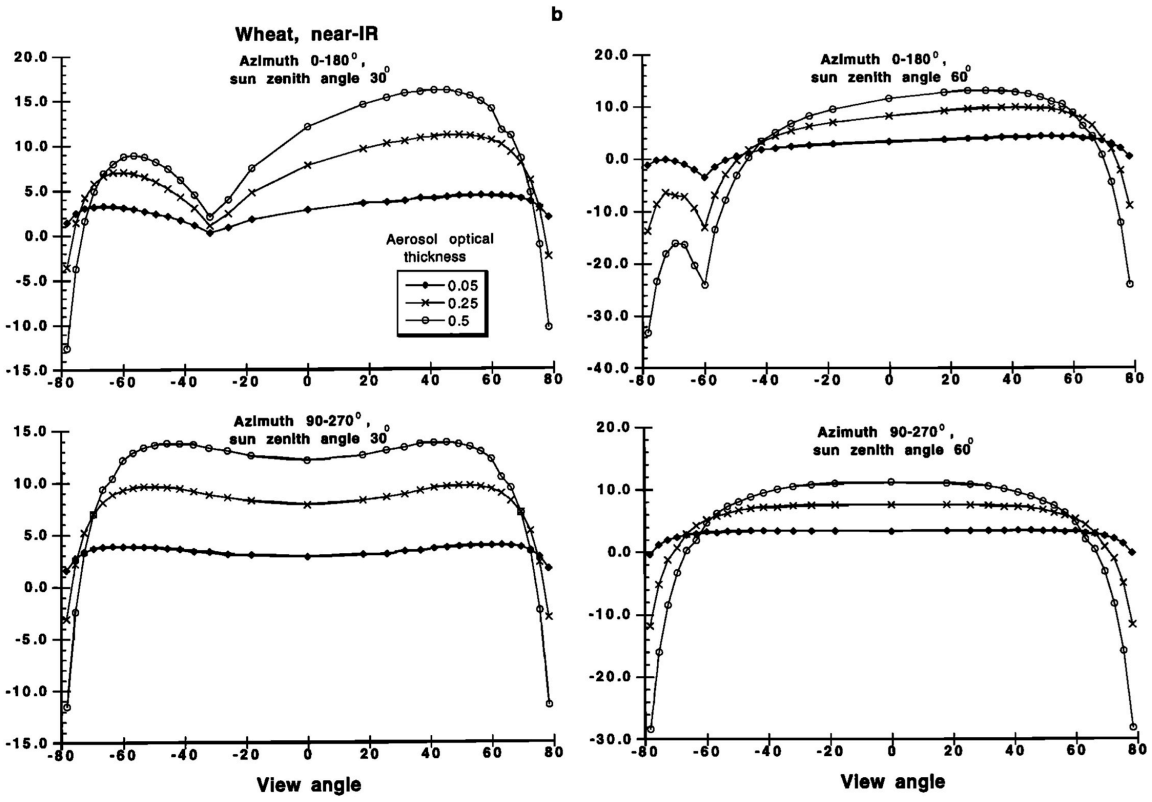

Figure 5.3.: Errors of BDRF retrieval from space in the Lambertian approximation for different atmospheric opacities ($\tau = 0.05$, 0.25 and 0.5). The retrievals are performed for a wheat surface presenting a high anisotropy in the NIR. Credit: [111].

2. Multi-angle imaging spectroscopy carried out by cameras such as CRISM provides unprecedented sets of TOA radiance values from the same target at different observation angles. These unique data sets may help constraining the present inverse problem. I therefore propose to exploit the angular coverage of CRISM in a integrated manner in order to carry out accurate atmospheric correction. This can be achieved by introducing the BRDF of the surface in the RT formulation, thus considering the anisotropy of the surface in addition to that of atmospheric aerosols.

Eventually, I highlight the recent work of Cull et al. in which surface retrievals are carried out for multi-angle CRISM data considering a non-Lambertian surface driven by a Hapke's model [42]. In that study a DISORT-based LUT is generated by storing surface spectra corresponding to multiple atmospheric situations. Although this algorithm does not assume a Lambertian surface, it cannot be used for our purposes, nor in a general case, since it is developed to work for a specific mineral region of Mars. This atmospheric correction procedure assumes that the surface in the processed images has similar scattering properties than some materials previously characterized by independent studies.

To our knowledge, an inversion method for the retrieval of surface reflectance from CRISM targeted observations considering a non-Lambertian surface without any a priori on the surface properties has not been proposed yet.

5.2. Outline

The algorithm MARS-ReCO that I propose in this thesis inherits the basis of currently adopted methods for imaging spectrometers in Earth observation[1]. In this twin field of research simultaneous AOT and surface retrievals are carried out for series of multi-temporal MODIS images by the algorithm referred to as MAIAC (MultiAngle Implementation of Atmospheric Correction) [108, 110]. MAIAC inherits the basis of previous works developed for MISR [113] and Meteosat [142] data that incorporate the surface BRDF in the RT formulation to account for variations of the surface according to viewing geometry. In contrast to other methods MAIAC solves the aerosol/surface coupling problem considering a non-Lambertian surface without strong reductionist assumptions.

In the AOT retrieval step MAIAC uses an initial estimate of the surface BRF that is obtained from a MODIS waveband for which the effects of aerosols are negligible. The final BRF is re-estimated with the retrieved AOT value. Unfortunately this strategy is not valid in our case since there is no homologous waveband in the CRISM instrument. Martian aerosols are mostly formed by mineral particles that are larger than those found drifting over Earth and therefore their contribution to the at-sensor signal is strong in the SWIR range [93]. In this context I propose an atmospheric correction chain for CRISM multi-angle observations resulting from the combination of (i) the AOT retrieval approach adopted by the IPAG-DP (see section 14.2), (ii) the gas correction strategy also adopted by the IPAG-DP, and (iii) the aerosol correction method MARS-ReCO inspired by the surface retrieval algorithm of MAIAC (see Figure 5.4). Contrarily to MAIAC or the MODIS BRDF/Albedo algorithm in [153], MARS-ReCO is devised to process multi-angle data acquired practically at the same time instead of multi-temporal series of images.

[1]This work has been carried out in collaboration with Dr. Alexei Lyapustin from the NASA Goddard Space and Flight Center, MD, USA, and Dr. Mike Wolff form the Space Science Institute, Boulder, Colorado.

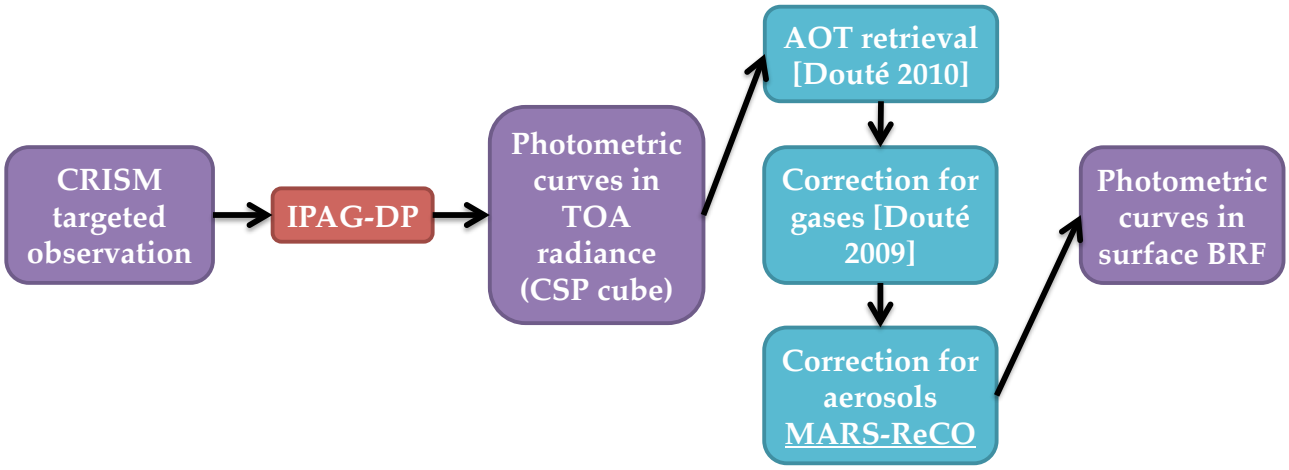

Figure 5.4.: Block diagram illustrating the atmospheric correction chain for CRISM multi-angle observations. The AOT and the photometric curves of the surface in BRF units are retrieved using the corresponding CSP cube produced by the IPAG-DP.

I summarize the key points of the MARS-ReCO approach as follow:

- The surface is assumed to be flat or, in other words, there are no adjacency effects between neighboring areas.
- The TOA reflectance is expressed using a RT formulation of the atmosphere/surface system based on a Green's function of the atmosphere. This formulation was originally developed by Lyapustin and Knyazikhin in [107] and has been detailed in subsection 2.2.1. The Green's function method allows the analytical combination of the atmospheric reflectance and transmissivity with the surface BRDF in order to calculate the radiance reaching the sensor for an arbitrary AOT and acquisition geometry.
- The surface anisotropy is taken into account by expressing its BRF using a semi-empirical RTLS model (see subsubsection 2.3.1.4). This reflectance model used by the algorithms MAIAC and BRDF/Albedo allows the linearization of the TOA reflectance expression, thus enabling a highly efficient inversion by a classical least-square method. As a matter of fact the RTLS coefficients characterizing the surface BRF model can be calculated analytically from measurements. Besides its mathematical properties, the RTLS model has proved to be appropriate for recreating scattering properties of natural surfaces such as soils.
- The AOT is an input parameter which is generally provided by the β-method integrated in the IPAG-DP (see section 14.2). In the case that the β-method does not work (e.g. in the presence of surfaces covered by CO_2 ice), MARS-ReCO may be fed by other means such as the AOT estimates provided by the Pancam instrument aboard the MER rovers.
- Contrarily to MAIAC, the gaseous contribution in the at-sensor signal is corrected before using MARS-ReCO. This is done by the IPAG-DP following the procedure described in section 14.2 which takes into consideration the coupling between the gases and the aerosols. In this way MARS-ReCO deals exclusively with the correction for aerosol effects, which are conjugated with the signal coming from the surface.
- A LUT is generated using DISORT to store atmospheric quantities that are needed for the atmospheric correction of CRISM observations. Each quantity is computed for multiple scenarios of

the remote sensing of Mars by CRISM. The use of a precomputed LUT implies an initial and sole calculation of the atmospheric quantities that shall be used repeatedly afterwards. The LUT of MARS-ReCO does not depend on the surface properties because of the qualities of the Green's function method and the RTLS model. The current LUT considers an homogeneous atmosphere exclusively composed by mineral aerosols. The radiative properties of these suspended particles are used in the calculation of the LUT and are obtained from the study of Wolff et al. [187] based on CRISM multi-angle observations (review subsection 2.1.3). Nonetheless, there is not any intrinsic restriction for considering different or more complex atmospheres (e.g. considering gases or water ice aerosols). A new LUT must be computed in this case. The current LUT depends on the state of the atmosphere, by means of the AOT, and on the acquisition geometry, by means of the angles θ_0, θ_0 and φ.

- Surface retrieval is carried out using a fast and robust iterative least-square strategy based on a matrix inversion similar to what is done in the algorithm MAIAC. The reliability of the retrieved BRF is validated by an ensemble of tests.

In this framework the MARS-ReCO approach aims at providing the BRF that is associated to each super-pixel forming a CSP cube (see subsection 4.2.4 for definition of super-pixel). The properties of the atmosphere (i.e. the AOT and the radiative properties of the aerosols) are known. In its current implementation MARS-ReCO processes each spectral band individually, treating all super-pixels in a sequential manner. In the conclusions of this part of the thesis I shall give some details on the improvement of MARS-ReCO toward the simultaneous consideration of the angular and spectral information contained in CRISM observations. The atmospheric correction of the at-sensor photometric curve corresponding to a given super-pixel is threefold:

1. The RT model based on the Green's function of the atmosphere is first fitted to the angular measurements forming the photometric curve. This is done by knowing the acquisition geometry corresponding to each measurement (retrieved from the ancillary DDR) and the AOT.
2. The coefficients of the RTLS surface model are retrieved by inversion of the fitted TOA reflectance expression.
3. The retrieved BRF model undergoes a validation step that aims at detecting and excluding those solutions that are not realistic.

The algorithm MARS-ReCO represents an original tool to infer crucial properties of the surface, namely the surface BRF and the albedo. The proposed technique provides unprecedented data from CRISM targeted observations while being fully operational. As a matter of fact MARS-ReCO processes a single spectral band of a CSP CRISM cube in a few tens of seconds. In the following two sections I describe the theoretical background and the technical aspects of the proposed atmospheric correction.

5.3. Algorithm theoretical background

The RT formulation on which MARS-ReCO is based is adopted from the processing of MODIS multi-temporal data by the MAIAC algorithm [108]. This formulation was initially put forward by Lyapustin and Knyazikhin some years ago in [107]. The main novelty of MARS-ReCO in front of other LUT-based methods is the injection into the RTE of the diffuse Green's function of the atmosphere and the RTLS expression to model the surface BRF.

5.3.1. The Green's function method in radiative transfer

The concept of the Green's function, developed in neutron transport several decades ago [10], represents a powerful approach to solve the RT problem with complex boundary conditions and internal sources. This mathematical concept entails the reformulation of the general problem in terms of simpler basic sub-problems and the expression of the general solution as a superposition of these basic solutions. The virtues of the Green's function method in the problem of atmospheric radiative transport are demonstrated in [64, 145, 22]. I recommend the work of Lyapustin and Knyazikhin in which further development of this method is offered for one-dimensional RT problems with a non-Lambertian surface [107]. A brief introduction to the mathematical principles of the Green's function can be found in the appendix section 13.1.

The Green's function describes the solely atmospheric radiative transport and serves to find radiance in an arbitrary direction and altitude in the atmosphere, given the angular orientation of an exciting beam at the surface level. The Green's function can be used to compute the radiation field generated by virtually any source. The benefit of using such an explicit expression for the Green's function is twofold. Firstly, an analytical expression for the superposition of the basic solutions allows for analytical computations of the total radiation field. Secondly, computing the Green's function is much more efficient than solving for the integrated surface-RT. The Green's function approach is especially suitable for inversion problems such as the one addressed in this thesis where the radiation field needs be computed repeatedly for changing surface BRDF [145].

5.3.2. Expression of the top-of-atmosphere reflectance

The parametrization of the surface/aerosol RT problem on which MARS-ReCO is based is detailed as follows. Throughout this section I use the notation and atmospheric quantities that have been introduced in subsection 2.2.1. Some parameters are summarizes as follow:

- s_0, s: incidence and view directions defined by pairs of zenith and azimuthal angles (θ, φ); in this thesis I do not consider surfaces with privileged scattering directions and therefore $\varphi_0 = 0$. For brevity, φ stands for the relative azimuthal angle between both directions $\varphi - \varphi_0$.
- μ_0, μ: cosines of the SZA and VZA $(\mu = \cos\theta)$; the z axis is pointed downward, so $\mu_0 > 0$ for the solar beam and $\mu < 0$ for the reflected beam.
- πS: extraterrestrial solar spectral irradiance.
- ρ: surface BRF.
- c_0, q: spherical albedo of the atmosphere and the surface, respectively.
- τ_{aer}: aerosol optical thickness, or the atmospheric opacity exclusively due to aerosols.

As stated before, CRISM data are previously corrected for atmospheric gases following the method adopted by the IPAG-DP and detailed in the appendix section 14.2. In this appendix the symbol L_{aer} stands for the TOA radiance in a gas-free atmosphere, that is, only altered by the aerosols. In the present part of the dissertation I shall use the symbol L for simplicity. Likewise, the following formulation does not express the dependence of atmospheric quantities on wavelength for brevity.

The TOA radiance L reaching the CRISM instrument can be expressed as it is done in subsection 2.2.1 by means of Equation 2.6. Rearranging atmospheric quantities depending on their scattering nature,

radiance L can be decomposed as a sum of the atmospheric path radiance (D), and the radiance reflected by the surface and that is directly (L_s) and diffusely (L_s^d) transmitted through the atmosphere,

$$L(s_0, s) = D(s_0, s) + L_s(s_0, s)e^{-\frac{\tau_{aer}}{|\mu|}} + L_s^d(s_0, s). \tag{5.1}$$

The first term of the surface-reflected radiance can be written as

$$L_s(s_0, s) \cong S\mu_0 e^{-\frac{\tau_{aer}}{\mu_0}} \left\{\rho\left(s_0, s\right) + \alpha c_0 \rho_1\left(\mu\right)\rho_2\left(\mu_0\right)\right\} + \frac{\alpha}{\pi}\int_{\Omega^+} D_s\left(s_0, s'\right)\rho\left(s', s\right)\mu' ds', \tag{5.2}$$

where D_s is the path radiance incident on the surface and

$$\rho_1\left(\mu\right) = \frac{1}{2\pi}\int_{\Omega^+}\rho\left(s', s\right)ds', \rho_2\left(\mu_0\right) = \frac{1}{2\pi}\int_{\Omega^-}\rho\left(s_0, s\right)ds. \tag{5.3}$$

Parameter α is a multiple reflection factor, $\alpha = (1 - q(\mu_0)c_0)^{-1}$, that depends on the surface albedo q.

The diffusely transmitted surface-reflected radiance at the TOA is calculated from L_s with the help of one-dimensional diffuse Green's function of the atmosphere G^d,

$$L_s^d(s_0, s) = \int_{\Omega^-} G^d(s_1, s)L_s(s_0, s_1)ds_1. \tag{5.4}$$

The function πG_d is often called bidirectional upward diffuse transmittance of the atmosphere. The method of its calculation is discussed in detail in section 5.4.

The surface albedo is defined as a ratio of reflected and incident radiative fluxes at the surface,

$$q(\mu_0) = F^{Up}(\mu_0)/F^{Down}(\mu_0), \tag{5.5}$$

$$F^{Down}(\mu_0) = \pi S\mu_0 e^{-\frac{\tau_{aer}}{\mu_0}} + \int_{\Omega^+} D_s\left(s_0, s'\right)\mu' ds' = F_s^{Dir}(\mu_0) + F_s^{Dif}(\mu_0), \tag{5.6}$$

$$F^{Up}(\mu_0) = \pi S\mu_0 e^{-\frac{\tau_{aer}}{\mu_0}} q_2(\mu_0) + \int_{\Omega^+}\mu' q_2(\mu') D_s\left(s_0, s'\right)ds', \tag{5.7}$$

and its moment,

$$q_2(\mu_0) = \frac{1}{\pi}\int_{\Omega^-}\rho\left(s_0, s\right)\mu ds. \tag{5.8}$$

These formulas give an explicit expression for the TOA radiance as a function of surface BRF. The accuracy of the above formulas is high, usually within a few tenths of a percent [107].

In the following, I use the TOA apparent reflectance in a gas-free atmosphere at a given wavelength λ defined as

$$R = L/\left(\mu_0 S\right). \tag{5.9}$$

For simplicity, I shall use the symbol R instead of R_{aer} to refer to units of TOA apparent reflectance in a gas-free atmosphere populated by aerosols.

5.3.3. Including a surface model

Based on the described semi-analytical solution, TOA apparent reflectance is expressed as an explicit function of the parameters involved in the parametrization of the surface BRF. In this case I use the linear, kernel-driven, semi-empirical RTLS model (review subsubsection 2.3.1.4), which is reminded here as follows

$$\rho\left(\mu_0,\mu,\varphi\right) = k^L + k^G f_G\left(\mu_0,\mu,\varphi\right) + k^V f_V\left(\mu_0,\mu,\varphi\right). \tag{5.10}$$

The BRF of a pixel is thus characterized by a combination of three kernel weights, $\vec{K} = \left\{k^L, k^G, k^V\right\}^T$. The substitution of Equation 5.10 into Equation 5.1-Equation 5.8 radically modifies the RT formulation into a quasi-linear expression. This attribute of the RTLS is crucial for the fast and robust inversion of multi-angle data. After normalization to the apparent reflectance units following Equation 5.9, I detail the last two terms of equation Equation 5.1 after incorporating the RTLS model as

$$\begin{aligned} R_s\left(\mu_0,\mu,\varphi\right) \;=\; & e^{-\frac{\tau_{aer}}{\mu_0}}\left\{k^L + k^G f_G\left(\mu_0,\mu,\varphi\right) + k^V f_V\left(\mu_0,\mu,\varphi\right)\right. \\ & +\alpha c_0 \rho_1\left(\mu\right)\rho_2\left(\mu_0\right)\} + \alpha\mu_0^{-1}\{k^L E_0^d\left(\mu_0\right) \\ & \left.+k^G D_G^1\left(\mu_0,\mu,\varphi\right) + k^V D_V^1\left(\mu_0,\mu,\varphi\right)\right\}, \end{aligned} \tag{5.11}$$

$$\begin{aligned} R_s^d\left(\mu_0,\mu,\varphi\right) \;=\; & e^{-\frac{\tau_{aer}}{\mu_0}} \times \left\{\left[k^L G^{av}\left(\mu\right) + k^G G_G^1\left(\mu_0,\mu,\varphi\right) + k^V G_V^1\left(\mu_0,\mu,\varphi\right)\right]\right. \\ & +\alpha c_0\left[k^L G^{av}\left(\mu\right) + k^G G_G^{11}\left(\mu_0,\mu,\varphi\right) + k^V G_V^{11}\left(\mu_0,\mu,\varphi\right)\right]\rho_2\left(\mu_0\right)\} \\ & \left.+\alpha\mu_0^{-1}\left\{k^L E_0^d\left(\mu_0\right) G^{av}\left(\mu\right) + k^G H_G^1\left(\mu_0,\mu,\varphi\right) + k^V H_V^1\left(\mu_0,\mu,\varphi\right)\right\}. \right. \end{aligned} \tag{5.12}$$

The surface albedo is now written as

$$q\left(\mu_0\right) = E_0^{-1}\left(\mu_0\right)\left\{e^{-\frac{\tau_{aer}}{\mu_0}} q_2\left(\mu_0\right) + k^L E_0^d\left(\mu_0\right) + k^G D_G^3\left(\mu_0\right) + k^V D_V^3\left(\mu_0\right)\right\}. \tag{5.13}$$

Different functions in these equations represent different integrals of the incident path radiance on the surface (D_s) and diffuse atmospheric Green's function (G^d) with the BRF kernels. The method of

their numerical calculation is described in section 5.4. Below, I give the integral expressions for these functions:

$$\rho_1(\mu) = k^L + k^G f_G^1(\mu) + k^V f_V^1(\mu), \tag{5.14}$$

$$\rho_2(\mu) = k^L + k^G f_G^2(\mu) + k^V f_V^2(\mu), \tag{5.15}$$

$$q_2(\mu) = k^L + k^G f_G^3(\mu) + k^V f_V^3(\mu), \tag{5.16}$$

$$D_k^1(\mu_0, \mu, \varphi) = \frac{1}{\pi} \int_0^1 \mu' d\mu' \int_0^{2\pi} d\varphi' D_s(\mu_0, \mu', \varphi') f_k(\mu', \mu, \varphi - \varphi'), \tag{5.17}$$

$$D_k^3(\mu_0) = \frac{1}{\pi} \int_0^{2\pi} d\varphi' \int_0^1 \mu' f_k^3(\mu') D_s(\mu_0, \mu'; \varphi') d\mu', \tag{5.18}$$

$$G^{av}(\mu) = \int_{-1}^0 d\mu_1 \int_0^{2\pi} G^d(\mu_1, \mu, \varphi - \varphi_1) d\varphi_1, \tag{5.19}$$

$$G_k^{11}(\mu) = \int_{-1}^0 f_k^1(\mu_1) d\mu_1 \int_0^{2\pi} G^d(\mu_1, \mu, \varphi - \varphi_1) d\varphi_1, \tag{5.20}$$

$$G_k^1(\mu_0, \mu, \varphi) = \int_{-1}^0 d\mu_1 \int_0^{2\pi} G^d(\mu_1, \mu, \varphi - \varphi_1) f_k(\mu_0, \mu_1, \varphi_1) d\varphi_1, \tag{5.21}$$

$$H_k^1(\mu_0, \mu, \varphi) = \int_{-1}^0 d\mu_1 \int_0^{2\pi} G^d(\mu_1, \mu, \varphi - \varphi_1) D_k^1(\mu_0, \mu_1, \varphi_1) d\varphi_1. \tag{5.22}$$

The subscript k in the above expressions refers to either geometric-optical (G) or volumetric (V) kernels.

The moments of the geometric BRF kernels are given by

$$f_k^1(\mu) = \frac{1}{2\pi}\int_0^1 d\mu' \int_0^{2\pi} f_k(\mu', \mu; \varphi' - \varphi)\, d\varphi', \tag{5.23}$$

$$f_k^2(\mu_0) = \frac{1}{2\pi}\int_{-1}^0 d\mu_1 \int_0^{2\pi} f_k(\mu_0, \mu_1, \varphi_1)\, d\varphi_1, \tag{5.24}$$

$$f_k^3(\mu') = \frac{1}{\pi}\int_{-1}^0 \mu d\mu \int_0^{2\pi} f_k(\mu', \mu, \varphi - \varphi')\, d\varphi. \tag{5.25}$$

The diffuse and total spectral surface irradiance are calculated from Equation 5.6 as

$$E_0^d(\mu_0) = F^{Dif}(\mu_0) / (\pi S), E_0(\mu_0) = F^{Down}(\mu_0) / (\pi S). \tag{5.26}$$

Let us rewrite equations Equation 5.11 and Equation 5.12 separating the kernel weights. First, separate the small terms proportional to the product $c_0\rho_2(\mu_0)$ into the non-linear term

$$\begin{aligned} R^{nl}(\mu_o, \mu) &= \alpha c_0 \rho_2(\mu_o) e^{-\tau_{aer}/\mu_0} \{e^{-\tau_{aer}/|\mu|}\rho_1(\mu) \\ &\quad + k^L G^{av}(\mu) + k^G G_G^{11}(\mu) + k^V G_V^{11}(\mu)\}. \end{aligned} \tag{5.27}$$

Second, collect the remaining multiplicative factors for the kernel weights,

$$F^L(\mu_o, \mu) = \left(e^{-\tau_{aer}/\mu_0} + \alpha\mu_0^{-1} E_0^d(\mu_0)\right)\left(e^{-\tau_{aer}/|\mu|} + G^{av}(\mu)\right), \tag{5.28}$$

$$\begin{aligned} F^k(\mu_o, \mu; \varphi) &= \left\{e^{-\tau_{aer}/\mu_0} f_k(\mu_0, \mu, \varphi) + \alpha\mu_0^{-1} D_k^1(\mu_0, \mu, \varphi)\right\} e^{-\tau_{aer}/|\mu|} \\ &\quad + e^{-\tau_{aer}/\mu_0} G_k^1(\mu_0, \mu, \varphi) + \alpha\mu_0^{-1} H_k^1(\mu_0, \mu, \varphi), k = V, G. \end{aligned} \tag{5.29}$$

With these notations, the TOA apparent reflectance becomes

$$\begin{aligned} R(\mu_o, \mu, \varphi) &= R^D(\mu_o, \mu, \varphi) + k^L F^L(\mu_o, \mu) + k^G F^G(\mu_o, \mu, \varphi) \\ &\quad + k^V F^V(\mu_o, \mu, \varphi) + R^{nl}(\mu_o, \mu). \end{aligned} \tag{5.30}$$

This last equation, representing TOA apparent reflectance as an explicit function of the BRF model parameters, provides us with the means for an efficient atmospheric correction by MARS-ReCO.

5.4. LUT generation and numerical aspects

Look-up tables are a very convenient way to store numerical results that are used repeatably by other calculations. In MARS-ReCO I precompute a LUT to store the RT quantities that are related only to the atmosphere and the acquisition geometry. The LUT of MARS-ReCO does not depend on the surface kernel weights $\left(k^L, k^G, k^V\right)$ thanks to the Green's formalism that I use in the RT formulation. The precomputed LUT for processing CRISM data is devised by inheriting basic principles from the MISR and MODIS surface retrieval algorithms. In this matter I follow the recommendations of King et al. in [91] that define the best LUT as the one that preserves the realistic physical variability while keeping its size within reasonable limits. In particular I follow the next principles to minimize the size of the LUT and the computational cost to generate it:

1. Only data coming from multiple scattering of light are stored in the LUT. Single-scattering, which is less computational expensive, is calculated analytically for a given set of parameters, or super-pixel, in the inversion process.
2. I use a dense grid of acquisition angles, namely μ_o, μ, φ, to use a nearest neighbor strategy for inversion instead of costly multi-dimensional interpolation.
3. In the current version of LUT CRISM observations have been previously corrected for gas effects and only mineral aerosols are considered. The AOT, or τ_{aer}, is therefore the integrated optical depth produced exclusively by mineral aerosols.
4. A single-layer homogeneous atmosphere is selected as it is accurate enough for modeling the aerosol effects. Likewise, I choose this strategy to reduce the computational time to generate the LUT.

The LUT is defined to store functions f_k^1, f_k^2, f_k^3, which depend on geometry of observations; c_0, which depends on aerosol content AOT; and functions D_k^1 , D_k^3 , G^{av}, G_k^1 , G_k^{11}, H_k^1, E_0^d, E_0 and R^D, which depend on both the geometry and the aerosol content. Index k refers to either volumetric (V) or geometric-optical (G) kernel function of the RTLS model. I compute the LUT for a dense grid of μ, μ_o, and φ angles ($\Delta\mu = \Delta\mu_0 = 0.02$ and $\Delta\varphi = 3^\circ$ for the ranges $\theta_0 = \{14^\circ \ldots 81^\circ\}$, $\theta = \{0^\circ \ldots 70^\circ\}$, and $\varphi = \{0^\circ \ldots 180^\circ\}$). I choose the range of viewing and illumination angles according to the functioning of CRISM. For example, the investigation of several CRISM observations reveal that viewing conditions never exceed $\theta = 70^\circ$, which is the highest value for the first and last EPF scan (see section 1.4). Similarly to processing of MISR and MODIS data, I select the nearest neighbor angle to fit the CRISM multi-angle measurements due to its higher speed. In this way MARS-ReCO avoids costly 3D interpolation in angles. Eventually, I calculate the LUT for a set of twelve atmospheric opacities values $\tau_{aer} = \{0, 0.05, 0.1, 0.2, 0.33, 0.5, 0.75, 1, 1.4, 2.0, 2.8, 4.0\}$. The selected set of AOT values are not homogeneously distributed because the contribution of a varying aerosol content to the remotely sensed signal is more variable for low dust concentrations (see Figure 5.6). In this case the consideration of a nearest neighbor strategy is not adequate since increasing the number of AOT values would increase substantially the size of the LUT as well. A linear interpolation is therefore used to extrapolate the LUT functions for the required AOT. This rather simple interpolation strategy is appropriate in our case because of its speed and the fact that functions stored in the LUT vary rather smoothly according to AOT, thus not presenting high variations that could not be reproduced by a linear interpolation. The grid density in terms of acquisition and atmospheric configurations is selected empirically from

considerations of accuracy and of minimal required memory as it is done in [108]. The current size of the LUT is ∼50 megabytes for each CRISM spectral band.

At this point, a few basic input radiative functions are necessary in order to compute the functions stored in the LUT. I decide to compute these four functions, namely $\left(R^D, D_s, G^d, c_0\right)$, for the aforementioned set of atmospheric conditions and acquisition angles using the RT program DISORT [168]. In Figure 5.5 I show a scheme illustrating the role of each of the aforementioned functions that play a role in the atmospheric RT. In the following I detail each input function and the way in which they are computed.

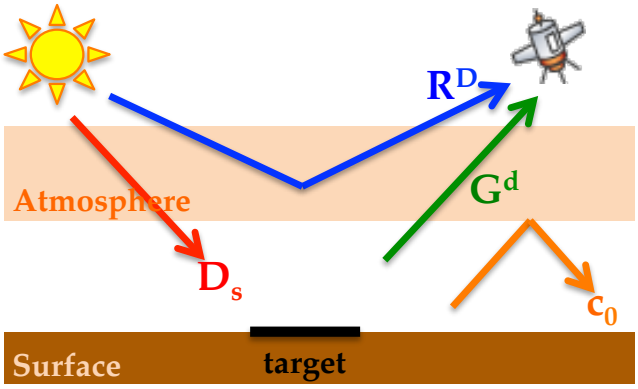

Figure 5.5.: Scheme depicting the four input atmospheric functions $\left(R^D, D_s, G^d, c_0\right)$ that are needed to calculate all the functions stored in the LUT of MARS-ReCO. In this figure, straight lines stand for direct and diffuse radiation.

- $R^D\ \left[sr^{-1}\right]$: The **atmospheric path reflectance** refers to the additive component of radiation divided by $\mu_0 S_\lambda$ received by a sensor that does not originate from the surface but exclusively through scattering in the atmosphere. I compute this term using DISORT by considering a dark surface (surface albedo set to 0) and simulating the TOA radiation at the sensor level.
- $D_s\ \left[Wm^{-2}sr^{-1}\right]$: The **path radiance incident on the surface** can be computed at the bottom-of-atmosphere, the inferior boundary condition of the RTE. Again, I consider a completely dark surface in order to avoid multiple reflections between the surface and the atmosphere.
- $G^d\ \left[sr^{-1}\right]$: The **diffuse Green's function** is also called the bi-directional upward diffuse transmittance divided by π. I calculate this term similarly to the path radiance incident on the surface D_s by simply reversing the direction of light propagation or, in other words, by setting the atmospheric layers in reverse order and normalizing the result by πS_λ. In the case of an homogeneous atmosphere like ours, the problem for the Green's function becomes identical to the problem for D_s provided that the substitution $s_0 \rightarrow s$ is done. In the calculation of G^d I also put the surface albedo to 0.
- c_0: The **spherical albedo of the atmosphere** is the fraction of the total light falling on the atmosphere that is reflected from it in all directions. I choose a special option of DISORT that allows retrieving the albedo of the entire medium as a function of SZA cosine. In this way I obtain the final spherical albedo of the atmosphere of Mars after integration of this DISORT output in μ_0 following Equation 1.5. Figure 5.6 illustrates the albedo of the entire medium depending on illumination angle and dust content.

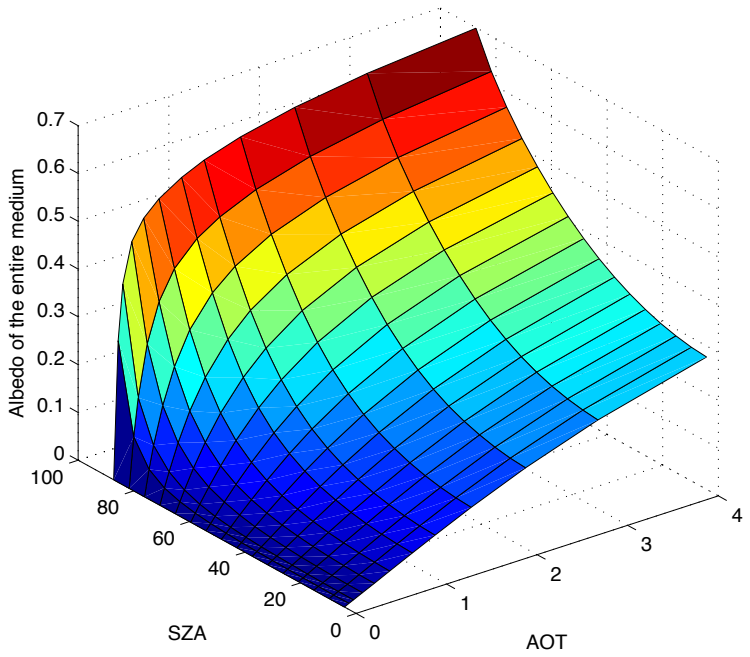

Figure 5.6.: Albedo of the atmosphere depending on illumination angle SZA and AOT. As expected, albedo is higher for high dust contents and large optical path lengths ν ($\nu \propto \theta_0$). These data have been generated using DISORT by considering an atmosphere with different values of AOT and a completely dark surface. The integration of these data in SZA provides the spherical albedo c_0 that is used in the generation of the LUT of MARS-ReCO.

Once these basic functions are precomputed, I calculate the derived quantities from Equation 5.17 to Equation 5.26 for the specified set of geometries and atmospheric opacities of the LUT. For this purpose, I utilize classical numerical methods in order to solve the different types of integrals in a smart yet accurate manner. I distinguish two types of integrals (see Equation 5.23 as reference), namely (i) integrals in azimuthal angle φ from 0 to 2π and (ii) integrals in cosine of illumination μ_0 or viewing angle μ from 0 to 1 or from -1 to 0.

First, I propose to solve the first type of integrals using the Fourier series expansion. Being $f(\varphi)$ an arbitrary function to be integrated in φ, it can be decomposed such that

$$f(\varphi) = \frac{1}{2}a_0 + \sum_{n=1}^{\infty} a_n \cos(n\varphi) + \sum_{n=1}^{\infty} b_n \sin(n\varphi). \tag{5.31}$$

Given the 2π-periodicity in azimuthal angle of all functions used in RT, the solution of the first type of integrals can be expressed such that

$$\int_0^{2\pi} f(\varphi)\, d\varphi = \frac{1}{2}a_0 2\pi = \pi a_0. \tag{5.32}$$

The first term of the Fourier series expansion a_0 can be calculated by computational techniques such as the FFT. This technique allows the calculation of the frequency components for any data. More details on this mathematical method as well as the Fourier series expansion are given in section 13.2.

Second, integrals in μ_0 or μ may be resolved by approximating them to a quadrature rule in the domain of integration equal $[0 \dots 1]$ or $[-1 \dots 0]$. In particular I use a n-point Gaussian quadrature rule that yields an accurate result by a suitable choice of the evaluation points and corresponding weights. The rule is stated as

$$\int_a^b f(x)\, dx \approx \sum_{i=1}^{n} \omega_i f(x_i)\,, \tag{5.33}$$

where x_i are the evaluation points and ω_i are the corresponding weights, which are tabulated in the literature. Gaussian quadratures produce accurate results if the function $f(x)$ is well approximated by a polynomial function within the integration range. In our case all atmospheric functions are quite smooth and thus Gaussian quadratures are appropriate. Severe testing revealed that a 16-point Gaussian quadrature is satisfactory to compute all integrals since higher orders did not improve the results. More details on this mathematical method are given in section 13.3.

Eventually, I highlight Equation 5.17, Equation 5.21 and Equation 5.22 which represent a different type of integral. Indeed, these functions depend on an integral in φ' that is formed by one function that depends on φ' and another that depends on $\varphi - \varphi'$. Under these circumstances I propose to solve this type of integrals using the convolution theorem that is defined as

$$\int_a^b f(\varphi')g(\varphi - \varphi')\mathrm{d}\varphi' = \mathcal{F}^{-1}\left\{\mathcal{F}\left\{f * g\right\}\right\} = \mathcal{F}^{-1}\left\{\mathcal{F}\left\{f\right\}\mathcal{F}\left\{g\right\}\right\}, \tag{5.34}$$

where $\mathcal{F}\{f\}$ is the Fourier transform of function f. Again I use a FFT algorithm to compute the Fourier transform. This mathematical theorem is summarized in section 13.4.

By following the previous numerical methods, I build the LUT by computing functions f_k^1, f_k^2, f_k^3, c_0, D_k^1 , D_k^3 , G^{av}, G_k^1 , G_k^{11}, H_k^1, E_0^d, E_0, and R^D for every geometric and atmospheric combination that is defined at the beginning of the present section. Results are stored in memory individually for each CRISM spectral band, ready to use for processing with MARS-ReCO.

5.5. Inversion strategy for surface retrieval

At this point I have introduced the RT formulation and the LUT on which MARS-ReCO is built. This two key elements provide the means for a robust and fast retrieval of the surface BRF by considering a non-Lambertian surface. In the present section I describe the strategy that is adopted to perform atmospheric correction. This strategy is inspired by the approach referred to as ASRVN (AERONET-based Surface Reflectance Validation Network) developed by Wang et al. in [183] and based on the RT formulation described in section 5.3.

Given an arbitrary CRISM multi-angle observation the IPAG-DP introduced in chapter 4 generates the corresponding CSP product. I remind the reader that this data set is composed by a collection of photometric curves in TOA apparent reflectance units, each one corresponding to a given super-pixel. Each super-pixel corresponds to a given ~180×180 m^2 area at the surface (see section 14.3 for

details). MARS-ReCO is devised to perform atmospheric correction due to aerosols of all photometric curves within a given spectral band of the CSP product by sequentially processing each super-pixel independently.

Being $\mathbf{R}_p = \{R_1, \dots R_{Ng}\}$ the photometric curve corresponding to the p^{th} super-pixel of an arbitrary CSP spectral band, the set of three RTLS coefficients that determine the surface BRF of the associated area at the surface are directly retrieved by fitting the RT solution described in Equation 5.30 to the set of N_g ($N_g \leq 11$) available angular measurements. The quasi-linear form of Equation 5.30 leads to a very efficient iterative algorithm aimed at minimizing the root mean square error (RMSE) between the angular measurements and the RT model defined as

$$RMSE = \sum_j \left(r_j^{(n)} - F_j^L k^{L(n)} - F_j^V k^{V(n)} - F_j^G k^{G(n)} \right)^2, \tag{5.35}$$

where

$$r_j^{(n)} = R_j - R_j^D - R_j^{nl(n-1)}, \tag{5.36}$$

where index j denotes each measurement at a different viewing angle, and n is the iteration number. Equation 5.35 provides an explicit least-squares solution for the RTLS kernel weights $\vec{K} = \{k^L, k^G, k^V\}^T$. In matrix form the solution is written as:

$$\vec{K}^{(n)} = A^{-1}\vec{b}^{(n)}, \tag{5.37}$$

where

$$A = \begin{bmatrix} \sum_j \left(F_j^L\right)^2 & \sum_j F_j^G F_j^L & \sum_j F_j^V F_j^L \\ \sum_j F_j^G F_j^L & \sum_j \left(F_j^G\right)^2 & \sum_j F_j^V F_j^G \\ \sum_j F_j^V F_j^L & \sum_j F_j^V F_j^G & \sum_j \left(F_j^V\right)^2 \end{bmatrix}, \; \vec{b}^{(n)} = \begin{bmatrix} \sum_j r_j^{(n)} F_j^L \\ \sum_j r_j^{(n)} F_j^G \\ \sum_j r_j^{(n)} F_j^V \end{bmatrix}. \tag{5.38}$$

At each iteration the retrieved $\vec{K}$ provides a refined estimate of the surface BRF that will be used in the upcoming iteration. The iterative process starts with a couple of assumptions regarding the surface (detailed in subsection 5.5.1) and stops when an intrinsic process checking the validity of the retrieved BRF (detailed in subsection 5.5.2) decides that the current $\vec{K}$ is satisfactory. MARS-ReCO then addresses the correction of the associated photometric curve of the following super-pixel and so forth.

The described inversion strategy represents the core of the algorithm MARS-ReCO and has proved to be very robust and fast when processing CRISM multi-angle data. In particular I observe computational times of roughly 20 seconds to process one spectral band of a CSP product (~3000 photometric curves) in a traditional computer. The computational burden is insignificant in front of traditional inversion algorithms. The major reason of this improvement stems from the linearization of the RT

formulation and the low size of the LUT due to the RTLS model and the Green's function method, respectively.

5.5.1. Initial assumptions

In the following I detail a couple of hypothesis regarding the surface that must be done to start the described iterative strategy. The non-linear term R_{nl} and the multiple reflection factor α depend on the surface reflectance, which is unknown at first, making Equation 5.30 weakly non-linear.

- On the one hand, function R_{nl} describes the contribution resulting from the direct or diffuse transmission of the upward radiance at the surface arising from the reflection of the environmental illumination. This function is due to the multiple reflections of the direct-beam sunlight between the surface and the atmosphere. Since function R_{nl} is small in front of other terms because $R_{nl} \propto qc_0$, Wang et al. propose to neglect this term in the first iteration of the ASRVN strategy putting $R_j^{nl(0)} = 0$ [183].
- On the other hand, functions F^k are still weakly non-linear via parameter α, which describes the contribution resulting from the direct or diffuse transmission of the upward radiance at the surface arising from the reflection of the direct and the diffuse incident sunlight. This non-linearity is also omitted by Wang et al. by setting $\alpha^{(0)} = 1$.

Considering these two assumptions Equation 5.30 becomes a linear function of the RTLS parameters and MARS-ReCO can thus estimate the coefficients $\vec{K}$ in the first iteration. In following iterations both terms R_{nl} and α are calculated using the $\vec{K}$ values of the previous iteration until convergence is achieved. In this study I decided to investigate the impact of these two assumption on the final retrieved BRF.

Regarding the assumption for $R_j^{nl(0)}$, MARS-ReCO proves to converge with high accuracy in a few iterations because the non-linear terms are usually quite small. Nevertheless, the assumption regarding the multiple reflection factor $\alpha^{(0)}$ is adapted to work for dark surfaces whose albedo q is close to zero (if $\alpha = (1 - qc_0)^{-1} = 1$, then $q = 0$). It is straightforward to realize that the inversion problem will converge more slowly for brighter surfaces such as snow-covered terrains with $q \approx 1$. In this matter Lyapustin et al. performs surface retrievals from snow-covered images with a similar inversion strategy than Wang et al. but assuming a spectrally dependent albedo such that $\alpha^{(0)} \neq 1$ [106]. In this case convergence is achieved over bright snow in the visible range in a higher number of iterations than for longer wavelengths where snow is less reflective. This strategy, however, requires a priori knowledge on the reflectance properties of the surface in order to set $\alpha^{(0)}$ for each spectral band.

Given the large variety of surface types that exist on Mars I propose to adopt a different strategy for MARS-ReCO. Since the proposed atmospheric correction approach is intended to work on any type of surface I do not consider appropriate to consider any a priori on the surface. I therefore propose to set the surface albedo for the first iteration $q^{(0)}$ as the value resulting from averaging the TOA apparent reflectances that correspond to those viewing geometries for which aerosol contribution is less predominant. This first guess is usually close to the real surface albedo as aerosols mostly scatter in the forward direction. As a consequence, measurements acquired under low phase angles are less affected by aerosols and are appropriate for the first guess on $q^{(0)}$. This approach is made possible because of the two modes in terms of relative azimuth (one of them corresponding to low phase

angles) that are generally present in CRISM observations (review section 1.4 for details). The proposed strategy is intended to speed up the convergence of the inversion strategy and to avoid potential false solutions.

5.5.2. Checking the validity of the retrieved surface

The quality and the physical sense of the retrieved BRF are not always assured by the inversion performed by Equation 5.37. Although the RTLS model leads to an efficient inversion algorithm there are some limitations associated with this BRF model (review subsubsection 2.3.1.4). These factors reduce the stability and uniqueness of the solutions such that small perturbations in measurements may lead to significantly different solutions. In some cases a mathematical solution may exist for the inverse problem (i.e. a triplet of RTLS coefficients k^L, k^G, k^V minimizing the RMSE) while its physical correctness may be unsatisfactory. As a matter of fact, the high goodness-of-fit at the measurement angles does not guarantee the correct shape of the retrieved BRF and may result in negative BRF values at other angles not considered in the inversion.

For this reason, the approach MARS-ReCO adopts a set of original tests inspired by the work of Wang et al. [183] that aims at validating the retrieved BRF of a given super-pixel by checking its quality and physical sense. If the solution is found to be deficient, the current inversion is aborted, and MARS-ReCO proceeds with the following super-pixel. The inversion of a given photometric curve is carried out iteratively. For each iteration n, the retrieved solution undergoes the following tests.

1. Before carrying out the inversion at iteration n MARS-ReCO checks if the photometric curve has sufficient angular sampling. A simple criterion is chosen based on the range of cosine of the VZA, namely $\mu_{max} - \mu_{min} \geq 0.2$. This simple yet efficient test is usually sufficient to ensure robust retrievals as Wang et al. prove with MODIS multi-temporal data. Furthermore, I devise MARS-ReCO such that the inversion is only performed if there are at least three angular measurements. This threshold is adopted according to the results obtained from the sensitivity study that I shall carry out in section 6.1. As might be expected, if the number of available measurements goes below three or the range of VZA cosine goes below 0.2, the retrieval of the photometric curve is aborted for the current spectral band. The inversion continues with the next test otherwise.
2. After the inversion performed following Equation 5.38 we check that the maximal difference over all points of the photometric curve between measured and computed TOA reflectance does not exceed a given threshold ϑ such that

$$\left| R_j^{CRISM} - R_j^{RTLS} \right| > \vartheta, \tag{5.39}$$

   Experiments proved that $\vartheta = 0.05$ provides a good trade-off between rejection of unsatisfactory solutions and intrinsic limitations of the inversion strategy. Whether some angular measurements surpass the previous threshold, the one with the highest deviation is excluded from the process and the inversion is repeated in iteration $n + 1$. Contrarily, if a set of angular measurements greater than three provides a good agreement with the model within ϑ for all points, MARS-ReCO proceeds with the next test.
3. The third trial verifies that the values of the direct-beam albedo $q(\theta_0)$ at $\theta_0 = 15^o, 45^o, 60^o$ are

positive and lower than unity. The inversion of the current photometric curve is discarded otherwise as we consider that the retrieved $\vec{K}$ coefficients do not recreate a physically meaningful BRF. The albedo, being an integral function of BRF and a fraction of radiation ranging from 0 to 1, is especially sensitive to an incorrect BRF shape.

4. Whether the albedo values are found to be positive the new solution n is checked to be consistent with the previous solution $n-1$. This is done by checking that $\left|q^n\left(\theta_0\right) - q^{n-1}\left(\theta_0\right)\right| < \kappa$, where κ is a threshold that has been empirically set to $1e^{-3}$. As might be expected, this test is only performed when $n > 0$.
5. The consistency of the derived BRF and albedo from the photometric curve is further assured by defining a confidence index. The confidence in the solution is initially low ($flag = 0$, when $n = 0$). Each time the new retrieval agrees with the previous retrieval according to test number four, $flag$ is increased by 1 and MARS-ReCO proceeds with the following iteration $n+1$. The $\vec{K}$ coefficients used in the $n+1$ iteration when $flag$ increases are calculated as follow

$$\vec{K}^{(n)} = w\vec{K}^{(n)} + (1-w)\vec{K}^{(n-1)}. \tag{5.40}$$

The weight w depending on the confidence in the previous solution, which increases with the value of $flag$. In particular the weight is $w = 1$ when $flag = 1$, $w = 0.8$ when $flag = 2$, $w = 0.6$ when $flag = 3$, and $w = 0.5$ thereafter. The retrieval is considered to be reliable when $flag = 4$. This updating method mitigates the random noise of retrievals and increases the quality of solutions when the non-linear term $R_j^{nl(0)}$ is not negligible and the first guess of $\alpha^{(0)}$ is far from reality.

According to this validation step super-pixels passing test number 2 may reach convergence after $n = 4$, which is the minimum number of iterations to reach $flag = 4$. The number of iterations may be higher $n > 4$ for those super-pixels for which an angular measurement is discarded in test number 2. In general most successfully inverted super-pixels reach convergence after 4-5 iterations. The presented validity process has proved to reject the majority of physically meaningless BRF solutions provided by MARS-ReCO.

6 Validation

In this chapter I aim at testing thoroughly the atmospheric correction addressed by MARS-ReCO. In this way its suitability to process data acquired by the CRISM spectrometer is tested. On the one hand, the accuracy of the semi-analytical formula for the TOA radiance derived with the Green's function method expressed by subsection 5.3.3 is proved to be very high, usually within a few tenths of a percent, in [107, 109]. The accuracy of the RT formulation on which MARS-ReCO is based is hence not evaluated in this dissertation. On the other hand, I propose to test the capabilities of MARS-ReCO on simulated data mimicking the surface and atmospheric properties of the planet Mars before applying it to real CRISM data. This goal is achieved by a sensitivity study that aims at identifying the acquisition geometries and atmospheric configurations under which MARS-ReCO becomes less reliable. With this aim the use of synthetic data is required as a sensitivity study based on real data would be limited to a few sites of Mars and dates for which ground truth data are available.

6.1. Sensitivity study

In this section I perform the validation of the proposed algorithm for atmospheric correction of CRISM targeted observations. With this goal I carry out the inversion of realistic simulated data by MARS-ReCO. Synthetic data sets are made available by considering the optical properties of the martian atmosphere and several types of martian materials that have characterized in the past using data from the MER Spirit (see section 1.2). In the generation of the simulated data I consider a large range of atmospheric conditions in order to test MARS-ReCO under clear and turbid atmospheric conditions. Likewise, I mimic the functioning of the CRISM instrument to generate CRISM-like data sets within the range of acquisition geometries in which this sensor operates. The goal of this sensitivity study is to identify the potential atmospheric or geometric conditions that may substantially decrease the quality of the surface retrievals or may simply make then unfeasible.

6.1.1. Validation strategy

Figure 6.1 details the sensitivity study devised to test the algorithm MARS-ReCO. First, I consider four types of mineral materials that are present in the Gusev crater of Mars and whose reflectances were acquired by the Pancam instrument aboard the MER Spirit at 753 nm and fitted to a BRDF model in [84]. In that study Johnson et al. use a Hapke's model accounting for the roughness of the surface (see subsubsection 2.3.1.2 and Equation 2.11). The Gusev crater represents a benchmark in the martian community and shall be further detailed in section 7.1. Second, the surface BRDF data are manipulated to simulate an overlaying atmosphere composed of mineral aerosols. For that purpose I use the radiative transfer properties of aerosols retrieved from CRISM multi-angle data by Wolff et al. in order to be consistent with the functioning of MARS-ReCO. Simulated TOA radiances encompassing the contributions of the surface and of the aerosols are generated by DISORT using several combinations of illumination geometry, azimuthal geometry and dust content, from typical to extreme configurations. I then manipulate the synthetic TOA radiances in order to build CRISM-like photometric curves at 753 nm by mimicking the typical viewing angles of a CRISM multi-angle observation. The construction of CRISM-like data sets from these realistic photometric (see bullet number 1 in Figure 6.1) curves is described in subsection 6.1.2. Afterward all simulated data sets are processed by MARS-ReCO to retrieve the RTLS coefficients $\vec{K}$ that model the surface BRDF corresponding to each configuration set by a given acquisition geometry and atmospheric opacity. The configurations for which MARS-ReCO fails to provide a satisfactory result are investigated in subsection 6.1.3 (see bullet number 2 in Figure 6.1). Eventually I carry out BRF comparisons between the original Hapke's model and the retrieved BRF one for a large range of angles (see bullet number 3 in Figure 6.1) in subsection 6.1.4. In this way the potential limitations of MARS-ReCO are identified. In the processing of CRISM-like simulated data I feed MARS-ReCO with the exact AOT value, which is not the case in reality. I hence remark that observed errors come only from the intrinsic limitations of MARS-ReCO under unfavorable conditions.

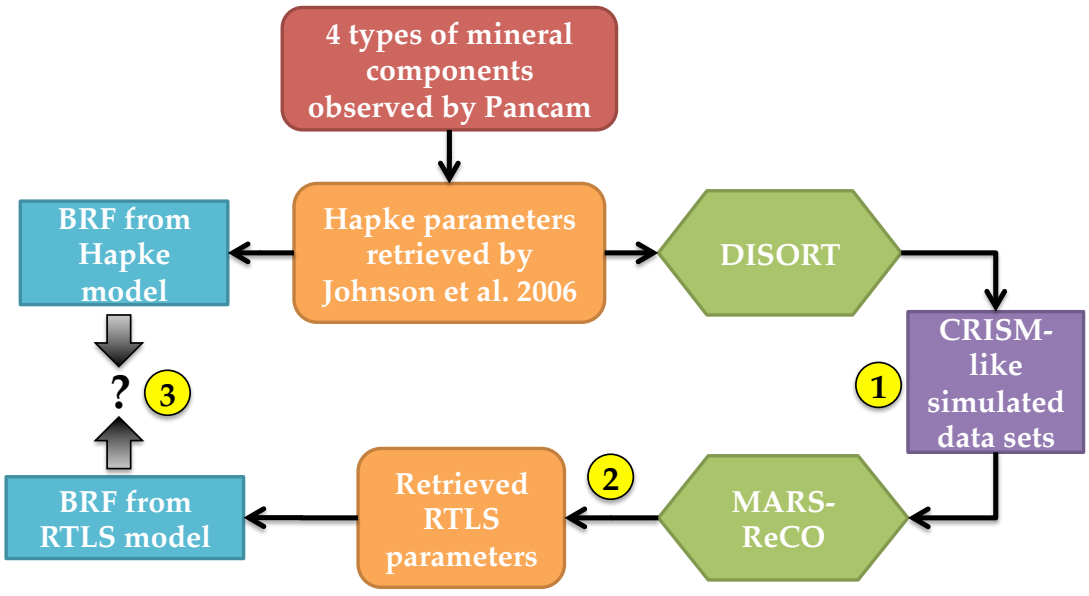

Figure 6.1.: Schematic diagram of the comparison strategy performed for the sensitivity study. The accuracy of MARS-ReCO is studied by comparing the retrieved surface BRF from simulated CRISM-like data with the original Hapke's model for the surface reflectance. Yellow bullets refer to the three major steps described in the text.

6.1.2. Simulated data

I consider two types of endmembers to recreate the properties of the surface of Mars. Two regions of interest identified by Johnson et al. in [84] are selected, namely "Soil", which corresponds to typical soils of intermediate redness and albedo, and "Red rock", which is related to rock facets exhibiting redness and albedo comparable to typical soils. I choose the endmember "Soil" because it is representative at the spatial scale of analysis that is carried out using orbital CRISM data. To expand the simulation, the endmember "Red rock" is also chosen as its photometric properties are more anisotropic than soils'. Figure 6.2 shows a set of composite images acquired by Pancam illustrating the two selected endmembers and others.

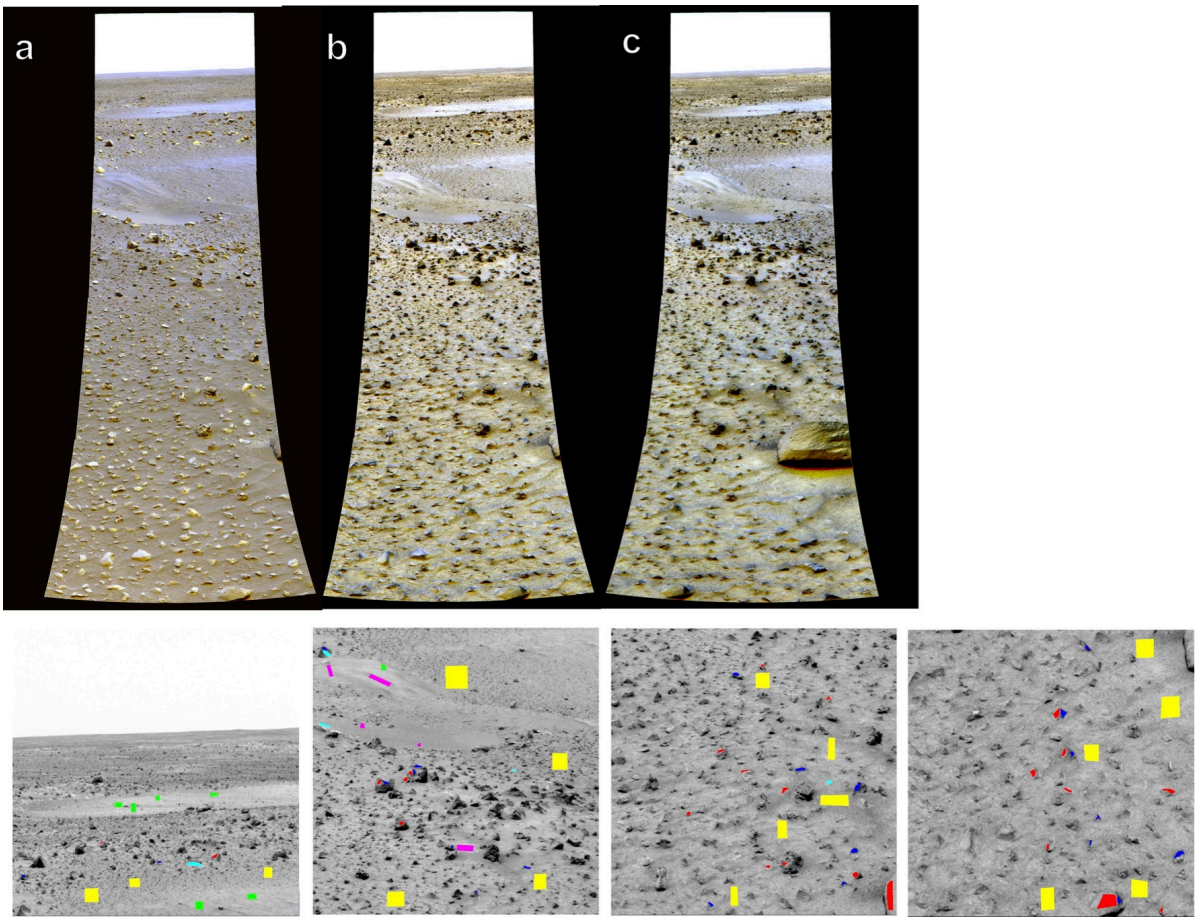

Figure 6.2.: (top) Color composite mosaics derived from three different times of day for the same wavelength: (a) 432 nm, (b) 753 nm, and (c) 1009 nm. (bottom) Regions of interest selected for photometric analyses: green = Bright soil; yellow = Soil; magenta = Dark soils; cyan = Bright rocks; red = Red rocks; blue = Gray rocks. Credit: [84].

Table 6.1 details the Hapke's parameters retrieved by Johnson et al. for each endmember of study. In [84] measurements are fitted using a Hapke's model using a 1-lobe and a 2-lobe Henyey-Greenstein phase functions. I consider the second case in order to test the validity of the RTLS model in the challenging case accounting for the variation of the surface BRDF in azimuthal angle in the presence of two scattering lobes. The Pancam measurements that were used to fit the surface model by Johnson et al. are related to a phase domain of 0-100° for the endmember "Red rock" and 0-125° for the endmember "Soil". I consider this phase domain as sufficient to constrain the BRDF model that will

be eventually compared with the one retrieved from CRISM data by MARS-ReCO. As it is shown in Table 6.1 I consider two cases, one bright and one dark (indexes 1 and 2, respectively), for every selected surface endmember. In this way the consequences of processing brighter surfaces with MARS-ReCO are also explored. For instance, the endmember Soil-2 represents a backscattering ($c_{Soil-2} = 0.55 > 0.5$, see subsection 2.1.2) and more darker ($w_{Soil-2} = 0.65$) surface than Soil-1 ($w_{Soil-2} = 0.69$) probably because to its rocky nature, while Red rock-1 is related to the brightest and most forward scattering surface ($w_{Red\,rock-1} = 0.83$, $c_{Red\,rock-1} = 0.25$) out of the four endmembers considered in this study. In this way the present sensitivity study deals with a complete and diverse range of martian mineral surfaces embracing the variability of dusty and rocky surface properties in a representative manner.

Endmember / Hapke's param. at 753 nm	w	$\bar{\theta}$	b	c	h	B_0
Soil-1 (table 4c in [84])	0.69	11	0.24	0.48	0.085	1
Soil-2 (table 6c in [84])	0.65	12	0.17	0.55	0.073	1
Red rock-1 (table 4b in [84])	0.83	19	0.45	0.25	0.0079	0.14
Red rock-2 (table 8b in [84])	0.65	14	0.17	0.80	0.069	1

Table 6.1.: Hapke's parameters of the four endmembers considered in the sensitivity study. These data are retrieved from the study of Johnson et al. with Pancam data of the Spirit Mars Exploration Rover [84].

In Figure 6.1 I detail how the DISORT engine is fed by the Hapke's BDRF model in Equation 2.11 using one of the four sets of parameters described in Table 6.1, depending on the chosen endmember. Alternatively, Table 6.2 details the set of 264 combinations of geometric and atmospheric properties that are chosen to generate the CRISM-like photometric curves. I decide to use a single configuration in terms of VZA since the set of eleven viewing angles in CRISM observations is quite constant. As it can be seen, the first and last measurements correspond to the most extreme VZA values while the sixth point is acquired at 25°, which corresponds to the average VZA value of CRISM central scans. Up to six SZA values are considered to embrace the angular range in which CRISM works, going from equatorial observations ($60° > \theta_0 > 30°$) to polar acquisitions ($\theta_0 > 70°$) . Regarding the phase domain I select four archetypal types of photometric curves in terms of azimuthal mode of a CRISM observation (see section 1.4). The sole case with a single azimuthal mode is the fourth combination which represents the extreme case when the Sun and the satellite positions are orthogonal ($\varphi_{in} = \varphi_{out} = 90°$). It is straightforward to see that the azimuthal combination number 1 is related to the photometric curves with higher phase domain while number 4 represents the poorer one. Since surfaces are not considered to have privileged scattering directions, and I therefore work with relative azimuthal angles ($\varphi_0 = 0°$), azimuthal angles such that $\varphi > 180°$ are not considered in this study. I finally consider a varying range of atmospheric opacities to alter the CRISM-like data sets by simulating TOA radiance at eleven different atmospheric opacities. The determination of the highest AOT for which MARS-ReCO is able to retrieve surface signatures satisfactorily is one of the major objectives of this sensitivity study.

6.1.3. Atmospheric correction

In this section the simulated data set introduced above is corrected for aerosol effects using the proposed algorithm MARS-ReCO. Each CRISM-like photometric curve is processed by the inversion strategy described in section 5.5. In Figure 6.3 I illustrate the quality of the inversion process in terms of (i)

Parameter	Combinations
θ (deg.)	1 comb.: [70, 63.5, 57.5, 52, 46.5, 25, 46.5, 52, 57.5, 63.5, 70]
θ_0 (deg.)	6 comb.: [30; 40; 50; 60; 70; 80]
φ_{in}, φ_{out} (deg.)	4 comb.: [0, 180; 30, 150; 60, 120; 90, 90]
τ_{aer}	11 comb.: [0; 0.1; 0.33; 0.5; 1; 1.5; 2; 2.5; 3; 3.5; 4]

Table 6.2.: Geometric and atmospheric configurations that are considered for the simulated CRISM-like data set of the sensitivity study of MARS-ReCO.

percentage of super-pixels that have failed to be inverted and (ii) average RMSE between the simulated measurements and the TOA expression fed by the LUT (see Equation 5.35). The two indicators are presented individually for every surface endmember and their dependence. The parameters of study (i.e. AOT, SZA and phase domain) are explored as follow.

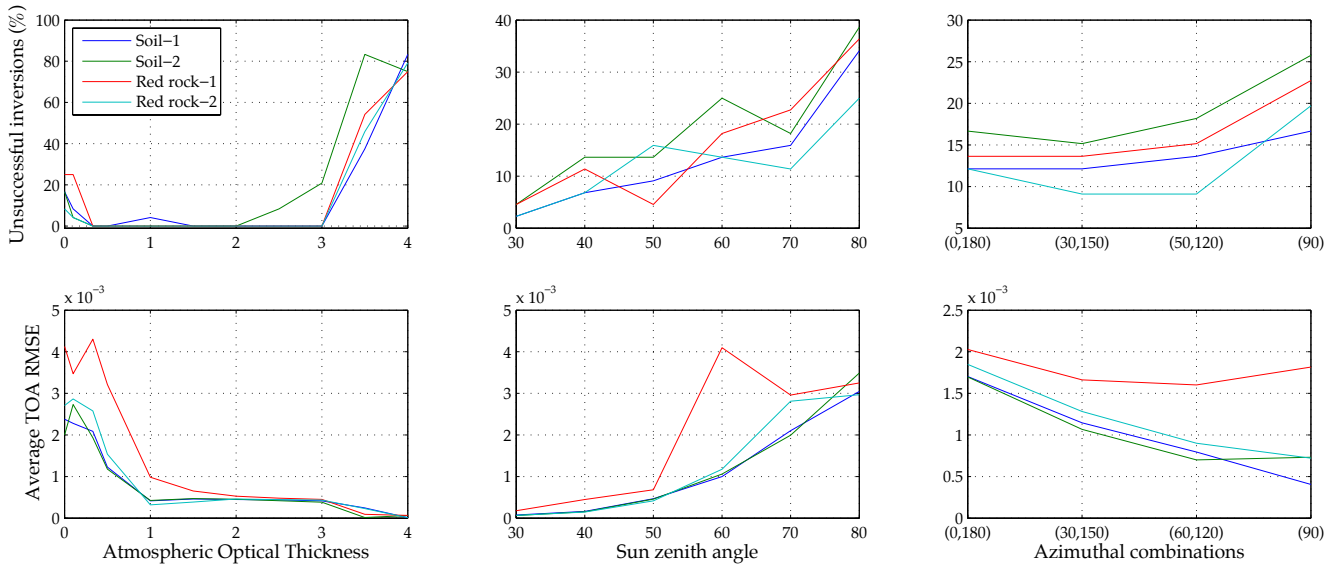

Figure 6.3.: (top) Percentage of unsuccessful retrievals obtained by MARS-ReCO according to AOT, SZA and azimuthal configuration detailed in Table 6.2. (bottom) Average RMSE resulting from fitting the TOA reflectance expression fed by the LUT to the synthetic data.

According to the percentage of unsuccessful surface retrievals detailed in Figure 6.3 (top-left) I conclude that MARS-ReCO performs satisfactorily for AOT values up to 3 regardless of the geometric configuration. Endmember Soil-2 represents the sole exception as the atmospheric correction fails when $\tau_{aer} > 2.5$. Unsatisfactory retrievals usually happen when negative values of surface albedo or high errors between the measurements and the RTLS model are obtained (review subsection 5.5.2). As it can be seen, more than 50% retrievals are unsuccessful when processing photometric curves that have been generated with an AOT greater than 3. In this case the higher contribution of the atmosphere disables the retrieval of the weaker signal coming from the surface. I draw the attention to the case of very clear atmospheric conditions ($\tau_{aer} \leq 0.1$) for which MARS-ReCO surprisingly performs several unsuccessful retrievals. Further investigation carried out in Figure 6.1.4 and Figure 6.1.4 shows that these results correspond to the configurations with poor phase domain and maximum SZA. I deduce that these results point to the lower performance of the RTLS model to recreate surfaces in these rather extreme configurations (see subsubsection 2.3.1.4). As regards the study on the SZA, experiments

summarized in Figure 6.3 (top-center) show that MARS-ReCO does not perform satisfactorily with a rejection rate up to 40% when the simulated data are acquired with the most extreme illumination angle, namely $\theta_0 = 80^o$. This circumstance may be explained again by the intrinsic limitations of the RTLS parametrization under these illumination conditions (see subsubsection 2.3.1.4). Regarding the phase domain, MARS-ReCO becomes more unstable for those simulated super-pixels that are related to a poor sampling in terms of azimuth. I consider this result as evident since photometric curves related to a single mode of azimuthal angle have theoretically half measurements that are similar to the other half. In this extreme case I deal with the shortest range of phase angles, thus justifying the worse results. As for the four types of endmembers, results show that the endmember Soil-2 is more problematic in terms of unsatisfactory retrievals. This circumstance could be caused by its lower albedo and anisotropy that make this endmember less distinguishable by MARS-ReCO under turbid atmosphere conditions.

Figure 6.3 (bottom) details the average error in terms of RMSE between the observations and the model. According to the results I note that the error of fitting made by MARS-ReCO decreases with higher atmospheric opacities. I do not consider this result to be surprising since the additive term of the atmosphere, namely the atmospheric path reflectance R^D, predominates in this range of AOT while the contribution of the surface is minimal. In this case the RT model does not need an accurate estimate of the surface (i.e. coefficients $\vec{K}$) to recreate satisfactorily the TOA reflectance. Contrarily, the TOA reflectance fitting is less satisfactory for higher SZA values similarly to what it happened with the percentage of unsuccessful retrievals. As for the azimuthal configuration, lower RMSE values are obtained for those configurations related to poorer phase domain. At this point I note that lower RMSE values do not necessarily mean better surface retrievals since the RTLS model can satisfactorily fit the multi-angle measurements while providing a physically incorrect solution. This is the case of the data combinations generated at high AOT as it is explained in Figure 6.6. Eventually, I underline that the endmember Soil-2 shows one of the lowest RMSE errors while Figure 6.3 (top) shows that it corresponds to the highest rate of unsuccessful retrievals. This result may mean that although this endmember is harder to retrieve because of its lower albedo and lower degree of anisotropy ($w = 0.65$ and $c = 0.55$), the corresponding bland BRF is fitted in a more accurate manner by the RTLS model. Contrarily, endmember Red rock-1 presents the higher RMSE reasonably because of its higher albedo and anisotropy ($w = 0.83$ and $c = 0.25$). In this matter I suggest that the forward scattering peak of endmember Red rock-1 might be more difficult to be retrieved accurately due to the predominant contribution of aerosol at these specific azimuthal angles.

I conclude this experiment by stating the BRF retrieval by MARS-ReCO is generally possible, yet not necessary accurate, when the signal coming from the surface is significant compared to the signal coming from the atmosphere. By significant I mean a favorable combination of (i) surface albedo, which must not be too low; (ii) surface anisotropy, which must be different from the photometric curve of the aerosols; (iii) and AOT, which must not be very high.

6.1.4. Evaluation of retrieved surface

After the $\vec{K}$ coefficients of the RTLS model are obtained for every super-pixel that has been satisfactorily processed, I propose to evaluate MARS-ReCO in the following manner:

1. The retrieved BRF of a given super-pixel, which corresponds to a specific endmember and a

specific geometric/atmospheric configurations, is reconstructed based on the estimated $\vec{K}$ coefficients and the RTLS model described in Equation 5.10.

2. The same set of BRF values are generated based on the Hapke's model in Equation 2.11 and the reference parameters summarized in Table 6.1. This second data set represents the reference BRF.

The second stage of the sensitivity study aims at evaluating the differences between the reference BRF derived from Pancam measurements and the BRF retrieved by MARS-ReCO from the the CRISM-like data set. I remind the reader that the simulated data set is generated by DISORT by feeding it with the scattering properties of the surface retrieved by Pancam. In order to perform this evaluation I consider a large and representative grid of geometries that explores the whole upper hemisphere (i.e. $\theta = [0^o \dots 85^o];\ \Delta\theta = 2^o;\ \varphi = [0^o \dots 180^o];\ \Delta\varphi = 3^o$) at the Sun incidence angle θ_0 that was used for the generation of each super-pixel. I restrict the evaluation of the retrieved BRF model to this sole illumination direction since it would be too unpredictable to investigate other ranges of θ_0 in which the BRF can be completely different.

Figure 6.4 shows the average absolute difference in BRF units between the retrieved RTLS model and the reference Hapke's model. Results according to AOT illustrate the goodness of the BRF retrievals when $\tau_{aer} < 2$. In the interval $2 < \tau_{aer} < 3$ all endmembers are also characterized satisfactorily (error ~ 0.1) except for Soil-2. I underline the agreement of this result with Figure 6.3 (top), which detects the endmember Soil-2 as the most problematic material in terms of percentage of satisfactory retrievals. Again, the darker nature of this endmember along with its less marked anisotropy may make it less distinguishable under turbid atmospheres when the contribution of aerosols predominates. The Figure 6.4 (center) and Figure 6.4 (right) are computed for all geometric combinations when $\tau_{aer} \leq 2$. I make this decision according to Figure 6.3 (top-left), which proves that retrievals above this atmospheric opacity are not reliable enough. In this case none of the two graphs provides valid information that can be generalized as the BRF retrieval error seems quite homogeneous according to SZA and azimuthal configuration. I remark, however, that Figure 6.4 (center) and Figure 6.4 (right) do not consider the unsuccessful retrievals that mostly happen for high SZA values and poor phase domains. According to these two figures I draw the conclusion that the BRF error mostly depends on the AOT and the intrinsic photometric properties of the surface or, in other words, the selected endmember. Regarding the latter I remark that endmember Red rock-1 is related to the less accurate surface retrievals according to the associated error, which is the highest among the four endmembers regardless of SZA and phase domain. Contrarily, endmember Soil-1 obtains the most accurate retrievals. According to these results I deduce that lower BRF errors may be obtained for darker and more isotropic surfaces, albeit the retrieval of this type of surface is more problematic in presence of turbid atmospheres. This conclusion agrees with the deductions drawn based on Figure 6.3. Contrarily, bright and anisotropic surfaces may be easier to distinguish even in rather turbid atmospheres while the difficulty to derive an accurate BRF model becomes higher. The previous inferences regarding the properties of the observed surface shall be of great interest for the atmospheric correction of real CRISM data.

The present investigation continues by exploring the surface BRF reconstructed from the retrieved coefficients $\vec{K}$ for a set of specific acquisition configurations in terms of AOT, SZA and phase domain. The following plots from Figure 6.5 to Figure 6.10 show the reconstructed BRF in polar coordinates with fixed SZA and in which the radial and angular coordinates correspond to the VZA and the relative azimuth, respectively. Note that the backscattering direction, $\varphi = 0^o$, is situated at the right-

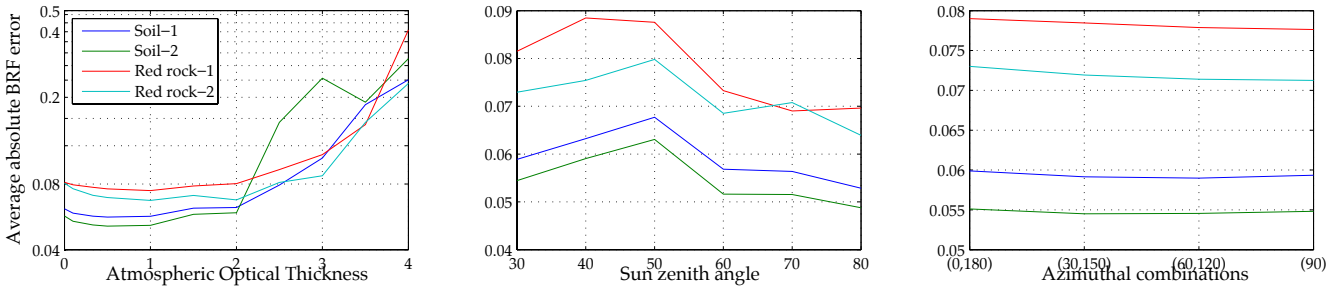

Figure 6.4.: Average absolute error between the BRF computed by the reference Hapke's model and the RTLS model fed by the kernel weights retrieved by MARS-ReCO. (left) Error according to aerosol optical thickness. Y axis is in logarithmic scale to appreciate the differences among endmembers under a clear atmosphere. (center) Error according to illumination angle. (right) Error according to the four azimuthal configurations. In the last two plots, only data with AOT<2 are considered.

hand side of the plots.

- **Impact of the AOT.** Figure 6.5 illustrates the validation of the retrieved RTLS model that is estimated by MARS-ReCO for the endmember Soil-2 when $\tau_{aer} = 1$ and $\theta_0 = 30^o$. In this case I select the first combination in azimuthal angle in which CRISM acquires the eleven measurements with $\varphi_{in}, \varphi_{out} = \{0^o, 180^o\}$, resulting in an acquisition phase domain $g = \{5^o - 100^o\}$. First, the reference surface BRF is generated for the value of acquisition SZA (the one that was used in the generation of the synthetic photometric curve) and a dense grid of VZA and φ using the Hapke's parameters inferred by Johnson et al. in [84] [see Figure 6.5 (left)]. Similarly, the RTLS model described in Equation 5.10 is then used to reconstruct the estimated BRF based on the RTLS coefficients retrieved by MARS-ReCO [see Figure 6.5 (center)]. I use the same geometrical grid for the evaluation of the retrieved RTLS. Eventually, Figure 6.5 (right) expresses the quality of the estimated surface BRF by plotting the difference between both BRF data sets in terms of percentage. As it can be seen, the RTLS model retrieves a predominantly backscattering surface, which corresponds satisfactorily to the BRF shown by the Hapke's model. I note a relatively low average error around 4%. The sole exception is observed at azimuthal angle 0° where the RTLS model is not able to reproduce the strong backscattering lobe of the Hapke's model. I consider this limitation of MARS-ReCO as expectable since the eleven available measurements do not sample such a narrow lobe. As a possible solution to recreate the opposition effect, I propose the combination of several CRISM observations corresponding to different configurations in terms of azimuth and solar incidence angle. However, it is important to remember that the RTLS model does not consider the opposition effect. This strategy will be adopted in chapter 7.

  The same experiment is now repeated for a greater atmospheric opacity in order to study the effects of more turbid atmospheres on the accuracy of MARS-ReCO. In Figure 6.6 I consider an opacity of $\tau_{aer} = 3$ which corresponds to a much higher probability of non-satisfactory retrievals according to Figure 6.4. In this case I select one of the few configurations for which MARS-ReCO works and, theoretically, provides a valid solution. As a matter of fact all tests detailed in subsection 5.5.2 are satisfactorily passed by the configuration of study. According to Figure 6.6 MARS-ReCO, however, retrieves a surface BRF model that is far from being close to that used in the generation of the synthetic data. This is especially the case for high viewing angles. Under these extreme conditions MARS-ReCO overestimates the surface reflectance up to 100%

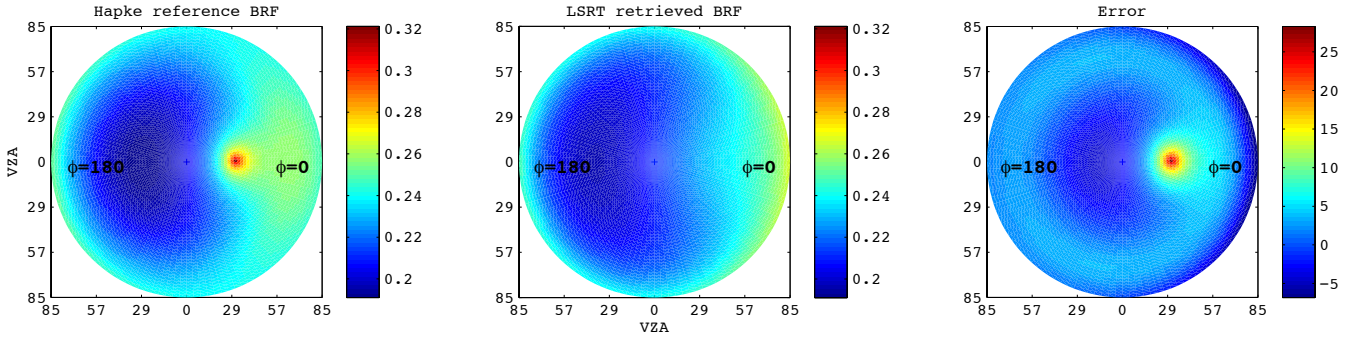

Figure 6.5.: Surface BRF corresponding to the endmember Soil-2 generated using (left) the reference Hapke's model and (center) the RTLS model estimated by MARS-ReCO when $\tau_{aer} = 1$, $\theta_0 = 30^o$ and $\varphi_{in}, \varphi_{out} = \{0^o, 180^o\}$. (right) Relative difference in percentage between the BRF obtained by the Hapke's model and the RTLS one. The BRF is plotted in polar coordinates for a dense range of VZA and azimuthal angle and for the value of SZA that is used for generating the investigated photometric curve.

in terms of BRF. I interpret this result as an under-correction of the aerosol contribution resulting in an overestimation of the signal coming from the surface. This example illustrates that surface retrievals may be physically incorrect despite a low inversion RMSE as it is shown in Figure 6.3 (bottom-left).

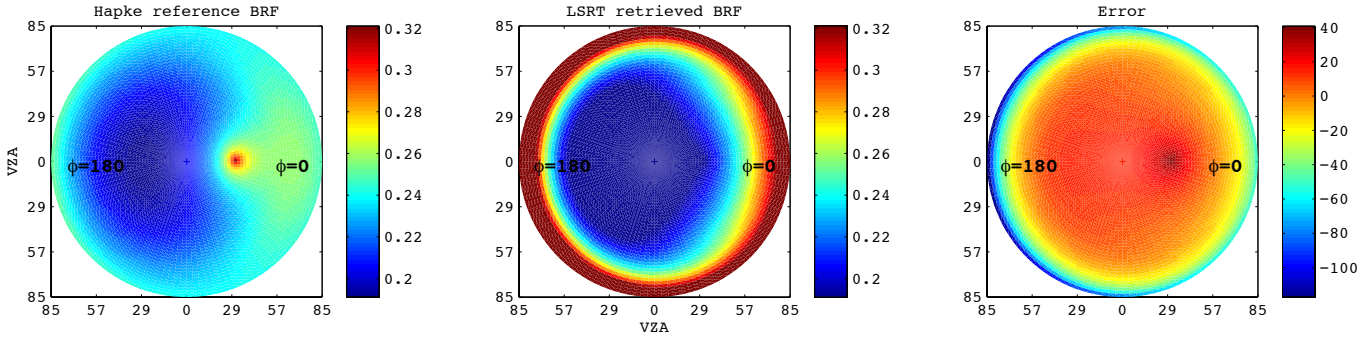

Figure 6.6.: Same as Figure 6.5 when $\tau_{aer} = 3$.

- **Impact of the SZA**. In Figure 6.7 and Figure 6.8 I investigate the validation of the retrieved surface BRF according to the illumination angle of acquisition. In this case the anisotropic endmember Red rock-1 is retrieved by MARS-ReCO using a synthetic CRISM observation built with a quite clear atmosphere ($\tau_{aer} = 0.5$) and a large azimuthal domain ($\varphi_{in}, \varphi_{out} = \{0^o, 180^o\}$). Two different values $\theta_0 = 30^o$ and $\theta_0 = 80^o$ are selected to explore the impact of high acquisition illumination angles on the retrieval of very anisotropic surfaces such as endmember Red rock-1. As it can be seen in Figure 6.7, when $\theta_0 = 30^o$ (corresponding phase domain of acquisition $g = \{5^o - 100^o\}$) the RTLS model reproduces satisfactorily a surface that presents a main forward scattering lobe. Again, the narrow backscattering lobe of Red rock-1 is slightly detected (see higher BRF values when $\varphi = 0^o$) but not well reproduced as TOA measurements are restricted to the principal plane. Except for this problematic scattering feature, a closer look to Figure 6.7 (right) reveals that the average absolute error is 5% in percentage, even for the forward scattering peak.

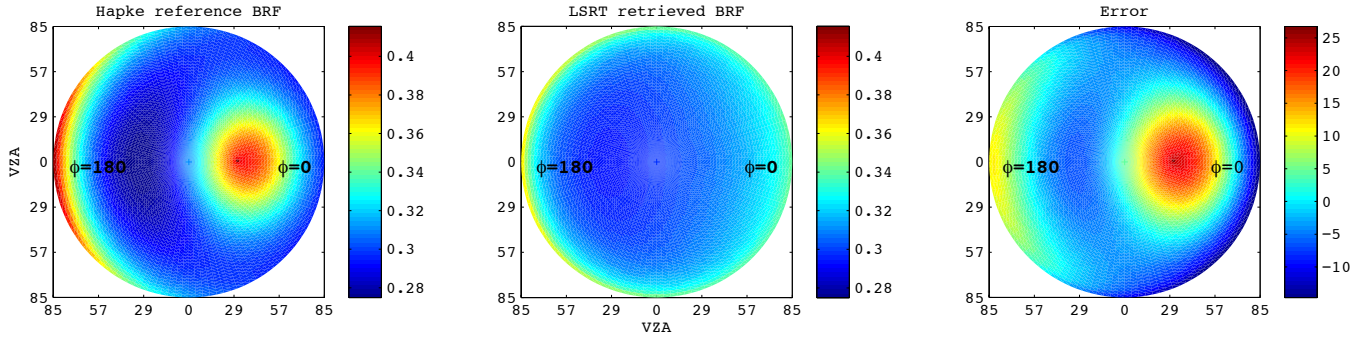

Figure 6.7.: Surface BRF corresponding to the endmember Red rock-1 generated using (left) the reference Hapke's model and (center) the RTLS model retrieved by MARS-ReCO with $\tau_{aer} = 0.5$, $\theta_0 = 30^o$ and $\varphi_{in}, \varphi_{out} = \{0^o, 180^o\}$. (right) Relative difference between the BRF obtained by the Hapke's model and the RTLS one. The BRF is plotted in polar coordinates for a dense range of VZA and azimuthal angle and the value of SZA that is used for generating the investigated photometric curve.

Contrarily, the higher Sun zenith angle that is used to acquire the TOA measurements related to Figure 6.8 (i.e. $\theta_0 = 80^o$, acquisition phase domain $g = \{10^o - 50^o, 105^o - 150^o\}$) results in a greater misclassification of endmember Red rock-1. In this case MARS-ReCO succeeds in retrieving the backscattering lobe while it totally fails in detecting the forward scattering one. Although the lobe at azimuth 0^o is predominant at this specific SZA I cannot consider this retrieval to be satisfactory because of the large average error (up to 140% in BRF units) that happen especially in the forward scattering direction and the cross-principal plane. This result may explain the results summarized in Figure 6.3 (top-left) in which some unsatisfactory retrievals are detected under clear atmospheres. Albeit the present photometric curve of study is related to a low atmospheric opacity ($\tau_{aer} = 0.5$) the extreme SZA used in the acquisition may prevent the RTLS model to accurately fit the observations (see subsubsection 2.3.1.4). Furthermore, the phase domain is not continuous in this case, which may also trouble the BRF retrieval.

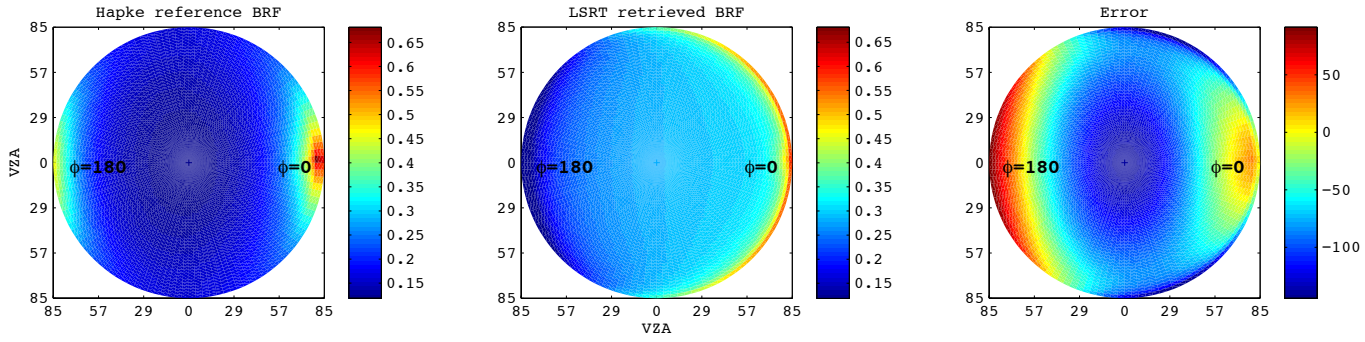

Figure 6.8.: Same as Figure 6.7 when $\theta_0 = 80^o$.

- **Impact of the azimuthal modes**. In order to study the phase domain of photometric curves I carry out an experiment using a synthetic CRISM-like data set composed by endmember Red rock-2 and observed by CRISM with $\tau_{aer} = 0$ and $\theta_0 = 30^o$. I select a completely clear atmosphere to further investigate the few unsatisfactory retrievals that are found under these conditions [see Figure 6.3 (top-left)]. Figure 6.9 and Figure 6.10 explore the two extreme cases in azimuthal angle when $\varphi_{in}, \varphi_{out} = \{0^o, 180^o\}$ (acquisition phase domain $g = \{5^o - 100^o\}$) and $\varphi_{in}, \varphi_{out} = \{90^o, 90^o\}$

(acquisition phase domain $g = \{38^o - 73^o\}$), respectively. I remind that the phase domain that can be explored by CRISM also depends on the solar incidence angle. Since considering multiple solar incidence angles would considerably expand this section I decide to only consider one value of acquisition SZA (i.e. $\theta_0 = 30^o$). In the first case MARS-ReCO succeeds in reconstructing the photometry of the endmember of study although it reproduces a broader and more diffuse backscattering lobe. This limitation is in agreement with the lack of angular measurements that has been detailed in previous experiments. As it is shown by Figure 6.9 (right) the average error in percentage is roughly 5%, except for the opposition effect in which the limitations of the RTLS model are visible.

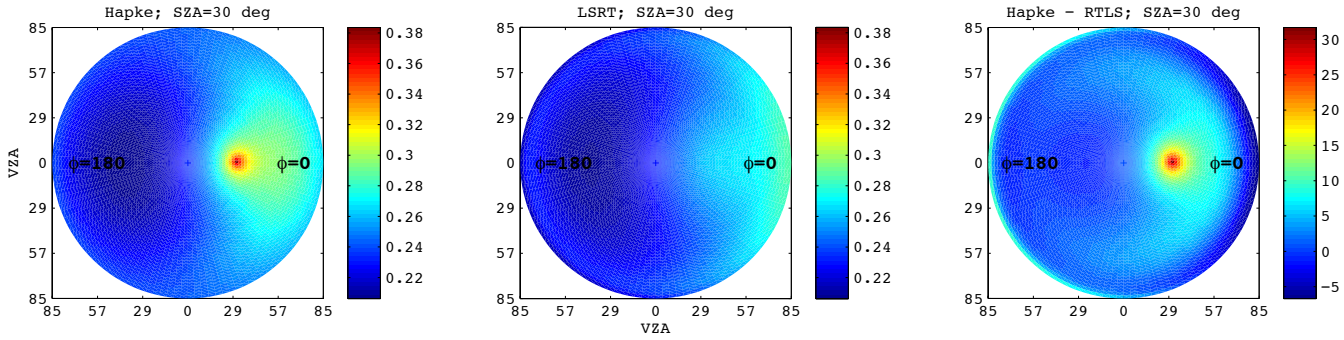

Figure 6.9.: Surface BRF corresponding to the endmember Red rock-2 generated using (left) the reference Hapke's model and (center) the RTLS model retrieved by MARS-ReCO with $\tau_{aer} = 0$, $\theta_0 = 30^o$ and $\varphi_{in}, \varphi_{out} = \{0^o, 180^o\}$. (right) Relative difference between the BRF obtained by the Hapke's model and the RTLS one. The BRF is plotted in polar coordinates for a dense range of VZA and the value of SZA that is used for generating the investigated photometric curve.

In the second case illustrated by figure Figure 6.10 I perform the same experiment but considering a narrower acquisition phase domain. In this experiment the photometric curve of study is exclusively acquired at $\varphi = 90^o$. Surprisingly, MARS-ReCO retrieves the backscatter properties of the endmember Red rock-2 with retrieval errors that are quite similar to the previous case with a larger phase domain. I consider this result to be totally fortuitous as the available measurements do not correspond to the principal plane. Nevertheless, some relatively high inaccuracies are observed in the forward scattering direction where the reconstructed BRF is underestimated by a 30% in average. This result does not happen in the case when $\varphi_{in}, \varphi_{out} = \{0^o, 180^o\}$ and may point to the reason why a few unsatisfactory retrievals happen under clear atmosphere conditions [see Figure 6.3 (left)]. I conclude that unsatisfactory retrievals may indeed happen for limited phase domains.

To conclude this experiment I remark that MARS-ReCO generally succeeds in retrieving a satisfactory model for the surface reflectance. The proposed atmospheric correction method infers the primary scattering properties of the surface (i.e. backscatter or forward scattering) for most of the cases. As for the type of material MARS-ReCO presents some difficulties in retrieving surfaces characterized by a weakly anisotropic BRF under relatively turbid atmospheric conditions. Contrarily, brighter and strongly anisotropic materials are detected satisfactorily, while the retrieved BRF is more susceptible to contain some inaccuracies. In general higher discrepancies occur under extreme illumination and viewing angles in which the BRF is more anisotropic and less easily reproduced by the RTLS model. I conclude that the eleven viewing geometries are generally not enough to represent narrow scattering

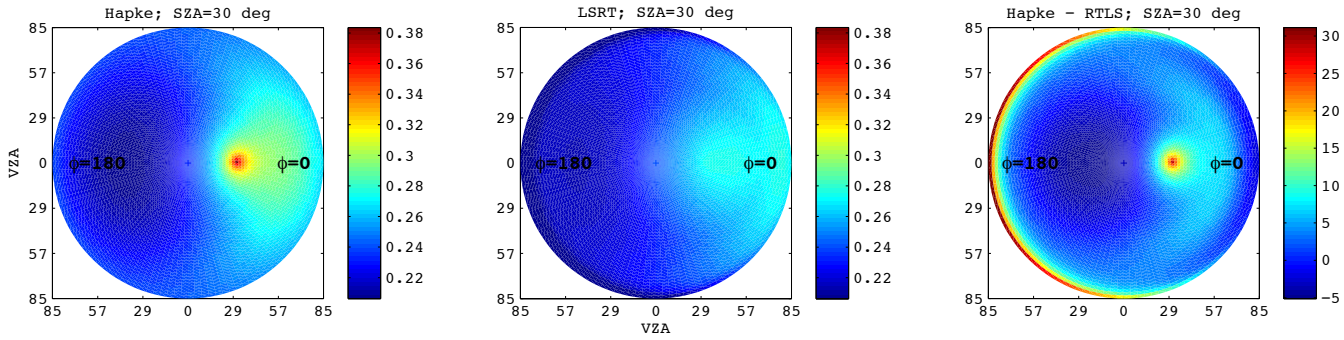

Figure 6.10.: Same as Figure 6.9 when $\varphi_{in}, \varphi_{out} = \{90^o, 90^o\}$.

lobes (e.g. the opposition effect) in an accurate manner. Another reason to this limitation is that the RTLS model does not have a kernel to model such a scattering effect. Nonetheless, experiments show that the average BRF value is generally retrieved satisfactorily in most of the cases, especially at mild VZA angles. I deduce that the Lambertian component of the RTLS model k_L is generally estimated accurately. Contrarily, the volumetric k_V and geometric-optical k_G kernel coefficients are harder to constrain due to the scarcity of angular measurements. Special attention must be paid to data acquired at high AOT, high SZA or poor phase domain for which the inversion may not be satisfactory as it is shown in Figure 6.6, Figure 6.8 and Figure 6.10, respectively. This information must be taken into account while processing CRISM observations acquired over the high latitudes of Mars, which are usually acquired at $\theta_0 \leq 80$. Regarding turbid atmospheres, Mars atmospheric conditions are usually related to $\tau_{aer} < 1$ and thus MARS-ReCO is suitable for processing most of the CRISM observations. Eventually, CRISM observations related to poor phase domains must be handled with care as it is shown in subsection 7.3.1.

I propose a last experiment to conclude the present sensitivity study. Until now, eleven measurements have been made available to perform atmospheric correction. Unfortunately, this is not the common case for real CRISM observations as less than 40% of the area encompassed by a given observation is observed by more than four geometries (see Figure 14.3). In this experiment I aim at determining the worst case in terms of available measurements for which MARS-ReCO can operate with an acceptable level of accuracy. With that aim I degrade the simulated CRISM-like data set by randomly removing an increasing number of measurements of each photometric curve. I detail the results of performing atmospheric correction by MARS-ReCO on the resulting data set as follow:

- **Impact of the available measurements**. Figure 6.11 plots the two parameters that have been used to monitor the quality of MARS-ReCO in the previous experiments. First Figure 6.11 (left) shows the percentage of unsuccessful surface retrievals. As it can be seen, this indicator is quite stable up to four removed measurements while it increases by 10% for the range between six and three available measurements. According to these results I state that MARS-ReCO is quite robust when dealing with low numbers of angular measurements. Beyond the threshold of three measurements the success rate drops as expected by more than 50%, reaching a 80% of unsuccessful retrievals when only a couple of measurements are available. On the other hand, I consider the inversion RMSE indicator as not being relevant in this particular experiment since it is easier to fit the RTLS model when there are a few available measurements.

  Further experiments are performed by evaluating the average absolute error between the BRF

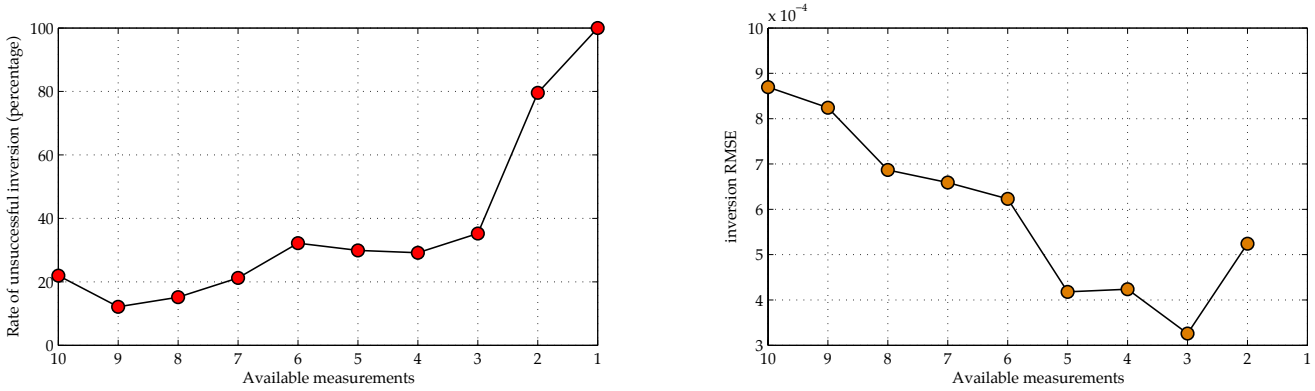

Figure 6.11.: (left) Percentage of deficient retrievals for a decreasing number of available measurements. (right) Inversion RMSE depending on available angular measurements.

retrieved by MARS-ReCO and the one generated using the reference Hapke's model. Figure 6.12 details experiments performed with 11, 9, 7, 5 and 3 available measurements. According to the presented results I remark that the performances observed for the eleven measurements are severely degraded when more than six measurements are removed. However, the average error remains relatively acceptable, especially if low dust contents and SZA values are considered.

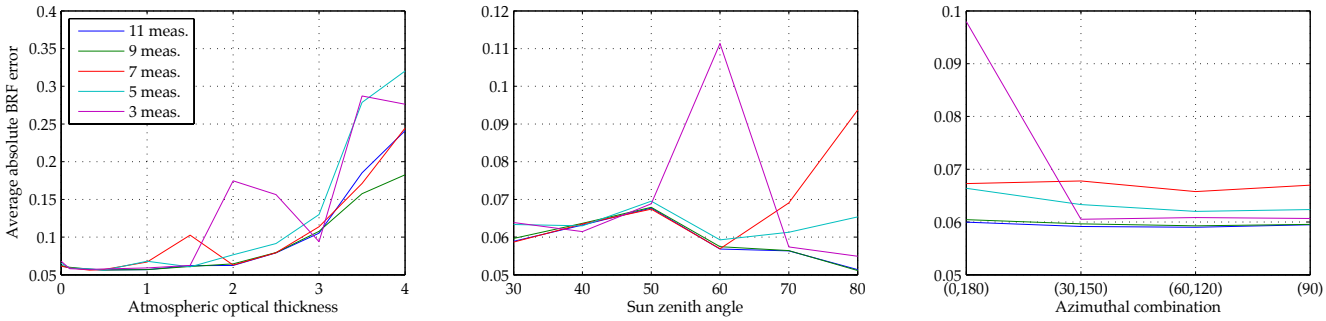

Figure 6.12.: Same as Figure 6.4 but the average absolute error is now plotted according to the available measurements.

In conclusion of this last experiment I determine that the minimum number of available measurements assuring the reliability of MARS-ReCO is equal to three as indicated by Figure 6.11 (left). This value is defined as a minimum threshold in the inversion strategy detailed in subsection 5.5.2. The reason for such a low value in comparison with the maximum number of measurements (i.e. 11) may be the intrinsic angular functioning of the CRISM instrument. As a matter of fact, multi-angle measurements are always aligned onto the same axis and therefore three appropriate measurements (e.g. one in the forward scattering direction, one at nadir and one in the backscattering direction) may be enough to retrieve the primary photometric properties of the investigated surface. While a higher number of measurements may improve the retrieved BRF model I stress that the angular position of the measurements may be much more relevant. Eventually, retrievals with a few measurements under non favorable conditions (e.g. high dust contents and high SZA values) must be considered with skepticism according to Figure 6.12.

7

Experiments on CRISM data

After testing the capabilities of MARS-ReCO on simulated data, the goal of the present chapter is to evaluate the suitability of the proposed atmospheric correction algorithm when applied to real CRISM targeted observations[1]. For this purpose we define a validation strategy focused on CRISM data acquired over a specific area of Mars, the Gusev crater, and summarized in Figure 7.1. The Gusev crater is a suitable martian site to validate any atmospheric correction algorithm since it corresponds to the landing site of the MER Spirit. Since 2004 this rover has acquired data on the terrains surrounding the landing site under different atmospheric conditions. In particular photometric properties of the minerals at the surface of this crater have been made available using data acquired by the Pancam instrument aboard the rover Spirit. In the present experiment we propose to contrast the photometric properties retrieved from orbital CRISM images using the MARS-ReCO approach with those presented in previous works using Pancam data. With that aim four CRISM targeted observations of the Gusev crater are selected and initially processed by the IPAG-DP proposed in this thesis in Part II. Afterward, each corresponding multi-angle CSP product is individually processed by MARS-ReCO to compensate for atmospheric effects and retrieve the BRF of each super-pixel. According to the sensitivity study performed in section 6.1 the four retrieved data sets in BRF units are combined into a single data set in order to increase the available angular sampling and therefore improve the photometric properties of the materials in the crater to be retrieved from orbital data. This is possible since each CRISM observation is related to a different acquisition geometry. The resulting integrated BRF data set is fitted to a Hapke's model as it is done in the experiments using Pancam data in [84]. MARS-ReCO is eventually evaluated by performing a comparison, for several super-pixels, between the Hapke's parameters derived from the CRISM observations and those from the Pancam instrument.

This chapter is organized as follows. First, I present the study site in section 7.1 by giving details on

[1] This work has been done in collaboration with the "Institut de Recherche en Astrophysique et Planétologie", Toulouse, France, and the "Laboratoire Interactions et Dynamique des Environnements de Surface", Paris, France, under the framework of the M.Sc. thesis of Jennifer Fernando [60].

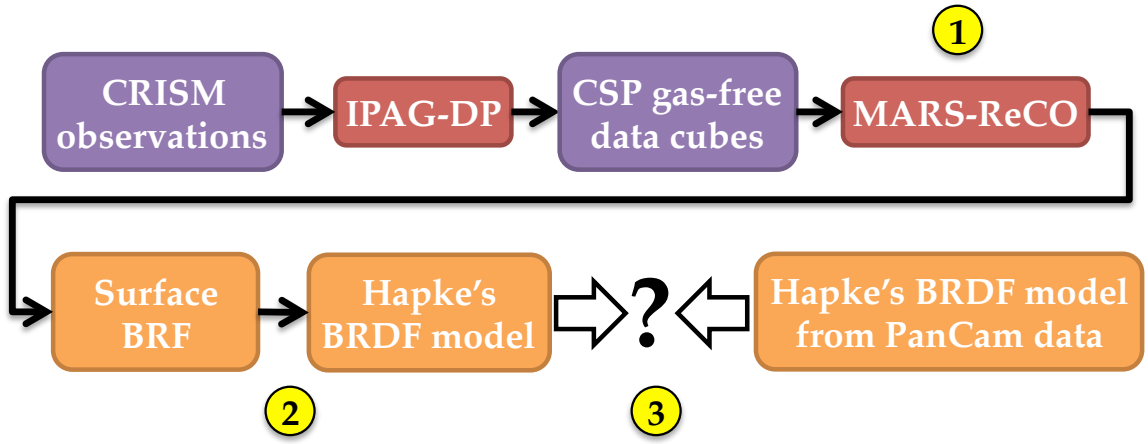

Figure 7.1.: Scheme of the validation of the MARS-ReCO approach using real CRISM observations and photometric properties retrieved from data acquired by the MER Spirit. Yellow bullets refer to the three major steps described in the text.

the Gusev crater and the MER mission. In section 7.2 I introduce the data sets used in this study. section 7.3 then details the comparison between the results of the surface retrieval and those from independent studies. In section 7.4 I eventually report on a short experiment that is carried out to evaluate the benefits of using an atmospheric correction algorithm that does not assume a Lambertian surface.

7.1. The Gusev crater and the MER Spirit

The Gusev crater is a martian impact crater dated from the Noachian Period (between 4.1 and about 3.7 billion years ago) that is located at latitude 14.5° S and longitude 176.5° E (see Figure 7.2). This geological structure measures about 160 km of diameter and was named in 1976 after the Russian astronomer Matvei Gusev. The Gusev crater is located between the high cratered terrains of the southern hemisphere and the flat plains of the northern hemisphere.

The Gusev crater was selected as a landing site for one of the MER in the NASA "Follow the water" mission. This mission aimed at understanding how the water may have affected the martian environment in the past. The Gusev crater was chosen by international scientists due to the hypothesis that it could have played the role of a former lake where water and sediments carried by the southern canyon Ma'adim Vallis might have been unloaded. Given this scientific interest the robotic rover Spirit landed in the Gusev crater on January 4, 2004, in the region formed by the cratered plains in the west of Columbia Hills. Spirit explored the surface of the crater from 2004 to 2010 in search of evidence of water activity in the past (e.g. hydrated minerals). Figure 7.3 details the traverse map through the two main types of terrain that have been explored by Spirit, the cratered plains and the Columbia Hills. Both terrains are mainly composed of basalts rich in olivine [6].

In this scenario we choose to carry out the following experiments on the cratered plains that are close to the landing site of Spirit. Indeed, photometric studies have been conducted in this region in the past using in situ measurements acquired by the Pancam instrument aboard Spirit [84] and orbital HRSC images [81]. The results presented in the literature represent a unique opportunity to evaluate the

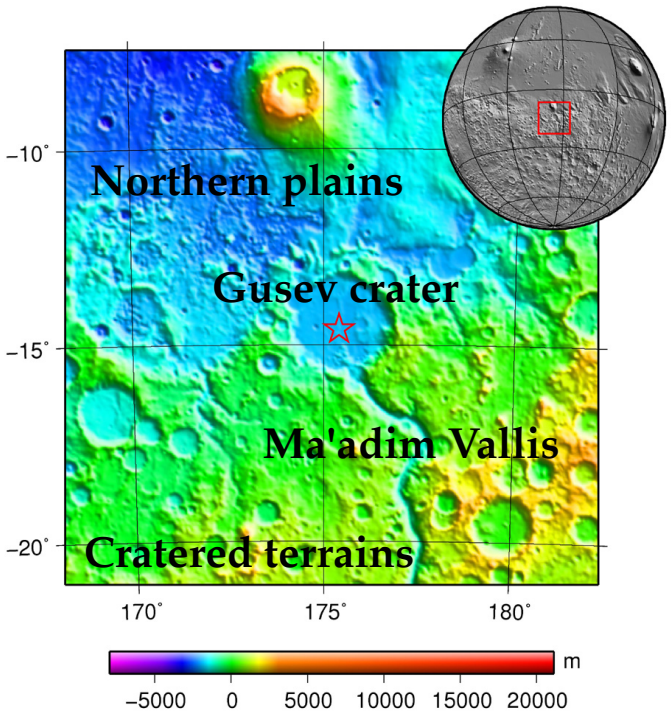

Figure 7.2.: An overall view of MER-A Spirit landing site (denoted with a star). Plotted using Generic Mapping Tools and gridded MOLA data.

quality of the photometric properties retrieved by MARS-ReCO.

7.2. Selection of CRISM observations

Many CRISM observations have been acquired over the landing zone of the rover Spirit due to the scientific interest of this area. Among all of them, we select four CRISM observations, namely FRT3192, FRT553B, FRT8CE1 and FRTCDA5. These observations are chosen according to their corresponding acquisition characteristics. All observations present a substantial spatial overlapping among them and a high diversity of geometric conditions (i.e. various illumination configurations). The latter element is crucial to constitute a complete data set in terms of angular sampling from which to retrieve accurate and reliable photometric properties of the materials at the surface. According to the results of the sensitivity study in chapter 6 we decide to discard those observations with high atmospheric contributions (i.e. $\tau_{aer} \geq 2$) according the results of the sensitivity study in section 6.1. Figure 7.4 shows the central scan of each observation, which is roughly centered at the Columbia Hills (review Figure 7.3). Additionally, Table 7.1 details each observation by the corresponding illumination angle, azimuthal mode, AOT and time of the martian year. As it can be seen, the four images represent a comprehensive collection of data on the Gusev crater in terms of acquisition angles.

First, selected observations are processed by the IPAG-DP as described in chapter 4. In this way, the AOT values detailed in Table 7.1 are estimated by the β-method as explained in section 14.2. The eleven hyperspectral images forming each FRT CRISM observation are combined by the step described in subsection 4.2.4 using an output spatial resolution of ~180 m/pixel. Figure 7.4 (left) shows the four 180×180-meter super-pixels that are chosen close to the landing site of Spirit and from which

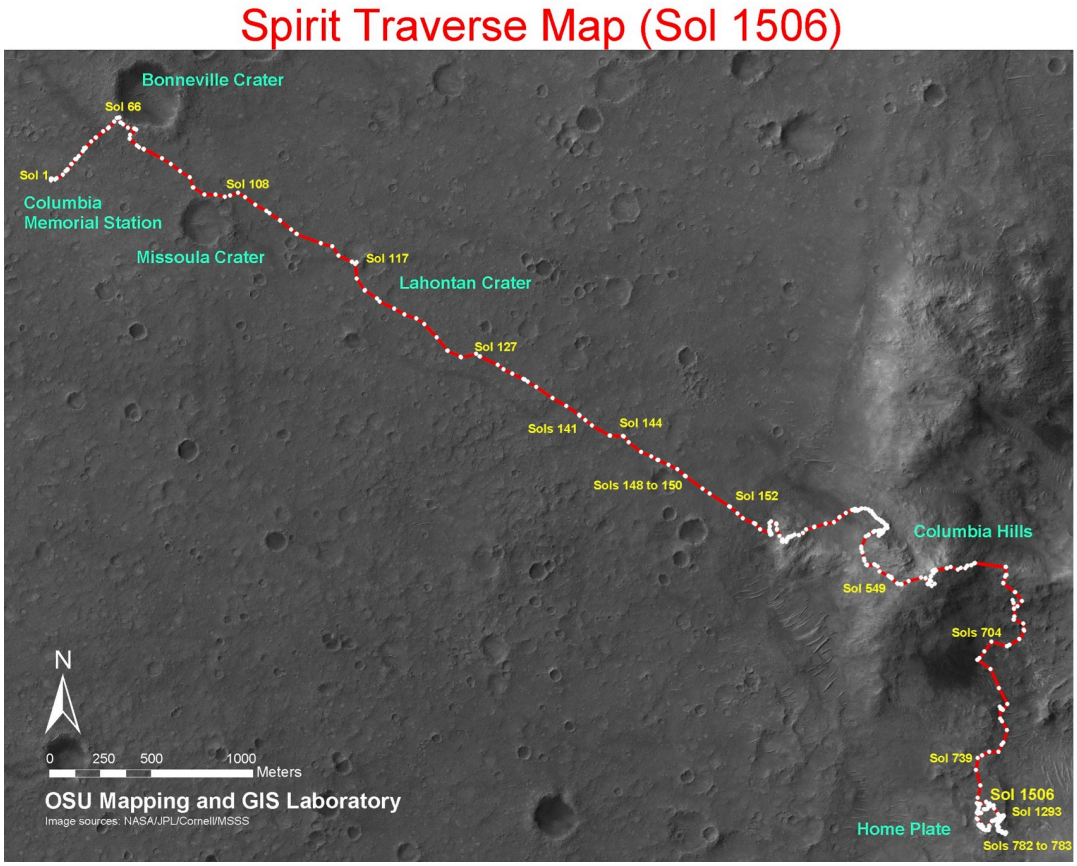

Figure 7.3.: Spirit traverse map, up to sol 1506 (April 02,2008). The term sol refers to the duration of a solar day on Mars (24 hours, 39 minutes, and 35 seconds). The landing site is in the upper left.

the corresponding photometric properties will be estimated and evaluated. Super-pixels are selected according to the availability of measurements and the average slope of the terrain. As a matter of fact, each super-pixel is related to a high number of available angular measurements (up to eleven) and a flat area. The latter condition is important to assure the validity of the traditional photometric normalization adopted by the IPAG-DP (see subsection 4.2.3 for details). Eventually, we conduct the photometric study at 750 nm for two reasons. First, this wavelength corresponds to a spectral window in which the transmittance of the atmosphere is maximum and therefore the photometric results are less sensitive to the potential residues of the correction for atmospheric gases (see Figure 2.2). Second, similar studies such as [84, 81] were performed at this very wavelength and therefore our results can be contrasted.

7.3. Retrieving photometric properties of the surface

The validation of the surface BRF retrieved by the MARS-ReCO algorithm is carried out for the set of CRISM observations as follows. First, CRISM data are corrected for aerosol effects using the MARS-ReCO approach (see bullet number 1 in Figure 7.1) in subsection 6.1.4. For that purpose the AOT estimation at 1 μm as detailed in Table 7.1 is used. We then fit the retrieved surface BRF of every super-pixel to a Hapke's macroscopic model with a two-term Henyey-Greenstein phase function (see bullet number 2 in Figure 7.1). As it will be shown in the validation step (see bullet number 3 in

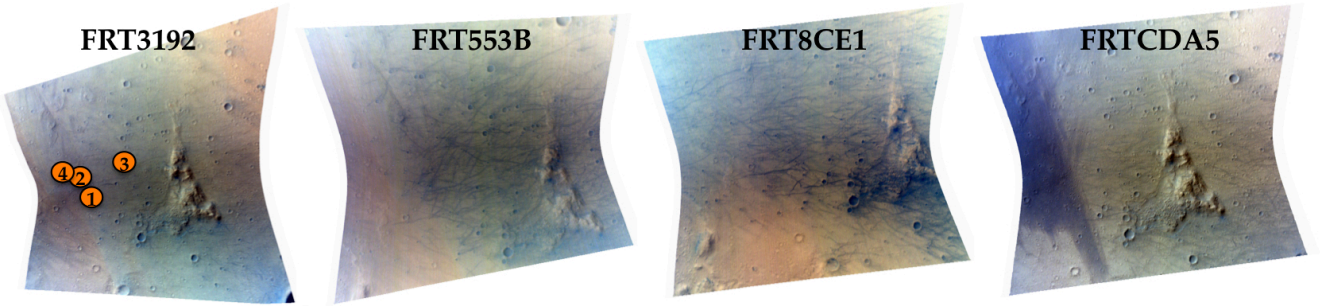

Figure 7.4.: Selection of CRISM observations for the photometric study of the Gusev crater. The high-resolution central scan of each observation is shown. The Columbia Hills are the triangular geological formation that appear in each image. The approximative position of the four super-pixels are highlighted by orange circles in the snapshot corresponding to image FRT3192.

Param.\Obs.	FRT3192	FRT553B	FRT8CE1	FRTCDA5
SZA	60.4°	53.1°	40.2°	62.8°
Azimuthal mode	65°, 135°	90°	60°, 120°	55°, 125°
AOT at 1 μm	0.38	1.00	0.40	0.95
Solar longitude	139° (summer)	218° (fall)	4° (spring)	138° (summer)

Table 7.1.: Acquisition details of the CRISM observations used in chapter 7. AOT is retrieved with the β-method. Seasons correspond to the northern hemisphere.

Figure 7.1), the satisfactory agreement between the results obtained from orbital CRISM data and from previous studies underlines the validity of the retrieved photometric curves at 750 nm.

7.3.1. Atmospheric correction

Atmospheric correction of the four CRISM observations corresponding to the Gusev crater is performed by MARS-ReCO. Table 7.2 details the results of the surface retrieval by means of the percentage of successfully processed super-pixels and the corresponding average RMSE of the TOA reflectance fit. As it can be seen, a maximum of ~20% photometric curves are corrected satisfactorily for atmospheric effects. I consider this result to be fully coherent as less than 30% of the super-pixels of a CRISM observation are usually sensed by more than three scans (see subsection 4.2.4). According to the small RMSE of fit, I consider the surface retrievals to be robust while results cannot be assured to be physically meaningful yet.

CRISM observation	FRT3192	FRT553B	FRT8CE1	FRTCDA5
# processed super-pixels	15.0%	0%	19.9%	12.5%
RMSE with RTLS model	1.4e-03	NaN	4.9e-04	3.1e-03

Table 7.2.: Results obtained by MARS-ReCO applied to the selection of CRISM observations over the Gusev crater.

At this point I draw the attention to observation FRT553B. As it can be seen in Table 7.2 MARS-ReCO fails to retrieve the surface BRF of all the photometric curves of the corresponding CSP cube. As a matter of fact the validity testing step of MARS-ReCO (see subsection 5.5.2) finds the inferred surface

albedo to be negative for each processed photometric curve and therefore the inversion is aborted. I highlight two different causes that may explain this series of unsuccessful retrievals:

1. **Overestimation of the AOT**. If the IPAG-DP overestimates the signal coming from dust aerosols, the contribution of the surface may be extremely low after atmospheric correction, thus resulting in negative surface albedos.
2. **Poor acquisition conditions**. As it is proved in section 6.1 some extreme acquisition conditions may trouble the retrieval of realistic BRFs.

I investigate the most likely cause of this unsatisfactory functioning by repeating the inversion process using the AOT estimation provided by the Pancam instrument aboard the rover Spirit (available at http://starbrite.jpl.nasa.gov/pds) and the retrieval method of Wolff et al. in [187]. In practice the latter option is not considered since the corresponding AOT estimate is greater ($\tau_{aer}^{Wolff} = 1.4$) than the one provided by the IPAG-DP ($\tau_{aer}^{\beta-method} = 1.0$). In this case the processing of FRT553B by MARS-ReCO with this AOT value would definitely fail too. As for the Pancam estimate, the corresponding AOT is slightly lower ($\tau_{aer}^{PanCam} = 0.8$) and thus MARS-ReCO should work if reason number 1 is true. However, only 0.3% of the CSP cube (8 super-pixels out of 2667) were inverted satisfactorily in this case. Further experiments proved that the inversion provides an acceptable rate of inverted super-pixels when $\tau_{aer} < 0.2$. If reason 1 is right, it would mean that all the available AOT estimations for observation FRT553B are wrong. Given the robustness demonstrated by the three AOT retrieval methods in other experiments I discard reason number 1.

On the other hand, the inspection of the angular coverage of FRT553B shows that there is only one mode in azimuthal angle (review Table 7.1). According to the results shown by Figure 6.3 in the sensitivity study, the inversion of observation FRT553B may not be satisfactory caused by its poor angular coverage in terms of phase domain. Another outcome of the sensitivity study is that MARS-ReCO has some trouble retrieving rather isotropic materials under relatively turbid atmospheric conditions. As it shall be explained in the following sections, soils predominate in the Gusev crater at the CRISM resolution. This type of material is less anisotropic than other martian components at the surface (review Table 6.1). Eventually, FRT553B corresponds to the highest AOT out of the four selected observations. All these limitations may explain the failure of MARS-ReCO in processing observation FRT553B. According to this interpretation I thus exclude this observation from the photometric study.

Following sections detail the numerical method used to fit the Hapke's model to the retrieved BRF photometric curves and the comparisons with the previous studies.

7.3.2. Fitting the retrieved surface to a Hapke's model

The Hapke's formalism has been widely used to study the bidirectional reflectance of planetary surfaces, including cases in which the phase angle coverage is incomplete (review subsubsection 2.3.1.2). This is the case of previous studies with Mars data in the region of Gusev such as [84, 81, 43]. In terrestrial remote sensing I highlight a similar study using MISR data over desert areas performed by Wu et al. in [188].

As it is introduced in the beginning of chapter 7 the selected overlapping observations under varied geometry conditions in units of surface BRF are combined as in [81] to better constrain the photometric modeling. A single CRISM observation senses the surface of Mars at a maximum of eleven different

emergence angles. This set of measurements are distributed along the same line of trajectory that corresponds to two different azimuthal angles at best. Unfortunately, this range of angles may not be enough to determine robustly the photometric parameters of the materials at the surface as it is shown in subsection 6.1.4. In order to improve the number of observational geometries we propose to combine the surface BRF retrieved by MARS-ReCO corresponding to observations FRT3192, FRT8CE1 and FRTCDA5.

In this study we select a Hapke's BRDF model taking into account the roughness of the surface as detailed in Equation 2.11. As for the phase function we choose a two-term Henyey-Greenstein phase function (see Equation 2.4) as Johnson's in [84]. Given the three photometric curves in BRF units of a given super-pixel observed by the three observations, the set of parameters involved in the Hapke's model are determined by the approach described in [40]. Cord et al. put forward a regression method founded on a genetic algorithm. The principal advantages in applying this technique are (i) all Hapke's parameters are treated simultaneously with no a priori additional assumptions, (ii) all the available data have the same weight and are used to solve the problem, (iii) it requires less computational time than a Monte Carlo routine. This genetic algorithm starts with a set of randomly generated suitable solutions. After evaluating the error between the model and the measurements, the best solutions are combined among them. In this way a new set of solutions is formed, expecting that the error of the fitting is lower than the previous one. This is repeated until a threshold is attained.

In the absence of small phase angles (CRISM data acquired over the region of Gusev present phase angles above 20°), we ignore the opposition parameters (h and B_0) in the regression because they are inconsequential (review subsubsection 2.3.1.2).

7.3.3. Evaluation

Table 7.3 shows the values of the Hapke's parameters w, $\bar{\theta}$, b and c provided by the regression algorithm detailed in subsection 7.3.2 for the four super-pixels of study. The robustness of the regression is assessed by monitoring the relative and absolute RMSE between the Hapke's model and the BRF measurements. As it can be seen, results show that the Hapke's model reproduces the retrieved surface BRF with low absolute and relative quadratic residues.

	w	$\bar{\theta}$ (°)	b	c	Abs. RMSE	Rel. RMSE	# of meas.
SP I	0.72±0.01	18.9±0.3	0.24±0.01	0.52±0.03	0.010	0.037	24/33
SP II	0.71±0.02	19.0±0.4	0.25±0.02	0.46±0.03	0.011	0.039	22/33
SP III	0.69±0.02	18.3±0.5	0.22±0.02	0.57±0.04	0.013	0.039	24/33
SP IV	0.69±0.01	18.3±0.3	0.21±0.01	0.54±0.02	0.013	0.045	25/33
Avg.	**0.70**	**18.6**	**0.23**	**0.52**	**0.012**	**0.040**	**24/33**

Table 7.3.: Retrieved physical parameters corresponding to the Hapke's macroscopic model fitted to CRISM multi-angle surface reflectance. Parameters correspond to the fusion of CRISM observations FRT3192, FRT8CE1 and FRTCDA5. SP stands for super-pixel.

In this section we aim at validating the photometric properties inferred from CRISM orbital data based on the results provided by MARS-ReCO by comparison to previous photometric studies. We propose the seminal work of Johnson et al. in which spectro-photometric observations acquired using

the Pancam instrument aboard the robot Spirit are processed to study the photometric properties of the rocks and soils in the cratered plains close to the Columbia Hills [84]. In that study in situ reflectance data are fitted to the Hapke's RT model at 750 nm, among other wavelengths. We also highlight the study of Jehl et al. which was carried out using HRSC data in [81]. In that study, photometric parameters of the Gusev crater are determined under some limitations, namely the lack of atmospheric correction of the HRSC images. To mitigate this inconvenient, HRSC observations with low atmospheric opacities ($\tau_{aer} < 0.9$) and VZA are selected. Nonetheless, as some inaccuracies are expected (e.g. overestimation of the single scattering albedo w caused by the misinterpretation of the brightness caused by aerosols as coming from the surface), we therefore decide to focus exclusively on the work of Johnson et al. Alternatively, Cull et al. retrieve photometric properties of the Gusev crater from CRISM data using an algorithm that is specifically developed for this region of Mars [43]. The retrieved physical properties presented in that study are similar to those inferred in [84].

Hapke's parameters w, $\bar{\theta}$, b and c retrieved from CRISM observations are evaluated by contrasting them with the results obtained by Johnson et al.. We remark that the present study compares two types of results that are arguably contrastable under some specific situations. As a matter of fact Pancam provides in situ measurements while CRISM acquires data from orbit corresponding to lower spatial resolution. Figure 6.2 shows how soils are the most predominant terrain class while endmembers named as Red Rock and Gray Rock are much more spatially confined. The most appropriate Pancam observations for our study are consequently selected in the cratered plains, namely the NW of Missoula at Sol 102-103, where the endmember Soil is predominant (see [84] for more details on this specific location).

Regarding the **single scattering albedo** w, Johnson et al. find variations from 0.65 to 0.85, for the three endmembers studied by the robot at different sites (see Figure 7.5). In particular a value of $w = 0.69$ is derived for measurements at Sol 102-103. These values are consistent with those obtained using the CRISM targeted observations as the average w is 0.70 when the three observations are combined (see Table 7.3).

As for the two **parameters of the Henyey-Greenstein phase function** b and c, values obtained by the genetic algorithm are plotted along with the results obtained from Pancam measurements at Sol 102-103 in Figure 7.6. In addition, we plot the b and c values from the study carried out by McGuire and Hapke on the photometric properties of artificial particles [116]. The results presented in Figure 7.6 show that the photometric properties retrieved from orbital CRISM data are close to the Soil endmember.

Regarding the **macroscopic roughness of the surface**, parameter $\bar{\theta}$ is found to be between 10 and 14 degrees in the site NW of Missoula at Sol 102-103 for the endmember Soil (see Figure 7.7). These values are slightly lower than those obtained in our study (average $\bar{\theta}$ of 18.6°). We interpret this difference as a higher concentration of rocks in the field of view of CRISM that may result in a higher roughness of the surface. Indeed, rocks are generally have a higher macroscopic roughness than soils as it can be seen in Figure 7.7.

We conclude that the Hapke's parameters w, $\bar{\theta}$, b and c estimated by the genetic algorithm from retrieved BRF of the Gusev crater are substantially consistent with independent studies based on in-situ Pancam data. These results validates the atmospheric correction approach MARS-ReCO proposed in this thesis. We draw the attention to the spatial resolution of CRISM observations as MARS-ReCO

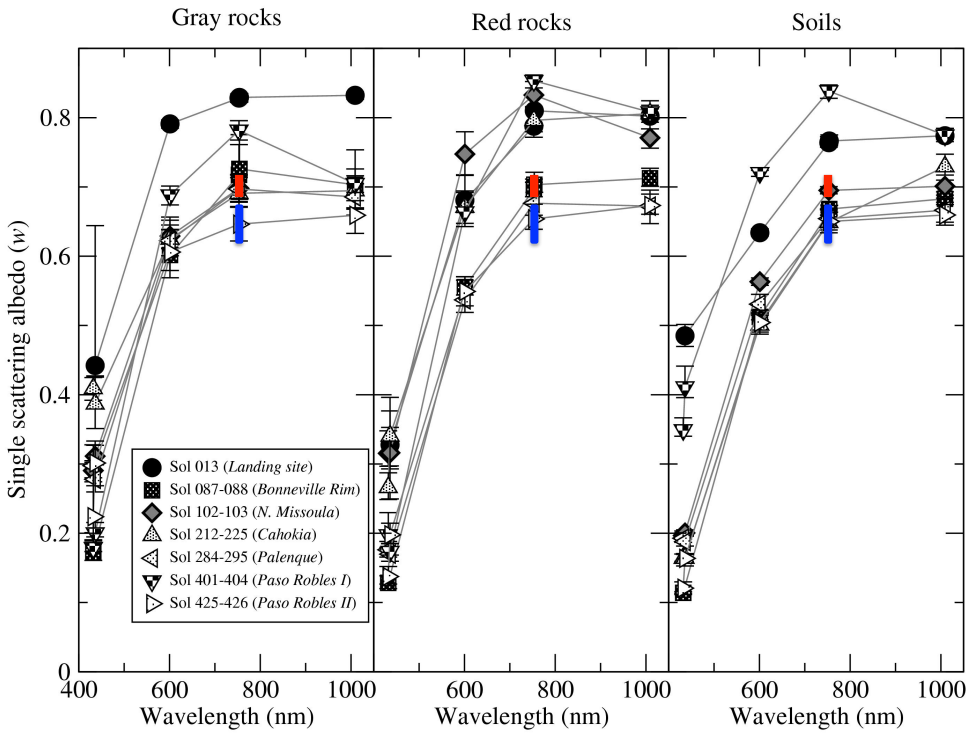

Figure 7.5.: Single scattering albedo (w) values for the three endmembers studied in [84] at different wavelengths. The range of parameter w retrieved from CRISM data by MARS-ReCO is shown using a red marker. The blue box corresponds to the results obtained by the method based on the Lambertian assumption in [52]. Credit: [84]

infers surface BRF from areas that are homogeneous within an extent of ~180×180 m^2. Indeed, the spatial resolution of the EPFs (down to ~180 m/pixel) sets the minimum resolution of the super-pixels in a CSP product (see section 14.3). On the other hand, we note that the accuracy of the BRF retrieved by MARS-ReCO benefits from the combination of several CRISM observations of the same area. In this matter I conclude that, contrarily to what is done in this section, it may be beneficial to combine the observations in units of TOA radiance, that is to say, before the atmospheric correction performed by MARS-ReCO. By slightly modifying the expression in Equation 5.35 such that a different AOT is considered for each CRISM observation, the surface retrieval can be performed based on all available TOA radiances at once. In this way inversion results may become more robust due to the higher number of angular measurements. With this modification data from observation FRT553B could be exploited in the present study. This issue represents an immediate future prospect of this work. Further investigations will be led toward a finer validation of MARS-ReCO by combining more observations of the Gusev crater and by performing this study on other study sites. The complementary study of Johnson et al. focused on the landing site of the MER Opportunity represents a potential validation site [85].

7.4. On the benefits of assuming a non-Lambertian surface

To conclude the present part of the dissertation I propose to look into the benefits of performing atmospheric correction based on a non-Lambertian surface with regard other traditional methods adopting

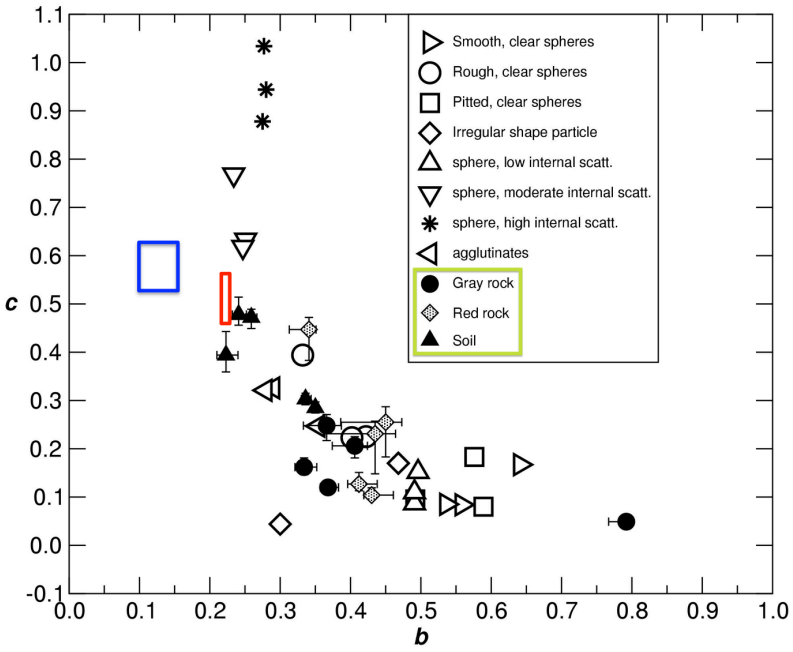

Figure 7.6.: Asymmetry parameters (b) versus backward scattering fraction parameters (c) for end-members retrieved by Johnson et al. from Pancam data at Sol 102-103 (see green box). Values for different types of artificial particles estimated by McGuire and Hapke [116] are also shown by hollow symbols. Artificial materials correspond to varied shapes, absorption coefficients, and conditions of surface roughness, and containing differing densities of internal scatterers. The range of parameters b and c retrieved from CRISM data using MARS-ReCO is shown using a red box. The blue box corresponds to the results obtained by the method based on the Lambertian assumption in [52]. Credit: [84]

the isotropic assumption. As it is discussed in chapter 5, although the Lambertian hypothesis greatly simplifies the RT modeling and allow more operational and faster algorithms, this assumption creates systematic biases in retrieved surface reflectance, particularly reducing the estimated anisotropy of the surface. In particular the Lambertian assumption enhances the derived reflectance where BRF is low and reduces it where BRF is high. The magnitude of this error increases with higher aerosol contents since the amount of scattering in the atmosphere is more important [111].

In this section I assess the impact of the Lambertian assumption on retrieved scattering properties of the surface by comparing two different surface retrieval methods. With this aim experiments presented in section 7.3 are repeated using the algorithm based on a Lambertian assumption described in [52]. The latter method is based on a RT formulation based on the Green's function of the atmosphere and a Lambertian surface. The retrieved photometric properties are contrasted with the results obtained using the proposed algorithm MARS-ReCO. The error bias caused by the Lambertian assumption is assessed by comparing both results.

Table 7.4 shows the retrieved values for the Hapke's parameters w, θ, b and c provided by the method in [52]. For comparison, the results obtained with MARS-ReCO are also shown. Likewise, the results of the method based on the Lambertian hypothesis are also shown by means of blue markers in Figure 7.5, Figure 7.6 and Figure 7.7.

According to the results we note that the retrieved photometric properties under the Lambertian assumption differ substantially from those obtained by MARS-ReCO. For example, an underestimation

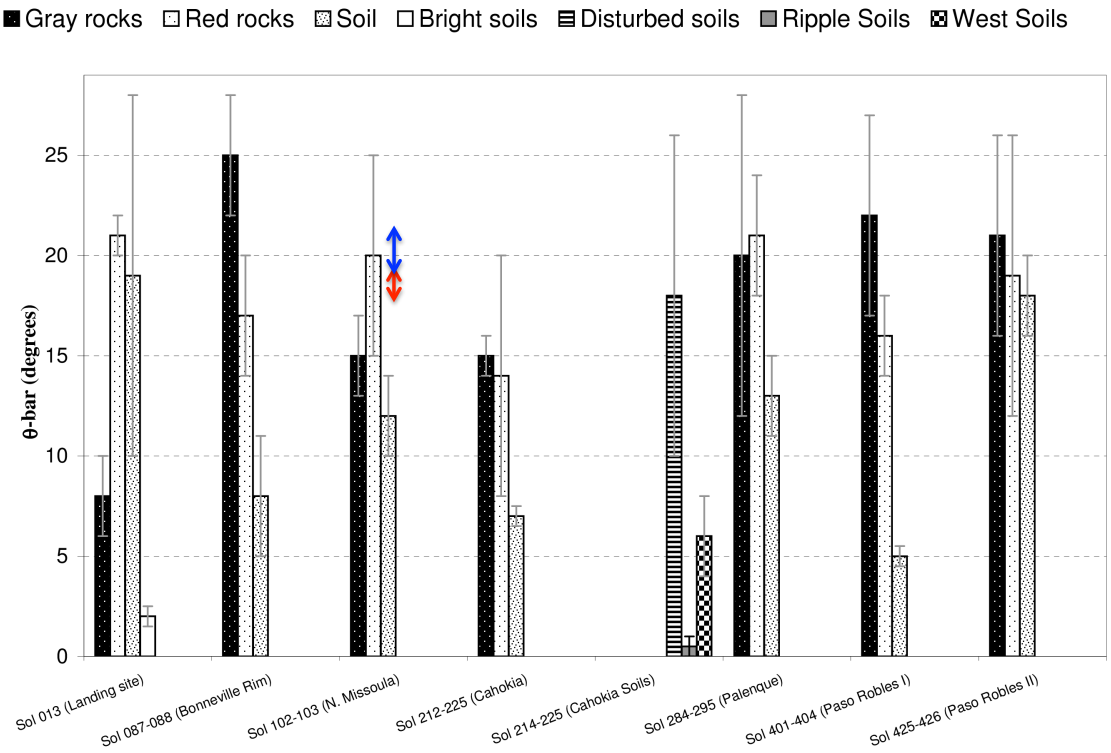

Figure 7.7.: Average macroscopic roughness ($\bar{\theta}$) values and their standard deviations derived from 2-term HG models for the main unit types studied in [84]. The range of parameter $\bar{\theta}$ retrieved from CRISM data by MARS-ReCO is also shown using a red arrow. The blue arrow corresponds to the results obtained by the the method based on the Lambertian assumption in [52]. Credit: [84]

	w	θ (°)	b	c	Abs. RMSE	Rel. RMSE	# of meas.
MARS-ReCO	0.69-0.72	18.0-19.0	0.22-0.25	0.46-0.57	0.012	0.040	24/33
Lamb. [52]	0.62-0.67	18.7-20.5	0.10-0.15	0.53-0.63	0.016	0.073	24/33

Table 7.4.: Retrieved physical parameters corresponding to the Hapke's macroscopic model fitted to the surface reflectance obtained from CRISM data. Surface BRF is retrieved using MARS-ReCO and the method based on the Lambertian assumption in [52]. Parameters correspond to the fusion of CRISM observations FRT3192, FRT8CE1 and FRTCDA5.

of 17% is observed regarding the single scattering albedo. This effect may be due to a overcorrection of the aerosol effects for low azimuthal angles when they are negligible. Figure 7.5 underlines this underestimation when compared to the parameters obtained by Johnson et al. for the area of study at Sol 102-103. In addition, results do not agree any more with the endmembers "Gray Rock" and "Red Rock". Contrarily, Figure 7.7 shows how the average roughness suffers from an overestimation of 6% when the Lambertian assumption is considered that makes the parameter $\bar{\theta}$ less similar to the values obtained in [84]. According to Table 7.4, the Henyey-Greenstein parameters b and c undergo an underestimation of 90% and an overestimation of 11%, respectively. Figure 7.6 suggests that results obtained under the Lambertian assumption are biased as the corresponding b and c ranges of values do not correspond to the comprehensive selection of materials that McGuire and Hapke used in [116].

Another way of assessing the quality of the retrieved photometric properties is by means of the RMSE associated to the photometric fitting in subsection 7.3.2. Assuming that the Hapke's model expressed

by Equation 2.11 is suitable to represent granular surfaces, the higher absolute and relative errors obtained by the atmospheric correction method under the Lambertian assumption in Table 7.4 indicate a somewhat worse quality of the surface BRF measurements.

To conclude this experiment, we provide an outlook of the impact of the atmospheric correction on real photometric curves. Figure 7.8 details the BRF curve corresponding to super-pixel IV after the two investigated atmospheric corrections and the fitting by the Hapke's model. In Figure 7.8 (top) we show how the atmospheric correction under the Lambertian assumption overcorrects the released data for lower phase angles while it overestimates the contribution of aerosols for the large phase angles. This result is in agreement with the previously cited study of Lyapustin in [111]. Additionally, Figure 7.8 (bottom) highlights the lower RMSE that results from fitting by the measurement by the Hapke's model when we use the BRF retrieved by MARS-ReCO. As a matter of fact, the regression method described in subsection 7.3.2 does not succeed in fitting the processed BRF under the Lambertian assumption as it does with the results obtained with MARS-ReCO. We conclude that this result may come from the fact that BRF retrieved by the proposed algorithms is substantially more physically meaningful than the one produced assuming a Lambertian surface.

I bring to an end the present part of the thesis by remarking that the impact produced by the Lambertian assumption on the photometric properties of the surface is substantial according to the presented quantitative assessment. In this context original and advanced atmospheric corrections such as the proposed MARS-ReCO algorithm are necessary. In addition, I note that the presented inaccuracies are likely to increase for surfaces presenting stronger anisotropic properties. The obtained results in this section agree with previous works such as [76, 111].

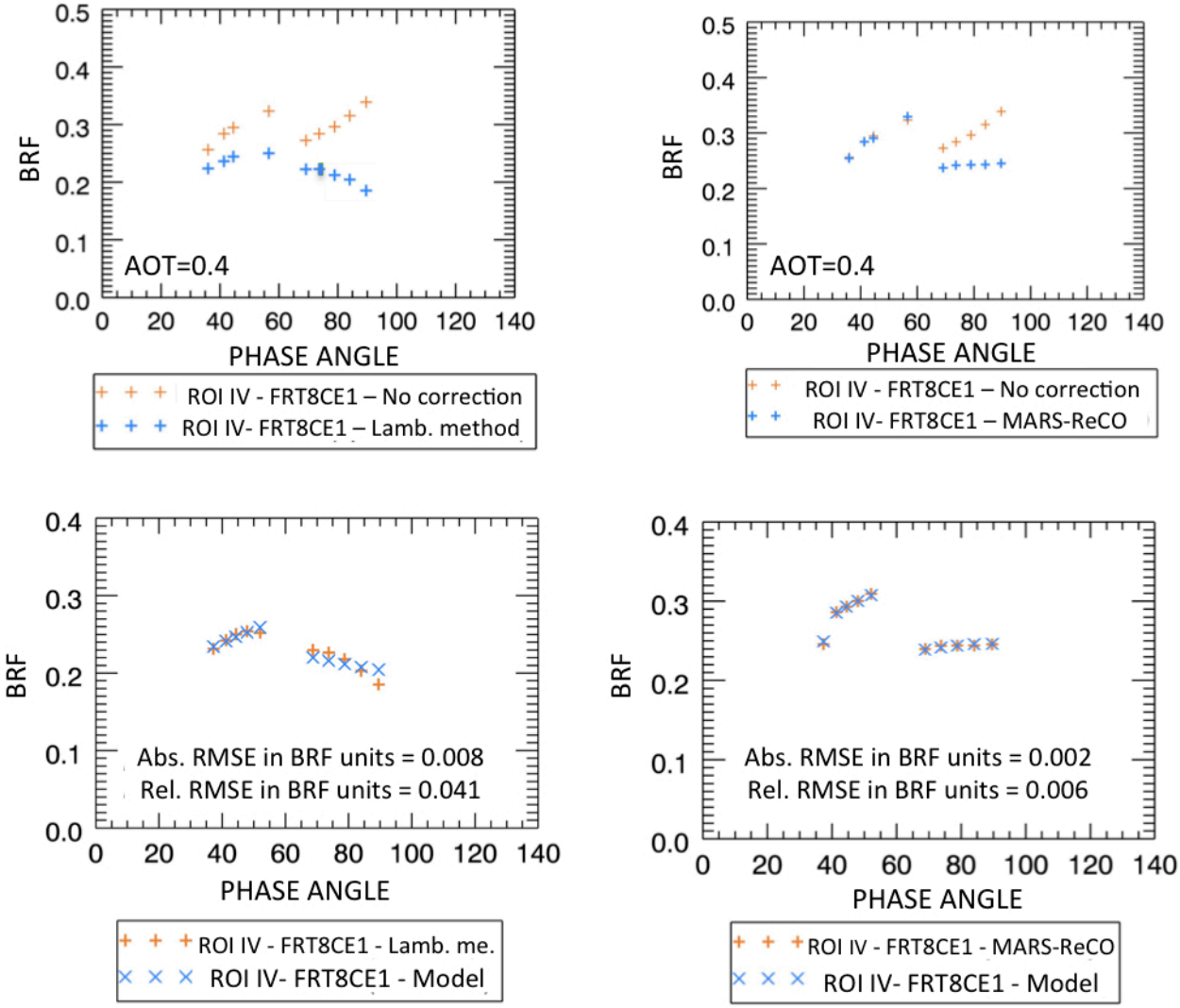

Figure 7.8.: BRF according to phase angle for super-pixel IV. (top-left) Photometric curve after being released and after atmospheric correction under a Lambertian assumption with the method in [52]. (top-right) Photometric curve after being released and after atmospheric correction by MARS-ReCO. (bottom-left) BRF corresponding to the atmospheric correction with a Lambertian assumption and after fitting it to a Hapke's model. (bottom-right) (bottom-left) BRF corresponding to the atmospheric correction MARS-ReCO and after fitting it to a Hapke's model. Credit: [60]

Summary and future prospects

In the present part of this dissertation I have proposed an original method to retrieve surface reflectance from orbital CRISM data by performing accurate atmospheric correction. The Multi-angle Approach for Retrieval of Surface Reflectance for CRISM Observations, or MARS-ReCO, takes advantage of the multi-angle capabilities of the CRISM instrument to perform an accurate separation between the contributions of the atmosphere and of the surface. The main novelty of the proposed method is the consideration of the anisotropic scattering properties of the materials at the surface, as well as those of the atmospheric aerosols, into the atmospheric correction. A complete sensitivity study has been carried out to determine the suitability of the algorithm MARS-ReCO under varied atmospheric and geometric configurations. It has been proved that MARS-ReCO is suitable to operate for most CRISM observations. Afterward, the application of MARS-ReCO on real CRISM data has been carried out. A specific region of Mars has been selected since data coming from other independent studies are available for validation. Results show a satisfactory agreement between the retrieved photometric properties of the surface by MARS-ReCO and those from previous independent studies. Furthermore, the benefits of considering a non-Lambertian surface has been investigated through original experiments.

I conclude that the proposed method for retrieval of surface reflectance is a powerful tool to study the surface reflectance of the martian surface using orbital CRISM data. According to the presented experiments the use of the RTLS model may be appropriate for recreating the scattering properties of martian surfaces. To our knowledge MARS-ReCO is the first algorithm for retrieval of surface reflectance of any region of Mars assuming a non-Lambertian surface. Nonetheless, it is important to note that MARS-ReCO is not meant to immediately replace the currently adopted atmospheric correction method for CRISM images detailed in section 14.2. Indeed, the lower spatial resolution of the EPF data makes impossible the direct atmospheric correction of the central scan of targeted observations at full spatial resolution. The resolution of the resulting CSP cubes, roughly 180 m/pixel, is not acceptable to generate significant spatial products due to the limited spatial coverage at this resolution (e.g. the central scan of CRISM at 180 m/pixel is formed by only 60×15 pixels which are not sufficient to distinguish spatial features). Further research will address the extrapolation of the results obtained by MARS-ReCO to the atmospheric correction of the central scan at high resolution. In the meantime I propose to use MARS-ReCO for the retrieval of photometric properties of the surface of Mars while the method adopted by the IPAG-DP will be used for operational correction of CRISM hyperspectral data. As I state in the conclusions of Part II the results produced by the IPAG-DP must be handled with care as the adopted method for atmospheric correction is based on the Lambertian assumption.

In this thesis the approach MARS-ReCO is based on a LUT that considers a homogenous atmosphere composed by a single layer of mineral aerosols. These dust particles are characterized by the radiative

transfer properties inferred by Wolff et al. in [187]. This atmospheric model is suitable for most of CRISM observations acquired over the equatorial regions of Mars. Future versions of MARS-ReCO may nonetheless consider a LUT encompassing different atmospheric situations such as the presence of mineral aerosols with different grain size or the existence of icy aerosols, typical from the high latitudes of Mars. In this matter the LUT may also consider the gases in the atmosphere of Mars in order to perform a full compensation for atmospheric effects. Furthermore, the MARS-ReCO approach may be adapted to work for multi-angle data acquired by other sensors orbiting Mars and other bodies of the Solar system such as Titan. The properties of the aerosols surrounding this moon of Saturn start getting documented by several authors (e.g. [172]).

The following step is the mapping of the photometric properties of several study sites on Mars. For instance, MARS-ReCO represents an unprecedented tool to study the photometric properties of the polar regions of Mars, mainly made of frozen CO_2. To our knowledge this study has never been carried out before. The properties retrieved from this type of surfaces will be interpreted using scattering models and experiments carried out in the laboratory. In this matter MARS-ReCO needs to be further tested on polar observations. As a matter of fact snow-covered and icy terrains represents theoretically the most challenging scenario for atmospheric correction as they are related to very bright and anisotropic surfaces. In addition, the illumination configurations of CRISM are usually rather extreme at these latitudes. In this situation a reliable AOT estimate is crucial to avoid inaccuracies coming from a deficient characterization of the atmospheric opacity. Unfortunately, the currently adopted β-method for AOT retrieval does not work for snow-covered and icy surfaces due to the presence of frozen CO_2. Therefore, the capabilities of other AOT retrieval methods must be tested for this type of scenario.

In this matter I have recently drawn an outline of an evolution of MARS-ReCO that shall perform simultaneous retrievals of atmospheric AOT and surface BRF. The improved MARS-ReCO algorithm will be a self-consistent method (i.e. it will not depend on the quality of the AOT estimate provided by independent methods) that will be operative for any type of surface. This new version of the proposed method for atmospheric correction of CRISM observations is in an early stage of development and thus is not presented in this thesis.

To conclude I detail another future prospect that is related to the work addressed in the present section. Contrarily to inferring surface properties based on the knowledge of the scattering properties of the aerosols, the latter could be further refined if the former are known. As I previously stated, aerosol properties are still largely undocumented. For example, the RT properties from the work of Wolff et al. in [187] are retrieved based on CRISM observations during highly dusty periods. In this case the nature of the aerosol particles might be different from that of clearer atmospheric conditions. The Gusev crater of Mars represents, again, a unique benchmark to refine the current RT properties of aerosols as in situ data of the surface are available. Based on the robust MARS-ReCO technique, an improved photometric curve of martian aerosols could be retrieved by finding the scattering properties that provide the exact surface parameters observed with Pancam data.

Part IV.

On the use of spectral unmixing for the study of Mars

Introduction

In Part III of this dissertation I have proposed an original method to infer the reflectance of the surface of Mars from hyperspectral images acquired by the CRISM instrument. This algorithm is founded on physical laws that explain the RT happening in planetary atmospheres with the surface as a boundary condition. As it has been seen, physically-based approaches may enhance our understanding on specific areas of Mars when applied to orbital images as they take into account the physical elements and phenomena that shape the remote sensing signal.

Hyperspectral images are also traditionally processed with analysis methods that treat these data without any a priori knowledge on the physics of the observed scene. In the literature it has been widely proved that this type of algorithms may produce reliable information on the spatial distribution of compounds and processes as well as on the recognition of objets. Efficient analysis algorithms become decisive for processing hyperspectral data in front of the recent trends that influence the field of planetary remote sensing. Constant technological improvements such as the multi-angle capabilities of CRISM contribute to the increase of the volume and the complexity of planetary data sets. In addition, planetary remote sensing entails the additional challenge regarding the scarcity of ground truth data to confront and to validate the outcomes of analysis methods. In this context there is an increasing need for automatic, operational, and accurate algorithms to extract the most meaningful features from remotely sensed hyperspectral images. The most relevant features unveiled by these analysis methods can be further analyzed by more specific and complete physically-based tools.

Spectral unmixing techniques are potentially relevant unsupervised analysis tools in planetary sciences. As it is introduced in section 1.3, materials at the surface are characterized by their spectral signatures that are shaped by their intrinsic chemical composition and physical state. Limited spatial resolution of orbital sensors and multiple scattering of photons between distinct components, with or without transfer through the atmosphere, generate linear and non-linear combinations of several spectral signatures in the remotely sensed signal that forms the at-sensor spectra. Spectral unmixing methods can be successfully applied to hyperspectral data in order to decompose mixed spectra into the original contributions. Two products are generated in this process. First, a representative spectral signature is extracted for every data source, or endmember, that is detected in the image. Second, optimization strategies allow the generation of fraction abundance maps that reveal the spatial distribution of each endmember over the area covered by the processed image. In this way the spectral unmixing concept allows the transformation of a hyperspectral cube into a few feature bands. This dimensionality reduction may benefit extensive analysis of collections of planetary data.

In the fourth part of the dissertation I aim at evaluating the potential of spectral unmixing techniques for retrieving accurate information on the surface and the atmosphere of Mars. This family of analysis techniques is potentially useful to complement the physically-based methods such as the MARS-ReCO

approach presented in Part III. In chapter 8 I first introduce the basis of the spectral unmixing problem and give some details on the use of these techniques in remote sensing applications. In chapter 9 I investigate the suitability of these techniques on simulated data that recreate a realistic martian scenario observed by the imaging spectrometers orbiting around it. In chapter 10 I process real hyperspectral data acquired by CRISM over a specific region of Mars, the Russell crater megadune, using the spectral unmixing concept. This area of Mars is of great interest from a methodological point of view since a ground truth can be built in order to evaluate the capabilities of different spectral unmixing techniques. An accurate intercomparison based on this ground truth is performed among a comprehensive selection of state-of-the-art unmixing techniques in order to discriminate those that are more suitable to process CRISM data. I eventually conclude Part IV by introducing an original strategy in chapter 11 to retrieve atmospheric AOT based on spectral unmixing and without any information regarding the radiative transfer properties of the aerosols or of the surface.

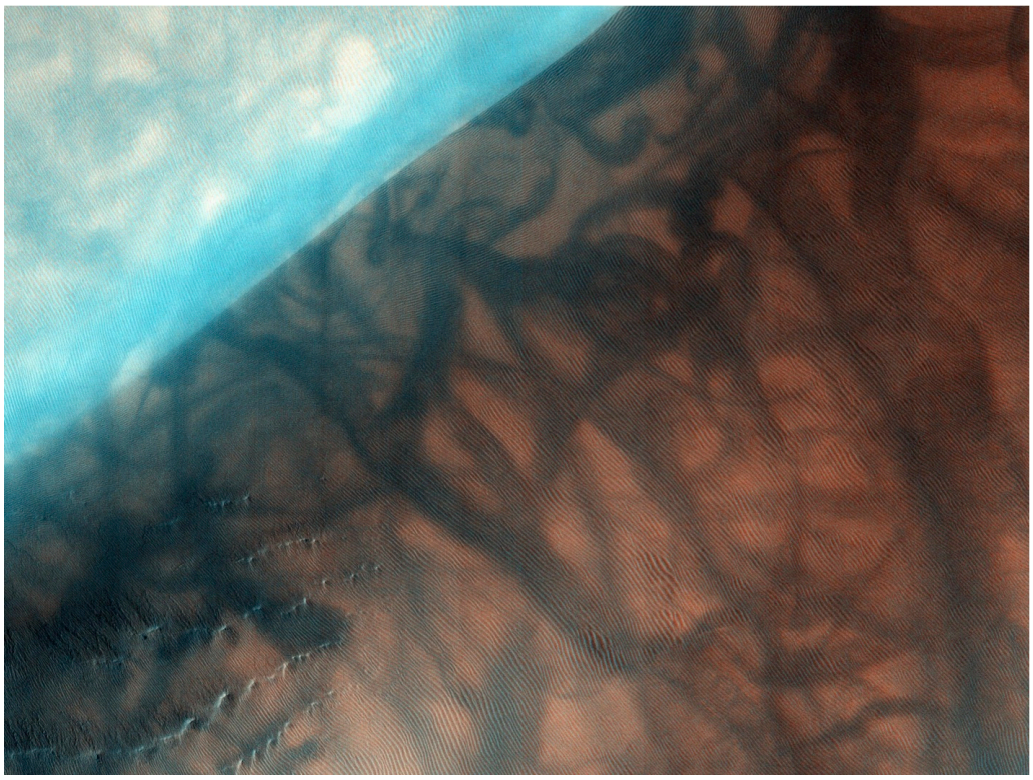

The Russell crater dune field is covered seasonally by carbon dioxide frost which has already sublimated in this HiRISE image. Numerous dark dust devil tracks can be seen meandering across the dunes. Credit: University of Arizona.

Contents

8

Introduction to spectral unmixing

The concept of spectral unmixing goes further than traditional analysis algorithms by exploiting the sub-pixel information. Spectral unmixing techniques originate in the concept of blind signal separation that is introduced by Jutten et al. in [88]. In a signal, or source, separation problem we consider that each signal is the result of several contributions, each one corresponding to a source, or **endmember**. Extending this definition to the field of image processing in remote sensing, endmembers may be shaped not only to the contributions coming from materials at the surface but also to the contribution of the atmosphere or even to instrumental artifacts.

In remote sensing spectral unmixing techniques are used to deconvolve complex surface signatures and open a number of possibilities for characterizing and monitoring mineralogical surface properties and changes in both planetary sciences [32] and Earth observation [140]. Extending the concept of source separation to hyperspectral imagery, each spectrum may be decomposed into the combination of several spectral signatures corresponding to distinct materials at the surface in the absence of atmosphere and instrumental artifacts [90]. It is important to note that the concept of an endmember is generally ill-posed since there is often a degree of detail in which a given endmember can be considered to be formed by a combination of a few sub-endmembers (e.g. an arbitrary endmember "ice" sensed by the OMEGA instrument at 300 m/pixel can be observed as a combination of a few sub-endmembers, "ice slab", "granular ice", and "dusty ice", at the higher resolution of CRISM, 18 m/pixel). When applied to hyperspectral imagery spectral unmixing techniques extract, for each endmember, a **representative spectral signature** and an **abundance map** (i.e. an ensemble of weights for all pixels in the image). The most common reasons for the existence of mixed spectra in a remote sensing problem are:

1. Insufficient spatial resolution to resolve "pure" endmembers [2] and overlapping among the PSFs attached to each pixel of the image [161].
2. Mixtures of different chemical species, or the same species with different physical properties, at the grain scale [25]. This kind of scenario is common to natural surfaces such as those on Mars.

3. Stratified surfaces whose upper layers are optically-thin enough to let the solar photons go through [157].
4. Adjacency effects between pixels by transfer of photons through the atmosphere (see subsection 2.1.3). Such effects make spectra dependent on their corresponding area on the surface but also on the surrounding ones [178].

The first reason is the origin of the so-called sub-pixel geographical mixtures or, simply, geographical mixtures [see Figure 8.1 (right) for an example]. In the absence of an atmosphere the spectrum of the leaving reflectance is the result of adding the weighted spectral signatures of each component within the conjugated footprint at the surface. In this particular case weights correspond to the surface fraction of each endmember [e.g. in Figure 8.1 (right) each material covers an area of one third of the pixel, thus all weights are equal to one third]. **Linear spectral unmixing** methods assume this linear relationship among the different endmembers. All the remaining reasons are related to non-linear mixtures, namely intimate granular mixtures for reason number 2 [see Figure 8.1 (left)] or stratified intimate mixtures for reason number 3 [see Figure 8.1 (center)]. This type of mixtures are addressed by the so-called **non-linear spectral unmixing** techniques.

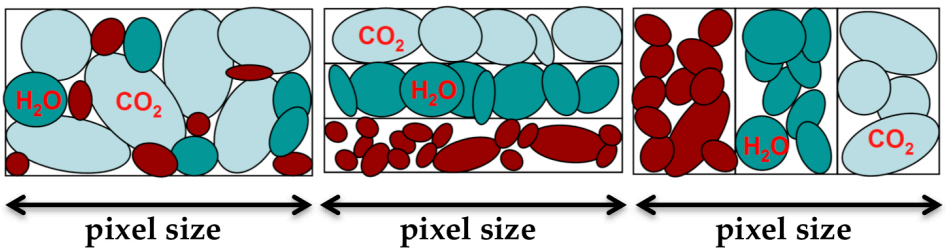

Figure 8.1.: Different types of sub-pixel mixtures corresponding to distinct arrangements of chemical species: (left) intimate granular mixture, (center) stratified intimate mixture, and (right) sub-pixel geographical mixture. Credit: [157].

Another major division in spectral mixing analysis is set by the origin of the constituent spectral signatures that are used to reconstruct the at-sensor spectra. In this matter I highlight two main families of strategies as:

- **Unsupervised spectral unmixing**, or blind source separation, in which spectral signatures are directly derived from the image without any a priori on the endmembers.
- **Supervised spectral unmixing**, in which spectral signatures are obtained from libraries of endmembers.

In this thesis I focus on the first group of techniques since I aim at developing automatic analysis tools that can deal with any type of scenario. In addition, a major disadvantage of library endmembers is that they may have not been collected at the same scale or under the same conditions than the data to be analyzed. In that case library endmembers are less easily associated with real features in the scene [150]. This drawback is especially significant for ices as they are potentially related to more physical states than minerals, for example. Unsupervised spectral unmixing becomes, however, more complex and unstable when considering non-linear mixtures. First, a priori data on the image are required. For example, accurate information on the scattering properties of the atmosphere is needed to consider reason number 4 of the list above. Second, non-linear spectral unmixing must be monitored due to the intrinsic risk of dealing with an infinite number of solutions otherwise [89].

In this context this part of the dissertation is focused on the evaluation of unsupervised linear unmixing algorithms when applied to hyperspectral images of Mars. In particular I propose to investigate the ability of these methods to decompose each measured spectrum into a combination of a set of significant endmembers described by their corresponding spectral signatures and abundance maps. I remark that the concept of blind source separation is potentially very useful to complement those products produced by physically-based methods. For instance, abundance maps may be useful to explore the presence of a given endmember over the whole area covered by the image. While physically-based methods require some knowledge on the physics that rule the scene of investigation analysis approaches such as those based on the unmixing concept may produce accurate results without any a priori information.

In order to illustrate the typical outcomes produced by spectral unmixing techniques I illustrate the main results of the study of Moussaoui et al. in [125] in Figure 8.2. In that work a hyperspectral image acquired by the OMEGA sensor over the south polar cap of Mars is processed by a strategy based on source separation techniques. After three endmembers related to martian dust and two types of ice are detected, the corresponding spectral signatures and abundance maps are extracted and estimated, respectively. The products shown in Figure 8.2 are of great interest for the characterization and the mapping of the chemical species that predominate in the polar cap. These goals are achieved in a more efficient way than when dealing with the few hundreds of spectral bands that form the original hyperspectral data set.

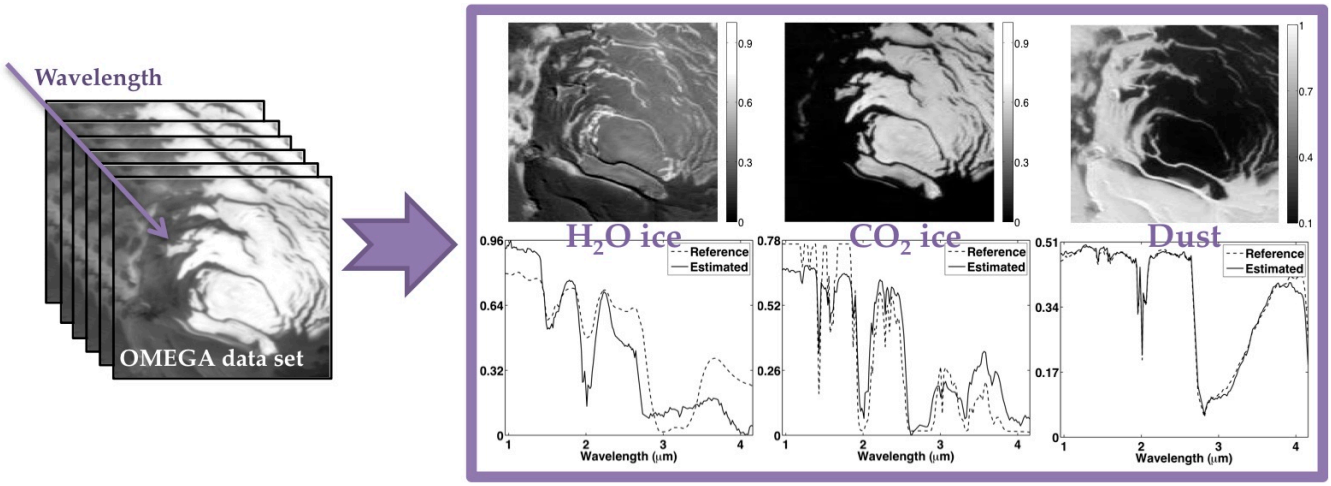

Figure 8.2.: Reference and retrieved spectral signatures (bottom) and abundance maps (top) of the three endmembers detected in the south polar cap of Mars observed by the OMEGA instrument. Credit: [125].

In the following I investigate the limitations of the linear mixture assumption, or linear mixture model. Again I highlight the work of Moussaoui et al. in [125] in which the physical assumptions that lead to the linearity of the remotely sensed signal are enumerated as:

1. Predominance of geographical sub-pixel mixing at the ground [see Figure 8.1 (right)].
2. Absence of non-linear mixing at the surface in the form of intimate granular mixtures or stratified mixtures.
3. Lambertian surface or homogeneity of illumination conditions. Procedures aimed at performing photometric normalization may be used to satisfy this assumption (see subsubsection 4.2.3.1).

4. Absence of adjacency effects, especially at high spatial resolutions such as the one made possible by the CRISM instrument. Advanced atmospheric correction may be carried out to meet this assumption.

In addition to the previous hypothesis I include the supposition that there are no non-linearities coming from instrumental artifacts such as the spectral smile effect (see subsubsection 4.1.2.1). As Schmidt argues in his Ph.D. dissertation, all these assumptions are, in practice, invalid in a real planetary situation [157]. I therefore underline that the interpretation of the results obtained by spectral unmixing based on the linear mixture model must take into account this evidence. Nonetheless, results obtained on data sets which meet, or are close to meet, the previous requirements can be considered as approximative estimates of the reality.

One of the major objectives of this thesis is to propose strategies to perform efficient dimensionality reduction. Spectral unmixing techniques are able to transform a data set of hundreds of spectral bands into a few abundance maps or, in other words, a thousand spectra into a few significative spectral signatures. Therefore, this part of the thesis investigates the potential of exploiting the subpixel information contained in hyperspectral images in order to extract the most physically meaningful features. In this matter I recommend the Ph.D. thesis of Villa in which spectral unmixing techniques are used to optimize the processing of terrestrial remote sensing data [179]. In the following section I first describe the spectral unmixing problem based on a linear mixture model from a mathematical point of view. Afterward, section 8.2, section 8.3, and section 8.4 detail the three main steps in a classical spectral unmixing problem and provide an overview of the state of the art in this subject.

8.1. Mathematical background

We note $\mathbf{X}$ the matrix representing the flatten hyperspectral image cube such that $\mathbf{X} = \{\mathbf{x}_1, \mathbf{x}_2, \ldots, \mathbf{x}_{N_p}\}$, where $\mathbf{x}_k = \{x_{1,k}, x_{2,k}, \ldots, x_{N_s,k}\}^T$ are the constituent spectra. The terms $x_{\lambda,k}$ represent the value of the k^{th} pixel at the λ^{th} channel, N_p is the number of pixels and N_s is the number of spectral channels. We assume that the spectrum of each pixel can be reduced to a linear mixture of N_c endmember spectra, leading to the following instantaneous model:

$$\mathbf{X} = \mathbf{M} \cdot \mathbf{S} + \mathbf{e}, \tag{8.1}$$

where $\mathbf{e}$ stands for the additive noise in the image, $\mathbf{M} = \{\mathbf{m}_1, \mathbf{m}_2, \ldots, \mathbf{m}_{N_c}\}$ is the mixing matrix, being $\mathbf{m}_n$ the spectral signature, or the characteristic spectrum, of the n^{th} endmember, and $\mathbf{S} = \{\mathbf{s}_1, \mathbf{s}_2, \ldots, \mathbf{s}_{N_c}\}^T$ is the source matrix with $\mathbf{s}_n = \{s_{n,1}, s_{n,2}, \ldots, s_{n,N_p}\}$. Coefficients $s_{n,k}$ correspond to the abundance of the n^{th} endmember at the k^{th} pixel.

Two physical constrains are traditionally imposed on the model described in Equation 8.1 as it is introduced by Heinz et al. in [73]. Positivity of $\mathbf{s}_n = \{s_{n,1}, s_{n,2}, \ldots, s_{n,N_p}\}$ is generally imposed such that $s_{n,k} \geq 0$ to avoid unphysical negative abundances. In addition, if we assume that there are only N_c endmembers in the image, endmember abundances must respect the sum-to-one constraint such that $\sum_{n=1}^{Nc} s_{n,k} = 1$, $\forall k$. I remark that these two assumptions are crucial in planetary remote sensing as we are interested in retrieving physically meaningful endmembers that help understanding the planetary

scenes.

Regarding the linear mixture assumption, I remark that existent non-linear contributions in the data may lead to perturbations on the mixture model described in Equation 8.1. For example, non-linear residues coming from the surface or a deficient photometric, artifact or atmospheric correction may corrupt the linear model (this point is further discussed in chapter 10). All the existent non-linear factors $\mathbf{F} = \{\mathbf{f}_1, \mathbf{f}_2, \ldots, \mathbf{f}_{N_c}\}$ may transform the linear mixing assumption into the following degenerated model

$$\mathbf{X} = \Im\left(\mathbf{M} \cdot \mathbf{S}\right) + \mathbf{e} \simeq \mathbf{F} \cdot \mathbf{M} \cdot \mathbf{S} + \mathbf{e}, \tag{8.2}$$

where $\Im\left(X\right) = \mathbf{F} \cdot X + \mathbf{F}_2 \cdot X^2 + ... \simeq \mathbf{F} \cdot X$. In this case the term $\mathbf{e}$ not only includes the noise of the image but also residues coming from the non-linearities. As a conclusion, special attention must be paid to those results obtained in this situation when performing spectral unmixing under the linear mixture hypothesis.

Figure 8.3 shows the classical scheme of a spectral unmixing problem in which $\mathbf{M}$ and $\mathbf{S}$ are estimated from $\mathbf{X}$ without any a priori information. In the first place the number of endmembers N_c in the data is estimated. An endmember extraction approach is then applied to retrieve $\mathbf{M}$, followed by the reconstruction of $\mathbf{S}$ based on the extracted spectra and the linear mixture model expressed by Equation 8.1. I shall further detail these three steps in the three following sections.

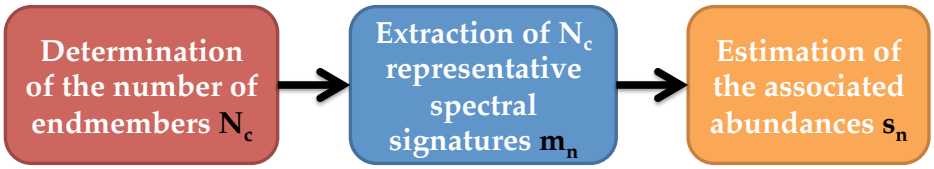

Figure 8.3.: Outline of a classical spectral unmixing problem.

8.2. Estimation of the number of endmembers

The first step in a spectral unmixing problem consists in estimating the number of sources, or endmembers, that exist in the image. In this matter I highlight the seminal work of Chang et al. who define the concept of virtual dimensionality (VD) as the minimum number of spectrally distinct signal sources that characterize a hyperspectral data set [31]. The VD is one of the most critical parameters for resolving satisfactorily a spectral unmixing problem, thus many efforts have been done to address this issue. In the literature PCA-based thresholding is a classical method to determine the number of endmembers in a hyperspectral image. In [125] Moussaoui et al. set $N_c = 7$ after observing that more than the 98% of the variance of the image of study is concentrated in the first seven principal components. The main drawback of this strategy, however, is to set the cut-off threshold since the eigenvalues caused by the relevant sources and those caused by the noise are usually comparable. In this context more sophisticated approaches have been proposed in the literature. I distinguish two main families of techniques, the first one based on the eigenvalues of the covariance and correlation matrices

of the data, and the second one based on the minimization of the error resulting from projecting the data onto another subspace.

In the following I briefly detail three illustrative methods that aim at estimating the VD of a given hyperspectral data set. First, I introduce the seminal method Harsanyi–Farrand–Chang (HFC) whose theoretical concept is used by many other state-of-the-art methods. This is the case of the Eigenvalue Likelihood Maximization (ELM) algorithm that was first tested on martian data acquired by OMEGA. These two algorithms are part of the first family of methods. Finally, I detail the widely used Hyperspectral Signal-subspace Identification by Minimum Error (HySime) method that belongs to the second family of approaches.

- **Harsanyi–Farrand–Chang**. Probably the most known detection theory-based thresholding method developed to determine the VD of hyperspectral imagery is the HFC method. This approach was originally developed to determine the number of endmembers in AVIRIS data [72].

  HFC is based on the difference between the eigenvalues of the sample correlation matrix and sample covariance matrix. The VD is assumed to be equal to the total number of relevant eigenvalues, each eigenvalue specifying a component dimension and providing an indication of the relevance of that particular component in terms of energy. If a particular component does not contain signal source, the corresponding correlation and covariance eigenvalues should reflect only the noise energy. In that case the correlation and covariance eigenvalues are equal because the noise is assumed to have zero mean. This fact provides with a base on which we can formulate that the VD is determined as the number of eigenvalues which associated difference between the correlation eigenvalue and its corresponding covariance eigenvalue is greater than zero.

  The main disadvantage of the HFC approach is the setting of an internal parameter, namely the false alarm probability, as Bioucas-Dias states in [14]. As a matter of fact the estimated number of endmembers by HFC is quite sensitive to this parameter. Furthermore, the HFC approach may fail to give the exact number in front of colored noise.

- **Eigenvalue Likelihood Maximization**. In the flavor of the approach HFC the technique referred to as ELM is based on the difference between the eigenvalues corresponding to the correlation and covariance matrices [104].

  Contrarily to HFC, the algorithm ELM is proposed as a parameter-free automatic method to estimate the number of endmembers in hyperspectral images. ELM assumes that the distribution of the difference between a couple of eigenvalues z_n is asymptotically modeled by a Gaussian probability density function centered at zero for $n > N_c$ for the noise features, and a non-zero value otherwise, that is, for the data features. Based on this property ELM builds a likelihood function depending on z_n that presents a global maximum when $n = N_c$. This approach has been validated on simulated and real data acquired by the OMEGA and the CRISM instruments in [104] and [28], respectively.

  According to the experiments that shall be performed in the following chapters I remark that the main drawback of the approach ELM resides in its assumption that the noise is Gaussian. Unfortunately, the noise of the CRISM instrument is hardly Gaussian [126].

- **Hyperspectral Signal-subspace Identification by Minimum Error**. The approach referred to as HySime has been recently proposed as a minimum MSE-based approach to infer the signal subspace in hyperspectral imagery in an unsupervised manner [14]. HySime uses multiple re-

gression theory to accurately determine the noise value per pixel. Afterward, the noise vector is subtracted from the sample vector for each pixel. Eventually HySime estimates the signal and noise correlation matrices before selecting the subset of eigenvalues that best represents the signal subspace in the least squared error sense. In [14] this approach has been tested on simulated and real hyperspectral AVIRIS data and its performances have been proved to be satisfactory in front of other widely used algorithms such as HFC.

The work that shall be presented in chapter 10 (and that is fully detailed in [28]) concludes that HySime might be related to a high sensitivity that may lead to the detection of subtle, yet unwanted, contributions such as residual artifacts.

8.3. Endmember extraction

After the number of endmembers of a given hyperspectral image is estimated as N_c, the next task in spectral mixing analysis consists in extracting an appropriate set of N_c constituent spectral signatures. Over the past decade many algorithms have been developed to accomplish this task. In this section I briefly summarize the use of endmember extraction techniques based on the linear mixture model and applied to planetary and terrestrial hyperspectral images. The following review does not pretend to be exhaustive and I detail only the state-of-the-art algorithms that shall be used in this thesis.

According to the literature I define four major divisions as follow:

- The so-called **geometric methods** exploit the parallelism between mixing models and the geometric orientation of hyperspectral data in multi-dimensional spaces. A detailed review of these algorithms can be found in [143]. I point out two sub-families that are separated by the so-called **pure pixel assumption**:
  - Geometric methods belonging to the first sub-family seek for endmembers in the data of investigations and therefore require the existence of a pure sample (i.e. a pure spectrum) for each endmember. These methods include the widely-used algorithms referred to as Vertex Component Analysis (VCA) [131] and N-FINDR [186] that have been satisfactorily applied to planetary remote sensing data [104, 171, 27].
  - The second sub-family embraces those techniques which are able to extract endmembers whose representative spectra do not exist in the hyperspectral image. This is the case of the approaches referred to as Minimum Volume Simplex Analysis (MVSA) [100], Minimum-Volume Enclosing Simplex [29], and Simplex Identification via Split Augmented Lagrangian [13]. All these methods have proved to be very efficient when dealing with highly mixed data.

  In order to illustrate the pure pixel assumption I show in Figure 8.4 the extraction of endmembers from synthetic data by the methods named VCA, MVSA and Minimum Volume Constrained Non-negative Matrix Factorization (MVC-NMF). The last algorithm is a hybrid technique that is not based on the pure pixel assumption and that shall be introduced in the next family of algorithms. In Figure 8.4 the simulated data set has been generated based on three endmembers and then, the purest samples have been removed. These data are projected on a 2-D subspace in which the so-called **data simplex** (i.e. the cloud formed by the data points, that is, the spectra) is

observed as a triangle with eroded extrema. As it can be seen, VCA extracts the endmembers by selecting the extrema of the data cloud while MVSA and MVC-NMF select the extrema of the so-called **minimum volume simplex**, which embraces the data cloud as tightly as possible (see the red triangle in Figure 8.4). Strategies based on the minimum volume constraint are able to extract endmembers for which a pure sample does not exist in the data set of analysis. Alternatively, Figure 8.5 illustrates the benefits of the second sub-family of methods in the unmixing of data acquired by OMEGA over the icy terrains of Mars [55]. In this case the hyperspectral image is formed by three endmembers (i.e. water ice, CO_2 ice and mineral dust). Nevertheless, a pure spectrum is available only for the endmember dust. The majority of the spectra result from mixtures of two or three endmembers. In this case I remark that a method based on the pure pixel assumption would inevitably fail to extract the pure spectral signatures corresponding to the endmembers water ice and CO_2 ice. By contrast, techniques such as MVSA or MVC-NMF are theoretically able to do so. The disadvantage of the second sub-family of geometric methods, however, is that they may extract endmembers that are not physically correct (e.g. showing non-meaningful absorption features or negative reflectance values).

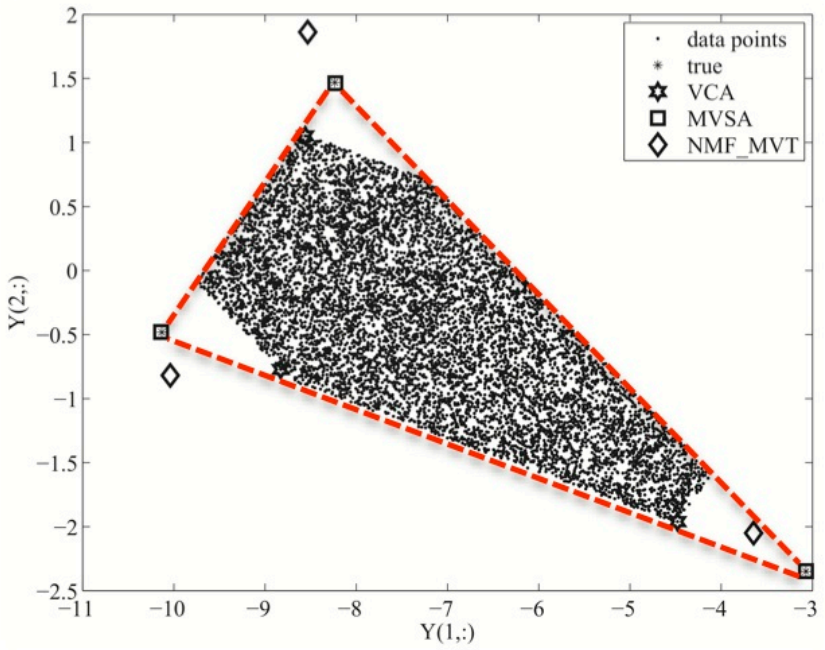

Figure 8.4.: Extraction of endmember spectral signatures from a synthetic data set formed by three endmembers by the algorithms MVSA, MVC-NMF, and VCA. Dots represent spectral vectors. All other symbols represent inferred endmembers by the unmixing algorithms. The minimum volume constraint imposed by MVSA is highlighted by a red triangle. Credit: [100].

- An alternative method to solve the linear unmixing problem is based on the seminal concept called **non-negative matrix factorization** (NMF) and proposed by Lee et al. in [97]. In multivariate analysis and linear algebra NMF embraces a group of algorithms where a matrix $\mathbf{X}$ is usually factorized into two matrices, $\mathbf{W}$ and $\mathbf{H}$. The concept NMF differs from classical matrix factorization methods such as PCA by enforcing the constraint that factors $\mathbf{W}$ and $\mathbf{H}$ must be non-negative, that is, all elements must be equal to or greater than zero. Approaches based on NMF have been used for processing terrestrial remotely sensed hyperspectral data in [77] and

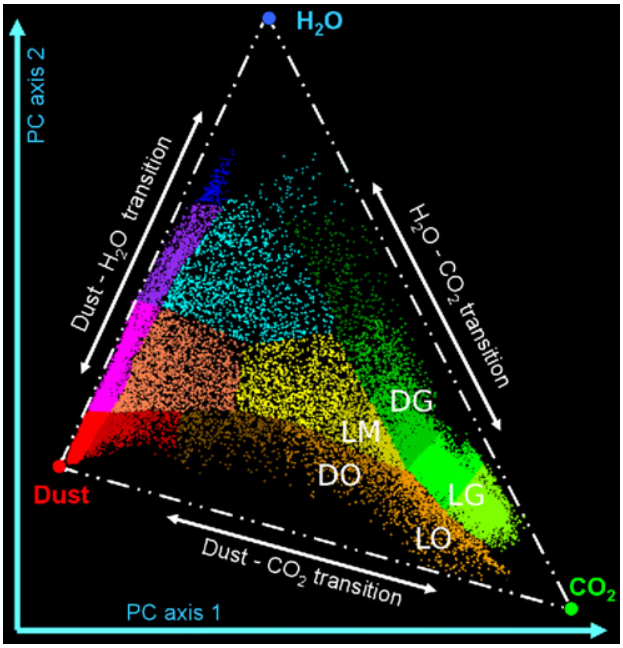

Figure 8.5.: Cloud diagram obtained by applying a MNF transform to a set of OMEGA hyperspectral observations. Three endmembers are found in this case, water ice, CO_2 ice and mineral dust. The transitions between each couple of endmembers reveal that there is only a pure sample for endmember dust. Each color represents an identified class in the work of Douté et al. in [55]. Credit: [55].

in planetary exploration to characterize the surface composition of Mars in [137]. In particular I highlight the MVC-NMF algorithm that is a hybrid geometric/NMF-based method because it is regularized by minimization of the simplex volume [119]. MVC-NMF is not based on the pure pixel assumption and therefore is able to extract endmembers whose representative spectra are not included in the analyzed hyperspectral image.

- Mixed spectra are also processed using statistical representations by **statistical methods**. For example, the classical PCA is widely used along with a linear mixture model to access relevant information from natural scenes [98, 32]. Likewise, the alternative transformation ICA is also used to perform endmember extraction by supposing that the physical sources are mutually independent and non-Gaussian. In [58] meaningful endmembers are retrieved applying ICA to images acquired by the VIRTIS instrument on the nightside of Venus. In that study extracted endmembers are related to physical processes or components in view of the good correlation of the endmember spectra with known atmospheric structures of Venus. The role of ICA to carry out spectral unmixing is, however, questioned by Nascimento and Bioucas-Dias in [130]. As a matter of fact hyperspectral data do not satisfy the independence of abundance distributions. Furthermore, ICA does not consider the positivity constrain. Alternatively, the NMF problem has been solved in a Bayesian framework by the algorithm referred to as Bayesian Positive Source Separation (BPSS) [124]. In [125] a robust BPSS-based strategy applied to data acquired by the OMEGA instrument leads to endmembers whose associated spectra and abundance maps are physically meaningful. Traditionally, this family of endmember extraction methods does not take into account the pure pixel assumption.
- Last but not least there exists a recent trend to include **spatial information** into the endmem-

ber extraction process. All aforementioned methods do not take into consideration the spatial organization of the spectra and therefore they do not consider the cross-information that may exist among adjacent pixels. I remark that this fact does not mean, however, that the previously introduced methods are pixel-wise as the extraction of the endmembers is based on the consideration of the complete collection of spectra at once. A few studies have recently addressed the inclusion of spatial information into the extraction of endmembers such as the works in [82, 191]. For instance, the authors of [191] propose a spatial preprocessing that enhances the search for endmembers in the unmixing problem. This procedure has proved to provide better extracted spectra and more relevant abundance maps after its combination with a traditional endmember extraction method.

In the following I detail five state-of-the-art algorithms that belong to the four mentioned families and that are based on different principles. Albeit this list is not exhaustive, it is meant to be representative of the different types of algorithms that are used for endmember extraction nowadays. The following methods shall be used in chapter 10 and chapter 11.

- **Vertex Component Analysis**. The algorithm VCA is proposed as a fast geometric method for extracting endmembers under a linear mixing supposition [131]. According to the sum-to-one condition the data vectors $\mathbf{x}_k$ are always inside the simplex formed by $\mathbf{M} \cdot \mathbf{S}$ whose vertex are the spectra of the endmembers. VCA iteratively projects the data onto the orthogonal direction to the subspace spanned by the already extracted endmembers, designating the most extreme projection as the next endmember. The process is repeated until N_c endmembers are found. In this process VCA assumes that (i) there are pure pixels in the data and (ii) there is no noise. In practice, vectors $\mathbf{x}_k$ (i.e. the spectra) may be outside the simplex if noise is present, which is actually the common case.

  The method VCA represents a powerful tool in planetary exploration as it has been evaluated satisfactorily on OMEGA and CRISM data in [104] and [27], respectively.

- **Minimum Volume Simplex Analysis**. The method MVSA belongs to the family of geometric algorithms and addresses spectral unmixing by fitting a minimum volume simplex to the hyperspectral data [100]. The main weakness of the minimum volume constraint is that even a single outlier may force it to be far away from a reasonable solution. In order to cope with outliers and noise the positivity constraint imposed on the abundance fractions is replaced by a soft constraint. This formulation seeks for a minimum volume simplex where most abundance fractions are non-negative but allowing, however, some negative values.

  In [100] the performances of the MVSA algorithm are confirmed when applying it to simulated mixed data and comparing the results with those obtained with the state-of-the-art and more complex method MVC-NMF. As a matter of fact MVSA can be considered as a method lying between MVC-NMF and the simpler VCA.

- **Minimum Volume Constrained Non-negative Matrix Factorization**. The geometrically regularized technique MVC-NMF is proposed for endmember extraction of highly mixed hyperspectral data [119]. This method is developed to deal with the realistic scenario in which the pure pixel assumption is not fulfilled (see Figure 8.4 for an example). In these conditions the method MVC-NMF yields much better performances than the pure pixel-based algorithms. MVC-NMF decomposes mixed pixels by analyzing the connection between the spectral unmixing analysis

and the NMF. A minimum volume constraint makes the MVC-NMF learning robust to different levels of noise, less sensitive to the estimated number of endmembers and applicable to images with or without pure pixel representations.

Experiments in [119] and [27] indicate that MVC-NMF has the potential of identifying less-prevalent endmembers, which is relevant in planetary sciences. In chapter 10 I shall show that MVC-NMF is indeed a very pertinent technique to detect rare sources in planetary data sets.

- **Bayesian Positive Source Separation**. The statistical algorithm referred to as BPSS proposes to estimate the matrices **M** and **S** in a Bayesian framework, under a linear mixture model, with inherent positivity and additivity constraints, and without pure pixel assumption [51]. The noise and the matrices **S** and **M** are assumed to follow a Gaussian, Dirichlet and Gamma probability density functions, respectively. The algorithm BPSS is based on hierarchical Bayesian models to encode prior information regarding the parameters of interest. The complexity of the estimation from the resulting posterior distribution is overcome using Markov chain Monte Carlo methods. In BPSS the degree of uncertainty affecting the extracted endmember spectra can be estimated since results are computed as probability distribution functions.

  This statistical method has been applied satisfactorily on OMEGA and CRISM hyperspectral images in [125] and [27], respectively.

- **Spatial preprocessing**. The authors of [191] propose a preprocessing to incorporate spatial information into the unmixing of hyperspectral images. First, the importance of the spectral information associated to each spectrum is weighted based on its spectral similarity as regards a certain spatial neighborhood. After applying a traditional endmember extraction technique on the preprocessed image, the spatial position of each endmember is retrieved. Second, the reconstruction of the abundance maps (see section 8.4) is carried out using the analogous spectra from the original image and the linear mixture model. This preprocessing enhances the search for endmembers in spatially homogeneous areas while it may penalize the detection of anomalous sources as it is shown in [27]. This preprocessing can be combined only with methods based on the pure pixel assumption, which is required to retrieve the position of the endmembers in the preprocessed image.

8.4. Abundance determination

After the spectral signatures representing the endmembers **M** are extracted, each spectrum of the original image is reconstructed based on the linear model. The goal is to estimate the abundances, or weights, **S** that must be applied to each endmember to recreate the data spectra **X** by a linear combination such that $\mathbf{X} = \mathbf{M}\cdot\mathbf{S}$. Abundances are generally obtained using least square error approximations that eventually generate fraction abundance maps. These products are unique to explore the spatial distribution of a given endmember, or associated chemical component, over the area at ground covered by remotely sensed images.

A common choice to estimate endmember abundances consists in the so-called algorithm UnConstrained Least Squares (UCLS) because of its efficiency in terms of computation. By unconstrained we mean that both the non-negativity and the sum-to-one conditions are not considered. The expression

of the UCLS strategy is

$$\hat{\mathbf{S}}_{\mathbf{UCLS}} = \arg\min_{\mathbf{S}} \|\mathbf{X} - \mathbf{MS}\|^2 . \tag{8.3}$$

A more realistic choice consists in the so-called Fully Constrained Least Squares (FCLS) algorithm that is proposed by Heinz and Chang in [73]. In addition to its efficiency in terms of computation, both the non-negativity and the sum-to-one conditions are satisfied to get rid of unphysical solutions. The expression of the FCLS strategy is

$$\begin{aligned} \hat{\mathbf{S}}_{\mathbf{FCLS}} &= \arg\min_{\mathbf{S}} \|\mathbf{X} - \mathbf{MS}\|^2 , \\ &\ni \ \mathbf{S} \geq 0; \ \sum_{n=1}^{N_e} s\,(n,k) = 1, \ \forall k. \end{aligned} \tag{8.4}$$

This optimization method does not have a closed-form mathematical solution due to the non-negativity constraints and therefore a numerical solution is required. The non-negativity constraint is considered first. The idea is to minimize the least squared error by estimating the non-negative abundance values using Lagrange multipliers in an iterative process. The sum-to-one constraint is handled by a slight modification of the aforementioned algorithm. I recommend the reader the Ph.D. dissertation of Villa to find more details on this method [179].

9

Evaluation of spectral unmixing to analyze hyperspectral data of Mars

In this chapter I carry out a first experiment to investigate the performances of unsupervised linear unmixing to analyze hyperspectral data of Mars. The goal is to explore whether or not these techniques are suitable to discriminate between the spectral signatures of different martian chemical species. For this purpose I generate a simulated data set that mimics the composition of the surface of Mars as well as the acquisition conditions under which spacecrafts operate from orbit. In this experiment three chemical components are linearly combined to generate mixed spectra. First, the technique ELM is applied to the resulting synthetic data set in order to estimate the number of endmembers. Second, the widely used algorithm VCA is applied in its UCLS flavor to evaluate its capabilities to decompose mixed spectra of martian materials[1].

9.1. Simulated data

Synthetic spectra are simulated with a RT-based model of the surface based on the work of Douté et al. in [54]. Three chemical species that are common of the surface of Mars are considered, (i) CO_2 ice, (ii) H_2O ice, and (iii) mineral dust. In particular I use the optical properties of the two types of ice from the study of Schmitt et al. [158]. As for the mineral dust I use data retrieved from OMEGA observations of dusty sites of Mars. The spectral signatures in the NIR and SWIR of the three chemical species are shown in Figure 9.1 and form the matrix $\mathbf{M}$ of the unmixing problem.

A synthetic data set of 4224×21 spectra is generated based on the linear mixture model (see Equation 8.1) fed by the spectral signatures $\mathbf{M}$ and the fraction maps detailed in Figure 9.2. These abundance maps

[1] This work was carried out in collaboration with the GIPSA-Lab of the Grenoble Institute of Technology. More details on this experiment can be found in [105].

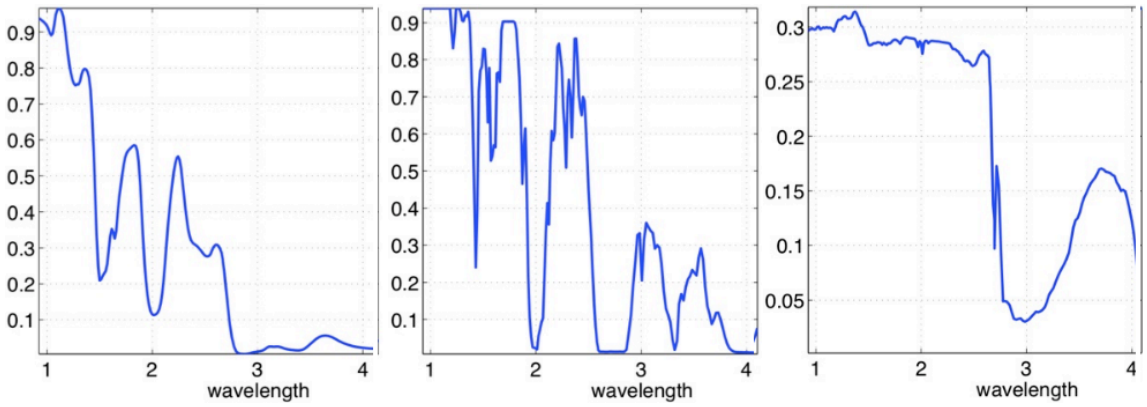

Figure 9.1.: Reference spectral signatures of the three chemical species used in the simulated data set when illumination angle SZA is equal to 45 degrees. (left) $\mathbf{m}_1$: H_2O ice. (center) $\mathbf{m}_2$: CO_2 ice. (right) $\mathbf{m}_3$: mineral dust.

form the matrix $\mathbf{S}$ of the unmixing problem and illustrate how the three chemical species are spatially distributed. The resulting 4224 linear combinations among the three materials are arranged along the vertical axis of the synthetic data set. In order to consider the consequences of sensing planetary surfaces under varying illumination conditions I define the horizontal axis to include 21 different configurations in terms of SZA within the range $\theta_0 = \{45^o \ldots 85^o\}$. This acquisition parameter is considered in the simulated data as the shape of sensed spectra depends on illumination conditions. Gaussian noise is included into the data set according to Equation 8.1. The noise variance of every spectral band is adjusted to the values estimated for the CRISM imaging spectrometer.

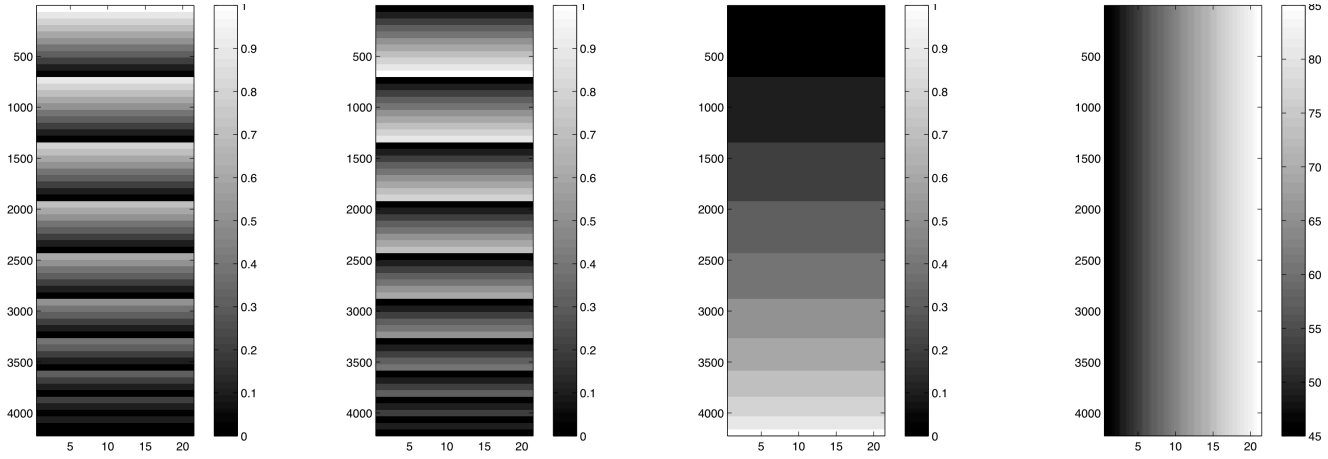

Figure 9.2.: Reference abundance maps of the three chemical species. The distribution of the illumination angle, or SZA, is also shown. From left to right: (1) $\mathbf{s}_1$: H_2O ice abundance. (2) $\mathbf{s}_2$: CO_2 ice abundance. (3) $\mathbf{s}_3$: mineral dust abundance. (4) $\mathbf{s}_4$: SZA in degrees. For example, the spectrum corresponding to the first column and the first row is made of 100% of H_2O ice, 0% of CO_2 ice, 0% of mineral dust and has been simulated using $\theta_0 = 45^o$.

9.2. Experiments

The synthetic data set is first processed by the algorithm ELM. The first goal of this study is to investigate if this method succeeds in detecting the three chemical species that have been used to generate the data set of study. The algorithm ELM distinguishes, however, the existence of four endmembers (i.e. $N_c = 4$). The number of endmembers is therefore overestimated.

The spectral signature representing each endmember is extracted as a second step using the technique VCA. Figure 9.3 shows the extracted signatures along with the reference spectra that have been used in the data simulation. As it can be seen, the VCA approach extracts two endmembers corresponding to the species CO_2 ice due to the overestimation of the number of endmembers by ELM. The two associated spectral signatures differ only in terms of average reflectance value and spectral slope. Further investigation showed that $\hat{\mathbf{m}}_3$ and $\hat{\mathbf{m}}_4$ correspond to a CO_2 ice surface observed at 45^o and 85^o in SZA, respectively. I identify the reason of this outcome to be related to the so-called **source splitting effects**. These effects stand for the phenomena for which a given data source (e.g. a chemical species) is split into two or more endmembers due to the existence of non-linearities in the data. These non-linear, typically residual, components corrupt the linear mixture model expressed by Equation 8.1 and therefore impact the extraction of the real endmembers. In the present experiment the varying SZA results in a non-linear effect that impacts the spectral signature of the CO_2 ice extracted by VCA. The reason why the source splitting effects affect the data source corresponding to the frozen carbon dioxide may be related to the higher energy of its spectral signature due to a higher value of reflectance and its numerous strong absorption bands. The issue of the source splitting effects shall be further investigated in section 10.2.

As for the quality of the extracted spectral signatures, the reference spectra in Figure 9.3 underline the satisfactory estimation of the spectral shape for all chemical species. Likewise, the average reflectance value is well estimated in all cases except for the fourth endmember for which the reference spectrum has been scaled to fit the extracted signature. This exception comes from the source splitting effects.

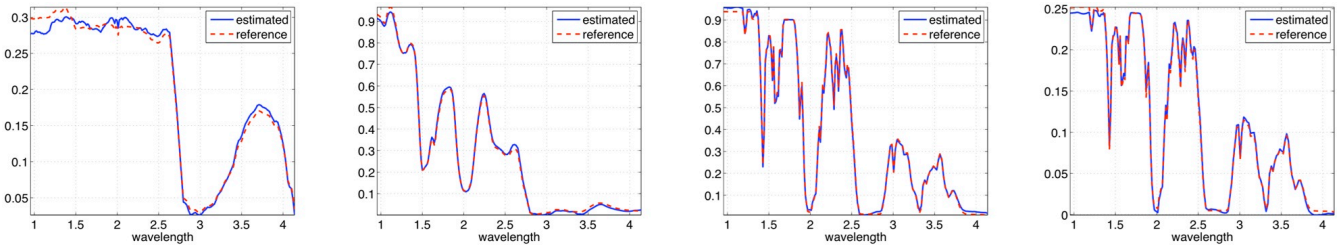

Figure 9.3.: Spectral signatures of the four endmembers extracted by VCA. From left to right: (1) $\hat{\mathbf{m}}_1$: mineral dust estimated spectrum. (2) $\hat{\mathbf{m}}_2$: H_2O ice estimated spectrum. (3) $\hat{\mathbf{m}}_3$: CO_2 ice estimated spectrum. (4) $\hat{\mathbf{m}}_4$: CO_2 ice estimated spectrum.

Figure 9.4 shows the abundance maps reconstructed following the UCLS strategy described in Equation 8.3. The choice of this rather simple reconstruction strategy is made to investigate the consequences of ignoring the additivity and positivity constraints. Regarding the spatial distribution of the estimated abundances, the maps $\hat{\mathbf{s}}_1$ and $\hat{\mathbf{s}}_2$ present a high correlation coefficient as regards $\mathbf{s}_3$ and $\mathbf{s}_1$, 0.954 and 0.948, respectively (see Figure 9.2 and Figure 9.4). Similarly, the fraction map resulting from the sum of $\hat{\mathbf{s}}_3$ and $\hat{\mathbf{s}}_4$, both corresponding to the CO_2 ice, is related to a correlation coefficient of 0.963 with regard the original input $\mathbf{s}_2$. Nevertheless, the quality of the estimated abundances is not satisfactory

from an absolute point of view since $\hat{\mathbf{s}}_1$, $\hat{\mathbf{s}}_3$ and $\hat{\mathbf{s}}_4$ show abundances out of the physical range $[0 \dots 1]$. I therefore conclude that the abundance maps provided by the UCLS strategy are clearly unphysical and do not agree with the ground truth in Figure 9.2. Furthermore, the abundances corresponding to the spectra whose corresponding SZA is greater that 70^o (right-hand side of the abundance maps in Figure 9.4) present a reconstruction noise that comes from the presence of the fourth endmember $\hat{\mathbf{m}}_4$.

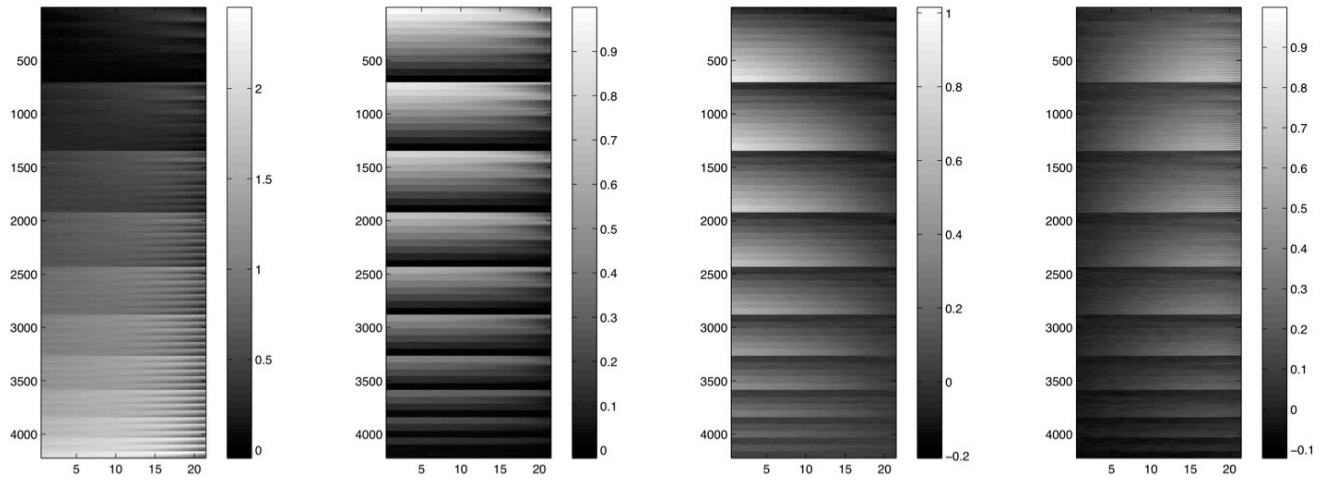

Figure 9.4.: Estimated abundance maps of the four endmembers extracted by VCA. From left to right: (1) $\hat{\mathbf{s}}_1$: mineral dust abundance fraction. (2) $\hat{\mathbf{s}}_2$: H_2O ice abundance fraction. (3) $\hat{\mathbf{s}}_3$: CO_2 ice abundance fraction. (4) $\hat{\mathbf{s}}_4$: CO_2 ice abundance fraction.

9.3. Conclusions

I conclude this experiment by stating that the combination of the algorithms ELM and VCA may be suitable to decompose mixed data if certain precautions are taken. First, non-linearities in the data such as varying illumination conditions may produce source splitting effects that may alter the real number of endmembers estimated by ELM. As a matter of fact, the homogeneity of the illumination conditions makes part of the requirements stated at the beginning of chapter 8 to assure the absence of non-linearities in the remotely sensed signal. Second, special attention must be paid when ignoring the positivity and sum-to-one constraints in the reconstruction of the abundance maps based on the spectra extracted by VCA. In particular the physical sense of the retrieved maps cannot be assured when using the UCLS strategy. The quality of these spatial outputs being critical for mapping purposes in planetary sciences, I therefore recommend to use the FCLS strategy in order to constrain the retrieved abundances in the physical range $[0 \dots 1]$. This decision shall be taken in the following study described in chapter 10. Despite these two limitations, results prove that the ELM+VCA strategy may provide satisfactory spectral signatures and abundance maps of the chemical species present in a martian scene, at least in a qualitative manner. As a matter of fact, the absence of the physical constraints on the estimated abundances severely impacts the quantitative quality of the present study. Eventually the unmixing process has proved to be robust in front of the typical noise in imaging spectrometers. Similar experiments carried out on real planetary data acquired by the OMEGA sensor and presented in [105] show similar satisfactory results. In the following chapter I take into account of the conclusions drawn in this chapter when using the spectral unmixing concept to analyze real planetary data.

10

Spectral unmixing for the study of planetary surfaces

In chapter 9 I have investigated the capabilities of blind source separation to decompose simulated data under a linear mixture model. One could argue, however, that the reality is much more complex than the scenario considered in the synthetic data set. In this matter many authors have recently addressed satisfactorily the unmixing of real planetary remotely sensed data. For example, Moussaoui et al. [125] and Luo et al. [105] obtain satisfactory results when processing data acquired by the imaging spectrometer OMEGA by the aforementioned techniques BPSS and VCA, respectively. In this matter one could argue that the conditions under which OMEGA senses the surface of Mars may be suitable for the existence of linear mixtures because of its moderate spatial resolution, up to 350 m/pixel. As a matter of fact several terrain units are likely to coexist geographically within a given pixel at this spatial resolution. By contrast, the CRISM instrument provides data with an unprecedented detail, up to 18 m/pixel, thus increasing the complexity of the observed surface. As detailed in chapter 8 the probability of dealing with non-linear mixtures typically increases with higher spatial resolutions, thus questioning the suitability of spectral unmixing techniques based on a linear mixture model in the CRISM case.

In this chapter I go further than in chapter 9 by investigating the suitability of the linear mixture model in the planetary context made available by the CRISM instrument. By suitability I mean the capacity of linear unmixing techniques to reveal relevant features related to the chemical composition and the physical state of planetary surfaces. Scientists working with CRISM hyperspectral data may benefit substantially from this original study since spectral unmixing approaches are potential tools to map and quantify the abundance of chemical species such as minerals (e.g. [137]). Additionally, these techniques allow the transformation of a hyperspectral cube formed by hundreds of spectral bands into a set of a few relevant features, each one characterized by a spectral signature and an abundance map.

In this matter the second objective of this chapter is defined as the evaluation of the capacity of unmixing techniques to perform dimensionality reduction. In front of the volume increase of planetary data collections the potential of source separation to ease this problem is explored in this chapter. With this aim I focus on unsupervised techniques that allow the automatic processing of such collections of data. As I shall conclude in section 10.4 the concept of spectral unmixing is appropriate to generate significant quick look products that squeeze out the meaningful information from hyperspectral images.

Eventually spectral unmixing has proved to be a unique tool to detect rare minerals provided that the corresponding, often weak, signals are conserved in the process. This issue has been recently investigated by some authors in [119, 138, 27, 1]. This point shall also be investigated in the present chapter as planetary scientists usually require methods that are sensitive to rare materials at the ground (e.g. [37]). At this point I remark that the aim of this study is not to explore the capability of spectral unmixing to detect rare signals that are different to the rest (e.g. anomalies). In this special case anomaly detection algorithms or unmixing techniques considering the sparsity of the data must be used and this is out of the scope of this thesis.

In order to address these objectives I put forward an original validation strategy to assess the performances of spectral unmixing applied on CRISM data in a quantitative manner[1]. The validation of spectral unmixing techniques is a very challenging issue in planetary sciences because ground truth data are very scarce. Similarly to what is done in chapter 9 the validation of unmixing outputs is traditionally addressed either by comparison of the extracted endmembers with reference spectral signatures [35, 48, 122, 189] or by using simulated data [82, 83, 191]. In the martian case I do not consider this evaluation strategy as fully satisfactory as only a few specific areas of Mars are characterized to the extend of making available reliable reference spectral signatures. Contrarily, the validation of abundance maps obtained from unmixing real martian data has never been addressed. I highlight the work of Jia et al. that represents to our knowledge the sole attempt in this direction. In that work the authors perform the validation of spectral unmixing techniques by comparing abundance maps with reference data [82]. Nevertheless I cannot consider this validation to be independent of the unmixing problem since the abundance maps of reference are built from spectra that are manually extracted from the original image. To our knowledge, the validation of spectral unmixing techniques applied on real data through the evaluation of extracted abundance maps in an independent manner has been never addressed.

In this chapter I present an innovative strategy to validate unsupervised spectral unmixing techniques applied to CRISM data. For this purpose a specific CRISM observation displaying the Russell crater megadune is selected. This particular area of Mars is very suitable to validate spectral unmixing techniques based on the linear mixture model. First, the existence of geographic sub-pixel mixtures coming from two predominant materials at the ground is confirmed by very high-resolution imagery. Second, it is possible to build a ground truth for validating the extracted abundance maps using the same independent imagery. Following original experiments I perform quantitative assessment of surface abundances obtained by a selection of state-of-the-art unmixing algorithms. This choice is performed among spectral unmixing techniques that are widely used in planetary sciences and/or

[1] This work has been carried out in collaboration with the Laboratoire IDES, Orsay, France, the GIPSA-lab, Grenoble, France, and the LIESMARS, Wuhan, China. More details can be found in the published article [27] that has been attached to this dissertation in chapter 16.

Earth observation. In this experiment the most appropriate and efficient techniques for analyzing CRISM data are identified by evaluating their spatial outcomes.

This chapter is organized as follows. In section 10.1 I present the site of study by describing the Russell dune and the corresponding data sets. Experiments are carried out in section 10.2 followed by the intercomparison and validation of the spectral unmixing techniques using the reference ground truth in section 10.3. In section 10.4 I draw the conclusions on the proposed strategy, the tested unmixing techniques, and the potential of spectral unmixing in planetary sciences.

10.1. The Russell crater megadune

The Russell crater is a 134-km wide impact crater situated in the southern hemisphere of Mars. Figure 10.1 (top-right) shows an image of the 1700 km^2 dune field situated on the northeastern part of the Russell crater. This uncommon 500-m high megadune is made of mineral materials that are completely covered by seasonal CO_2 ice during the southern winter of Mars [63].

In this experiment I propose to study the southwest facing scarp of the Russell megadune because it displays many defrosting features in late winter. These features appear at the beginning of the retreat of the CO_2 ice in the form of dark elongated patterns (mainly along the gullies that erode the scarp) and dark spots (mostly on the top of the dune) as it is shown in Figure 10.1. In late winter the Russell dune represents a potential benchmark for testing spectral unmixing algorithms in a planetary context. With the beginning of the sublimation of predominant ice, the sandy mineral substratum is gradually uncovered. This geographical coexistence of two components has been observed during the MRO mission by very high resolution imagery and imaging spectroscopy with the HiRISE and the CRISM instruments, respectively. The former sensor fully resolves the geographical coexistence of dark dusty features and brighter ice while the latter instrument does not. In this case I consider that assumption of linear mixtures in the hyperspectral signal leaving from the Russell dune becomes reasonable at the CRISM resolution. Figure 10.1 illustrates the existence of geographical sub-pixel mixtures by superposing the footprint of a CRISM pixel onto the HiRISE image. The displayed pixel actually encompasses two potential endmembers that are distinctly defined.

Another reason that I consider to be valid to designate the Russell dune as a study site is the possibility of constructing a ground truth based on high resolution HiRISE imagery. These ground truth data can be used to evaluate the capabilities of spectral unmixing techniques as it will be done in section 10.3.

I distinguish two major difficulties linked to the choice of the Russell dune, the quite accentuated relief and the presence of icy materials. The former hurdle is related to the multiple scattering that may occur between the different tilted facets of the dune and that is not considered in the unmixing process. Second, the remaining CO_2 ice over the main scarp of the dune is susceptible to display quite strong anisotropic photometric effects throughout the image. In addition, the presence of ice increases the complexity of the atmospheric correction that the selected CRISM image will undergo.

10.1.1. CRISM data and preprocessing

In this study I select the central scan of the CRISM observation FRT42AA acquired in late winter when the CO_2 sublimation starts and the defrosting features appear. Figure 10.2 shows the 80-km^2 area of

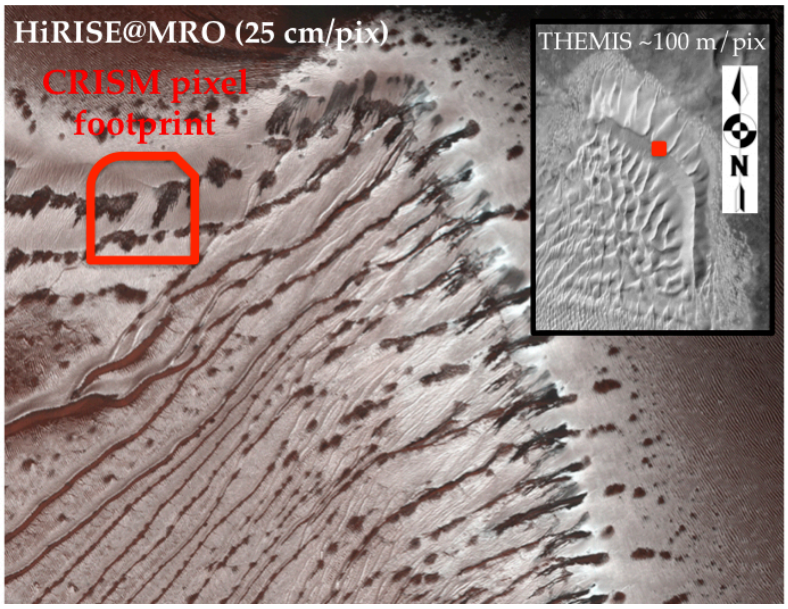

Figure 10.1.: Detail of the HiRISE image PSP_002482_1255_RED over the Russell dune showing the geographical coexistence of brighter areas made of CO_2 ice and the dark features. The dark spots and the elongated patterns are observed. The approximative footprint of a 18×18 m^2 CRISM pixel is superposed on the HiRISE image at 25 cm/pix to illustrate the likely geographical mixtures happening in the remotely sensed signal.

study embracing a large portion of the southern facing scarp of the Russell dune. A region of interest (ROI) is defined to enclose the southwest facing scarp containing the defrosting features (see yellow line in Figure 10.2). As regards the spectral dimension, I only consider the CRISM spectral bands ranging from 1.0 to 2.6 μm because of the less marked features of CO_2 ice in the visible range (<1.0 μm) and the high impact of thermal noise for greater wavelengths (>2.6 μm) due to the second order leakage detailed in subsection 4.1.2.

Before the spectral unmixing stage, the FRT42AA central scan is processed by the IPAG-DP introduced in chapter 4 as Figure 10.3 illustrates. In this way the test image is compensated for instrumental artifacts, atmospheric effects and photometric issues. These contributions are not related to the materials at the surface and therefore may introduce non-linearities in the data that would invalidate the linear mixture assumption. At this point I make the following comments as regards the application of the IPAG-DP on the FRT42AA central scan:

1. The correction of the FRT42AA central scan for smile effects is particularly challenging due to the presence of CO_2 ice (review subsubsection 4.1.2.1). While the proposed desmiling method compensates the majority of the smile effects some residues are therefore expected.
2. Imprecisions in the adopted scattering properties of the aerosols (review subsection 2.1.3) may result in atmospheric residues affecting the spectra corresponding to the upper and lower rows of the image (corresponding to the most extreme VZA values) by means of spurious spectral slopes.
3. Correction for photometric effects is performed on the FRT42AA central scan by considering the average illumination conditions of the ROI. The average SZA used in the photometric normalization is estimated from the HiRISE DTM covering the Russell dune (see Figure 4.25).

As a consequence of the mentioned limitations residues coming from the heterogeneous photometry,

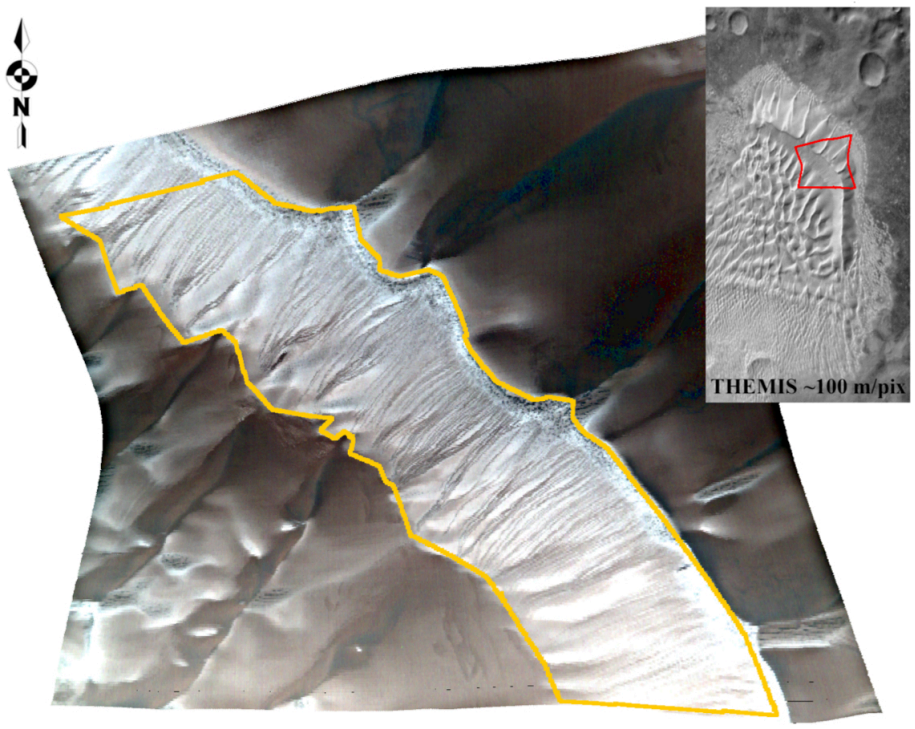

Figure 10.2.: True color image of the central scan of FRT42AA showing the Russell dune. The still frosted scarp displays dark spots on the ridge of the dune and dark elongated patterns along the gullies. The ROI is highlighted in yellow. The upper-right figure displays the location of the test image over the megadune observed by the THEMIS instrument.

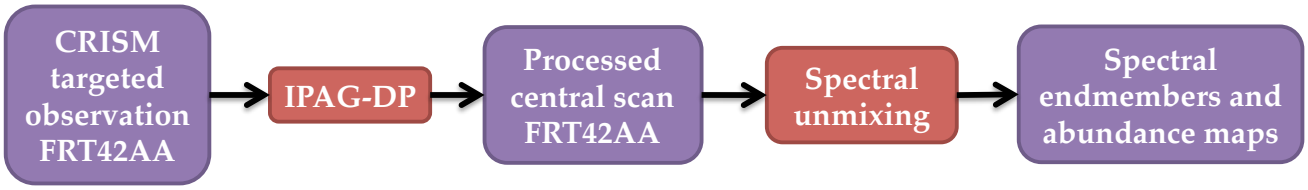

Figure 10.3.: Block diagram illustrating the spectral unmixing of the central scan of the CRISM observation FRT42AA after processing by the IPAG-DP.

instrumental artifacts and atmospheric effects may still affect the data related to the surface after the IPAG-DP. This point is made obvious in the following section 10.2 where I show how these non-linear residues have an impact on the linear mixture model. In any case I consider the central scan FRT42AA to be suitable to perform linear spectral unmixing according to the conditions stated in chapter 8. First, the presence of geographic sub-pixel mixtures in the Russell dune is proved by inspecting HiRISE imagery. Figure 10.1 shows that the radiance leaving the surface may be reasonably composed by a linear combination of, at least, two physically distinct components at the spatial resolution of CRISM. Despite the likely presence of residues I assume the absence of atmospheric effects as well as the homogeneity of the solar illumination after the IPAG-DP. The lack of non-linear contributions coming from the surface cannot be, however, guaranteed. In this situation the linear mixture model is subject to be degenerated, as it is expressed in Equation 8.2, and spurious transformations arising from the non-linear factors $\mathbf{F} = \{\mathbf{f}_1, \mathbf{f}_2, \ldots, \mathbf{f}_{N_c}\}$ may alter the estimated endmembers $\mathbf{M}$ as it happened in chapter 9. The semi-validity of the linear mixture model is taken into consideration in the analysis that is carried out in the following section.

10.2. Experiments

Experiments are conducted on the area of the FRT42AA central scan delimited by the introduced ROI. As for the unmixing stage I define a comprehensive selection of state-of-the-art algorithms based on geometric, NMF-based, statistical and spectral-spatial first principles[2]. In this selection I discard those algorithms typically used in planetary sciences that are supervised [e.g. the Iterative Linear Spectral Unmixing Model (ILSUM) [122]] or that have been proved to be less appropriate to retrieve physically meaningful features (e.g. the PCA and the MNF transformations, see [55]). With the resulting comprehensive selection of algorithms I aim at performing an intercomparison to determine those that are more suitable to analyze CRISM data. The essential result in order to consider an analysis technique to be reliable is the obtention of physically meaningful endmembers that are related to the materials at the surface such as the dark features presented in Figure 10.1.

10.2.1. Spectral unmixing

As detailed in chapter 8 the first step toward the unmixing of hyperspectral data consists in the determination of the number of endmembers. With this aim I use the state-of-the-art technique referred to as ELM (review section 8.2). In this case ELM detects the coexistence of six endmembers in the hyperspectral image of investigation. This result is considered satisfactory given that the Russell dune is assumed to be composed by at least two major components (i.e. CO_2 ice and mineral dust). The slight disagreement existing between the expected (i.e. ~2) and the detected (i.e. $N_c = 6$) number of materials is explained by the so-called source splitting effects (see section 9.2). I note that the alternative method HySime was discarded in this study as it determined the presence of 14 endmembers, a result largely exceeding the expected number of sources. The reason of this result may be related to the higher sensitivity of HySime to the non-linearities in the data which severely impact the endmember reconstruction.

In this investigation experiments are carried out by a selection of four endmember extraction methods based on different principles detailed as follow:

1. The geometric method VCA with assumption of pure pixels.
2. The statistical technique BPSS with no assumption of pure pixels and based on a Bayesian framework.
3. The hybrid approach MVC-NMF with no assumption of pure pixels and suitable for identifying less-prevalent endmembers.
4. The algorithm spatial-VCA resulting from the fusion of the method VCA and the preprocessing procedure introduced in Figure 8.3. The latter routine aims at incorporating the existent spatial information in the image into the unmixing problem.

The MVSA algorithm is not used in this study as it is based on similar principles than MVC-NMF. As for the reconstruction of the abundance maps using the linear mixture model I take into account the non-negativity and the sum-to-one constraints by considering the FCLS strategy (see Equation 8.4) as it is concluded from the study performed in chapter 9. In this framework one spectral signature and

[2]In this thesis I present only results obtained by a selection of four algorithms that provided satisfactory results on the FRT42AA image. Further experiments were carried out with other techniques (see article in chapter 16).

one abundance map is provided for each of the six endmembers by each the analysis methods. I make the following comments at this point:

- After the scrutiny of the extracted spectral signatures by a team of planetary scientists, all spectra are considered to be physically meaningful. This is also the case of those provided by the techniques MVC-NMF and BPSS, which are not based on the pure pixel assumption. Nonetheless, residual non-linear contributions make that one physical source, typically a material at the surface, can be split into two or more endmembers. This outcome is caused by source splitting effects (see section 9.2).
- After the inspection of the six spectral signatures and the six corresponding abundance maps provided by each method, I distinguish three physical data sources related to the surface in the central scan of the FRT42AA observation. These three materials are detected in the outcomes provided by the four endmember extraction methods that are tested in this study.
- A recombination effort is therefore needed to reconstruct each physical source (three in total) based on the forming endmembers (six in total). The algorithms MVC-NMF and BPSS are the sole techniques providing a self-consistent endmember embracing the dark features observed in Figure 10.1.

In the following section I detail the recombination process that is carried out on the endmembers extracted by the method MVC-NMF. Details on the recombination efforts done for the rest of techniques are given in the enclosed article in chapter 16.

10.2.2. Analysis and recombination of endmembers

The spectral signatures corresponding to the six endmembers extracted by the method MVC-NMF are plotted in Figure 10.4. Alternatively, Figure 10.5 shows the associated abundance maps.

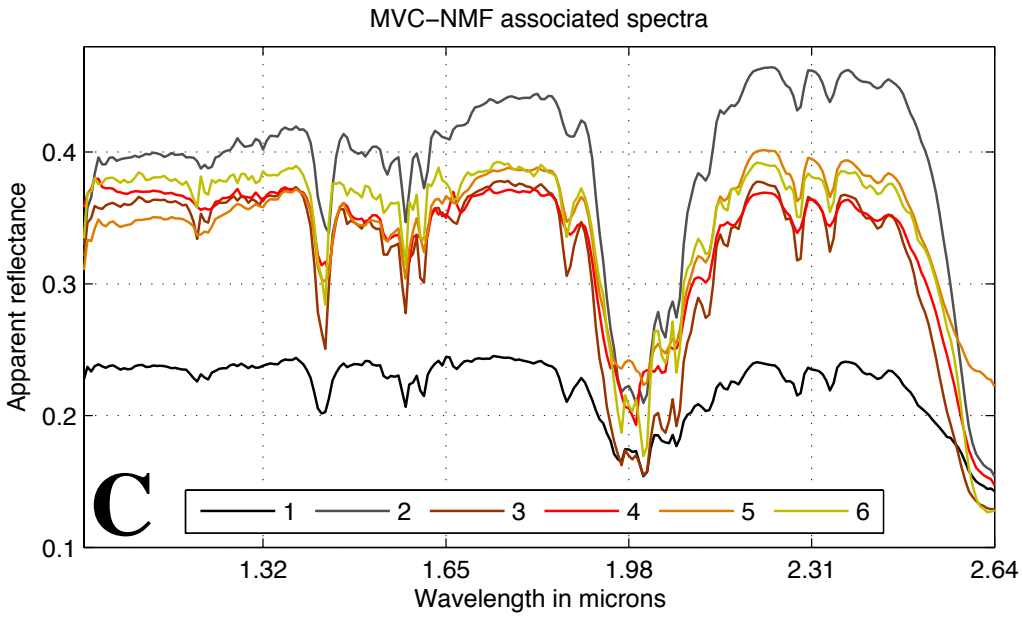

Figure 10.4.: Spectral signatures extracted by the method MVC-NMF.

In order to identify the origin of each endmember I define two parameters that characterize each extracted spectrum. Let $R_{1.1}$ be the apparent reflectance value at 1.1 μm and let $B_{2.3}$ be the absorption

depth at 2.3 μm such that $B_{2.3} = 1 - R_{2.3}/R_{2.2}$. These two spectral parameters are decisive for the interpretation of the spectral signatures together with the information coming from the abundance maps. In particular large values of $R_{1.1}$ and $B_{2.3}$ are related to a higher content of CO_2 ice because of the higher reflectance of ice in comparison to dust and the fact that absorption at 2.3 μm is specific to ice, respectively. Due to inaccuracies in the atmospheric correction extracted spectra may have an anomalous positive or negative slope that must be accounted for in the calculation of $B_{2.3}$. In order to overcome this anomaly I propose to multiply $B_{2.3}$ by the spectrum average slope $b_{1.1-2.2}$ that is calculated as $R_{2.2}/R_{1.1}$. Table 10.1 details the two spectral parameters for each endmember extracted with MVC-NMF.

Endmember:	1 (D)	2 (W)	3 (S)	4 (W)	5 (W)	6 (W)
$R_{1.1}$:	**0.24**	**0.39**	**0.36**	**0.37**	**0.34**	**0.38**
$b_{1.1-2.2}$:	1.01	1.17	1.04	1.00	1.16	1.03
$B_{2.3}$:	**0.08**	**0.08**	**0.16**	**0.08**	**0.10**	**0.10**

Table 10.1.: Spectral parameters of the endmembers extracted by MVC-NMF. Apparent reflectance at 1.1 μm and absorption depth at 2.3 μm - (D): dark source, (S): strong bright source, (W): weak bright source.

According to the defined spectral parameters and the abundance maps in Figure 10.5 three physical sources are defined to coexist in the central scan of FRT42AA. They are characterized by their spectral and spatial characteristics as follow:

1. Definition of **dark source**: physical source related to the presence of dark features. The corresponding $R_{1.1}$ and $B_{2.3}$ are the lowest among the three sources due to a high content in dust and a few residual CO_2 ice. This source predominates along the ridge of the dune and within the gullies in the form of dark spots and elongated patterns, respectively.
2. Definition of **strong bright source**: physical source related to a high content of CO_2 ice. The corresponding $B_{2.3}$ is the highest among the three sources while $R_{1.1}$ is higher than for the dark source due to a lower dust content. This source predominates principally in the areas surrounding the dark source.
3. Definition of **weak bright source**: physical source related to a high content of CO_2 ice. The corresponding $R_{1.1}$ is the highest among the three sources while $B_{2.3}$ is higher than for the dark source but lower than for the strong bright source. This source greatly predominates on the dune scarp and may correspond to a different physical state of the ice than the one of the strong bright source.

In the following I detail the designation of each endmember to one of the physical sources. This classification is conducted based on the spectral parameters detailed in Table 10.1, the associated spectra in Figure 10.4, and the abundance maps in Figure 10.5. Afterward, the abundance map of each physical source is obtained by adding the individual abundance maps of the endmembers associated by the assignation. The results of the recombination are shown for the MVC-NMF case in Figure 10.6 (C).

- Reconstruction of **dark source**: I identify endmember 1 to be related to the dark source due to the lowest $R_{1.1}$ among all endmembers and a moderately low values of parameter $B_{2.3}$. This choice is justified by the abundance map related to endmember 1, revealing the dark structures over the Russell dune [see Figure 10.5 upper-left and red pixels in Figure 10.6 (C)]. The composite

abundance map highlights the areas that are prone to contain dark sources as it is observed with HiRISE imagery, namely the dark spots on the top of the dune, the dark elongated patterns along the gullies, and some areas belonging to the base of the northeast-facing defrosted scarp.

- Reconstruction of **strong bright source**: I establish endmember 3 to be related to the strong bright source due to the highest $B_{2.3}$ among all the extracted endmembers. The abundance map of the strong bright source [see Figure 10.5 upper-right and green pixels in Figure 10.6 (C)] shows a spatial coherence with the dark source as the green areas typically surround the red pixels, particularly on the top of the dune.
- Reconstruction of **weak bright source**: I identify endmembers 2, 4, 5, and 6 as belonging to the weak bright source due to a common higher $R_{1.1}$ and a moderately low $B_{2.3}$. In this case source splitting phenomena coming from non-linear residues affect this physical source. On the one hand, the predominance of the CO_2 ice leads to a typical cross-track pattern due to spectral smile affecting the abundance map of endmember 6 (see subsubsection 4.1.2.1). This is pointed out by the anomalous lower abundances that happen in the horizontal edges similarly to what is shown in Figure 4.7. In this context residues of the smile effect make endmember 6 energetic enough to be extracted separately. On the other hand, the differences in terms of reflectance of the spectral signature corresponding to endmember 2 are explained by the different illumination conditions that happen in the scene. This result is similar to the outcome of the experiment in section 9.2 in which the non-uniform SZA results in the splitting of the ice source into two endmembers. The inspection of the HiRISE DTM corresponding to the Russell dune revealed that endmember 2 predominates at low SZA while other endmembers correspond to SZA values that are similar to the average SZA used in the photometric normalization of the IPAG-DP. An optimal normalization by the real SZA would decrease the average reflectance of endmember 2, thus matching the rest of endmembers in terms of $R_{1.1}$. Eventually, the splitting of endmembers 4 and 5 is justified by the opposite vertical trend that affects the corresponding abundance maps. As it is seen in Figure 10.5 (bottom-left) and in Figure 10.5 (bottom-center), both maps show very low spurious abundances, either for the top or the bottom rows, coming from the atmospheric residue described in subsection 10.1.1. This interpretation is also pointed out by the complementary slopes of the spectra ($b_{1.1-2.2} > 1$ for endmember 4 and $b_{1.1-2.2} < 1$ for endmember 5). Figure 10.6 (C) highlights in blue the abundance map resulting from the fusion of endmembers 2, 4, 5 and 6 the areas and that is complementary to the dark and strong bright sources.

Eventually I propose to assess the quality of the spectra reconstruction based on the absence of non-linearities as it is done in [143]. The accuracy of the conducted spectral unmixing is evaluated by reconstructing the CRISM central scan using the extracted spectral signatures $\mathbf{m}_n$ and their associated abundance maps $\mathbf{s}_n$ based on the linear mixture model as follows:

$$\hat{\mathbf{X}}_k = \mathbf{M}\cdot\mathbf{S} = \sum_{n=1}^{N_c} \mathbf{m}_n s_{n,k},\ n = \{1 \dots N_c\},\ k = \{1 \dots N_p\}. \tag{10.1}$$

If the linear mixture hypothesis is fully satisfied and the endmember extraction is performed satisfactorily the resulting error (the term e in Equation 8.1) is equal to the noise of the data. In practice, however,

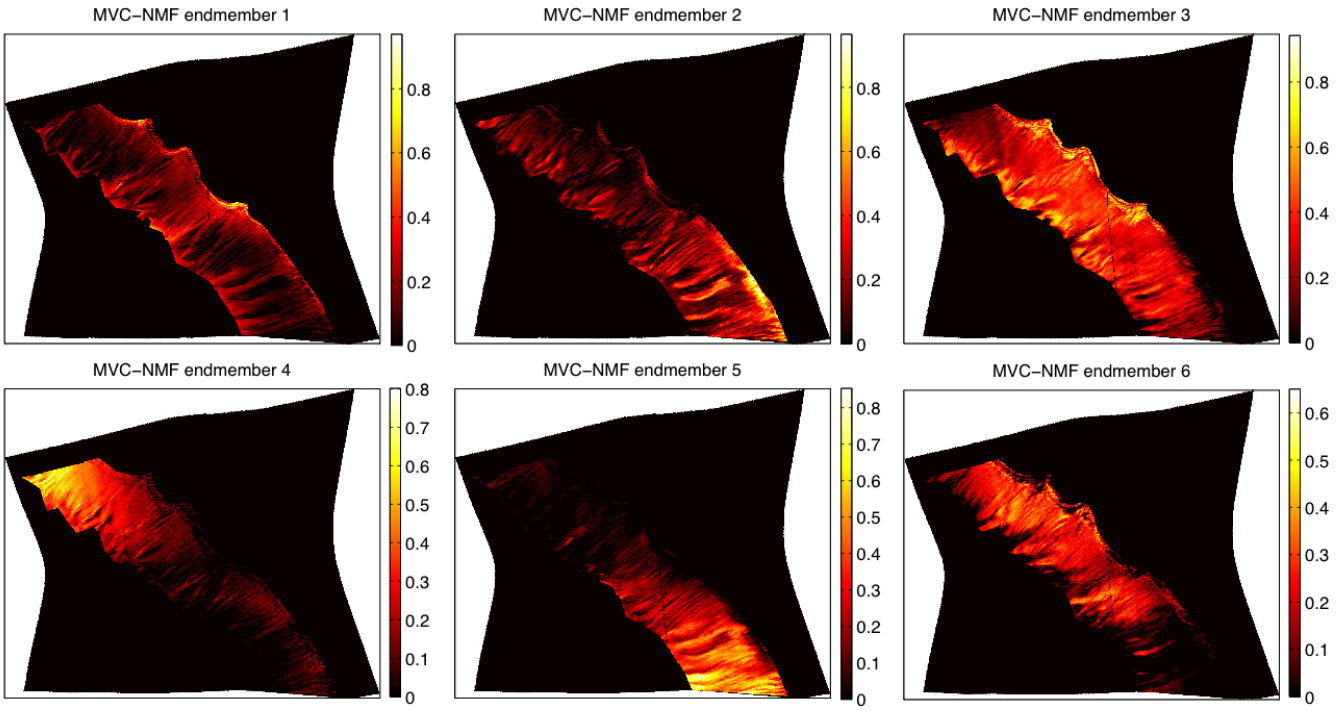

Figure 10.5.: Abundance maps corresponding to the six endmembers extracted from the FRT42AA central scan using the endmember extraction algorithm MVC-NMF.

the term e corresponds to the reconstruction error of the image coming from the non-linearities that exist in the data. The reconstruction error is calculated for each endmember extraction approach in terms of signal-to-noise ratio such as 36 dB for VCA, 41 dB for BPSS, 43 dB for MVC-NMF, and 35 dB for spatial-VCA. These results along with the fact that the abundance maps are accurate (as it shall be shown in the next section) prove an accurate reconstruction in all cases. The results of this last experiment are a solid evidence that the linear mixture model is appropriate for the study of the Russell dune observed by CRISM.

10.3. Validation

In the previous section the robustness of the planetary scenario formed by three physical sources is validated in a qualitative manner by the four composite abundance maps in Figure 10.6. As a matter of fact the notable spatial similarities among these four products coming from different techniques validate the spectral unmixing step. In the following I perform further validation of the obtained outcomes using a ground truth that expresses the abundance fractions of the dark source for every pixel. This reference in the form of an abundance map is constructed from HiRISE imagery, assuring the independence of the resulting ground truth. I propose to use this ground truth to validate the planetary scenario unveiled by spectral unmixing. In particular I propose to evaluate the abundance maps related to the dark features of each tested technique in a quantitative manner.

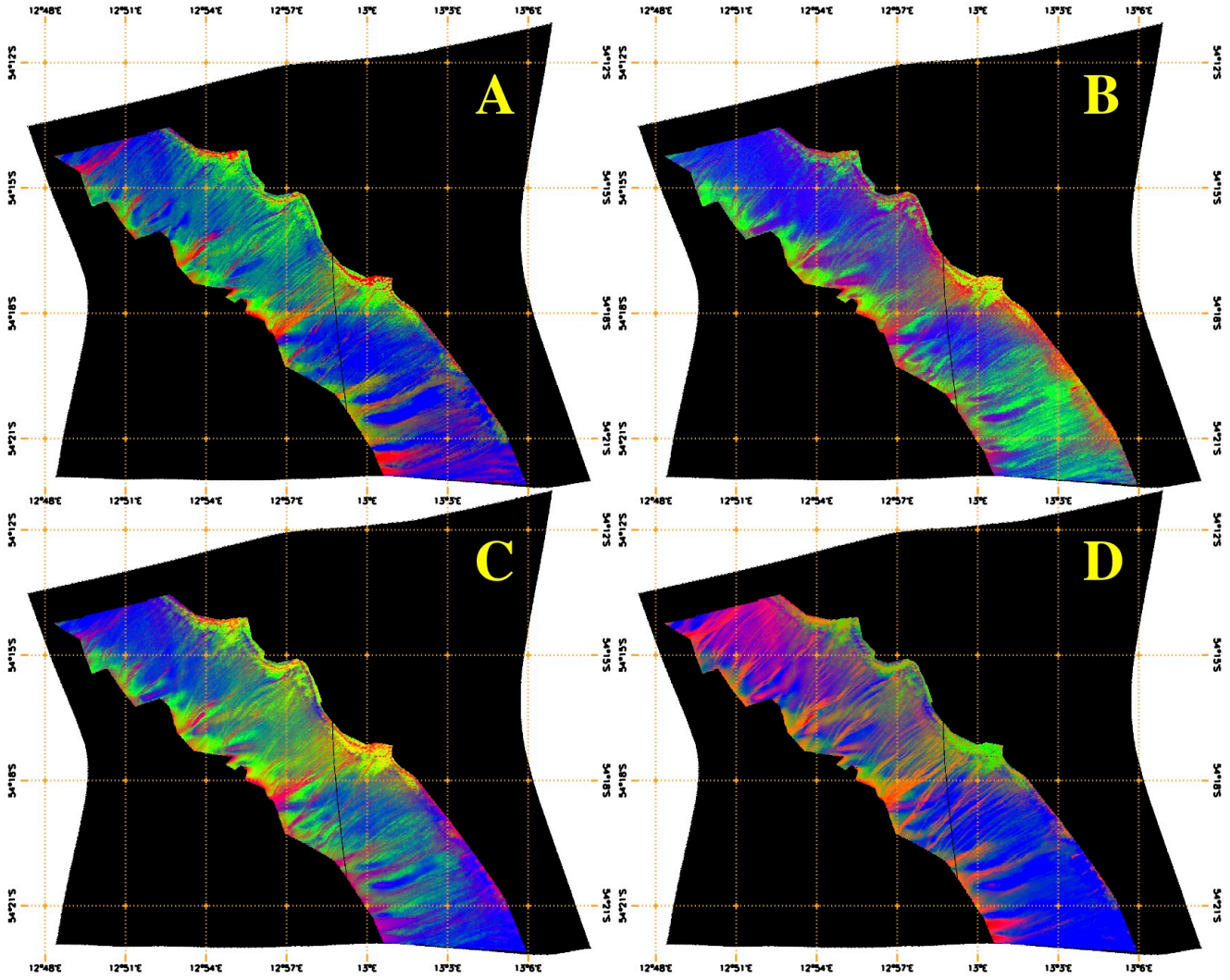

Figure 10.6.: A: Color composite image illustrating the spatial distribution of the three physical sources over the Russell dune extracted by VCA. The dark, strong bright and weak bright sources are show in red, green and blue, respectively. B, C and D: Same as Figure Figure 10.6-A for BPSS, MVC-NMF and spatial-VCA.

10.3.1. Ground truth

The validation of outcomes coming from planetary data is a very challenging issue in front of the scarcity of available ground truth data. Only a few specific sites on Mars have been explored to a sufficient degree to allow contrasting data coming from different instruments. The Gusev crater presented in chapter 7 represents one of the few sites on Mars that have been scrutinized by the combination of spacecrafts from orbit and rovers on the ground. Nonetheless, confronting different kinds of results is not a straightforward task because of the different spatial resolution and conditions under which the measurements are acquired. In this chapter I present a novel strategy to validate the outcomes provided by unmixing strategies from planetary data by building a ground truth based on HiRISE imagery.

10.3.1.1. HiRISE image

The HiRISE camera is an unprecedented tool to explore the surface of Mars. HiRISE consists of a half-meter reflecting telescope that allows sensing geological formations of the Red Planet at a very high spatial resolution, up to 0.25 m/pixel [115]. HiRISE is aboard MRO and thus explores the planet Mars simultaneously with CRISM. Figure 10.7 (upper-right) shows the footprints of the HiRISE image PSP_002482_1255 that was acquired at the same time than CRISM's FRT42AA. Likewise, Figure 10.7 shows a small area of the Russell dune observed simultaneously by the CRISM and the HiRISE instruments. As it can be seen, HiRISE is able to resolve spatially the dark features from the surrounding brighter ice while the CRISM image is composed of highly mixed pixels. In this situation I propose to exploit the HiRISE image PSP_002482_1255_RED at 550-850 nm to build a reference abundance map for the dark features that shall be used in the evaluation of the corresponding spectral unmixing outcomes (i.e. the red pixels in Figure 10.6).

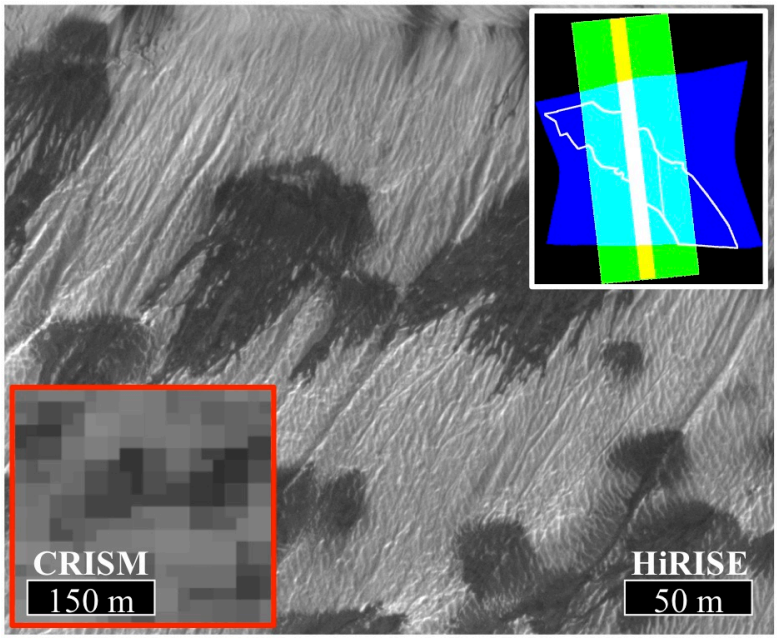

Figure 10.7.: (main) Detail of the Russell dune observed by the CRISM and the HiRISE instruments. (upper-right) footprints of the images CRISM FRT42AA in blue (604×420 pixels, non-map projected), HiRISE PSP_002482_1255_RED in green (29862×63004 pixels, map projected) and HiRISE PSP_002482_1255_COLOR in yellow (11776×61257 pixels, map projected). In this study, the COLOR product is discarded in favor of the RED image because of its smaller coincident footprint with the CRISM image and twice worse spatial resolution (see chapter 16 for more details). The ROI is enclosed with a white line.

I propose the following threefold strategy to generate the ground truth:

1. The HiRISE image is first classified in order to extract the dark features.
2. The resulting classification map is registered with the CRISM hyperspectral image. The HiRISE geographic space is preferred as output in order to keep its higher spatial resolution for the final comparison between the two products.
3. The reference abundance map is generated by counting the labels classified as dark features that fall within the footprint of a given CRISM pixel.

In the following sections I further detail these three steps.

10.3.1.2. Image classification

The dark features are first extracted from the HiRISE image PSP_002482_1255_RED by classifying each pixel of the image as belonging to the class "dark features" or the class "brighter ice". The definition of these two classes is straightforward according to the geomorphologic analysis based on Figure 10.1 and Figure 10.7. I use a traditional unsupervised k-means strategy that was introduced in the 60s and firstly applied to remote sensing data by Richards et al. in [149]. After splitting the image into $k = 7$ clusters according to the gray value of the HiRISE image, the darkest cluster is selected to represent the dark features. Some manual improvement based on local thresholding is performed in order to avoid misclassifying other dark zones in the image such as shadows that could be misinterpreted as dusty features of interest. Figure 10.8 (a) shows the resulting classification map encompassing the dark spots and the dark elongated features.

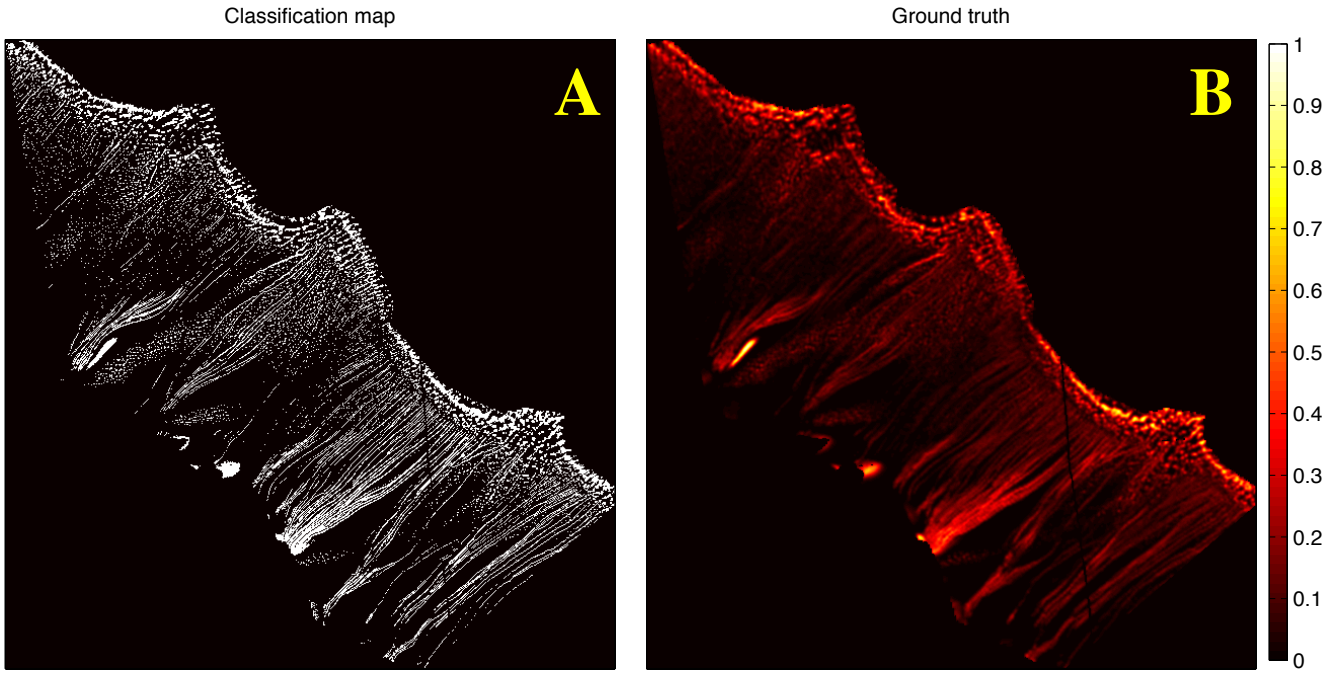

Figure 10.8.: A: Classification map embracing the dark features after extraction from the original HiRISE image. The label occurrences corresponding to the dark features are represented by white points. B: Reference abundance map used as ground truth.

10.3.1.3. Image registration

The resulting classification map must be transformed into an abundance map to be comparable to the spatial outcomes of the unmixing stage. For this purpose I propose to overlap the grid formed by the footprints of all CRISM pixels onto the classification map in order to calculate the fraction of dark features within each CRISM pixel. Nonetheless, the generation of an abundance map from HiRISE imagery to be compared to products coming from CRISM data is a challenging problem due to the different functioning of both instruments. The major hurdle is related to the spatial resolution

of the instruments, differing by more than a factor 70 (18 m/pixel for CRISM against 0.25 m/pixel for HiRISE). For this purpose I first project the CRISM hyperspectral image, originally in its image space, onto the HiRISE geographic space[3] using the DDR ancillary data [127]. At this point both images should be theoretically correctly registered. Nevertheless, this processing step is not enough since there exist incompatibilities between the instrument models that are used to generate the geographic data of each sensor.

In this context I decide to perform the direct registration of both images for the sake of an accurate pixel-wise comparison between the two products of interest (i.e. the HiRISE-based ground truth and the abundance maps resulting from the spectral unmixing of CRISM data). With this aim I use a feature matching method that warps a CRISM spectral band of control (i.e. the one at 1.1 μm, in the continuum of the spectra) to fit the original HiRISE image. As a matter of fact it would not be safe to perform the direct registration of the unmixing abundance maps as they could be wrong. After this processing step is satisfactorily achieved the registration procedure can be repeated for the unmixing abundance maps.

I define a threefold procedure to register both images as follows:

1. The control spectral band of the CRISM image is projected onto the geographic space of the HiRISE data using its geographic data in the ancillary DDR (i.e. latitude and longitude).
2. A coarse registration is first performed by applying to the CRISM product the spatial translation in the vertical and horizontal dimensions that maximizes the correlation coefficient between both images.
3. A fine registration is eventually carried out using a classical Delaunay triangulation [49]. In this way the CRISM image is warped based on a set of more than 200 manually-selected ground control points defined over the southwest-facing scarp and, in particular, for the dark spots along the ridge of the dune. This registration method is chosen for its simplicity and robustness.

The registration process is illustrated in Figure 10.9 (A) and Figure 10.9 (B) showing, respectively, the HiRISE and the CRISM images with the associated ground control points. The quality of the registration is expressed by Figure 10.9 (C) depicting the spatial distribution of the local correlation coefficient r_{reg} between the HiRISE image and the control CRISM spectral band after registration. The r_{reg} values are obtained using a 10×10 sliding window over the coinciding area resulting from the intersection of the two images and the ROI (review Figure 10.7). Figure 10.9 (C) underlines the satisfactory accuracy of the registration with an average correlation of ~0.7. I remark that the manual selection of control points may introduce misregistration inaccuracies, particularly on the borders of the processed area where control points are difficult to define due to the lack of information on the surrounding areas.

10.3.1.4. Reference abundance map

After registration the classification map obtained based on HiRISE imagery is ready to be transformed into an abundance map that is comparable to the unmixing results. Given that the data manipulation has been performed on the HiRISE geographic space, each CRISM pixel is now associated to a footprint containing several pixels at the HiRISE resolution (see red polygon in Figure 10.1 for an example). I

[3]HiRISE products are released using an equidistant cylindrical projection.

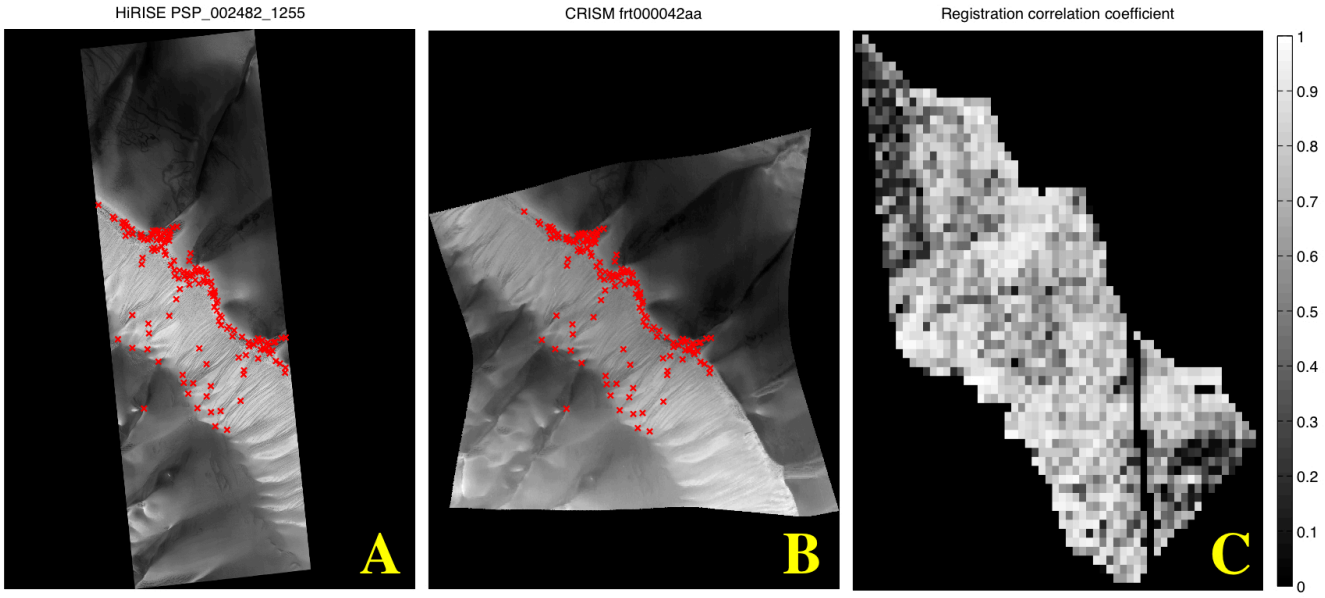

Figure 10.9.: (A): HiRISE image with the corresponding registration control points as red crosses. (B): The same as Figure Figure 10.9 (A) for the CRISM image. (C): Registration accuracy map displaying the local correlation coefficient computed on the intersection between the two images and the ROI on a 10×10-pixel basis.

therefore compute the reference abundances by counting the number of dark labels (i.e. white points in Figure 10.8) occurring in each CRISM footprint, and then normalizing by the total number of labels. In this way I obtain a ground truth product that provides the fraction of dark features at the CRISM resolution.

The resulting ground truth is eventually improved to become more realistic. In remote sensing any sensed radiance value of a given pixel is determined by the contribution coming from the conjugated area on the surface and spurious contributions originated by two principal causes:

1. The overlapping of the PSFs corresponding to the pixel of interest and those of the neighboring detectors (review section 1.4).
2. The so-called adjacency effect introduced in subsection 2.1.3.

In the spatial dimension this effect result in a blurring of the whole hyperspectral image that has not been taken into account in the generation of the ground truth. I therefore mimic an image blurring by filtering the reference abundance map by a Gaussian low-pass filter. More details on this image degradation can be found in chapter 16.

Figure 10.8 shows the transformation of the classification map into the final ground truth that is used for validation of the unmixing products. Additionally, Figure 10.10 provides a summary of the different steps in the construction of the ground truth on a small area of the Russell dune.

10.3.2. Evaluation of abundance maps

The abundance maps related to the dark source produced by spectral unmixing of the FRT42AA central scan are validated using the introduced ground truth. For this purpose I make the reasonable assumption that the dark features resolved by the HiRISE instrument correspond to the extracted

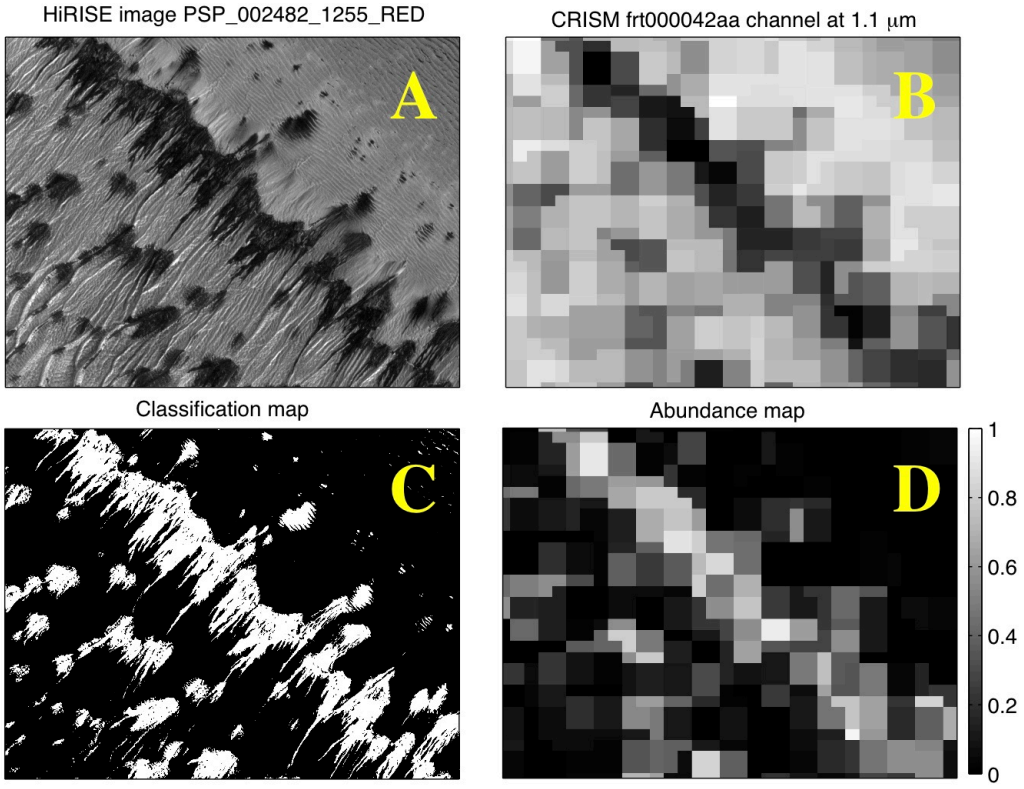

Figure 10.10.: Detail of the ground truth generation. A, B: HiRISE and CRISM images after registration. C: Classification map highlighting the dark features. D: Reference abundance map after pixel counting.

dark source. As it is introduced in subsubsection 10.3.1.3 the registration step is repeated, using the same parameters, on the abundance maps provided by the algorithms VCA, BPSS, MVC-NMF, and spatial-VCA. Figure 10.11 displays the products related to the dark source after cropping them to be comparable to the ground truth in Figure 10.8 (B).

I propose two indicators to assess the similarity between the ground truth and the unmixing abundance maps, namely the Pearson correlation coefficient r and the average absolute error ϵ. The former indicator is chosen to measure the spatial similarity of both products, while the latter is selected to give a more quantitative assessment of the comparison. As it is shown in Figure 10.9 (C), misregistration problems may alter the comparison on some specific areas. Consequently, I carry out three experiments by calculating r and ϵ according to the registration accuracy. Each experiment is detailed in the caption of Table 10.2 and results are summarized as follow:

1. According to the results of the first experiment the unmixing outcomes are quite satisfactory with r up to 0.69 and ϵ as small as 0.08.

    - The algorithms MVC-NMF and spatial-VCA provide the best and the worst results in terms of r, respectively. BPSS performs slightly worse than VCA and MVC-NMF because of the noisy background that affects the dark abundance map (see Figure 10.11). I interpret this result as a higher sensitivity of BPSS to the presence of residual dust invisible to HiRISE within the ice surrounding the dark features.
    - The examination of results in terms of ϵ reveals that abundances provided by spatial-VCA

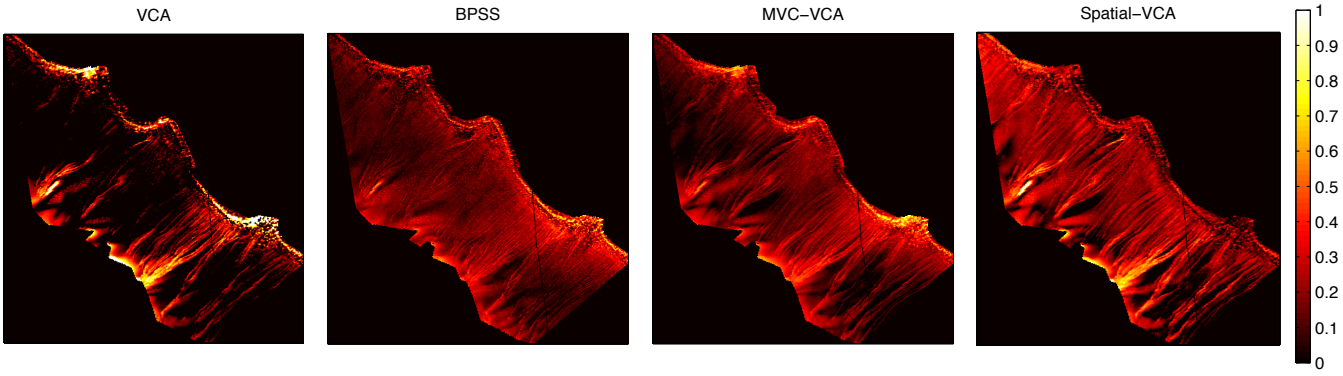

Figure 10.11.: From left to right, abundance maps corresponding to the dark source extracted by the algorithms VCA, BPSS, MVC-NMF and spatial-VCA. The matching ground truth is found in Figure 10.8 (B) for comparison.

Method	VCA		BPSS		MVC-NMF		spatial-VCA	
Indicator	r	ϵ	r	ϵ	r	ϵ	r	ϵ
1: All pixels	0.68	0.08	0.57	0.10	0.69	0.09	0.50	0.14
2: Accurate registration	0.73	0.08	0.59	0.09	0.72	0.08	0.56	0.13
3: Best registration	0.81	0.19	0.80	0.13	0.83	0.14	0.77	0.33

Table 10.2.: Pearson correlation coefficient r and average absolute error ϵ for (1) all pixels ($mean(r_{reg}) = 0.7$), (2) the moderately well registered areas ($r_{reg} > 0.7$, ∼50% of the pixels with $mean(r_{reg}) = 0.83$) and (3) an area with an improved registration (∼1% of the pixels with $mean(r_{reg}) = 0.96$). The region corresponding to the third experiment is shown in Figure 10.10.

are slightly worse than the rest with $\epsilon = 0.14$. This bias is mostly originated in the atmospheric residue affecting the upper rows in the form of a small overestimation that is conjugated with a poorer registration accuracy [see Figure 10.9 (C) and Figure 10.11]. Additionally, Figure 10.6 (D) shows an excess of red pixels in the upper rows that may indicate a deficient endmember recombination in the spatial-VCA case.

2. Misregistration issues are proved to be an important source of error since the obtained results in the second experiment outperform those from the first experiment.
   - All methods undergo a significant correlation improvement up to 0.06 in terms of r.
   - The improvement of ϵ is less notable as this indicator is less sensible to the spatial distribution of the abundance values. According to this result, I remark that the best value $\epsilon = 0.08$ may represent the intrinsic accuracy of the proposed methodology.
3. The third experiment corroborates the improvement according to the registration quality underlined by the second experiment.
   - There is a clear trend of improvement in terms of r with values up to 0.83 for the algorithm MVC-NMF.
   - The average error ϵ is slightly higher in this case because of the high heterogeneity of the selected area in terms of dark abundance [see Figure 10.10 (A)]. This heterogeneity of the area makes the comparison more sensitive to PSF and adjacency effects that especially degrade the absolute levels of the abundance maps. Another reason to such error increase may come

from potential non-linearities coming from the selected portion of surface. As regards the tested techniques, parameter ϵ reveals a notable disagreement between the results obtained with VCA and, especially, spatial-VCA with regard to the ground truth. I consider this result to point to a faulty extraction of the dark source by these two approaches.

Eventually I perform a last experiment by computing the distribution of abundance values for the ground truth and the unmixing outcomes. Results of this experiment are summarized in Figure 10.12 and conclusions are detailed as follow:

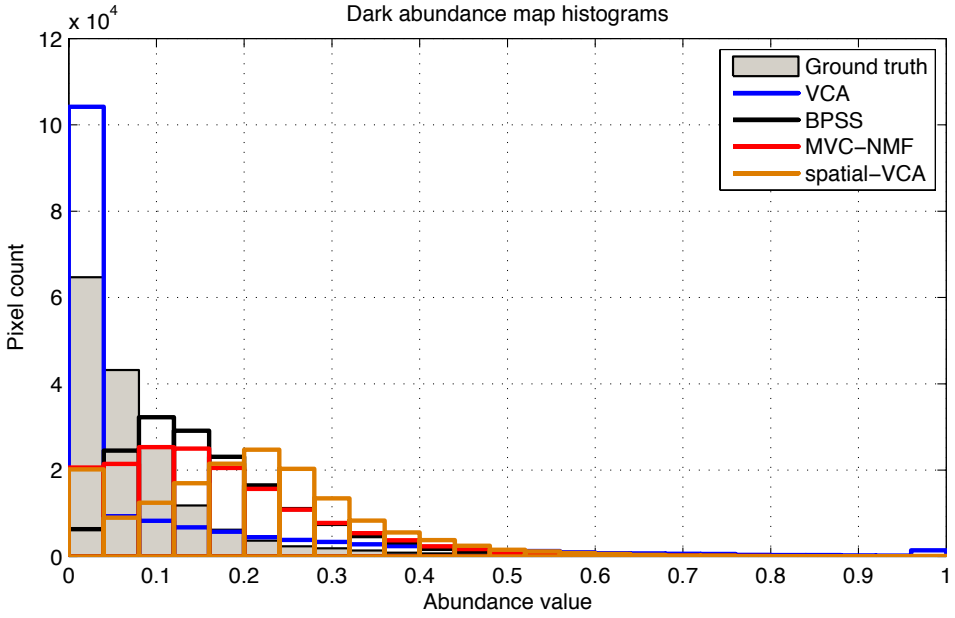

Figure 10.12.: Distribution of the dark abundances corresponding to the ground truth and the unmixing abundance maps.

- VCA: this approach severely underestimates the dark abundances in comparison with the ground truth according to the presence of null abundances. This result may be originated from the truncation of the actual abundance maps caused by the non-positivity and the sum-to-one constraints. These two restraints result in a more restrictive final abundance map of the dark sources.
- BPSS: the statistical technique presents a notable agreement with the ground truth as the corresponding histogram suffers only from a small overestimation (average abundance of 0.17 for BPSS and 0.08 for the ground truth). At this point I underline the relevance of Figure 10.12 as first conclusions drawn based on Table 10.2 seem to indicate a lower accuracy of BPSS in front of other techniques.
- MVC-NMF: the hybrid geometric/NMF-based method provides the best histogram in terms of average abundance, equal to 0.16. A little overestimation is still observed in comparison with the ground truth.
- spatial-VCA: the histogram of this approach confirms the initial conclusions drawn according to Table 10.2. As a matter of fact the dark abundances are generally overestimated with an average abundance of 0.21. The side effects resulting from the truncation imposed by the unmixing constraints is observed as it happens for the VCA case, especially for low abundance values.

I conclude this section by questioning the relatively small abundance overestimation that is observed

for the majority of the methods. This anomaly could be misleading as it may be explained conversely by underestimated abundances in the reference abundance map. In this study the ground truth is built by selecting the dark regions in the HiRISE image, that is, those pixels whose radiance values are lower than the neighboring pixels. Nevertheless, I can reasonably assume that the surrounding ice is contaminated by dust particles that are not considered in the classification process as they are not resolved spatially by HiRISE. These particles are, however, likely sensed by the CRISM instrument because of its accurate spectral discrimination. Consequently, I conclude that the average abundance of the real ground truth may be slightly higher. This would therefore shift the corresponding reference histogram in Figure 10.12 to higher abundances, thus increasing the average accuracy of methods BPSS, MVC-NMF, and spatial-VCA. The remaining differences may be related to the intrinsic limitations of the endmember extraction methods and to spurious non-linear contributions.

10.4. Conclusions

The present investigation represents an unprecedented study regarding the performances of spectral unmixing techniques applied to high resolution planetary data. First, I prove that the Russell dune of Mars is suitable to be considered as a benchmark to evaluate the capabilities of spectral unmixing under the linear mixture model. The satisfactory results obtained after comparison of the unmixing outcomes to the ground truth prove that the linearity assumption may be valid for processing CRISM images corresponding to areas of Mars with similar properties than the Russell dune. Second, relevant planetary information on the physical state of the Russell megadune has been provided by unmixing techniques. The planetary community may benefit of these results as the phenomena happening on the Russell dune are an ongoing research topic for the understanding of Mars geology and activity [63]. These two conclusions mean that the presented methodology could be applied to other CRISM observations similar to Russell's.

As for the intercomparison of endmember extraction techniques, albeit all tested methods reveal the same three physically meaningful sources, an effort of recombination is required due to repeated splitting of physical sources into a few endmembers. The reason of such anomaly is the existence of residual non-linearities that come either from the surface or from residues of the IPAG-DP. Based on original experiments I have proved that most of the discrepancies in the validation using the ground truth come from limitations of the registration process between the HiRISE and CRISM images. I draw some conclusions on each of the tested endmember extraction methods as follow:

- **VCA**. I conclude that this geometric method provides satisfactory spectral signatures while the estimated abundance maps after the endmember recombination are not satisfactory. This limitation is caused by the lack of sensitivity due to the positivity and sum-to-one constrains that are imposed on the original abundance maps. This side effect of the physical constraints causes extremely low dark abundances, frequently set to zero. I therefore deduce that the physical constraints may be less relevant when a recombination effort is needed since the physical meaning imposed by these constraints is required for the recombined sources and not for the intermediary endmembers. Nonetheless, VCA is the fastest among all techniques and therefore is of great interest to perform dimensionality reduction of large collections of hyperspectral data sets.
- **BPSS**. According to the presented results the abundance maps provided by this statistical method

are generally accurate, that is, sufficient for an initial planetary interpretation. BPSS shows significantly satisfactory performances according to its histogram and the second lowest reconstruction error in terms of reconstruction error. In addition, no recombination is needed to retrieve the abundance map related to the dark source. An advantage of BPSS is that this method provides error bars for estimated abundance due to its statistical basis. The main disadvantage of BPSS is, however, related to the high computational time. An issue deserving further research would be to evaluate the risks of extracting unphysical endmembers when performing unmixing with BPSS as it does not consider the pure pixel assumption.

- **MVC-NMF**. This method holds the first position of the ranking since it provides the best results among the four tested techniques. The abundance map corresponding to the dark source is indeed the most accurate when compared to the ground truth. In addition, MVC-NMF extracts the dark source directly without the need of the recombination process, which reasonably increases the accuracy. I deduce that this result may come from the higher sensitivity of MVC-NMF in front spatially confined physical sources as it is stated in [119]. Furthermore MVC-NMF is a very fast algorithm and results can be considered by planetary scientists as a primary quick look to reveal physical sources in a hyperspectral data set. Additionally, I propose to use this method in order to detect and evaluate subtle residues coming from faulty instrumental or atmospheric corrections.
- **spatial-VCA**. According to presented results I deduce that the combination between the VCA technique and the spatial preprocessing are affected by the lack of sensitivity induced by the physical constraints, similarly to what it happens with VCA. While spectral signatures are quite significant due to the pure pixel assumption, experimental results point to somewhat unsatisfactory abundance maps with regard to other methods. I relate this underperformance to the inherent penalization of the spatial preprocessing for spatially confined sources such as the dark features on the Russell dune [191].

As a conclusion I remark that linear spectral unmixing can be considered as a relevant tool to infer physical information on specific areas of Mars. In this study the products provided by these techniques are related to a high accuracy when compared to the independent ground truth and therefore constitute a valuable product for planetary scientists. These techniques are certainly not limited to the Russell dune and can be applied to other sites of Mars as along as the linear mixture assumption is met. An issue deserving further research is the evaluation of residual non-linearities in the central scan of observation FRT42AA. Non-linear contributions may come from the intrinsic spectral variability of the physical sources, the presence of granular intimate mixtures, and the occurrence of adjacency effects due to multiple scattering between the atmosphere and the surface. As it has been seen, these factors may result in inaccuracies affecting the estimated abundance maps. In order to improve the accuracy of the results I propose a thorough study of the image FRT42AA that would account for non-linearities by inverting a physical model of the spectra. The simulation of the spectral signatures of the physical sources using RT codes can drive the determination of a physical model of the scene based on the source abundances among other parameters. CRISM spectra can then be inverted using the determined physical model and constraining it with the estimated abundance maps as the most probable solution.

11

Retrieval of AOT using spectral unmixing

Up to this point I have proposed to exploit the concept of spectral unmixing to infer physical parameters of planetary surfaces. Nonetheless, the radiation sensed by orbital instruments is shaped by the atmospheric contribution as well as the signal that comes from the surface. Atmospheric studies are typically addressed by physically-based methods that aim at characterizing the atmospheric by means of the AOT, or τ_{aer}, for example. These methods are often unstable since the inverse problem is highly unconstrained or they are limited by the properties of the materials at the surface (e.g. the β-method adopted by the IPAG-DP does not operate for surfaces covered by CO_2 ice). In addition, physically-based methods do not typically exploit the coherency between neighboring pixels whereas it is widely known that the AOT varies slowly in the spatial dimension in most of cases, for example.

In this context our group proposes to exploit the fingerprint of atmospheric aerosols, as well as the existent spatial coherency, to derive atmospheric properties using analysis techniques based on the spectral unmixing concept[1]. In particular we address the retrieval of AOT from hyperspectral images based on linear unmixing techniques as those that have been previously presented. As it has been proved in Part III the AOT is a crucial atmospheric parameter for performing fine analysis of surface reflectance. Unlike materials at the surface, the contribution of aerosols cannot be extracted as a regular endmember as it is done for surface materials such as the dark features in chapter 10. The impact of aerosols on the radiation leaving the surface is indeed non-linear and therefore is not linearly mixed with spectral signatures of surface materials. In order to illustrate this I refer the reader to Figure 2.5 where the effect of mineral aerosols on a water ice spectrum is illustrated.

In order to account for the contribution of aerosols we propose to introduce a parametric model of the remote sensing signal into an iterative solving procedure. The TOA data are first corrected for gaseous absorption based on an initial assumption regarding the content and the spatial distribution of aerosols. Eventually, the iterative use of linear spectral unmixing techniques and a gaseous correction that is improved at each iteration allows the final estimation of the correct AOT.

[1] This work has been carried out in collaboration with the Gipsa-lab, Grenoble, France. More details are given in [103].

The outline of this chapter is as follows. First, in section 11.1 I introduce the algorithm for AOT retrieval based on a parametrized model of the TOA apparent reflectance accounting for the gas transmission and the aerosol scattering. I then report on the test of the proposed algorithm in section 11.2 on realistic synthetic data simulating the typical atmospheric conditions on Mars. Eventually, I draw the conclusions and detail the future prospects of this work in section 11.3.

11.1. Description of the algorithm

The proposed AOT retrieval algorithm is based on the RT formulation that is adopted by the IPAG-DP to perform atmospheric correction. I therefore recommend the lecture of the appendix section 14.2 since only some concepts shall be remembered in the present chapter. The TOA apparent reflectance $R_{TOA}(k;\lambda)$ at a given wavelength λ and for pixel k is expressed as a function of the gaseous vertical transmission T_{Gas} and the surface reflectance only altered by the aerosols R_{aer} as follows:

$$R_{TOA}(k;\lambda) = T_{Gas}(k;\lambda)^{\epsilon(k)} R_{aer}(k;\lambda). \tag{11.1}$$

In this formulation I remind the reader that the AOT is closely related to the exponent parameter ϵ because of the dependencies of the latter (see Equation 14.2). Based on this physically-based expression we propose an iterative strategy aiming at estimating the AOT by means of the ϵ parameter as schemed in Figure 11.1. I summarize the most important points as follows:

1. In iteration j, the original hyperspectral image $R_{TOA}(k;\lambda)$ is corrected for atmospheric effects as it is done by the IPAG-DP by following

$$R_{aer,j}(k;\lambda) = \frac{R_{TOA,j}(k;\lambda)}{T_{Gas}(k;\lambda)^{\epsilon_j(k)}}. \tag{11.2}$$

- $T_{Gas}(k;\lambda)$ is the vertical transmission of the gases and is computed depending on the topography and meteorological conditions of the processed image as it is explained in section 14.2. This parameter is not updated during the iterative process.
- In the first iteration $j = 1$, we assume a homogeneous distribution of the AOT $\tau_1(k)$ fixed at a typical average value $\bar{\tau_{aer}}$. The exponent parameter $\epsilon_1(k)$ is readily computed from the AOT following Equation 14.2.

2. Spectral unmixing is then performed on the atmospherically-corrected data set $R_{aer,j}(k;\lambda)$ using the unsupervised MVSA approach based on the linear mixture model (review Figure 8.3). The MVSA algorithm is adopted for the proposed AOT retrieval approach as MVSA is fast, simple yet not based on the pure pixel assumption. In this way, MVSA may extract the spectral signatures of the existing endmembers. Following the linear mixture model, the hyperspectral data are decomposed into a ensemble of spectral signatures $\mathbf{m}_n$ and abundance maps $\mathbf{s}_n$ that are related to the components at the surface as follows

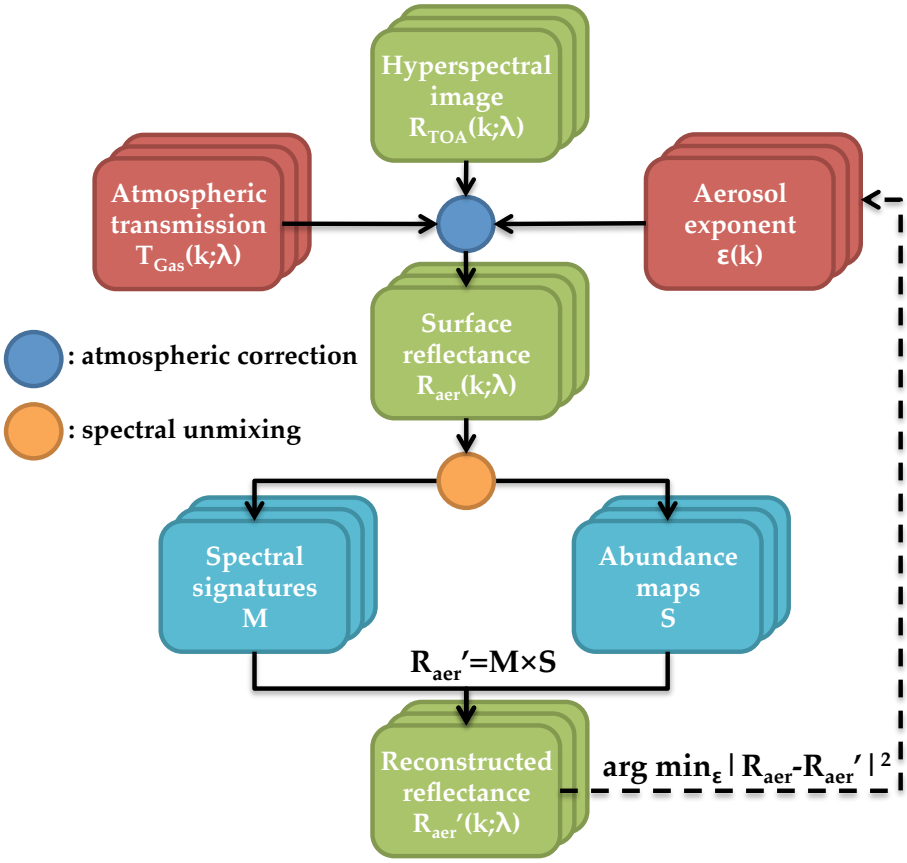

Figure 11.1.: Scheme of the algorithm for retrieval of AOT using the unmixing-based strategy.

$$R_{aer,j}(k;\lambda) = \sum_{n=1}^{N_c} \mathbf{m}_{j,n}(\lambda)\, s_{j,n,k} + e_j(\lambda), \tag{11.3}$$

$n = \{1 \ldots N_c\}, k = \{1 \ldots N_p\}$.

3. The original atmospherically-corrected image is then reconstructed using $\mathbf{m}_{j,n}$ and $\mathbf{s}_{j,n,k}$ based on Equation 10.1

$$\hat{R_{aer,j}}(k;\lambda) = R_{aer,j}(k;\lambda) - e_j(\lambda) = \sum_{n=1}^{N_c} \mathbf{m}_{j,n} s_{j,n,k}. \tag{11.4}$$

4. Then, the difference between the original and the reconstructed data set $e_j(\lambda) = R_{aer,j}(k;\lambda) - \hat{R_{aer,j}}(k;\lambda)$ is assumed to come from the atmospheric absorption residues induced by the erroneous AOT estimation. Under this assumption, the optimal exponent parameter $\epsilon(k)$ minimizes the reconstruction error as follows

$$\epsilon_{j+1}(k) = \arg\min_{\epsilon\in\Re} \left\| \ln\left(R_{TOA}(k;\lambda) - T_{Gas}(k;\lambda)^{\epsilon_{j+1}(k)} R_{aer,j}(k;\lambda) \right) \right\|, \tag{11.5}$$

$$\epsilon_{j+1}(k) = \frac{\ln\left(\sum_\lambda T_{Gas}(k;\lambda)\left(R_{TOA}(k;\lambda) - \hat{R_{aer,j}}(k;\lambda)\right)\right)}{\ln\left(\sum_\lambda T_{Gas}(k;\lambda)^2\right)}. \tag{11.6}$$

5. Points 1-4 are repeated using the retrieved $\epsilon_{j+1}(k)$ until convergence is achieved in terms of the reconstruction error.

11.2. Experiments

In order to evaluate the capabilities of the proposed AOT retrieval method based on spectral unmixing I set up an original validation based on simulated data that recreate realistic atmospheric and acquisition conditions. The following experiment constitutes the preliminary evaluation that has been done toward the full validation of the proposed algorithm.

11.2.1. Simulated data

Experiments are performed on an original 128×128-pixel synthetic data set. I consider two typical components of the surface Mars, namely mineral dust and H_2O ice, as it is done in chapter 9. CO_2 ice is not considered in the preliminary tests as the similarities between the absorption bands of the gaseous and the solid carbon dioxide may make the problem much more challenging. Similarly to chapter 9 synthetic spectra are simulated using the RT model described in [54]. In this experiment TOA apparent reflectance is simulated in the SWIR range 0.93-2.73 μm at 128 wavelengths. Figure 11.2 shows the complementary abundance maps that are used to generate the synthetic data set $R_{TOA}(k;\lambda)$. By using these two fraction maps I recreate the sub-pixel geographic mixtures between the two endmembers. As it can be seen, the majority of the pixels contains highly mixed spectra. In order to introduce some intrinsic variability into the data set I randomly generate the spectra using a varying grain size for the mineral dust particles as well as for the granular H_2O ice. The ranges of grain size are selected according to the observed properties of these materials on Mars as it is done in the study of Bernard-Michel et al. [12]. Furthermore, I simulate the acquisition conditions corresponding to the high latitudes of Mars by generating synthetic spectra at nadir ($\theta = 0^o$) with $\theta_0 = \{65^o \dots 85^o\}$. The latter angle of acquisition follows the geometry map shown in Figure 11.3 (left). By setting high SZA values, the proposed algorithm is tested under a challenging scenario as the signal coming from the surface at these incidence angles is especially fainter due to aerosols. The AOT is given by the simulated abundance map $\tau_{aer}(k)$ shown in Figure 11.3 (right). The corresponding $\epsilon(k)$ is computed following Equation 14.2 and is shown in Figure 11.4 (left). I propose to generate the AOT map using plasma fractals to give a cloud-like realistic result. In the final aerosol product [see Figure 11.3 (right)], AOT varies from 0.1 to 1.6 and the average opacity is equal to 1.2, which corresponds to a quite dusty atmospheric scenario[2].

The previous conditions set by the surface, the illumination geometry, and the atmospheric opacity are taken into account to generate the image $R_{aer}(k;\lambda)$. I then combine this intermediary product with the atmospheric effects by simply multiplying the synthetic image $R_{aer}(k;\lambda)$ by an atmospheric data set $T_{Gas}(k;\lambda)^{\epsilon(k)}$ to obtain $R_{TOA}(k;\lambda)$ according to Equation 11.1. In this way the surface, which has been previously altered by the aerosols, is altered this time by the transmission of the atmospheric gases $T_{Gas}(k;\lambda)$ also modulated by the suspended aerosols according to parameter $\epsilon(k)$. For the purpose of simulating a real scenario I adopt the gas transmission estimated from a real OMEGA image acquired over the polar regions Mars. In this way the variability of atmospheric effects depending on a heterogeneous topography are reproduced.

[2]The MATLAB code that is used for simulating plasma fractals can be found in http://library.thinkquest.org/26242/full/progs/a8.html.

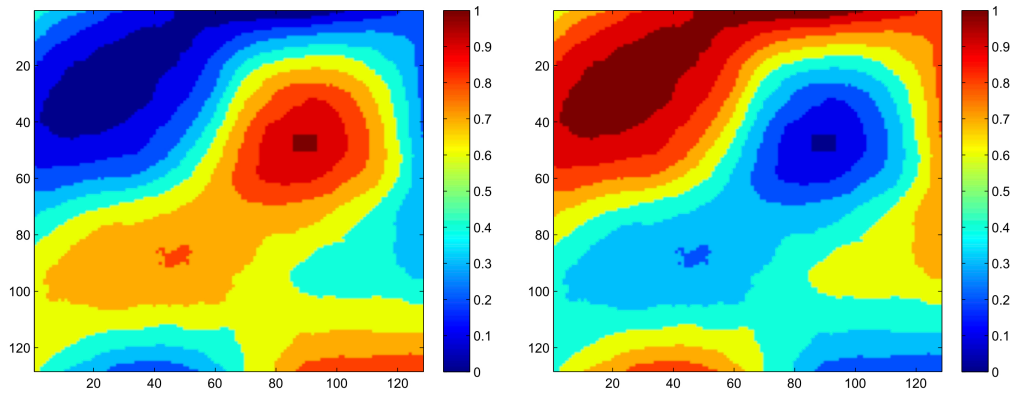

Figure 11.2.: Ground truth describing the fraction abundance of the two synthetic endmembers (water ice on the left, and mineral dust on the right) forming the simulated image.

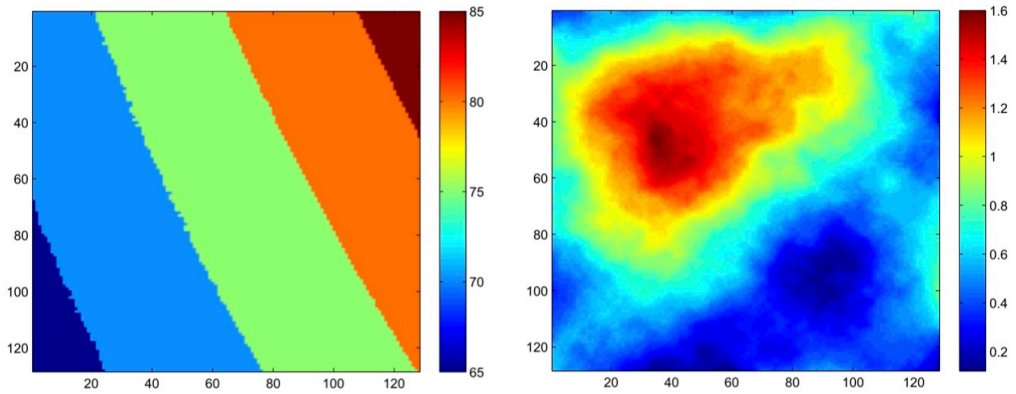

Figure 11.3.: Ground truth describing the distribution in the simulated data set of (left) the solar incident angle, and (right) the AOT or τ_{aer}.

11.2.2. Results and analysis

In the present experiment a number of 3000 iterations are carried out to estimate the original exponent $\epsilon(k)$ that is originally used in the simulation of $R_{TOA}(k;\lambda)$. The initial atmospheric conditions were previously set such as $\epsilon_0(k) = 2,\ \forall k$. The adopted value corresponds to the average value of the ground truth shown in Figure 11.4 (left). In order to evaluate the quality of the retrieval the correlation coefficient r_j and the mean squared error (MSE) e_j between the ground truth $\epsilon(k)$ and the retrieval $\epsilon_j(k)$ are computed at the j^{th} iteration such that

$$r_j = \frac{\sum\left(\epsilon_{j,k} - \sum\epsilon_{j,k}\right)\left(\epsilon_k - \sum\epsilon_k\right)}{\sqrt{\sum\left(\epsilon_{j,k} - \sum\epsilon_{j,k}\right)^2 \sum\left(\epsilon_k - \sum\epsilon_k\right)^2}}, \tag{11.7}$$

$$e_j = \sum\left(\epsilon_{j,k} - \epsilon_k\right)^2, \tag{11.8}$$

where all sums are done over all pixels, that is, $\sum_{k=1}^{Np}$.

Figure 11.5 monitors the two quality parameters according to the number of iterations. The robustness of the iterative algorithm in terms of convergence is observed as the correlation coefficient constantly increases from 0.55 to 0.75 while the MSE decreases exponentially by more than 60%.

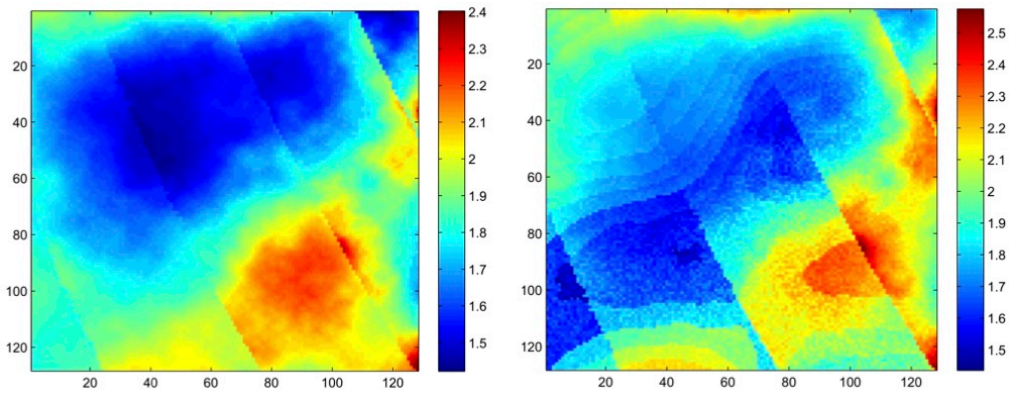

Figure 11.4.: (left) Ground truth exponent $\epsilon\,(k)$, and (right) estimate after 3000 iterations $\epsilon_{3000}\,(k)$.

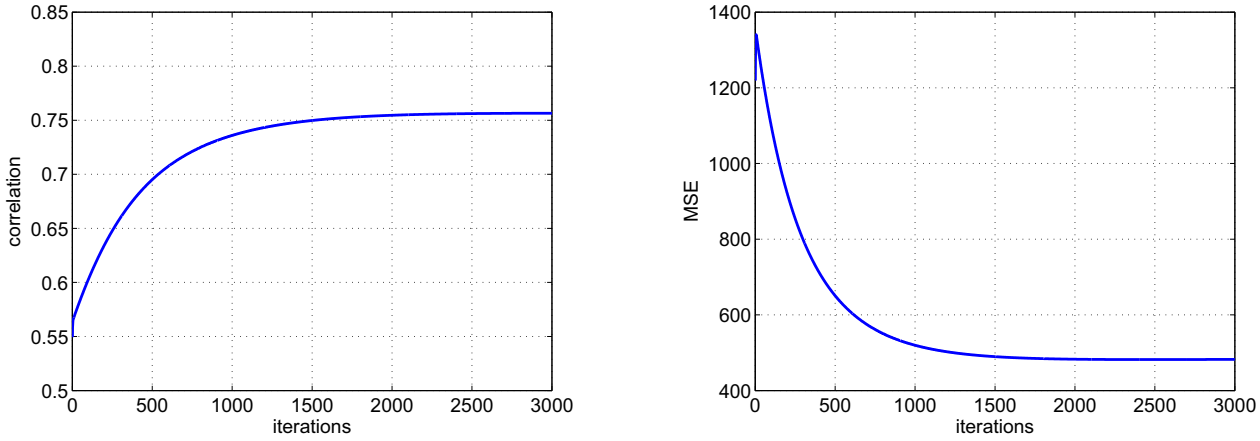

Figure 11.5.: (left) Correlation coefficient and (right) MSE between the original $\epsilon\,(k)$ and the estimate $\epsilon_j\,(k)$. j stands for the number of iteration in the AOT retrieval process.

Figure 11.4 (right) shows the estimation of the exponent parameter retrieved after 3000 iterations $\epsilon_{3000}\,(k)$ for comparison with the ground truth in Figure 11.4 (left). According to results, the retrieved AOT agrees with the ground truth at first order. First, the range of retrieved ϵ_{3000} values agree with that of the ground truth according to the color bars of each plot in Figure 11.4. Second, areas corresponding to high/low dust contents (i.e. low/high ϵ values) are assigned satisfactorily to low/high estimations of ϵ_{3000}. Nonetheless, we detect some disagreements at the contour lines corresponding to the distribution in SZA and the abundance maps. As for the former product, the related impact on the retrieval of ϵ seems to be quite critical when the illumination angle varies. We explain this effect by the relatively high incremental step that is used in the variation of θ_0. In this matter I remark that the impact on ϵ produced by the variations in θ_0 are expected as it is already present in the exponent ground truth [see Figure 11.4 (left)]. The exponent parameter actually depends on the airmass, and thus the SZA. Eventually, the retrieval strategy reveals a moderate sensitivity to the grain size of the components according to the granular pattern affecting the $\epsilon_{3000}\,(k)$ map [see Figure 11.4 (right)]. However, this source of inaccuracy is not considered to be as critical as other parameters since the variation in grain size that has been considered in the ground truth is somewhat exaggerated and is not expected to be found on the surface of Mars.

11.3. Conclusions

In this chapter an innovative approach has been introduced to retrieve the AOT of a hyperspectral image based on the spectral unmixing concept. I stress that the proposed analysis method is not based on any information on the properties of the components at the surface nor in the atmosphere. As a consequence this method is theoretically suitable to retrieve the AOT over snow-covered surfaces for which the β-method currently adopted by the IPAG-DP does not work. According to results obtained on realistic simulated data, this strategy provides rather satisfactory estimates of the dust content in the atmosphere. The main limitation is that all non-linearities in the data are assumed to come from the contribution of the aerosols. This assumption is, however, not true in reality as other non-linear contributions such as those coming from the surface or the varying acquisition conditions are expected. As a matter of fact results show an important sensitivity to the varying grain size of the surface components and to the heterogeneous illumination conditions that are considered to generate the synthetic spectra. In this matter we propose further testing to determine the limitations of the presented retrieval strategy. Subject to the obtention of satisfactory results, real CRISM and OMEGA data will be then processed and retrieved AOT values will be compared to those estimated by independent techniques.

According to the preliminary results I conclude that this original method represents the first step toward a non-physically-based analysis approach for retrieval of AOT. For instance, the results obtained in this study prove that the retrieved AOT may be suitable to be used as a first guess that may be refined afterward by more sophisticated methods.

Summary and future prospects

This part of the dissertation has been dedicated to investigate the capabilities of the concept referred to as source separation in the analysis of hyperspectral images of Mars. Source separation is also referred to as spectral unmixing when dealing with hyperspectral images since it aims at "unmixing" the observed spectra into constituent spectral signatures. In the present part of the thesis I have investigated the role of spectral unmixing as a robust tools to identify and extract endmembers related to the surface, the atmosphere or even the instrument itself. In spectral unmixing each endmember is characterized spectrally and spatially by means of a spectral signature and a fraction abundance map, respectively. These outcomes have proved to be decisive in the analysis of collections of terrestrial and planetary remotely sensed data.

A major issue that I have addressed in this part is the evaluation of the linear mixture model. Only spectral unmixing methods based on this somewhat reductionist supposition have been considered as techniques based on a non-linear model are generally supervised and more complex to implement. In chapter 9 and chapter 10 I have carried out experiments on simulated data and real CRISM images, respectively. In the first study I have proved that the widely used endmember extraction method VCA is suitable to process mixed data composed of geographic sub-pixel mixtures that are similar to those found on Mars. The results of this first study have been then questioned in the second investigation by arguing that the spatial resolution of the CRISM instrument may be too high for the existence of this type of linear mixtures. Nonetheless, results obtained in chapter 10 on the Russell crater megadune observed by CRISM prove that the linear mixture model may be accurate enough to distinguish surface materials and provide reliable information on their composition. In this chapter I have also introduced an original strategy to evaluate the capabilities of any endmember extraction algorithm in an independent manner by means of a ground truth.

Globally the results obtained on the Russell dune are satisfactory according to the presented reference. The reason to this success is the predominance of geographic sub-pixel mixtures in this particular area of Mars. Similarly I conclude that other regions of Mars observed by CRISM may be appropriate for being analyzed by these techniques. Based on this original study I propose the use of unsupervised unmixing techniques based on the linear mixture model to process large collection of planetary hyperspectral images. While some attention must be paid to the most challenging cases techniques such as MVC-NMF or BPSS are theoretically suitable to provide accurate results at first order. Nonetheless, I underline the likely difficulty of these algorithms to extract satisfactorily the physical sources in the image in some cases. In the study of the Russell dune an endmember recombination is required by some of the tested methods to reconstruct the test dark source. This postprocessing is done manually as it requires the analysis of the unmixing outcomes based on some knowledge on the expected scenario. This drawback prevents the processing of large collections of planetary data sets in a fully

unsupervised manner. I hence infer that the adoption of the linear mixture model at the CRISM spatial resolution may restrain the unsupervised analysis of hyperspectral data to the rather restricted case where a single type of mixture predominates (i.e. linear geographical mixtures). This issue points out that future prospects may consider the incorporation of physical constraints into the unmixing process to obtain accurate results without the need of any postprocessing. I propose that these constraints consider phenomena such as the intimate mixtures that may happen at the surface or the multiple scattering in the atmosphere. In fact these two factors of the remote sensing problem cause non-linear mixtures at the signal level that are not considered by a linear mixture model. In the future I suggest the consideration of improved non-linear methods that gradually become an interesting alternative such as those in [18, 75]. Another future prospect in this matter would be to use the BRDF of the materials at the surface estimated with the MARS-ReCO approach to project the data onto a more linear space in which perform a classical linear unmixing such as it is done in [41].

An undeniable benefit of spectral unmixing is the ability of performing dimensionality reduction. In this matter I have proved that a hyperspectral image can be transformed from a set of a few hundreds spectral bands into a few relevant feature bands. This information can definitely benefit planetary scientists who are interested in analyzing large series of images. This key advantage is based on the low computational time of the so-called geometric techniques that typically perform endmember extraction in a few tens of seconds. The outcomes coming from these techniques can be considered as a quick-look that helps unveiling the prevailing components in the data. In this matter I also propose the use of fast unmixing techniques to drive iterative postprocessing strategies that may use the endmembers to detect and monitor residues coming from faulty atmospheric or instrumental corrections.

In chapter 11 I have eventually explored the potential of spectral unmixing for characterizing planetary atmospheres. Albeit further investigations must be performed in the future preliminary results evidence that unmixing techniques may be appropriate to drive retrieval strategies. According to the obtained results I conclude that the proposed iterative strategy based on the MVSA method and a formulation of the at-sensor signal can provide satisfactory initial estimates of AOT over an arbitrary scene of Mars. Subject to further testing, at the present time there is no theoretic limitation regarding the composition of the surface on which the AOT is estimated. I underline this last property to be very interesting for processing hyperspectral images acquired over the high latitudes of Mars for which traditional AOT retrieval algorithms (e.g. the β-method adopted by the IPAG-DP) do not often work.

Finally I envisage the investigation of the benefits of spectral unmixing on different types of data. Up to this time I have used these tools to decompose at-sensor spectra into constituent spectral signatures while the source separation concept can be applied to any type of data. In subsection 4.2.4 I have presented a new type of planetary product derived from the multi-angle capabilities of the CRISM sensor, namely photometric curves depending on viewing angle. Similarly to the spectral unmixing of spectra, photometric curves may be potentially decomposed into constituent angular endmembers. In this case source separation techniques shall aim at separating components related to the physical state of the materials rather than their chemical composition. The moderate spatial resolution of the photometric curves (~180 m/pixel) should be enough to include several terrain units corresponding to a different photometric nature. In addition to the angular dimension source separation techniques may also consider the spectral dimension when applied to spectro-photometric curves. To our knowledge this type of investigation has never been addressed before.

Conclusions and future prospects

Under the title **Evaluating the potential of statistical and physical methods to analyze hyperspectral images of Mars - Application to the multi-angle instrument CRISM**, this Ph.D. thesis proposes a series of tools to analyze the information encompassed by observations of Mars produced by the CRISM instrument. The Compact Reconnaissance Imaging Spectrometer for Mars is a hyperspectral imager aboard the Mars Reconnaissance Orbiter that provides unique data on the surface and the atmosphere of the Red Planet. In the targeted mode CRISM acquires systematically multi-angle observations that allow an innovative and fine exploration of Mars. The complexity and size of these data represent nonetheless a real hurdle for planetary scientists. This thesis proposes a series of tools that facilitates the visualization, manipulation and analysis of CRISM observations while considering the whole information that they encompass. Although the proposed algorithms are recurrently tested and validated on selected CRISM images they are designed to be reusable for other images belonging to many different contexts.

The present work is divided into four main parts. The first part establishes the environment in which the work is framed. The others refer explicitly to the three major contributions that have been made in response to the need of a combined set of unsupervised tools to process hyperspectral data in a fast and efficient manner and of physically-based algorithms to fully exploit the potential of the multi-angle hyperspectral CRISM instrument. Going into more detail:

1. In Part I I have defined the framework of this thesis by firstly detailing the reason why imaging spectrometers constitute a key tool in the exploration of the Solar system and, in particular, of Mars. In this matter I have introduced the basis of hyperspectral imaging by detailing the related instruments, the resulting products, the major families of tools for processing hyperspectral images, and the related challenges in terms of data visualization and analysis. The first chapter ends by describing the CRISM instrument whose key technological attributes are its high spatial resolution up to 18 m/pixel and its multi-angle capabilities, the latter feature making available up to eleven viewing geometries from a same martian target. The second chapter describes the physical background in planetary remote sensing, with special attention to the processes that shape the spectral radiation arriving to the MRO spacecraft. Based on a radiative transfer model, I have proposed to adopt a robust and smart expression of the at-sensor signal that decomposes it into several simpler contributions. The theory in this chapter is the basis of the physically-based atmospheric correction approaches that are described in the following parts of the dissertation.
2. In Part II I have investigated the existent limitations of the CRISM data products as regards the objectives of this thesis. For instance, the radiometric quality of the released CRISM products is observed to be affected by spectral anomalies coming simultaneously from intrinsic limitations of push broom scanners and from the martian scenario itself. In the fourth chapter of this thesis

I have showed how the presence of carbon dioxide in the atmosphere, as well as in some specific regions of the surface of Mars, amplifies some technical limitations of the CRISM instrument. Furthermore the release of CRISM data does not consider the generation of an integrated multi-angle product to perform further processing on it nor classical issues in remote sensing such as the compensation for atmospheric effects. In this context I have proposed an original and automatic data pipeline that addresses the previous issues among others in a sequential and efficient manner. The recurrent and successful use of the data pipeline throughout the thesis for processing CRISM observations corresponding to different martian scenarios validates it as a convenient and automatic tool for planetary scientists interested in improving meaningfully the original radiometric quality of CRISM data and in advanced products such as atmospherically-corrected CRISM images.

3. In Part III I have exploited the multi-angle capabilities of the CRISM instrument in order to define an original method to correct for atmospheric effects. As originally intended the multi-angle dimension of CRISM eases the separation of the contributions coming from the surface and the atmosphere using radiative transfer modeling. Traditional single-shot instruments must inevitably assume a Lambertian surface to correct satisfactorily for anisotropic effects of atmospheric aerosols. Unfortunately this assumption is proved to bias severely the obtained estimates of the surface properties. The use of multiple measurements from a given target observed at different observation angles eases considerably this complexity. The problem remains, however, complicated as the consideration of the surface BRDF in radiative transfer-based inversion methods increases exponentially the computational burden. Under these circumstances I have proposed a robust atmospheric correction method that is based on an original expression of the at-sensor radiation using a semi-empirical model for the surface BRDF and a Green's function to model the atmosphere. The proposed algorithm MARS-ReCO inherits the state of the art from atmospheric correction of multi-angle sensors in Earth observation.

4. In Part IV I have looked into the use of spectral unmixing techniques for an unsupervised analysis of CRISM hyperspectral images. Hyperspectral images are not only associated to a unique information but also to a high dimensionality that might seem redundant at first. As a consequence the retrieval of meaningful information on the different contributions enclosed in a hyperspectral image cannot be done straightforwardly by simple inspection. Moreover, although physically-based approaches are very useful to perform fine analysis of specific martian areas, they prove to be limited when a priori information on the scene is not available. In front of this hurdle automatic algorithms are increasingly demanded to accurately process large collections of hyperspectral observations. In this context I have investigated the use of spectral unmixing techniques that automatically decompose a hyperspectral image into a set of physically meaningful endmembers. An intercomparison between several state-of-the-art endmember extraction methods has been carried out based on an original strategy using high resolution imagery as a reference. As shown by the results unmixing techniques are able to detect significant martian endmembers and to quantify their fraction at the surface by means of abundance maps. This type of product constitutes a valuable quick look for planetary scientists. Also in this thesis I have explored the use of unmixing techniques for the retrieval of physical quantities related to the atmosphere.

Many statements and conclusions have been highlighted in the individual conclusions of each part of this thesis. I outline some of them here as the main concluding remarks:

- The **improvement of the radiometric quality of CRISM data** by the data pipeline represents a major contribution of this thesis. Fine analysis of hyperspectral data requires low levels of noise and accurate sensed radiances. For instance, physical models are complex tools that often seek weak signals and therefore become sensitive to minor artifacts affecting the images. The CRISM instrument represents a unique tool as regards its accuracy, performances and design. Unfortunately, the increasingly demanding applications along with the also demanding martian scenario result in an inevitable sensitivity of the former to instrumental artifacts. The proposed data pipeline is designed to overcome these technical limitations. I highlight the **correction for the spectral smile effect** that is addressed in this dissertation. Although the presented results show a notable improvement of severely affected images in terms of radiometric quality, I remark that the smile effect may result in the degradation of meaningful data that might become unrecoverable. As it is shown in chapter 4 spectral features encompassed by the most affected columns might be too much degraded to be recovered by desmiling methods. In my opinion the main reason of this drawback is not linked to CRISM itself but to the martian scenario itself. CRISM has been designed with a push broom concept and therefore the smile effects are somehow inevitable. However, the remote sensing of Mars with hyperspectral pushbroom scanners is particularly affected by the carbon dioxide that predominates in the atmosphere and in the high latitudes of Mars. This chemical component has strong and steep absorption bands that increase the smile effects, as well as the complexity of other technical issues. In this situation slight non-uniformities affecting the two-dimensional matrix of pushbroom scanners are severely magnified when sensing carbon dioxide, resulting in data artifacts such as the smile effect. According to my experience acquired throughout this thesis an improved spectral calibration of the instrument would inevitably end up in smile effects due to the strong steepness of the mentioned spectra. This is especially the case of images acquired over the high latitudes of Mars that are rich in frozen CO_2 on the surface and gaseous CO_2 in the atmosphere. This limitation could be overcome in the future by advanced methods inspired by the desmiling algorithm presented in this dissertation. As I detail in the conclusions of Part II, advanced indicators of the spatial distortion induced by the smile effect may be used for the sake of a refined desmiling. To conclude this point I stress the potential ability of the presented desmiling technique to carry out an improved flat fielding of CRISM hyperspectral images. This goal can be achieved by incorporating the desmiling approach into the CRISM-DP. In this way the bland images that are used to generate the flat fields could be corrected for the smile effect, which is the cause of the faulty flat fielding mentioned in the second part of this dissertation.
- Another contribution of this thesis as regards the data pipeline is the **generation of advanced products**, namely atmospherically corrected images and the multi-angle CSP product. These two outcomes of the proposed IPAG-DP have proved to be crucial in many experiments carried out in this thesis. I highlight the study of the Russell dune based on spectral unmixing techniques applied to the central scan of the observation FRT42AA. Before the unmixing step this image is corrected for atmospheric effects by the IPAG-DP. This preprocessing is crucial to focus exclusively on the features linked to the surface. Similarly, the MARS-ReCO method processes the CSP products created from CRISM observations by the IPAG-DP. This multi-angular product has

revealed to be key for the exploitation of CRISM multi-angle observations that are originally released as a set of eleven independent products. As for the drawbacks of the proposed pipeline, I spotlight the **correction for heterogeneous illumination conditions** within a single targeted CRISM observation. After some investigation I have come to the conclusion that an improved photometric normalization using digital terrain models is not possible nowadays from an operational point of view. Such an advanced correction requires DTMs linked to a high resolution and a high accuracy as it is shown in [182]. Although the DTMs provided by the HiRISE instrument may satisfy these requirements, the required registration process represents the major hurdle. First, registration algorithms are often supervised as they require a set of control points. Second, even the slightest error in the registration results may end in large bias affecting the photometrically corrected CRISM image. In this context I recommend to conduct future efforts toward the accurate fusion of these two products by advanced unsupervised registration methods that start to emerge nowadays. Eventually, I draw the attention to the fact that processes such as multiple reflections between multiple facets must be considered for the sake of an improved photometric normalization, especially when dealing with high resolution imagery such as CRISM's.

- The algorithm **MARS-ReCO** symbolizes one of the major contributions of this thesis. In this matter we are pioneers in developing an atmospheric correction method that can consider a non-Lambertian surface regardless of its location and its composition. Presented results obtained on CRISM observations acquired over the Gusev crater confirm this statement. Nonetheless, I stress that further testing of MARS-ReCO is required when dealing with other areas on Mars. First, the testing shall be performed on the landing site of the MER Opportunity, Meridiani Planum, for which photometric data are available in [85]. Although the proposed atmospheric correction has proved to be accurate over minerals surfaces, the real challenge is found in the high latitudes of Mars. As mentioned throughout this thesis, these regions of Mars are very challenging in terms of acquisition geometry and estimation of the aerosol optical thickness. First, the poles of Mars are related to high Sun zenith angles that may put in trouble MARS-ReCO as it was shown by the sensitivity study. A second sensitivity study should be therefore carried out simulating reference data using scattering properties of martian ices. The main problem is, however, that these data are unknown, the retrieval of the photometric properties of martian ices and snow being exactly one of the main objectives of MARS-ReCO. In this context I propose to use scattering models built from measurements in laboratory. Second, the currently adopted AOT retrieval algorithm is not operational for surfaces covered by frozen carbon dioxide due to the superposition of the ice absorption bands with those belonging to the gaseous state of this component. In this matter I have proposed in the partial conclusions of Part III the development of a new version of MARS-ReCO by taking into account the spectral information enclosed by hyperspectral imagery. By increasing the information in the present inverse problem, it should be possible to retrieve simultaneously the surface BRF and the AOT regardless of the surface type.
- Also regarding the atmospheric correction of CRISM multi-angle observations, the MARS-ReCO algorithm represents a unprecedented tool to study the **photometric properties of the surface of Mars from space**. While this type of study has been already done by rovers on the surface, these robots are limited to very precise locations on Mars. By contrast, CRISM makes available data regarding 15 by 15 km sites spread over the entire planet. Similar to what I have done on the Gusev crater, any location can be potentially considered to be atmospherically corrected using

MARS-ReCO as long as the acquisition and the atmospheric conditions under which the corresponding image has been acquired are in agreement with the results of the sensitivity study. The study of the photometry of the surface is crucial to understand the physical state of the materials coexisting in it. As mentioned, the next step in this matter is the processing of polar images encompassing geological formations made of frozen carbon dioxide or water. Although the existence of the former component has been repeatedly ensured in the past, the different physical states that this type of ice can adopt on Mars still remain a mystery. I therefore conclude that an operating tool such as the MARS-ReCO method represents a unique opportunity to address such an issue. Again, the success in the future improvement of this atmospheric correction algorithm shall be crucial in the achievement of the mentioned goal. Eventually, another future prospect would be to use the retrieved BRDF for the whole spectral range of CRISM to map the bolometric albedo (i.e. the reflectance integrated in all angular directions and in the spectral dimension) of several martian sites as Bell et al. do using Pancam data [78].

- As for the use of the spectral unmixing concept to analyze CRISM hyperspectral images, the presented results have proved that the estimated abundances maps of the Russell dune largely agree with the independent ground truth. Therefore, it seems reasonable to state that this result can be repeated for other site of Mars sharing the conditions happening in the Russell dune. Nonetheless, a closer look to the results reveals a meaningful issue, the non-validity of the **linear mixing model**. Although this assumption has proved to be largely correct for data with a moderate spatial resolution such as OMEGA's, the higher performances of CRISM expose some intrinsic limitations of the linear mixing model. I therefore stress that while unmixing techniques based on this assumption can be considered to be reliable, results must be considered as a first approximation of the planetary reality embodied in a CRISM hyperspectral image. As it is has been shown, the presence of often weak non-linearities in the data such as residual instrumental artifacts or atmospheric residues results in a significant impact on the unmixing outcomes. Unfortunately, such impact transforms the unmixing of the data into a semi-supervised process due to the required recombination step. In my opinion two main considerations must be done at this point. First, the extracted endmembers in their spectral and abundance forms represent a remarkable product reducing a few hundred spectral bands to a few features, highlighting the major contributions enclosed in the data. Even in the presence of non-linearities, these outcomes provide useful information on the radiometric quality of the data, the accuracy of the atmospheric correction and the major terrain units. Some postprocessing is of course necessary if more refined products are desired. Second, non-linear spectral unmixing algorithms represent a potential and more robust alternative to linear-based techniques. Recent technical advances are gradually developing more unsupervised methods that may be used in broader situations. Unfortunately, non-linear methods are nowadays related with several technical hurdles toward the automatic processing of hyperspectral images.

Part V.

Appendices

12 Acronyms

- AERONET: AErosol RObotic NETwork.
- AOT: Aerosol Optical Thickness.
- ASRVN: AERONET-based Surface Reflectance Validation Network.
- AVIRIS: Airborne Visible Infrared Imaging Spectrometer.
- BRDF: Bidirectional Reflectance Distribution Function.
- BRF: Bidirectional Reflectance Factor.
- BPSS: Bayesian Positive Source Separation.
- CAT: CRISM Analysis Toolkit.
- CDR: Calibration Data Records.
- CHRIS: Compact High Resolution Imaging Spectrometer.
- CRISM: Compact Reconnaissance Imaging Spectrometer for Mars.
- CSP: "Courbe Spectro-Phometrique, spectro-photometric in French.
- DDR: Derived Data Record.
- DISORT: Discrete Ordinates Radiative Transfer Program for a Multi-Layered Plane-Parallel Medium.
- DN: Digital Number.
- DTM: Digital Terrain Model.
- EPF: Emission Phase Function.
- ESA: European Space Agency.
- FCLS: Fully Constrained Least Squares.
- FFT: Fast Fourier Transform.
- FOV: Field Of View.

- FRT: Full-Resolution Targeted.
- FWHM: Full-Width at Half Maximum.
- HDRF: Hemispherical Directional Reflectance Function.
- HFC: Harsanyi–Farrand–Chang.
- HiRISE: High Resolution Imaging Science Experiment.
- HRL: Half-Resolution Long.
- HRS: Half-Resolution Short.
- HRSC: High Resolution Stereo Camera.
- HySime: Hyperspectral Signal-subspace Identification by Minimum Error.
- ICA: Independent Component Analysis.
- IFOV: Instantaneous Field Of View.
- IR: InfraRed.
- ISM: Infrared SpectroMeter.
- LUT: Look-up table.
- MAIAC: MultiAngle Implementation of Atmospheric Correction.
- MGS: Mars Global Surveyor.
- MER: Mars Exploration Rovers.
- MEX: Marx EXpress.
- MISR: Multi-angle Imaging SpectroRadiometer.
- MNF: Maximum Noise Fraction.
- MOLA: Mars Orbiter Laser Altimeter.
- MODIS: Moderate Resolution Imaging Spectroradiometer.
- MRF: Markov Random Field.
- MRO: Mars Reconnaissance Orbiter.
- MSE: Mean Squared Error.
- MVC-NMF: Minimum Volume Constrained Non-negative Matrix Factorization.
- MVSA: Minimum Volume Simplex Analysis.
- NASA: National Aeronautics and Space Administration.
- NIMS: Near Infrared Mapping Spectrometer.
- NMF: Non-negative Matrix Factorization.
- OMEGA: Observatoire pour la Minéralogie, l'Eau, les Glaces, et l'Activité.
- OSU: Optical Sensor Unit.
- Pancam: Panoramic Camera.
- PCA: Principal Component Analysis.
- PDS: Planetary Data System.
- PROBA: PRoject for On–Board Autonomy.
- PSF: Point Spread Function.

- RMSE: Root Mean Square Error.
- ROI: Region Of Interest.
- RT: Radiative Transfer.
- RTE: Radiative Transfer Equation.
- VCA: Vertex Component Analysis.
- VD: Virtual Dimensionality.
- VIRTIS: Visible and Infrared Thermal Imaging Spectrometer.
- VNIR: Visible and Near-InfraRed.
- VZA: View Zenith Angle.
- SNR: Signal to Noise Ratio.
- SWIR: Short Wavelength InfraRed.
- SZA: Sun Zenith Angle.
- THEMIS: Thermal Emission Imaging System.
- TRDR: Targeted Reduced Data Records.

13

Mathematical appendix

13.1. Green's function

A Green's function is an integral kernel that can be used to solve an inhomogeneous differential equation with boundary conditions. It serves roughly an analogous role in partial differential equations as do Fourier series in the solution of ordinary differential equations. Here we expose a brief introduction. Further reading can be obtained in [5].

For an arbitrary linear differential operator $\widetilde{L}$ in three dimensions, the Green's function $G(\mathbf{r}, \mathbf{r}')$ is defined by analogy with the one-dimensional case by

$$\widetilde{L}G(\mathbf{r}, \mathbf{r}') = \delta(\mathbf{r} - \mathbf{r}'). \tag{13.1}$$

The solution to $\widetilde{L}\phi = f$ is then

$$\phi(\mathbf{r}) = \int G(\mathbf{r}, \mathbf{r}') f(\mathbf{r}') d^3\mathbf{r}'. \tag{13.2}$$

Explicit expressions for $G(\mathbf{r}, \mathbf{r}')$ can often be found in terms of a basis of given eigenfunctions $\phi_n(\mathbf{r}_1)$ by expanding the Green's function

$$G(\mathbf{r}_1, \mathbf{r}_2) = \sum_{n=0}^{\infty} a_n(\mathbf{r}_2) \phi_n(\mathbf{r}_1), \tag{13.3}$$

and delta function,

$$\delta^3 (\mathbf{r}_1 - \mathbf{r}_2) = \sum_{n=0}^{\infty} \phi_n (\mathbf{r}_1) \phi_n (\mathbf{r}_2) . \tag{13.4}$$

By plugging in the differential operator, solving for the variables a_n, and substituting into G, the original non-homogeneous equation then can be solved.

The coefficient S of $\ln(1/r)$ in all normalized fundamental Green's function solutions

$$\phi (x, y; x_0, y_0) = S (x, y; x_0, y_0) \ln (1/r) + T (x, y; x_0, y_0) , \tag{13.5}$$

with

$$r = \sqrt{(x - x_0)^2 + (y - y_0)^2}, \tag{13.6}$$

of the elliptic partial differential equation

$$Ku = u_{xx} + v_{yy} + A(x, y)u_x + B(x, y)u_y + C(x, y)u = 0, \tag{13.7}$$

with analytic coefficients is an analytic function of four variables and is equal to the Riemann function $S = R^*(\xi, \eta; \xi_0, \eta_0)$ of the conjugate equation

$$K^*v = v(\xi, \eta) - (av)(\xi) - (bv)(\eta) + cv = 0, \tag{13.8}$$

which can be produced from $Ku = 0$ by the change of variables

$$\begin{aligned} \xi &= x + iy, \\ \eta &= x - iy, \\ \xi_0 &= x_0 + iy_0, \\ \eta_0 &= x_0 - iy_0, \\ 4a (\xi, \eta) &= A (x, y) + iB (x, y) , \\ 4b (\xi, \eta) &= A (x, y) - iB (x, y) , \\ 4c (\xi, \eta) &= C (x, y) . \end{aligned} \tag{13.9}$$

13.2. Fourier transform

13.2.1. Fourier series expansion

In this section, $f(x)$ denotes a function of the real variable x. This function is usually taken to be periodic, of period 2π, which is to say that $f(x+2\pi) = f(x)$, for all real numbers x. I attempt to write such a function as an infinite sum, or series of simpler 2π-periodic functions. I start by using an infinite sum of sine and cosine functions on the interval $[-\pi, \pi]$ and we then discuss different formulations and generalizations. More details on Fourier series expansions can be found in [152].

For a periodic function $f(x)$ that is integrable on $[-\pi, \pi]$, the numbers

$$a_n = \frac{1}{\pi}\int_{-\pi}^{\pi} f(x)\cos(nx)\,dx, \quad n \geq 0,$$

and

$$b_n = \frac{1}{\pi}\int_{-\pi}^{\pi} f(x)\sin(nx)\,dx, \quad n \geq 1,$$

are called the Fourier coefficients of f. One introduces the partial sums of the Fourier series for f, often denoted by

$$(S_N f)(x) = \frac{a_0}{2} + \sum_{n=1}^{N} [a_n \cos(nx) + b_n \sin(nx)], \quad N \geq 0.$$

The partial sums for f are trigonometric polynomials. One expects that the functions $S_N\, f$ approximate the function f, and that the approximation improves as N tends to infinity. The infinite sum

$$\frac{a_0}{2} + \sum_{n=1}^{\infty} [a_n \cos(nx) + b_n \sin(nx)],$$

is called the Fourier series of f. The notion of a Fourier series can also be extended to complex coefficients to become the basis for the Discrete Fourier transform (DFT).

13.2.2. Fast Fourier transform

A fast Fourier transform (FFT) is an efficient algorithm to compute the DFT and its inverse. A FFT algorithm computes the DFT and produces exactly the same result as evaluating the DFT definition directly in a much faster manner. More details can be found in [17].

Let $x_0, ..., x_{N-1}$ be complex numbers. The DFT is defined by the formula

$$X_k = \sum_{n=0}^{N-1} x_n e^{-i2\pi k \frac{n}{N}},\ k = 0, \dots N-1.$$

Evaluating this definition directly requires $O(N^2)$ operations: there are N outputs X_k, and each output requires a sum of N terms. An FFT is any method to compute the same results in $O(N \log N)$ operations.

To illustrate the savings of an FFT, consider the count of complex multiplications and additions. Evaluating the DFT's sums directly involves N^2 complex multiplications and $N(N-1)$ complex additions [of which $O(N)$ operations can be saved by eliminating trivial operations such as multiplications by 1]. The well-known radix-2 Cooley–Tukey algorithm, for N a power of 2, can compute the same result with only $(N/2)\log_2 N$ complex multiplies (again, ignoring simplifications of multiplications by 1 and similar) and $N \log_2 N$ complex additions. In practice, actual performance on modern computers is usually dominated by factors other than arithmetic and is a complicated subject, but the overall improvement from $O(N^2)$ to $O(N \log N)$ remains.

By far the most common FFT is the Cooley-Tukey algorithm [39]. This is a divide and conquer algorithm that recursively breaks down a DFT of any composite size $N = N_1 N_2$ into many smaller DFTs of sizes N_1 and N_2, along with $O(N)$ multiplications by complex roots of unity traditionally called twiddle factors.

The most well-known use of the Cooley-Tukey algorithm is to divide the transform into two pieces of size $N/2$ at each step, and is therefore limited to power-of-two sizes, but any factorization can be used in general. These are called the radix-2 and mixed-radix cases, respectively. Although the basic idea is recursive, most traditional implementations rearrange the algorithm to avoid explicit recursion. Also, because the Cooley-Tukey algorithm breaks the DFT into smaller DFTs, it can be combined arbitrarily with any other algorithm for the DFT.

13.3. Gaussian quadrature rule

In numerical analysis, a quadrature rule is an approximation of the definite integral of a function, usually stated as a weighted sum of function values at specified points within the domain of integration. An n-point Gaussian quadrature rule, named after Carl Friedrich Gauss, is a quadrature rule constructed to yield an exact result for polynomials of degree $2n-1$ or less by a suitable choice of the points x_i and weights w_i for $i = 1, ..., n$. Further reading can be obtained in [169].

The domain of integration for such a rule is conventionally taken as $[-1, 1]$, so the rule is stated as

$$\int_{-1}^{1} f(x)dx \approx \sum_{i=1}^{n} w_i f(x_i).$$

Gaussian quadrature as above will only produce accurate results if the function $f(x)$ is well approximated by a polynomial function within the range $[-1, 1]$. The method is not, for example, suitable for functions with singularities. However, if the integrated function can be written as $f(x) = W(x)g(x)$,

where $g(x)$ is approximately polynomial, and $W(x)$ is known, then there are alternative weights w_i such that

$$\int_{-1}^{1} f(x)dx = \int_{-1}^{1} W(x)g(x)dx \approx \sum_{i=1}^{n} w_i g(x_i).$$

For the integration problem stated above, the associated polynomials are Legendre polynomials, $P_n(x)$. With the n^{th} polynomial normalized to give $P_n(1) = 1$, the i^{th} Gauss node, x_i, is the i^{th} root of P_n; its weight is given by

$$w_i = \frac{2}{\left(1 - x_i^2\right)\left[P_n'(x_i)\right]^2}.$$

Some low-order rules for solving the integration problem are listed in Table 13.1. The integration problem can be expressed in a slightly more general way by introducing a positive weight function ω into the integrand, and allowing an interval other than $[-1, 1]$.

Number of points, n	Points, x_i	Weights, w_i
1	0	2
2	$\pm 1\sqrt{3}$	1
3	0 $\pm\sqrt{3/5}$	$8/9$ $5/9$
4	$\pm\sqrt{(3-2\sqrt{6/5})/7}$ $\pm\sqrt{(3+2\sqrt{6/5})/7}$	$8/9$ $5/9$
5	0 $\pm\frac{1}{3}\sqrt{(5-2\sqrt{10/7}}$ $\pm\frac{1}{3}\sqrt{(5+2\sqrt{10/7}}$	$128/225$ $\frac{322+13\sqrt{70}}{900}$ $\frac{322-13\sqrt{70}}{900}$

Table 13.1.: Low-order rules of the Legendre polynomials

The error of a Gaussian quadrature rule can be stated as follows. For an integrand which has $2n$ continuous derivatives,

$$\int_a^b \omega(x)f(x)dx - \sum_{i=1}^{n} w_i f(x_i) = \frac{f^{(2n)}(\xi)}{(2n)!}(p_n, p_n),$$

for some ξ in (a, b), where p_n is the orthogonal polynomial of degree n and where

$$(f, g) = \int_a^b \omega(x)f(x)g(x)dx.$$

In the important special case of $\omega(x) = 1$, we have the error estimate

$$\frac{(b-a)^{2n+1}(n!)^4}{(2n+1)[(2n)!]^3} f^{(2n)}(\xi), \qquad a < \xi < b.$$

Important consequence of the above equation is that Gaussian quadrature of order n is accurate for all polynomials up to degree $2n-1$.

13.4. Convolution theorem

Let f, g belong to $L^1(\mathbf{R}^n)$. Let F be the Fourier transform of f and G be the Fourier transform of g:

$$F(\nu) = \mathcal{F}\{f\} = \int_{\mathbb{R}^n} f(x) e^{-2\pi i x\cdot\nu} \mathrm{d}x,$$
$$G(\nu) = \mathcal{F}\{g\} = \int_{\mathbb{R}^n} g(x) e^{-2\pi i x\cdot\nu} \mathrm{d}x,$$

where the dot between x and ν indicates the inner product of $\mathbf{R}^n$. Let h be the convolution of f and g

$$h(z) = \int_{\mathbb{R}^n} f(x) g(z-x) \mathrm{d}x.$$

Now notice that

$$\begin{aligned}\int\int |f(z)g(x-z)|\, dx\, dz &= \int |f(z)| \int |g(z-x)| dx dz \\ &= \int |f(z)|\, \|g\|_1\, dz = \|f\|_1 \|g\|_1.\end{aligned}$$

Hence by Fubini's theorem we have that $h \in L^1(\mathbb{R}^n)$ so its Fourier transform H is defined by the integral formula

$$H(\nu) = \mathcal{F}\{h\} = \int_{\mathbb{R}^n} h(z) e^{-2\pi i z\cdot\nu} dz = \int_{\mathbb{R}^n}\int_{\mathbb{R}^n} f(x) g(z-x) dx e^{-2\pi i z\cdot\nu} dz.$$

Observe that $|f(x)g(z-x)e^{-2\pi i z\cdot\nu}| = |f(x)g(z-x)|$ and hence by the argument above we may apply Fubini's theorem again:

$$H(\nu) = \int_{\mathbb{R}^n} f(x) \left(\int_{\mathbb{R}^n} g(z-x) e^{-2\pi i z\cdot\nu} dz \right) dx.$$

Substitute $y = z - x$; then $dy = dz$, so:

$$\begin{aligned} H(\nu) &= \int_{\mathbb{R}^n} f(x) \left(\int_{\mathbb{R}} g(y) e^{-2\pi i (y+x)\cdot \nu} dy \right) dx, \\ &= \int_{\mathbb{R}^n} f(x) e^{-2\pi i x \cdot \nu} \left(\int_{\mathbb{R}^n} g(y) e^{-2\pi i y \cdot \nu} dy \right) dx, \\ &= \int_{\mathbb{R}^n} f(x) e^{-2\pi i x \cdot \nu} dx \int_{\mathbb{R}^n} g(y) e^{-2\pi i y \cdot \nu} dy. \end{aligned}$$

These two integrals are the definitions of $F(\nu)$ and $G(\nu)$, so:

$$H(\nu) = F(\nu) \cdot G(\nu).$$

QED [185].

14

Postprocessing CRISM images

In this appendix I describe those blocks of the IPAG-DP that have been adopted from existing procedures in the CAT, that have not been completely devised in the framework of this thesis, or that were already developed.

14.1. Destriping algorithm

A destriping technique is proposed by the CRISM team via the CAT. This filtering method in the flavor of [65] is described by Parente in [136] as follows:

1. First, the hyperspectral data cube is averaged over the along-track direction for each spectral band resulting in a two-dimensional image representing an estimate of the detector matrix. A trimmed average is used instead of a regular mean because of the presence of dropout pixels (see subsubsection 4.1.1.2).
2. A Gaussian smoothing filter is used over this image to remove calibration variations among detector elements. The destriping method for CAT users allows the adjustment of the input spatial kernel size and the standard deviation in the Gaussian filter (the larger the spread, the smoother the results). After exhaustive testing on several CRISM images, I propose to adopt a 30-pixel kernel size and a 15-pixel Gaussian spread for the 600-column FRT images. These values are divided by a factor two for HRL and HRS observations while they are set to 4 and 2 for the 60-column EPF images, respectively. Experiments demonstrate that these values provide a good trade-off between destriping accuracy and preservation of the radiometric accuracy.
3. A residual image is generated by dividing the original detector image by the smoothed one, being the residual image the correction factor to be applied in order to obtain the optimal calibration from the initial one.
4. This residual factor is applied to filter each line of the original image.

In order to evaluate the destriping method proposed by the CAT, Figure 14.1 shows the results of destriping the original IR spectral band 10 of the central scan FRT64D9, which is originally shown in Figure 4.2. As it can be seen, the stripes have nearly disappeared while preserving the main features of this area of Mars.

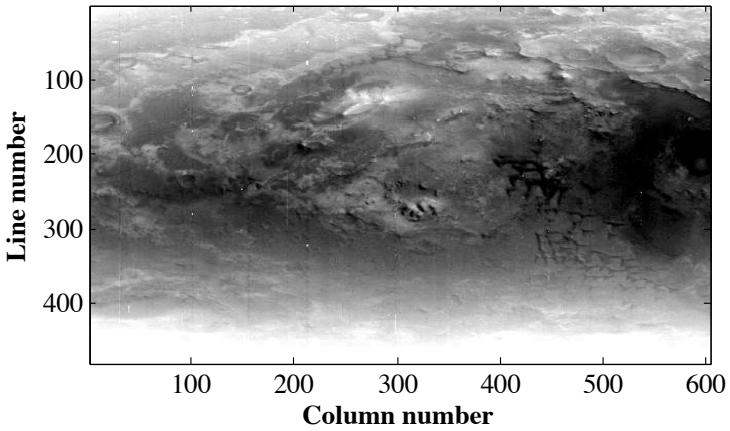

Figure 14.1.: Destriped FRT64D9 IR band 10.

I propose to carry out further investigation by investigating the central scan FRT64D9 in another data space defined by an MNF transformation (see subsubsection 1.3.2.3). An **MNF rotation** produces new components, or eigenimages, that are ordered according to SNR after two cascaded PCA transformations and a noise whitening step [67]. The first PCA decorrelates and rescales the noise in the data based on the noise covariance matrix. In the case of CRISM the covariance matrix of the noise is calculated based on the noise file of each image stored in the UB CDR (see Table 3.1). Eventually, a second PCA is applied to the noise-whitened data. The transformed data set can be divided into significant eigenimages with high eigenvalues (i.e. corresponding to high SNR) and noise-dominated components corresponding to low eigenvalues. The MNF transformation is very appropriate to determine the features that exist in the data and their relevance in terms of SNR.

Figure 14.2 shows the three eigenimages corresponding to the largest eigenvalues of the CRISM central scan FRT64D9 before and after destriping. The three eigenimages represent the spatial features that are related to a higher SNR, that is, the most robust components against noise. First, Figure 14.2 (top) illustrates how the striping effect affects the second and the third MNF eigenimages, which embrace the average albedo of the scene and the typical cross-track pattern due to the spectral smile artifact (see subsubsection 4.1.2.1 for more details), respectively. Indeed, the stripes are quite energetic and therefore impact other features due to their non-linear properties. As it can be seen in Figure 14.2 (bottom), the adopted destriping method overcomes this residual bias as the columnar pattern due to stripes is satisfactorily removed from the MNF eigenimages. Further experiments showed that the stripping effect reappears in eigenimages corresponding to lower eigenvalues, closer to the noise domain.

The present results show satisfactory performances in the original and the MNF space. Similar results were obtained for other CRISM images. The filtering method is very fast and process a single CRISM observation (encompassing the eleven hyperspectral images) in some tens of seconds in a traditional computer. In addition, the correction can be tuned to embrace a large range of cases. However, this option also represents a disadvantage as the cut-off frequency, which is defined by kernel size and

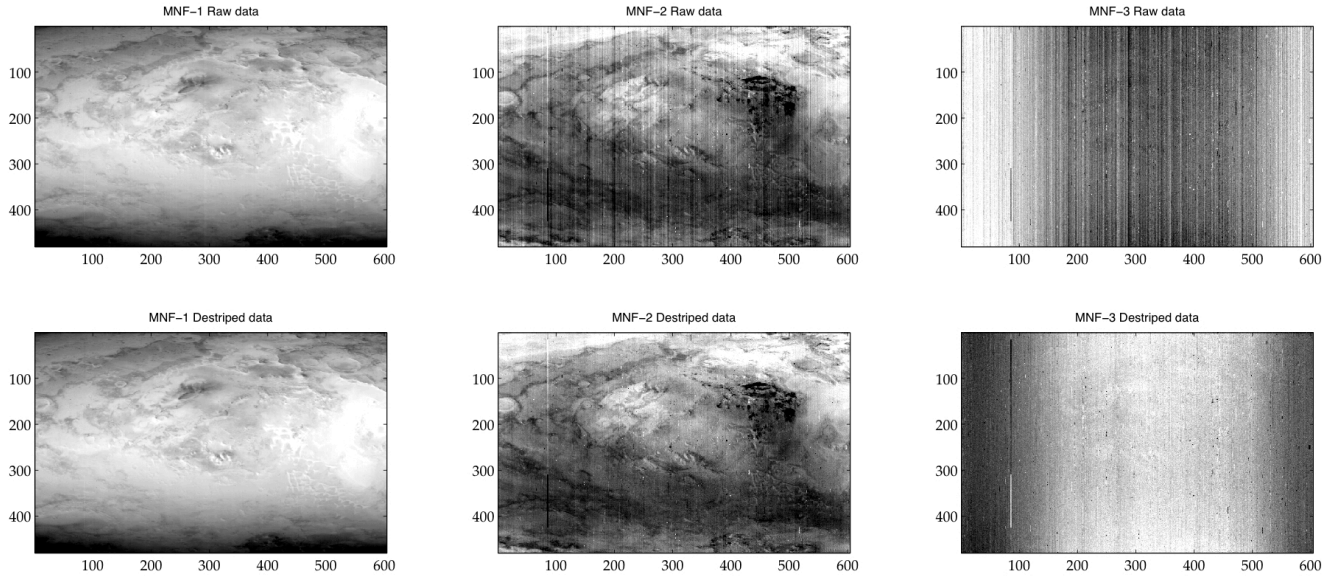

Figure 14.2.: MNF eigenimages of the central scan of observation FRT64D9 corresponding to the three highest eigenvalues. Eigenimages are plotted before (first row) and after (second row) applying the destriping method proposed in the CAT. Note the columnar pattern introduced by stripes in the second and third eigenimages corresponding to the PDS-released data.

width, must be set, making the destriping method somewhat semi-supervised. Eventually, I remark that even though a satisfactory cut-off value is selected, any high-frequency vertical structure within a martian scene may be considered as a stripe by the destriping algorithm and thus it is suitable to be mistakenly filtered. This side effect must be considered in the subsequent processing of the data.

14.2. Atmospheric correction

The adopted method by the IPAG-DP for atmospheric correction is based on the work of Douté in [52, 53]. In short, atmospheric effects are compensated by using a parametrization of the radiative coupling that happens between mineral aerosols and CO_2 gas and by determining the absorption band depth at 2 μm, among other factors. This coupling comes from the absorption and multiple scattering that photons undergo when interacting with the gas particles and the aerosols. The strategy for atmospheric correction is based on several reasonable assumptions:

1. Water ice aerosols are not considered by assuming that there are not ice clouds or their contribution to the remotely sensed signal is minimal.
2. The optical thickness of aerosols τ_{aer} is constant over the area covered by a CRISM observation. This assumption is reasonable because of the limited spatial extent of CRISM targeted observations (~80 km^2).
3. The optical path length of the observation, expressed by the airmass ν, is long enough such that the coupling between the gases and the aerosols is predominant over other effects. This condition is satisfied by CRISM multi-angle observations because of their intrinsic range in emergence angle from -70° to 70°.
4. The optical depth layer is assumed to follow an exponential drop off with a typical scale. The

scale height of the aerosols, or H, is considered to be known, adopting a value around 8-11 km as suggested by several studies such as [181].

5. The surface is assumed to behave as a Lambertian scatterer. In this way the surface is characterized by its Lambertian albedo q_L, only depending on wavelength. Nonetheless, the proposed algorithm minimizes the sensitivity of the aerosol retrieval on this assumption. Because the radiative coupling between aerosols and gas is sensitive to the surface properties through multiple scattering between the surface and the atmosphere, the AOT is weakly dependent on the Lambertian assumption.
6. The absence of frozen carbon dioxide on the surface is assumed. As a matter of fact, the currently adopted method for atmospheric correction does not operate for icy surfaces as the related absorption features at 2 μm overlap with those coming from the CO_2 gas.
7. Absorption of atmospheric gases behaves as a multiplicative factor on the TOA radiance resulting from the reflection of solar light by the surface and the aerosols.

According to the last assumption, the TOA radiance observed by the CRISM instrument is written such that (the dependence of all parameters on wavelength have been omitted for brevity):

$$L_{TOA}\left(\theta_0,\theta,\varphi\right) \approx T_{gas}\left(h,lat,long\right)^{\epsilon\left(\theta_0,\theta,\varphi,\tau_{aer},H,q_L\right)} L_{aer}\left(\theta_0,\theta,\varphi\right), \tag{14.1}$$

where the effects of gases are characterized by the spectral transmission of the atmosphere along the vertical dimension T_{gas} and L_{aer} is the TOA radiance altered only by aerosols. The former term is calculated for each pixel of a hyperspectral image based on the Line-By-Line radiative transfer model (LBLRTM) described in [38]. In this calculation we consider the vertical compositional and thermal profiles of the actual date, location and altitude using the European Mars climate database [61]. More details on the generation of T_{gas} for a given CRISM observation can be found in [52].

According to Equation 14.1, the contribution of the gases is scaled by an exponent ϵ that accounts for the acquisition geometry defined by the angular triplet $(\theta_0,\theta,\varphi)$, the dust content by means of the AOT τ_{aer}, the scale height H, and the Lambert albedo of the surface q_L. Factor ϵ is further decomposed into two terms such that

$$\epsilon\left(\theta_0,\theta,\varphi,\tau_{aer},H,q_L\right) = \psi\left(\nu\right)\beta\left(\theta_0,\theta,\varphi,\tau_{aer},H,q_L\right). \tag{14.2}$$

First, factor ψ only depends on the acquisition geometry and thus can be easily determined from ancillary data. Second, factor β expresses specifically the effect of aerosol particles on the gaseous absorption and depends on the aerosol content, their vertical distribution, the acquisition geometry, and, to a lesser extend, the surface albedo.

The atmospheric parameter β provides the means for retrieving the dust content over a given scene because it directly depends on the AOT and is invertible provided that H is known and q_L can be estimated. On the one hand, factor β can be readily evaluated from CRISM observations. This done by comparing the absorption depth at 2 μm in an observed spectrum with the equivalent feature in the aerosol-free transmission spectrum $T_{gas}(h,lat,long)$ that is calculated by the LBLRTM and subsequently

scaled by $\psi(\nu)$. On the other hand, a LUT of synthetic data stores the dependency of factor β regarding aerosol content and vertical distribution, acquisition geometry, and surface albedo. In this way, the AOT, as well as the Lambertian albedo of the surface q_L, are retrieved by iterative inversion of the LUT embodying the TOA model by using the TOA radiance L_{TOA} at 2 μm and the estimation of factor β as input parameters. The choice to work at this specific wavelength range makes that the previous desmiling of the data is crucial for a good atmospheric correction. The LUT is computed by a radiative transfer algorithm based on the optical properties of aerosols derived from multi-angle CRISM observation by Wolff et al. in [187].

The AOT values estimated by the presented method have proved to be robust in comparison with other independent techniques. Table 14.1 summarizes the comparison of the estimated AOT values by the so-called β-method for a set of CRISM observations that have been acquired on the landing site of the MER Spirit. This rover is equipped with the Pancam instrument that can measure the AOT by directly looking at the Sun and comparing the observed transmission with solar reference data. As it can be seen, the agreement between the two data sets is quite notable. The slight differences between the estimated AOTs may be explained by the fact that the β-method cannot see low aerosol layers contrarily to the Pancam instrument.

Retrieval method \ CRISM observation	7D6C	812F	B6B5	3192	CDA5
Proposed method	1.41	1.00	0.46	0.38	0.33
Pancam instrument on MER	1.29	0.90	0.47	0.31	0.41

Table 14.1.: AOT retrieved for a set of CRISM observations based on the proposed β-method and on-ground measurements realized by the Pancam instrument aboard the MER Spirit.

Once the AOT, or τ_{aer}, over a given image is estimated, the radiative transfer formulation in Equation 14.1 allows the calculation of the radiance coming from the surface that is altered only by the atmospheric aerosols, that is, $L_{aer}(\theta_0, \theta, \varphi)$. The absorption by the gases is compensated by ratioing the observed spectrum by the corresponding modified transmission spectrum such that

$$L_{aer}(\theta_0, \theta, \varphi) \approx \frac{L_{TOA}(\theta_0, \theta, \varphi)}{T_{gas}(h, lat, long)^{\epsilon(\theta_0, \theta, \varphi, \tau_{aer}, H, q_L)}}. \tag{14.3}$$

The resulting TOA parameter $L_{aer}(\theta_0, \theta, \varphi)$ is used in Part III to retrieve the surface reflectance using a method which is not based on the Lambertian assumption. This expression stresses the importance of an accurate wavelength calibration of L_{TOA} as the one proposed in subsubsection 4.1.3.2. Equation 14.3 indeed requires the position of the several strong atmospheric absorption bands to be equal in the L_{TOA} and the T_{gas} spectra. Strong spectral spurious spikes can happen otherwise.

The presented algorithm for correction of atmospheric effects allows an operational processing of CRISM observations. On the one hand, the retrieved AOT values have been proved to be robust against other independent measurements. Furthermore, the assumptions on which the proposed retrieval method is based have been proved to be reasonable in the processing of CRISM observations. On the other hand, a first order estimate of the surface reflectance is inferred by means of the ratioing by the modified gaseous transmission of Equation 14.3 and by means of the correction of the aerosol

contribution. This product is refined by further processing in Part III of this thesis.

14.3. Generation of an integrated multi-angle product

The first step toward the extraction of spectro-photometric curves from a CRISM observation is the generation of a data object that incorporates the eleven hyperspectral images forming a single multi-angle observation. In this way, the proposed IPAG-DP spatially rearranges the spectra corresponding to the set of eleven hyperspectral images to generate the so-called CSP cube. With this aim, the central scan is first binned by a factor ten to match the spatial resolution of the EPF images. The CRISM team did not consider necessary to preserve the full resolution for the bracketing images due to downlink limitations and since the downgraded resolution of the EPF is enough for the characterization of the atmosphere. This represents a disadvantage of the CRISM instrument in front of other multi-angle spectrometers such as MISR in which all angular images are acquired at the same spatial resolution. The whole sequence of images are then projected onto a common geographical space in which a regular grid of **super-pixels** is defined. Figure 14.3 illustrate this fusion step by showing the approximative grid over the projected footprints of individual images for a given CRISM observation. We note the rather good overlap of the set of hyperspectral images, thus assuring the existence of a high number of super-pixels that are sensed at several emergence angles. In this matter, approximatively 30% of the scene defined for a CRISM observation are scanned by 4 or more angular scans.

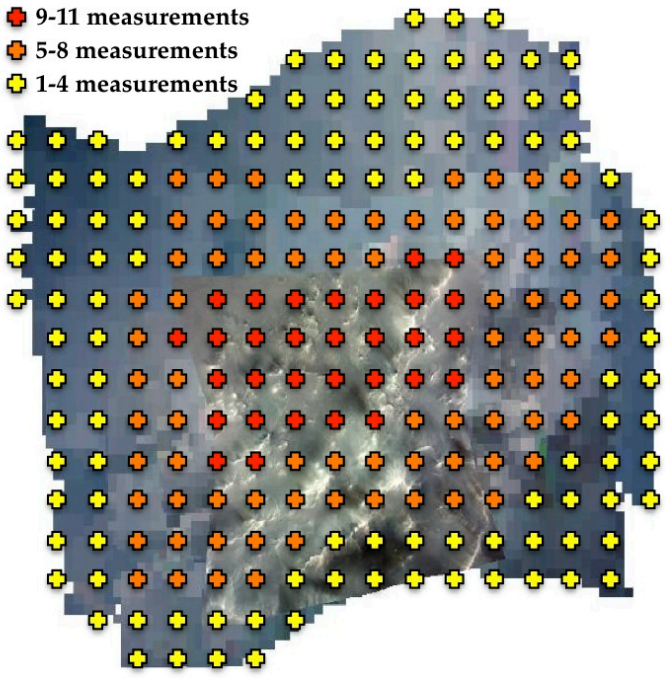

Figure 14.3.: Same as Figure 1.20 with overlapping grid pointing to the location of the super-pixel centers (colored crosses) that are used in the construction of the CSP cube corresponding to the CRISM observation. The color code describes the number of available angular measurements. The grid presented here is approximative and it is usually more dense, generally one super-pixel for each pixel of the EPF images (~180 m/pixel).

After the definition of the set of super-pixels, the CSP data cube is constructed by arranging the corresponding spectra according to the angular configuration (i.e. the rank of the scan from '01' to '0D',

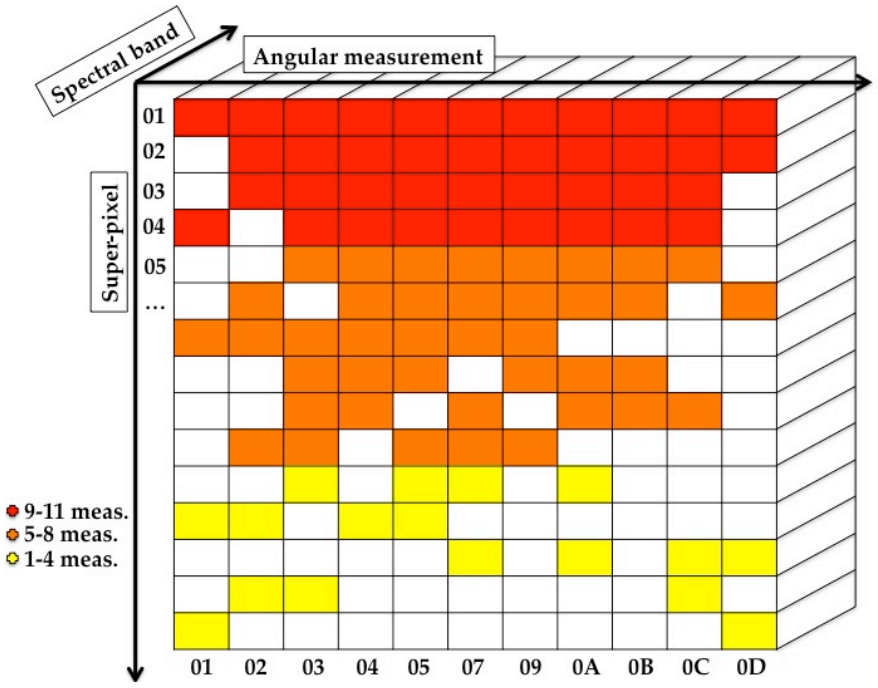

Figure 14.4.: Scheme of a CSP cube in which we define a horizontal dimension containing the photometric curves ordered by scan rank from '01' to '0D' Central measurement '07' corresponds to a binned version of the central scan. The set of super-pixels to which the photometric curves belong are arranged sequentially along a vertical dimension by the number of available angular measurements. Each line corresponds to a cross in Figure 14.3 and follows the same color code. The spectral dimension corresponds to the set of wavelengths of a typical CRISM spectrum.

horizontal dimension. See section 1.4) and the super-pixel index (vertical dimension). Consequently the sequence of up to eleven spectra forming each super-pixel, or spectro-photometric curve is arranged along the horizontal dimension. Figure 14.4 shows a scheme of a CSP data product to illustrate the arrangement. Under this configuration, a spectro-photometric curve corresponds to a horizontal matrix of elements, while a photometric curves is composed by a line of elements. This new data cube provides the means to utilize the multi-angle data provided by the CRISM sensor as it is shown in Part III. However, we remind the reader that the spatial resolution of the CSP data cube is degraded in front of the maximum capabilities of CRISM as its spatial resolution can be up to ~180 m/pixel, the resolution of the EPF images.

15

Article detailing the method for correction of the smile effect affecting CRISM data appeared in the IEEE Transactions on Geoscience and Remote Sensing

Spectral Smile Correction of CRISM/MRO Hyperspectral Images

Xavier Ceamanos, *Student Member, IEEE*, and Sylvain Douté

***Abstract*—The Compact Reconnaissance Imaging Spectrometer for Mars (CRISM) is affected by a common artifact to pushbroom-type imaging spectrometers, the so-called "spectral smile." For this reason, the central wavelength and the width of the instrument spectral response vary according to the spatial dimension of the detector array. As a result, the spectral capabilities of CRISM get deteriorated for the off-axis detector elements while the distortions are minimal in the center of the detector array, the so-called "sweet spot." The smile effect results in a data bias that affects hyperspectral images and whose magnitude depends on the column position (i.e., the spatial position of the corresponding detector element) and the local shape of the observed spectrum. The latter is singularly critical for images that contain chemical components having strong absorption bands, such as carbon dioxide on Mars in the gas or solid phase. The smile correction of CRISM hyperspectral images is addressed by the definition of a two-step method that aims at mimicking a smile-free spectral response for all data columns. First, the central wavelength is uniformed by resampling all spectra to the sweet-spot wavelengths. Second, the nonuniform width of the spectral response is overcome by using a spectral sharpening which aims at mimicking an increase of the spectral resolution. In this step, only spectral channels particularly suffering from the smile effect are processed. The smile correction of two CRISM images by the proposed method show remarkable results regarding the correction of the artifact effects and the preservation of the original spectra.**

***Index Terms*—Compact Reconnaissance Imaging Spectrometer for Mars (CRISM), hyperspectral imagery, imaging spectrometers, Mars, planetary remote sensing, spectral smile.**

I. Introduction

THE COMPACT Reconnaissance Imaging Spectrometer for Mars (CRISM) is a visible/short-wave infrared hyperspectral imager on board of the Mars Reconnaissance Orbiter spacecraft. In the targeted mode, CRISM aims at mapping the mineralogy of Martian key areas at high spectral (544 spectral channels) and spatial (15–19 m/pixel) resolution. This is done by two spectrometers (VNIR for the visible and near-infrared and IR for the short-wave infrared) that cover the 362–3920 nm range [1]. Each targeted CRISM observation is composed of a nadir hyperspectral image at high-spatial resolution and a sequence of ten spatially binned off-nadir images that are acquired before and after flying over the target. Thanks to this particularity of CRISM, multiangle hyperspectral data from the same Martian site are made available. The set of low-spatial resolution images, the so-called emission phase function (EPF), was originally intended for atmospheric studies as it is done in [2] and [3]. Nevertheless, the multiangle capabilities of CRISM can be further exploited for the 4-D exploration (i.e., one spectral, one angular, and two spatial dimensions) of Mars, as it is done for other Earth-based spectrometers such as the Compact High Resolution Imaging Spectrometer/Project for On Board Autonomy (CHRIS/PROBA) [4], [5]. In particular, this type of multiangular imaging spectrometers may be used for retrieving spectrophotometric signatures of materials in the surface, depending on the observation geometry. These signatures would be of great interest in order to delineate and characterize Martian sites by image processing and modeling.

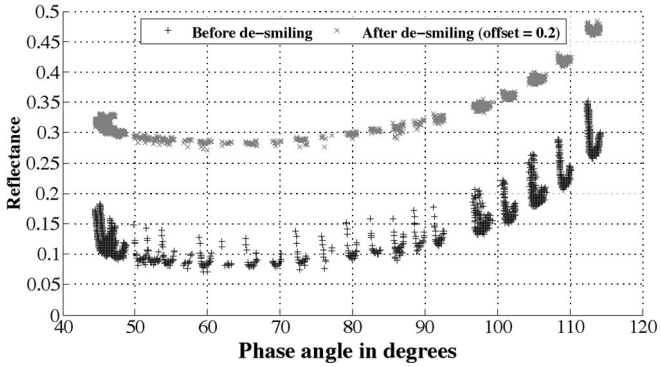

Fig. 1. Reflectance values of channel IR 155, observation FRT5AE3. Data of the 11 scans are plotted before and after desmiling (offset for clarity).

Nevertheless, pushbroom-type spectrometers need to be carefully corrected for instrumental artifacts before data exploitation. In particular, CRISM is affected by spectral smile, a common artifact to pushbroom-type sensors to which CRISM belongs. The smile effect is caused by optical distortions onto the spatial/spectral detector array which make the instrument spectral response nonuniform for the cross-track dimension. As a consequence, data belonging to the same spectral channel are acquired according to different spectral parameters, and therefore, the coherent analysis of the spectra making the image turns into an unreliable task [2], [6], [7]. In this paper, we propose a "desmiling" method that minimizes the smile effects of a CRISM hyperspectral observation while preserving the information coming from the observed Martian site.

Spectrophotometric signatures may be particularly corrupted by the smile effect. Fig. 1 shows a sample of the 4-D object

Manuscript received December 4, 2009; revised May 31, 2010. Date of publication September 20, 2010; date of current version October 27, 2010. The work within the Vahiné project was supported in part by the Centre National d'Etudes Spatiales through its R&T Systèmes Orbitaux program and in part by the Agence Nationale de la Recherche under Grant ANR-07-MDCO-013.

The authors are with the Laboratoire de Planétologie de Grenoble (Centre National de la Recherche Scientifique—Université Joseph Fourier), 38041 Grenoble Cedex 9, France (e-mail: xavier.ceamanos@obs.ujf-grenoble.fr; sylvain.doute@obs.ujf-grenoble.fr).

Color versions of one or more of the figures in this paper are available online at http://ieeexplore.ieee.org.

Digital Object Identifier 10.1109/TGRS.2010.2064326

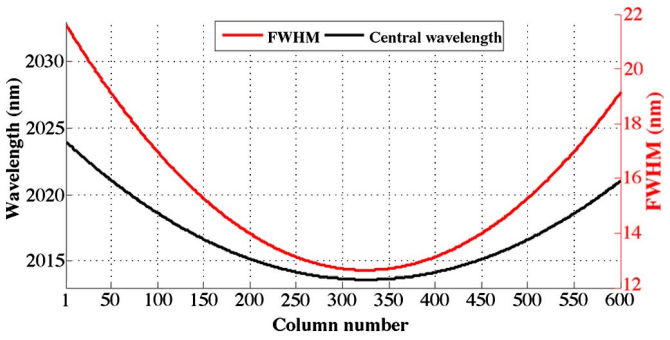

Fig. 2. Central wavelength and $FWHM$ according to column position of CRISM spectral channel IR 155.

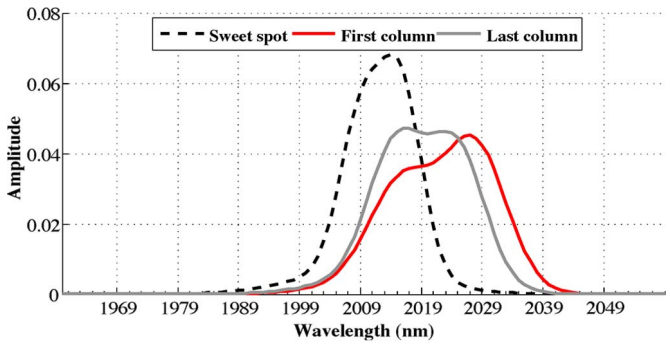

Fig. 3. PSF belonging to three cross-track positions of CRISM channel IR 155. Dashed line corresponds to the average PSF of the sweet spot.

that we constituted from CRISM observation FRT5AE3. The black crosses represent all reflectance values of a single channel before the correction while the gray ones show the same data after applying the desmiling method that is presented in this paper. Both data are plotted according to the phase angle, which describes the acquisition geometry. First, the CRISM data show a repetitive smile pattern that is caused by the correlation of the smile bias (depending on the column position) and the cross-track variation of the phase angle. This effect may corrupt the spectrophotometric signatures since a given terrain unit is typically sensed by detector elements belonging to different column positions (and thus different spectral responses) throughout the 11 acquisitions. It can be seen that the addressed desmiling method strongly reduces the smile bias while preserving the main reflectance dependence on the phase angle.

This paper is organized as follows. First, spectral smile is introduced in Section II along with its consequences on the CRISM spectral response and data. The desmiling method is put forward in Section III, then followed by experiments in Section IV. Finally, conclusions are drawn in Section V.

II. Spectral Smile

A. Definition and Consequences

Spectral smile is widely referred as cross-track low-frequency artifacts that affect spectroimages. In pushbroom-type spectrometers, the received light corresponding to a line of adjacent terrain units is scattered according to wavelength before being projected onto a spatial/spectral detector array. Due to aberrations in imaging optics, the projection becomes defective, thus resulting in spatial and spectral artifacts (i.e., keystone and spectral smile, respectively) [8].

The smile effect results in two main consequences that affect the instrument spectral response. First, the distortions in the projection make that the light corresponding to a given wavelength is sensed by more than one line of detector elements, some of them assigned to a different spectral range. Second, the spectral resolution becomes poorer progressing toward the off-axis detector elements due to a decrease in the projection sharpness. As a result of these effects, both the central wavelength and the width of the point spread function (PSF) of the detector elements vary according to the spatial dimension of the instrument which corresponds to the columns in the data. Fig. 2 shows the central wavelength and the full-width at half maximum (*FWHM*) of the spectral channel corresponding to 2013 nm. In particular, CRISM shows an increasing error as the off-axis detector elements are inspected. Fig. 3 depicts the PSF of three different positions within the same spectral channel. The dashed line corresponds to the average PSF of the so-called "sweet spot", the central detector elements where the distortions are minimal. The plain lines illustrate the PSF shifting and broadening that happen at the edges of the detector array.

The distortions in the PSF parameters affect the data acquisition. In particular, off-axis spectra suffer from spectral shifting and amplitude smoothing. The magnitude of both effects depends on the column position and the shape of the observed spectra, the latter being critical for steep spectra (e.g., absorption bands). In this case, the slightest inaccuracy in the acquisition may result in a significant error bias. Fig. 8 (left) shows the typical cross-track brightness gradient due to the smile effect of a spectral channel encompassing an absorption band.

B. Mars Case

The planet Mars represent a challenging scenario regarding the smile correction due to the presence of carbon dioxide (CO_2). In fact, the atmosphere of Mars consists of 95% CO_2 gas, which has very strong absorption bands for the near and short-wave infrared. As a result, the atmosphere of Mars is a source of the smile effect that must be taken into account in each image for the sake of a good data analysis. An accurate atmospheric correction may remove most of the smile effects since the surface of Mars is mostly composed by "flat-spectrum" minerals that do not lead the smile effect. In the literature, CRISM hyperspectral images are typically corrected for atmospheric effects (and thus partially desmiled) by techniques based on the volcano-scan technique that was originally developed by the Observatoire pour la Minéralogie, l'Eau, les Glaces et l'Activité (OMEGA) team. A description of this technique can be found in the supplementary materials of [9].

However, the prior strategy becomes unsatisfactory in two cases. First, atmospheric signatures in CRISM data may be of interest for some studies such as a surface pressure investigation based on the probing of the atmospheric CO_2 absorption bands [10] or water vapor and carbon monoxide observations [2]. This type of atmospheric studies becomes unviable in the presence of the smile effect. Second, CO_2 is also found in the form of dry

ice (frozen carbon dioxide) in the polar caps of Mars [11]. CO_2 ice shows similar spectral features to atmospheric CO_2, and therefore, it becomes a strong source of the smile effect. In this case, an accurate atmospheric correction would not be enough since the smile effects coming from the strong absorption bands of the CO_2 ice would still affect the data.

C. State of the Art

In the literature, the problem of the smile effect in CRISM data has been tackled differently by some authors. McGuire *et al.* overcome the varying spectral response by modifying their albedo retrieval method, as discussed in [12]. In that study, CRISM spectra are corrected for atmospheric effects in the major CO_2 gas absorption bands by using an approach that is applied separately for the sweet spot and the off-axis columns. By contrast, Smith *et al.* overcome the smile effects by considering only the central 100 columns of the images, thus minimizing the optical distortions in the data [2]. A similar procedure is done in [6], where the presence of the smile effect restricts the detection of gypsum in the north polar cap of Mars to the center of the image. To the best of our knowledge, a method aiming a full correction of the smile effect has not yet been proposed for CRISM.

Nevertheless, several studies have addressed the correction of the smile effects in other pushbroom-type sensors. Dadon *et al.* propose the use of derivative calculations issued from atmospheric absorption features and the maximum noise fraction (MNF) transformation for detecting and correcting the smile effects in Hyperion/Earth Observing 1 (Hyperion/EO-1) images [13]. In that study, the spectral smile is overcome by adapting the MNF component that embodies the cross-track effects before rotating the MNF data set back to the radiance space. The main drawback of this method, however, is the lack of an instrumental basis. The desmiling of Hyperion images has also been addressed by Goodenough *et al.* in [14]. The problem is first tackled by a method that uniforms all column average values to the spectral channel mean. This technique proves to be inadequate when performed on either the radiance or the MNF space due to the apparition of false spectra caused by the assumption of the image cross-track uniformity. A second technique resamples spectra to a set of wavelengths resulting from the Hyperion prelaunch calibration after linearly interpolating the data. This approach provides reasonable results, although a residual smile is still detected after the correction. Jupp *et al.* also investigate the desmiling of Hyperion images in [15]. First, the MNF component that encompasses the smile effects is detrended by a polynomial fit before rotating the data back to the radiance space. Another strategy is based on the cross-track illumination correction in the ENVI software. In this method, each value is corrected by subtracting the difference regarding a polynomial that is fitting the averaged line of the corresponding spectral channel. Finally, the resampling of the spectra after interpolation is also proposed. All techniques, excluding the resampling, fail to provide satisfactory results because of the apparition of false spectra. Unlike the preceding methods, Schläpfer *et al.* address the correction of the bias induced by the nonuniformity of the PSF width [16]. In that study, a degradation of the imagery is suggested to obtain a uniform spectral response on the basis of the broadest occurring PSF. However, this method is not tested on real data.

III. Methods

Most desmiling techniques are driven by the artifacts observed in the data [13]–[15]. We believe that an approach aiming an accurate correction of the smile effect must take into account the instrument parameters as well as the shape of the observed spectra. In fact, the error bias induced by the smile effect depends on both attributes. Consequently, we propose a two-stage smile correction technique aiming at correcting the data sensibly by mimicking an optimal smile-free spectral response (in the case of CRISM, the PSFs owned by the sweet-spot detector elements). The nonuniformities affecting the central wavelength and the width of the instrument PSFs are overcome by a resampling strategy and a sharpening approach, respectively. Furthermore, the evolution of the smile effect in the data is assessed throughout the desmiling process by using a smile indicator.

A. Spectral Smile Indicator

Assessing the impact of the smile effect is crucial for evaluating the capabilities of a desmiling method. Hence, a measure of the extent of the artifact in a CRISM image is investigated.

First of all, the original hyperspectral space proves to be unsatisfactory to define a reliable quantitative indicator. Hence, an MNF transformation of the hyperspectral data is proposed as in [13]–[15]. An MNF rotation produces new components (eigenimages) that are ordered according to signal-to-noise ratio (SNR) after two cascaded principal components analysis (PCA) transformations and a noise whitening step [17]. The first transformation decorrelates and rescales the noise in the data based on the noise covariance matrix. Then, a standard PCA transformation is applied to the noise-whitened data. As a result, the transformed data can be divided into two parts: coherent eigenimages with large eigenvalues (i.e., high SNR) and noise-dominated components corresponding to lower eigenvalues. Although many authors have discussed the determination of the noise-free eigenimages (e.g., [18]), we propose the widely used criterion that defines the unity as the threshold between both types of eigenimages [17].

After an MNF rotation, CRISM images typically show an eigenimage (hereafter called MNF-smile) that embodies the cross-track brightness gradient of all spectral channels that are affected by the smile effect [see, e.g., Fig. 4 (center)]. The eigenvalue of the MNF-smile can be then considered as a measure of the artifact energy due to its relation to the SNR. Nonetheless, the MNF-smile must be handled carefully since it may contain other spatial components apart from the artifact [13].

Two other data rotations were studied to derive a smile indicator: PCA and independent component analysis (ICA). The PCA transforms a series of probably correlated variables into a smaller number of uncorrelated variables arranged by variance. By contrast, the ICA aims at separating a multivariate signal into additive subcomponents supposing the mutual statistical independence of the non-Gaussian source signals. Neither of

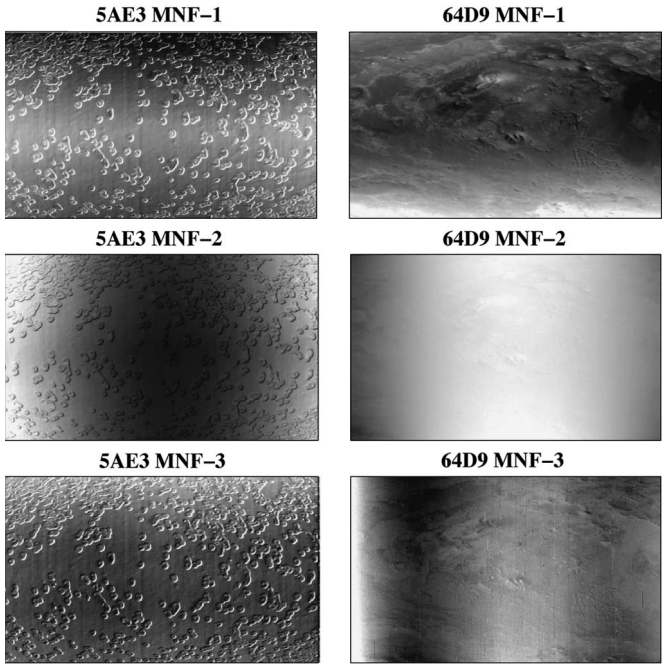

Fig. 4. MNF eigenimages corresponding to the three largest eigenvalues of nadir scans FRT5AE3 and FRT64D9.

the two transformations provided a reliable measure of the smile effect in comparison to the MNF. First, the PCA does not take into account the noise in the data, and therefore, the transformation axes might be ill defined. On the other hand, the ICA does not result in a clear "ICA-smile" eigenimage probably because of the dependence of the smile effect on other components in the data.

B. Spectra Resampling by Cubic Spline Interpolation

The first desmiling step aims at overcoming the nonuniform central wavelength by resampling all spectra to the sweet-spot parameters. First, CRISM Calibration Data Records (CDR) are used to retrieve the central wavelength of each detector element in the detector array (see Appendix). Then, each reflectance value is reevaluated at its corresponding sweet-spot wavelength after locally interpolating each spectrum. The interpolation is meaningful since wavelength shifts are hardly ever a whole number of the spectral sampling $(\Delta\lambda)$. By doing this, the approach assumes that the missing data between two consecutive spectels correspond to the points resulting from the interpolation. We consider this hypothesis reasonable since CRISM is close in meeting the Nyquist sampling theorem $FWHM \geq 2\Delta\lambda$ since $\Delta\lambda \approx 6.55$ nm/channel and $FWHM \approx$ 8–15 nm for the sweet spot [1]. Moreover, $FWHM$ increases by $\sim$2 nm for the off-axis detector elements, whose data are the most likely to undergo a significant correction.

Now, we investigate the error due to interpolation. Three different types of interpolation (linear, piecewise cubic Hermite, and cubic spline) are tested to study the preservation of the spectra shape. First, a CO_2 ice laboratory spectrum at high spectral resolution is separately convolved by the sweet-spot spectral response and the CRISM "poorest" one (the one corresponding to the first column). The PSFs of the latter are modified to make the wavelength shift the only difference between the two spectra. Then, the smile-affected spectrum is interpolated by the three methods to be eventually sampled to the sweet-spot wavelengths. The accuracy of the reconstruction is determined by computing the mean square error as

$$MSE = \frac{1}{n}\sum_{\lambda=1}^{n}\left[s^{\mathrm{corr}}(\lambda) - s^{\mathrm{SS}}(\lambda)\right]^2$$

where n is the number of channels and s^{corr} and s^{SS} are the resampled and the sweet spot spectra, respectively.

TABLE I
MEAN SQUARE ERROR IN THE RECONSTRUCTION OF A SWEET SPOT CO_2 ICE SPECTRUM FROM A SMILE-SHIFTED ONE

Interpolation type	MSE
Linear	4.33×10^{-3}
Piecewise cubic Hermite	3.93×10^{-3}
Cubic spline	3.71×10^{-3}

The results in Table I show how the cubic spline interpolation yields the best reconstruction error. Although all methods provide apparently similar errors, the difference among them is significant for the absorption maxima where the data are modified the most. In fact, the strong absorption bands are likely to be oversmoothed by a linear interpolation method as it is done in [14]. Furthermore, cubic splines have been used satisfactorily in other complex situations such as the spatial resampling of hyperspectral data [19]. Hence, we propose a spectral resampling algorithm based on cubic splines which is individually performed on each image of a CRISM observation (nadir scan + EPF).

C. Spectral Sharpening of Smile-Affected Spectral Channels

The second step of the proposed approach aims at overcoming the nonuniform spectral resolution within a given spectral channel. This heterogeneity causes that the strong absorption bands that are convolved by increasingly wider PSFs become oversmoothed progressively, thus contributing to the cross-track brightness gradient. A global degradation of the spectral resolution as in [16] would not be satisfactory since the CRISM capabilities would be drastically reduced by losing an average 30% of the spectral resolution.

A spectral sharpening approach inspired by image processing techniques is addressed in this paper. The proposed method mimics an increase of the spectral resolution up to the sweet-spot reference by enhancing the local contrast of the data that are most affected by the smile effect.

1) Estimation of the Spectral Smile Energy: First of all, the relevance of the smile effect in the data is investigated by estimating its energy as it was introduced in Section III-A.

First, the MNF-smile component from the nadir hyperspectral image is determined as the eigenimage which maximizes

$$\arg\max_{\lambda^{\mathrm{MNF}}} \xi(\lambda^{\mathrm{MNF}}) = \left\{ \frac{\mathrm{var}\left[\Phi(\lambda^{\mathrm{MNF}})\right]}{\sigma\left[\Theta(\lambda^{\mathrm{MNF}})\right]} \right\} \qquad (1)$$

where $\Phi(\lambda^{\mathrm{MNF}})$ and $\Theta(\lambda^{\mathrm{MNF}})$ are the average line and average column of the MNF eigenimage with index λ^{MNF}, respectively.

$\mathrm{var}[\cdot]$ and $\sigma[\cdot]$ are the variance and the standard deviation operators, respectively. The MNF-smile eigenimage maximizes ξ since the smile bias mostly depends on the column position. The impact of the existing along-track structures in the image on the MNF-smile (due to their correlation with the smile effect) is minimized by calculating the standard deviation instead of the variance. The smile energy (hereafter denoted as E^S) is estimated as the eigenvalue corresponding to the selected MNF-smile.

2) Selection of Smile-Affected Spectral Channels: Sharpening techniques bear the inherent risk of increasing the noise in the data. In order to avoid this, the second step of the desmiling approach is only performed on those spectral channels that are significantly affected by the smile effect.

For a given CRISM observation, the smile-affected channels are regrouped as

$$\beta = \Psi[\psi^{\mathrm{MNF}} \cup \psi^{\mathrm{CO_2}}] \tag{2}$$

where ψ^{MNF} is the ensemble of channels showing a greater cross-track smile gradient and $\psi^{\mathrm{CO_2}}$ encompasses those that are systematically critical in all observations. $\Psi[\cdot]$ includes a conservative spectral neighborhood for every selected channel.

First of all, an automatic strategy is put forward to define ψ^{MNF}. The MNF rotation of a hyperspectral image I with n spectral channels can be expressed as $I^{\mathrm{MNF}} = I \times \boldsymbol{A}$, where I^{MNF} is the rotated image and $\boldsymbol{A}$ is the MNF composite transformation matrix such that

$$\boldsymbol{A} = \begin{pmatrix} \alpha_1^1 & \dots & \alpha_1^n \\ \dots & \dots & \dots \\ \alpha_n^1 & \dots & \alpha_n^n \end{pmatrix}$$

where $\boldsymbol{\alpha}_i$ is the eigenvector of the MNF-i component that expresses the linear combination of the spectral channels that give rise to the eigenimage MNF-i.

The absolute value of the eigenvector corresponding to the MNF-smile (hereafter called $|\boldsymbol{\alpha}_S|$) is examined for outliers that reveal those channels whose cross-track brightness gradient is more significant. ψ^{MNF} is then defined as the channels whose corresponding $|\boldsymbol{\alpha}_S^j|$ departs by more than $1\sigma_{|\boldsymbol{\alpha}_S|}$.

The previous thresholding may prove to be inaccurate due to the noisy nature of $\boldsymbol{\alpha}_S$ caused by the correlation of the smile effect with other data components. As a result, $|\boldsymbol{\alpha}_S|$ may contain strong outliers not corresponding to the smile effect that may entail the absence of some moderately-affected channels (corresponding to medium $|\boldsymbol{\alpha}_S^j|$ values) that need to be corrected. This problem is overcome by the definition of $\psi^{\mathrm{CO_2}}$ that regroups the spectral channels that are most likely to be affected by the smile effect according to a Martian scenario: the channels encompassing the CO_2 gas absorption bands. In [11], the spectral channels of the OMEGA sensor, whose wavelengths correspond to the main absorption features of the atmospheric CO_2, were specified. We update these data according to CRISM and define $\psi^{\mathrm{CO_2}}$ as the spectral channels in Table II.

Lastly, an ensemble of adjacent spectral channels (hereafter called "packet") is added for the correction of every previously selected channel. This last step is done to avoid spurious differential effects that may degrade the spectra integrity if single channels are processed. A packet is defined as

TABLE II
CRISM CHANNELS WITHIN THE MAJOR CO_2 GAS ABSORPTION BANDS

CRISM IR spectral channel	Spectral channel center (μm)
88	1.572
99	1.644
148	1.969
155	2.011
163	2.067
205	2.341
245-249	2.611–2.637
255-258	2.673–2.695

$$\Psi[\lambda_j] = \{\forall\lambda\epsilon[\lambda_{j-p}\dots\lambda_{j+q}]/\mathrm{sgn}\,[\overline{s}''(\lambda)] = \mathrm{sgn}\,[\overline{s}''(\lambda_j)]\} \tag{3}$$

where $\overline{s}''$ is the second local derivative of the average spectrum. In doing so, the fidelity of the original data is preserved since each packet encompasses the local spectral concavity or convexity instead of a single spectel.

3) Sharpening: The sharpening technique is performed on every smile-affected channel belonging to β by

$$r_\lambda^{\mathrm{sh}}(\theta) = \frac{r_\lambda(\theta) - \frac{1}{2}\omega_\lambda(\theta)\left(r_{\lambda-v}(\theta) + r_{\lambda+v}(\theta)\right)}{1 - \omega_\lambda(\theta)} \tag{4}$$

where $r_\lambda(\theta)$ is the reflectance of channel λ for column θ and for any line position, v sets the pair of bracketing channels that are considered for the correction, and $\omega_\lambda(\theta)$ is the sharpening degree within $[0\dots1)$.

Equation (4) aims at increasing the local resolution of the spectra, an operation that becomes more significant for off-axis data. This sharpening process is individually adapted to each spectral channel by taking into account the local shape of the spectra and the instrument parameters.

First, v is set to be equal to unity to correspond to thin absorption bands that are represented by three adjacent spectels. Furthermore, (4) is suitable for false alarms in β that may be linked to other components than the smile effect. In fact, the sharpening approach becomes negligible when flat spectra are processed since

$$r_\lambda^{\mathrm{sh}}(\theta) \approx r_\lambda(\theta), \qquad \text{if } r_{\lambda-v}(\theta) \approx r_\lambda(\theta) \approx r_{\lambda+v}(\theta).$$

Second, $\omega_\lambda(\theta)$ is linked to the ratio between the current PSF width and that of the sweet spot by the relation

$$\omega_\lambda(\theta) = \rho_\lambda \kappa_\lambda(\theta) \tag{5}$$

where ρ_λ is the largest sharpening degree for the current channel and $\kappa_\lambda(\theta)$ provides the shape of $\omega_\lambda(\theta)$ such that

$$\kappa_\lambda(\theta) = \frac{f_\lambda(\theta) - \min(f_\lambda)}{\max(f_\lambda) - \min(f_\lambda)} \tag{6}$$

where f_λ is the $FWHM$ of all detector elements corresponding to spectral channel λ (see, e.g., Fig. 2). In doing so, $\omega_\lambda(\theta)$

TABLE III
MNF-SMILE EIGENVALUE EVALUATION

	FRT5AE3						FRT64D9					
Stage:	Smile-affected data		Resampled data		Sharpened data		Smile-affected data		Resampled data		Sharpened data	
	Eigenimage	E	Eigenimage	E	Eigenimage	E	Eigenimage	E	Eigenimage	E	Eigenimage	E
MNF-1	Photom.	193.8	Photom.	188.5	Photom.	188.4	Albedo	71.7	Albedo	71.7	Albedo	71.6
MNF-2	**Smile**	**100.1**	Albedo	13.8	Albedo	13.5	**Smile**	**12.3**	**Smile**	**1.7**	**Smile**	**0.3<1**
MNF-3	Albedo	12.5	**Smile**	**7.6**	**Smile**	**2.1**	Noise	<1	Noise	<1	Noise	<1

is close to zero for the sweet-spot spectra (i.e., negligible sharpening) and at the maximum for the image edges.

4) Sharpening Degree Determination: Setting ρ_λ is not straightforward since the optimal sharpening degree mainly depends on the shape of the observed spectra. Hence, ρ_λ is not unique, and it differs from channel to channel.

A strategy based on the examination of the smile energy E^S is proposed to determine the ensemble of ρ_λ values. Specifically, for every spectral channel in β, ρ_λ is set as the sharpening degree which makes E^S minimal. An iterative procedure is proposed as follows:

Input: a hyperspectral cube $I = [I_{\lambda_1} \dots I_{\lambda_n}]$, an ensemble of spectral channels $\beta = [\beta_1 \dots \beta_m]$, with $I_{\beta_j} \in I, \forall \beta_j$, and an initial smile energy E^S

1) FOR every β_j
2) $E_0^S = E^S$
3) $i = 1$
4) $\rho_{\beta_j}^i = \rho^1$
5) WHILE 1
6) Sharpening of I_{β_j} with $\omega_\lambda(\theta) = \rho_{\beta_j}^i \kappa_{\beta_j}(\theta)$
7) Compute new smile energy E_i^S
8) IF $E_i^S \geq E_{i-1}^S$ BREAK
9) $i = +1$
10) $\rho_{\beta_j}^i = \rho_{\beta_j}^{i-1} + \Delta\rho$
11) IF $\rho_{\beta_j}^i = \rho^{\max}$ BREAK
12) END
13) $P(\beta_j) = \rho_{\beta_j}^i - \Delta\rho$
14) END

where ρ^1 and $\Delta\rho$ are the initial sharpening degree and the increasing step, respectively. Both are typically set to be equal to 0.1.

Finally, the impact of the sharpening approach on the noise in the data is studied by SNR investigation. By doing this, the sharpening degree from which the noise increase becomes critical ($\rho^{\max}$) is defined. The SNR is estimated by the method in [20], which performs a linear regression of λ_{j-1} and λ_{j+1} to estimate λ_j. The data resulting from $\hat{\lambda}_j - \lambda_j$ are considered as noise. The SNR probing of several CRISM channels showed that the SNR generally becomes unacceptable when $\rho_\lambda > 0.5$. Hence, the iterative process is stopped when ρ_λ is equal to $\rho^{\max} = 0.6$.

5) Desmiling of CRISM Observations: CRISM observations are processed by the sharpening of the high-resolution nadir scan in the first place. Then, the same β and P are used for the correction of the corresponding EPF images. In this way, a spectrally uniform sharpening is performed on the whole observation.

IV. EXPERIMENTS

The proposed desmiling approach is applied to CRISM data for evaluation. Two targeted observations are considered, each one belonging to a science case for which an atmospheric correction is not of interest (or enough) to desmile the data.

A. CRISM Observations

First, an icy surface of the residual south polar cap is considered by selecting FRT5AE3. This observation shows the "Swiss cheese" pits that are supposed to be formed in a thin layer of CO_2 ice [21]. FRT5AE3 is singularly challenging in terms of desmiling due to the presence of dry ice in addition to the atmospheric CO_2. Second, observation FRT64D9, revealing the Nili Fossae fracture, is chosen. This near equatorial zone of Mars presents a mineral surface that is singularly rich in carbonate minerals. In this case, the desmiling of FRT64D9 must be considered for an accurate analysis of the atmosphere.

B. Data Postprocessing

CRISM data products are delivered in apparent I/F units (the ratio of the reflected intensity to the incident intensity of sunlight). We assume a Lambertian surface and divide the data by the cosine of the solar incidence angle to transform the data into reflectance units [1]. Although CRISM data are radiometrically calibrated, electronic artifacts such as spikes and stripes must be corrected. Both test images were corrected for these distortions by the method in [22] prior to the smile correction.

C. Spectral Smile Correction

Spectral channels 138–168 of the IR spectrometer are considered for the evaluation of the smile correction method. The corresponding spectral range of study (1902–2099 nm) is particularly challenging since it contains the strong 2-μm CO_2 absorption triplet that is of great interest in many research investigations [10], [23].

The quality of the proposed technique is evaluated in detail by examining the correction of the nadir scan of both test observations. First, the smile energy is investigated throughout the desmiling process in Table III, illustrating the evolution of the three largest MNF eigenvalues. Then, the spectra are carefully inspected to evaluate their physical correctness. Figs. 5 and 6 represent the evolution of four spectra corresponding to different column positions. The plotted spectra are the result of averaging the central 100 lines of the nadir scan, so the likely effects coming from the surface photometry are minimized.

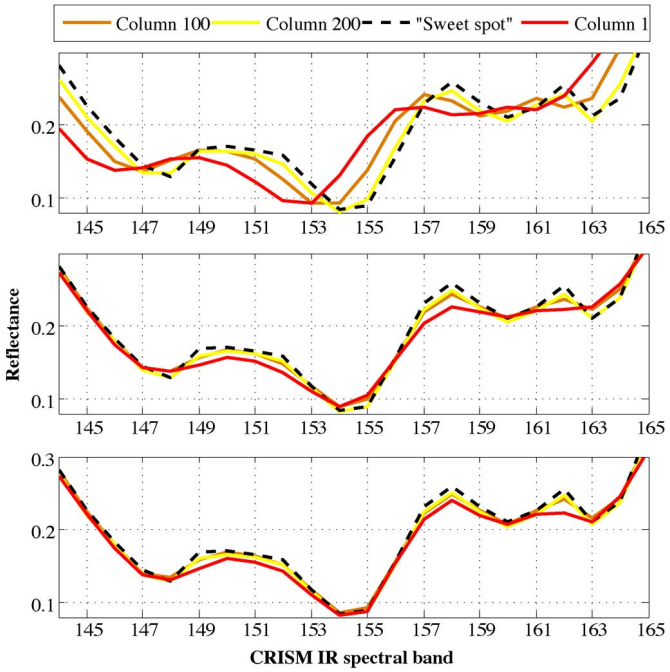

Fig. 5. FRT5AE3 spectra belonging to four different column positions throughout the desmiling process (top to bottom). All spectra are the result of averaging the 100 central lines of the image.

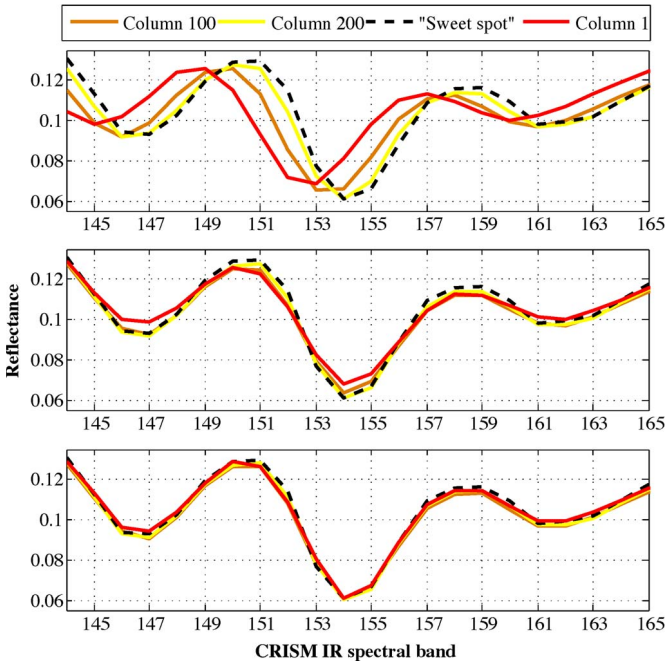

Fig. 6. FRT64D9 spectra belonging to four different column positions throughout the desmiling process (top to bottom). All spectra are the result of averaging the 100 central lines of the image.

Finally, Fig. 8 depicts FRT5AE3 spectral channel IR 155 before and after the correction. This channel is particularly of interest since its sweet spot falls precisely on the maximum of the CO_2 absorption at 2 μm.

The desmiling process starts with the MNF rotation of both nadir images for the evaluation of the smile impact. Fig. 4 shows the MNF eigenimages corresponding to the three largest eigenvalues of both images (see also Table III). First, FRT5AE3 MNF-1 shows a correlation with the image photometry caused

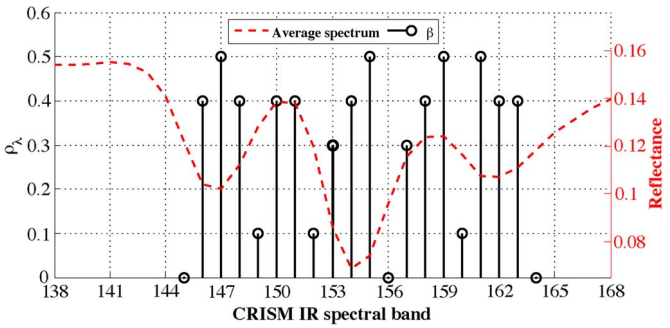

Fig. 7. (Red dashed line) FRT64D9 average spectrum after resampling and (black circles) ρ_λ values corresponding to (vertical lines) the ensemble of selected spectral channels β.

by the ice bidirectional reflectance anisotropy and the along-track variation of the solar emergence angle. MNF-2 shows a significant cross-track brightness gradient, and therefore, it is considered as the MNF smile of FRT5AE3 by (1). The smile eigenimage is far from being negligible since its eigenvalue ($E^S = 100.1$) is ten times larger than MNF-3's, which is depicting the average albedo. On the other hand, MNF-1 of image FRT64D9 illustrates the average albedo. Again, MNF-2 is designated as the smile eigenimage due to the high cross-track variance. In the absence of dry ice, the atmospheric CO_2 is the only source of the smile effect in this image, and therefore, the smile energy is lower ($E^S = 12.3$). MNF-3 of image FRT64D9 corresponds to the noise since its corresponding eigenvalue is lower than unity. Regarding Figs. 5 and 6 (top), the spectra appear to be shifted and smoothed as the off-axis columns are investigated. Lastly, Fig. 8 (left) shows the typical cross-track brightness gradient corresponding to the smile-affected bands. In fact, the reflectance values of channel IR 155 increase when moving toward the edges since the weight of the absorption wings intensifies as a result of the PSF shifting and broadening.

Once the smile energy is determined, the desmiling process proceeds with the resampling of each image to the sweet-spot wavelengths. By doing this, E^S is drastically reduced by $\sim$90% in both cases, and the spectra are no longer shifted [see Table III and Figs. 5 and 6 (center)]. However, the data belonging to the edges are still corrupted by smoothing as a result of the still nonuniform spectral resolution.

The resampled data are now corrected by the proposed spectral sharpening strategy. After following the procedure introduced in Section III-C2, the nadir scans of FRT5AE3 and FRT64D9 present the same β. In fact, spectral channels IR 145–164 are selected for the correction in both cases as they encompass the CO_2 absorption triplet. Fig. 7 gives the details on the sharpening of FRT64D9. The average spectrum, the selected spectral channels β, and the corresponding degrees of sharpening ρ_λ are shown. At first, the 2.07-μm ($\sim$IR band 161) feature, which is oversmoothed after resampling, is missed in ψ^{MNF} due to the high impact of the smile effect on the 2.01-μm ($\sim$IR band 154) and the 1.97-μm ($\sim$IR band 147) absorption bands. However, this feature is also processed in the sharpening procedure thanks to $\psi^{\mathrm{CO_2}}$. Finally, Ψ includes the entire CO_2 absorption triplet, and it is corrected as a whole feature. Regarding the optimal sharpening degrees, a high correlation between the positions of the CO_2 absorption maxima and the greatest

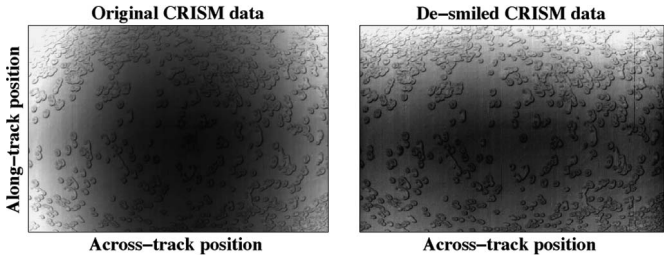

Fig. 8. IR spectral channel 155 of FRT5AE3 before and after smile correction.

values can be observed (e.g., IR channels 147 and 155). Furthermore, Fig. 7 illustrates how the procedure based on the E^S examination assigns low ρ_λ values for the channels showing a low impact after the resampling, e.g., IR 145 and 164.

Concerning the final evaluation of the desmiling technique, Figs. 5 and 6 (bottom) illustrate how the local contrast of the CO_2 absorption bands are enhanced by the proposed sharpening technique. As expected, the spectra belonging to off-axis columns are further corrected than the sweet-spot ones, whose correction is negligible. It can be observed that the integrity of the spectra is preserved, conserving their physical meaning and free of spikes due to a faulty correction. Regarding E^S, the smile energy of FRT5AE3 is reduced by $\sim$70%, being eventually close to the noise threshold (see Table III). The complexity of the correction due to the presence of both types of CO_2 explains why the smile effects are not entirely corrected by the desmiling process. Fig. 8 (right) shows, however, how the smile correction strongly attenuates the cross-track brightness gradient in FRT5AE3 channel IR 155. FRT64D9 smile also experiences a notable reduction by $\sim$80% thanks to the second desmiling step as the MNF-smile eigenvalue is reduced below unity. In this case, the residual smile can be considered as noise [17]. Lastly, Table III illustrates how the proposed desmiling method involves a minimal impact on other components in the data since their eigenvalues do not change significantly.

V. Conclusion

In this paper, the correction of the smile effect affecting CRISM hyperspectral images has been addressed. First, an exhaustive study of the artifact was carried out, and its main effects on the instrument spectral response and the acquisition of the data were identified. The Martian scenario was also investigated, and two different science cases were defined as critical regarding the smile effect. Then, a two-stage method for desmiling CRISM observations was put forward. The presented approach takes into account both the instrument parameters and the shape of the observed spectra. In addition, a smile indicator is defined in order to evaluate the artifact energy throughout the correction process. First, the spectral shifting due to the drift of the central wavelength of the detector elements is corrected. Spectels are first interpolated by cubic splines and then resampled by taking into account the ground calibration of the instrument. The fidelity of the spectra shape is preserved because of the properties of the interpolation method. Second, the nonuniformities of the PSF width of the detector elements are adjusted by a spectral sharpening technique that enhances the local contrast of the spectra. The method reliability is emphasized since the sharpening is only performed on spectral channels particularly suffering from the smile effect. As a result, the noise increase is minimized, and other components in the data are not affected by the desmiling process. Again, the sharpening method is based on the instrument parameters by choosing a degree of correction that depends on the variations of the spectral resolution among the detector elements. In addition, the increase of the spectral resolution is mimicked by taking account of the observed spectra shape. In fact, the optimal degree of the sharpening is set individually for every spectral channel depending on the decrease of the spectral smile energy induced by the correction method. By contrast, the sharpening procedure might prove to be unsatisfactory for correcting the spectral features having nearly disappeared for the off-axis columns.

The previous statements have been confirmed by the presented experimental results. The CRISM nadir images FRT5AE3 and FRT64D9 show a notable reduction of the smile energy after following the proposed method. Regarding the whole observation correction, Fig. 1 corroborates the validity of the introduced approach as the smile pattern greatly disappears for all scans. Furthermore, the approach may be improved with new versions of the CRISM data calibration. Future research will be conducted on the extraction of spectrophotometric signatures, followed by their inversion to obtain sampled bidirectional reflectance distribution functions of the Martian surface.

Appendix
Calibration Data Records

CRISM Calibration Data Records (CDR) are used in the desmiling process. In particular, WA CDR, which contain the calibrated central wavelength of each detector element, are used in the resampling process. Then, SB CDR, containing the parameters to calculate the spectral PSF for each detector element, are used for $\kappa_\lambda(\theta)$ in the sharpening process. Finally, UB CDR, which give the standard deviation of each detector element in a CRISM shutter closed measurement, are used to compute the noise covariance matrix in all MNF transformations.

References

[1] S. Murchie, R. Arvidson, P. Bedini, K. Beisser, J.-P. Bibring, J. Bishop, J. Boldt, P. Cavender, T. Choo, R. T. Clancy, E. H. Darlington, D. Des Marais, R. Espiritu, D. Fort, R. Green, E. Guinness, J. Hayes, C. Hash, K. Heffernan, J. Hemmler, G. Heyler, D. Humm, J. Hutcheson, N. Izenberg, R. Lee, J. Lees, D. Lohr, E. Malaret, T. Martin, J. A. McGovern, P. McGuire, R. Morris, J. Mustard, S. Pelkey, E. Rhodes, M. Robinson, E. Schaefer, G. Seagrave, F. Seelos, P. Silverglate, S. Slavney, M. Smith, W.-J. Shyong, K. Strohbehn, H. Taylor, P. Thompson, B. Tossman, M. Wirzburger, and M. Wolff, "Compact Reconnaissance Imaging Spectrometer for Mars (CRISM) on Mars Reconnaissance Orbiter (MRO)," *J. Geophys. Res.*, vol. 112, p. E05 S03, May 2007.

[2] M. D. Smith, M. J. Wolff, R. T. Clancy, and S. L. Murchie, "Compact reconnaissance imaging spectrometer observations of water vapor and carbon monoxide," *J. Geophys. Res.*, vol. 114, p. E00 D03, Jun. 2009.

[3] M. J. Wolff, M. D. Smith, R. T. Clancy, R. Arvidson, M. Kahre, F. Seelos, IV, S. Murchie, and H. Savijärvi, "Wavelength dependence of dust aerosol single scattering albedo as observed by the Compact Reconnaissance Imaging Spectrometer," *J. Geophys. Res.*, vol. 114, p. E00 D04, Jun. 2009.

[4] W. H. Davies, P. R. J. North, W. M. F. Grey, and M. J. Barnsley, "Improvements in aerosol optical depth estimation using multiangle

CHRIS/PROBA images," *IEEE Trans. Geosci. Remote Sens.*, vol. 48, no. 1, pp. 18–24, Jan. 2010.
[5] R. Duca and F. D. Frate, "Hyperspectral and multiangle CHRIS–PROBA images for the generation of land cover maps," *IEEE Trans. Geosci. Remote Sens.*, vol. 46, no. 10, pp. 2857–2866, Oct. 2008.
[6] M. Massé, O. Bourgeois, S. L. Mouélic, C. Verpoorter, L. Le Deit, and J.-P. Bibring, "Martian polar and circum-polar sulfate-bearing deposits: Sublimation tills derived from the north polar cap," *Icarus*, 2010, DOI: 10.1016/j.icarus.2010.04.017, to be published.
[7] A. J. Brown, W. M. Calvin, and S. L. Murchie, "MRO (CRISM/MARCI) mapping of the south pole—First Mars year of observations," in *Proc. 40th Lunar Planet. Sci. Conf.*, 2009, p. 1860.
[8] P. Mouroulis, R. O. Green, and T. G. Chrien, "Design of pushbroom imaging spectrometers for optimum recovery of spectroscopic and spatial information," *Appl. Opt.*, vol. 39, no. 13, pp. 2210–2220, May 2000.
[9] Y. Langevin, S. Douté, M. Vincendon, F. Poulet, J.-P. Bibring, B. Gondet, B. Schmitt, and F. Forget, "No signature of clear CO_2 ice from the 'cryptic' regions in Mars' south seasonal polar cap," *Nature*, vol. 442, no. 7104, pp. 790–792, Aug. 2006.
[10] A. Spiga, F. Forget, B. Dolla, S. Vinatier, R. Melchiorri, P. Drossart, A. Gendrin, J.-P. Bibring, Y. Langevin, and B. Gondet, "Remote sensing of surface pressure on Mars with the Mars Express/OMEGA spectrometer: 2. Meteorological maps," *J. Geophys. Res.*, vol. 112, no. E8, p. E08 S16, Aug. 2007.
[11] S. Douté, B. Schmitt, Y. Langevin, J.-P. Bibring, F. Altieri, G. Bellucci, B. Gondet, and F. Poulet, "South pole of Mars: Nature and composition of the icy terrains from Mars Express OMEGA observations," *Planet. Space Sci.*, vol. 55, no. 1/2, pp. 113–133, Jan. 2007.
[12] P. C. McGuire, M. J. Wolff, M. D. Smith, R. E. Arvidson, S. L. Murchie, R. T. Clancy, T. L. Roush, S. C. Cull, K. A. Lichtenberg, S. M. Wiseman, R. O. Green, T. Z. Martin, R. E. Milliken, P. J. Cavender, D. C. Humm, F. P. Seelos, K. D. Seelos, H. W. Taylor, B. L. Ehlmann, J. F. Mustard, S. M. Pelkey, T. N. Titus, C. D. Hash, and E. R. Malaret, "MRO/CRISM retrieval of surface lambert albedos for multispectral mapping of Mars with DISORT-based radiative transfer modeling: Phase 1—Using historical climatology for temperatures, aerosol optical depths, and atmospheric pressures," *IEEE Trans. Geosci. Remote Sens.*, vol. 46, no. 12, pp. 4020–4040, Dec. 2008.
[13] A. Dadon, E. Ben-Dor, and A. Karnieli, "Use of derivative calculations and minimum noise fraction transform for detecting and correcting the spectral curvature effect (smile) in Hyperion images," *IEEE Trans. Geosci. Remote Sens.*, vol. 48, no. 6, pp. 2603–2612, Jun. 2010.
[14] D. G. Goodenough, A. Dyk, K. O. Niemann, J. S. Pearlman, H. Chen, T. Han, M. Murdoch, and C. West, "Processing Hyperion and ALI for forest classification," *IEEE Trans. Geosci. Remote Sens.*, vol. 41, no. 6, pp. 1321–1331, Jun. 2003.
[15] D. L. B. Jupp, B. Datt, T. McVicar, T. G. V. Niel, J. S. Pearlman, J. L. Lovell, and E. A. King, "Improving the analysis of Hyperion red-edge index from an agricultural area," in *Proc. SPIE Image Process. Pattern Recog. Remote Sens.* S. G. Ungar, S. Mao, and Y. Yasuoka, Eds., 2003, vol. 4898, pp. 78–92.
[16] D. Schläpfer, J. Nieke, and K. I. Itten, "Spatial PSF nonuniformity effects in airborne pushbroom imaging spectrometry data," *IEEE Trans. Geosci. Remote Sens.*, vol. 45, no. 2, pp. 458–468, Feb. 2007.
[17] A. A. Green, M. Berman, P. Switzer, and M. D. Craig, "A transformation for ordering multispectral data in terms of image quality with implications for noise removal," *IEEE Trans. Geosci. Remote Sens.*, vol. 26, no. 1, pp. 65–74, Jan. 1988.
[18] U. Amato, R. M. Cavalli, A. Palombo, S. Pignatti, and F. Santini, "Experimental approach to the selection of the components in the minimum noise fraction," *IEEE Trans. Geosci. Remote Sens.*, vol. 47, no. 1, pp. 153–160, Jan. 2009.
[19] F. Tsai and W. W. Chen, "Striping noise detection and correction of remote sensing images," *IEEE Trans. Geosci. Remote Sens.*, vol. 46, no. 12, pp. 4122–4131, Dec. 2008.
[20] R. E. Roger and J. F. Arnold, "Reliably estimating the noise in AVIRIS hyperspectral imagers," *Int. J. Remote Sens.*, vol. 17, no. 10, pp. 1951–1962, Jul. 1996.
[21] S. Byrne and A. P. Ingersoll, "A sublimation model for Martian south polar ice features," *Science*, vol. 299, no. 5609, pp. 1051–1053, Feb. 2003.
[22] M. Parente, "A new approach to denoising CRISM images," in *Proc. Lunar Planet. Sci. Conf.*, 2008, p. 2528.
[23] S. Douté and X. Ceamanos, "Retrieving Mars aerosol optical depth from CRISM/MRO imagery," in *Proc. IEEE Workshop Hyperspectral Image Signal Process., Evol. Remote Sens.*, Reykjavik, Iceland, 2010.

Xavier Ceamanos (S'10) received the M.S. degree in electrical engineering from the Universitat Politècnica de Catalunya, Barcelona, Spain, in 2007, and the M.S. degree in electronics from the Institut National Polytechnique de Grenoble, Grenoble, France, in 2008. He is currently working toward the Ph.D. degree in the Laboratoire de Planétologie de Grenoble, Centre National de la Recherche Scientifique–Université Joseph Fourier, Grenoble. His Ph.D. work is devoted to developing statistical and physical methods for Martian hyperspectral images. In particular, he is working with hyperspectral data acquired by the multiangular Compact Reconnaissance Imaging Spectrometer for Mars/Mars Reconnaissance Orbiter (CRISM/MRO) spectrometer.

His research interests include the calibration of imaging spectrometers and the processing of hyperspectral images, including atmospheric correction algorithms, spectral unmixing, and statistical inversion techniques to retrieve surface reflectance.

Sylvain Douté received the M.S. degree in physics from the Université Joseph Fourier, Grenoble, France, in 1994, and the Ph.D. degree in remote sensing from the Université Denis Diderot, Paris, France. His Ph.D. work was devoted to modeling light scattering properties of planetary icy surfaces with applications to the study of Io and Pluto.

For two years, he was a Postdoctoral Researcher with the Institute of Geophysics and Planetary Physics, University of California, Los Angeles, where he worked in analyzing the images of the Galilean satellites acquired by the near-infrared mapping spectrometer (Galileo, National Aeronautics and Space Administration). He is currently a Researcher in planetary physics with the Laboratoire de Planétologie de Grenoble, Centre National de la Recherche Scientifique—Université Joseph Fourier, Grenoble. His research interests include the study of the Mars cryosphere and polar atmosphere by imaging spectroscopy because he was a Coinvestigator of the spatial Observatoire pour la Minéralogie, l'Eau, les Glaces et l'Activité/Mars Express (OMEGA/MEX) and Compact Reconnaissance Imaging Spectrometer for Mars/Mars Reconnaissance Orbiter (CRISM/MRO) experiments. He is also the Leader of the Vahiné project, Laboratoire de Planétologie de Grenoble, where physical models and statistical inversion techniques as well as signal processing methods are developed.

Dr. Douté is a member of the "Programme National de Planétologie" science committee and American Geophysical Union.

16

Article detailing the application of blind source separation techniques to CRISM data appeared in the IEEE Transactions on Geoscience and Remote Sensing

Intercomparison and Validation of Techniques for Spectral Unmixing of Hyperspectral Images: A Planetary Case Study

Xavier Ceamanos, *Student Member, IEEE*, Sylvain Douté, Bin Luo, Frédéric Schmidt, Gwenaël Jouannic, and Jocelyn Chanussot, *Senior Member, IEEE*

***Abstract*—As the volume of hyperspectral data for planetary exploration increases, efficient yet accurate algorithms are decisive for their analysis. In this paper, the capability of spectral unmixing for analyzing hyperspectral images from Mars is investigated. For that purpose, we consider the Russell megadune observed by the Compact Reconnaissance Imaging Spectrometer for Mars (CRISM) and the High-Resolution Imaging Science Experiment (HiRISE) instruments. In late winter, this area of Mars is appropriate for testing linear unmixing techniques because of the geographical coexistence of seasonal CO_2 ice and defrosting dusty features that is not resolved by CRISM. Linear unmixing is carried out on a selected CRISM image by seven state-of-the-art approaches based on different principles. Three physically coherent sources with an increasing fingerprint of dust are recognized by the majority of the methods. Processing of HiRISE imagery allows the construction of a ground truth in the form of a reference abundance map related to the defrosting features. Validation of abundances estimated by spectral unmixing is carried out in an independent and quantitative manner by comparison with the ground truth. The quality of the results is estimated through the correlation coefficient and average error between the reconstructed and reference abundance maps. Intercomparison of the selected linear unmixing approaches is performed. Global and local comparisons show that misregistration inaccuracies between the HiRISE and CRISM images represent the major source of error. We also conclude that abundance maps provided by three methods out of seven are generally accurate, i.e., sufficient for a planetary interpretation.**

Manuscript received October 22, 2010; revised February 2, 2011; accepted March 30, 2011. Date of publication May 19, 2011; date of current version October 28, 2011. This work was done within the framework of the Vahiné project funded by the "Agence Nationale de la Recherche" (ANR) and the "Centre National d'Études Spatiales" (CNES). We also acknowledge support from the "Centre National de la Recherche Scientifique" (CNRS) through the "Programme National de Planétologie."

X. Ceamanos and S. Douté are with the Institut de Planétologie et d'Astrophysique de Grenoble (IPAG), UJF-CNRS, UMR 5274, 38041 Grenoble, France (e-mail: xavier.ceamanos@obs.ujf-grenoble.fr; sylvain.doute@obs.ujf-grenoble.fr).

B. Luo is with the Gipsa-lab, Grenoble Institute of Technology, 38402 Grenoble, France and also with the State Key Laboratory of Information Engineering in Surveying, Mapping and Remote Sensing (LIESMARS), Wuhan University, Wuhan 430079, China (e-mail: robinlb2002@gmail.com).

F. Schmidt is with the Université Paris-Sud, Laboratoire IDES, UMR 8148 and CNRS, 91405 Orsay, France (e-mail: frederic.schmidt@u-psud.fr).

G. Jouannic is with the Université Paris-Sud, Laboratoire IDES, UMR 8148 and CNRS, 91405 Orsay, France and also with the International Research School of Planetary Sciences, Università G. d'Annunzio, 65127 Pescara, Italy (e-mail: gwenael.jouannic@u-psud.fr).

J. Chanussot is with the Gipsa-lab, Grenoble Institute of Technology, 38402 Grenoble, France (e-mail: jocelyn.chanussot@gipsa-lab.grenoble-inp.fr).

Color versions of one or more of the figures in this paper are available online at http://ieeexplore.ieee.org.

Digital Object Identifier 10.1109/TGRS.2011.2140377

Index Terms—**Blind source separation, Compact Reconnaissance Imaging Spectrometer for Mars (CRISM), ground truth, High-Resolution Imaging Science Experiment (HiRISE), hyperspectral imagers, Mars, remote sensing of planetary surfaces, spectral analysis, unsupervised linear unmixing.**

I. Introduction

VISIBLE and near-infrared imaging spectroscopy is a key remote sensing technique to study planetary objects. Since their first appearance in 1989, imaging spectrometers have been aboard an increasing number of orbiters aimed at exploring our solar system. This kind of sensors have been decisive when addressing issues related to the surface or the atmosphere of Mars, Venus, Jupiter, Saturn, and their moons [1]–[5]. In particular, imaging spectroscopy gives outstanding results regarding the chemical composition and physical state of solid surfaces, thus providing clues about present and past activity and environmental conditions. Constant technological improvements promote the acquisition of dramatically expending collections of hyperspectral images. For instance, the Compact Reconnaissance Imaging Spectrometer for Mars (CRISM) aboard Mars Reconnaissance Orbiter (MRO) is the first hyperspectral imager to operate systematically in multiangle mode at high spatial resolution from orbit [1].

Because of the increasing volume and complexity of planetary hyperspectral data such as CRISM's, efficient yet accurate algorithms are decisive for their analysis. Unsupervised spectral unmixing techniques are potentially relevant tools, particularly in planetary sciences for which only few ground truth data are available. These techniques aim at separating the existent mixtures between the different contributions—coming mainly from materials at the surface—that form the remotely sensed signal. Materials (i.e., physical sources) at the surface are characterized by their spectral signatures determined by their intrinsic chemical composition. Due to limitations of sensor spatial resolution and multiple scattering of solar photons occurring among distinct physical sources, different spectral signatures may be combined both linearly (i.e., geographic mixtures) and nonlinearly (e.g., intimate mixtures).

First attempts in applying spectral unmixing techniques to planetary hyperspectral data are based on a linear model of the signal, even though nonlinear processes might prevail. The Independent Component Analysis (ICA) has been proposed to extract the existent spectral components (i.e., endmembers) in a hyperspectral image by assuming that physical sources are

non-Gaussian and mutually independent. Application of ICA on images acquired by the Observatoire pour la Minéralogie, l'Eau, les Glaces et l'Activité (OMEGA) hyperspectral imager allows the retrieval of meaningful endmembers in [6]. Likewise, spectra measured by the Visible and Infrared Thermal Imaging Spectrometer (VIRTIS) on the nightside of Venus are analyzed with ICA in [7]. In that study, several extracted endmembers are related to physical components or processes due to good correlation of the corresponding distribution maps with known structures of the Venusian atmosphere. Nonetheless, the role of ICA to carry out spectral unmixing is questioned in [8] since the independence of abundance distributions is not satisfied. Another important limitation of ICA is the potential unphysical results in the form of negative values affecting the extracted spectra or abundances. On the other hand, for more than a decade, the Non-negative Matrix Factorization (NMF) has been an alternative method to solve the unmixing problem under a linear model with non-negative constraint [9]. For instance, the NMF approach has been used in planetary exploration to estimate the surface composition of Mars using data acquired by the Martian rovers [10]. Likewise, the NMF problem has been solved in a Bayesian framework through the Bayesian Positive Source Separation (BPSS) [11] ensuring a unique robust solution. In [12], a combination of spatial ICA and BPSS applied on OMEGA data leads to endmembers whose associated spectra and abundance maps correlate satisfactorily with reference signatures and outcomes of physical models, respectively.

In terrestrial remote sensing, many approaches have been proposed as efficient tools for linear unmixing of hyperspectral data. These methods include the Vertex Component Analysis (VCA) [13] which retrieves the spectra of the existent endmembers by extracting the extrema of the simplex formed by the hyperspectral data. In [14], this geometric method is performed on OMEGA data from Mars with satisfactory results. Similarly to VCA, the widely used N-FINDR [15] algorithm is proposed for endmember extraction of linearly mixed data, showing notable performances on many types of hyperspectral data such as CRISM's in [16]. Contrary to VCA and N-FINDR that require the existence of pure pixels in the data, many methods have been developed without the pure pixel assumption. This is the case of the techniques referred to as Minimum Volume Constrained Non-negative Matrix Factorization (MVC-NMF), Minimum Volume Enclosing Simplex (MVES), and Simplex Identification via Split Augmented Lagrangian (SISAL), which are proposed for endmember extraction of highly mixed data. MVC-NMF decomposes mixed pixels based on the NMF and a minimum volume constraint and has proved to be very efficient on simulated and real data and less sensitive to the estimated number of endmembers [17]. In the same way, MVES proposes a convex analysis by minimizing the simplex volume subject to the constraint that all dimension-reduced pixels are enclosed in it [18]. Eventually, SISAL [19] has been recently proposed to solve the linear unmixing problem based on a non-convex optimization problem with convex constraints [19]. Last but not least, many studies have recently addressed the inclusion of spatial information into endmember extraction [20], [21]. For instance, the authors of [21] propose a spatial preprocessing that enhances the search for endmembers in the unmixing problem. This procedure has proved to provide better extracted spectra and more relevant abundance maps after combination with a traditional endmember extraction method.

In this paper, we propose to evaluate the suitability of spectral unmixing techniques in a planetary context by testing the following comprehensive selection of state-of-the-art algorithms: BPSS, VCA, N-FINDR, MVC-NMF, MVES, and SISAL. In addition, spatial information is integrated into the unmixing process by considering the spatial preprocessing proposed in [21]. In this way, a large scope of methods based on geometric, Bayesian, and spectro-spatial first principles is considered. Unfortunately, the validation of spectral unmixing techniques is a very challenging yet crucial issue, particularly in planetary sciences due to the scarcity of ground truth. In that matter, previous studies traditionally address the validation of unmixing outcomes either through comparison of endmember spectra extracted from real data with reference spectral signatures [22], [23] or by using simulated data [20], [21], [24]. As for abundance maps obtained from unmixing of real data, only the authors of [20] perform their validation by comparing these outcomes with a reference. In that study, reference abundance maps are built from reference spectra manually extracted from the original image. To our knowledge, the validation of spectral unmixing techniques applied on real data through the evaluation of extracted abundance maps in an independent and quantitative manner has never been addressed. We therefore propose an innovative case study that overcomes this hurdle by choosing a CRISM image displaying the Russell dune of Mars. In late winter, this particular area is very suitable for validation of spectral unmixing techniques under a linear model due to two principal reasons: (i) The very likely existence of geographic subpixel mixtures coming from the two predominant materials at the surface and (ii) the possibility of building a ground truth for validation of extracted abundance maps using very high-resolution imagery and geomorphological techniques. Based on original experimentations, we perform quantitative assessment of surface proportions obtained by spectral unmixing techniques on real hyperspectral data. In addition, an intercomparison of the selected unmixing methods is carried out by evaluating their spectral and spatial outcomes independently. Eventually, the linear mixing model and the limitations of the assumptions made by the algorithms are evaluated for the problem at hand.

This paper is organized as follows. In Section II, we present the case study of the Russell dune through the description of the area of interest, the data sets that are used, and the construction of the ground truth. Then, the selection of spectral unmixing algorithms is briefly described in Section III by highlighting the properties of each method that may be suitable for our case study. Likewise, the techniques used for estimating the number of endmembers are introduced. Experiments are carried out in Section IV followed by the intercomparison and validation of the unmixing methods in Section V. Section VI concludes by discussing on the proposed methodology based on unmixing techniques and preprocessing, drawing some conclusions on the potential of unmixing techniques for planetary sciences, and giving some indications for further research.

II. Case Study: The Russell Crater Megadune

A. Description of the Area

The selected area of study is the megadune in the Russell crater of Mars (55° S 12° E). This 134-km wide crater hosts a 1700 km^2 dune field with an uncommon large dune on its northeastern part. This megadune is about 500 m high, 20 km wide, and 40 km long. In particular, the southwest facing scarp of the dune displays many defrosting features in late winter when the retreat of CO_2 ice starts. These phenomena in the form of dark spots—mostly on the top of the dune—and dark elongated patterns—all over the scarp—precede the global sublimation of the ice, eventually uncovering the sandy mineral substratum [25]. The defrosting features as well as the gullies are an ongoing key research topic for the understanding of Mars geology and activity.

The Russell dune represents a potential benchmark for testing spectral unmixing algorithms in a planetary context. During the MRO mission, this area of Mars has been extensively scrutinized in a coordinated manner by very high-resolution imagery and imaging spectroscopy. In late winter, the former fully resolves the geographical coexistence of dark features—mostly made of dust—and brighter ice while the latter does not. Hence, the assumption of linear mixing in the hyperspectral signal coming from the contributions of both components is very reasonable. In addition, the use of very high-resolution imagery can be used for constructing a ground truth against which abundance maps provided by unmixing techniques applied to hyperspectral images can be evaluated.

B. CRISM Data

In the targeted mode, the CRISM instrument maps the mineralogy of Martian key areas at high spectral (362–3920 nm, 6.5 nm/channel) and spatial (up to 18 m/pix) resolution [1]. CRISM offers a new insight into the planet Mars because of its high resolution and its multi-angle capabilities provided by its gimbaled optical sensor unit (OSU). In this way, each targeted observation is composed of a central hyperspectral image at full spatial resolution and a sequence of ten bracketing spatially binned images that are acquired before and after MRO flies over the target.

In July 2009, CRISM had scanned the Russell megadune 15 times of which 4 in late winter when the CO_2 sublimation starts and the defrosting features appear. We therefore select the central image of the targeted observation frt000042aa covering an area of 80 km^2, in which the southern facing scarp of the Russell dune is visible (see Fig. 1). Due to the OSU functioning, this image was acquired with view zenith angles (VZA) varying by more than 60° from the first to the last image row.

1) Preprocessing: Before the unmixing stage, the test image frt000042aa is processed to get rid of the contributions that are not related to the components at the surface. In particular, these contributions may introduce nonlinearities in the data affecting the linear mixture model of the signal. In this way, the test image is corrected for instrumental artifacts, atmospheric effects, and photometric issues. First, residual stripes and spikes are corrected as in [26]. Likewise, the spectral smile effect affecting CRISM images is corrected by the method in [27]. This step is particularly challenging due to the presence of CO_2 ice, which results in a higher strength of the smile artifacts. Second, the contribution of the Martian atmosphere, which is mainly composed by CO_2 gas and mineral aerosols, is corrected as in [28], [29]. The widely used volcano scan algorithm for CRISM data in [30] is not applicable as it does not operate for icy surfaces nor corrects it for aerosol contribution. Imprecisions in the adopted scattering properties of the aerosols as a function of VZA may induce atmospheric residues in the upper and lower rows of the image by means of spurious spectral slopes. Third, atmospherically corrected spectra are transformed into apparent reflectance units R in a similar way as it is done in [1]. For this photometric correction, we take into account the average illumination conditions on the whole scarp by means of the solar zenith angle (SZA). The average SZA of the scarp is retrieved by using a digital terrain model (DTM) of the Russell dune generated by the High-Resolution Imaging Science Experiment (HiRISE) camera. This procedure results in better levels of R for the majority of the spectra when compared to the traditional procedure in which the surface is approximated by the Martian areoid [1]. A complete pixel-wise photometrical correction is not realizable due to noise in the DTM. Likewise, a procedure based on clustering the image according to SZA had to be abandoned as the spatial information coming from the surface is critically corrupted after correcting for the average photometry of each SZA-similar area. Hence, residues coming from the heterogeneous photometry, as well as instrumental artifacts and atmospheric effects, may remain after the data pipeline.

Eventually, an region-of-interest (ROI) is defined as we are only interested in the southwest facing scarp displaying the defrosting features (see yellow line in Fig. 1). In addition, only the 250 CRISM channels ranging from 1.0 to 2.6 μm are considered due to the high impact of thermal noise for greater wavelengths and the less marked features of CO_2 ice in the visible range.

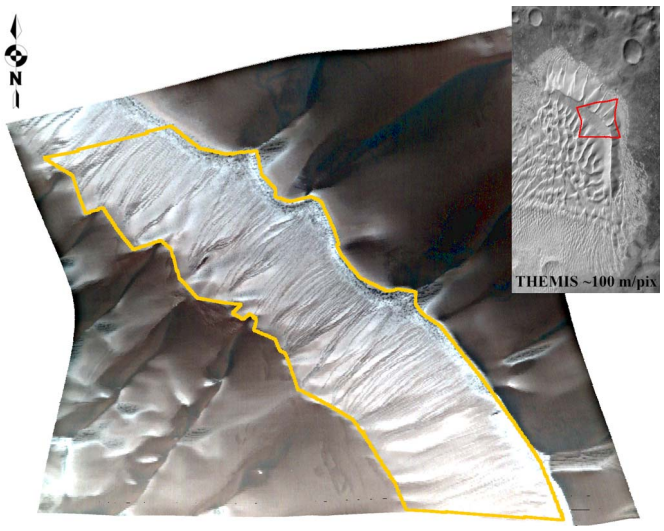

Fig. 1. CRISM frt000042aa true color image showing the Russell dune. The still-frosted scarp displays dark spots on the ridge of the dune and dark elongated patterns along the gullies. The region-of-interest (ROI) is highlighted in yellow. The upper right figure displays the location of the test image over the megadune observed by the THEMIS instrument.

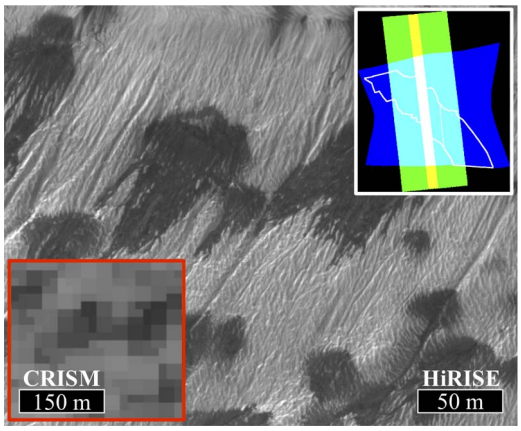

Fig. 2. Detail of the Russell dune observed by the CRISM and the HiRISE instruments. Upper right image: footprints of the images CRISM frt000042aa in blue (604 × 420 pixels, non-map projected), HiRISE PSP_002482_1255_RED in green (29 862 × 63 004 pixels, map projected), and HiRISE PSP_002482_1255_COLOR in yellow (11 776 × 61 257 pixels, map projected). The ROI is enclosed with a white line.

C. Building a Ground Truth

Although Mars is the planet other than Earth for which more data are available, the scarcity of ground truth to validate the statistical and physical algorithms that are used to retrieve information on the surface of the red planet is a crucial issue. On the one hand, only a few specific areas of Mars are enough characterized by a combined coverage of spacecrafts and rovers. Furthermore, both types of experiments provide information at very different spatial scales and thus confronting their results is a very challenging task. On the other hand, validation using simulated data generated from realistic surface and atmosphere models is not fully satisfactory due to the unavoidable limitations of the models. In this paper, a new strategy to validate the processing of planetary data is introduced. In particular, we propose the use of another type of imagery acquired over the Russell dune to build a ground truth for validation of spectral unmixing techniques.

1) HiRISE Data: The HiRISE camera is a unique tool to study the surface of Mars due to its very high spatial resolution. HiRISE consists of a half-meter reflecting telescope which allows taking three-channel (near-infrared, red, and blue-green) pictures with resolutions up to 25 cm/pix [31]. Two products are made available by HiRISE, a red-channel image making use of the full field of view and a three-channel image whose extent on the ground is significantly reduced.

Being aboard MRO, HiRISE is coordinated with CRISM to generate pair of images CRISM-HiRISE, displaying the same area of Mars. Fig. 2 (upper right) shows the footprints of the two products corresponding to the HiRISE image PSP_002482_1255 to be compared to the CRISM image frt000042aa. In this paper, the red-channel product is selected because of its larger coincident footprint as regards the CRISM image and twice better spatial resolution in comparison with the three-band image. Likewise, Fig. 2 shows the same area of the Russell dune observed by the CRISM and the HiRISE instruments. As it can be seen, HiRISE displays the dark features with a much greater detail, making them very distinguishable from the surrounding brighter ice. Hence, we propose to use the red-channel image PSP_002482_1255_RED to generate a reference abundance map corresponding to the dark features. The resulting ground truth will be then compared to the abundance maps obtained from the image frt000042aa, thus evaluating the performances of each unmixing technique in a similar and independent way.

The generation of the ground truth is as follows. First, the HiRISE image is classified by extracting the dark features. The resulting classification map and the CRISM image—previously projected onto the HiRISE geographic space—are registered by means of a feature matching method. Then, labels corresponding to the dark features are counted within the footprint of each CRISM pixel projected on the classification map. By doing this, the classification outcome is transformed into a reference abundance map against which the unmixing abundance maps will be compared in a pixel-wise manner.

2) Classification Map: The dark features are extracted by classifying the image PSP_002482_1255_RED into two classes, dark features and brighter ice, as suggested by geomorphologic analysis and the image histogram. With this aim, the image is split into k clusters according to gray value using a k-means strategy [32]. A value of $k = 7$ is satisfactory in our case. We note $\{L_1, \ldots, L_7\}$ the labels of the clusters and $\{C_1, \ldots, C_7\}$ their average values such that $(C_1 < \ldots < C_7)$. In order to represent the dark features, we select the darkest cluster L_1 which is manually improved by locally thresholding the original image. This operation takes into account the presence of shadows within the gullies that can be confused with elongated dark structures. Eventually, only the dark spots and the dark elongated features are classified as dark features while the rest of the image is classified as brighter ice. Fig. 3(a) shows the resulting classification map.

3) Image Registration: The classification map must be processed along with the CRISM image to allow an accurate pixel-wise comparison between the two final products (i.e., the ground truth coming from the HiRISE image and the abundance maps coming from the unmixing techniques). With this aim, we perform the registration of the HiRISE original image and the CRISM channel at 1.1 μm, which corresponds to the continuum of the spectra. One should note that the direct registration of the unmixing products is not reasonable since this might introduce some bias (e.g., if the unmixing results are wrong). The registration of CRISM and HiRISE images is very challenging because of the notable differences as regards the spatial resolution of both cameras ($\sim$72 times larger for HiRISE).

First, the selected CRISM channel is projected onto the HiRISE geographic space using the ancillary data of the image frt000042aa, which provide the latitude and longitude coordinates for each pixel. After this step, the two images are not correctly registered due to inaccuracies of pointing and limitations of the instrument models used to generate the geographical data of each sensor. That being so, we first perform a coarse registration of both images by applying a spatial translation whose Δl and Δc (where l and c stand for line and column, respectively) maximize the correlation coefficient between both images. Eventually, a Delaunay triangulation refines the registration by warping the CRISM image using a set of manually selected ground control points.

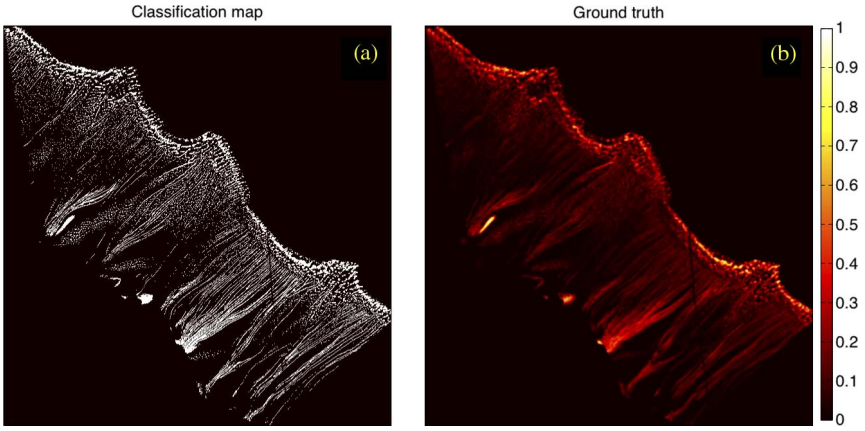

Fig. 3. (a) Classification map corresponding to the dark features extracted from the original HiRISE image. The label occurrences corresponding to the dark features are represented by white points. (b) Reference abundance map used as ground truth.

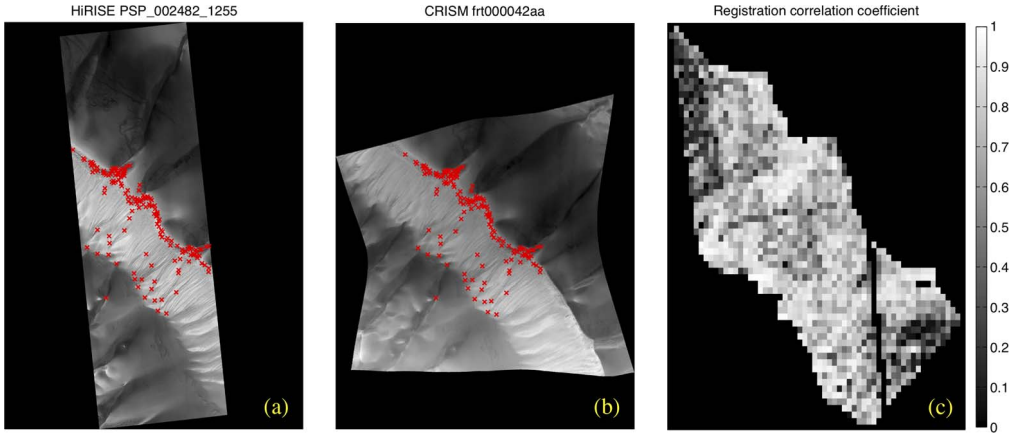

Fig. 4. (a) HiRISE image with the corresponding registration control points as red crosses. (b) The same as Fig. 4(a) for the CRISM image. (c) Registration accuracy map displaying the local correlation coefficient computed on the intersection between the two images and the ROI on a 10 × 10-pixel basis.

The registration step is detailed in Fig. 4. Fig. 4(a) and (b) show, respectively, the HiRISE and the CRISM images with the corresponding ground control points. More than 200 reference points are defined over the southwest-facing scarp, particularly for the dark spots along the ridge of the dune as they are critical features in the upcoming comparison. The accuracy of the registration is evaluated by calculating the local correlation coefficient r_{reg} between the HiRISE image and the CRISM channel at 1.1 μm after registration. Fig. 4(c) shows the ensemble of r_{reg} values that are obtained using a 10 × 10 sliding window over the area, resulting from the intersection of the two images and the ROI [see Fig. 2 (upper right)]. The resulting correlation map underlines the accuracy of the registration with an average correlation $r_{reg} = 0.7$. In addition, Fig. 4(c) provides valuable information on the distribution of the registration accuracy that will be used in the validation stage. Given the manual selection of control points and the size of the images (29 862 × 63 004 pixels for the HiRISE image), misregistration inaccuracies affect this processing step, particularly on the borders of the processed area.

4) Reference Abundance Map: After registration, the HiRISE classification map is transformed into an abundance map. Since the data manipulation is performed on the HiRISE geographic space, each CRISM pixel is now associated to a footprint containing several pixels at the HiRISE resolution. That being so, the reference abundances are calculated by counting the number of dark labels occurring in each CRISM footprint. The result is then divided by the total number of labels. By doing this, we obtain an image that provides the abundance of dark features at the CRISM resolution.

One should note that the remotely sensed signal that determines the radiance value of each CRISM pixel comes not only from its conjugated area at the Martian surface (i.e., the theoretical footprint) but also the areas corresponding to the neighboring pixels. This additive contribution to the signal is originated by two principal causes. First, the spatial response of a single CRISM detector element—characterized by its Gaussian-shaped point spread function (PSF)—partially overlaps the PSFs of the neighboring detectors [1]. As a consequence, the final radiance value is the weighted sum of the contribution coming from the target pixel and its neighbors. In addition, CRISM images suffer from the so-called adjacency effect that is common to all 2-D imagers [33]. Due to the aerosol particles in the atmosphere, some photons coming from the neighboring area of a given pixel are scattered toward its corresponding detector element, thus contributing to the final radiance value. These two effects result in a blurring of the image that is not taken into account by the label counting process introduced previously. Since evaluating the coupling of the adjacency and PSF effects is not straightforward, the image blurring is mimicked

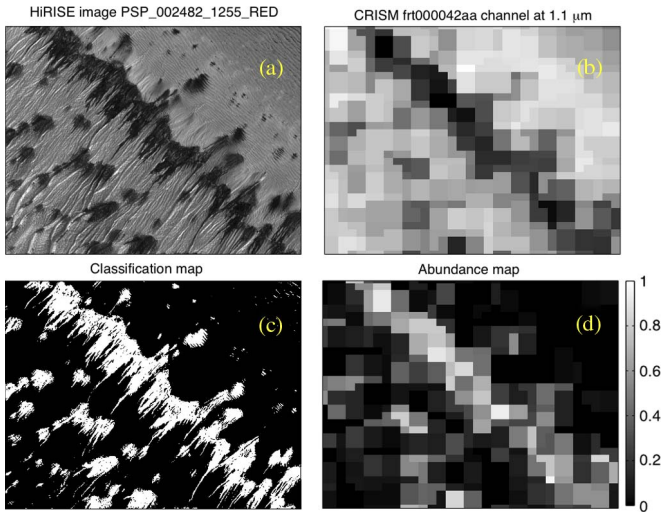

Fig. 5. Detail of the ground truth generation. (a), (b) HiRISE and CRISM images after registration. (c) Classification map highlighting the dark features. (d) Reference abundance map after pixel counting.

by filtering the reference abundance map by a Gaussian low-pass filter. The size of the Gaussian kernel is determined by optimizing the correlation coefficient between the registered CRISM channel at 1.1 μm and the filtered HiRISE image.

Fig. 3(b) shows the final ground truth that will be used for validating the unmixing products. Lastly, Fig. 5 illustrates the different processing steps on a small area of the Russell dune.

III. Spectral Unmixing

We note $\mathbf{X}$ the matrix representing the flatten hyperspectral image cube such that $\mathbf{X} = \{\mathbf{x}_1, \mathbf{x}_2, \ldots, \mathbf{x}_{N_p}\}$, where $\mathbf{x}_k = \{x_{1,k}, x_{2,k}, \ldots, x_{N_s,k}\}^T$. $x_{l,k}$ represents the value of the kth pixel at the lth channel, N_p is the number of pixels, and N_s is the number of spectral channels. We assume that the spectrum of each pixel can be reduced to a linear mixture of N_c endmember spectra, leading to the following instantaneous model:

$$\mathbf{X} = \mathbf{M} \cdot \mathbf{S} + \mathbf{e} \tag{1}$$

where $\mathbf{e}$ stands for the additive noise in the image, $\mathbf{M} = \{\mathbf{m}_1, \mathbf{m}_2, \ldots, \mathbf{m}_{N_c}\}$ is the mixing matrix, being $\mathbf{m}_n$ the spectral signature—the characteristic spectrum—of the nth endmember, and $\mathbf{S} = \{\mathbf{s}_1, \mathbf{s}_2, \ldots, \mathbf{s}_{N_c}\}^T$ is the source matrix with $\mathbf{s}_n = \{s_{n,1}, s_{n,2}, \ldots, s_{n,N_p}\}$. $s_{n,k}$ correspond to the abundance of the nth endmember at the kth pixel and its positivity is generally imposed. Besides, the endmember abundances must respect the sum-to-one constraint such that $\sum_{n=1}^{Nc} s_{n,k} = 1, \forall k$. In order to extract $\mathbf{M}$ and $\mathbf{S}$ from $\mathbf{X}$ without any *a priori* information, N_c must be estimated in the first place. An endmember extraction approach is then applied to retrieve $\mathbf{M}$, followed by the reconstruction of $\mathbf{S}$ based on the extracted spectra and the linear model of (1).

Physical assumptions leading to the linearity of the remote sensing signal are enumerated in [12] as: (i) predominance of linear subpixel mixing at the ground; (ii) absence of nonlinear mixing; (iii) Lambertian surface or homogeneity of surface illumination conditions; and (iv) absence of atmospheric absorption and scattering. In this paper, the presence of linear subpixel mixing in some specific areas of the Russell dune has been demonstrated by the scrutiny of the HiRISE image in Section II-C-1. Due to the lower spatial resolution of the CRISM instrument, the hyperspectral signal corresponding to some specific areas is composed by the signatures of two physically distinct components at the surface, resulting in geographic subpixel mixtures. By contrast, the absence of nonlinear mixtures cannot be assured as that would require data at the grain-size scale. A first attempt to address this point is presented in Section V by relating the reconstruction error of the spectra to the existence of nonlinearities. Future work will further expand this issue by performing a complete physical analysis of the test image as it is stated in Section VI. As regards atmospheric contributions, assumptions of linearity are met after the preprocessing in Section II-B-1. However, potential residues may lead to perturbations on the spectral unmixing process. Likewise, the heterogeneity of surface illumination may also result in some artifacts. All the previous factors $\mathbf{F} = \{\mathbf{f}_1, \mathbf{f}_2, \ldots, \mathbf{f}_{N_c}\}$, including residues coming from instrumental artifacts, may transform the linear mixing assumption into the degenerated model

$$\mathbf{X} = \Im(\mathbf{M} \cdot \mathbf{S}) + \mathbf{e} \simeq \mathbf{F} \cdot \mathbf{M} \cdot \mathbf{S} + \mathbf{e} \tag{2}$$

where $\Im(X) = \mathbf{F} \cdot X + \mathbf{F}_2 \cdot X^2 + \ldots \simeq \mathbf{F} \cdot X$. Furthermore, spurious transformations arising from $\mathbf{F}$ may affect the physical sources $\mathbf{M}$. In that case, the number of endmembers estimated by the following methods may become higher for $\mathbf{F} \cdot \mathbf{M} \cdot \mathbf{S}$ than it is for $\mathbf{M} \cdot \mathbf{S}$.

A. Estimation of the Number of Endmembers

Two methods are considered in order to estimate the number of endmembers in the image frt000042aa, the widely used Hyperspectral Signal Subspace Identification by Minimum Error (HySIME) approach and the recent Eigenvalue Likelihood Maximization (ELM) technique, which has been originally developed for hyperspectral data from Mars.

1) HySIME*:* This approach has been recently proposed as a minimum mean square error-based approach to infer the signal subspace in hyperspectral imagery [34]. HySIME is eigendecomposition-based, unsupervised, and fully automatic. It first estimates the signal and noise correlation matrices and then selects the subset of eigenvalues that best represents the signal subspace in the least squared error sense. The performances of HySIME have been validated satisfactorily by using simulated and terrestrial remotely sensed hyperspectral data.

2) ELM: This technique is proposed as an automatic and unsupervised algorithm for estimating the number of endmembers of hyperspectral images [14]. This approach is based on the distribution of the eigenvalues corresponding to the correlation and covariance matrices of $\mathbf{X}$. In particular, ELM assumes that the couple of nth eigenvalues of both matrices correspond to the variance of the noise for $n > N_c$. That being so, the distribution of the difference between a couple of eigenvalues z_n is asymptotically modeled by a Gaussian probability density function centered at zero for $n > N_c$ and a non-zero value otherwise. Based on this property, ELM builds a likelihood function depending on z_n that shows a global maximum for

$n = N_c$. In [14], this approach is validated using simulated data and hyperspectral images from Mars acquired by the OMEGA instrument. However, ELM supposes the Gaussianity of the noise while CRISM noise is hardly Gaussian.

B. Endmember Extraction

After estimating the number of endmembers N_c of the test image, we perform a selection of state-of-the-art algorithms based on different principles as follows: (i) geometric techniques assuming the presence of pure pixels in the image; (ii) geometric approaches without pure pixel assumption; and (iii) statistic methods based on a Bayesian framework. In addition, we consider the incorporation of spatial information by performing spatial preprocessing on the image frt000042aa. The endmember extraction techniques considered in this paper are briefly explained as follow.

1) VCA: VCA has been proposed as an efficient and fast geometric method for extracting endmembers under a linear mixing supposition [13]. According to the sum-to-one condition, the data vectors $\mathbf{x}_k$ are always inside a simplex formed by $\mathbf{M} \cdot \mathbf{S}$ whose vertex are the spectra of the endmembers. VCA iteratively projects the data onto the orthogonal direction to the subspace spanned by the already extracted endmembers, designating the most extreme projection as the next endmember. The process is repeated until N_c endmembers are found. That being so, VCA assumes that (i) there are pure pixels in the data and (ii) there is no noise. However, the latter means that $\mathbf{x}_k$ may be outside the simplex if noise is present. In [14], VCA is evaluated satisfactorily on OMEGA data from Mars and therefore it may be suitable for spectral unmixing of CRISM data.

2) N-FINDR: The widely used N-FINDR algorithm extracts extreme points of the simplex of maximum volume that can be inscribed within $\mathbf{X}$ using a simple nonlinear inversion [15]. This approach iteratively selects random endmembers and evaluates whether the volume of the simplex sustained by those endmembers changes or not. The convex nature of hyperspectral data allows this operation to be performed in a quick and relatively straightforward manner. Contrarily to VCA, N-FINDR is a truly simplex volume-based technique. However, this method may become less efficient and not reproducible due to its randomness. N-FINDR has been applied on CRISM data with satisfactory results in [16].

3) MVC-NMF: This technique is proposed for endmember extraction of highly mixed hyperspectral data without the pure pixel assumption [17]. MVC-NMF decomposes mixed pixels by analyzing the connection between the spectral unmixing analysis and the non-negative matrix factorization. A minimum volume constraint makes the MVC-NMF learning less dependent on the initializations, robust to different levels of noise, less sensitive to the estimated number of endmembers, and applicable to images with or without pure pixel representations. Experiments in [17] indicate that MVC-NMF has the potential of identifying less prevalent endmembers and thus it may be suitable for extracting the dark features in frt000042aa.

4) MVES: The recent MVES approach proposes a convex analysis without involving pure pixels [18]. Through an affine set fitting of observed pixels followed by the use of Craig's unmixing criterion, the MVES problem aims at minimizing a simplex volume subject to the constraint that all the dimension-reduced pixels are enclosed in the simplex. MVES utilizes linear programs to approximate the unmixing problem in a cyclic fashion. MVES might be suitable for this paper since it has proved to work well for endmembers with low purity levels and to outperform the VCA and MVC-NMF algorithms [18].

5) SISAL: Recently, the SISAL method has been proposed to solve the linear unmixing of the minimum volume simplex without pure pixel assumption [19]. Being a non-convex optimization problem with convex constraints, the positivity constraints are replaced by soft constraints, forcing the spectral vectors to belong to the convex hull of the endmember signatures. The resulting problem is solved by a sequence of augmented Lagrangian optimizations. SISAL may be appropriate for the unmixing of the test image due to its effectiveness. In [19], SISAL is satisfactorily validated on simulated data through comparison to other state-of-the-art methods such as VCA and MVES.

6) BPSS: This algorithm proposes to estimate the matrices $\mathbf{M}$ and $\mathbf{S}$ in a Bayesian framework under a linear model with inherent positivity and additivity constraints and no pure pixel assumption [35]. In BPSS, the noise $\mathbf{S}$ and $\mathbf{M}$ are assumed to follow a Gaussian, Dirichlet, and Gamma probability density functions, respectively. BPSS is based on hierarchical Bayesian models to encode prior information regarding the parameters of interest. The complexity of the estimation from the resulting posterior distribution is overcome using Markov chain Monte Carlo methods. In BPSS, the degree of uncertainty affecting the extracted endmember spectra can be estimated since results are computed as probability distribution functions. In [36], numerical schemes are devised to reduce the computation time which is a critical point of BPSS. This method has been applied satisfactorily on OMEGA hyperspectral images in [12] yet never on CRISM's.

7) Spatial Preprocessing: The authors of [21] propose a preprocessing to incorporate spatial information into the unmixing of hyperspectral images. For each pixel, a scalar factor related to the spectral similarity of spectra lying within a certain spatial neighborhood—determined by the window size w_s—is estimated. This value is then used to weigh the importance of the spectral information associated to each spectrum in terms of its spatial context. After applying a traditional endmember extraction technique on the preprocessed image, the spatial position of each endmember is retrieved. Then, the reconstruction of the abundance maps is carried out by using the analogous spectra from the original image and a linear mixture model. This preprocessing enhances the search for endmembers in spatially homogeneous areas while it may penalize the detection of anomalous sources. This Preprocessing can be combined only with methods such as VCA and N-FINDR, as the existence of pure pixels is required to retrieve the position of the endmembers in the preprocessed image.

IV. Experiments

Experiments are conducted on the preprocessed image frt000042aa. We recall that only the spectra encompassed by

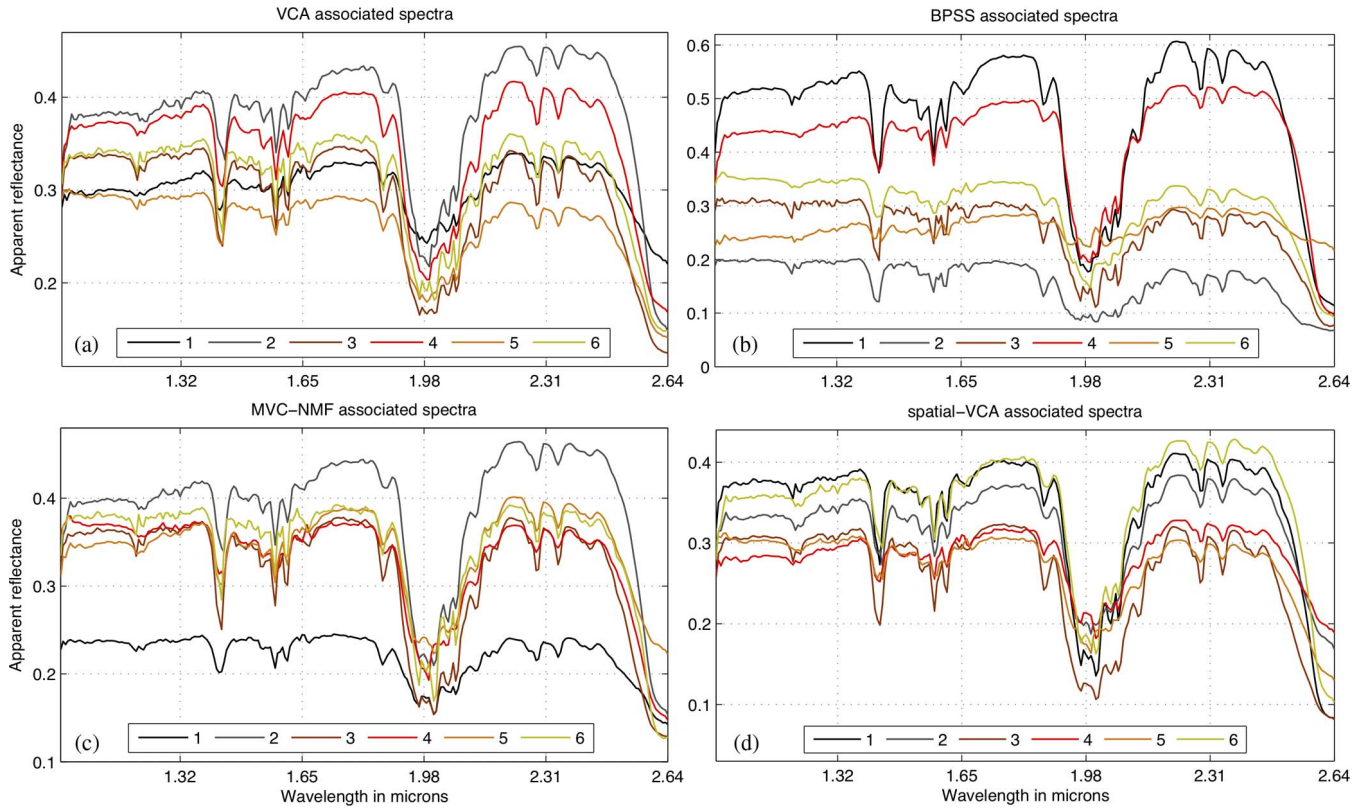

Fig. 6. Extracted spectra by the (a) VCA, (b) BPSS, (c) MVC-NMF, and (d) spatial-VCA methods.

the defined ROI are considered. By performing spectral unmixing, we consider two main objectives, (i) the extraction of physically meaningful sources and their corresponding distribution maps that help understanding the physical state of the Russell dune and (ii) the obtention of a physical source related to the dark features to be compared to the ground truth generated in Section II-C. One should note that while the achievement of the second purpose is not mandatory (yet desirable), the first objective is crucial for the validation of spectral unmixing techniques in a planetary context.

First, the number of endmembers in the image frt000042aa is determined by the two methods presented in Section III-A. On one hand, the HySIME technique determines $N_c = 14$. Given that the Russell dune is assumed to be composed by two components—CO_2 ice and dust—this result largely exceeds the expected number of sources in the image. Furthermore, the analysis of 14 extracted endmembers turns into a rather unfeasible task. The reason of this result may come from a higher sensitivity of HySIME to subtle contributions in the image that could be valuable in other situations out of the scope of this paper such as the detection of residual artifacts. Therefore, HySIME is not further considered in this paper. On the other hand, the ELM technique detects the presence of six endmembers. This result seems to correspond more satisfactorily to the physical scenario prevailing in the Russell dune and corroborates the good performances of ELM when applied to OMEGA hyperspectral data from Mars [14]. As regards the requirement of Gaussian noise by ELM, the VCA endmember extraction was conducted with $N_c = \{4 \ \ldots \ 8\}$ in order to evaluate the robustness of the N_c estimation by ELM. However, experiments with $N_c \neq 6$ did not provide any significant improvement regarding the unveiling of the physical sources. For this reason and since a similar conclusion would be likely drawn from operating the other methods in the same way, all the presented experiments are carried out by using $N_c = 6$.

As regards endmember extraction, all the techniques introduced in Section III-B are applied on the test image. However, the results of a few methods are not shown in this paper, as they do not meet the main objectives detailed above. For example, MVES and SISAL are not further considered as they both extract an endmember whose associated spectrum cannot be explained from a physical point of view. This is in agreement with the fact that both methods are based on simplex volume optimization and therefore may extract endmembers absent in the image. Although MVC-NMF and BPSS do not consider the pure pixel assumption either, they provide satisfactory endmembers and therefore are considered in this paper. Likewise, the results of the N-FINDR algorithm are not shown in this section since a satisfactory source related to the dark features could not be extracted, contrarily to VCA. As a consequence, the spatial preprocessing introduced in Section III-B7 is exclusively combined with the VCA approach, thus defining the method referred to as spatial-VCA. The window size w_s is set equal to five as it is recommended in [21] and given that larger values may affect the endmembers related to the spatially confined dark features. Hence, in this paper, we present the experimental results of performing spectral unmixing of the image frt000042aa by the following endmember extraction methods based on different principles: (i) the VCA method with assumption of pure pixels; (ii) the BPSS technique based on

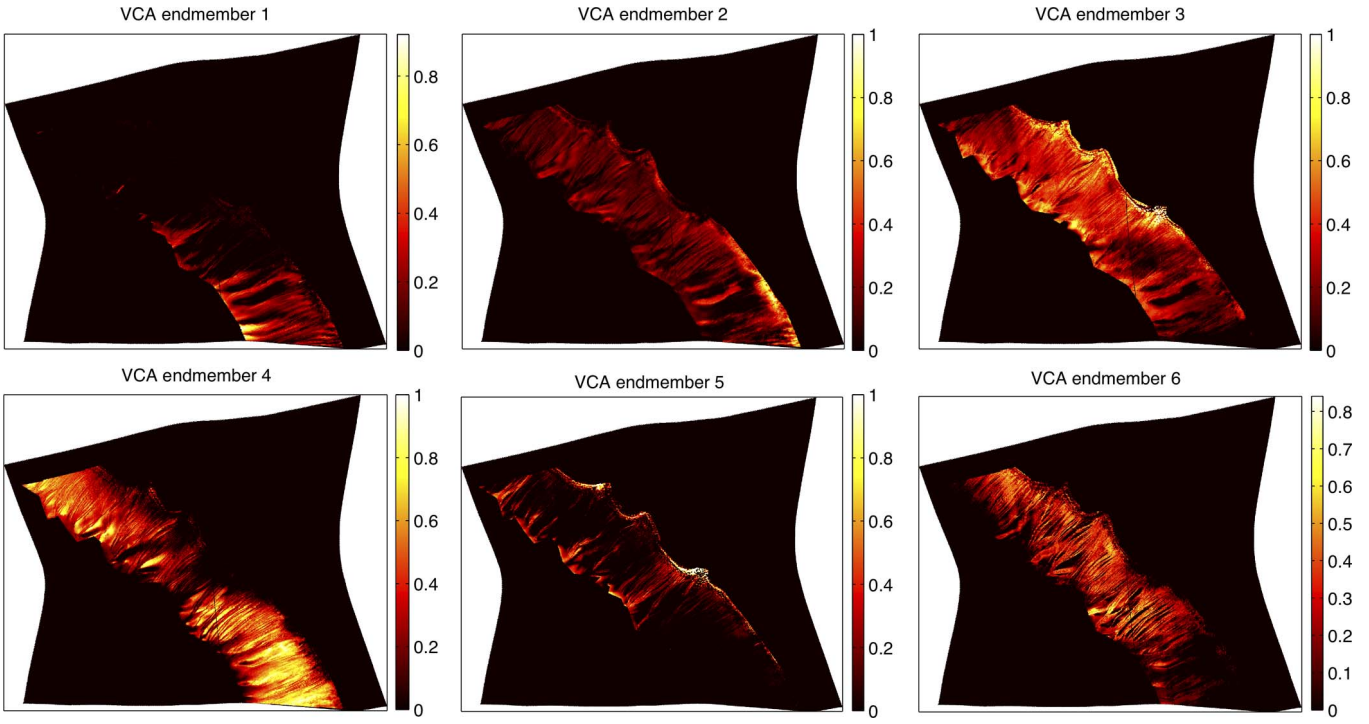

Fig. 7. Abundance maps corresponding to the six endmembers extracted using VCA.

a Bayesian framework; (iii) the MVC-NMF approach with no assumption of pure pixels; and (iv) the spatial-VCA algorithm that incorporates the existent spatial information in the image. As for the reconstruction of the abundance maps using the linear mixing model, the non-negativity and the sum-to-one constraints are considered for all methods.

A. General Interpretation

The spectra corresponding to the six endmembers extracted by each method are plotted in Fig. 6. Then, Figs. 7–10 show the associated abundance maps. Based on the information coming from both products, a similar physical interpretation of the scene is performed independently for each method, leading to the definition of three physical sources. Due to residual artifacts and other nonlinearities, the spectral unmixing of the image frt000042aa is affected by source splitting effects (see Section III), thus making necessary the recombination of the six endmembers into three physical sources. After assigning each extracted endmember to one of the three physical sources, the abundance map of a given physical source is obtained by adding the individual abundances of the associated endmembers. The results of this recombination are shown in Fig. 11. The robustness of the proposed interpretation is underlined by the notable similarities among the physical sources that are reconstructed for each method.

In order to identify the origin of each endmember, two parameters are defined from each extracted spectrum. Let $R_{1.1}$ be the apparent reflectance value at 1.1 μm and let $B_{2.3}$ be the absorption depth at 2.3 μm such that $B_{2.3} = 1 - R_{2.3}/R_{2.2}$. These two spectral parameters are decisive for the interpretation of the endmembers together with the information coming from the abundance maps. In particular, large values of $R_{1.1}$ and $B_{2.3}$ are related to a higher content of CO_2 ice because of its higher reflectance in comparison to dust and the fact that absorption at 2.3 μm is specific to ice, respectively. Due to inaccuracies in the atmospheric correction (see Section II-B-1), extracted spectra may have an anomalous positive or negative slope that must be accounted for the calculation of $B_{2.3}$. With this aim, we multiply $B_{2.3}$ by the spectrum average slope $b_{1.1-2.2}$ that is calculated as $R_{2.2}/R_{1.1}$. Tables I–IV detail the previous parameters for each endmember extracted with VCA, BPSS, MVC-NMF, and spatial-VCA, respectively.

The three physical sources that are defined based on the unmixing results are briefly described by detailing their spectral and spatial characteristics. The physical interpretation of each source is kept to a minimum since it is not the aim of this paper.

- Dark source: physical source related to the presence of dark features. The corresponding $R_{1.1}$ and $B_{2.3}$ are the lowest among the three sources due to a high content in dust and a few residual CO_2 ice. This source predominates along the ridge of the dune and within the gullies in the form of dark spots and elongated patterns, respectively.
- Strong bright source: physical source related to a high content of CO_2 ice. The corresponding $B_{2.3}$ is the highest among the three sources while $R_{1.1}$ is higher than for the dark source due to a lower dust content. This source predominates principally in the areas surrounding the dark source.
- Weak bright source: physical source related to a high content of CO_2 ice. The corresponding $R_{1.1}$ is the highest among the three sources while $B_{2.3}$ is higher than for the dark source but lower than for the strong bright source. This source may correspond to a physical state of the ice—different from the strong bright source—that greatly predominates on the dune scarp.

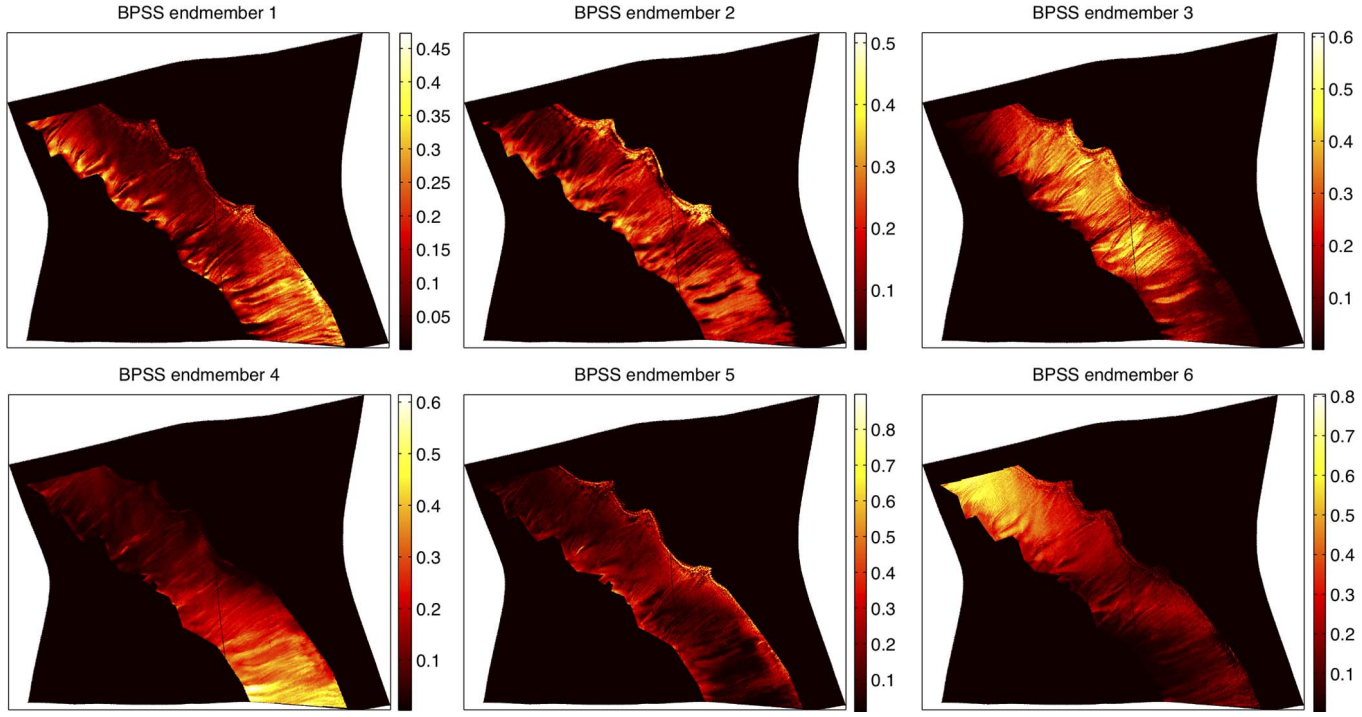

Fig. 8. Abundance maps corresponding to the six endmembers extracted using BPSS.

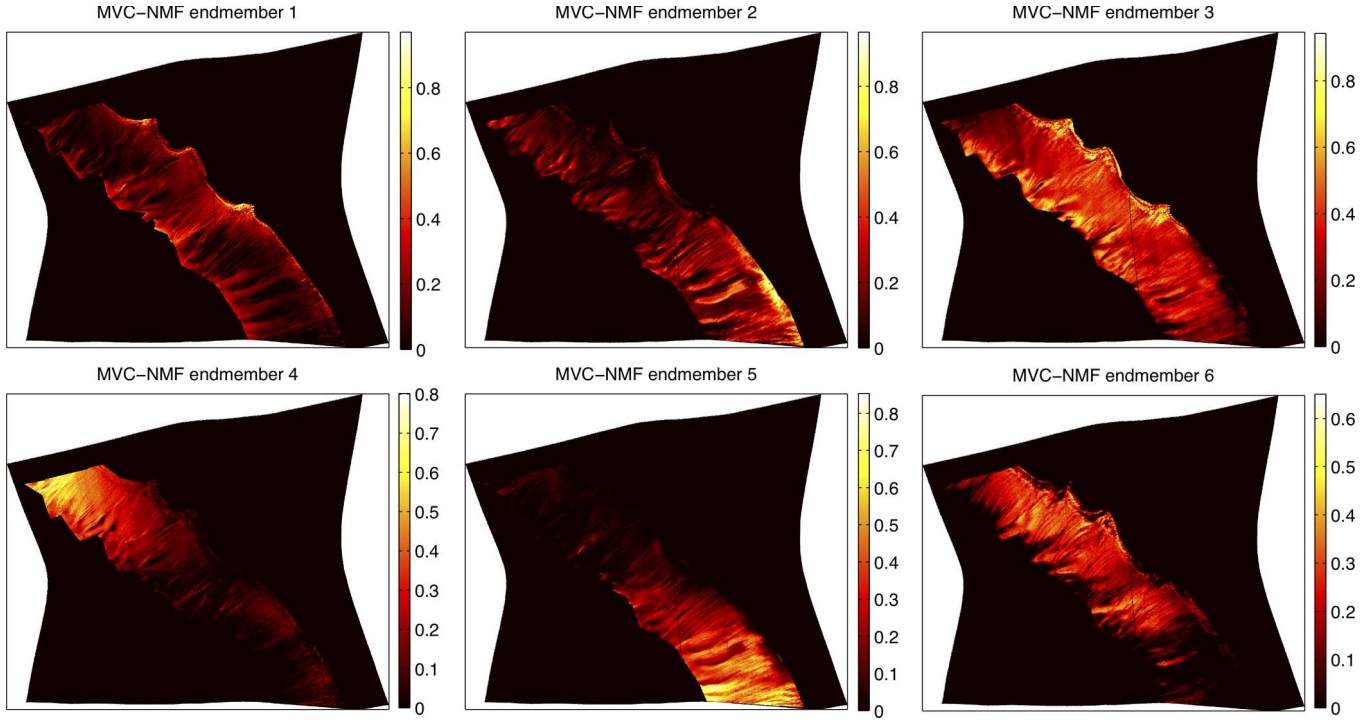

Fig. 9. Abundance maps corresponding to the six endmembers extracted using MVC-NMF.

In the following sections we detail, for each method, the recombination process that is carried out to reconstruct the three physical sources.

B. VCA

The interpretation of the endmembers extracted by VCA is conducted by examining the associated spectra and abundance maps in Figs. 6(a) and 7, respectively. The spectral parameters $R_{1.1}$ and $B_{2.3}$ are detailed in Table I. Lastly, the recombined abundance maps corresponding to the physical sources are displayed in Fig. 11(a).

1) Dark Source: Endmembers 1 and 5 are identified to be related to the dark source due to the lowest $R_{1.1}$ and $B_{2.3}$ among the six endmembers.

The combination of the two endmembers into a single physical source is also justified by the opposite vertical trends that affect the abundance maps 1 and 5. Both maps show

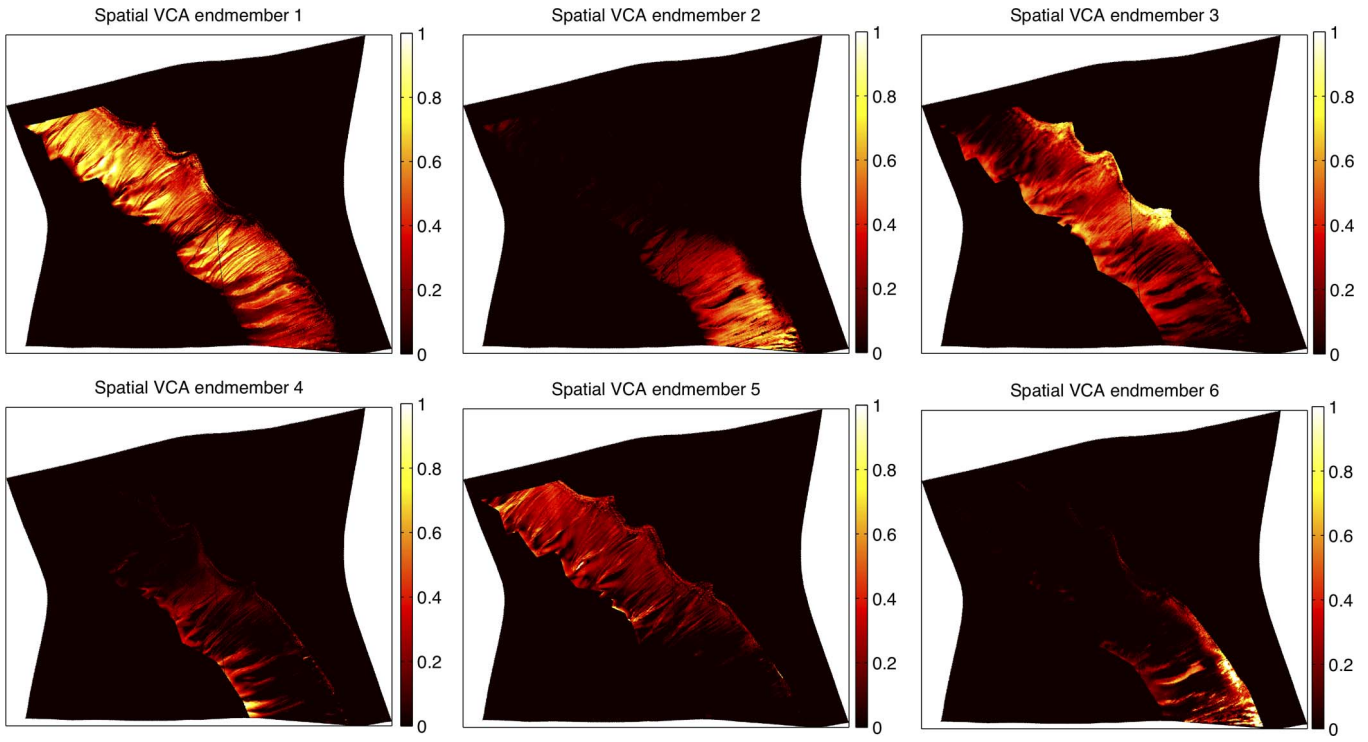

Fig. 10. Abundance maps corresponding to the six endmembers extracted using spatial-VCA.

very low spurious abundances, either for the top or the bottom rows, coming from the atmospheric residue described in Section II-B-1. This interpretation is also pointed out by the complementary slopes of the spectra ($b_{1.1-2.2} > 1$ for endmember 1 and $b_{1.1-2.2} < 1$ for endmember 5).

The abundance map resulting from the fusion of the two initial abundance maps eliminates the vertical trend, thus revealing the dark structures over the Russell dune. As a matter of fact, the red pixels of the recombined abundance map highlight the dark spots on the top of the dune, the dark elongated patterns along the gullies and some areas belonging to the base of the northeast-facing defrosted scarp.

2) Strong Bright Source: Endmember 3 is identified to represent the strong bright source due to the highest $B_{2.3}$ among all the extracted endmembers and a medium $R_{1.1}$.

The abundance map of the strong bright source shows a spatial coherence with the dark source as the green areas surround the red pixels, particularly on the top of the dune.

3) Weak Bright Source: Endmembers 2, 4, and 6 are identified as being related to the weak bright source as they all correspond to the highest $R_{1.1}$ and a medium $B_{2.3}$.

The splitting phenomenon that affects this physical source comes from the coupling of two nonlinear residues. On the one hand, the predominance of CO_2 ice for this physical source leads to a typical smile pattern in the abundance map of endmember 6 (see Section II-B-1). This is pointed out by the anomalous lower abundances for the horizontal edges. The presence of a spectral smile residue makes endmember 6 enough energetic to be extracted independently. On the other hand, the differences of $R_{1.1}$ among the three endmembers are explained by the different illumination conditions that happen over the scene. A qualitative study of the HiRISE DTM corresponding to the Russell dune (see Section II-B-1) reveals that endmember 6 predominates at low SZA while endmembers 2 and 4 correspond to SZA values that are similar to the average angle used in the photometric correction. An accurate photometric correction by the real SZA would increase $R_{1.1}$ for endmember 6, thus matching the other two endmembers in terms of apparent reflectance.

The abundance map resulting from the fusion of the three endmembers highlights in blue the areas which are poor in dark and strong bright sources.

C. BPSS

Given the nature of the BPSS algorithm the interpretation of the corresponding results must be carried out differently than it is done for VCA. As it is stated in Section III-B, BPSS may extract associated spectra that do not exist in the hyperspectral image. As a consequence, the parameters $R_{1.1}$ and $B_{2.3}$, shown in Table II, are less relevant and must be taken into account in an indicative manner. Similarly to VCA, Figs. 6(b), 8, and 11(b) detail the results of BPSS.

1) Dark Source: Endmember 5 is identified to be related to the dark features according to the lowest $B_{2.3}$. While having the lowest $R_{1.1}$, endmember 2 is not interpreted as representing the dark source since such a low level of apparent reflectance does not exist in the image and is unphysical (see Section IV-C2 for more details).

Besides the agreement of the extracted spectrum with the characteristic spectral features of the dark source, the abundance map of endmember 5 is correlated with the dark structures revealed by the other methods.

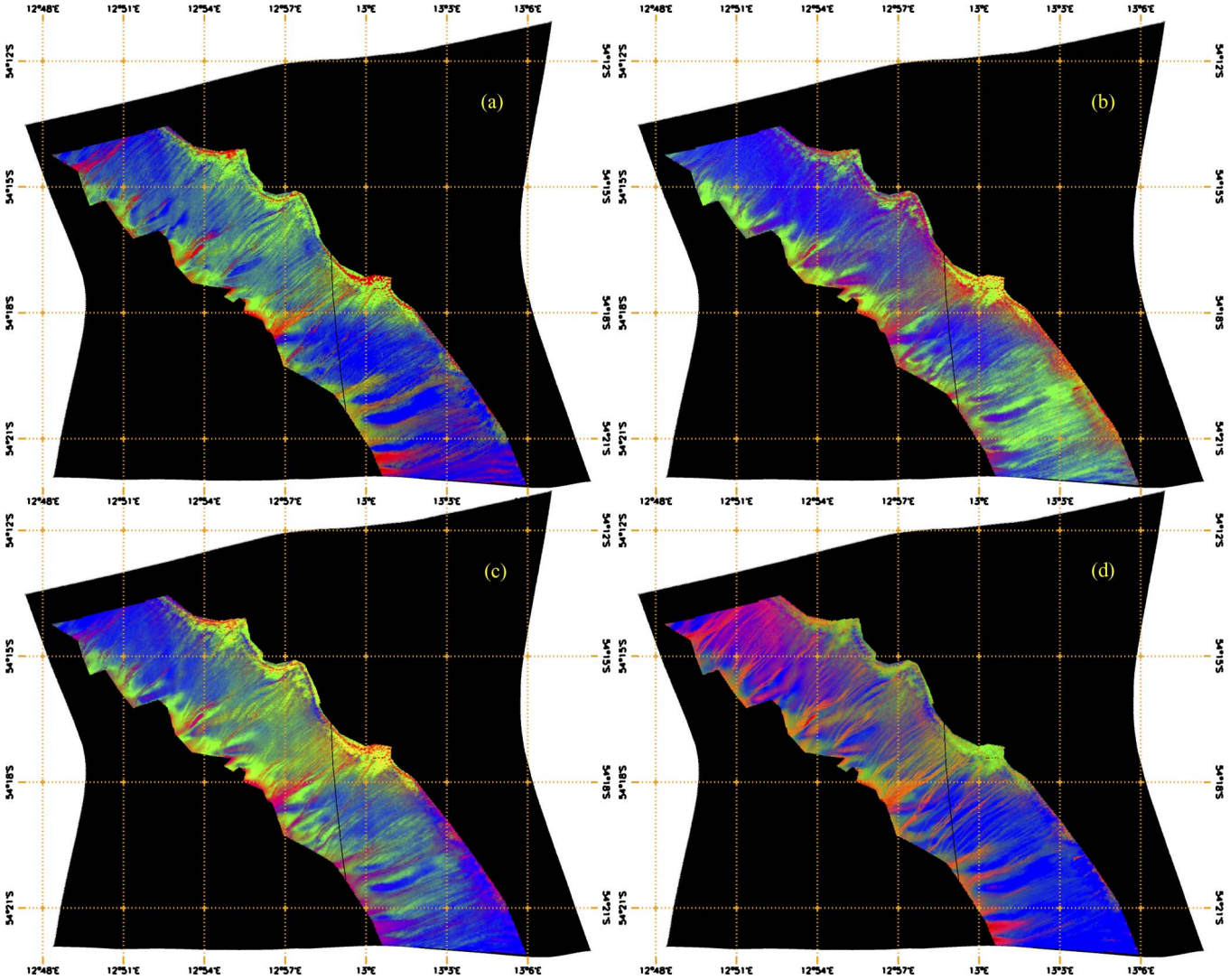

Fig. 11. (a) Color composite image illustrating the spatial distribution of the three physical sources over the Russell dune extracted by VCA. The dark, strong bright, and weak bright sources are show in red, green, and blue, respectively. (b), (c) and (d) Same as Fig. 11(a) for BPSS, MVC-NMF, and spatial-VCA.

TABLE I
VCA ENDMEMBERS—APPARENT REFLECTANCE AT 1.1 μm AND ABSORPTION DEPTH AT 2.3 μm—(D): DARK SOURCE, (S): STRONG BRIGHT SOURCE, (W): WEAK BRIGHT SOURCE

Endmember:	1 (D)	2 (W)	3 (S)	4 (W)	5 (D)	6 (W)
$R_{1.1}$:	**0.29**	**0.38**	**0.34**	**0.37**	**0.29**	**0.35**
$b_{1.1-2.2}$:	1.15	1.20	1.02	1.13	0.98	1.06
$B_{2.3}$:	**0.07**	**0.10**	**0.17**	**0.12**	**0.09**	**0.13**

TABLE II
BPSS ENDMEMBERS—APPARENT REFLECTANCE AT 1.1 μm AND ABSORPTION DEPTH AT 2.3 μm—(D): DARK SOURCE, (S): STRONG BRIGHT SOURCE, (W): WEAK BRIGHT SOURCE

Endmember:	1 (S)	2 (S)	3 (W)	4 (W)	5 (D)	6 (W)
$R_{1.1}$:	**0.51**	**0.20**	**0.31**	**0.43**	**0.24**	**0.35**
$b_{1.1-2.2}$:	1.18	0.91	0.95	1.20	1.25	0.96
$B_{2.3}$:	**0.15**	**0.25**	**0.17**	**0.09**	**0.08**	**0.11**

TABLE III
MVC-NMF ENDMEMBERS—APPARENT REFLECTANCE AT 1.1 μm AND ABSORPTION DEPTH AT 2.3 μm—(D): DARK SOURCE, (S): STRONG BRIGHT SOURCE, (W): WEAK BRIGHT SOURCE

Endmember:	1 (D)	2 (W)	3 (S)	4 (W)	5 (W)	6 (W)
$R_{1.1}$:	**0.24**	**0.39**	**0.36**	**0.37**	**0.34**	**0.38**
$b_{1.1-2.2}$:	1.01	1.17	1.04	1.00	1.16	1.03
$B_{2.3}$:	**0.08**	**0.08**	**0.16**	**0.08**	**0.10**	**0.10**

TABLE IV
spatial-VCA ENDMEMBERS—APPARENT REFLECTANCE AT 1.1 μm AND ABSORPTION DEPTH AT 2.3 μm—(D): DARK SOURCE, (S): STRONG BRIGHT SOURCE, (W): WEAK BRIGHT SOURCE

Endmember:	1 (W)	2 (W)	3 (S)	4 (D)	5 (D)	6 (W)
$R_{1.1}$:	**0.37**	**0.33**	**0.30**	**0.28**	**0.29**	**0.36**
$b_{1.1-2.2}$:	1.10	1.16	1.04	1.18	0.97	1.20
$B_{2.3}$:	**0.11**	**0.11**	**0.21**	**0.09**	**0.09**	**0.10**

2) Strong Bright Source: Endmembers 1 and 2 are related to the strong bright source. Due to the combination of the atmospheric residue and the BPSS properties, this source has been split into two endmembers that do not exist in the image and are difficult to explain from a physical point of view. The combination of both endmembers is necessary to obtain

a coherent strong bright source in terms of spectrum and abundance map. This interpretation is justified by the following reasons based on the examination of the associated spectra: (i) The spectral slope of both spectra is complementary due to the atmospheric residue as in Section IV-B1 ($b_{1.1-2.2} > 1$ for endmember 1 and $b_{1.1-2.2} < 1$ for endmember 2); (ii) a spurious fingerprint at 2 μm for endmember 1, which is reversed for endmember 2; and (iii) the $R_{1.1}$ values of both endmembers are either too high or too low from a physical point of view. Likewise, the abundance maps also confirm this interpretation since (i) the endmembers 1 and 2 show a strong anticorrelation (for all k pixels with $s_{1,k} + s_{2,k} > 50\%$, $correlation(s_{1,k}, s_{2,k}) = -0.62$) and (ii) endmembers 1 and 2 are always present in similar proportions (for all k pixels with $s_{1,k} + s_{2,k} > 50\%$, $mean(s_{1,k}) = 0.26$, $var(s_{1,k}) = 3.10^{-3}$, $mean(s_{2,k}) = 0.30$, $var(s_{2,k}) = 4.10^{-3}$). It is straightforward to verify that the combination of these two endmembers using similar proportions results in a spectrum with similar $R_{1.1}$ and $B_{2.3}$ to the strong bright source extracted by the other methods.

Similarly to VCA, the resulting abundance map of the strong bright source shows a strong correlation with those areas surrounding the dark source pixels. In addition, several yellow pixels coming from the combination of the dark and strong bright sources are observed over the dune ridge. This is in agreement with a linear mixing scenario for which the spatial resolution of CRISM may not suffice to resolve both sources.

3) Weak Bright Source: The weak bright source is composed by endmembers 3, 4, and 6. The associated spectra of endmembers 4 and 6 correspond to a high $R_{1.1}$ and medium $B_{2.3}$. Again, the spectrum of endmember 3 presents a $R_{1.1}$ and $B_{2.3}$ that cannot be found in the image.

Similarly to the VCA dark source, endmembers 4 and 6 show strong values at the bottom or the top of the image. This anomaly is originated in the atmospheric residue as the slopes of the two endmembers underline ($b_{1.1-2.2} > 1$ for endmember 4 and $b_{1.1-2.2} < 1$ for endmember 6). Contrarily, endmember 3 is particularly dominant in the center of the image with abundance values up to 0.6, indicating an origin linked with the smile effect residue (see Section IV-B3).

The regions corresponding to the weak bright source are widespread over the dune scarp as shown by the combined abundance map.

D. MVC-NMF

The examination of the endmembers extracted by the MVC-NMF algorithm are conducted by examining the associated spectra and abundance maps shown in Figs. 6(c) and 9, respectively. The corresponding spectral parameters $R_{1.1}$ and $B_{2.3}$ are detailed in Table III while the combined abundance maps corresponding to the physical sources are displayed in Fig. 11(c). Similarly to BPSS, MVC-NMF may extract spectra that are absent from the image and thus the spectral parameters must be considered carefully.

1) Dark Source: Endmember 1 is identified as the dark source due to the lowest $R_{1.1}$ among all endmembers. Contrary to VCA and BPSS, the parameter $B_{2.3}$ is less discriminative for MVC-NMF as all spectra, except for number 3, have similar low values.

Again, the corresponding abundance map reveals the structures related to the dark features with high accuracy.

2) Strong Bright Source: Endmember 3 is identified to be related to the strong bright source due to the highest $B_{2.3}$ among all the extracted endmembers.

Similarly to the other methods, the corresponding abundance map highlights the areas that surround the dark features, particularly on the top of the dune.

3) Weak Bright Source: Endmembers 2, 4, 5, and 6 are identified as belonging to the weak bright source due to a high $R_{1.1}$ and a medium $B_{2.3}$.

Again, the splitting phenomenon affecting this physical source comes from atmospheric and photometric residues. For example, the abundance maps of the endmembers 4 and 5 present the vertical dichotomy detailed in Section IV-B1.

The abundance map obtained by combining the original ones is in agreement with the spatial distribution of the weak bright source extracted by the other methods.

E. Spatial-VCA

The scrutiny of the endmembers extracted by the spatial-VCA algorithm is based on the examination of the corresponding extracted spectra and abundance maps shown in Figs. 6(d) and 10, respectively. Likewise, the spectral parameters are detailed in Table IV and the combined abundance maps are shown in Fig. 11(d).

1) Dark Source: Endmembers 4 and 5 are identified to be related to the dark source due to the lowest $R_{1.1}$ and $B_{2.3}$ among the six endmembers.

Similarly to VCA, the fusion of the two endmembers is justified by spectral and spatial reasons, respectively, the vertical dichotomy and the complementary spectral slopes caused by the atmospheric residue.

Although the combined abundance map is broadly in agreement with the dark sources extracted by the other methods, a slight overestimation of abundance is detected for the upper rows probably due to a persistent residual contribution from the atmosphere.

2) Strong Bright Source: Endmember 3 is recognized as being the strong bright source because of the highest $B_{2.3}$ among all the extracted endmembers and a higher $R_{1.1}$ than for the dark source.

Contrarily to other methods, the associated abundance map shows some differences as the green areas mask the red pixels on some places of the top of the dune. This may come from the penalization of spatially confined sources—such as the dark source—coming from the spatial preprocessing.

3) Weak Bright Source: Endmembers 1, 2, and 6 are associated to the weak bright source due to the highest $R_{1.1}$ and a medium $B_{2.3}$.

This source splitting may come from both atmospheric and photometric residues. The recombination of these three endmembers is justified by the coherence of the resulting abundance map in comparison to other methods.

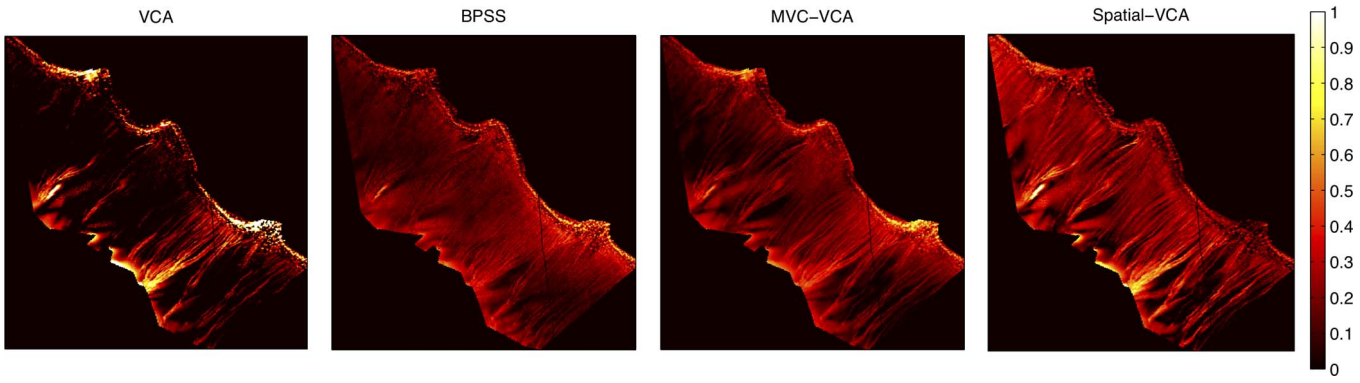

Fig. 12. From left to right, abundance maps corresponding to the dark source extracted by the algorithms VCA, BPSS, MVC-NMF, and spatial-VCA.

V. Validation

In this section, we aim at validating the results obtained by the proposed methodology based on spectral unmixing followed by recombination of the extracted endmembers into meaningful sources. First, Fig. 11 underlines the validity of both processes in a qualitative way as a quite similar relevant planetary scenario is unveiled after interpretation of the color composite images. The notable spatial similarities among the four composite abundance maps represent a cross-validation of the different endmember extraction techniques as well as it validates the corresponding recombination effort. A more in-depth validation is carried out by using the ground truth for the dark source that was introduced in Section II-C. In this matter, abundance maps are validated using the ground truth assuming that the dark features resolved by the HiRISE instrument correspond to the extracted dark source. Unfortunately, reference abundance maps cannot be built for the bright sources from the HiRISE image as they are not distinct by neither markedly different level of apparent reflectance nor structural specificities. Prior to the comparison, the registration procedure (see Section II-C3) is repeated using the same parameter values for the abundance maps provided by the VCA, BPSS, MVC-NMF, and spatial-VCA algorithms. Fig. 12 displays the four maps related to the dark source after cropping them to fit the intersection between the CRISM ROI and the HiRISE image. These products must be compared with the reference map in Fig. 3(b).

Several indicators are used to assess the similarity between the ground truth and the unmixing abundance maps. First, the Pearson correlation coefficient r is computed between both types of abundance maps to measure the similarity as regards to relative spatial distribution. Second, the average value of the absolute error ϵ is computed to complete the quantitative validation. Since misregistration is expected to be one of the main sources of error, several experiments are carried out by calculating r and ϵ according to registration accuracy [see Fig. 4(c)]. In this way, r and ϵ are summarized in Table V by (1) considering all pixels ($mean(r_{reg}) = 0.7$), (2) taking into account only those areas whose associated registration correlation meets $r_{reg} > 0.7$ ($\sim$50% of the pixels with $mean(r_{reg}) = 0.83$), and (3) by selecting the best registered area ($\sim$1% of the pixels with $mean(r_{reg}) = 0.96$). The region corresponding to the third experiment is shown in Fig. 5. A last experiment is performed for the whole population of pixels by computing the distribution of abundance values for the ground truth and the unmixing results (see Fig. 13).

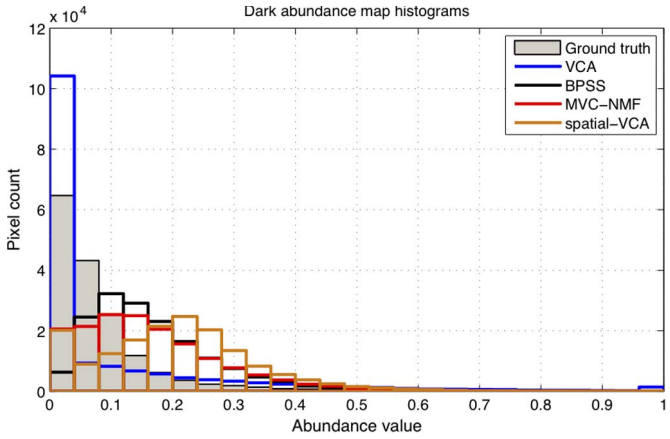

Fig. 13. Distribution of the dark abundances corresponding to the ground truth and the unmixing abundance maps.

In the first experiment, results show a quite good agreement between the unmixing results and the ground truth with r and ϵ values up to 0.69 and down to 0.08, respectively. As regards to correlation, all methods provide notable r values—close to 0.7—except for BPSS, which attains $r = 0.57$. This slight underperformance may be explained by the noisy background of the BPSS dark abundance map displayed in Fig. 12 and may point to a higher sensitivity of this method to the presence of dust. On the other hand, the examination of ϵ reveals that the abundances provided by the spatial-VCA approach are slightly worse with $\epsilon = 0.14$. This bias is mostly originated in the atmospheric residue affecting the upper rows in the form of a small overestimation that is conjugated with a poorer registration accuracy [see Figs. 4(c) and 12]. Contrarily, the average error for other methods is always $\epsilon \leq 0.10$. As for the second experiment, misregistration issues are proved to be an important source of error since the corresponding results outperform those of the first experiment, particularly in terms of r. As a matter of fact, all methods undergo a significant correlation improvement up to 0.06. The improvement of ϵ is less important as this indicator is less sensible to the spatial distribution of the abundance values. In this matter, the best value $\epsilon = 0.08$ seems to represent the intrinsic accuracy of the proposed methodology.

TABLE V
VALIDATION RESULTS REGARDING (1) ALL PIXELS($mean(r_{reg}) = 0.7$), (2) THE MODERATELY WELL-REGISTERED AREAS ($r_{reg} > 0.7$, $mean(r_{reg}) = 0.83$), AND (3) AN IMPROVED REGISTRATION ($mean(r_{reg}) = 0.96$). r IS THE PEARSON CORRELATION COEFFICIENT AND ϵ IS THE AVERAGE VALUE OF THE ABSOLUTE ERROR

Method	VCA		BPSS		MVC-NMF		*spatial*-VCA	
Indicator	r	ϵ	r	ϵ	r	ϵ	r	ϵ
(1) All pixels	0.68	0.08	0.57	0.10	0.69	0.09	0.50	0.14
(2) Accurate registration	0.73	0.08	0.59	0.09	0.72	0.08	0.56	0.13
(3) Best registration	0.81	0.19	0.80	0.13	0.83	0.14	0.77	0.33

Likewise, the third experiment corroborates the improvement tendency according to registration accuracy as r increases up to 0.83 for the MVC-NMF algorithm. Contrarily, the average error is slightly higher in this particular case probably because of the high heterogeneity of the selected area in terms of dark abundance [see Fig. 5(a)] or the presence of nonlinearities coming from the surface. As for the spatial-VCA algorithm, parameter ϵ reveals a notable disagreement with the ground truth that may underline a somewhat faulty extraction of the dark source by this approach.

Several conclusions can be drawn regarding the experiment expressed by Fig. 13. First, the VCA approach underestimates dark abundances in comparison with the ground truth as many pixels correspond to null abundances. This fact may come from the non-positivity and the sum-to-one constraints that result in more restrictive abundance maps. Second, BPSS shows a rather good agreement with the reference abundance map as the abundance distribution only suffers from a small overestimation (average abundance of 0.17 for BPSS and 0.08 for the ground truth). This point underlines the relevance of Fig. 13 since conclusions drawn based on Table V might have indicated an inferior accuracy of BPSS as regardss the other techniques. Third, MVC-NMF presents the best histogram in comparison to the ground truth (average abundance of 0.16) even though a little overestimation is still observed. Eventually, the results of the spatial-VCA approach confirm the initial conclusions drawn according to Table V. As a matter of fact, the dark abundances are generally overestimated with an average abundance of 0.21.

In relation to the small overestimation affecting the majority of the methods, it should be noted that the ground truth may contain slightly underestimated abundances. The reference abundance map generated from the HiRISE image is built by selecting those pixels whose radiance value is much lower than the neighboring pixels. Nonetheless, the dark source may exist in areas classified as brighter ice in the form of a minor dust contamination. The corresponding dust particles may be too small to be resolved spatially by the HiRISE instrument while the corresponding spectral contribution may be strong enough to be detected by the CRISM instrument. As a consequence, the corresponding abundances in the unmixing outcomes would be wrongly considered as being overestimated in comparison to the ground truth. In that case, the average abundance of the ground truth would increase and so would the accuracy of the methods BPSS, MVC-NMF, and spatial-VCA. Another reason to explain the differences between the results coming from the unmixing and the reference may be related to nonlinear contributions and limitations of the endmember extraction methods.

Eventually, an indication of the accuracy of the conducted unmixing is provided by the reconstruction of the original image with the estimated endmembers and their associated abundances. This is done by using the linear mixture model to approximate each pixel by the corresponding linear combination of endmembers weighted by the estimated abundances. By doing this, the average reconstruction error of the image [i.e., the term $\mathbf{e}$ in (1)] is calculated by means of the signal-to-noise ratio as 36 dB for VCA, 41 dB for BPSS, 43 dB for MVC-NMF, and 35 dB for spatial-VCA. These results show a very satisfactory reconstruction by all methods, BPSS and MVC-NMF particularly. After inspection of the signal-to-noise ratio maps, the reconstruction error was found to be very homogeneous with no pixels under 30 dB. These results are an additional proof that the linear model is indeed relevant and may be valuable in future research to locate those confined areas with slightly higher reconstruction errors that may point to nonlinear effects.

VI. CONCLUSIONS

In this paper, we have carried out validation and intercomparison of a comprehensive selection of state-of-the-art spectral unmixing techniques applied on planetary hyperspectral data. An appropriate case study has been defined by choosing a hyperspectral image acquired by the CRISM instrument displaying the Russell dune. This particular area of Mars is suitable for testing the benefits of spectral unmixing under a linear model because of the coexistence of two distinct materials—dark features and brighter ice—resulting in geographic subpixel mixtures at the CRISM resolution.

First, while two methods were considered for evaluating the number of endmembers in the test image only the ELM technique provided a realistic input for the subsequent endmember extraction. Then, spectral signatures extracted by the selected unmixing techniques were characterized and examined by spectral indicators to ensure their physical correctness. As a result, the initially selected methods N-FINDR, MVES, and SISAL were discarded due to unsatisfactory results. By contrast, the techniques VCA, BPSS, MVC-NMF, and spatial-VCA revealed the same three physically meaningful sources. An effort of recombination was however required due to repeated splitting of physical sources into a few endmembers caused by residual nonlinearities. For that purpose, the spectral indicators were considered together with spatial correlations among the endmember abundance maps. In that matter, we noted that spectra belonging to the physical sources are better reconstructed from endmembers extracted by the VCA and spatial-VCA methods

due to the pure pixel assumption. Exhaustive evaluation of the unmixing outcomes was also conducted by comparison of derived abundance maps with a reference. In that matter, very high-resolution HiRISE imagery and geomorphological techniques were used to generate a reference abundance map for the physical source related to the dark features happening in the Russell dune.

The quality of the results is estimated through several indicators— the correlation coefficient and average error between the reconstructed abundance maps and the groud truth and the superposition of the abundance distributions by means of the corresponding histograms. To our knowledge, this quantitative assessment represents the very first attempt to validate abundance maps produced by spectral unmixing of real data in an independent and quantitative manner. In that matter, global and local comparisons show that misregistration inaccuracies between the HiRISE and CRISM images represent the major source of error. For the best registered areas, the MVC-NMF and VCA methods outperform the BPSS and spatial-VCA techniques in terms of correlation coefficient. This ranking is however put into perspective after considering the average error and, particularly, the distribution of abundance values and average reconstruction error. As a matter of fact, BPSS shows significantly better performances than stated by the correlation indicator, agreeing quite satisfactorily with the reference histogram and showing the second lowest reconstruction error in terms of signal-to-noise ratio. On the other hand, the first position of the MVC-NMF method is never questioned since it generally provides the best results. As for the spatial-VCA, experimental results point to slightly lower performances which are probably due to the inherent penalization of the spatial preprocessing as for spatially confined sources such as the dark features on the Russell dune [21]. Eventually, the side effect of imposing the positivity and sum-to-one constrains turns into a lack of sensitivity, particularly in the VCA case, in the form of extremely low dark abundances frequently set to zero. As matter of fact, the abundance constraints might be less relevant in our case since physical sources—related to positive abundance values—are obtained after recombination of initial endmembers.

We conclude that abundance maps provided by VCA, BPSS, and MVC-NMF are generally accurate, i.e., sufficient for an initial planetary interpretation. In this matter, the results given by VCA and MVC-NMF—rather than BPSS which is much more computer intensive—can be considered as a primary quick look that helps revealing physical sources in the scene of study together with subtle residues of instrumental or atmospheric corrections. As a matter of fact, unmixing results may be used to iteratively drive the improvement of the image preprocessing, which has proved to be critical as for the existence of nonlinearities in this paper. As regards to the pure pixel assumption, the algorithms BPSS and MVC-NMF seem to outperform the VCA-based approaches in terms of estimated abundances while the latter extract more physically coherent spectra. An issue deserving further research would be to evaluate the risks of extracting unphysical endmembers when performing unmixing with BPSS and MVC-NMF as it happens for the MVES and SISAL algorithms.

Although examination of the HiRISE image and experimental results regarding reconstruction error confirm the linear mixing hypothesis in our case, some residual nonlinearities may prevail. Major causes are (i) intrinsic variability of the physical sources, (ii) nonlinear mixing at the grain size scale, and (iii) adjacency effects due to multiple scattering between the atmosphere and the surface. All these factors may be related to uncertainties affecting the abundance maps provided by spectral unmixing. In order to take into account existent nonlinearities and improve the accuracy of the results, linear unmixing must be followed by a complete physical analysis of the image through the inversion of a physical model. First, simulating the spectra of the physical sources with radiative transfer algorithms will allow building a comprehensive physical model of the scene with some free parameters including the source abundances. Second, model inversion will be performed for all CRISM spectra using the estimated abundance maps as the most probable solution. By doing this, the risk of multiple solutions will be diminished as regards to the improved abundance maps.

ACKNOWLEDGMENT

The authors would like to thank the anonymous reviewers for their constructive comments that helped improving this paper.

REFERENCES

[1] S. Murchie, R. Arvidson, P. Bedini, K. Beisser, J.-P. Bibring, J. Bishop, J. Boldt, P. Cavender, T. Choo, R. T. Clancy, E. H. Darlington, D. Des Marais, R. Espiritu, D. Fort, R. Green, E. Guinness, J. Hayes, C. Hash, K. Heffernan, J. Hemmler, G. Heyler, D. Humm, J. Hutcheson, N. Izenberg, R. Lee, J. Lees, D. Lohr, E. Malaret, T. Martin, J. A. McGovern, P. McGuire, R. Morris, J. Mustard, S. Pelkey, E. Rhodes, M. Robinson, T. Roush, E. Schaefer, G. Seagrave, F. Seelos, P. Silverglate, S. Slavney, M. Smith, W.-J. Shyong, K. Strohbehn, H. Taylor, P. Thompson, B. Tossman, M. Wirzburger, and M. Wolff, "Compact Reconnaissance Imaging Spectrometer for Mars (CRISM) on Mars Reconnaissance Orbiter (MRO)," *J. Geophys. Res. (Planets)*, vol. 112, no. E05, p. E05 S03, 2007.

[2] Eur. Space Agency, ESA SP-1240 J.-P. Bibring, A. Soufflot, M. Berthé, Y. Langevin, B. Gondet, P. Drossart, M. Bouyé, M. Combes, P. Puget, A. Semery, G. Bellucci, V. Formisano, V. Moroz, and V. Kottsov, "OMEGA: Observatoire pour la Minéralogie, l'Eau, les Glaces et l'Activité," Mars Express: The Scientific Payload, Noordwijk, The Netherlands, Aug. 2004, ESA SP-1240.

[3] P. Drossart, G. Piccioni, A. Adriani, F. Angrilli, G. Arnold, K. H. Baines, G. Bellucci, J. Benkhoff, B. Bézard, J.-P. Bibring, A. Blanco, M. I. Blecka, R. W. Carlson, A. Coradini, A. di Lellis, T. Encrenaz, S. Erard, S. Fonti, V. Formisano, T. Fouchet, R. Garcia, R. Haus, J. Helbert, N. I. Ignatiev, P. G. J. Irwin, Y. Langevin, S. Lebonnois, M. A. Lopez-Valverde, D. Luz, L. Marinangeli, V. Orofino, A. V. Rodin, M. C. Roos-Serote, B. Saggin, A. Sanchez-Lavega, D. M. Stam, F. W. Taylor, D. Titov, G. Visconti, M. Zambelli, R. Hueso, C. C. C. Tsang, C. F. Wilson, and T. Z. Afanasenko, "Scientific goals for the observation of Venus by VIRTIS on ESA/Venus express mission," *Planet. Space Sci.*, vol. 55, no. 12, pp. 1653–1672, Oct. 2007.

[4] R. W. Carlson, P. R. Weissman, W. D. Smythe, and J. C. Mahoney, "Near-infrared mapping spectrometer experiment on Galileo," *Space Sci. Rev.*, vol. 60, no. 1–4, pp. 457–502, May 1992.

[5] R. H. Brown, K. H. Baines, G. Bellucci, J.-P. Bibring, B. J. Buratti, F. Capaccioni, P. Cerroni, R. N. Clark, A. Coradini, D. P. Cruikshank, P. Drossart, V. Formisano, R. Jaumann, Y. Langevin, D. L. Matson, T. B. McCord, V. Mennella, E. Miller, R. M. Nelson, P. D. Nicholson, B. Sicardy, and C. Sotin, "The Cassini Visual and Infrared Mapping Spectrometer (VIMS) investigation," *Space Sci. Rev.*, vol. 115, no. 1–4, pp. 111–168, Dec. 2004.

[6] O. Forni, F. Poulet, J.-P. Bibring, S. Erard, C. Gomez, Y. Langevin, and B. Gondet, "Component separation of OMEGA spectra with ICA," in *Proc. 36th Lunar Planet. Sci. Conf.*, 2005, p. 1623.
[7] S. Erard, P. Drossart, and G. Piccioni, "Multivariate analysis of Visible and Infrared Thermal Imaging Spectrometer (VIRTIS) Venus Express nightside and limb observations," *J. Geophys. Res. (Planets)*, vol. 114, no. E00, p. E00 B27, 2009.
[8] J. M. P. Nascimento, "Does independent component analysis play a role in unmixing hyperspectral data?" *IEEE Trans. Geosci. Remote Sens.*, vol. 43, no. 1, pp. 175–187, Jan. 2005.
[9] D. D. Lee and H. S. Seung, "Learning the parts of objects by non-negative matrix factorization," *Nature*, vol. 401, no. 6755, pp. 788–791, Oct. 1999.
[10] M. Parente, J. L. Bishop, and J. F. Bell, III, "Spectral unmixing for mineral identification in pancam images of soils in Gusev crater, Mars," *Icarus*, vol. 203, no. 2, pp. 421–436, Oct. 2009.
[11] S. Moussaoui, D. Brie, A. Mohammad-Djafari, and C. Carteret, "Separation of non-negative mixture of non-negative sources using a Bayesian approach and MCMC sampling," *IEEE Trans. Signal Process.*, vol. 54, no. 11, pp. 4133–4145, Nov. 2006.
[12] S. Moussaoui, H. Hauksdóttir, F. Schmidt, C. Jutten, J. Chanussot, D. Brie, S. Douté, and J. A. Benediktsson, "On the decomposition of Mars hyperspectral data by ICA and Bayesian positive source separation," *Neurocomputing*, vol. 71, no. 10–12, pp. 2194–2208, Jun. 2008.
[13] J. M. P. Nascimento and J. M. B. Dias, "Vertex component analysis: A fast algorithm to unmix hyperspectral data," *IEEE Trans. Geosci. Remote Sens.*, vol. 43, no. 4, pp. 898–910, Apr. 2005.
[14] B. Luo and J. Chanussot, "Unsupervised hyperspectral image classification by using linear unmixing," in *Proc. 16th IEEE Int. Conf. Image Process.*, Cairo, Egypt, 2009, pp. 2877–2880.
[15] M. E. Winter, "Fast autonomous spectral end-member determination in hyperspectral data," in *Proc. 13th Int. Conf. Appl. Geologic Remote Sens.*, Vancouver, BC, Canada, 1999, vol. II, pp. 337–344.
[16] D. R. Thompson, L. Mandrake, M. S. Gilmore, and R. Castano, "Superpixel endmember detection," *IEEE Trans. Geosci. Remote Sens.*, vol. 48, no. 11, pp. 4023–4032, Nov. 2010.
[17] L. Miao and H. Qi, "Endmember extraction from highly mixed data using minimum volume constrained non-negative matrix factorization," *IEEE Trans. Geosci. Remote Sens.*, vol. 45, no. 3, pp. 765–777, Mar. 2007.
[18] T.-H. Chan, C.-Y. Chi, Y.-M. Huang, and W.-K. Ma, "A convex analysisbased minimum-volume enclosing simplex algorithm for hyperspectral unmixing," *IEEE Trans. Signal Process.*, vol. 57, no. 11, pp. 4418–4432, Nov. 2009.
[19] J. Bioucas-Dias, "A variable splitting augmented Lagrangian approach to linear spectral unmixing," in *Proc. 1st IEEE Workshop Hyperspectral Image Signal Process.: Evolution Remote Sens.*, Grenoble, France, Aug. 2009, pp. 1–4.
[20] S. Jia and Y. Qian, "Spectral and spatial complexity-based hyperspectral unmixing," *IEEE Trans. Geosci. Remote Sens.*, vol. 45, no. 12, pp. 3867–3879, Dec. 2007.
[21] M. Zortea and A. Plaza, "Spatial preprocessing for endmember extraction," *IEEE Trans. Geosci. Remote Sens.*, vol. 47, no. 8, pp. 2679–2693, Aug. 2009.
[22] P. Debba, E. J. M. Carranza, F. D. van der Meer, and A. Stein, "Abundance estimation of spectrally similar minerals by using derivative spectra in simulated annealing," *IEEE Trans. Geosci. Remote Sens.*, vol. 44, no. 12, pp. 3649–3658, Dec. 2006.
[23] A. Zare and P. Gader, "PCE: Piecewise convex endmember detection," *IEEE Trans. Geosci. Remote Sens.*, vol. 48, no. 6, pp. 2620–2632, Jun. 2010.
[24] S. Jia and Y. Qian, "Constrained non-negative matrix factorization for hyperspectral unmixing," *IEEE Trans. Geosci. Remote Sens.*, vol. 47, no. 1, pp. 161–173, Jan. 2009.
[25] E. Gardin, P. Allemand, C. Quantin, and P. Thollot, "Defrosting, dark flow features, and dune activity on Mars: Example in Russell crater," *J. Geophys. Res.*, vol. 115, no. E06, p. E06 016, 2010.
[26] M. Parente, "A new approach to denoising CRISM images," in *Proc. 39th Lunar Planet. Sci. Conf.*, 2008, p. 2528.
[27] X. Ceamanos and S. Douté, "Spectral smile correction of CRISM/MRO hyperspectral images," *IEEE Trans. Geosci. Remote Sens.*, vol. 48, no. 11, pp. 3951–3959, Nov. 2010.
[28] S. Douté, "Retrieving Mars surface reflectance from OMEGA/MEX imagery," in *Proc. 1st IEEE Workshop Hyperspectral Image Signal Process.: Evolution Remote Sens.*, Grenoble, France, Aug. 2009, pp. 1–4.
[29] S. Douté and X. Ceamanos, "Retrieving Mars aerosol optical depth from CRISM/MRO imagery," in *Proc. 2nd IEEE Workshop Hyperspectral Image Signal Process.: Evolution Remote Sens.*, Reykjavik, Iceland, Jun. 2010, pp. 1–4.
[30] P. C. McGuire, J. L. Bishop, A. J. Brown, A. A. Fraeman, G. A. Marzo, M. F. Morgan, S. L. Murchie, J. F. Mustard, M. Parente, S. M. Pelkey, T. L. Roush, F. P. Seelos, M. D. Smith, L. Wendt, and M. J. Wolff, "An improvement to the volcano-scan algorithm for atmospheric correction of CRISM and OMEGA spectral data," *Planet. Space Sci.*, vol. 57, no. 7, pp. 809–815, Jun. 2009.
[31] A. S. McEwen, E. M. Eliason, J. W. Bergstrom, N. T. Bridges, C. J. Hansen, W. A. Delamere, J. A. Grant, V. C. Gulick, K. E. Herkenhoff, L. Keszthelyi, R. L. Kirk, M. T. Mellon, S. W. Squyres, N. Thomas, and C. M. Weitz, "Mars Reconnaissance Orbiter's High Resolution Imaging Science Experiment (HiRISE)," *J. Geophys. Res. (Planets)*, vol. 112, no. E5, p. E05 S02, 2007.
[32] J. A. Richards and X. Jia, *Remote Sensing Digital Image Analysis*. Berlin, Germany: Springer-Verlag, 1999.
[33] E. F. Vermote, N. El Saleous, C. O. Justice, Y. J. Kaufman, J. L. Privette, L. Remer, J. C. Roger, and D. Tanré, "Atmospheric correction of visible to middle-infrared EOS-MODIS data over land surfaces: Background, operational algorithm and validation," *J. Geophys. Res.*, vol. 102, no. D14, pp. 17 131–17 141, 1997.
[34] J. M. Bioucas-Dias and J. M. Nascimento, "Hyperspectral subspace identification," *IEEE Trans. Geosci. Remote Sens.*, vol. 46, no. 8, pp. 2435–2445, Aug. 2008.
[35] N. Dobigeon, S. Moussaoui, J.-Y. Tourneret, and C. Carteret, "Bayesian separation of spectral sources under non-negativity and full additivity constraints," *Signal Process.*, vol. 89, no. 12, pp. 2657–2669, Dec. 2009.
[36] F. Schmidt, A. Schmidt, E. Tréguier, and M. Guiheneuf, "Implementation strategies for hyperspectral unmixing using Bayesian source separation," *IEEE Trans. Geosci. Remote Sens.*, vol. 48, no. 11, pp. 4003–4013, Nov. 2010.

Xavier Ceamanos (S'09) received the M.Sc. degree in electrical engineering from the Universitat Politècnica de Catalunya (UPC), Barcelona, Spain, in 2007, and from the Grenoble Institute of Technology (Grenoble INP), Grenoble, France, in 2008. He is currently working toward the Ph.D. degree at the Institut de Planétologie et d'Astrophysique de Grenoble (Centre National de la Recherche Scientifique-Université Joseph Fourier), Grenoble, France. His Ph.D. work is devoted to developing statistical and physical methods for analyzing remotely sensed hyperspectral images. In particular, he is working with multi-angular hyperspectral data acquired by the CRISM/MRO spectrometer (NASA).

His research interests include calibration and processing of data acquired by imaging spectrometers, spectral unmixing techniques, and atmospheric correction and inversion algorithms to retrieve surface reflectance from top-of-atmosphere radiances.

Sylvain Douté received the M.Sc. degree in physics from the Université Joseph Fourier (UJF), Grenoble, France, in 1994, and the Ph.D. degree in remote sensing from the Université Denis Diderot, Paris, France. His Ph.D. work was devoted to modeling light scattering properties of planetary icy surfaces with application to the study of Io and Pluto.

He held a postdoctoral position for two years at the Institute of Geophysics and Planetary Physics (University of California, Los Angeles) to analyze images of the Galilean satellites acquired by the near-infrared mapping spectrometer Galileo (NASA). He is currently a Researcher in planetary physics at the Institut de Planétologie et d'Astrophysique de Grenoble (Centre National de la Recherche Scientifique-UJF), Grenoble. His research interests are directed toward the study of Mars cryosphere and polar atmosphere by imaging spectroscopy thanks to his status of co-investigator regarded the spatial OMEGA/MEX and CRISM/MRO experiments. This research is supported by R&T activities in hyperspectral image post-processing and analysis carried out in the framework of the Vahiné project led by Dr. Douté. Physical models, statistical inversion technics, as well as signal processing methods are developed in this framework.

Dr. Douté is a member of the "Programme National de Planétologie" science committee and of the American Geophysical Union.

Bin Luo received the M.Sc. degree from École Normale Supérieure (ENS) Cachan, France, and the Ph.D. degree from École Nationale Supérieure de Telecommunication (ENST) Paris, France, in 2007.

He worked as Postdoctoral Researcher at Gipsa-lab, Grenoble Institute of Technology (Grenoble INP), Grenoble, France, from 2008 to 2010. He is currently an Associate Professor at the Laboratory of Information Engineering in Surveying, Mapping and Remote Sensing (LIESMARS), Wuhan University, Wuhan, China. His research interests include hyperspectral data analysis, high-resolution image processing, and indexation of images at different resolutions.

Frédéric Schmidt received the Ph.D. degree from the Laboratoire de Planétologie de Grenoble (Centre National de la Recherche Scientifique-Université Joseph Fourier), Grenoble, France, in 2007.

He spent two years at the European Space Astronomy Centre, European Space Agency (ESA), Madrid, Spain, as a Postdoctoral Fellow. Since 2009, he has been an Assistant Professor with the Laboratoire Intéractions et Dynamique des Environnements de Surface, University Paris-Sud, Orsay, France, and is also with the Centre National de la Recherche Scientifique. He is a Co-investigator of the OMEGA imaging spectrometer onboard Mars Express (ESA). His research interests are in analysis of hyperspectral data, ices, and polar processes on planet Mars.

Gwenaël Jouannic received the M.Sc. degree in earth sciences from the Université Pierre et Marie Curie, Paris, France, in 2009. He is currently working toward the Ph.D. degree in the team "Géomorphologie planétaire" in the Laboratoire Intéractions et Dynamiques des Environnements de Surface, Université Paris-Sud, Orsay, France. His Ph.D. work is devoted to the geomorphological study of Martian debris flows on dunes. In particular, he is working with High-Resolution Imaging Science Experiment (HiRISE) images and high-resolution Digital Topographic Models in order to better characterize 3-D geometry of Martian debris flows.

His research interests include the seasonal processes on Mars as present flow activities currently observed on Martian dunes slopes.

Jocelyn Chanussot (SM'04) received the M.Sc. degree in electrical engineering from the Grenoble Institute of Technology (Grenoble INP), Grenoble, France, in 1995, and the Ph.D. degree from Savoie University, Annecy, France, in 1998.

In 1999, he was with the Geography Imagery Perception Laboratory for the Délégation Générale de l'Armement (DGA—French National Defense Department). Since 1999, he has been with Grenoble INP, where he was an Assistant Professor from 1999 to 2005, an Associate Professor from 2005 to 2007, and is currently a Professor of signal and image processing. He is currently conducting his research at the Grenoble Images Speech Signals and Automatics Laboratory (GIPSA-Lab). His research interests include image analysis, multicomponent image processing, nonlinear filtering, and data fusion in remote sensing.

Dr. Chanussot is the founding President of IEEE Geoscience and Remote Sensing French chapter (2007–2010) which received the 2010 IEEE GRS-S Chapter Excellence Award "for excellence as a Geoscience and Remote Sensing Society chapter demonstrated by exemplary activities during 2009". He was a member of the IEEE Geoscience and Remote Sensing AdCom (2009–2010), in charge of membership development. He was the General Chair of the first IEEE GRSS Workshop on Hyperspectral Image and Signal Processing, Evolution in Remote sensing (WHISPERS). He is the Chair (2009–2011) and was the Cochair of the GRS Data Fusion Technical Committee (2005–2008). He was a member of the Machine Learning for Signal Processing Technical Committee of the IEEE Signal Processing Society (2006–2008) and the Program Chair of the IEEE International Workshop on Machine Learning for Signal Processing, (2009). He was an Associate Editor for the IEEE GEOSCIENCE AND REMOTE SENSING LETTERS (2005–2007) and for *Pattern Recognition* (2006–2008). Since 2007, he is an Associate Editor for the IEEE TRANSACTIONS ON GEOSCIENCE AND REMOTE SENSING. Since 2011, he has been the Editor-in-Chief of the IEEE JOURNAL OF SELECTED TOPICS IN APPLIED EARTH OBSERVATIONS AND REMOTE SENSING.

Sixième partie .

Résumé en français

Résumé

Une nouvelle technique de télédétection émerge dans le domaine de l'exploration spatiale. L'imagerie spectroscopique classique est dotée d'une dimension de mesure supplémentaire - la dimension angulaire - afin de permettre une meilleure séparation des signaux provenant de l'atmosphère et de la surface. Elle peut fournir aussi une caractérisation plus précise des matériaux planétaires. Le capteur Compact Reconnaissance Imaging Spectrometer for Mars (CRISM) à bord de la sonde Mars Reconnaissance Orbiter est une caméra hyperspectrale qui fonctionne systématiquement dans le mode multi-angulaire depuis l'orbite. Néanmoins, les images multi-angulaires hyperspectrales posent certains problèmes de manipulation, de visualisation et d'analyse en raison de leur taille et de leur complexité. Dans ce cadre, cette thèse propose des algorithmes statistiques et physiques pour analyser les images acquises par l'instrument CRISM de manière efficace et robuste. Premièrement, je propose une chaîne de post-traitement visant à améliorer la qualité radiométrique des données CRISM et à générer des produits avancés, ces dernières données étant conçues pour permettre une analyse fine de la planète Mars. Deuxièmement, je m'intéresse à la correction atmosphérique des images CRISM en exploitant les capacités multi-angulaires de cet instrument. Un algorithme innovant, à base physique est mis en oeuvre pour compenser les effets atmosphériques afin d'estimer la reflectance de surface. Cette approche est particulièrement utilisée dans cette thèse pour déduire les propriétés photométriques des matériaux qui coexistent dans un site spécifique de Mars, le cratère de Gusev. Troisièmement, j'effectue une comparaison d'une sélection des meilleures techniques existantes, visant à réaliser une déconvolution spectrale des données acquises par l'instrument CRISM. Cette famille de techniques s'est avérée très utile lors de l'analyse d'images hyperspectrales de manière non supervisé, c'est à dire, sans aucun à priori sur la scène. Une stratégie originale est proposée pour discriminer les techniques les plus appropriées pour l'exploration de Mars par CRISM à partir d'une vérité du terrain construite à partir d'images indépendantes à haute résolution .

Introduction

Parmi toutes les planètes du système solaire, Mars a donné lieu depuis toujours à de nombreuses questions telles que l'existence de vie extraterrestre. Cette curiosité persiste aujourd'hui grâce aux informations fournies par un ensemble de technologies dites de télédétection. La télédétection permet l'exploration d'objets planétaires par des sondes en orbite. Depuis le début de la télédétection, il y a plus de cinquante ans, des améliorations technologiques ont rendu possible le développement d'instruments sophistiqués qui sont installés sur ces sondes. Aujourd'hui, plusieurs types d'instruments fournissent des données uniques sur la formation, la géologie et l'atmosphère des objets planétaires, parmi d'autres sujets. La planète Mars a particulièrement bénéficié des missions planétaires avec quelques dizaines de sondes qui ont fourni une vue sans précédent de la planète rouge.

Les instruments de mesure utilisés typiquement en télédétection sont basés sur des techniques dites passives ou actives. En particulier, les capteurs passifs acquièrent des photons provenant du soleil après passage dans l'atmosphère dans un premier temps, réflection sur la surface et passage dans l'atmosphère une deuxième fois. Les interactions physiques qui ont lieu sur ce chemin modulent le signal qui est finalement détecté par ces scanners. Ainsi, le signal acquis contient des informations sur la

composition des composants de surface et d'atmosphère. La convergence des domaines de la spectroscopie et de l'imagerie traditionnelle a donné lieu à l'imagerie hyperspectrale qui vise à cartographier ces propriétés. Cette technique passive est devenue cruciale pour la détection, la caractérisation et la cartographie des matériaux qui coexistent sur les surfaces planétaires. Les capteurs hyperspectraux, ou spectro-imageurs, ont en effet la capacité de discriminer parmi des matériaux différents, qui peuvent parfois se ressembler dans le domaine visible. Devant ce potentiel, les sondes spatiales ont été équipées avec un spectro-imageur depuis la fin des années 1980.

Aujourd'hui, deux spectro-imageurs tournent autour de la planète Mars : l'Observatoire pour la Minéralogie, l'Eau, les Glaces, et l'Activité (OMEGA) à bord de la sonde Mars Express et le Compact Reconnaissance Imaging Spectrometer for Mars (CRISM) à bord de la sonde Mars Reconnaissance Orbiter (MRO). Bien que ces deux instruments fournissent des informations sur Mars sans précédent, le volume et la complexité des images hyperspectrales impliquent des défis concernant leur manipulation et exploitation. Ceci est particulièrement le cas de CRISM, dont les principales améliorations techniques par rapport à OMEGA sont une meilleure résolution spatiale et une acquisition systématique d'images hyperspectrales à plusieurs angles de visée sur un même site de Mars. Le premier attribut permet à CRISM de fournir une vue très fine de la surface de Mars. Deuxièmement, chaque observation CRISM est composée par onze images hyperspectrales acquises à des angles d'observation différents, comme le montre la Figure 16.1. L'image centrale est acquise à haute résolution (18 m/pixel) tandis que les images à des angles d'observations plus importants (dites EPF) sont acquises à 180 m/pixel. Cette particularité permet une meilleure caractérisation de l'atmosphère et une exploration innovatrice de la surface de Mars, mais aussi comporte une augmentation de la complexité et la taille des données.

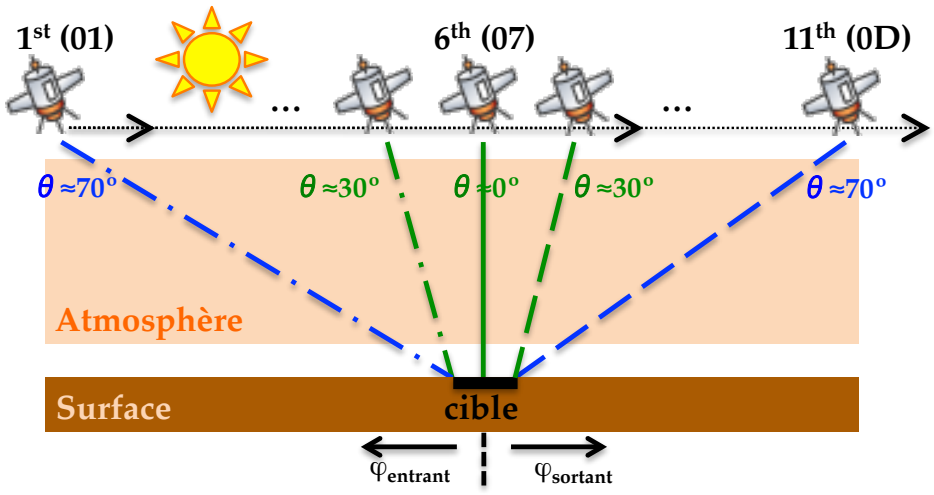

Figure 16.1.: Schéma d'une observation CRISM. Trois images hyperspectrales des onze au total sont montrées. La couleur verte correspond à l'image centrale à haute résolution tandis que seulement les images les plus extrêmes de l'EPF sont détaillées en bleu. θ est l'angle d'observation et φ l'azimut relatif.

Dans ce contexte, cette thèse propose une série d'outils pour faciliter la visualisation, le post-traitement et l'analyse d'observations multi-angulaires CRISM, tout en considérant l'ensemble des informations qu'elles contiennent. Les techniques développées dans cette thèse sont conçues vis-à-vis de l'état de l'art en traitement d'images de télédétection, que cela soit en planétologie ou en observation de la Terre. L'objectif principal est le développement de techniques non supervisées pour extraire des informations

planétaires significatives ainsi que des approches à base physique pour effectuer une analyse fine des propriétés physiques et chimiques des matériaux à la surface de Mars. Ceci est abordé en tenant compte des capacités multi-angulaires de l'instrument CRISM, non seulement pour une meilleure caractérisation de l'atmosphère mais aussi pour l'estimation de propriétés photométriques de la surface. Ces dernières données fournissent des indices précieux sur l'état physique des matériaux martiens qui sont encore largement inconnus. De plus, cette thèse étudie l'impact de plusieurs artefacts instrumentaux sur l'analyse des données CRISM et propose une amélioration de la qualité radiométrique des images. Bien que les algorithmes proposés dans ce manuscrit sont validés de manière récurrente sur des images dites de test, ils ont été conçus pour être utilisés dans d'autres contextes et ils ne sont pas limités au cas CRISM en particulier.

Le présent manuscrit est divisé en quatre parties. La première établit le contexte dans lequel le travail est encadré tandis que les autres se réfèrent aux trois contributions qui ont été réalisées vis-à-vis du besoin d'outils pour traiter des données CRISM de façon précise et automatique. Plus en détail :

- Dans la première partie, je présente le contexte de la thèse. D'abord je résume l'exploration de Mars par des techniques de télédétection et, en particulier, par des spectro-imageurs. Les raisons pour lesquelles ces instruments constituent des outils clefs en exploration planétaire sont précisées. Ensuite, je détaille le fonctionnement des spectro-imageurs et les produits qu'ils génèrent, suivi par une description détaillée de l'instrument CRISM. Dans un deuxième temps, je donne un aperçu sur la physique en télédétection passive : le transfert radiatif entre les photons, l'atmosphère et la surface. Ce contexte physique est décrit avec une attention particulière portée aux processus qui façonnent le signal acquit par les sondes. Finalement, je détaille les objectifs de la thèse et les solutions proposées pour surmonter les défis associés à la télédétection de Mars par CRISM.
- Dans la deuxième partie, j'étudie les limitations des données CRISM concernant les objectifs de la thèse. D'abord, la qualité radiométrique de ces produits est affectée par des anomalies provenant des limitations intrinsèques du type de scanner dont CRISM fait partie ainsi que par les propriétés spectrales de Mars. Pour surmonter ceci, je propose un traitement automatique des observations CRISM par une chaîne de traitement. Cet ensemble de routines vise à améliorer la qualité radiométrique des données à travers la correction de plusieurs artefacts instrumentaux. Dans un deuxième temps, la chaîne de traitement génère des produits avancés qui prennent en considération les conditions atmosphériques et géométriques dans lesquelles les images ont été acquises. En effet, celles-ci peuvent masquer les informations provenant de la surface. Finalement, la chaîne de traitement génère des produits multi-angulaires intégrés. Cet outil de traitement s'avère donc clef pour les planétologues qui sont intéressés par une amélioration significative de la qualité radiométrique des données CRISM et par des produits avancés.
- Dans la troisième partie, j'exploite les capacités multi-angulaires de CRISM dans la définition d'une méthode de correction des effets atmosphériques à base physique. Ces méthodes se basent traditionnellement sur l'hypothèse d'une surface dite lambertienne quand elles sont appliquées sur des images acquises par des instruments ayant une seule prise de vue (nadir). Dans ce cas, le problème est souvent sous-contraint. Malheureusement, cette hypothèse biaise l'estimation des propriétés photométriques de surface. Par contre, l'utilisation de plusieurs mesures d'une même cible à des angles d'observation différents dans une modélisation du transfert radiatif

facilite la séparation des contributions provenant de la surface et l'atmosphère. Cependant, la correction atmosphérique d'observations multi-angulaires CRISM reste compliquée, en ce qui concerne l'algorithmique, et chère, en temps de calcul. Dans ces circonstances, je propose une méthode de correction atmosphérique basée sur une formulation originale de la luminance en haut de l'atmosphère qui permet une inversion rapide et robuste. Cet algorithme, nommé MARS-ReCO, est inspiré par l'état de l'art en correction atmosphérique utilisée en observation de la Terre et permet de récupérer des informations relatives à la surface avec une meilleure fidélité que celle fournie par les méthodes classiques. Dans cette partie de la thèse, j'étudie aussi les propriétés photométriques des matériaux dans le cratère de Gusev grâce à MARS-ReCO à partir d'imagerie orbitale, ce qui constitue une étude pionnière.

- Dans la quatrième partie, j'étudie l'utilisation de techniques dites de déconvolution spectrale pour réaliser une analyse non supervisée des données CRISM. Les images hyperspectrales sont typiquement formées de la combinaison de multiples contributions qui fait de l'extraction d'informations significatives une tâche compliquée. Vis-à-vis de cet obstacle, des algorithmes automatiques sont de plus en plus demandés afin de traiter des grandes collections d'images hyperspectrales avec une précision satisfaisante. Dans ce contexte, j'étudie l'utilisation de techniques de déconvolution spectrale qui visent la décomposition automatique d'une image hyperspectrale en un ensemble de composantes spectrales physiquement significatives, tout en exploitant les informations sous-pixel. Avec ce but, j'effectue une comparaison entre plusieurs techniques de déconvolution spectrale qui sont typiquement utilisées pour l'analyse d'images hyperspectrales terrestres ou planétaires. Les méthodes les plus appropriées pour les données CRISM sont identifiées par une stratégie de validation basée sur une vérité du terrain construite à partir d'imagerie à haute résolution.

Dans ce résumé en français, je détaille les trois dernières parties dédiées aux contributions majeures de cette thèse.

1. Chaîne de traitement de données CRISM

Les spectro-imageurs doivent conjuguer une haute résolution spatiale et spectrale, tout en assurant un rapport signal sur bruit satisfaisant [123]. Le capteur CRISM appartient à la famille de spectro-imageurs du type push broom qui satisfait à ces exigences en raison de leur matrice de détection à deux dimensions. Néanmoins, la qualité spectroscopique des données résultantes est soumise aux non-uniformités qui affectent les éléments de détection de cette matrice. Les spectres acquis peuvent donc contenir des artéfacts d'origine thermique, optique ou électronique qui compromettent l'identification des informations d'intérêt par les algorithmes d'analyse. Dans ce contexte, l'équipe CRISM a établi une chaîne de traitement (ci-après nommée CRISM-DP) qui traite les observations CRISM avant les rendre publiques. Néanmoins, le traitement des données hyperspectrales est délicat car une correction erronée des artefacts peut entraîner des perturbations plus importantes que celles de départ, notamment dans la dimension spectrale. Ainsi, la chaîne CRISM-DP a été conçue pour corriger exclusivement les artefacts majeurs. La précision radiométrique résultante est donc acceptable pour des nombreuses études scientifiques dans lesquelles un certain degré d'inexactitude peut être toléré. Ainsi l'équipe CRISM a développé le CRISM Analysis Toolkit (CAT) qui représente un outil d'analyse opérationnel pour de

nombreux planétologues. Toutefois, le CAT ne traite que certains artefacts et donc plusieurs questions restent toujours non résolues.

Dans ce cadre, un traitement supplémentaire des observations CRISM est nécessaire. Dans la première partie de la thèse, je présente une chaîne de post-traitement automatique (ci-après dénommée IPAG-DP) pour une calibration fine des observations CRISM (voir Figure 16.2). Cet ensemble de routines propose également une transformation des données originales en produits avancés prenant en compte, par exemple, les capacités multi-angulaires de CRISM. En effet, ceci n'est pas fait par le CRISM-DP.

Figure 16.2.: Schéma du traitement des données CRISM depuis leur acquisition.

La chaîne de traitement IPAG-DP est résumée dans la Figure 16.3. Je note deux parties principales : la première liée à l'amélioration de la qualité radiométrique des données, et la seconde impliquant la génération de produits avancés. L'outil IPAG-DP est formé par deux types de blocs de traitement différents : ceux qui ont été adoptés du CAT ou qui n'ont pas été conçus dans le cadre de cette thèse, et ceux que j'ai conçu afin de surmonter les obstacles qui ne sont pas résolus ni par le CRISM-DP ni par le CAT. L'outil IPAG-DP corrige les artefacts suivants :

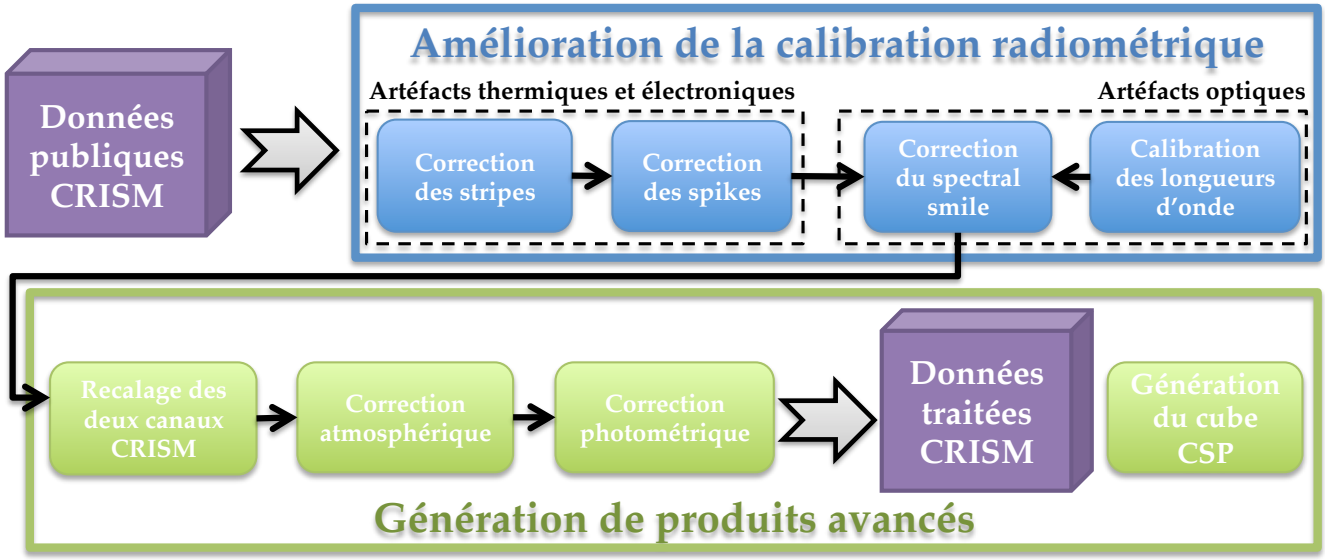

Figure 16.3.: Schéma de la chaîne de traitement IPAG-DP.

- **Stripes** : cet artefact provoque des perturbations complexes sur les données acquises par des instruments du type push broom. Ces anomalies dans la dimension spatiale sont caractérisées par des structures verticales (ou horizontales) causées par la variation aléatoire de l'intensité d'une zone homogène de l'image selon la dimension des colonnes (ou des lignes). Les stripes sont intrinsèques au processus de formation de l'image et affectent la qualité radiométrique des données des capteurs tels que CRISM. Dans cette thèse, je surmonte cet artefact en intégrant à l'IPAG-DP la méthode de correction proposée dans le CAT. Le CAT propose un filtrage qui vise

à éliminer les fausses contributions instrumentales afin de produire une sortie constante pour une entrée constante [136]. Ceci est obtenu en appliquant un filtre passe-bas sur les données perturbées avec une fréquence de coupure qui est estimée de façon indépendante pour chaque image. Selon des expériences faites dans cette thèse sur des données réelles, cette méthode est appropriée pour les observations CRISM.

- **Spikes** : les spikes se réfèrent aux pixels dont le rapport signal sur bruit est anormalement bas, résultant en valeurs de luminance anormales [65]. La localisation de ces pixels, ainsi que leur erreur associée, est totalement aléatoire. Les spikes forment souvent des ensembles de quelques pixels qui sont très visibles dans les observations CRISM. Dans cette thèse, j'étudie cet artefact à origine électronique en comparant la stratégie adoptée par le CAT pour surmonter cet artefact avec l'état de l'art dans ce sujet. Cette fois, je suggère de développer une méthode alternative qui convient mieux aux buts de cette thèse. La stratégie proposée se déroule en deux étapes : (i) la première consiste à détecter les spikes comme les pixels possédant une valeur anormale par rapport à celle de leurs voisins spatiaux, (ii) les pixels détectés sont ensuite corrigés dans une seconde étape par une stratégie de restauration qui remplace leur valeur de luminance anormale par la valeur moyenne de leurs voisins.

- **Effet du spectral smile** : cet artefact à origine optique est décrit comme des anomalies à faible fréquence affectant certaines bandes spectrales des images hyperspectrales. Le spectral smile provient des limitations intrinsèques des spectro-imageurs du type push broom. L'impact de ces aberrations se résume par deux effets sur la réponse spectrale de CRISM : (i) une partie de la luminance à une longueur d'onde est détectée par des éléments de détection assignés à d'autres longueurs d'onde, et (ii) la résolution spectrale devient de plus en plus pauvre pour les détecteurs hors axe de la matrice de détection. Ces effets font que les spectres des images sont acquis en utilisant des réponses spectrales différentes en fonction de la position de la colonne. Dans ce contexte, une analyse spectrale fine devient très difficile car les techniques d'analyse supposent que toutes les données dans une même bande spectrale ont été acquises dans les mêmes conditions. Je propose d'aborder la correction du spectral smile par le développement d'une méthode innovante et robuste car il n'en existe pas de pareil dans le CAT. Cette stratégie est basée sur les données de calibration fournies par l'équipe CRISM qui permettent de gérer cet artefact, l'objectif principal étant la minimisation des anomalies dans les données tout en préservant l'information utile. La méthode de correction suit trois étapes : (i) d'abord, un indicateur de l'énergie du spectral smile est défini grâce à une transformation de données dites Maximum Noise Fraction [67], (ii) la longueur d'onde centrale non-uniforme est normalisée par un ré-échantillonnage de tous les spectres aux paramètres optimaux de CRISM, et (iii) la résolution spectrale non-uniforme est surmontée par une technique dite de sharpening inspirée sur le traitement d'image traditionnel. Selon les expériences présentées dans ce manuscrit, la méthode proposée est robuste, même pour les observations CRISM les plus difficiles.

- **Images à champ-plat erronées** : la visualisation des spectres CRISM révèle un décalage anormal des spectres dans la dimension spectrale, dont la magnitude dépend du numéro de colonne. Cet artefact affecte notamment la position de certaines bandes d'absorption liées à des composants chimiques, notamment à celles du CO_2. Dans le CRISM-DP, des images de champ-plat sont générées pour normaliser ensuite la sensibilité de tous les éléments de la matrice de détection

de CRISM. Des aberrations ont lieu car cette correction ne prend pas en compte les effets du spectral smile. Ainsi, les longueurs d'onde de CRISM en vol ne correspondent pas à celles mesurées avant le lancement, et qui sont utilisées dans le traitement des images. La chaîne IPAG-DP prend en compte ces anomalies en considérant une mauvaise calibration des longueurs d'onde avant le lancement. Je propose donc une méthode de calibration qui détermine, pour une image CRISM donnée, toutes les longueurs d'onde réelles par une comparaison avec des données de référence bien calibrées. Selon les résultats obtenus sur des données réelles, les longueurs d'onde récupérées par cette méthode permettent ensuite une compensation satisfaisante de la distorsion produite par les images de champ-plat défectueuses.

La deuxième étape de la chaîne IPAG-DP transforme les observations CRISM en produits avancés qui sont utilisés pour réaliser une analyse fine de la planète Mars. Plus en détail :

- **Recalage des deux canaux CRISM** : l'instrument CRISM est composé de deux voies différentes qui travaillent respectivement dans le visible/proche infrarouge et dans l'infrarouge. Les données correspondantes aux deux voies doivent parfois être combinées pour mener à bien des études basées sur des bandes spectrales à l'interface c'est à dire sur des spectres dites full spectrum. Un simple empilement des bandes spectrales correspondantes à chaque voie n'est pas approprié car la zone de surface conjuguée est légèrement différente dans les deux cas. Ainsi, je décide de considérer cette problématique comme un recalage défectueux entre les deux voies. Pour surmonter cela, je mets en oeuvre une méthode originale qui effectue un recalage précis entre les deux voies sur la base de données géographiques auxiliaires. Des expériences sur des données réelles prouvent la validité de cet algorithme de fusion.
- **Correction atmosphérique** : l'atmosphère de Mars est dominée par les nombreuses bandes d'absorption liées au CO_2 atmosphèrique qui souvent recouvrent des signatures provenant de la surface. En plus des gaz, des particules dites aérosols sont généralement en suspension au dessus de la surface martienne. Les aérosols ont souvent une forte influence sur les spectres observés. Comme cette thèse se place dans le cadre d'une analyse des matériaux à la surface, une stratégie de correction des effets atmosphériques se révèle donc nécessaire. La chaîne IPAG-DP intègre une méthode originale pour corriger les observations CRISM des effets des gaz et des aérosols atmosphériques. Cette méthode, développée au laboratoire parallèlement à cette thèse [52, 53], prend en compte les capacités multi-angulaires du capteur CRISM. Par contre, elle suppose que la surface est lambertienne ou, en d'autres termes, que la quantité de lumière diffusée par celle-ci est la même quelle que soit la direction d'observation. Dans ce contexte, la chaîne IPAG-DP estime l'épaisseur optique des aérosols (AOT, sigles en anglais) ainsi que l'albédo de surface lambertien.
- **Normalisation photométrique** : dans une observation CRISM, l'angle d'éclairage local est généralement hétérogène en raison de la topographie souvent accidentée de Mars. L'angle d'observation peut varier pour la même raison mais aussi en raison des fonctionnalités multi-angulaires de CRISM. Toutes ces variations se reflètent dans les valeurs de luminance acquises au sommet de l'atmosphère par les capteurs de télédétection [174]. Dans ce contexte, des modèles photométriques de surface sont habituellement utilisés pour transformer des données de luminance en unités de reflectance, limitant donc les effets d'une acquisition variable. Les données CRISM sont délivrées dans des unités de luminance et donc dépendent des effets photométriques de surface. La normalisation photométrique au premier ordre la plus adoptée dans la littérature se

base sur la loi de Lambert et produit des données de reflectance par une division par le cosinus de l'angle d'éclairage. Toutefois, ce modèle photométrique est valable uniquement pour le cas restrictif dans lequel la surface est lambertienne. Malgré les limitations de ce modèle, l'hypothèse lambertienne est largement adoptée pour le traitement des données de télédétection en raison de sa simplicité et sa précision au premier ordre. Le modèle de Lambert peut être remplacé par des modèles plus réalistes, mais une connaissance à priori sur les propriétés de diffusion de la surface est nécessaire dans ce cas. Suite au besoin de méthodes automatiques non supervisées, la chaîne IPAG-DP adopte donc cette normalisation classique.

- **Génération du produit multi-angulaire** : les spectro-imageurs multi-angulaires sont des instruments uniques pour récupérer des signatures inédites des matériaux de surface dites des courbes spectro-photométriques. Une courbe spectro-photométrique est définie comme l'ensemble des spectres correspondant à la même unité de terrain observée dans des conditions géométriques différentes. De la même façon, une courbe photométrique est définie comme étant la luminance observée d'une zone à la surface donnée à des géométries différentes et à une seule longueur d'onde. Bien que CRISM représente une occasion unique pour étudier la surface de Mars à plusieurs géométries, la chaîne CRISM-DP délivre de façon séparée chacune des onze images hyperspectrales qui forment une observation CRISM. La chaîne IPAG-DP conclut donc en réarrangeant spatialement les spectres correspondants à l'ensemble des onze images dans un cube nommé CSP. Chaque zone à la surface observée par plus d'une prise de vue (ci-après nommée super-pixel) est associé à la courbe photométrique correspondante par la chaîne IPAG-DP.

2. Correction atmosphérique d'observations multi-angulaires CRISM

Les capacités multi-angulaires de CRISM sont conçues pour réaliser une caractérisation fine de l'état de l'atmosphère martienne pour une observation donnée [192]. Par exemple, l'EPF de chaque observation CRISM peut être exploité pour la caractérisation physique des aérosols [187]. Les études atmosphériques bénéficient substantiellement des mesures multi-angulaires dans la mesure où ces dernières rendent accessibles des parcours atmosphériques différents. Cette caractéristique instrumentale améliore substantiellement le traitement que l'on peut faire par rapport à ceux qui s'appliquent aux données des spectro-imageurs traditionnels. Dans cette thèse, j'étudie le potentiel de la couverture angulaire de CRISM pour compenser les effets atmosphériques présents dans le signal de télédétection. L'objectif étant ensuite de caractériser la reflectance bidirectionnelle de surface.

Les aérosols atmosphériques et les matériaux à la surface présentent des propriétés de diffusion anisotropes, c'est à dire, qui varient avec les directions d'éclairage et d'observation. Les méthodes de correction atmosphérique conçues pour des spectro-imageurs ayant une seule prise de vue ne peuvent pas traiter correctement le problème du transfert radiatif qui a lieu dans l'atmosphère et dans la surface. L'hypothèse que la surface se comporte comme un diffuseur isotrope, ou lambertien, est donc généralement adoptée afin de contraindre l'inversion des données orbitales pour récupérer la reflectance de surface. Ceci est le cas, par exemple, de la technique de correction atmosphérique intégrée dans la chaîne IPAG-DP. Néanmoins, l'hypothèse lambertienne n'est pas réaliste puisque la plupart de surfaces sont anisotropes. La stratégie afin de résoudre correctement ce problème inverse implique la considération de la fonction distribution de la reflectance bidirectionnelle (BRDF, sigles en anglais) de surface

dans un modèle de transfert radiatif. En pratique, cette procédure rend le problème sous-contraint si une seule mesure angulaire est disponible car la BRDF est typiquement inconnue. Toutefois, l'imagerie multi-angulaire est capable de contraindre mieux ce problème.

La communauté scientifique en observation de la Terre a récemment mené des efforts vers l'utilisation de mesures multi-angulaires pour améliorer les résultats de la correction atmosphérique de données satellitaires. Dans cette thèse, je propose une stratégie originale à base physique pour traiter des observations CRISM. Cette méthode hérite du travail effectué en observation de la Terre et porte le nom de Multi-angle Approach for Retrieval of Surface Reflectance for CRISM Observations (MARS-ReCO). Ceci est un algorithme de correction atmosphérique qui estime la reflectance de surface suite à l'inversion d'une formulation du signal en haut de l'atmosphère (TOA, sigles en anglais). Cette approche représente une amélioration par rapport à d'autres techniques de correction atmosphérique en considérant une surface qui n'est pas lambertienne. Ainsi, l'algorithme MARS-ReCO réalise une extraction précise de signatures photométriques des matériaux de surface en fonction de la géométrie d'acquisition et de la longueur d'onde à partir d'observations multi-angulaires CRISM. Comme le montre la Figure 16.4, ces données sont corrigées auparavant des effets des gaz atmosphériques tandis que l'épaisseur optique des aérosols est estimée par une méthode indépendante. Je résume les points clés de MARS-ReCO comme suit :

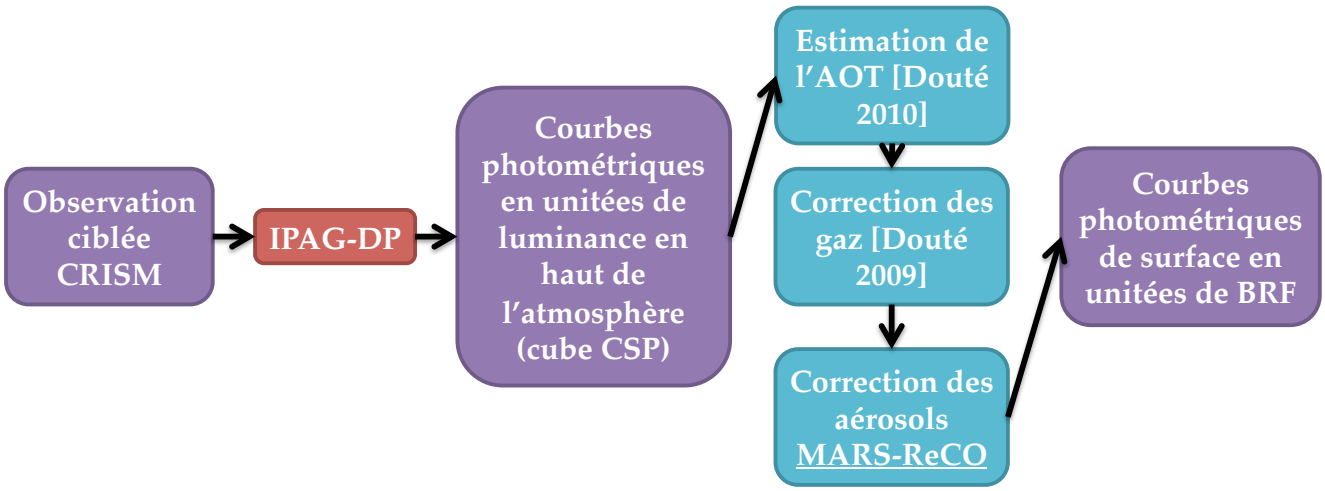

Figure 16.4.: Schéma de la chaîne de correction atmosphérique d'observations multi-angulaires CRISM. L'AOT et les courbes photométriques de surface sont estimés à partir du cube CSP produit par la chaîne de traitement IPAG-DP.

- La reflectance en haut de l'atmosphère est exprimée en utilisant une formulation de Green du transfert radiatif dans le système atmosphère/surface [107]. Cette méthode mathématique permet la combinaison analytique de la réflectivité et la transmissivité atmosphériques avec la BRDF de surface afin de calculer la luminance atteignant le capteur pour une épaisseur optique et une géométrie d'acquisition arbitraires.
- L'anisotropie de la surface est prise en compte en paramétrisant sa BRDF par un modèle semi-empirique dite de Ross-Thick Li-Sparse (RTLS). Ce modèle de reflectance rend linéaire l'expression du signal arrivant au capteur, permettant ainsi une inversion très efficace. Outre ses propriétés mathématiques, le modèle RTLS s'est avéré être approprié pour recréer les propriétés de diffusion des surfaces naturelles telles que les sols.

- L'épaisseur optique des aérosols, ou AOT, est un paramètre d'entrée fournie par la chaîne IPAG-DP. De même, la contribution gazeuse dans le signal reçu par le capteur CRISM est corrigée par la chaîne de traitement avant l'utilisation de MARS-ReCO. De cette façon, MARS-ReCO traite exclusivement la correction des effets des aérosols.
- Un abaque, ou look-up table (LUT, sigles en anglais), est généré pour stocker des quantités atmosphériques nécessaires pour la correction atmosphérique d'observations CRISM. L'utilisation d'un LUT implique un seul calcul initial de ces quantités qui sont ensuite utilisées de façon répétée. Le LUT de MARS-ReCO ne dépend pas des propriétés de surface en raison des qualités de la formulation de Green et du modèle RTLS. Le LUT actuel considère une atmosphère homogène composée exclusivement par des aérosols minéraux. Les propriétés radiatives élémentaires de ces particules qui sont utilisées dans le calcul de la LUT sont obtenues grâce à l'étude de Wolff et al. basée sur des observations CRISM [187]. Le LUT sauvegarde chaque quantité atmosphérique calculée pour plusieurs valeurs d'AOT et plusieurs géométries d'acquisition.
- L'estimation des propriétés de surface est réalisée par une stratégie basée sur une minimisation de l'erreur aux moindres carrés qui consiste à ajuster la courbe photométrique d'un super-pixel avec le modèle basé sur le LUT. Cette stratégie est très rapide car elle est basée sur une simple inversion de matrice. La fiabilité de la BRDF estimée par MARS-ReCO est ensuite validée par une stratégie itérative basée sur un ensemble de tests.

L'approche MARS-ReCO fournit un échantillonnage de la BRDF associée à chaque super-pixel aux géométries d'acquisition CRISM. Dans son implémentation actuelle, MARS-ReCO traite individuellement chaque bande spectrale, en corrigeant les effets atmosphériques pour tous les super-pixels d'une manière séquentielle. La traitement de la courbe photométrique en unités de luminance TOA correspondant à un super-pixel donnée est décrite comme suit :

1. L'expression de la luminance TOA basée sur la formulation de Green du transfert radiatif est ajustée tout d'abord aux mesures angulaires CRISM qui forment la courbe photométrique. Ceci est fait en connaissant l'AOT et la géométrie d'acquisition correspondant à chaque point de mesure (extraites à partir des données auxiliaires CRISM).
2. Les coefficients du modèle de surface RTLS sont ainsi obtenus par inversion de l'expression de la luminance TOA.
3. Les valeurs de BRDF estimées subissent finalement une étape de validation qui vise à détecter et à exclure les solutions qui ne sont pas réalistes.

L'algorithme MARS-ReCO représente un outil non seulement original mais aussi opérationnel pour déduire les propriétés de surface à partir d'observations CRISM. En effet, une bande spectrale d'un cube CSP est traitée en quelques dizaines de secondes.

Dans cette thèse, je teste la correction atmosphérique adressée par MARS-ReCO grâce à des données simulées qui imitent les propriétés de surface et atmosphériques de la planète Mars. Une étude de sensibilité basée sur ces données de référence identifie les géométries d'acquisition et les configuration atmosphériques dans lesquelles MARS-RECO devient moins fiable. Cette étude conclue que l'estimation de la BRDF de surface par MARS-ReCO est possible en général, mais pas nécessairement précise, lorsque le signal provenant de la surface est significatif par rapport à celui provenant de l'atmosphère. Par significatif je veux dire une combinaison favorable de (i) un albédo de surface pas trop bas, (ii) une anisotropie de la surface différente de celle des aérosols, (iii) et un AOT pas très élevé. Si ces circons-

tances sont satisfaites, MARS-ReCO estime un modèle de la reflectance de surface qui est satisfaisant dans la plupart des cas. Toutefois, les lobes de diffusion très étroits ne sont pas estimés de manière précise en raison du nombre relativement petit des mesures angulaires (jusqu'à onze) et les limitations intrinsèques du modèle RTLS. En ce qui concerne le type de surface, l'étude de sensibilité prouve que MARS-ReCO présente quelques difficultés pour estimer les propriétés des surfaces caractérisées par une faible anisotropie dans des conditions atmosphériques relativement opaques. Au contraire, les matériaux très brillants et fortement anisotropes sont détectés de manière satisfaisante, tandis que la BRDF récupérée est plus susceptible de contenir des inexactitudes. En général, les erreurs les plus importantes se produisent pour les angles d'éclairage et d'observation extrêmes. Dans ce cas, la BRDF est plus anisotrope et moins facilement reproduite par le modèle RTLS. En conséquence, une attention particulière doit être accordée aux observations CRISM acquises avec un grand AOT ou un angle d'observation élevé. Toutes ces informations sont prises en compte dans la thèse lors du traitement d'observations CRISM réelles.

Après avoir testé les capacités de MARS-ReCO sur des données simulées, cette thèse évalue la pertinence de cette correction atmosphérique lorsqu'elle est appliquée à de vraies observations CRISM. A cet effet, nous définissons une stratégie de validation basée sur des observations acquises sur une zone spécifique de Mars, le cratère de Gusev. Cette zone de Mars est un site approprié pour valider des algorithmes de correction atmosphérique puisqu'il est le site d'atterrissage du robot Spirit. Depuis 2004, ce robot a acquis des données de terrain sous différentes conditions atmosphériques. En particulier, les propriétés photométriques des minéraux à la surface de ce cratère ont été mis à disposition en utilisant des données acquises par l'instrument Pancam à bord de Spirit. Dans cette thèse, je compare les propriétés photométriques extraites à partir d'observations orbitales CRISM par MARS-ReCO avec celles présentées dans des travaux basés sur des données Pancam. Dans ce résumé en français, je ne discute que deux paramètres relatifs à la fonction de phase de surface et correspondant au modèle dit de Henyey-Greenstein à deux lobes de diffusion. La première quantité est le paramètre d'asymétrie b, décrivant la largeur des deux lobes et allant de $0 < b < 1$. Des grandes valeurs de b correspondent aux lobes les plus étroits décrivant alors une BRDF très anisotrope. La fraction de rétrodiffusion c est également comprise dans l'intervalle $0 < c < 1$. Si $c > 0,5$, la particule est principalement rétrodiffusante, tandis que $c < 0,5$ implique une diffusion vers l'avant prédominante. Les valeurs de ces deux paramètres obtenues à partir d'observations CRISM par MARS-ReCO sont tracées avec les résultats obtenus à partir des mesures Pancam dans la Figure 16.5. En outre, je trace les valeurs b et c de l'étude réalisée par McGuire et Hapke sur les propriétés photométriques de quelques surfaces artificielles [116]. Les résultats montrent que les propriétés photométriques récupérées à partir des données orbitales CRISM sont proches des propriétés des sols, qui est le matériel le plus présent dans le cratère de Gusev. Ceci valide la correction atmosphérique effectuée par MARS-ReCO dans ce cas et dans d'autres pour lesquels des observations CRISM similaires vont être traitées.

3. Déconvolution spectrale d'images hyperspectrales CRISM

En plus des méthodes à base physique, les images hyperspectrales sont traditionnellement traitées avec des méthodes d'analyse qui utilisent très peu ou pas d'à priori concernant les phénomènes physiques ayant lieu dans la scène observée. Par contre ces méthodes intègrent souvent des données mesurées sur

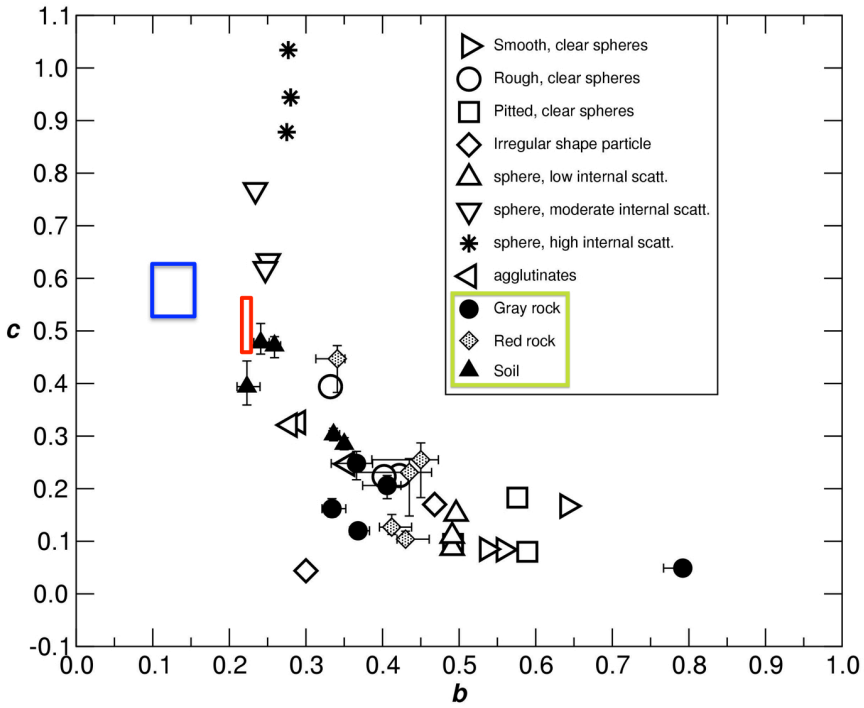

Figure 16.5.: Paramètres d'Hapke d'asymétrie b et de rétrodiffusion c pour les pôles extrêmes définis par Johnson et al. à partir de données Pancam (dans le carré vert). Les valeurs estimées par McGuire et Hapke [116] pour plusieurs types de surfaces artificielles sont aussi présentées. L'intervalle des paramètres b et c estimé à partir de données CRISM par l'algorithme MARS-ReCO est montré par un carré rouge. Afin de montrer les avantages de considérer une surface non-lambertienne dans une correction atmosphérique, le carré bleu correspond aux résultats obtenus par la méthode basée sur une hypothèse Lambertienne détaillée en [52]. Crédit : [84]

le terrain ou en laboratoire pour réaliser des apprentissages. Ces algorithmes dont la mise en oeuvre est en général plus aisée peuvent être décisifs pour le traitement de volumes croissants de données hyperspectrales. Cependant la télédétection planétaire implique un défi supplémentaire lié à la rareté des données dites de vérité du terrain pour éduquer les méthodes d'analyse ou valider leurs résultats. Dans ce contexte, il existe un besoin croissant d'algorithmes automatiques qui soient à la fois précis et opérationnels pour extraire les informations significatives des images hyperspectrales de télédétection.

Les techniques dites de déconvolution spectrale, ou démixage en aveugle, sont des outils d'analyse non supervisés potentiellement utiles en planétologie. Les matériaux à la surface sont caractérisés par des signatures spectrales qui sont façonnées par leur composition chimique et leur état physique. La résolution spatiale limitée des capteurs orbitaux et la diffusion multiple des photons entre plusieurs matériaux génèrent des combinaisons linéaires et non linéaires entre plusieurs signatures spectrales dans le signal de télédétection. Ces facteurs, parmi d'autres, conduisent à l'existence des spectres dites mélangés dans les données fournies par les capteurs hyperspectraux. Dans ce contexte, des méthodes de déconvolution spectrale sont conçues pour décomposer ces spectres mélangés en leurs contributions spectrales originales. Après avoir estimé le nombre de sources, ou pôles extrêmes, dans une image hyperspectrale, deux produits sont générés par le processus de déconvolution spectrale. Comme la Figure 16.6 le montre, une signature spectrale représentative est extraite tout d'abord pour chaque pôle extreme détecté dans l'image. Deuxièmement, des stratégies d'optimisation permettent la génération des cartes d'abondance qui révèlent la distribution spatiale de chaque pôle extrême sur la zone cou-

verte par l'image. De cette manière, la déconvolution spectrale permet la transformation d'une image hyperspectrale en quelques produits significatifs, facilitant donc l'analyse de grandes collections de données planétaires.

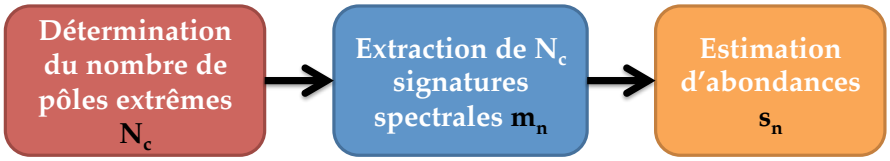

Figure 16.6.: Schéma de déconvolution spectrale en aveugle d'une image hyperspectrale.

Concernant les différents types de mélanges existants, une résolution spatiale modérée est typiquement à l'origine des mélanges dites géographiques [voir Figure 16.7 (droite)]. Dans ce cas, le spectre de luminance montante est le résultat d'une combinaison linéaire des signatures spectrales des matériaux à la surface pondérées par leurs couvertures spatiales dans le pixel [par exemple, dans la Figure 16.7 (droite) chaque matériel couvre une superficie d'un tiers du pixel, et donc tous les poids sont égaux à un tiers]. Les méthodes de déconvolution spectrale du type linéaire supposent cette relation linéaire impliquant les pôles extrêmes. Par contre, les autres types de mélanges sont abordés par des techniques de déconvolution spectrale du type non-linéaire. Cette partie de la thèse se focalise sur l'évaluation d'algorithmes de démixage linéaire non supervisés pour estimer des informations relatives à la surface et à l'atmosphère de Mars à partir d'images hyperspectrales. En particulier, j'examine la pertinence de ces techniques sur des données simulées et d'autres réelles acquises par CRISM sur une région spécifique de Mars. La quatrième partie de la thèse se termine par la description d'une stratégie pour estimer l'épaisseur optique atmosphérique basée sur des techniques de déconvolution spectrale. Dans ce résumé, je détaille seulement l'étude sur des données CRISM.

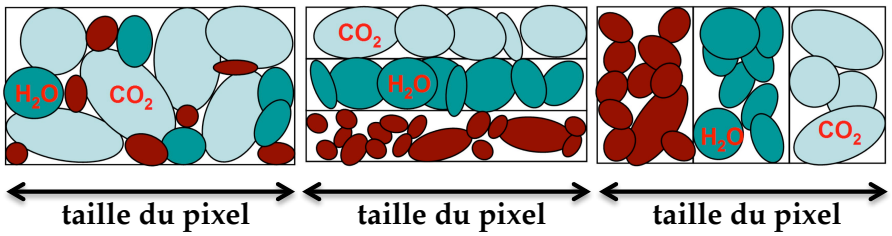

Figure 16.7.: Différents types de mélange sous-pixel : (gauche) mélange intime granulaire, (centre) mélange intime stratifié, et (droite) mélange géographique. Credit : [157].

Bien que la déconvolution spectrale d'images acquises par le spectro-imageur OMEGA a été abordé de manière satisfaisante (e.g. [125]), on pourrait revendiquer que les conditions dans lesquelles OMEGA détecte la surface de Mars est adaptée à l'existence de mélanges linéaires en raison de sa résolution spatiale modérée (au mieux 350 m/pixel). En revanche, l'instrument CRISM fournit des données avec une précision spatiale sans précédent (jusqu'à 18 m/pixel), ce qui augmente la complexité de la surface observée et la probabilité de faire face à des mélanges non-linéaires. Dans cette thèse, j'examine la pertinence du modèle de mélange linéaire dans le contexte planétaire mis à disposition par CRISM. Par pertinence, j'entends la capacité des techniques de déconvolution linéaire de révéler des caractéristiques relatives à la composition chimique et l'état physique des surfaces planétaires. Avec ce but, des expériences sont menées sur l'image centrale de l'observation FRT42AA acquise par CRISM sur la

dune Russell de Mars [voir Figure 16.8 (en haut à gauche)]. Ce site est d'un grand intérêt pour valider des techniques de déconvolution spectrale basées sur un modèle linéaire. Premièrement, l'existence de mélanges géographiques qui ont lieu sur la dune en fin d'hiver (i.e. des structures sombres liées au dégivrage côtoyant, de la glace de CO_2 résiduelle) est confirmée par de l'imagerie à très haute résolution. Deuxièmement, il est possible de construire une vérité du terrain à partir de cette même imagerie afin de valider les cartes d'abondance estimées par déconvolution spectrale.

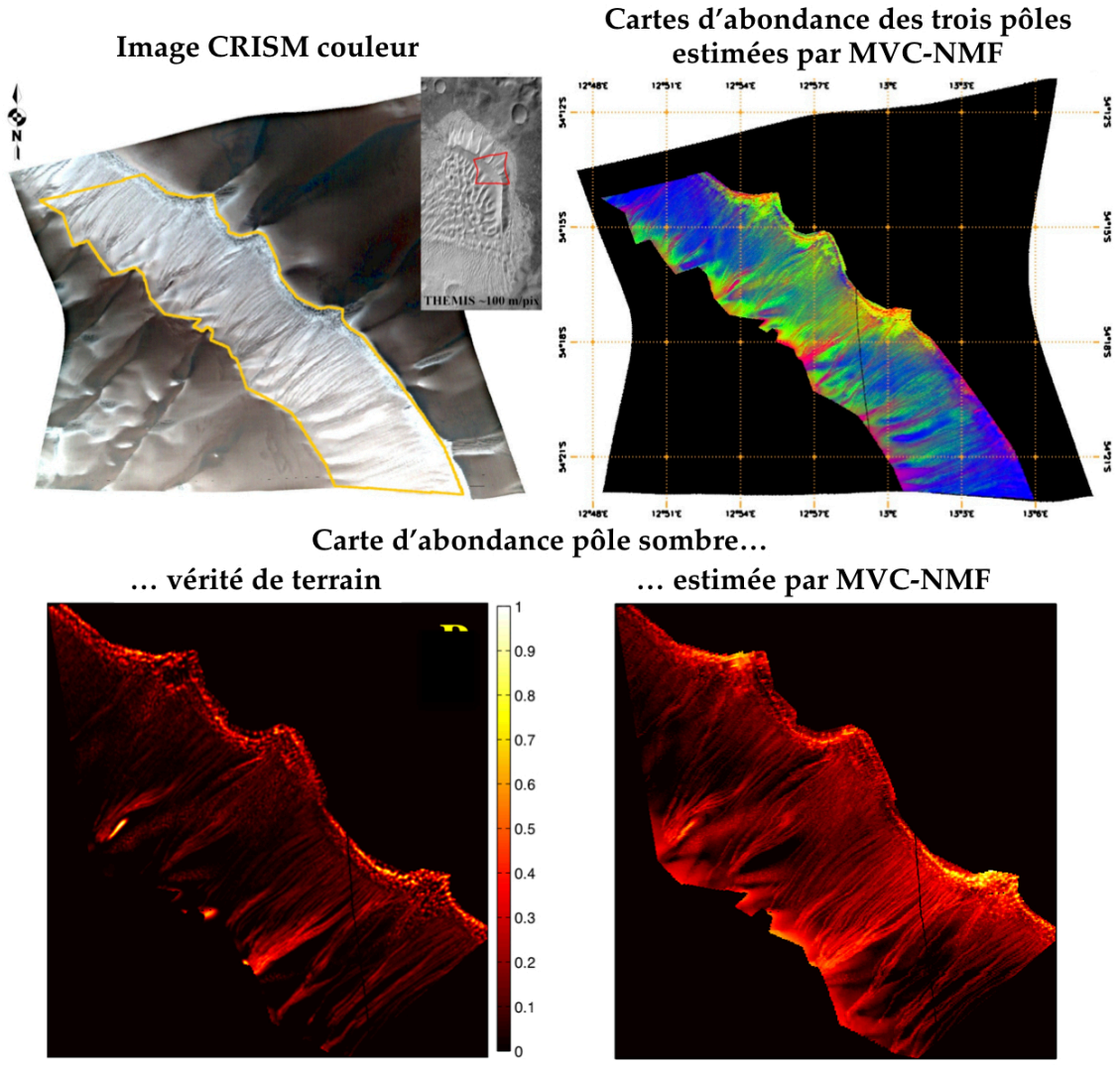

Figure 16.8.: (en haut à gauche) : Image centrale FRT42AA en vraies couleurs dans laquelle la dune du cratère de Russell est visible. (en haut à droite) : Carte d'abondance composite des trois pôles extrêmes extraits par la méthode MVC-NMF. (en bas à gauche) : Vérité du terrain du pôle sombre. (en bas à droite) : Carte d'abondance du pôle correspondant aux structures sombres estimée par la méthode MVC-NMF.

Suite à des expériences originales, j'effectue une évaluation quantitative des abondances de surface obtenues par une sélection de quatre algorithmes de déconvolution spectrales linéaires basés sur des principes différents qui portent le nom de : (i) Vertex Component Analysis (VCA) [131], (ii) Bayesian Positive Source Separation (BPSS) [51], (iii) Minimum Volume Constrained Non-negative Matrix Factorization (MVC-NMF) [119], et (iv) une combinaison de la méthode VCA avec un prétraitement spatial proposé dans [191] nommé spatial-VCA. Ce choix est effectué parmi les techniques non supervisées

les plus utilisées en planétologie et observation de la Terre. Des expériences sont menées sur la région d'intérêt encerclé en jaune dans la Figure 16.8 (en haut à gauche). Après avoir estimé le nombre de pôles extrêmes comme étant égal à six par une méthode automatique, l'image centrale FRT42AA est déconvoluée spectralement par les quatre algorithmes. Après l'examen des signatures spectrales et des cartes d'abondance extraites pour chacun, trois sources physiques liées à deux matériaux à la surface sont détectées par toutes les méthodes : une concerne les structures sombres et deux sont associées à la glace. Un effort de recombinaison est donc nécessaire pour reconstruire chaque source physique sur la base des pôles extrêmes. L'existence des non linéarités dans l'image est à l'origine de cette inégalité entre le nombre de pôles extrêmes (six au total) et celui des sources physiques (trois au total). Finalement, les résultats de chaque méthode sont comparés avec la vérité du terrain pour déterminer les techniques les plus appropriées dans l'analyse de données CRISM.

La Figure 16.8 (en haut à droite) montre la carte d'abondance composite des trois sources physiques reconstruites à partir des pôles extrêmes extraits par la méthode MVC-NMF. Je propose une stratégie originale pour évaluer les performances de la déconvolution spectrale de données CRISM de manière quantitative. La caméra High Resolution Imaging Science Experiment (HiRISE) est un outil sans précédent pour explorer Mars car elle offre une très haute résolution spatiale, jusqu'à 0,25 m/pixel [115]. HiRISE est en mesure de résoudre spatialement les structures sombres tandis que l'image CRISM est presque entièrement composée par des spectres mélangés. Dans cette situation, j'exploite l'image HiRISE PSP_002482_1255_RED afin de construire une carte d'abondance de référence des structures sombres. Cette vérité terrain sera utilisée dans l'évaluation des résultats de déconvolution spectrale [i.e. les pixels rouges dans la Figure 16.8 (en haut à droite) ou encore la Figure 16.8 (en bas à gauche)]. Je propose la stratégie suivante pour générer une telle vérité du terrain : (i) l'image HiRISE est classifiée afin d'extraire les structures sombres, (ii) la carte de classification qui en résulte est recalée avec l'image hyperspectrale CRISM, (iii) la carte d'abondance de référence est générée par le comptage des pixels classifiés comme étant des structures sombres dans l'empreinte de chaque pixel CRISM. Le produit issu de cette stratégie est montré dans la Figure 16.8 (en bas à gauche).

Je propose deux indicateurs pour évaluer la similarité entre la vérité du terrain et les cartes d'abondance issues de la déconvolution spectrale, à savoir le coefficient de corrélation r et l'erreur moyenne ϵ. Le premier indicateur mesure la similarité spatiale au sens relatif entre les deux produits, tandis que le deuxième exprime l'écart absolu. Étant donné que des problèmes de recalage lors de la génération de la vérité du terrain peuvent altérer cette comparaison sur certaines zones de l'image, je réalise trois expériences en calculant les deux indicateurs en fonction de la précision de recalage r_{reg}. Chaque expérience est détaillée dans la légende du Tableau 16.1. En général, les résultats de comparaison sont positifs pour toutes les méthodes sauf pour spatial-VCA. Cette méthode, basée sur l'information spatiale de la scène, pénalise les pôles extrêmes rares, et donc les structures sombres. En général, les résultats de comparaison montrent une amélioration pour un recalage de qualité croissante, les meilleurs résultats étant obtenus pour la troisième expérience. La méthode fournissant la meilleure carte d'abondance relative aux structures sombres par rapport la vérité du terrain est la technique MVC-NMF. Plus des détails peuvent être trouvés dans le manuscrit en anglais.

Le présent travail représente une étude sans précédent sur les performances des techniques de déconvolution spectrale appliquées sur des images hyperspectrales à haute résolution spatiale. Premièrement, je prouve que la dune Russell de Mars est une référence pour évaluer les capacités de ces

Méthode	VCA		BPSS		MVC-NMF		spatial-VCA	
Indicateur	r	ϵ	r	ϵ	r	ϵ	r	ϵ
1 : Tous les pixels	0.68	0.08	0.57	0.10	0.69	0.09	0.50	0.14
2 : Recalage précis	0.73	0.08	0.59	0.09	0.72	0.08	0.56	0.13
3 : Recalage optimale	0.81	0.19	0.80	0.13	0.83	0.14	0.77	0.33

Table 16.1.: Coefficient de corrélation r et erreur absolue moyenne ϵ pour (1) tous les pixels ($mean(r_{reg}) = 0.7$), (2) les zones qui sont bien recalées ($r_{reg} > 0.7$, $\sim$50% des pixels avec $mean(r_{reg}) = 0.83$) et (3) une zone avec un recalage optimale ($\sim$1% des pixels avec $mean(r_{reg}) = 0.96$).

techniques sous un modèle de mélange linéaire. Les résultats de démixage satisfaisants obtenus après comparaison avec une vérité du terrain indépendante prouvent que l'hypothèse de linéarité est valable pour le traitement d'images CRISM acquises sur des sites de Mars avec des propriétés similaires à la dune de Russell. Deuxièmement, j'ai évalué une série de techniques de déconvolution spectrale qui représentent l'état de l'art dans ce sujet. Les planétologues travaillant avec des données CRISM pourront profiter de cette étude car ces approches s'avèrent utiles pour cartographier et quantifier les abondances des espèces chimiques à la surface, aussi bien que pour effectuer une réduction de dimensionnalité à des fins de classification par exemple.

Bibliography

[1] N. Acito, M. Diani, and G. Corsini. Hyperspectral signal subspace identification in the presence of rare signal components. *IEEE Transactions on Geoscience and Remote Sensing*, 48(4):1940–1954, Apr. 2010.

[2] J. B. Adams, M. O. Smith, and P. E. Johnson. Spectral mixture modeling: a new analysis of rock and soil types at the Viking lander 1 site. *Journal of Geophysical Research*, 91:8098–8112, 1986.

[3] European Space Agency. Water at Martian south pole. http://www.esa.int/esaMI/Mars_Express/SEMYKEX5WRD_0.html, March 2004.

[4] T. Appéré, B. Schmitt, Y. Langevin, S. Douté, A. Pommerol, et al. Winter and spring evolution of northern seasonal deposits on mars from omega/mars express. *Journal of Geophysical Research*, 116(E05001), 2011.

[5] G. B. Arfken and H. J. Weber, editors. *Mathematical Methods for Physicists*, chapter "Non-homogeneous Equation–Green's Function," "Green's Functions–One Dimension," and "Green's Functions–Two and Three Dimensions.", pages 480–491 and 897–924. FL: Academic Press, 3rd ed. edition, 1985.

[6] R. E. Arvidson, S. W. Squyres, R. C. Anderson, J. F. Bell III, D. Blaney, et al. Overview of the Spirit Mars Exploration Rover mission to Gusev crater: Landing site to Backstay Rock in the Columbia Hills. *Journal of Geophysical Research*, 111(E02S01), 2006.

[7] A. Barducci and I. Pippi. Analysis and rejection of systematic disturbances in hyperspectral remotely sensed images of the Earth. *Applied optics*, 40:1464–1477, 2001.

[8] N. Barlow. *Mars: An Introduction to its Interior, Surface and Atmosphere*. Cambridge University Press, 2008.

[9] P. S. Barry, J. Shepanski, and C. Segal. Hyperion on-orbit validation of spectral calibration using atmospheric lines and on-board system. In *Proc. Int. Symp. Optical Science and Technology*, 2001.

[10] G. I. Bell and S. Glasstone. *Nuclear reactor theory*. Van Nostrand Reinhold Co., New York, 1970.

[11] J. Bell, editor. *The Martian Surface*. Cambridge University Press, 2008.

[12] C. Bernard-Michel, S. Douté, M. Fauvel, L. Gardes, and S. Girard. Retrieval of Mars surface physical properties from OMEGA hyperspectral images using regularized sliced inverse regression. *Journal of Geophysical Research*, 114(E06005), 2009.

[13] J. Bioucas-Dias. A variable splitting augmented Lagrangian approach to linear spectral unmixing. In *IEEE Workshop on Hyperspectral Image and Signal Processing: Evolution in Remote Sensing*, Grenoble, August 2009.

[14] J. M. Bioucas-Dias and J. M. Nascimento. Hyperspectral subspace identification. *IEEE Transactions on Geoscience and Remote Sensing*, 46(8):2435–2445, August 2008.

[15] M. Bouali. *Destriping data from multidetector imaging spectrometers: a study on the MODIS instrument*. PhD thesis, TELECOM ParisTech, April 2011.

[16] M. Bouali and S. Ladjal. Towards optimal destriping of MODIS data with a unidirectional variational model. *IEEE Transactions on Geoscience and Remote Sensing*, 2011.

[17] E. O. Brigham. *The Fast Fourier Transform*. New York: Prentice-Hall, 2002.

[18] J. Broadwater and A. Banerjee. A comparison of kernel functions for intimate mixture models. In *IEEE Workshop on Hyperspectral Image and Signal Processing: Evolution in Remote Sensing*, Grenoble, 2009.

[19] A. J. Brown and M. J. Wolff. Atmospheric modeling of the Martian polar regions: One Mars year of CRISM EPF observations of the south pole. In *Lunar and Planetary Science Conference*, number 1675, 2009.

[20] Adrian J. Brown, Wendy M. Calvin, Patrick C. McGuire, and Scott L. Murchie. Compact reconnaissance imaging spectrometer for mars (CRISM) south polar mapping: First Mars year of observations. *Journal of Geophysical Research*, 115(E00D13), 2010.

[21] S. Byrne and A. P. Ingersoll. A sublimation model for Martian south polar ice features. *Science*, 299:1051–1053, 2003.

[22] W. Cai, M. Xu, and R. R. Alfano. Three-dimensional radiative transfer tomography for turbid media. *IEEE Journal of Selected Topics in Quantum Electronics*, 9(2):189–198, March/April 2003.

[23] G. Camps-Valls and L. Bruzzone. Kernel-based methods for hyperspectral image classification. *IEEE Transactions on Geoscience and Remote Sensing*, 43(6):1351–1362, Jun. 2005.

[24] H. Carfantan and J. Idier. Statistical linear destriping of satellite-based pushbroom-type images. *IEEE Transactions on Geoscience and Remote Sensing*, 48(4):1860–1871, Apr. 2010.

[25] E. Carmina and V. Carrére. Spectral un-mixing of natural surfaces scenarios. In *IEEE IGARSS*, Hawai'i, 2010.

[26] X. Ceamanos and S. Douté. Spectral smile correction of CRISM/MRO hyperspectral images. *IEEE Transactions on Geoscience and Remote Sensing*, 48(11):3951–3959, Nov. 2010.

[27] X. Ceamanos, S. Douté, B. Luo, F. Schmidt, G. Jouannic, and J. Chanussot. Intercomparison and validation of techniques for spectral unmixing of hyperspectral images: A planetary case study. *IEEE Transactions on Geoscience and Remote Sensing*, 49(11):4341–4358, Nov. 2011.

[28] X. Ceamanos, B. Waske, J. A. Benediktsson, J. Chanussot, M. Fauvel, and J. R. Sveinsson. A classifier ensemble based on fusion of support vector machines for classifying hyperspectral data. *International Journal of Image and Data Fusion*, 1(4):293–307, Dec. 2010.

[29] T.-H. Chan, C.-Y. Chi, Y.-M. Huang, and W.-K. Ma. A convex analysis-based minimum-volume enclosing simplex algorithm for hyperspectral unmixing. *IEEE Transactions on Signal Processing*, 57(11):4418–4432, November 2009.

[30] S. Chandrasekhar. *Radiative Transfer*. Dover Publications, New York, 1960.

[31] C. I. Chang and Q. Du. Estimation of number of spectrally distinct signal sources in hyperspectral imagery. *IEEE Transactions on Geoscience and Remote Sensing*, 42(3):608–619, Mar. 2004.

[32] S. D. Chevrel, P. C. Pinet, Y. Daydou, S. Le Mouélic, Y. Langevin, et al. The Aristarchus Plateau on the Moon: Mineralogical and structural study from integrated Clementine UV–Vis–NIR spectral data. *Icarus*, 199:9–24, 2009.

[33] S. D. Chevrel, P. C. Pinet, and J. W. Head. Gruithuisen domes region: A candidate for an extended nonmare volcanism unit on the Moon. *Journal of Geophysical Research*, 104(E7):16515–16529, Jul. 1999.

[34] R. T. Clancy and S. W. Lee. A new look at dust and clouds in the Mars atmosphere: Analysis of emission-phase-function sequences from global Viking IRTM observations. *Icarus*, 93:135–158, 1991.

[35] R. N. Clark, G. A. Swayze, K. E. Livo, R. F. Kokaly, S. J. Sutley, et al. Imaging Spectroscopy: Earth and Planetary Remote Sensing with the USGS Tetracorder and Expert Systems. *Journal of Geophysical Research*, 108(5131), 2003.

[36] H. Clénet. *Hyperspectral remote sensing: mineralogy and petrology - Application to Syrtis Major volcano (Mars) and to Oman's ophiolite*. PhD thesis, Université Paul Sabatier, 2009.

[37] H. Clénet, C. Quantin, J. Flahaut, X. Ceamanos, P. C. Pinet, et al. Compositional diversity of mafic rocks in the vicinity of Valles Marineris, Mars, using Modified Gaussian Model. In *European Planetary Science Congres - Division for Planetary Sciences - Joint Meeting*, Nantes, Oct. 2011.

[38] S. A. Clough and M. J. Iacono. Line-by-line calculation of atmospheric fluxes and cooling rates 2. Application to carbon dioxide, ozone, methane, nitrous oxide and the halocarbons. *Journal of Geophysical Research*, 100(9):16519–16536, 1995.

[39] J. W. Cooley and J. W. Tukey. An algorithm for the machine calculation of complex Fourier series. *Mathematics of Computation*, 19:297–301, 1965.

[40] A. Cord, P. Pinet, Y. Daydou, and S. D. Chevrel. Planetary regolith surface analogs: optimized determination of Hapke parameters using multi-angular spectro-imaging laboratory data. *Icarus*, 165:414–427, 2003.

[41] A. M. Cord, P. C. Pinet, Y. Daydou, and S. D. Chevrel. Experimental determination of the surface photometric contribution in the spectral reflectance deconvolution processes for a simulated martian crater-like regolithic target. *Icarus*, 175:78–91, 2005.

[42] S. Cull, R. E. Arvidson, M. Mellon, S. Wiseman, R. Clark, et al. Seasonal H2O and CO2 ice cycles at the Mars Phoenix landing site: 1. Prelanding CRISM and HiRISE observations. *Journal of Geophysical Research*, 115(E00D16), 2010.

[43] S. Cull, R. E. Arvidson, R. V. Morris, M. Wolff, M. T. Mellon, et al. Seasonal H2O and CO2 ice cycles at the Mars Phoenix landing site: 2. Postlanding CRISM and ground observations. *Journal of Geophysical Research*, 115(E00E19), 2010.

[44] S. C. Cull, R. E. Arvidson, F. Seelos IV, and M. J. Wolff. Photometric properties of soils at the Mars Phoenix landing site: Preliminary analysis from CRISM EPF data. In *Lunar and Planetary Science Conference*, number 1416, 2010.

[45] A. Dadon, E. Ben-Dor, and A. Karnieli. Use of derivative calculations and minimum noise fraction transform for detecting and correcting the spectral curvature effect (smile) in Hyperion images. *IEEE Transactions on Geoscience and Remote Sensing*, 48(6):2603–2612, Jun. 2010.

[46] W. H. Davies, P. R. J. North, W. M. F. Grey, and M. J. Barnsley. Improvements in aerosol optical depth estimation using multiangle CHRIS/PROBA images. *IEEE Transactions on Geoscience and Remote Sensing*, 48(1):18–24, Jan. 2010.

[47] M. de Grenier and P. C. Pinet. Near-opposition martian limb-darkening: quantification and implication for visible-near-infrared bidirectional reflectance studies. *Icarus*, 115:354–368, 1995.

[48] P. Debba, E. J. M. Carranza, F. D. van der Meer, and A. Stein. Abundance estimation of spectrally similar minerals by using derivative spectra in simulated annealing. *IEEE Transactions on Geoscience and Remote Sensing*, 44(12):3649–3658, December 2006.

[49] B. N. Delaunay. Sur la sphère vide. *Bulletin of Academy of Sciences of the USSR*, (6):793–800, 1934.

[50] D. J. Diner, J. V. Martonchik, R. A. Kahn, B. Pinty, N. Gobron, et al. Using angular and spectral shape similarity constraints to improve MISR aerosol and surface retrievals over land. *Remote Sensing of Environment*, 94:155–171, 2005.

[51] N. Dobigeon, S. Moussaoui, J.-Y. Tourneret, and C. Carteret. Bayesian separation of spectral sources under non-negativity and full additivity constraints. *Signal Processing*, 89(12):2657–2669, 2009.

[52] S. Douté. Retrieving Mars Surface Reflectance from OMEGA/MEX Imagery. In *IEEE Workshop on Hyperspectral Image and Signal Processing : Evolution in Remote Sensing*, 2009.

[53] S. Douté and X. Ceamanos. Retrieving Mars aerosol optical depth from CRISM/MRO imagery. In *IEEE Workshop on Hyperspectral Image and Signal Processing : Evolution in Remote Sensing*, Reykjavik, 2010.

[54] S. Douté and B. Schmitt. A multi-layer bidirectional reflectance model for the analysis of planetary surface hyperspectral images at visible and near infrared wavelengths. *Journal of Geophysical Research*, 103(E13), 1998.

[55] S. Douté, B. Schmitt, Y. Langevin, J-P. Bibring, F. Altieri, et al. South pole of Mars: Nature and composition of the icy terrains from Mars Express OMEGA observations. *Planetary and Space Science*, 55:113–133, 2007.

[56] P. Drossart, J. Rosenqvist, S. Erard, Y. Langevin, J.-P. Bibring, and M. Combes. Martian aerosol properties from the Phobos/ISM experiment. *Annales geophysicae*, 9(11):754–760, 1991.

[57] R. Duca and F. Del Frate. Hyperspectral and multiangle CHRIS–PROBA images for the generation of land cover maps. *IEEE Transactions on Geoscience and Remote Sensing*, 46(10):2857–2866, Oct. 2008.

[58] S. Erard, P. Drossart, and G. Piccioni. Multivariate analysis of Visible and Infrared Thermal Imaging Spectrometer (VIRTIS) Venus Express nightside and limb observations. *Journal of Geophysical Research (Planets)*, 114(E00B27), 2009.

[59] S. Erard, J. Mustard, S. Murchie, and J-P. Bibring. Martian aerosols: near-infrared spectral properties and effects on the observation of the surface. *Icarus*, 111:317–337, 1994.

[60] J. Fernando. Propriétés physiques de la surface dans le cratère Gusev au moyen des observations CRISM à bord de la sonde MRO. Master's thesis, Université Pierre et Marie Curie (Paris XI), 2011.

[61] F. Forget, E. Millour, S. Lebonnois, L. Montabone, K. Dassas, et al. The new Mars climate database. In *Second workshop on Mars Atmosphere Modelling and Observations*, Granada, 2006.

[62] B.-C. Gao, M. J. Montes, and C. O. Davis. Refinement of wavelength calibrations of hyperspectral imaging data using a spectrum-matching technique. *Remote Sensing of Environment*, 90:424–433, 2004.

[63] E. Gardin, P. Allemand, C. Quantin, and P. Thollot. Defrosting, dark flow features, and dune activity on mars: Example in russell crater. *Journal of Geophysical Research*, 115(E06016), 2010.

[64] S. A. W. Gerstl. *Atmospheric Aerosols: Their Formation, Optical Properties and Effects*, chapter Application of the adjoint method in atmospheric radiative transfer calculations, pages 241–254. Spectrum Press, 1982.

[65] L. Gómez-Chova, L. Alonso, L. Guanter, G. Camps-Valls, J. Calpe, and J. Moreno. Correction of systematic spatial noise in push-broom hyperspectral sensors: application to CHRIS/PROBA images. *Applied optics*, 47(28):F46–F60, Oct. 2008.

[66] D. G. Goodenough, A. Dyk, K. O. Niemann, J. S. Pearlman, H. Chen, et al. Processing Hyperion and ALI for forest classification. *IEEE Transactions on Geoscience and Remote Sensing*, 41(6):1321–1331, Jun. 2003.

[67] A. A. Green, M. Berman, P. Switzer, and M. D. Craig. A transformation for ordering multispectral data in terms of image quality with implications for noise removal. *IEEE Transactions on Geoscience and Remote Sensing*, 26(1):65–74, Jan. 1988.

[68] L. Guanter. *New algorithms for atmospheric correction and retrieval of biophysical parameters in Earth Observation. Application to ENVISAT/MERIS data*. PhD thesis, Universitat de València, 2006.

[69] L. Guanter, L. Alonso, and J. Moreno. A method for the surface reflectance retrieval from PROBA/CHRIS data over land: Application to ESA SPARC campaigns. *IEEE Transactions on Geoscience and Remote Sensing*, 43(12), Dec. 2005.

[70] L. Guanter, R. Richter, and J. Moreno. Spectral calibration of hyperspectral imagery using atmospheric absorption features. *Applied optics*, 45(10):2360–2370, Apr. 2006.

[71] B. Hapke. *Theory of Reflectance and Emittance Spectroscopy*. Cambridge University Press, 1993.

[72] J. Harsanyi, W. Farrand, and C.-I Chang. Determining the number and identity of spectral endmembers: An integrated approach using Neyman–Pearson eigenthresholding and iterative constrained RMS error minimization. In *9th Thematic Conference on Geologic Remote Sensing*, Feb. 1993.

[73] D. Heinz and C.-I. Chang. Fully constrained least squares linear mixture analysis for material quantification in hyperspectral imagery. *IEEE Transactions on Geoscience and Remote Sensing*, 39:529–545, 2001.

[74] L.G. Henyey and J.L. Greenstein. Diffuse radiation in the galaxy. *Astrophysical Journal*, 93:70–83, 1941.

[75] R. Heylen and P. Scheunders. Non-linear fully-constrained spectral unmixing. In *IEEE International Geoscience And Remote Sensing Symposium*, Vancouver, 2011.

[76] B. Hu, W. Lucht, and A. H. Strahler. The interrelationship of atmospheric correction of reflectances and surface BRDF retrieval: A sensitivity study. *IEEE Transactions on Geoscience and Remote Sensing*, 37(2), Mar. 1999.

[77] A. Huck, M. Guillaume, and J. Blanc-Talon. Minimum dispersion constrained nonnegative matrix factorization to unmix hyperspectral data. *IEEE Transactions on Geoscience and Remote Sensing*, 48(6):2590–2602, Jun. 2010.

[78] J. F. Bell III, M. S. Rice, J. R. Johnson, and T. M. Hare. Surface albedo observations at Gusev Crater and Meridiani Planum, Mars. *Journal of Geophysical Research*, 113(E06S18), 2008.

[79] A. Jehl. *Etude photométrique de la surface de Mars à partir de la caméra HRSC à bord de la sonde Mars Express : Préparation aux observations orbitales multi-angulaires en exploration planétaire.* PhD thesis, Université Toulouse III - Paul Sabatier, 2008.

[80] A. Jehl, P. Pinet, D. Baratoux, Y. Daydou, S. Chevrel, et al. Gusev photometric variability as seen from orbit by HRSC/Mars-express. *Icarus*, 197:403–428, 2008.

[81] A. Jehl, P. C. Pinet, A. Cord, Y. D. Daydou, D. Baratoux, et al. Improved surface photometric mapping across Gusev and Apollinaris from an HRSC/Mars Express integrated multi-orbit dataset. In *Lunar and Planetary Science Conference*, 2006.

[82] S. Jia and Y. Qian. Spectral and spatial complexity-based hyperspectral unmixing. *IEEE Transactions on Geoscience and Remote Sensing*, 45(12):3867–3879, December 2007.

[83] S. Jia and Y. Qian. Constrained nonnegative matrix factorization for hyperspectral unmixing. *IEEE Transactions on Geoscience and Remote Sensing*, 47(1):161–173, January 2009.

[84] J. R. Johnson, W. M. Grundy, M. T. Lemmon, J. F. Bell III, M. J. Johnson, et al. Spectrophotometric properties of materials observed by Pancam on the Mars exploration rovers: 1. spirit. *Journal of Geophysical Research*, 111(E02S14), 2006.

[85] J. R. Johnson, W. M. Grundy, M. T. Lemmon, J. F. Bell III, M. J. Johnson, et al. Spectrophotometric properties of materials observed by Pancam on the Mars Exploration Rovers: 2. Opportunity. *Journal of Geophysical Research*, 111(E12S16,), 2006.

[86] D. L. B. Jupp. A compendium of kernel and other (semi-)empirical BRDF Models. Technical report, CSIRO. Office of Space Science Applications. Earth Observation Centre, April 2000.

[87] D. L. B. Jupp, B. Datt, T.R. McVicar, T. G. Van Niel, J. S. Pearlman, et al. Improving the analysis of Hyperion red-edge index from an agricultural area. In S. G. Ungar, S. Mao, and Y. Yasuoka, editors, *Proceedings of SPIE. Image Processing and Pattern Recognition in Remote Sensing*, volume 4898, pages 78–92, 2003.

[88] C. Jutten, J.Herault, and A.Guerin. *Artificial Intelligence and Cognitive Science*, chapter An independent components analyzer based on an adaptive neuromimetic network. Manchester University Press, 1998.

[89] C. Jutten and J. Karhunen. Advances in blind source separation (BSS) and independent component analysis (ICA) for nonlinear mixtures. *International Journal of Neural Systems*, 14(5):267–292, 2004.

[90] N. Keshava and J. F. Mustard. Spectral unmixing. *IEEE Signal Processing Magazine*, 19:44–57, 2002.

[91] M. King and R. Greenstone, editors. *EOS Reference Handbook: A Guide to Earth Science Enterprise and the Earth Observing System*. NASA GSFC, Greenbelt MD, 1999.

[92] P. Koepke and K. T. Kriebel. Influence of measured reflection properties of vegetated surfaces on atmospheric radiance and its polarization. *Applied optics*, 17:260–264, 1978.

[93] O. Korablev, V.I. Moroz, E.V. Petrova, and A.V. Rodin. Optical properties of dust and the opacity of the martian atmosphere. *Advances in Space Research*, 35(1):21–30, 2005.

[94] J. H. Lambert. *Photometria sive de mensure de gratibus luminis, colorum umbrae*. Eberhard Klett, 1760.

[95] Y. Langevin, J.-P. Bibring, F. Montmessin, F. Forget, M. Vincendon, et al. Observations of the south seasonal cap of Mars during recession in 2004-2006 by the OMEGA visible/near-infrared imaging spectrometer on board Mars Express. *Journal of Geophysical Research*, 112(E08S12), 2007.

[96] Y. Langevin, F. Poulet, J.-P. Bibring, and B. Gondet. Sulfates in the north polar region of Mars detected by OMEGA/Mars Express. *Science*, 307(5715):1584–1586, 2005.

[97] D. D. Lee and H. S. Seung. Learning the parts of objects by non-negative matrix factorization. *Nature*, 401:788–791, 1999.

[98] C. C. D. Lelong, P. C. Pinet, and H. Poilvé. Hyperspectral imaging and stress mapping in agriculture: A case study on wheat in Beauce (France). *Remote Sensing of Environment*, 66:179–191, 1998.

[99] J. M. Lerner. Imaging spectrometer fundamentals for researchers in the biosciences - a tutorial. *Cytometry Part A*, 69A(8):712–734, 2006.

[100] J. Li and J. M. Bioucas-Dias. Minimum volume simplex analysis: A fast algorithm to unmix hyperspectral data. In *IEEE International Geoscience And Remote Sensing Symposium*, Boston, Jul. 2008.

[101] J. G. Liu and L. K. Morgan. FFT selective and adaptive filtering for removal of systematic noise in ETM+ imageodesy images. *IEEE Transactions on Geoscience and Remote Sensing*, 44(12):3716–3724, Dec. 2006.

[102] W. Lucht, C. B. Schaaf, and Alan H. Strahler. An algorithm for the retrieval of albedo from space using semiempirical BRDF models. *IEEE Transactions on Geoscience and Remote Sensing*, 38(2):977–998, 2000.

[103] B. Luo, X. Ceamanos, S. Douté, and J. Chanussot. Martian aerosol abundance estimation based on unmixing of hyperspectral imagery. In *IEEE Workshop on Hyperspectral Image and Signal Processing : Evolution in Remote Sensing*, Iceland, 2010.

[104] B. Luo and J. Chanussot. Unsupervised hyperspectral image classification by using linear unmixing. In *16th IEEE International Conference on Image Processing*, Cairo, November 2009.

[105] B. Luo, J. Chanussot, S. Douté, and X. Ceamanos. Unsupervised endmember extraction of Martian hyperspectral images. In *IEEE Workshop on Hyperspectral Image and Signal Processing: Evolution in Remote Sensing*, 2009.

[106] A. Lyapustin, C. K. Gatebe, R. Kahn, R. Brandt, J. Redemann, et al. Analysis of snow bidirectional reflectance from ARCTAS spring-2008 campaign. *Atmospheric Chemistry and Physics*, 10:4359–4375, 2010.

[107] A. Lyapustin and Y. Knyazikhin. Green's function method for the radiative transfer problem. I. Homogeneous non-Lambertian surface. *Applied optics*, 40(21):3495–3501, Jul. 2001.

[108] A. Lyapustin, J. Martonchik, Y. Wang, and I. Laszlo. Multiangle implementation of atmospheric correction (MAIAC): 1. Radiative transfer basis and look-up tables. *Journal of Geophysical Research*, 116(D03210), 2011.

[109] A. Lyapustin and Y. Wang. Parameterized code SHARM-3D for radiative transfer over inhomogeneous surfaces. *Applied optics*, 44(35), 7602-7610 2005.

[110] A. Lyapustin, Y. Wang, I. Laszlo, R. A. Kahn, S. Korkin, et al. Multiangle implementation of atmospheric correction (MAIAC): 2. Aerosol algorithm. *Journal of Geophysical Research*, 116(D03211), 2011.

[111] A. I. Lyapustin. Atmospheric and geometrical effects on land surface albedo. *Journal of Geophysical Research*, 104(D4):4127–4143, Feb. 1999.

[112] D. Manolakis, C. Siracusa, and G. Shaw. Hyperspectral subpixel target detection using the linear mixing model. *IEEE Transactions on Geoscience and Remote Sensing*, 39(7):1392–1409, Jul. 2001.

[113] J. V. Martonchik, D. J. Diner, R. A. Kahn, T. P. Ackerman, M. M. Verstraete, et al. Techniques for the retrieval of aerosol properties over land and ocean using multiangle imaging. *IEEE Transactions on Geoscience and Remote Sensing*, 36(4):1212–1227, Jul. 1998.

[114] M. Massé, O. Bourgeois, S. Le Mouélic, C. Verpoorter, L. Le Deit, and J.-P. Bibring. Martian polar and circum-polar sulfate-bearing deposits: sublimation tills derived from the north polar cap. *Icarus*, 209(2):434–451, Oct. 2010.

[115] A. S. McEwen, E. M. Eliason, J. W. Bergstrom, N. T. Bridges, C. J. Hansen, et al. Mars Reconnaissance Orbiter's High Resolution Imaging Science Experiment (HiRISE). *Journal of Geophysical Research (Planets)*, 112(E05S02), 2007.

[116] A. F. McGuire and B. Hapke. An experimental study of light scattering by large, irregular particles. *Icarus*, 113:134–155, 1995.

[117] P. C. McGuire, J. L. Bishop, A. J. Brown, A. A. Fraeman, G. A. Marzo, et al. An improvement to the volcano-scan algorithm for atmospheric correction of CRISM and OMEGA spectral data. *Planetary and Space Science*, 57:809–815, 2009.

[118] P. C. McGuire, M. J. Wolff, M. D. Smith, R. E. Arvidson, S. L. Murchie, et al. MRO/CRISM retrieval of surface lambert albedos for multispectral mapping of Mars with DISORT-based radiative transfer modeling: Phase 1 - using historical climatology for temperatures, aerosol optical depths, and atmospheric pressures. *IEEE Transactions on Geoscience and Remote Sensing*, 46(12):4020–4040, Dec. 2008.

[119] L. Miao and H. Qi. Endmember extraction from highly mixed data using minimum volume constrained nonnegative matrix factorization. *IEEE Transactions on Geoscience and Remote Sensing*, 45(3):765–777, March 2007.

[120] G. Mie. Beiträge zur optik trüber medien, speziell kolloidaler metallösungen. *Annalen der Physik*, 330:377–445, 1908.

[121] M. Minnaert. The reciprocity principle in lunar photometry. *The Astrophysics Journal*, 93:403–410, 1941.

[122] S. Le Mouélic, J.-Ph. Combe, V. Sarago, N. Mangold, M. Massé, et al. An iterative least squares approach to decorrelate minerals and ices contributions in hyperspectral images: Application to Cuprite (Earth) and Mars. In *IEEE Workshop on Hyperspectral Image and Signal Processing: Evolution in Remote Sensing*, 2009.

[123] P. Mouroulis, R. O. Green, and T. G. Chrien. Design of pushbroom imaging spectrometers for optimum recovery of spectroscopic and spatial information. *Applied optics*, 39(13):2210–2220, May 2000.

[124] S. Moussaoui, D. Brie, A. Mohammad-Djafari, and C. Carteret. Separation of non-negative mixture of non-negative sources using a Bayesian approach and MCMC sampling. *IEEE Transactions on Signal Processing*, 54(11):4133–4145, 2006.

[125] S. Moussaoui, H. Hauksdóttir, F. Schmidt, C. Jutten, J. Chanussot, et al. On the decomposition of Mars hyperspectral data by ICA and Bayesian positive source separation. *Neurocomputing*, 71(10-12):2194–2208, June 2008.

[126] S. Murchie, R. Arvidson, P. Bedini, K. Beisser, J.-P. Bibring, et al. Compact Reconnaissance Imaging Spectrometer for Mars (CRISM) on Mars Reconnaissance Orbiter (MRO). *Journal of Geophysical Research*, 112(E05S03), 2007.

[127] S. Murchie, E. Guinness, and S. Slavney. *Mars Reconnaissance Orbiter. CRISM data product software interface specification. Version 1.3.5*, Aug. 2007.

[128] S. L. Murchie, F. P. Seelos, C. D. Hash, D. C. Humm, E. Malaret, et al. Compact Reconnaissance Imaging Spectrometer for Mars investigation and data set from the Mars Reconnaissance Orbiter's primary science phase. *Journal of Geophysical Research*, 114(E00D07), 2009.

[129] J. F. Mustard, S. L. Murchie, S. M. Pelkey, B. L. Ehlmann, R. E. Milliken, et al. Hydrated silicate minerals on Mars observed by the Mars Reconnaissance Orbiter CRISM instrument. *Nature*, 454(7202):305–309, 2008.

[130] J. M. P. Nascimento. Does independent component analysis play a role in unmixing hyperspectral data? *IEEE Transactions on Geoscience and Remote Sensing*, 43(1):175–187, 2005.

[131] J. M. P. Nascimento and J. M. B. Dias. Vertex component analysis: A fast algorithm to unmix hyperspectral data. *IEEE Transactions on Geoscience and Remote Sensing*, 43(4):898–910, April 2005.

[132] R. A. Neville, L. Sun, and K. Staenz. Spectral calibration of imaging spectrometers by atmospheric absorption feature matching. *Canadian Journal of Remote Sensing*, 34(1):S29–S42, 2008.

[133] F. E. Nicodemus, J. C. Richmond, J. J. Hsia, I. W. Ginsberg, and T. Limperis. Geometrical considerations and nomenclature for reflectance. *National Bureau of Standards*, 160, Oct. 1977.

[134] M. E. Ockert-Bell, J. F. Bell III, J. B. Pollack, C. P. McKay, and F. Forget. Absorption and scattering properties of the Martian dust in the solar wavelengths. *Journal of Geophysical Research*, 102(E4):9039–9050, Apr. 1997.

[135] D. Olsen, C. Dou, X. Zhang, L. Hu, H. Kim, and E. Hildum. Radiometric calibration for AgCam. *Remote Sensing*, 2:464–477, 2010.

[136] M. Parente. A new approach to denoising CRISM images. In *Lunar and Planetary Science Conference*, number 2528, 2008.

[137] M. Parente, J.L. Bishop, and J.F. Bell III. Spectral unmixing for mineral identification in Pancam images of soils in Gusev crater, Mars. *Icarus*, 203(2):421–436, 2009.

[138] M. Parente, J. Mustard, S. Murchie, and F. Seelos. Robust unmixing of hyperspectral images: Application to Mars. In *IEEE International Geoscience And Remote Sensing Symposium*, Vancouver, 2011.

[139] C. M. Pieters, J. Boardman, B. Buratti, A. Chatterjee, and R. Clark. The Moon Mineralogy Mapper (M3) on Chandrayaan-1. *Current Science*, 96(4):500–505, Feb. 2009.

[140] P. C. Pinet, C. Kaufmann, and J. Hill. Imaging spectroscopy of changing Earth's surface: a major step toward the quantitative monitoring of land degradation and desertification. *Comptes Rendus Geoscience*, 338:1042–1048, 2006.

[141] P. C. Pinet, V. V. Schevchenko, S. D. Chevrel, Y. Daydou, et al. Local and regional lunar regolith characteristics at Reiner Gamma Formation: Optical and spectroscopic properties from Clementine and Earth-based data. *Journal of Geophysical Research*, 105(E4):9457–9475, Apr. 2000.

[142] B. Pinty, F. Roveda, M. Verstraete, N. Gobron, Y. Govaerts, et al. Surface albedo retrieval from meteosat: 1. theory. *Journal of Geophysical Research*, 105(D14):18099–18112, 2000.

[143] A. Plaza, P. Martinez, R. Perez, and J. Plaza. A quantitative and comparative analysis of endmember extraction algorithms from hyperspectral data. *IEEE Transactions on Geoscience and Remote Sensing*, pages 650–663, 2004.

[144] F. Poulet, J-P. Bibring, Y. Langevin, B. Gondet, C. Gomez, et al. Phyllosilicate on Mars and implications for early Martian climate. *Nature*, 438:623–627, Nov. 2005.

[145] Y. Qin and M. A. Box. Vector green's function algorithm for radiative transfer in plane-parallel atmosphere. *Journal of Quantitative Spectroscopy and Radiative Transfer*, 97:228–251, 2006.

[146] H. Rahman, B. Pinty, and M. M. Verstraete. Coupled surface-atmosphere reflectance (CSAR) model. 2. Semiempirical surface model usable with NOAA advanced very high resolution radiometer data. *Journal of Geophysical Research*, 98(D11):20791–20801, 1993.

[147] J. W. Rayleigh. On the scattering of light by small particles. *Philosophical Magazine*, 41:274–279, 1871.

[148] W. G. Rees. *Physical Principles of Remote Sensing (Topics in Remote Sensing)*. Cambridge University Press, 2001.

[149] J.A. Richards and X. Jia. *Remote Sensing Digital Image Analysis*. Springer-Verlag, Berlin, 1999.

[150] D. A. Roberts, G. T. Batista, et al. *Remote Sensing Change Detection: Environmental Monitoring Applications and Methods*, chapter Change identification using multitemporal spectral mixture analysis: Applications in eastern Amazonia, pages 137–161. Ann Arbor Press, 1998.

[151] J.-L. Roujean, M. Leroy, and P.-Y. Deschamps. A bidirectional reflectance model of the Earth's surface for the correction of remote sensing data. *Journal of Geophysical Research*, 97(D18):20455–20468, Dec. 1992.

[152] G. Sansone. *Orthogonal Functions*, chapter Expansions in Fourier Series, pages 39–168. New York: Dover, 1991.

[153] C. B. Schaaf, F. Gao, A. H. Strahler, W. Lucht, X. Li, et al. First operational BRDF, albedo nadir reflectance products from MODIS. *Remote Sensing of Environment*, 83:135–148, 2002.

[154] G. Schaepman-Strub, M.E. Schaepman, T.H. Painter, S. Dangel, and J.V. Martonchik. Reflectance quantities in optical remote sensing definitions and case studies. *Remote Sensing of Environment*, 103:27–42, 2006.

[155] J. Schewe and B. Fraser. *Image Sharpening*. Peachpit Press, 2nd edition edition, 2009.

[156] D. Schläpfer, J. Nieke, and K. I. Itten. Spatial PSF nonuniformity effects in airborne pushbroom imaging spectrometry data. *IEEE Transactions on Geoscience and Remote Sensing*, 45(2):458–468, Feb. 2007.

[157] F. Schmidt. *Classification de la surface de Mars par imagerie hyperspectrale OMEGA. Suivi spatio-temporel et étude des dépôts saisonniers de CO2 et H2O*. PhD thesis, Université Joseph Fourier, Oct. 2007.

[158] B. Schmitt, E. Quirico, F. Trotta, and W. M. Grundy. *Solar System Ices*, chapter Optical properties of ices from UV to infrared. Kluwer, 1998.

[159] F. P. Seelos, S. L. Murchie, D. C. Humm, O. S. Barnouin, F. Morgan, et al. CRISM data processing and analysis products update – calibration, correction, and visualization. In *Lunar and Planetary Science Conference*, 2011.

[160] F. P. Seelos, M. Parente, T. Clark, F. Morgan, O. S. Barnouin, et al. CRISM hyperspectral data filtering with application to MSL landing site selection. In *American Geophysical Union (AGU) Fall meeting*, 2009.

[161] K. Segl, L. Guanter, H. Kaufmann, J. Schubert, S. Kaiser, et al. Simulation of spatial sensor characteristics in the context of the Enmap hyperspectral mission. *IEEE Transactions on Geoscience and Remote Sensing*, 48(7):3046–3054, July 2010.

[162] T. Shibata, W. Frei, and M. Sutton. Digital correction of solar illumination and viewing angle artifacts in remotely sensed image. In *Seventh International Symposium Machine Processing of Remotely Sensed Data*, 1981.

[163] Y. G. Shkuratov, D. G. Stankevich, D. V. Petrov, P. C. Pinet, A. M. Cord, et al. Interpreting photometry of regolith-like surfaces with different topographies: shadowing and multiple scattering. *Icarus*, 173:3–15, 2005.

[164] D. E. Smith, M. T. Zuber, H. V. Frey, J. B. Garvin, J. W. Head, et al. Mars Orbiter Laser Altimeter: Experiment summary after the first year of global mapping of Mars. *Journal of Geophysical Research*, 106:23689–23722, 2001.

[165] M. D. Smith, M. J. Wolff, R. T. Clancy, and S. L. Murchie. Compact Reconnaissance Imaging Spectrometer observations of water vapor and carbon monoxide. *Journal of Geophysical Research*, 114(E00D03), 2009.

[166] A. L. Souchon, P. C. Pinet, S. D. Chevrel, Y. H. Daydou, D. Baratoux, et al. An experimental study of Hapke's modeling of natural granular surface samples. *Icarus*, 215:313–331, 2011.

[167] A. Spiga, F. Forget, B. Dolla, S. Vinatier, R. Melchiorri, et al. Remote sensing of surface pressure on Mars with the Mars Express/OMEGA spectrometer: 2. Meteorological maps. *Journal of Geophysical Research*, 112(E08S16), 2007.

[168] K. Stamnes, S-C. Tsay, W. Wiscombe, and K. Jayaweera. Numerically stable algorithm for discrete-ordinate-method radiative transfer in multiple scattering and emitting layered media. *Applied optics*, 27(12), Jun. 1988.

[169] J. Stoer and R. Bulirsch. *Introduction to Numerical Analysis*. Springer, 3rd edition, 2002.

[170] G. E. Thomas and K. Stamnes. *Radiative Transfer in the Atmosphere and Ocean*. Cambridge University Press, 1999.

[171] D. R. Thompson, L. Mandrake, M. S. Gilmore, and R. Castano. Superpixel endmember detection. *IEEE Transactions on Geoscience and Remote Sensing*, 48(11):4023–4032, November 2010.

[172] M. G. Tomasko. *Titan from Cassini-Huygens*, chapter Aerosols in Titan's Atmosphere. Springer, 2009.

[173] M. G. Tomasko, L. R. Doose, M. Lemmon, P. H. Smith, and E. Wegryn. Properties of dust in the Martian atmosphere from the Imager on Mars Pathfinder. *Journal of Geophysical Research*, 104:8987–9008, 1999.

[174] J. Tovar-Pescador, D. Pozo-Vazquez, J. A. Ruiz-Arias, J. Batlles, G. López, and J. L. Bosch. On the use of the digital elevation model to estimate the solar radiation in area of complex topography. *Meteorological Applications*, 13:279–287, 2006.

[175] F. Tsai and W. W. Chen. Striping noise detection and correction of remote sensing images. *IEEE Transactions on Geoscience and Remote Sensing*, 46(12):4122–4131, Dec. 2008.

[176] S. Valero, P. Salembier, and J. Chanussot. Hyperspectral image segmentation using binary partition trees. In *IEEE International Conference on Image Processing*, Brussels, Sep. 2011.

[177] E. F. Vermote and S. Kotchenova. Atmospheric correction for the monitoring of land surfaces. *Journal of Geophysical Research*, 113(D23S90), 2008.

[178] E. F. Vermote, N. El Saleous, C. O. Justice, Y. J. Kaufman, J. L. Privette, et al. Atmospheric correction of visible to middle-infrared EOS-MODIS data over land surfaces: Background, operational algorithm and validation. *Journal of Geophysical Research*, 102(D14):17131–17141, July 1997.

[179] A. Villa. *Advanced Spectral Unmixing and Classication methods for Hyperspectral Remote Sensing Data*. PhD thesis, Grenoble INP and University of Iceland, June 2011.

[180] M. Vincendon, Y. Langevin, F. Poulet, J-P. Bibring, and B. Gondet. Recovery of surface reflectance spectra and evaluation of the optical depth of aerosols in the near-IR using a Monte Carlo approach: Application to the OMEGA observations of high-latitude regions of Mars. *Journal of Geophysical Research*, 112(E08S13), 2007.

[181] M. Vincendon, Y. Langevin, F. Poulet, J-P. Bibring, B. Gondet, and D. Jouglet. Dust aerosols above the south polar cap of Mars as seen by OMEGA. *Icarus*, 196:488–505, 2008.

[182] S. Walter, R. Kirk, P. C. McGuire, and G. Neukum. HRSC topographic correction by Minnaert photometric modeling. In *European Planetary Science Congres - Division for Planetary Sciences - Joint Meeting*, volume 6, 2011.

[183] Y. Wang, A. I. Lyapustin, J. L. Privette, T. Morisette, and B. Holben. Atmospheric correction at AERONET locations: A new science and validation data set. *IEEE Transactions on Geoscience and Remote Sensing*, 47(8):2450–2466, Aug. 2009.

[184] W. Wanner, X. Li, and A. H. Strahler. On the derivation of kernels for kernel-driven models of bidirectional reflectance. *Journal of Geophysical Research*, 100:21077–21090, 1995.

[185] E. W. Weisstein. Convolution Theorem. From MathWorld–A Wolfram Web Resource. http://mathworld.wolfram.com/ConvolutionTheorem.html.

[186] M. E. Winter. Fast autonomous spectral end-member determination in hyperspectral data. In *Proceedings of the Thirteenth International Conference on Applied Geologic Remote Sensing*, volume II, pages 337–344, Vancouver, 1999.

[187] M. J. Wolff, M. D. Smith, R. T. Clancy, R. Arvidson, M. Kahre, et al. Wavelength dependence of dust aerosol single scattering albedo as observed by the Compact Reconnaissance Imaging Spectrometer. *Journal of Geophysical Research*, 114(E00D04), 2009.

[188] Y. Wu, P. Gong, Q. Liu, and A. Chappell. Retrieving photometric properties of desert surfaces in China using the Hapke model and MISR data. *Remote Sensing of Environment*, 113:213–223, 2009.

[189] A. Zare and P. Gader. PCE: Piecewise Convex Endmember Detection. *IEEE Transactions on Geoscience and Remote Sensing*, 48(6):2620–2632, June 2010.

[190] B. Zitová and Jan Flusser. Image registration methods: a survey. *Image and Vision Computing*, 21:977–1000, 2003.

[191] M. Zortea and A. Plaza. Spatial preprocessing for endmember extraction. *IEEE Transactions on Geoscience and Remote Sensing*, 47(8):2679–2693, August 2009.

[192] R. W. Zurek and S. E. Smrekar. An overview of the Mars Reconnaissance Orbiter (MRO) science mission. *Journal of Geophysical Research*, 112(E05S01), 2007.